ICMP&C 2020

INTERNATIONAL E-CONFERENCE ON MATERIALS PROCESSING & CHARACTERIZATION

18th & 19th September 2020

Chief Editor

Prof. B. Linga Reddy

DEPARTMENT OF PHYSICS
CHAITANYA BHARATHI INSTITUTE OF TECHNOLOGY
(AUTONOMOUS)
GANDIPET, HYDERABAD 500 075 INDIA

INTERNATIONAL E-CONFERENCE ON MATERIALS PROCESSING & CHARACTERIZATION

CHIEF EDITOR

Prof. B. Linga Reddy

Head, Department of Physics

EDITORS

Dr. Y.S. Reddy

Assistant Professor, Department of Physics

Dr. K. Rajagopal

Assistant Professor, Department of Biotechnology

Dr. A. Santhosh Kumar

Assistant Professor, Department of Physics

Dr. K. Ramesh

Assistant Professor, Department of Chemistry

VANDANA PUBLICATIONS

UG-4, Avadh Tower, Naval Kishor Road,

Hazratganj, Lucknow – 226001, INDIA

Published by
Vandana Publications
UG-4, Avadh Tower, Naval Kishor Road,
Hazratganj, Lucknow – 226001, INDIA
On behalf of
Department of Physics
Chaitanya Bharathi Institute of Techonology
(Autonomous)
Gandipet, Hyderabad- 500 075, India

ISBN: 978-81-946476-9-0

Published : October, 2020

Printed At:
Vandana Publication Press
UG-17, Avadh Tower, Naval Kishor Road, Hazratganj,
Lucknow – 226001, INDIA.
Ph: +91-9005805403

Price : 600/- (Six hundred rupees only)

President's Message

I am delighted to know that the Department of Physics, Chaitanya Bharathi Institute of Technology is organizing a Two Day "**International e-Conference on Materials Processing & Characterization (ICMP&C-2020)**" during 18th& 19th September, 2020.

I am sure that the conference would focus on all facets of current research and advancements of the study of materials, which is essential for various applications. It is an opportunity for the faculty members, research scholars and scientists working in several organizations/Institutions to share the on-going research in various fields and also a platform to focus on the suitable methods which serves the society the best.

I congratulate the faculty for organizing this conference and wish the conference a great success

Dr. V. Malakonda Reddy
President - CBIT

Principal's Message

The Department of Physics, Chaitanya Bharathi Institute of Technology is hosting a Two Day "**International e-Conference on Materials Processing & Characterization (ICMP&C-2020)**" during 18th& 19th September, 2020. The major focus is on functional materials, smart materials and intelligent materials of 21st century technology needs. The modern structural materials have a tremendous advancement in science and technology of materials. In recent years, nanostructure materials and nano composites have become increasingly important because of their remarkable properties and permanently growing areas for practical applications. Various aspects of mechanical and physical properties of nano materials including analytical and computational modelling in combination with comprehensive experimental analysis of mechanical behaviour is yet to be investigated. In spite of the rapid progress in this field, mechanical properties of nano materials and composites are still need to focus on the developments. In the field of massive and complex manufacturing we are now in need of materials, with properties, that can be manipulated according to our needs.

Nature is full of magic materials, which are to be discovered in forms suitable to the needs. Such magical materials, also known as intelligent or smart materials, can sense, process, stimulate and actuate a response. There is an increasing awareness of the benefits to be derived from the development and exploitation of advanced materials and structures in applications ranging from hydrospace to aerospace. This conference will create a cross disciplinary summit that transcends departmental, institutional, industrial, public and private research organizations and global barriers and lends itself to the integration of research and education in the vital field of advanced materials. This conference definitely gives the chance to the researchers to deliberate on major sectors of advanced processing, material characterization, modelling and simulation, evolving properties, performance and more so device fabrication.

I congratulate the Department of Physics and the faculty for organizing this conference and wish the conference a great success.

Prof. P. Ravinder Reddy
Principal

HoD's Message

It is my pleasure to invite all of the great scientists, academicians, young researchers from all over the world to attend the International Conference on Materials Processing & Characterization-2020 (ICMP&C-2020) during 18th and 19th September 2020. The ICMP&C-2020, organized by Department of Physics Department, shares an insight into the recent research and cutting edge technologies, which gains immense interest with the colossal and exuberant presence of adept, young and brilliant researchers. This conference covers global aspects on Materials Processing and Characterization from fundamental issues to practical applications of the principles of Physics. We are looking forward to an excellent meeting with great scientists, academicians and research scholars from different parts of the country and also from other countries and sharing new and exciting results in the field of materials science.

Prof. B. Linga Reddy
Head, Department of Physics
Organizing Secretary, ICMP&C-2020

Convener's Message

It is a great pleasure and an honor to extend to you a warm invitation to attend International e-Conference on Materials Processing & Characterization – 2020 on 18th and 19th September 2020 being organized by Department of Physics, CBIT (A). The basic objective of the Conference is to bring together experts and young research scholars from different parts of the country and as well as the world to exchange knowledge and share ideas to provide deep understanding of the subject. The Conference will provide a wonderful forum for you to explore innovations in the field of materials science. The Conference will offer plenty of collaborative opportunities as you listen and interact with the leading academicians and scientists from all over the world.

All the staff members of the department have been working tirelessly for over two months to make this event a reality. From the bottom of my heart, I wish to thank you for all your support, dedication and hard work.

The Organizing Committee has put in all the efforts to ensure that all of you carry back long lasting memories of academic and research excellence from this Conference.

Dr. Y.S. Reddy
Assistant Professor, Department of Physics
Convener, ICMP&C-2020

ORGANIZING COMMITTEE

CHIEF PATRON
Hon'ble Kavi Kereeti Dr. V. Malakonda Reddy
President, CBIT

CONFERENCE CHAIRPERSON
Prof. P. Ravinder Reddy
Principal, CBIT

CONFERENCE ORGANIZING SECRETARY
Prof. B. Linga Reddy
Head, Department of Physics

CONFERENCE JOINT ORGANIZING SECRETARY
Prof. B. Sreenivasa Reddy

CONVENER
Dr. Y.S. Reddy

CO-CONVENERS
Dr. K. Vinay Kumar Reddy
Mr. G. Nataraju

COORDINATORS
Dr. K. Rajagopal
Dr. M. Subhadra

CO-COORDINATORS
Dr. Neelima Agarwal
Dr. S. Shravan Kumar Reddy
Dr. A. Santhosh Kumar

KEYNOTE SPEAKER

Prof. S. SRINATH
Department of Physics
University of Hyderabad

INVITED SPEAKERS

Dr. VENKATA SRINIVAS PULI
Scientist
Smart Nanomaterials Solutions (LLC) Florida, USA

Dr. SUBHASH THOTA
Associate Professor
Department of Physics
IIT - Guwahati

CHIEF EDITOR

Prof. B. Linga Reddy

Dr. B. Linga Reddy is a Professor of Physics in Chaitanya Bharathi Institute of Technology (A), Hyderabad, India. He published 15 research papers in international and national journals of repute. He presented 6 research papers at various national and international conferences. He is a life member of Indian Society for Radiation Physics and Alumni Association of Osmania University. He carried out one research project sanctioned by Telangana State Council of Science & Technology. He has been serving the Institution at various capacities for over a decade. Currently, he is HoD and Chairman, Board of Studies of Department of Physics.

He obtained his Ph.D. degree in Physics from Osmania University, Hyderabad. He has a total of 26 years of teaching and research experience. His areas of research interest include Solid State Physics and Environmental Radiation.

EDITORS

Dr. Y.S. Reddy

Dr. Y.S. Reddy is an Assistant Professor of Physics in Chaitanya Bharathi Institute of Technology (A), Hyderabad, India. He authored 3 text books and edited one. He published 40 research papers in international and national journals of repute. He presented 50 research papers at various national and international conferences. He is a life member of Materials Research Society of India, Ultrasonic Society of India and Indian Association of Physics Teachers. He is a member of editorial board for two scientific journals.

He obtained his Ph.D. degree in Physics from Osmania University, Hyderabad. He has a total of 16 years of teaching and research experience. His areas of research interest include Magnetic Materials, Magnetotransport Properties and Ultrasonic Studies.

EDITORS

Dr. K. Rajagopal

Dr. K. Rajagopal is an Assistant Professor of Biotechnology in Chaitanya Bharathi Institute of Technology (A), Hyderabad, India. He published 14 research papers in international and national journals of repute. He presented 20 research papers at various national and international conferences.

He obtained his Ph.D. degree in Physics from Osmania University, Hyderabad. He has a total of 24 years of teaching and research experience. His research specialization is Biophysics.

EDITORS

Dr. A. Santhosh Kumar

Dr. A. Santhosh Kumar is an Assistant Professor of Physics in Chaitanya Bharathi Institute of Technology (A), Hyderabad, India. He published 20 research papers in international and national journals of repute. He presented 18 research papers at various national and international conferences. He is a recipient of SERB-NPDF fellowship, DRDO-DIAT fellowship and MHRD-NITK fellowship.

He obtained his Ph.D. degree in Physics from National Institute of Technology Karnataka, Surathkal, Mangalore. He completed Post-Doctoral Fellowship from Department of Metallurgical and Materials Engineering, DRDO-DIAT, Pune. He has a total of 06 years of teaching and 11 years of research experience. His areas of research interest include Materials Science and Opto-electronic Nanostructures.

EDITORS

Dr. K. Ramesh

Dr. K. Ramesh is an Assistant Professor of Chemistry in Chaitanya Bharathi Institute of Technology (A), Hyderabad, India. He published 22 research papers in international and national journals of repute. He presented 10 research papers at various national and international conferences. He is a life member of Indian Society for Technical Education, Indian Association of Chemistry Teachers and Indian Science Congress Association. He is a member of editorial board of IASIR.

He obtained his Ph.D. degree in Chemistry from Osmania University, Hyderabad. He has a total of 16 years of teaching and research experience. His areas of research interest include Physical Organic Chemistry, Catalysis and Green Chemistry.

Contents

Characterization of Titanium Doped Nanocrystalline Tungsten Oxide Thin Films for Smart Windows

K.Pandurangarao[a,b*], V.Ravi Kumar[a*]
[a]*Department of Physics, AcharyaNagarjuna University, Guntur-522510, Andhrapradesh.*
[b]*Andhraloyola Institute of Engineering and Technology, Vijayawada-520008, Andhrapradesh*
Corresponding author's email: pandurangaraokankanala@gmail.com

Abstract
The electrochromic properties of titanium doped tungsten oxide thin films prepared at different sputtering pressures and substrate temperatures at constant dc power by DC reactive magnetron sputtering technique for the fabrication of smart windowhave been reported in this paper**.** The roughness and thickness of the films were measured by using Stylus profilometry. The opticalproperties, transmittanceand optical band gap of the films were recorded with UV-Vis spectrometer. The films were exhibited high transmittance in the visible region. The optical absorption edge of the films was observed in the range of 347-381 nm (blueshift). The refractive index of the films was measured with spectroscopic ellipsometry. The molecular arrangement and bonding in the films was recorded from micro Raman spectra. The films were exhibited two prominent reflections of the planes (0 2 1), and (4 2 1) is confirmed by X-Ray diffraction studies. The morphology and composition of the films were analyzed using filed emission scanning electron microscopy and energy dispersive spectroscopy. The diffusion coefficient of ions, switching speed and, coloration efficiency of the films were evaluated from electrochemical studies.
Keywords: Tungsten oxide films, XRD, FE-SEM and Cyclic voltammetry

1. Introduction
Transition metal oxides are very important class of compounds and they are used in many opto-electronic applications such as smart windows, information displays, optic memories and rear view mirrors and antiglare mirrors. Over few decades, electrochromic windows emerged as trend of materials which controls the intensity of visible light and sunlight while passing through them and make the indoor environment comfort. Tungsten oxide is one of the transition metal oxide emerged as good cathodic electrochromic material in both crystalline and amorphous states. Tungsten oxide is extensively studied electro chromic material in its amorphous form due to absorption mechanism whereas in crystalline form there is a limited study on electrochromism. But, of late by doping with suitable metal to a host material, the electro chromic properties have been improved considerably, which is investigated by many researches [1-2]. In this study, we have reported on the effect of deposition parameters along with titanium doping on different characterizations and electrochromic properties of tungsten oxide thin films. From the past studies, the coloration efficiency of pure tungsten oxide thin films has been less than or greater than that of titanium doped films, and depends upon the amount of titanium incorporated into the films [3]. Because, by doping there will be changes in structure and morphology of the films, which open channels for easy intercalation and deintercalation of the alkali metal ions into host material. For the fabrication of any electrochromic device (smart window), coloration efficiency is considered as key performance indicator. As per as possible, the coloration efficiency should be high for electrochromic device because, it provides high optical modulation even for small amount of charge intercalated into the films. By doping of titanium, molybdenum, nitrogen, niobium, vanadium and nickel to the WO_3 will change the coloration efficiency of the films [4]. Subramanyam andMuthuKaruppasamy [5] were reported on the coloration efficiency of the films decreased from 121 to 13 cm^2/C with

addition of vanadium of 9 at.% into the tungsten oxide thin films deposited by DC magnetron sputtering. Patil et al [6] also reported on the decrease in coloration efficiency of the films with the increase of niobium doping. Sun et al [7] investigated on the nitrogen doped tungsten oxide thin films by DC reactive pulsed sputtering having coloration efficiency of 45 cm^2/C at 5 at. %. Karuppasamy and Subramanyam [3] reported on the titanium doped tungsten oxide thin films and the coloration efficiency of the tungsten oxide. Gesheva et al [8] investigated on MoO_3-WO_3 thin films deposited by chemical vapour deposition and the films have coloration efficiency of 141 cm^2/Cwhich has higher than pure WO_3 films (84 cm^2/C) and MoO_3 films (39 cm^2/C).

Tungsten oxide thin films have been prepared by physical methods like Thermal evaporation [9], Electron beam evaporation [10], Pulsed Laser deposition [11], RF Magnetron sputtering [12], DC Magnetron sputtering [13] and chemical methods like Chemical Vapor Deposition [14] and Sol-gel [15].

In the present case, dc magnetron sputtering technique was used for the deposition of tungsten trioxide thin films. Since, it is industrially viable for coating the films in a large scale, high vacuum and low deposition temperature, good bonding of the film to the substrate and easy control of the thickness of the films over the other physical methods

2. Experimental Methods

The Si (100) Wafer, Quartz glass and ITO Coated glass substrates were used for the deposition of thin films. The samples are ultrasonically agitated for 10 minutes to remove surface dust particles and then cleaned using isopropyl alcohol and ethanol to remove any contamination on the surface of the substrates and finally dried under UV lamp for five minutes. The cleaned substrates were mounted on the substrate holder before going to deposition. Initially the sputtering chamber is evacuated to a base pressure of 4×10^{-6} mbar. Fix the target (2 inch in Diameter&5mm thickness with titanium strip) in the sputtering gun and target and substrate are separated by distance of 60 mm.The substrate temperature was fixed at 400 K and 600 K for all the depositions. Release the argon gas into the chamber for 10 minutes to remove any oxide layers on the target prior to deposition at that time the shutter is closed between target and substrate. Now release the reacting gas oxygen into the chamber to form tungsten oxide thin films [5, 16]. The flow rates of argon and oxygen was controlled by using mass flow controllers. A DC power of 100W is applied for the target. The ratio of argon to oxygen was 2 and 3 and the corresponding sputtering pressure is 17.6mTorr and 16.3mTorr. The substrate holder is rotated 360^0 to attain uniform thickness during the deposition and the deposition time was 20 minutes. All the parameters are listed in Table 1

Table1 Deposition Parameters

Target	Tungsten metal 2” Diameter and 5mm thickness and Titanium strip (length-2.0143 cm and width- 0.17 mm)
Substrates	Si(100), Quartz glass and ITO coated glass
Base pressure	4×10^{-6} mbar
Target substrate distance	60 mm
Sputtering pressure	16.3 mTorr and 17.6 mTorr
Substrate temperature	400 K and 600 K
Argon: Oxygen Flow rate	20:10 and 20:7.5 sccm
Sputtering power	100 W
Deposition time	20 min

The roughness and thickness of the deposited films were measured using a Bruker DXT-15-1022 stylus profilometry. For structural characterization of the films, a Rigaku X-ray

diffractometer was used. The optical studies of the films were recorded using SHIMAZDU UV-1800 UV-vis spectrometer in the spectral range of 300-1100 nm. Refractive index profiles of the films were recorded using spectroscopic ellipsometry with J.A.woollam model: M2000X in the wavelength range of 500-1100 nm. The Raman studies of the films were performed on Micro-Raman spectrometer (Model: STR-300) in the wave number range of 200-1200 cm^{-1}. The surface morphology and composition of the films was investigated with FE-Scanning Electron Microscope (Carl Ziess Model: Neon-40). The surface topography of the films was studied with the help of Atomic Force microscope (Veeco Model: Dimension V SPM). The electrochemical properties of the films were performed with a standard three electrode electrochemical work station (CHI Instruments- Auto 50436) where in Ag/AgCl is used as reference electrode, the film coated on ITO glass is used as working electrode and the platinum wire is used as counter electrode. The current across the working electrode (WO_3 film) was measured at three different scan rates (viz., 100, 200 and 300 mV/s) in the applied potential range of -2.0 to +2.0 V. Diffusion coefficients of the films were evaluated using these cyclic voltammograms obtained during the analysis. The time for coloration and bleaching of the films were measured using chronoamperometric studies and the amount of charge intercalated into the films was evaluated using chronocoulometric studies.

3. Results and Discussion

3.1 Thickness and Roughness measurement

The thickness and roughness of the deposited films were analyzed using stylus profilometry. The thin films which are deposited on quartz substrate are used for measuring the thickness. The thickness and roughness were increased with sputtering pressure and decrease with substrate temperature. This is attributed to changes in the mean free path of atoms during the deposition. The thickness and roughness of the samples are listed in the Table 2.

Table 2 Thickness and Roughness of the films.

Sputtering pressure (mTorr)	Substrate Temp. (K)	Thickness (nm)	Roughness (nm)
	400	832	15
17.6	600	811	4
	400	820	9
16.3	600	760	2

3.2 Optical spectral studies by UV-VIS Spectrophotometer

The optical properties of titanium doped tungsten oxide thin films were recorded using UV-VIS Spectrophotometer in the wavelength range of 300-1100 nm as shown in Fig. 1. The films were exhibited an optical transmittance of 87% in the visible region. The optical transmittance of the films was increased with the increase of sputtering pressure and decrease with the increase of substrate temperature. This fact is owing to improvement in stoichiometry of the films [3, 4, 5,17]. The oscillations in the transmittance spectrum are due to difference of refractive index between substrate and the film. The optical band gap of the films was measured from tauc's plots as shown in Fig .2. The optical band gaps of the films were found to be varied between 2.80 to 2.49 eV. It was confirmed that the substrate temperature significantly affect the optical band gap of the films [18]. The refractive index of the films was altered between 2.38 to 2.29 at 550 nm. This refractive index of the films was

increased with the increase of sputtering pressure as shown in Fig. 3. The thickness of the films also affects the refractive index of the films and as the thickness increases, the refractive index also increases in the present investigation and which has been reported earlier [19-20]. The optical transmittance, Optical band gap and refractive index of the films are listed in the below Table 3.

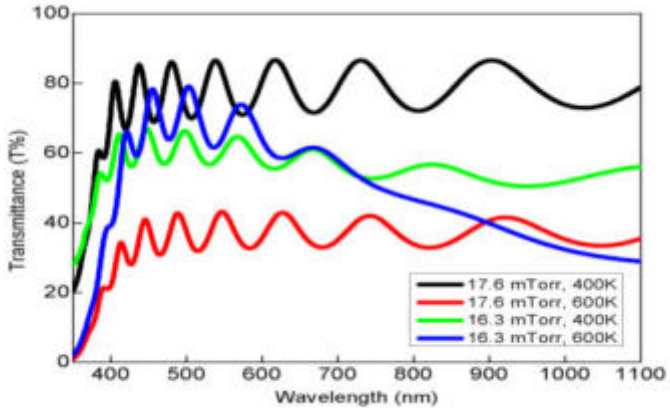

Fig. 1 Optical transmittance spectra of titanium doped tungsten trioxide thin films.

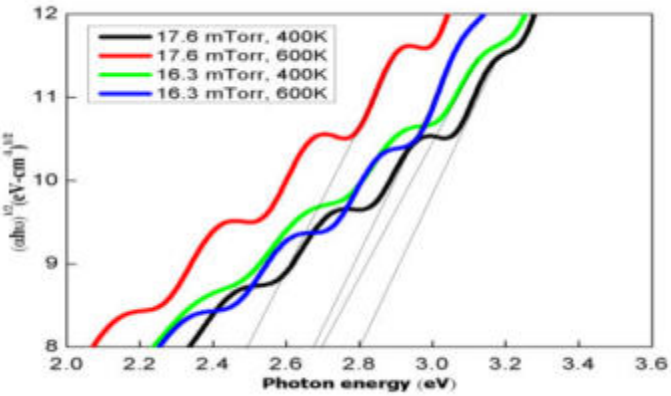

Fig. 2.Tauc's plot for Optical band gap of titanium doped WO_3 thin films

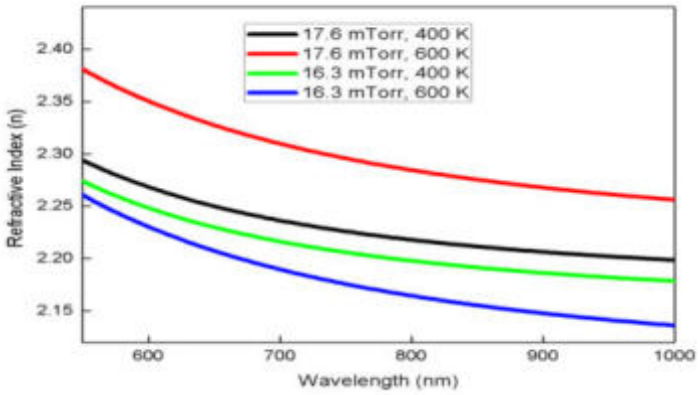

Fig. 3.The spectral dependence of Refractive index of titanium doped WO_3 thin films.

Table 3 Optical parameters of the films.

Sputtering pressure (mTorr)	Substrate temp. (K)	Transmittance (%)	Optical band gap (eV)	Refractive Index at λ=550 nm
17.6	400	87	2.80	2.38
	600	49	2.49	2.29
16.3	400	65	2.69	2.34
	600	39	2.67	2.28

3.3 Structural studies by X-Ray Diffraction

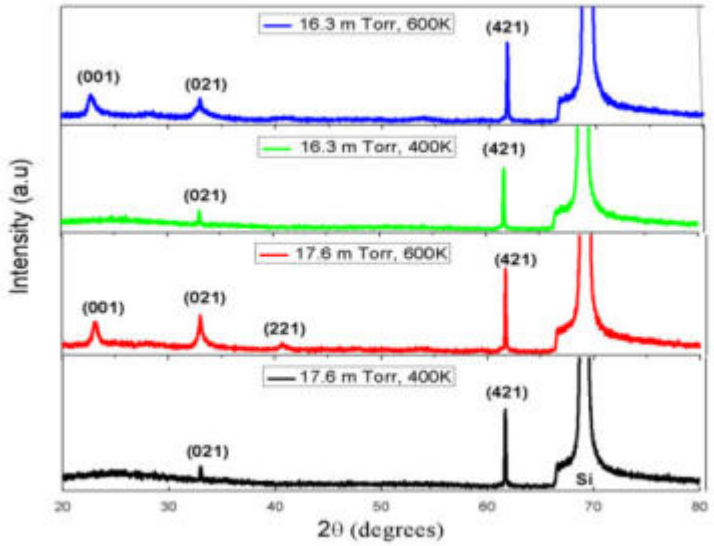

Fig. 4. XRD patterns of titanium doped WO_3 thin films.

The diffractograms of the films were shown in Fig.4. The [21-22]. The films exhibited reflections of the planes (0 2 1) and (4 2 1) at substrate temperature 400 K and as the substrate is increased to 600 K, the intensity of the peaks were increased and further we also observed two more additional peaks (0 0 1) and (2 2 1), and this fact suggest that the films are poly crystalline and all these peaks are corresponding to monoclinic phase of WO_3 (JCPDS card No-24-0747) [21, 22]. To be more particular, this polycrystallinity of the films was mainly attributed to titanium oxide present in the films and was presented in further studies of manuscript. But no significant peak of titanium oxide was observed in the diffractogram of the films. These observations suggest that titanium oxide doping leads to enhance the crystallinity of the films. The average crystallite size is calculated using Debye-Scherer relation and is altered between 62-83 nm.

To identify the phase composition and bonding in the films was analyzed through a non-destructive technique is called micro-Raman spectrometer at room temperature as shown in Fig. 5. The films exhibited two prominent peaks at 807 and 950 cm^{-1} and one weak knot at 327 cm^{-1}. The peaks are broad at low substrate temperature 400 K (at both the sputtering pressures) and become sharp at the substrate temperature 600 K [23, 24, 25]. The band

observed at 324 cm^{-1} is corresponding to O-W-O bending modes of the bridging oxygen of monoclinic phase of the films. Similarly the peak at 807 cm^{-1} corresponding to W^{6+}-O (O-W-O stretching modes of the films) and the peak at 950 cm^{-1} corresponds to stretching mode of W^{6+}=O. We have also observed another fact that, the films did not contain any significant peak related to titanium oxide. Hence the titanium oxide in the films helps to improve the crystallinity in the films.

3.4Micro-Raman Studies

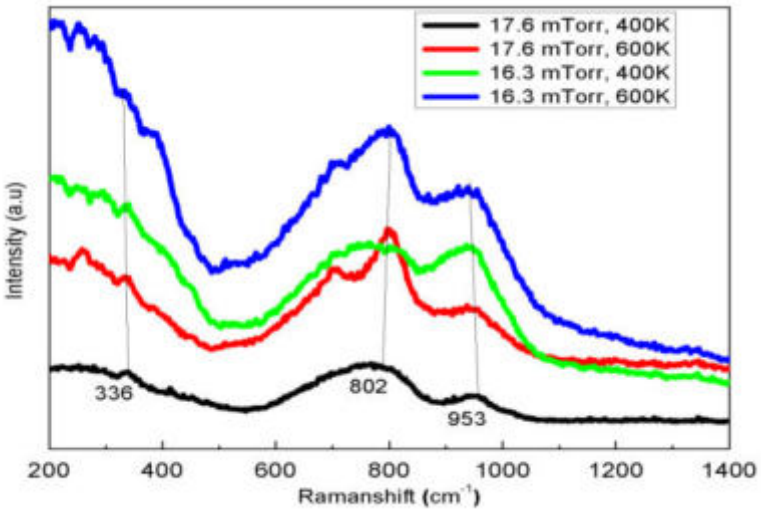

Fig. 5. Micro-Raman spectra of titanium doped WO_3 thin films.

4. Conclusions

The titanium doped nanocrystalline tungsten oxide thin films have deposited for electro chromic device by DC Magnetron sputtering. The effect of titanium on the host material and its characterizations were discussed in detail. The thickness and roughness of the films changes with deposition parameters. The films show good optical transmittance in the visible region up to 87% which is higher than that of the pure films. This is attributed to changes in the structure of the films. The optical band gap of the films decreases with substrate temperature and is owing to improvement in crystallinity of the films. The films shows good optical index of refraction and it was changedwith the deposition parameters. The films exhibited a prominent peaks from the reflections (021) and (421) and which are corresponding to monoclinic structure. The films were composed of sharp bands at the wave numbers 336,802 and 956 cm^{-1} corresponding to both bending and stretching vibrations of the molecule. The sputtering pressure, substrate temperature and titanium significantly affect the coloration efficiency of the films when compared to pure films in this route.

5. Acknowledgement

I take this opportunity to express my sincere thanks to Gobi Saravanan, Karthick , Suresh and DuraiNayak of Sathyabama university (Deemed) for their support in operating the Sputtering Unit instrument and other characterization techniques and Dr.Pradeeap Kumar Brahman of KL University (Deemed) for allowing me to utilize the facilities at the centre.

References

1. C.G. Granquist; Handbook of inorganic electrochromic materials; 1995, Amsterdam, ELSEVIER.
2. P.M.S. Monk et al., Electrochromism: Fundamentals and Applications, VCH, Weinheim, 1995.
3. Michal Mazur., Opt. Mater., 2017, **69**, 96-104.
4. V. Madhavi et al., 2014, **20**, 1737-1745.
5. K. MuthuKaruppasamyand et al., J. Phys.D., 2008, **41**(3).
6. S. R. Bathe., J. Phys. D., 2007, **40, 7423**–7427.
7. X. Sun et al., Thin Solid Films., 2011, **519**, 3032–3036.
8. K. A. Gesheva et al., J. Cryst Grow., 2010,**312**, 1188–1192.
9. A. Antonaia et al., Thin Solid Films., 1999, **354**, 73-81.
10. A.A. Joraid et al., Physica B., Phys. Cond Mat., 2007, **391**,199-205.
11. O.M. Hussain et al., Appl. Phys. A., 2005, **81**, 1291-1297.
12. S.M. Felicia et al., Mater.Sci. 2012,**47**,6593-6600.
13. B. Baloukas et al., Sola.Ener.Mat. Sola Cel., 2011, **95,** 2107-2112.
14. P. Tagtstrom et al., Thin Solid Films., 1999, **352**, 107-113.
15. C.S. Hsu et al., Thin Solid Films., 2008, **516**, 4839.
16. K. Salamon et al., J. Phys. D: Appl. Phys., 2013, **46**, 095304.
17. Guo-faCai et al., RSC Advances., 2013, **3**, 6896-6905.
18. K.J.Lethy et al., Appl. Surf. Sci. 2008, **254**, 2369-2376.
19. M. Vargas et al., J. Appl. Phys., 2014, **115**, 133511.
20. C.V. Ramana et al., App. Mat. Interfa, 2013, **5**, 4659-4666.
21. M. Meenakshi et al., doi:10.1063/1.4947948.
22. R. B. Suvarna et al., Solid state Ionics., 2008,**179**, 314-323.
23. M. Meenakshi et al., Mat.Today.Proc., 2016, **3S**, S30-S39.
24. H. Yuanrong et al., PlasSci and Technol., 2007, **9** (4).

Green Synthesis and studies of MultiWalledCarbonNanotube/ Polymer NanoComposites

Dr. Aparna Thakur
Vice-Principal, Birla Open Minds International School, Muzzaffarpur, Bihar.
Corresponding author's email: aparnathakur23@gmail.com

Abstract
The supercritical fluids have been used as inexpensive and environmentally benign media for the synthesis and processing of a variety of materials of technological significance. In the present work efforts have been made to synthesize a series of MWCNT/polymer nanocomposites through *in situ* polymerization of selected monomers in $scCO_2$. It was synthesized at 1200 psi and 90±1°C in $scCO_2$. Polypyrrole, polygycidyl methacrylate and their nanocomposites have been synthesized through chemical oxidative polymerization of monomer pyrrole in presence of ferric chloride and polygycidyl methacrylate through 2, 2-azobisisobutyronitrile initiated free radical polymerization. Their study has been done through FTIR, AFM and NMR spectroscopy.
Key words; Multi walled carbon Nanotube (MWCNT), super critical Carbondioxide ($scCO_2$), polypyrrole (PPy), polygycidyl methacrylate (PGMA)

1. Introduction
The potential of supercritical fluids as an alternative to organic reaction media for green synthesis of nanocompositeshas been recognized due to their inherent inexpensive, non-toxic, non-flammable features for synthesis of a variety of materials, no efforts has been made towards synthesis of the polymers and nanocomposites through chemical oxidative polymerization of Py and nanocomposites through free radical polymerization of GMA in presence of MWCNT in $scCO_2$ [1 – 6]. In the present investigation, supercritical carbon dioxide ($scCO_2$) has been used as environmentally benign alternative to organic solvents for synthesis of the proposed nanocomposites. The process of synthesis has been executed through *in situ* chemical oxidative and free radical polymerization of selected monomers in the presence of MWCNT in $scCO_2$.The nanocomposites and monopolymers have been characterized through AFM, FT-IR, ^{1}H NMR, and ^{13}C NMR spectra.

2. Experimental
MWCNT was purchased from the SES Research, Houston, Texas, USA. Which comprise outer diameter (nm) 80-100, length (µm) 10.3 and B.E.T area (m^2/g) 200.MWCNT was used without further purification. Monomers were purified through distillation under reduced pressure. AIBN was purified through recrystallization in hexane.
Supercritical carbondioxide Reactor was charged with withPy ($1.43X10^{-2}$mol/dL) ferric chloride (1.85X1 O'^{4}mol/dL), MWCNT ($5X10'^2$gm) and requisite quantity of carbon dioxide at 25±1°C. The contents were heated at 90±1°C to achieve the supercritical conditions therein at 1200 psi. MWCNT and Pyy was stirred for 40 hr under these condition, then dispersed in deionised water and filter using a PTFE membrane filter.
The reactor was charged with GMA ($3.67X10^{-2}$mol/dL), AIBN ($1.20X10^{-3}$mol/dL) and requisite quantity of carbon dioxide at 25±1°C. The contents were heated to 90±1°C to achieve the

supercritical conditions therein at 1200 psi. Under this stage, the contents were refluxed for 10 hr.

3. Results and Discussion

The formation of nanocompositeshas been ascertained through AFM, FT-IR and NMR spectra. FT-IR absorptions(cm-1) of monomers, respective polymers and nanocomposites are sketched in [Figure 2] Py shows absorptions at 3412.56(ν N-H), 2930.43(ν C-H), 1673.56(ν C=C) and 1469.57-1418.92(ν C-N).MWCNT shows absorptions 3439.11(ν O-H), 2841.32(ν C-H) and 2922.50(ν CH_2). The nanocomposite synthesized through polymerization of Py in presence of MWCNT shows absorption at 3446.59(ν N-H), 1653.45(ν N-H), 2937.26(ν C-H), 1023.04(ν C-H), 1561.29(ν C=C), 1458.36(ν C-N) and 798.15(ring deformation) (Turcu et al., 2006). GMA shows absorptions at 3752.4-3425.8(νO-H), 1722.5(ν C=O), 1637.4(νC=C), 1044.2(νC-H) and 760.50 out of plane. GMA shows absorptions at 3589.1-3276.2(νO-H), 3038.9(νCH_2), 1728.7(ν C=O), 1179.8(ν C-O), 1674.4-1631.0(νC=C) and 1044.2(νC-O-C). The respective nanocomposite shows absorption at 3607.1-3416.2(ν O-H), 2999.6(ν CH_2), 1731.1(ν C=O), 1130.9(ν C-O) and 1265.4(ν C-O-C).

Figure 5 shows the ^{1}H NMR spectra in DMSO-d6 of PPy and a representative nanocomposite. Due to insolubility in the solvent, the spectra show only characteristic peak of solvent centered around 2.5ppm. The peaks centered around 3-4 ppm in the spectra may be attributed to the presence of moisture. Comparative account of ^{13}C NMR of samples in TFA-d shows characteristic peak of solvent centered around 116.6 and 164.2ppm besides it signal at 127ppm corresponding to the presence of MWCNT.

The synthesized PGMA, extracted PGMA from crude Nano composite and MWCNT/PGMA show common ^{1}H NMR signals at δ-CH3 0.9-1.2 (a), -$CH_2$1.6-1.9 (b), CH_2 3.8-4.4(c), CH 3.3 (d), CH_2 6-2.9 (e) [7]. ^{13}C NMR spectra of Synthesized PGMA, extracted PGMA and MWCNT/PGMA shows common ^{13}C NMR signals at δ-CH3 18.10 (a), CH_2 124.00 (b), CH_2 53.22 (c), C=O 177.47(d), CH_2 adjacent to oxirane 65.71(e), CH of oxirane 49.06 (f) and CH_2 of oxirane 44.88, MWCNT at 127 [Figure 4], [7].

In Figures 1 the morphology of the MWCNT has been investigated into triethylenetetramine cured epoxy resin, with reference to the scale (μm) and height (nmX102).A comparative account of the topographic images at 5 μm, reveals the presence of amorphous grains (height, nm) of [Fig.1(c-d)] PPy (1.56), and MWCNT/PPy (3.02) [Fig.1(a-b)]. Nano indentation images indicate non-uniform distribution of grain. Under similar scale crystalline grains (height) have been observed for [Fig.1.(e-f)]PGMA(4.23) and MWCNT/PGMA(1.11) [Fig.1.(g-h)].

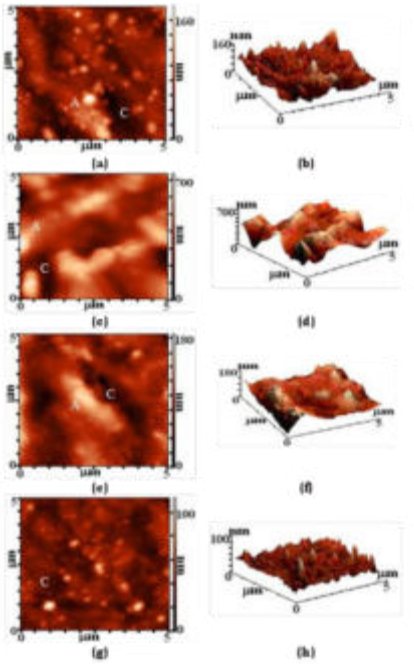

Fig1. Topography and Nanoindentation (a-b) MWCNT/PPy and (c-d) PPy (g-h) MWCNT/PGMA and (e-f) PGMA

Fig.2. FT-IR of Monomers (Py and GMA), MWCNT and Nano composites

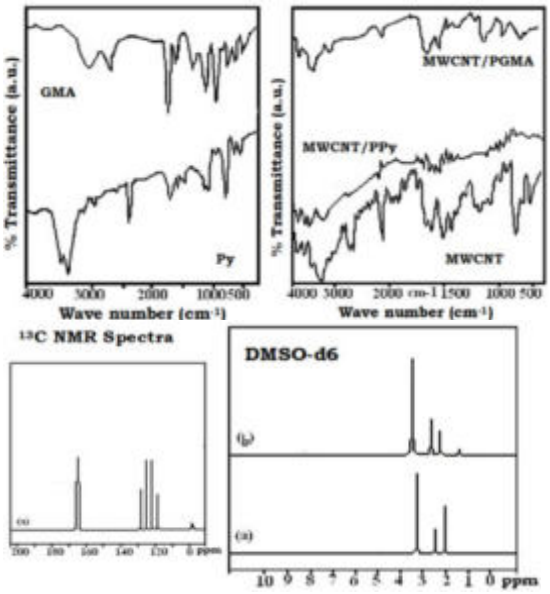

Fig5. 13C and 1H NMR of PPy and MWCNT/PPy

Fig.4. 1H NMR of PGMA
(I) synthesized
(II)extracted
(III)MWCNT/PGMA

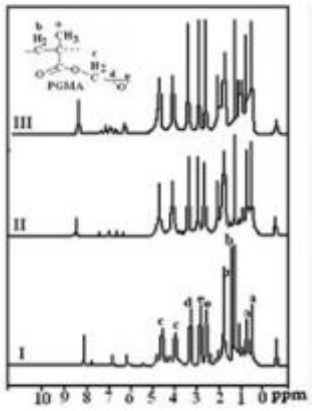

Fig.3. 13C NMR of PGMA
(I) synthesized
(II)extracted
(III) MWCNT/PGMA

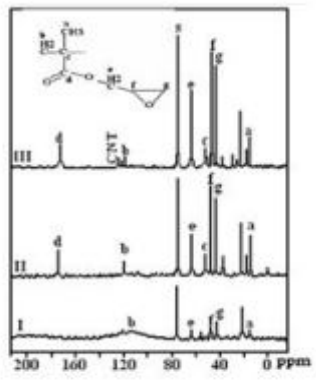

4. Conclusion

All the *in situ* polymerization reactions have been conducted under constant supercritical conditions maintained at 1200 psi and 90±1^{o}C. FT-IR spectra indicated characteristic wave numbers regarding the formation of homopolymers and their respective nanocomposites. Due to polymerization inhibitory nature of MWCNT, the nanocomposites derived from Pyy has been accomplished in 24 hr, whereas polymerization of GMA in presence of MWCNT has been accomplished in 10hr under the similar conditions.Due to poor solubility of conducting polymers and their nanocomposites in TFA and DMSO-d6 no relevant conclusion could be obtained from their ^{1}H NMR and ^{13}C NMR signals. But a significant result has been obtained from the ^{1}H NMR and ^{13}C NMR signals of PGMA and the respective nanocomposite due to the satisfactory solubility in $CDCl_3$.The morphology of the polymers and nanocomposites at 5nm scale reveals amorphous nature of PPy and its nanocomposites whereas PGMA and its nanocomposites show completely crystalline nature.

5. Acknowledgement

Thanks to DRDO and My supervisor Dr.MGHzaidi, HOD, Department of Chemistry, GBPUA&t, Pantnager, Uttarakhand.

References

1. S. G. Kazariann et al., Polymer science Series c., 2000, **42**(1), 78-101
2. H. Shiho et al., J. M. Macromolecules., 2001, **34**(5), 1198 -1203
3. L. I. Gang et al., Front. Chem. Chi., 2007, **2**(2), 118–122
4. C. M.Homenick et al., Poly. Rev., 2007, **47**(2), 265–290
5. M. N. Nadagouda., Green Synthesis of Nanocrystals and Nanocomposites (Chapter), 2012, DOI: 10.5772/29334
6. Z. Khanam et al., Poly.Adv.Technol., 2018, 29 (6), DOI; 10. 1002/pat.4357
7. R. M. Silverstein et al., John Wiley & Sons, INC. Spectrometric Identification of Organic Compounds, 2005.

Synthesis of Bioplastic Using Different Biopolymers

MaribelleLeocadiaViana* and Kevin D'Cruz
St. Xavier's College, Mumbai, India.
E-mail: maribelleviana@gmail.com

Abstract
This research investigates the effects of different biopolymers in production of bioplastic. Polysaccharide-based polymer/polymer blends from plant/algal sources were used, i.e. Potato Starch (PS), Corn Starch (CS), PS (50%) + CS (50%) blend, Sodium Alginate (SA) (40%) + PS (60%) blend, SA (20%) + PS (80%) blend, Pectin (20%) + SA (10%) + PS (70%) blend. The samples were analysed for swelling, solubility, thickness, mechanical properties, melting point, OTR, CO_2TR and biodegradability. All samples showed positive results although bioplastic prepared by the blend of SA (40%) and PS (60%) exhibited improved properties when compared to the other films. It showed the lowest engorgement, good solubility properties, good mechanical properties, the highest melting point and low Oxygen transmission rate as well as low Carbon dioxide transmission rate values.
Keywords: Bioplastic, Biopolymers, Potato Starch, Corn Starch, Sodium Alginate, Pectin

1. Introduction

Owing to their special characteristics, biopolymers have emerged as a major group of attractive and renewable substitutes for synthetic plastics.Biopolymers constitute a heterogenous group of naturally occurring polymers such as starch, cellulose, pectin, lignin, xylan, galactoglucomannan, chitosan, pullulan, alginates and PHA. The principal polymers used in bioplastics are obtained from plants, animals or micobiota, especially bacteria although, the polymers discussed in the present study focuses only on polysaccharide-based polymers from plant/algal sources [6]. The objectives of this study were to synthesize biodegradable plastic using different biopolymers and biopolymer blends, determine the swelling properties, solubility, biodegradability, mechanical properties (tensile strength, percentage elongation, young modulus), melting point, oxygen and carbon dioxide transmission rates, select the films showing best results and compare them with each other based on the above established properties. The findings of the research will help to determine the effect of different biopolymers in production of bioplastic. It will also aid in concluding which polymer or polymer blend is the most efficient one to produce biofilms and can be commercially utilised for manufacture of biodegradable plastic.

2. Experimental

2.1 Preparation of biodegradable films adapted [7]

A 2.5g of biopolymer was weighed and mixed with 25ml of distilled water. To this 0.8ml of 0.1MHCl was added. A 2ml of glycerol was added to the above mixture and boiled for 8 minutes at 150°. The solution was poured into a petri plate and kept in a hot air oven at 40ºC. After 24 hours, the film was carefully scraped off from the surface.

2.2 Swelling test adapted [7]

Pre-weighed pieces of samples were kept in petri plates containing 10 ml of water for 2 hours. The samples were taken out, excess solvent was wiped off and the final weight was recorded, and the amount of water uptake was calculated.

2.3 Solubility studies adapted [7]

Samples were cut into pieces and were inserted into test tubes containing different solvents viz., ammonia, acetic acid, chloroform, acetone, methanol, sulphuric acid, ortho-phosphoric acid, ethyl alcohol and water.

2.4 Film Thickness

Film thickness was measured at five different randomly selected spots using a micrometre screw gauge having a least count of 0.01mm. The mean value was calculated and used for rest of the calculations.

2.5 Mechanical property testing adapted [3]

The films were clamped between two clips and one end of the clip had a suspended beaker for placing weight in it. Once the sample was clamped, water was added in the beaker.The length of the strip was recorded after completion of the experiment. The average tensile strength, elongation at break and Young's modulus were calculated thereafter.

2.6 Melting point

2gm of sample was inserted in a 13x100mm test tube. The bulb end of the thermometer, along with the attached test tube was inserted in the Thiele tube containing paraffin oil. The Thiele tube was warmed until the sample had melted, thus getting an accurate melting point (Tm).

2.7 Oxygen Transmission Rate (OTR)

Oxygen transmission rate through the films was measured using PASPORT Oxygen as Sensor PS 212. A heated glass bead was added to the hydrogen peroxide solution present in a sampling bottle to accelerate its decomposition to H_2O and O_2. The gas produced was measured. The film samples were then wrapped around the sampling bottle and the amount of oxygen remaining was again measured after 15 minutes. Testing was performed at 27°C. Five replicates of each film type were tested and OTR was calculated.

2.8 Carbon Dioxide Transmission Rate

Carbon Dioxide transmission rate through the films was measured using PASCO CO_2 Sensor PS 320. 15 ml of Conc. HCl was added to 2 gm. calcium carbonate to produce CO_2 + CaCl2 + H_2O in a sampling bottle and the CO_2 gas produced was measured. The film samples were then wrapped around the sampling bottle and the amount of CO_2 remaining was again measured after 15 minutes. Testing was performed at 27°C. Five replicates of each film type were tested and CO_2TR was calculated

2.9 Biodegradability by soil burial test adapted [1]

Pre-weighed material was placed in a tray containing soil. The degradation of the samples was determined at regular time intervals (2 days) by carefully removing the samples from the soil and dusting the residual soil off gently. Weight loss of sample over time was used to indicate the degradation rate of the soil burial test.

3. Results and Discussion

Table 1: Film Characterization

Sr. No.	Bioplastic	Weight loss (%)	Solubility test	Elongati-on at break (%)	Tensile Strength (kPa)	Young's modulus (kPa)	Melting point (°C)	OTR (cc/m2/24hr)	CO2TR (cc/m2/24hr)
1	Potato Starch	46.76 ± 4.96	Partially soluble in NH_3 and H_2SO_4. Insoluble in rest.	1.4285	115.84±5	8108.98 ±355	218 ± 3.61	12033.82 ± 50.67	57001.31 ± 359.38
2	Corn Starch	123.38 ± 6.38	Partially soluble in NH_3,H_2SO_4 & H_2O. Insoluble in rest.	1.4285	132.65±12	9286.18±852	217 ± 7.55	12254.37 ± 42.90	62536.73 ± 110.20
3	Potato Starch (50%) + Corn Starch (50%) blend	68.02 ± 9.51	Partially soluble in NH_3 Insoluble in rest.	1.4285	131.62±12	9213.90±887	204 ± 5.03	11900.44 ± 26.90	55904.66 ± 189.23
4	Sodium Alginate (40%) + Potato Starch (60%) blend	22 ± 2.71	Insoluble in all solvents.	1.4285	195.82±3	13707.63±233	234 ± 2.88	9030.76 ± 21.52	40912.53 ± 177.43
5	Sodium Alginate (20%) + Potato Starch (80%) blend	57.62 ± 10.48	Partially soluble in NH_3 Insoluble in rest.	1.4285	179.47 ±6	12563.08±476	215 ± 2.51	9531.20 ± 49.92	46564.87 ± 202.60
6	Pectin (20%) + Sodium Alginate (10%) + Potato Starch (70%) blend	46.64 ± 2.72	Partially soluble in NH_3 Insoluble in rest.	2.8571±1.43	147.49±7	5162.21±277	222 ± 3.61	10627.84 ± 82.70	51733.38 ± 298.48

In the swelling test there is not much difference in the weight of the samples. Bioplastic 4 was comparatively the least effected among all the other films.Water insolubility may be useful for specific applications of films, such as the manufactureof biodegradable packaging, although, for example, edible films for candies require a high degree of water solubility. None of the samples were entirely soluble in the solvents. This shows that the biodegradable plastics are stable.

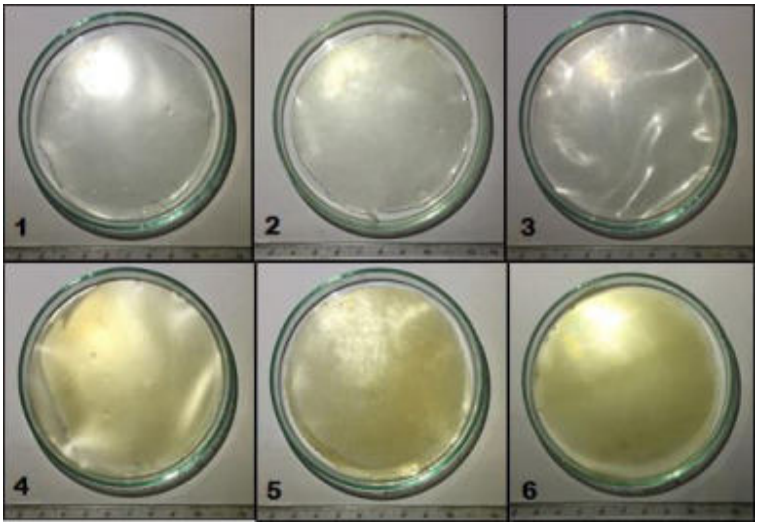

Figure 1: Visual aspect of the films

Tensile properties can be affected by molecular weight of the content of polymer, film thickness, polymer chain packing, chain interaction, and crystallinity of the film [2]. The tensile strength and the young's modulus of Bioplastic 4 was comparatively the highest among all the other bioplastics. Whereas there was no significant difference in Elongation (%) of all the bioplastics.

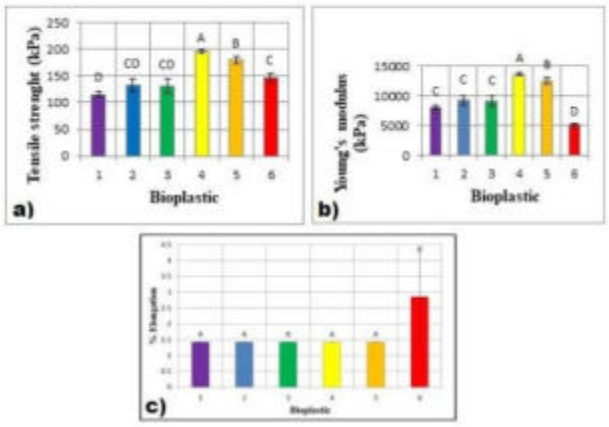

Figure 2: Mechanical properties of the bioplastics.* a) Tensile strength; b) Young's modulus; c) % Elongation

*The error bars indicate standard deviations. Different letters above the bars indicate statistically significant differences at $P < 0.05$.

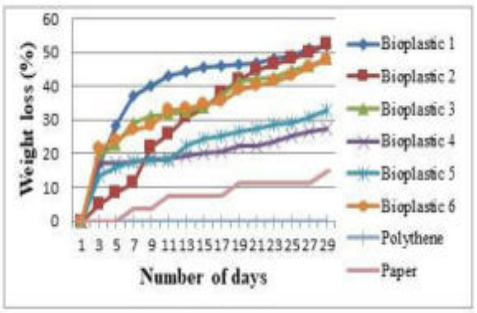

Figure3: Assessment of Biodegradability test using soil degradation method

All the bioplastics had a melting point above 200°C which was very high in contrast with polythene (Tm=133°C). Furthermore, Bioplastic 4 comparatively had the highest melting point (234°C) as sodium alginate contains hydroxyl and carboxylate groups, forming strong inter and intramolecular hydrogen bonding [4].

The oxygen and carbon dioxide barrier property of food packaging containers for fresh products (eg.fruits, salad) plays an important role in its preservation. When the polymer film packaging has low permeability, the O_2 and CO_2 pressure inside the container drops to the point where oxidation is retarded, extending the shelf life of the product [5]. Bioplastic2 had the highest OTR& CO_2TR followed by Bioplastic 1. Least OTR & CO_2TR was observed in Polythene. Further CO_2TR was 4 to 5 times the OTR value.

The longer the burial time, the higher the weight loss of bioplastic. It was seen that among the films, Bioplastic 2 and Bioplastic 4 had the highest and lowest % weight loss respectively. The reason being that starch had acetalbonds which were very easy to degrade. The magnitude of this mass reduction was due to the bioplastic composition due to which it was easily digested by microbes. Polymers containing hydroxyl groups (-OH) are easily degraded microbially.

4. Conclusions

Bioplastic 4 prepared by the blend of sodium alginate (40%) and potato starch (60%) exhibited improved properties when compared to the other films. It showed the lowest engorgement and solubility properties, good mechanical properties, the highest melting point and low OTR, CO_2TR values. With the above discussion, the biodegradable plastic films could have a potential uses for edible films and coatings due to their low degradability and low solubility in different solvents and low OTR and CO_2TR values. They can be also employed in controlled release of agrochemicals such as insecticides, pesticides, fungicides, germicides and growth stimulants.

References

1) N. A. Azahari et al., J.Physi. Sci., 2011, **22**(2), 15–31.
2) D. Domene-López et al., Polymers., 2019, **11**(7), 1084.
3) E. J. Eterigho et al., IJEE., 2017, 8 (2), 142-146.
4) Siddaramaiah et al., J. Appl. Poly Sci., 2008, **109**(6), 4075–4081.
5) V. Siracusa., Int. J. Poly Sci, 2012, 302029.
6) M. G. A. Vieira et al., Euro.Poly. J., 2011, **47**(3), 254–263.
7) Yaradoddi et al., Int. J.Pharma. Res& All Sci., 2016, 56-66.

*

Phase Transformation, Structural And Electrical Studies on Amorphous $Fe_{76}Nd_4B_{20}$ Alloy

B. Bhanu Prasad
Retired Professor of Physics,
Hyderabad – 501 510, Telangana State.
e-mail: bbpproofphys56@gmail.com

Abstract
X-ray Diffraction (XRD), Scanning Electron Microscopy (SEM) and electrical resistivity techniques have been used to study crystallization and the formation of crystalline phases in the crystallized samples of amorphous Fe76Nd4B20 alloy. The crystallized sample showed the formation of the primary crystalline phase α-Fe. The grain size of the grown crystalline phase for the annealed sample is about 20.08 nm.Fromthe resistivity measurements, the resistivity of amorphous Fe76Nd4B20 alloy at 300 K, ρ(300) is found to be 186 μΩ-cm.The Curie temperature (T_C), the first step of crystallization (T_{X1}) and the second step of crystallization (T_{X2}) of the amorphous sample are found to be 600 K, 800 K and 910 K, respectively. The temperarure coefficient if resistivity (TCR), α and the Debye temperarure (Θ_D) of the amorphous sample are found to be 8.065 X^{-4} K^{-1} and 408 K, respectively.

Keywords: hard ferromagnetic materials, melt spinning technique.thermal stability, magnetic materials, ferromagnetic alloys, temperature coefficient of resistivity, Debye temperature

1. Introduction

Hard ferromagnetic materials show high saturation and high coercivity with large area of B-H curve called energy product. The demand of these magnets is increasing because these magnets are indispensable for high performance motors in electrical vehicles. These magnets show good thermal stability since the properties of these materials significantly change by the onset of crystallization and crystallization is associated with nucleation and growth process. Thus, RE (Rare Earth) containing alloys (usually Fe-RE- B) obtained in amorphous state by Melt-Spinning technique and substantially annealed, have enhanced magnetic properties, compared to traditional permanent magnets. As the cost is lowered due to the substantial reduction of the rare-earth content, it therefore accounts for a new generation of permanent magnetic materials. The best permanent magnets are intermetallic compounds of a ferromagnetic 3d element and a 4f element; e.g. $SmCo_5$ or $Nd_2Fe_{14}B$. Their applications are magnetic resonance imaging, magnetic powder alignment, sensors, actuators, loudspeakers, generators, microphones, beam control, radiation sources (microwave, uv, X-ray) mineral separation, bearings, couplings, switchable clamps, brakes, metal separation. Other uses of magnets, in acupuncture, pain control, electrochemistry, suppression of wax formation in oil wells or control of lime scale deposits in pipes carrying hard water[1-6].In this paper, wemention Phase transformation, crystallization and structureand electrical properties of amorphous$Fe_{76}Nd_4B_{20}$ alloy to understand its structure and thermal stability after crystallization.

2. Experimental

Amorphous $Fe_{76}Nd_4B_{20}$ alloy ribbons were made using melt spinning technique which are procured from our other researchers. The width of these ribbons is about 1 mm and the thickness is about 30 μm. Structure of the crystallized samples were examined on the

MAXIMA_X 7000 XRD SERIES X-Ray diffractometerand computerized reflectedradiation recording system. For the fresh and annealed samples, X-ray diffraction patterns are recorded at room temperature. The structure of the crystallized samples is also examined using Scanning Electron Microscopy (SEM). Four probe resistance apparatus was used to make resistivity measurements in the temperature range 300 K – 950 K.

3. Results And Discussion

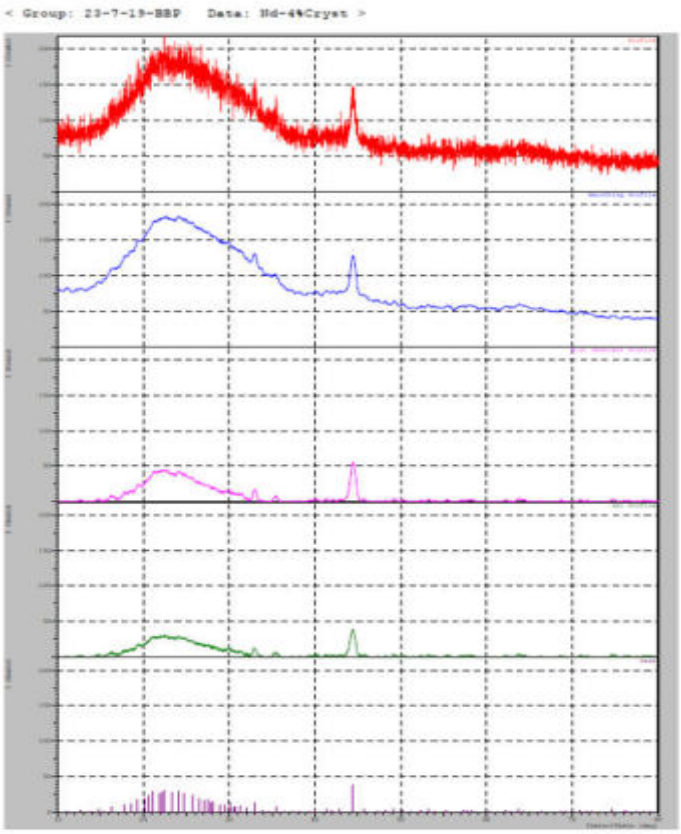

Figure 1 X-Ray diffraction pattern (XRD) of crystallized $Fe_{76}Nd_4B_{20}$

In the present study X-ray diffraction technique has been used to identify the crystalline phases as well as the grain size of the different samples by using Debye Scherrer's formula [7] given by

$$D = 0.94\lambda / \beta Cos\theta \quad \ldots\ldots\ldots\ldots\ldots\ldots\ldots\ldots\ldots\ldots(1)$$

Where D is the grain size, β is the full width at half maximum (FWHM), θ is the angle of diffraction and λ is the wave length of Cu-Kα radiation. The XRD pattern of the as-cast ribbon sample $Fe_{76}Nd_4B_{20}$ showed broad band revealing the amorphous nature of the sample. Another fresh ribbon sample of $Fe_{76}Nd_4B_{20}$ is heated to a temperature of about 1000 K and is cooled. As in Fig. 1 the XRD patterns show a sharp peak around $2\theta = 44.42^0$ which may be due to the presence of the primary crystalline phase α-Fe. The grain size of the grown crystalline phase is about 20.08 nm.

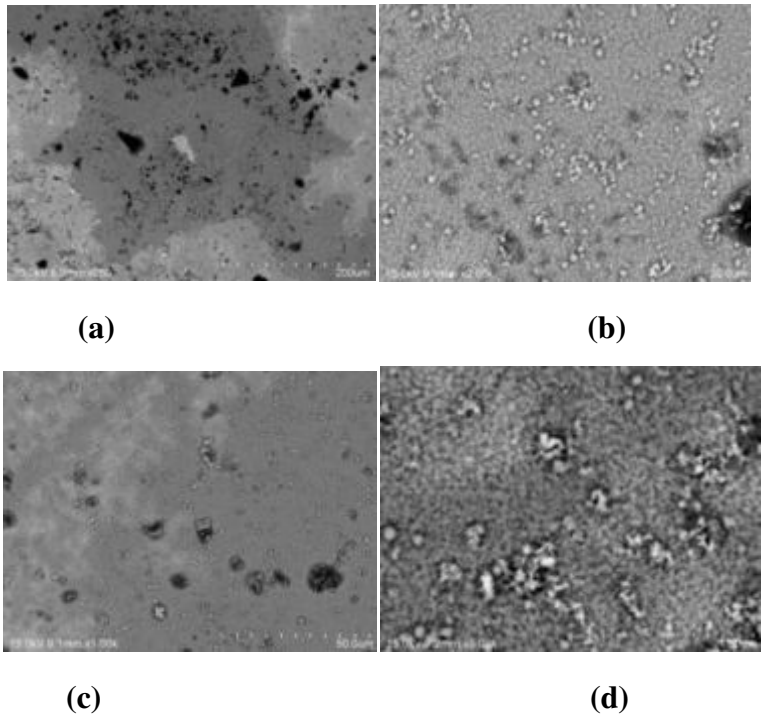

(a) **(b)**

(c) **(d)**

Figure 2 SEM photos of crystallized $Fe_{76}Nd_4B_{20}$at different resolutions
(a) 200 µm, (b) 50 µm, (c) 20 µm and (d) 10 µm

By using scanning electron microscope (SEM) micro structural studies were carried out. Thus, Figure 2 shows the SEM images of crystallized $Fe_{76}Nd_4B_{20}$ for different resolutions.. SEM micrographs of the crystallized sample thus shows the primary crystalline phase α-Fe as discussed in XRD results. Thus, XRD and SEM studies on crystallized $Fe_{76}Nd_4B_{20}$ shows the formation of α-Fe.

Figure 3 shows the variation of electrical resistivity, ρ (T) of amorphous $Fe_{76}Nd_4B_{20}$ alloy with temperature, T(K) in the temperature range 300 K – 950 K. As in Fig 1, resistivity of the amorphous alloy linearly increases from 300 K to 550 K. From 550 K the resistivity slowly decreases showing a small dip at 600 K. The small dip in the resistivity of the amorphous sample shows the Curie temperature (T_C) of the amorphous sample which is 600 K. Increase of temperature from 600 K increases the resistivity of the sample upto 700 K and from there the resistivity decreases rapidly up to 800 K. From 800 K, the resistivity more or less sharply increases up to 850 K. Thus, drop in the resistivity at 800 K gives the first step of crystallization (T_{X1}) in the amorphous sample. This occurs due to structural relaxation due to a variety of atomic rearrangements and growth of a primary crystalline phase. Similarly, in Fig.1, the resistivity suddenly drops at 910 K representing the second step of crystallization (T_{X2}) which occurs due to massive nucleation and the growth of another crystalline phase. From 910 K, the resistivity rapidly increases with increase in temperature. Thus, amorphous $Fe_{76}Nd_4B_{20}$ alloy undergoes two-step crystallization processes. This gives wide temperature interval between the two crystallization stages.

Figure 3 The variation of electrical resistivity, ρ(T) of amorphous $Fe_{76}Nd_4B_{20}$ alloy with temperature, T(K) in the temperature range 300 K – 950 K.

Observation of two step crystallization is more common in some amorphous ferromagnetic materials and metallic glasses. Thus, as spun samples of $Fe_{76}Nd_4B_{20}$ alloy crystallize in two steps to a final microstructure consisting of Fe_{14} Nd_2B and α-Fe phases [8]. Fe_{14} Nd_2B particles are surrounded by the bcc-Fe and amorphous phases which act as a magnetic exchange coupled medium [9, 10]. Comparison of our results with the published other similar systems reveals that amorphous $Fe_{76}Nd_4B_{20}$ alloy has good thermal stability for applications in the industries. From the resistivity measurements, the temperature coefficient of resistivity (TCR), α and the Debye temperature (Θ_D) of the amorphous sample are found to be 8.065 X 10^{-4} K^{-1} and 408 K, respectively.

4. Conclusions

For the fresh sample $Fe_{76}Nd_4B_{20}$heated to 1000 K and cooled, the XRD pattern at room temperature showed a sharp peak around $2\theta = 44.42^0$ which is due to the presence of α-Fe. The grain size of the grown crystalline phase for the annealed sample is about 20.08 nm. SEM studies on crystallized$Fe_{76}Nd_4B_{20}$showed the formation of α-Fe.From the resistivity measurements, the resistivity of amorphous $Fe_{76}Nd_4B_{20}$ alloy at 300 K is found to be 186 μΩ-cm. The Curie Temperature (T_C), the first step of crystallization (T_{X1}) and the second step of crystallization (T_{X2}) of the amorphous sample are found to be 600 K, 800 K and 910 K, respectively. The temperature coefficient of resistivity (TCR), α and the Debye temperarure (Θ_D) of the amorphous sample are found to be 8.065 X 10^{-4} K^{-1} and 408 K, respectively. The amorphous as spun samples of $Fe_{76}Nd_4B_{20}$ alloy crystallize in two steps to a final microstructure consisting of Fe_{14} Nd_2B and α-Fe phases.

5. Acknowledgements

The author would like to thank the Management members of Matrusri Education Society (MES), Principal, HOD, Faculty and Staff of Sciences & Humanities for their continuous support and encouragement in completing this work.

References

1. A. Inoue et al., MRS Bulletin., 2007, **32**, 651-658
2. J.S. Dugdale et al., Endeavour., 1985, **9**, 62-66
3. Y. Naitoh et al., J. Appl. Phys., 1998, **83**, 6332
4. A. Makino et al., J. Appl. Phys., 1997, **81**, 2736
5. A. Makino et al., JIM., 1995, **36**, 924
6. K. Hono et al., Acta. Metall. et Mat., 1992, **40**, 2137
7. A.K. Panda et al., J.Magn. Matter., 2003, **260**, 70.
8. L. Withanawasam et al., J. Magn.Magn. Mat., 1995, **1057**, 140-144,
9. A.Inoue et al., IEEE Trans. On Magn., 1995, **31**, 3626.
10. A. Grujic et al., Sci. Sint., 2007, **39**, 193.

Modelling Piezoelectric Effect of Flexible Substrates Using Finite Element Method

Dr.P.Geetha & H.D.Praveena
Electronics and Communication Engineering
Sree Vidyanikethan Engineering College,
Tirupati, India
Corresponding author's email: amailpgeetha213@gmail.com

Abstract
Different piezoelectric models are generated using COMSOL software before fabricating the hardware model. Software approach give the best design that can be developed as an hardware model. Best nano material is selected which gives more electric potential from the given materials i.e., Aluminium Nitride, Gallium Arsenide, Cadmium Sulphide and Zinc Oxide. Single rod is tested by applying different kind of forces. The effect of surface area of exposure in the generated output energy is determined. An electrical energy of 0.5268 pJ is produced when a force of 10 N/m2 is applied. By selecting the best design using software method a hardware model can be fabricated by using different materials such as paper, aluminium, textile.
Keywords: piezoelectric, nano rods, electric potential, electric energy, stress, flexible substrate.

1. Introduction

In recent past, more articles have reported the application zinc oxide (ZnO) nanostructures piezoelectric properties. In the same way, piezoelectric effect of various flexible substrates, such as paper, zinc foil, PET (polyethylene terephthalate) has been exploited by the research groups.

Fabrication of nanodevices with low cost and improved performance is of high demand [1]. Hence, different flexible substrates such as aluminum foil, paper, textile fabric, and plastic have been utilized to harvest electrical energy in the present study.

In addition to this, for paper and textile, an insulating layer is also needed to reduce the surface roughness [2-5]. This eliminates the use aluminum foil as a substrate as an insulating/conductive layer that is flexible and low cost.

Nano generator scavenges energy from the environment by utilizing the coupling between electrical and mechanical properties. Among the different tetrahedral coordinated compound semiconductors like GaN, ZnO, CdS, AIN, and CdSe it was found that ZnO has the highest piezoelectric coefficient [6]. ZnO is one of the Most important multi-functional semiconductors that possess a strong piezoelectric effect.

In this work, the electrical energy generator by the piezoelectric nano generator (NG) based on ZnO NWs/PVDF polymer hybrid structure has been studied. The study includes modeling the structure, characterizing it with various materials of dielectric strength [7, 8]. Modeling of devices reduces the burden of design during hardware implementation [9-16]. COMSOL multi physics software is used for the study. The total electrical potential, electric energy stored and total stored strain energy is calculated.

2. Experimental

The work flow is as follows. Two steps are followed. In step-1 simple 3D Parallel Plate Capacitor is developed and studied for different dielectric materials. In the next step 2: Elementary Piezoelectric Cylinder is developed for the ZnO as dielectric. The energy

generated has been simulated and the corresponding capacitance has been calculated. The results are compared for further discussions.

3. Results and Discussion

Step-1: Parallel Plate Capacitor

Poly silicon plates are used as conductive plates and air acts as a dielectric material between those parallel plates. The surface plot is displayed. The electric potential of 5V is applied blocks. As applied the upper block is at high potential of 5V. Table.1 contains the acquired results.

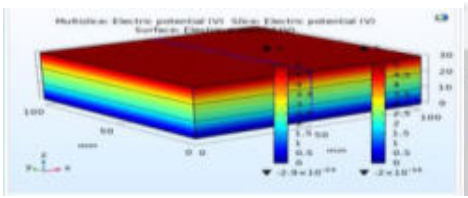

.

Figure 1: Colour legend of electric potential with ZnO as dielectric

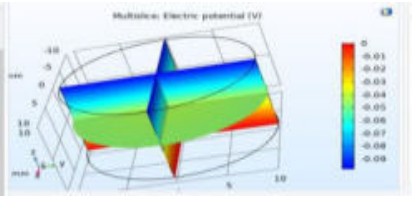

Figure:2 Multi slice view for electric potential of elementary piezoelectric cylinder with ZnO as dielectric material

Zinc Oxide, Cadmium Sulphide, and Bismuth Germanate can be used as a dielectric as they provide good capacitance value. But Zinc oxide is abundantly available, and the cost is much cheaper than the other two materials. So, consider Zinc Oxide as productive material for further courses.

TABLE 1 Tabulation of results obtained by varying materials

Material as	Electric	Capacitance	Consistency
Air	0.0766	0.0061	Non-
Aluminium	0.1992	0.0159	Not
Gallium	0.2109	0.0161	Barely
Cadmium	0.2014	0.0168	Uniform
Zinc Oxide	0.2040	0.0163	Good
Bismuth	0.2183	0.0174	Good

Step 2: Elementary Piezoelectric Cylinder

The next step is to construct the element that helps to study the pressure to voltage conversion. A cylinder considers as the elementary ZnO nanorod to study how a piezoelectric model can be created in COMSOL.

Fig:2 illustrates the color legend for the electric potential of the elementary piezoelectric cylinder. The total stored electric energy of 5.2675E-14 J and total strain of 7.2544E-14 J for an applied force on -100 N/m^2.

4. Conclusions

In summary different models of piezoelectric materials using COMSOL has been developed. It is observed that the piezoelectric nature of Zinc oxide is comparatively higher when compared to other piezoelectric materials such as Aluminum Nitride, Gallium Arsenide, Cadmium Sulphide etc. Zinc oxide nano rod produces an electrical energy of 5.2675E-14 J when a force of 10 N/m2 is applied. This simulation approach is promising, scalable and flexible before going to the hardware approach and it is easy to compare different materials, errors can be rectified easily, software model approach gives the best design that can be developed as an hardware model.

5. Acknowledgement

This work is developed in National MEMS Design Centre for Research at Sree Vidyanikethan Engineering College.

References

1. M. Hussain et al., Energy Harvesting and Systems, 2014, **1(1-2)**, 19-26.
2. E.S. Noura et al., Nano Energy, 2014, **9**, 221-228.
3. M. Willander et al., The International Society for optics and Photonics, 26 February 2016.
4. A. Khan et al., Chemical Physics Letters, 2014, **608**, 235-238.
5. Pu Xian Gao et al., Advanced Materials, 2007, **19**, 67-72.
6. M. Y. Soomro et al., Phys. Status Solidi RRL, 2012, **6(2)**, 80-82.
7. Zhong Lin Wang and Jinhui Song, Science, 2006, **312 (5771)**, 242-246
8. S. Khadarvali et al., International Conference on Applications of MEMS, Nano and Smart Materials, 2019.
9. P. Geetha et al., J. Compu. Electro., 2014, **13(4)**, 900-916.
10. P.Geetha et al., Carbon – Sci. & Technol., 2014, **6(2)**, 373 – 383.
11. P. Geetha et al., International Journal of Applied Engineering Research., 2015, **10 (10)**, 26401 -26421.
12. P.Geetha et al., Int. J. Sci Res & Devel., 2018, **5(5)**, 243-252.
13. P.Geetha et al., International Conference on Sustainable Approaches For Green Computing Economy and Environment, 2013.
14. P.Geetha et al., International Journal of Scientific and Engineering Research., 2014, **5 (3)**, 62-67.
15. P.Geetha et al., International Conference on Smart Computing and Control of systems, 2019, 17-19
16. P.Geetha et al., 2019., International Conference on MEMS, Nano and Smart Materials, 12-14.

Effect of Heat Treatment of the Microstructure of Al – Mg Alloys

M. S. SenthilSaravanan, Soorej K
Department of Mechanical Engineering,
Sree Buddha College of Engineering, Pattoor
Corresponding author's email: me.senthils@sbcemail.in

Abstract
In the present work, Al-Mg alloy was heat treated and the change in microstructure has been analyzed. The effect of microstructure variation on the hardness of the alloy also studied. Al-Mg alloy is a heat treatable alloy and mainly used in marine applications. AA 5083 alloy was taken for investigation. Five samples were prepared for the study. The samples were heat treated at different heat treatment process such as annealing and normalizing. Annealing was done at 250˚C and 400˚C. Similarly normalizing was done at 250˚C and 400˚C. The microstructure of heat treated samples was analyzed using Scanning electron microscope. The effect of heat treatment on hardness was measured using micro-hardness tester. The results show that hardness of the alloy is directly proportional to the heat treatment methods.
Keywords: AA5086; heat treatment; annealing; normalizing; SEM
Corresponding author e-mail-id

1. Introduction
The 5xxx-group contains magnesium as major addition element. These multiphase alloys belong to the group of commercial aluminum alloys, in which relative volume, chemical composition and morphology of structural constituents exert significant influence on their useful properties. In the technical aluminium alloys besides the intentional additions, transition metals such as Fe and Mn are always present. The 5083 aluminum alloy, which has high corrosion resistance, excellent weldability and good strength, is widely used in shipbuilding, automotive, aerospace and industrial construction. Recently, increasing attention has been paid to describing the quantitative influence of the heat treatment steps on the evolution of second-phase particles, including the dispersoidsand the precipitates in aluminum alloys [1 – 3].
In the present work, the effect of heat treatment on the microstructure and mechanical properties of AA 5083 is studied.

2. Experimental
The study material used for the present investigation is AA 5083 aluminium alloy. The chemical composition of AA 5083 alloy is given in Table 1.

Table 1: Chemical composition of AA 5083 alloy

Element	Al	Mg	Mn	Fe	Si	Cr	Ti	Cu
Wt. %	94.42	4.45	0.62	0.26	0.11	0.09	0.01	0.01

Five samples were prepared with dimension of 2 x 2 x 0.5 cm. the samples are heat treatedfor 90 minutes in muffle furnace at the temperatures of 250ºC and 400°C respectively. The samples were normalised with natural convection cooling process. The heat treated samples were polished using emery sheets (Grade 600, 400, 1/0, 2/0, 3/0 4/0) in the respective order. The samples were studied using X-ray diffraction analysis for elemental analysis. Further elemental analysis was carried out by Energy Dispersive X-Ray Analysis. The microstructural analysis was done by Scanning electron microscope. The mechanical properties of the heat treated samples were analysed by microhardness and tensile test.

The flowchart of the experiment procedure is shown below

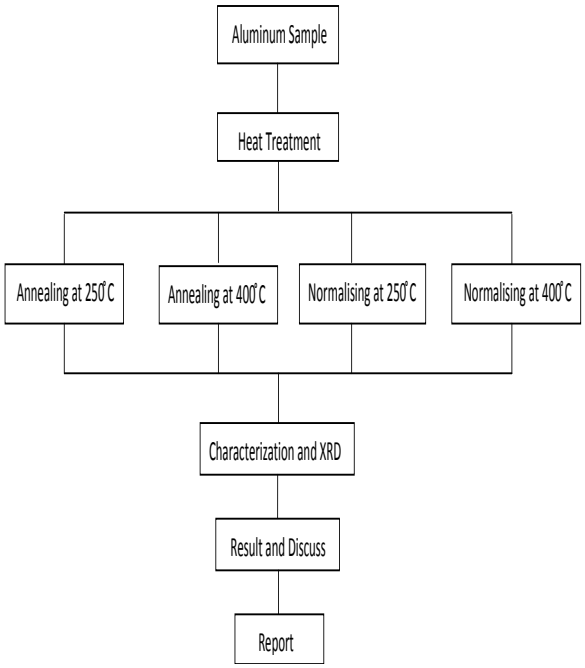

3. Results and Discussion

3.1 X-ray Analysis

XRD analysis of A confirms the material is Al 5083 and also it shows the deflection of x-ray in hkl planes, here hkl planes such as (111), (200), (220), (311) can identified at angles 38.4, 44, 66.3 and 78.4 degrees. The intensity of deflection of plane (111) is much larger as compared to other planes, plane (200) has the second highest value of intensity and the third is for plane (311), plane (220) has the least value of intensity.

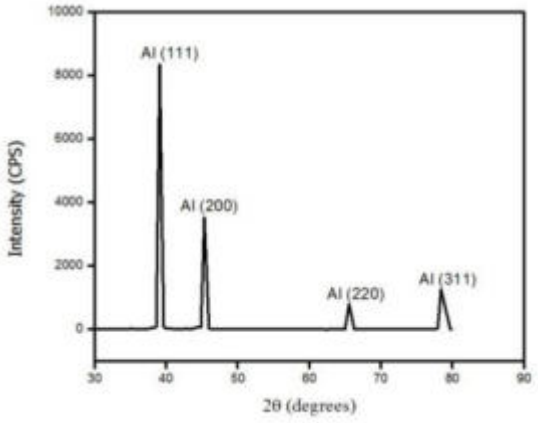

Fig 2 : XRD micrograph of AA-5083

3.2 Microstructure Analysis

The SEM micrograph of AA 5083 is shown in Fig 3. The microstructure is shown in fig (a). the elemental analysis of the alloy is confirmed with EDAX analysis which shows the predominant elements in the graph.

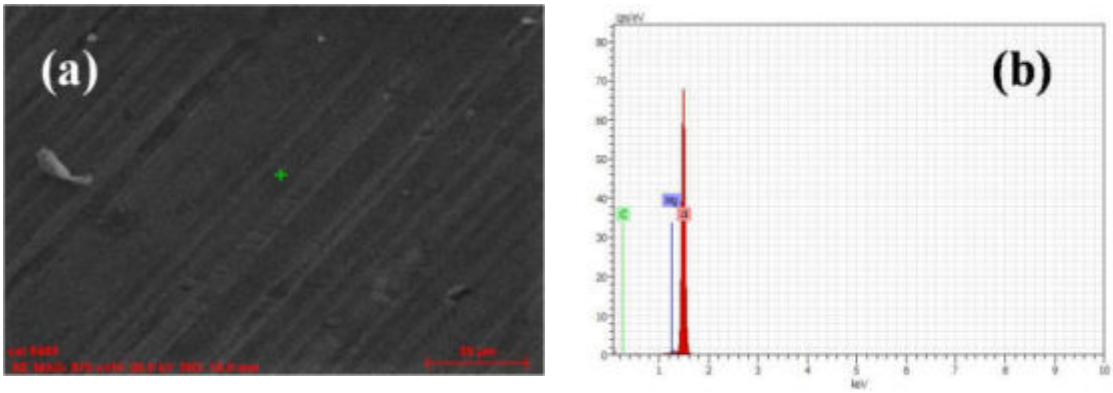

Fig 3: (a) SEM image of AA 5083; (b) EDAX analysis of AA 5083

3.3 Microhardness

The microhardness of AA 5083 at different heat treatment condition is shown in Fig 4. The high increase inmicrohardness values, compared to the base material (40 HV) is attributed mainly to the high presence of the Magnesium- copper based embeddedparticles. Those particles consisted mainly of different complex and hard intermetallic layers.Another possible reason for the hardnessincrease is the diffusion of the copper in the AA5083 matrix. The diffusion of the Mg and Cu inthe matrix could lead to a solid solution matrix that is mechanically tougher than the pure base metalmatrix. Furthermore, the embedded particles and the diffused copper in the AA5083 matrix could actas barriers to the movement of dislocations, thereby increasing the hardness of the material.

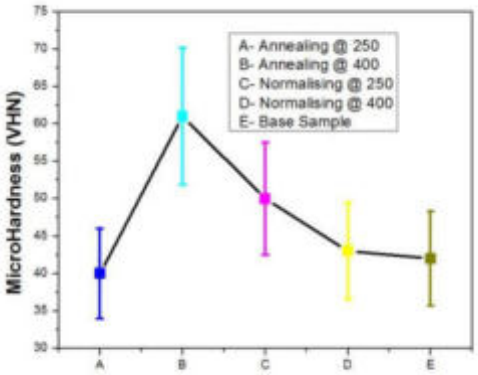

Fig 4: Microhardness of the sample at different heat treated condition

4. Conclusions

The heat treatment of AA 5083 was done at various temperatures to study its effect on mechanical property such as microhardness. Hardness increased at annealing and decreased during normalising.

References

1. K.T. Akhila et al., 2014, 12th global congress on manufacturing and management, GCMM 2014.
2. M. El-Shennawy et al., Int.J.Appl.Eng.Res., 2017, **12** (11).
3. Amit Kumar et al., Int.J.Appl.Eng. Res., 2017, **13** (9).

Structural and Optical Properties of Green Mediated Copper Oxide Nanoparticles

Dr. Divya.R[1] and Kathira.A[2]
[1]*Assistant Professor*
[2]*M.Sc. Scholar*
Corresponding author's email:divyar_86@yahoo.com

Abstract
Nature inspires researcher to carry out new research in science and technology, especially in the field of nanotechnology. Synthesis of Metal Oxide Nanoparticles using green is the recent trend. In the current study, we have attempted to synthesize CuO nanoparticles mediated with green by solvothermal method. CuO NPs were characterized by X-ray Diffraction (XRD), UV-Visible Spectroscopy (UV-Vis) and SEM studies.
Keywords: solanum lycopersicumextract (tomato fruit), Green synthesis, CuO nanoparticles, Structural properties, Optical Properties.

1. Introduction

Nanomaterials are cornerstones of nanoscience and nanotechnology. Nanostructure science and technology is a broad and interdisciplinary area of research and development activity that has been growing explosively worldwide in the past few years. It has the potential for revolutionizing the ways in which materials and products are created and the range and nature of functionalities that can be accessed. It is already having significant commercial impacts, which will assuredly increase in the future [1 - 8].

2. Experimental Method

In the present study, pure Copper oxide nanoparticles has been prepared using Solvothermal method. 10g of Copper acetate monohydrate is completely dissolved in 50 ml of Ethylene glycol and 9 grams of Urea is mixed with 50 ml of Ethylene glycol. The precursors are mixed together and heated in microwave oven for nearly half an hour to obtain pure copper oxide nanoparticles. Then separate this nanoparticle using what man filter paper and wash the resultant sample using distilled water repeatedly to remove the by-products, dry the sample for few days again its washed using acetone to remove the impurities.
To the above precursors solanum lycopersicum (tomato) fruit extract of different concentrations (3ml and 6ml) were added. The resultant solution was heated in microwave oven for about 30 min. The precipitate formed was allowed to settle down. After a minute the settled precipitate was washed with distilled water thrice and allowed to dry for a week. After a week the dried sample was again washed with acetone to remove the impurities. The samples were filtered and allowed to dry. The prepared samples were subjected to various studies

3. Results and Discussion

3.1 Structural properties:

3.1.1 XRD Analysis:

The structure analysis of the prepared CuO nanoparticle was done by X- ray diffraction. The prepared copper oxide powders were characterized by X-ray power diffraction meters using CuKλ radiation (wave length λ=0.15406nm). X-ray diffraction pattern is recorded for the as prepared samples. In x-ray diffraction, the Scherer formula that relates the size of sub-micrometer particles, or crystallites, in a solid to the broadening of a peak in a diffraction pattern. It is used in the determination of size of particles of crystals in the form of powder.

CuO nanoparticles exhibited Cubic crystal structure. The peak intensities are in agreement with the JCPDS. All diffraction peaks correspond to the characteristic face centered cubic (FCC) copper lines.

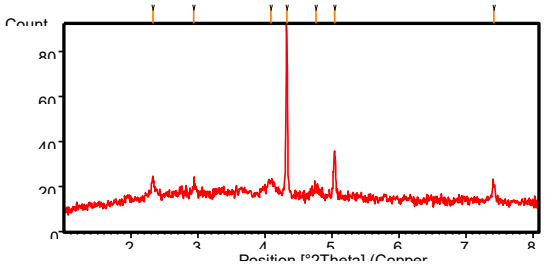

Figure 3.1: XRD spectrum for pure CuOnanoparticle

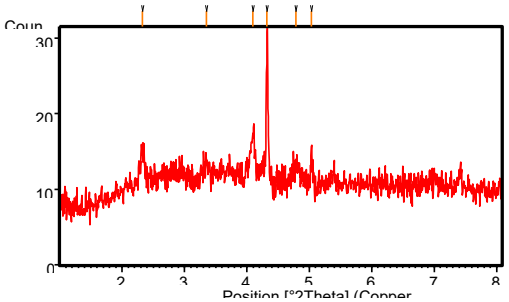

Figure 3.2: XRD spectrum for 3ml solanumlycopersicum mixed CuO nanoparticle

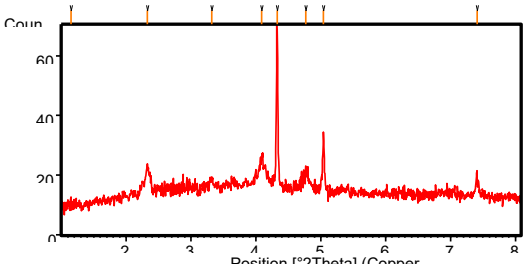

Figure 3.3: XRD spectrum for 6ml solanumlycopersicum mixed CuO nanoparticle

The crystalline size of the film is calculated using Debye Scherer formula by measuring FWHM from the diffraction pattern. The average size of CuO nanoparticles is calculated using the formula,

$$D = k\lambda/\beta cos\theta$$

Where, D is the average crystallite size of the particles, K is Debye-Scherer's constant (0.94), λ is the wavelength of the cuK α-radiation (1.5406 Å), β is the full width half maximum (FWHM) of the peak, θ is the Bragg`s angle.

Table 3.1: Crystalline size of CuO nanoparticles

Samples	Crystalline size
Pure CuO	19.7616 nm
3ml solanum lycopersicum mixed CuO	20.3484 nm
6ml solanum lycopersicum mixed CuO	22.6271 nm

3.2. Optical propertier

3.2.1 Ultraviolet-Visible Analysis:

Ultraviolet-visible spectroscopy or ultraviolet-visible spectrophotometers refers to absorption spectroscopy or reflectance spectroscopy in the ultraviolet-visible spectral region. This technique is based on the absorption of light in the ultra-violet (10-420nm) and visible (420-700nm) regions by a powder sample. From UV spectrum, the absorbance in each sample is studied.The optical band gap is determined using Tauc's relation,

$$\alpha h\upsilon = A(h\upsilon - E_g)^n$$

Table 3.2: Energy band gap for CuO nanoparticles

Samples	Energy band gap
Pure copper oxide	4.03eV
3ml solanum lycopersicum mixed CuO	4.63eV
6ml solanum lycopersicum mixed CuO	4.73eV

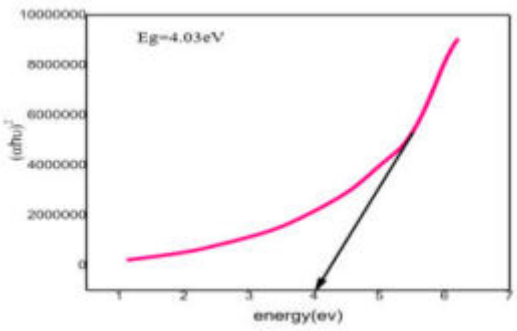

Figure 3.4: Tauc plot of pure CuOnanoparticle

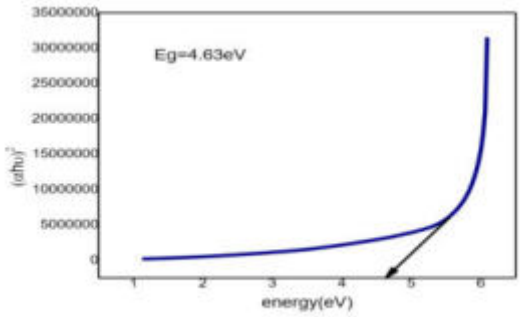

Figure 3.5: Taucplot of 3ml solanumlycopersicum mixed CuO nanoparticle

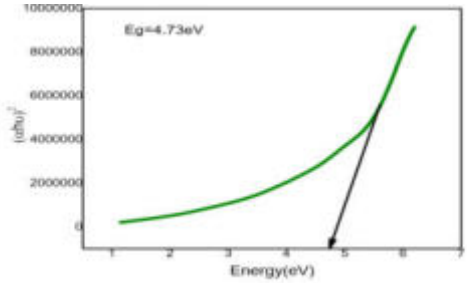

Figure 3.6: Taucplot of 6ml solanum lycopersicum mixed CuO nanoparticle

The results show that the energy band gaps of CuO nanoparticles increases with increasing in concentration. A larger bandgap means that more energy is required to excite an electron from the valance band to the conduction band.

3. SEM Studies

The structural features of the synthesized particles were investigated using scanning electron microscopy (SEM). The observed images are shown in Figure . This image was observed within the magnification of 25 nm. The nanostructured particles apparently exhibit a spherical morphology.

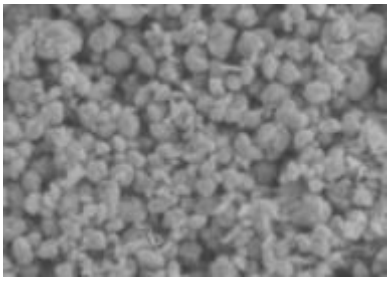

Figure 3.7 SEM Photograph of pure CuO

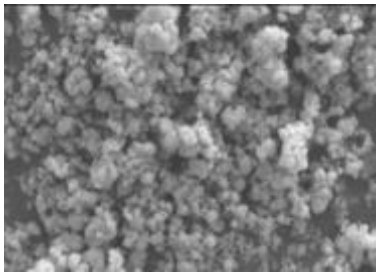

Fig 3.8 SEM Photograph of 3ml solanum lycopersicum mixed CuO np

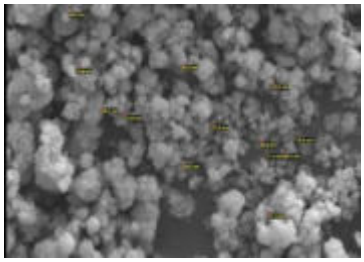

Fig 3.9 SEM Photograph of 6ml solanumlycopersicum mixed CuOnp

4. Conclusions

From XRD spectra, the prepared nanomaterials show the cubic crystal structure. The positions of the peaks are in excellent agreement with the standard reference pattern JCPDS data (No78-0428). The crystalline sizes of prepared nanomaterials are calculated from Scherer′s formula. The range of crystalline size lies between 19- 22nm.The results show that the crystallite size of CuO nanomaterials increases with increasing concentration. The absorbance of the pure copper oxide nanomaterial measured in the energy band gap is 4.03eV and the absorbance of the 3ml and 6ml solanum lycopersicum mixed CuO nanoparticles energy band gaps are 4.63eV and 4.73eV respectively. The optical band energies were calculated using Tauc plots. The grain size, shape and surface properties like morphology were investigated by the Scanning Electronic Microscopy shown in figure. The nanostructured particles apparently exhibit a spherical morphology. The results show that the energy band gaps of CuO nanoparticles increases with increase in concentration. The synthesized copper nanoparticles are of greater stability. Increased bandgap nanomaterials have potential applications in solar cells. The green synthesis of preparing CuO nanoparticles is economical and cheap with no hazardous effects.

5. Acknowledgement

I would like to thank the research centre of S.T.Hindu College, Nagercoil.

References

1. http://shodhganga.inflibnet.ac.in/bitsream/10603/22774/9/09_chapter1.pdf
2. http://www.emm-nano.org/what-is-nanoscience-nanotechnology/
3. https://www.researchgate.net/publication/259118068_Chapter_-
4. https://shodhganga.inflibnet.ac.in/bitstream/10603/176539/7/0_chapter%201.pdf
5. https://shodhganga.inflibnet.ac.in/bitstream/10603/175588/8/08_chapter2.pdf
6. http://www.ijnnonline.net/article_24532_2636a51c5bc94ff2de43dd7cba7bbbf0. pdf
7. https://www.ncbi.nlm.nih.gov/pmc/articles/PMC6206834/
8. Tan YW, et al., J Mater Chem., 2003, **13**, 1069-1075.

Effect of Multiwalled Carbon Nanotubes as Nano Additives in Canola Biodiesel Blends on Performance and Emission Characteristics of a Diesel Engine

A. Praveen
Department of Mechanical Engineering, Bapatla Engineering College, Bapatla, AP.
Corresponding author's email: praveen.tng@gmail.com

Abstract
The main aim of this work is to study the effect of Multiwalled carbon nanotubes used as nano additives in canola biodiesel blends on the performance and emission characteristics of a diesel engine. The MWCNTs were added into the canola biodiesel blend (CABD20) in the concentrations of 50 and 100 ppm with the aid of the ultrasonicator. The fuel properties of the test fuels were measured according to the ASTM standards. The performance and emission characteristics of a single cylinder diesel engine by using various fuel samples were determined. The CO, HC and smoke emissions were reduced with the addition of MWCNTs into the biodiesel blends compared to the biodiesel blends. It is concluded that addition of MWCNTs into the biodiesel blends shows the better results compared to the other fuel samples.
Keywords: Canola biodiesel, MWCNTs, Combustion, Emissions

1. Introduction
Recently, demand for energy was growing enormously which affects the improvement in the economy of developing nations. The majority of energy requirement was fulfilled by the fossil fuel resources which may result in environmental degradation, global warming and causes the air pollution [1]. Biodiesel is one of the substitute fuel for diesel engines due to its sustainable, eco-friendly nature, non-hazardous which is produced from the various sources such as vegetable oils, non-ediable sources, animal fats, waste cooking oil and algae etc. Nithya et al [2] studied the effect of additive nanoparticle TiO_2 in to canola biodiesel its emission properties were determined. The results revealed that the addition of the nanoparticle the emission of NOx was reduced 5% compared to neat canola biodiesel. Further, they also noticed the consistent reduction in other gases like CO, is 32%, HC 30% and the reduction of smoke is 52%. Mehrdad et.al [3] studied the effect of multiwall carbon nanotubes (MWCNT) to diesel–biodiesel blends in the diesel engine. The results reveal that NOx, CO, HC and soot emissions were reduced by up to 18.9%, 38.8%, 71.4% and 26.3%, respectively, for B20 (90 ppm) fuel compared to neat B20 fuel sample. Based on the literature review this work aims that the effect of multiwalled carbon nanotubes used in canola biodiesel blends on the performance and emission characteristics of a diesel engine [4, 5].

2. Experimental
Canola biodiesel was produced by the transesterfication process by using methanol to oil ratio of 6:1 with KOH as catalyst (1% of oil by weight). Next, this mixture was transferred to the reaction tank and heated at constant temperature of 60^0C with constant stirring process in one hour. Then this mixture was poured into the funnel and allowed to settle for 6 hours. After separation, the glycerol was removed from the bottom of the flask and then the biodiesel was collected and washed with water to remove the excess alcohol and dust particles. Canola biodiesel-diesel blend was prepared by blending of 20% of biodiesel with 80% of diesel in volumetric proportion and it was named as CABD20. In the CABD 20 fuel

sample multiwalled nanoparticles were added at proportions of 50 ppm and 100 ppm. The SEM image of multiwalled carbon nanotubes was shown in Figure 1. The properties of all fuel samples were determined according to the ASTM standards. The experimental investigation was carried out in a single cylinder four stroke vertical water cooled constant speed direct injection diesel engine was shown in figure 2. The various tests were conducted on a diesel engine to determine the performance and emission parameters by using various test fuel samples.

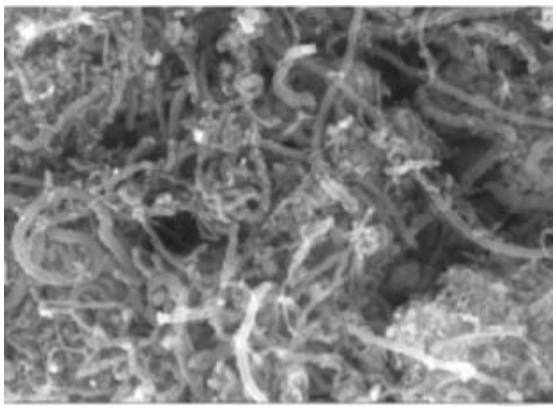

Figure 1: SEM Image

Figure 2: Test Engine

3. Results and Discussion

3. 1. Performance parameters:

The performance parameters such as brake thermal efficiency and brake specific fuel consumption were shown in Figure 3. The obtained results shows that the brake thermal efficiency of CABD20 fuel sample reduces compared to the diesel fuel due to the lower calorific value. The addition of MWCNTs to the biodiesel blend increases the brake thermal efficiency compared to the CABD20 fuel. The brake specific fuel consumption for the CABD20 higher than the diesel fuel. The addition of MWCNTs into the biodiesel blend the BSFC were reduced compared to the CABD20 fuel due to the improved combustion.

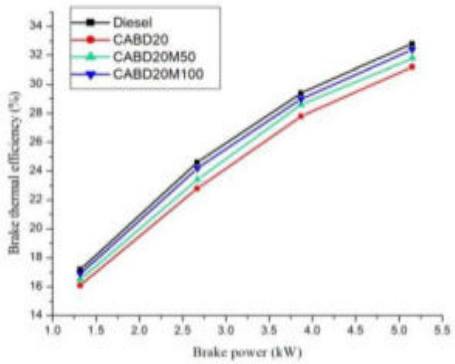

Figure 3: BTH Vs Brake power

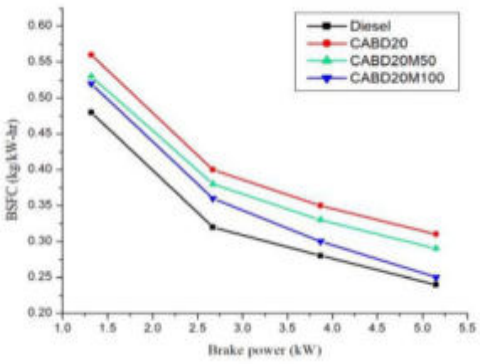

Figure 4: BSFC Vs Brake power

3. 2. Emission parameters:

The emission parameters such as CO, HC, NOx and smoke emissions were shown in Figure 5, 6, 7 and 8.The results shows that CO emissions for the CABD20 fuel were lower than the diesel fuel. The addition of multiwalled carbon nanotubes to the CABD20 fuel CO emissions were reduced due to shorter ignition delay period. The HC emissions for the CABD20 fuel were less compared to the diesel fuel at all load conditions. The addition of MWCNTs to the CABD20 fuel HC emissions further reduced due to the more surface to volume ratio of nanoparticles.

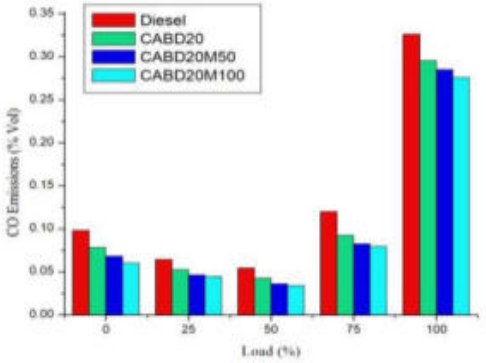

Figure 5: CO emissions Vs load

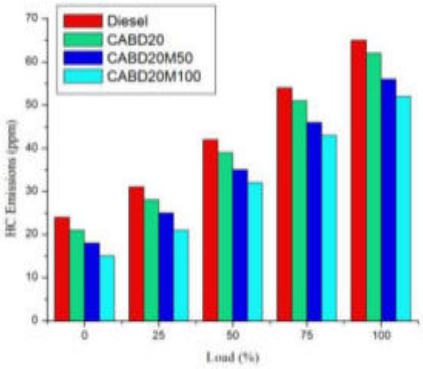

Figure 6: HC Emissions Vs load

The NOx emissions for the CABD20 fuel sample were higher compared to the diesel fuel at all load conditions. The addition of MWCNTs into the CABD20 fuel sample the NOx emissions were reduced compared to the CABD20 fuel due to the catalytic activity of nanoparticles. The smoke emissions for the CABD20 fuel were slightly increased compared to the diesel fuel at all load conditions. The addition of MWCNTs into the CABD20 fuel the smoke emissions were lowered compared to the CABD20 fuel due to the improved combustion.

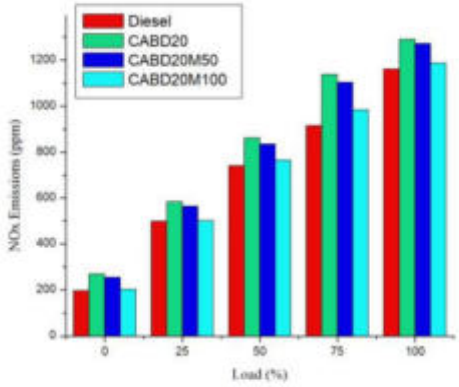

Figure 7: NOx Emissions Vs load

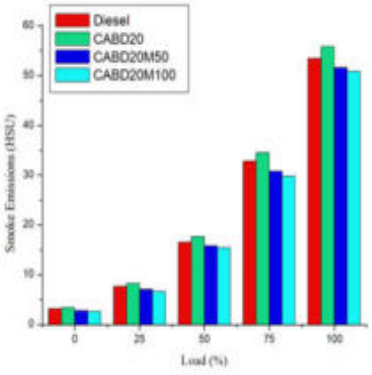

Figure 8: Smoke Vs load

4. Conclusions

The performance, combustion and emission characteristics of a diesel engine by using Canola biodiesel blend with MWCNT additives were investigated. The following on conclusions were obtained. The brake thermal efficiency was improved and BSFC was reduced with the addition of MWCNTs into the biodiesel blend compared to the CABD20 fuel sample. The emission parameters such as CO, HC, NOx and smoke emissions were reduced for the addition of the MWCNTs to the biodiesel blend than the CABD20 fuel.

References

1. M. Jayed et al., Renew & Sustain. Ener. Rev., 2009, **13**, 2452-62.
2. S. Nithya et al., Int.J. Amb. Energy., 2019, **40** (8), 838-841
3. M. Mehrdad et al., Fuel., 2015, **139**, 374–82.
4. A. Praveen et al., Egy. J. Petro., 2018, **27**, 731-38.
5. V. A. M. Selvan et al., Fuel., 2014, **30**,160–167.

Action of $[CaO]_{(y-x)}$- $[CuO]_x$Compositeson Bi_2O_3- SiO_2 GlassCeramics

G. Ravi Kumar[1,2], P. Mounika[2], Ch. Srinivasa Rao[2]
[1]*Department of Physics, Sreenidhi Institute of Science and Technology, JNT University, Hyderabad - 501301 India.*
[2]*Department of Physics, Andhra Loyola College, Krishna University, Vijayawada - 520008 India.*
E-Mail Address: raviguntu@sreenidhi.edu.in&drchsr1971@gmail.com

Abstract
The glasses of composition $[Bi_2O_3]_{10}$-$[SiO_2]_{60}$: $[CaO]_{(y-x)}$-$[CuO]_x$(where 'x'varies from 0.1 to 0.5, y = 30) are crystallized with heat treatment. Prepared test samples characterized by DTA& TLtechniques. More number of crystalline peaks in DTA reports strongly suggests that the test samplespreparedturned crystalline after required heat treatment.Elastic properties of both G & GC - δSeries of samples are also reported. TL measurements of both glassy (G - δ_4) and glass ceramic (GC - δ_3) exhibiting good SSF{$\boldsymbol{u}$(G - δ_4 = 0.484&GC - δ_3 = 0.247)} and low AE's {G - δ_4 (E_{τ} = 0.777, E_{δ} = 0.840& E_{ω} = 0.812)&GC - δ_3 (E_{τ} = 0.37, E_{δ} = 0.48& E_{ω} = 0.22)} under 30 min of γ - irradiation might be good TL asset.

Keywords
Micro hardness; thermal stability; trap depth parameters;

Abbrivations:
G- Glass; GC- Glass Ceramic; DTA - Differential Thermal Analysis; TL-hermoluminiscence; SSF-Shape Symmetry Factor; AE-Activation Energy; YM -Young's Modulus; MH-Micro Hardness; NBO- Non-Bridging Oxygen.

1. Introduction

Cu^{2+} ions of calcio bismuth silicates are extremely promising materials asa thermo- dielectric resource materials. Since most recent two decades to current years there has been significant research on Cu^{2+} ions of calcio bismuth silicates due to their anomalous TL and dielectric results. Generally, the Bi_2O_3-SiO_2 glass ceramics are hard in elastic nature, non-corrosive and possess high thermal stability [1]. The previous studies of these materials disclosed that the thermo radiative properties of Cu^{2+} ions of calcio bismuth silicates have very high credibility in many medical and engineering uses. Generally, Fe_2O_3 and CuO are mostly used to induce crystallization and nucleation in novel glass ceramics. Usually in glass ceramics, copper ions occur in multi stable valence states such as Cu^{+}, Cu^{2+} and Cu^{3+} induce thermo dielectric properties [2]. SiO_2 is one of the most complex and most abundant families of materials, existing as a compound of several minerals and as synthetic product (glass former). It is used in structural materials, microelectronics (as an electrical insulator) and as components in the thermo and dielectric industries. Silica of SiO_2 is an advocate among the most incredible and most abundant families of resources, existing as a compound of a glass former and as synthetic product. It is used in fundamental materials, microelectronics (as an electrical insulator) and as parts in the thermo and dielectric endeavours [3]. The addition of Bi_2O_3 to the silicate glass ceramic subordinates are believed to be of acceptable compound toughness and have ventured protection from gamma-light. For the most part, the corrosion diminishes with the expansion in the SiO_2 content within these glass ceramic network precisely true to form in perspective on the solid fundamental movement of silica in the glass coordinate. Bismuth silicate glasses, because of their favourable physical, TL characteristics, are used in numerous applications: in optoelectronics, and thermo dielectrics due to their low optical attenuation and dielectric dispersion.The addition of CuO to the calcio bismuth silicates are noble composite materials for nonlinear optical absorbers as passive modulators of thermo-

dielectric devices [4]. Most of the locations within the present glass ceramics are experienced distortion due to involvement of copper ions and induce condensed symmetry over octahedral or tetrahedral geometry. The existing calcio bismuth silicates glass ceramics have extensive certification as sealing resources in literature, as compressive seal needs an applied load during applications are electrically conductive and susceptible to oxidation [5]. The induced small degree of distortion within these glass ceramics is due to addition of copper oxide concentration split d-shell energy levels and improve the number of d-d transitions lead enhanced TL emission cause variations in values of trap depth parameters. Cu^{2+} ions of calcio bismuth silicates based non-crystallines have many excellent properties such as high refractive index medium and good at dielectric properties. Due to their wide range of characteristics of these glass ceramics are used in many applications like thermo dielectric sensors. Bismuth in present ceramics predominantly exist in Bi^{3+} state [6]. In the present investigation we have chosen $[Bi_2O_3]_{10}$- $[SiO_2]_{60}$:$[CaO]_{(y-x)}$- $[CuO]_x$as a chemical composition for synthesis to study the influence of CaO and CuO on structural changes in $Bi_2O_3 - SiO_2$ units before and after required heat treatment and to develop higher efficient thermoluminiscence and dielectric applications.

2. Methods & Measurements

The chemical composition of $[Bi_2O_3]_{10}$- $[SiO_2]_{60}$:$[CaO]_{(y-x)}$- $[CuO]_x$ (where 'x' varies from 0.1 to 0.5, y = 30) has chosen for present glass synthesis.Suitable quantities of analytic grades of pure CaO, Bi_2O_3, $SiO_2$and CuO chemicals are chosen in an agate mortar in a powder form. The chosen chemical powders were extremely mixed and liquefied in a thick walled crucible with in the temperature range of 1390 ^oC to 1430 ^oC in an automatic maintained temperature furnace for about 30 minutes until a bubble free transparent melt was produced. The final melt was discharged in a brass cast and successively annealed at 515 ^0C temperature in a muffle furnace. The following chemical composition represents the existing glass series of samples annealed at 515 ^0C.

G - δ_0 `	$[Bi_2O_3]_{10}$- $[SiO_2]_{60}$: $[CaO]_{(30)}$- $[CuO]_{0.0}$
G - δ_1 `	$[Bi_2O_3]_{10}$- $[SiO_2]_{60}$: $[CaO]_{(29.9)}$- $[CuO]_{0.1}$
G - δ_2 `	$[Bi_2O_3]_{10}$- $[SiO_2]_{60}$: $[CaO]_{(29.8)}$- $[CuO]_{0.2}$
G - δ_3 `	$[Bi_2O_3]_{10}$- $[SiO_2]_{60}$: $[CaO]_{(29.7)}$- $[CuO]_{0.3}$
G - δ_4 `	$[Bi_2O_3]_{10}$- $[SiO_2]_{60}$: $[CaO]_{(29.6)}$- $[CuO]_{0.4}$
G - δ_5 `	$[Bi_2O_3]_{10}$- $[SiO_2]_{60}$: $[CaO]_{(29.5)}$- $[CuO]_{0.5}$

Hitachi DTG-60 H (precision ± 1^OC & range ~ 27 to 1200^OC) was used to record DTA thermograms of existing glass tests. The observed thermo grams of present test samples showed different exothermic peaks at around 980 to 1010^oC. Through the observed analysis, further heat treatment given to the glass tests around 900^oC for 30 hours. Later on the glass tests are permitted to cool steadily to 27^oC. The following chemical composition represents the existing glass ceramic series of samples annealed at 900^0C.

GC - δ_0	$[Bi_2O_3]_{10}$- $[SiO_2]_{60}$:$[CaO]_{(30)}$- $[CuO]_{0.0}$
GC - δ_1	$[Bi_2O_3]_{10}$- $[SiO_2]_{60}$:$[CaO]_{(29.9)}$- $[CuO]_{0.1}$
GC - δ_2	$[Bi_2O_3]_{10}$- $[SiO_2]_{60}$:$[CaO]_{(29.8)}$- $[CuO]_{0.2}$
GC - δ_3	$[Bi_2O_3]_{10}$- $[SiO_2]_{60}$:$[CaO]_{(29.7)}$- $[CuO]_{0.3}$
GC - δ_4	$[Bi_2O_3]_{10}$- $[SiO_2]_{60}$:$[CaO]_{(29.6)}$- $[CuO]_{0.4}$
GC - δ_5	$[Bi_2O_3]_{10}$- $[SiO_2]_{60}$:$[CaO]_{(29.5)}$- $[CuO]_{0.5}$

The subsequent instruments are expended to characterize different measurements of existing both glass and glass ceramic tests. The samples are then optically refined and dimensionally prepared for both elastic (both length & breadth ≥ 1 cm, thick ness ≥ 0.5 cm) and optical (both length & breadth = 1 cm, thick ness = 0.2 cm) measurements. The following instruments are used to record structural, elastic & optical measurements. Scale Tec digital weighing balance (precision ~ 10^{-4} g/cm^3) was used to measure the weight of the present samples .PARAS WT - 311D Ultrasonic flaw detector (precision ~ 1 m/s, range ~ 10^4 m/s) was used to measure ultrasonic velocities.Shimadzu XRD – 7000 (precision ~ 0.1 degree) is used to record X-Ray diffraction. Hitachi S-3700N (precision ~ 0.1 μm & range ~ 1 to 200 μm) was used record SEM & EDS of present samples. Thermoluminiscence measurements are carried out by using Nucleonix TL/OSL Reader (precision ± 1 ^{O}C & range ~ 27 to 500 ^{O}C)and software - MAC OS Version -10.15.1 & MAT Lab 2.3 version were used plot all the figures.

3. Results & Discussion

3. 1. Structural Studies

X-Ray diffraction pattern of sample code GC - δ_3 represented in Fig.1.Observed XRDpattern exhibitingvarious crystalline phases [$CaSiO_3$, $CaSi_3O_7$, $CuBiO_3$, $Cu_2Bi_2O_7$ and $CaCuO_2$] after required heat treatment [7].The EDS of sample code GC - δ_3 represented in Fig 2. Elastic properties ofboth G& GC - δSeries of samples are reported. MH (H) and YM (Y) are also computed. The estimations of 'H'and 'Y' are stretching up with CuO concentration. The figured adaptable results give data about covalently linked structure. DTA traces of prevailingboth G & GC - δseries of samplesof present samplessignified in Fig 3. The values of T_g (glass transition temperature) of both G & GC - δseries of samples are also reported. Thermal stability (T_c– T_g) of both G & GC - δseries of samplesare computed from the DTA spectra [8]. The inset of the Fig.3 represents variation of thermal stability with increase in CuO content. The traces concerning GC - δseries of samples exhibit lower values of forming ability than the G - δseries of samples. The exothermic glass crystallization and endothermic glass transition of both existingboth G & GC - δseries of samples are due to variation in enthalpy. The information concerning all DTA thermo grams of existing bothG & GC - δseries of samples are furnished in Table 1. DTA, SEM & X-Ray diffraction characterization evidently directed that the prepared samples are transformed into glass ceramics after the required heat treatment.SiO_2 is a glass former and its tetrahedrons have a dissimilar in structure which are interlocked from side to side their corner sharing.

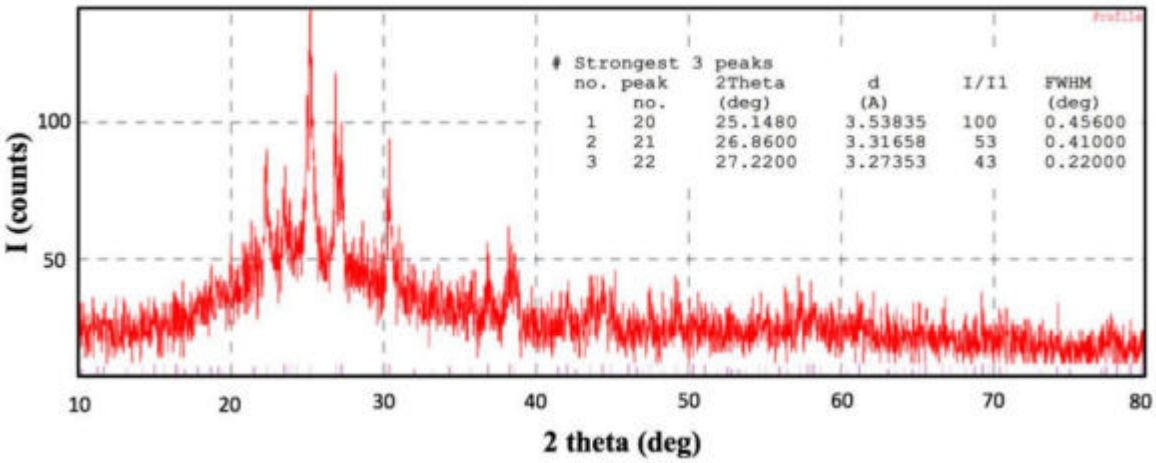

Fig. 1 XRD pattern of GC - δ_3 glass ceramic sample.

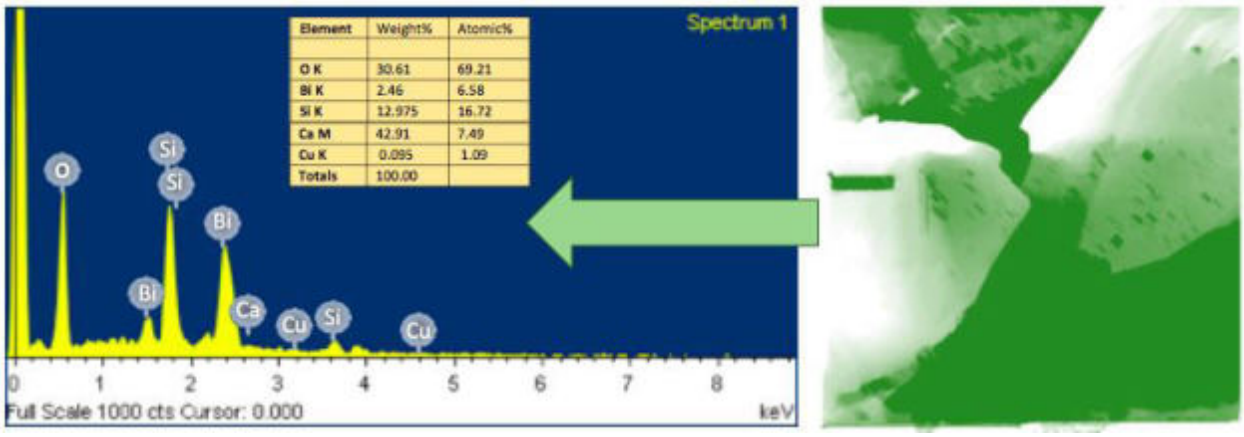

Fig. 2 Energy Dispersion Spectra of the glass samples GC - δ_4 glass ceramic sample.

The thought of Bi_2O_3 into pure SiO_2 will effects in the production of large number of NBO's. Bi_2O_3 is not a straight glass former yet in the event of modernizer like CaO it gets in interaction into the existing materials with BiO_6 (octahedral) and BiO_4 (tetrahedral) constituents. The BiO_4 structural units of Bi_2O_3 involve with silicate tetrahedral bonds with corner allocation, whereas the octahedral BiO_6 ions rule interstitial sites. The octahedral Bi^{3+} ions will effect as modifier like Ca^{2+} and Cu^{2+}ions which are further dependable for the signs of NBO's. In the present glass ceramic materials, the tetrahedral (or) octahedral occupancy of bismuth ions depends on the intensity of Bi_2O_3 with in the glass ceramic network [9].

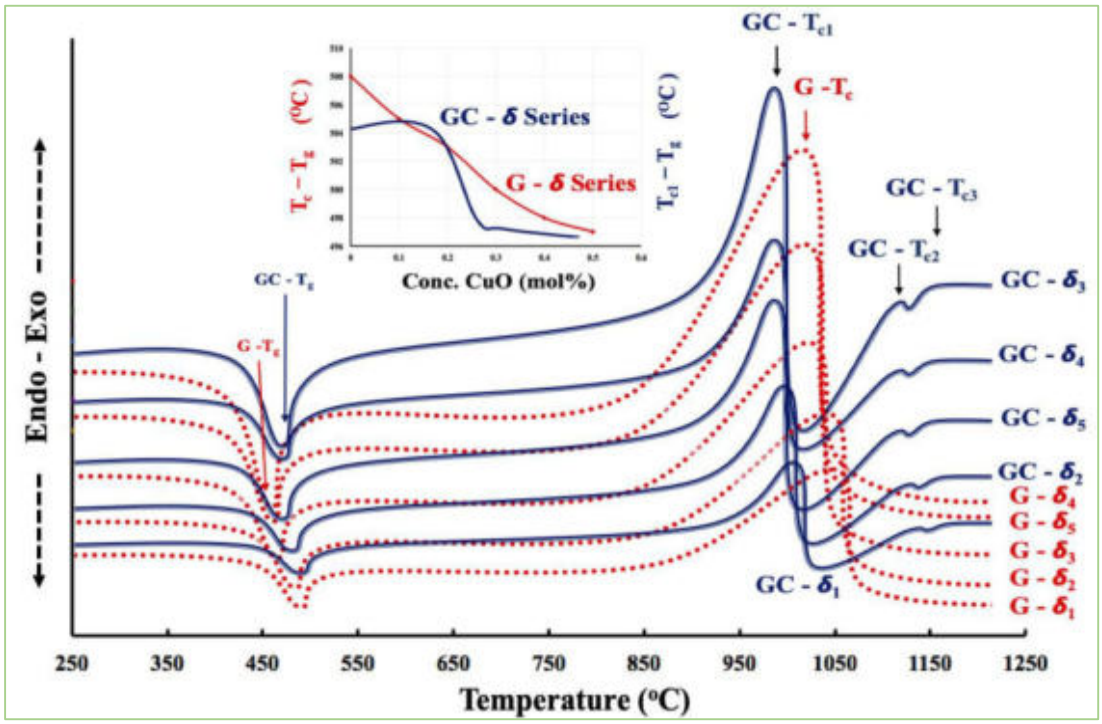

Fig. 3 DTA spectrum of $[Bi_2O_3]_{10}$- $[SiO_2]_{60}$:$[CaO]_{(y-x)}$- $[CuO]_x$ (where 'x' varies from 0.1 to 0.5, y = 30) glass ceramics, Insect represents variation in $T_c - T_g$ with CuO concentration of both G &GC - δ series of samples.

Table 1 Summary on DTA of $[Bi_2O_3]_{10}$ - $[SiO_2]_{60}$:$[CaO]_{(y-x)}$ - $[CuO]_x$ (where 'x' varies from 0.1 to 0.5, y = 30) glass ceramics

Sample	Before heat treatment (Pre-Crystallized State of Samples)					After required heat treatment (Crystallized State of Samples)				
	G - δ_1	G - δ_2	G - δ_3	G - δ_4	G - δ_5	GC - δ_1	GC - δ_2	GC - δ_3	GC - δ_4	GC - δ_5
T_g (^oC)	467	462	457	455	459	469	467	463	464	465
T_{c1} (^oC)	979	973	966	962	969	968	965	957	959	961
T_{c1}-T_g (^oC)	512	511	509	507	510	499	498	494	495	496

Instabilities in the dimensions of the interstitial holes and variation in coordination are causing change in the density of both G & GC - δseries of samples. The viewed temperatures such as both endothermic and exothermic peaks in DTA twists of the both G & GC - δseries of samples are a result of change in enthalpy [10]. For most of the part, the glass materials are supreme stretchable associationsbeneathany kind of glass progress. Generally, the elastic modulus is interrelated to the idea of holding and interatomic dominance. In a few glass materials, Young's modulus advances with in conventionalmagnitude to the atomic density. The expansion in elastic moduli with expanding CuO focus is the replacement of Bi^{3+} by divalent Cu^{2+} which lead to in the increment in covalent bond quality. The extension in atomic density can be authorized to the cumulative certainty and dimensionality of the glass materials are moreover cause increase in the elastic moduli [11].

3. 2 ThermoluminiscenceStudies

Fig. 4(a) and 4(b) signifies the thermoluminiscence spectra of both G & GC - δseries of samples (27 to 300 ^oC temperature range within the time interval of 0 to 30 minutes of γ–irradiation). The observed traces of GC - δseries of samples are exhibiting maximum TL effect comparatively with G - δseries of samples.

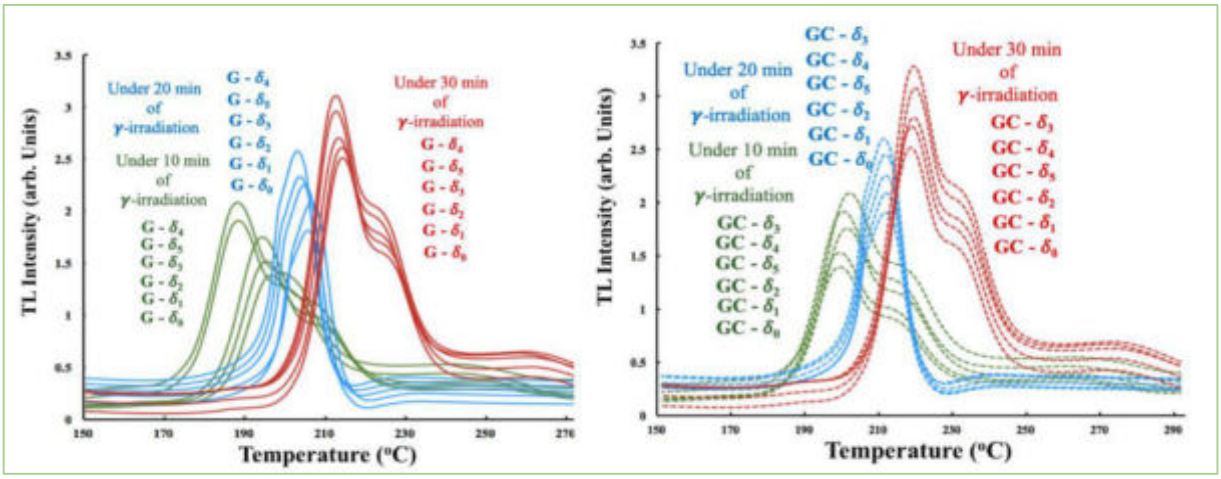

Fig.4 (A) & (B) Thermoluminiscence of $[Bi_2O_3]_{10}$- $[SiO_2]_{60}$:$[CaO]_{(y-x)}$- $[CuO]_x$ (where 'x' varies from 0.1 to 0.5, y = 30) glass ceramics under 0 to 30 min of γ – Irradiation, before (G - δSeries) and after (GC - δ Series) required heat treatment.

The observed glow curves are exhibiting maximum intensity around at 240 ^{o}C with in 30 min of γ -irradiation. The intensities of different peak positions corresponding to GC - δ series of samples shifted considerably towards higher temperature region whereas G - δ series of samples, follows reverse trend. The comparison of all various peak positions report that the significant improvement in TL emission peaks with the affecting of peak positions concerninggreater temperature with variation in CuO concentration. Table.2 represents the trap depth constraints related with the TL emission peaks contrasting with eachthese course of action of present materials are calculated by usual formulae's [12-15].

$E_\tau = C_\tau\left(\frac{KT_m^2}{\tau}\right) - b_\tau(2KT_m)$, $E_\delta = C_\delta\left(\frac{KT_m^2}{\delta}\right) - b_\delta(2KT_m)\&E_\omega = C_\omega\left(\frac{KT_m^2}{\omega}\right) - b_\omega(2KT_m)$;

Where

$\tau = T_m - T_1$, $\delta = T_2 - T_m\&\omega = T_2 - T_1$;

$C_\tau = 1.510 + 3(\mu - 0.42)$,$C_\delta = 0.976 + 7.3\ (\mu - 0.42)\&C_\omega = 2.52 + 10.2(\mu - 0.42)$;

$b_\tau = 1.510 + 3(\mu - 0.42)$, $b_\delta = 0\&b_\omega = 0\&\mu = \frac{\delta}{\omega}$;

T_m – peak temperature maximum

μ_{sf}– symmetry factor

TL studies of γ irradiated both G & GC - δseries of samples reported.The viewed GC - δseries of samples show improved TL emission under 30 min of γ irradiation.

Table 2 Summary on TL measurements of $[Bi_2O_3]_{10}$ - $[SiO_2]_{60}$:$[CaO]_{(y-x)}$ - $[CuO]_x$ (where 'x' varies from 0.1 to 0.5, y = 30) glass ceramics.

radiation dose	Glass	T_m (K)	**τ** (K)	**δ** (K)	**ω** (K)	***u***	E_τ (eV)	E_δ (eV)	E_ω (eV)
Pre-Crystallized State of Samples									
Under 30 min of γ radiation	G - δ_1	483	16.1	13.9	30	0.463	2.061	1.961	2.022
	G - δ_2	481	21.6	19.4	41	0.473	1.641	1.596	1.627
	G - δ_3	479	27.8	24.2	52	0.465	1.169	1.197	1.190
	G - δ_4	475	37.1	34.9	72	0.484	0.777	0.840	0.812
	G - δ_5	477	31.9	27.1	59	0.459	0.974	1.006	0.995
Crystallized State of Samples									
Under 30 min of γ radiation	GC - δ_1	493	22.7	9.3	32	0.29	0.94	0.06	0.69
	GC - δ_2	495	24.3	14.7	39	0.376	1.07	0.94	1.03
	GC - δ_3	497	38.4	12.6	51	0.247	0.37	0.48	0.22
	GC - δ_4	499	38.7	20.3	59	0.344	0.60	0.44	0.54
	GC - δ_5	502	38.3	29.7	68	0.436	0.74	0.79	0.77

With intensification in temperature up to 300^{o}C about the glass tests, there is a little activeness of electrons would initiateimproved thermionic emission. These thermally incited electrons are merging with the key D^+ traps cause TL at high temperature locale.With consistent increment of γ-irradiation upto 30 minutes, the viewed TL light yield under dosimetric apex is growing through and through and the peak viewed is additionally moving towards faintly higher temperature region [16, 17]. TL measurements of both glassy (G - δ_4) and glass ceramic (GC - δ_3) exhibiting good shape symmetry factor {***u*** (G - δ_4 = 0.484 &GC - δ_3 = 0.247)} and low AE's {G - δ_4 (E_τ = 0.777, E_δ = 0.840 & E_ω = 0.812) &GC - δ_3 (E_τ = 0.37, E_δ = 0.48 & E_ω = 0.22)} under 30 min of γ - irradiation might be good TL asset. The relationship between both G & GC - δseries of samples showed that the improvement in the

TL expression of the most critical intensity peak with the moving of apex positions towards higher temperature with change in different content of CuO.

4. Conclusions

For present investigation, we have synthesized $[Bi_2O_3]_{10}$- $[SiO_2]_{60}$:$[CaO]_{(y-x)}$- $[CuO]_x$ (where 'x' varies from 0.1 to 0.5 mol% in step size of 0.1 mol% & y = 30) glass materials and further crystallized them with required heat treatment. Both of the prepared glass (G - δ) and glass ceramic (GC - δ) series of samples characterized by structural andTL, techniques.

Elastic measurements of the samples 'G - δ_4' from glassy series and 'GC - δ_3' from glass ceramic series exhibiting good valuesofmicro hardness (G - δ_4 = 4.03 GPa&GC - δ_3 = 3.99 GPa)are suggesting that the materials prepared are mechanically hard. DTA, SEM & XRD reports evidently suggests that the materials prepared are initially amorphous, after required heat treatment they exhibit crystallinity. The glass forming ability of both G - δ and GC - δ series of samples decreasing with increase in CuO concentration.TL measurements of the samples 'G - δ_4' from glassy series and 'GC - δ_3' from glass ceramic series exhibiting good values of shape symmetry factor {$\boldsymbol{u}$ (G - δ_4 = 0.484 &GC - δ_3 = 0.247)} and low AE's {G - δ_4 (E_τ = 0.777, E_δ = 0.840 & E_ω = 0.812) &GC - δ_3 (E_τ = 0.37, E_δ = 0.48 & E_ω = 0.22)} under 30 min of γ - irradiation might be good TL asset.Based on Structural and TLresults of both G - δ and GC - δ series of samplesadvise that the glass ceramic test (GC - δ_3) might be bestdesirable for TLapplication.

Conflict of Interest: The authors declare that there is no conflict of interests regarding the publication of this paper.

Acknowledgements: The authorsthank SNIST-JNTU Hyderabad, Management for providingfinancial assistance to carry out present research work.

References

1. T. Srikumar et al., Ceram.Int., 2011, **37**, 2763 –2779.
2. S. Ardelean et al., J. Optoelectron. Adv. Mater., 2006, **8**, 1843–1847.
3. E. Cattaruzza et al., Appl. Surf. Sci., 2007, **254**, 1017–1021.
4. B. Sanyal et al., Radiat. Meas., 2010, **45**, 899 – 905.
5. A.Timar-Gabor et al., Appl. Rad. Isotopes., 2011, **69**, 780 – 784
6. O. Edison et al., J. Lumin., 2009, **129**, 657 – 660.
7. B. Karthikeyan et al., Opt. Commun., 2008, **281**, 2933–2937.
8. P.A. Loiko et al., Opt. Spectrosc., 2016, **121**, 497–502.
9. R. Kibar et al., Physica B., 2009, **404**, 105–110.
10. R. F. Bartholomew et al., J. Non-Cryst Solids., 1972, **7**, 221–235.
11. B. Eraiah et al., J. Phys. & Chem., 2010, **71**,153 – 155.
12. H.A.A. Sidek et al., Turk. J. Phys., 2004, **28**, 65 – 69.
13. M. Hamezan et al., J. Appl. Sci., 2006, **6** (4), 943 – 948.
14. B.J.R.S. Swamy et al., Ceram. International., 2014, **40**, 3707 – 3713.
15. A.R. Kadam et al., Ceram.International., 2020, **46**, 132-155
16. R.K Guntu et al., J.Lumin., 2019, **209**, 258-266
17. M.R. Chialanza et al., J. Mater. Sci., 2012, **47**, 2339 – 49.

Fabrication of PLA Based Nuts and Bolts

D. B. Naga Muruga
Dept of Mechanical Engineering, Sriram Engineering College, Tamil Nadu
Corresponding author's email:Nagamuruga403@gmail.com

Abstract
Today manufacturing has become one of the essential necessities for survival of humans. As technologies rise, complex machines and problems in manufacturing also rise. To overcome new methods in manufacturing is used. One such technology is Additive Manufacturing (or) 3D Printing. In this journal, we are going to view about origin and comparison study of Poly Lactic Acid (PLA) in Additive Manufacturing. In further, a product of PLA is Additive Manufactured and implied for tests. The results are cross-checked with standard data of PLA and comparison study of top preferred materials in 3D Printing is also discussed. In further, the advantages, limitations of Additive Manufacturing is also discussed. The upcoming tests to completely verify the PLA material is mentioned clearly. This journal also discusses the current advances of Additive Manufacturing in today's world.
Keywords: Additive Manufacturing, 3D Printing, PLA, ABS, PLA vs ABS, Fabrication and Analysis of PLA based materials.

1. Introduction

Manufacturing is divided into several categories based on necessities. One such category is Additional Manufacturing (or) 3D Printing and Subtractive Manufacturing. Subtractive Manufacturing is traditional manufacturing which is nothing but the removal of materials and its actions. This includes various operations like Drilling, Boring, Chamfering, Knurling, etc and to be collectively called Machining. But in Additive Manufacturing material an object is initially designed in Three Dimensions using modeling software like Creo, Auto CAD, etc. The obtained CAD file is converted into an STL file. This STL file is nothing but a file of CAD is split into thousands of layers with G-Codes. This language is suitable for reading 3D Printers. The G-Codes explains the movement of an extruder for every layer by layer. The extruder on the top end is connected with the Substrate material. In further it is connected with 3 Stepper Motors that reads the G-Codes and moves the extruder with X, Y, Z axes. The substrate material is melted in an extruder and that filament is applied layer by layer upon the bed, by which our material gets Additively Manufactured [1 – 4].

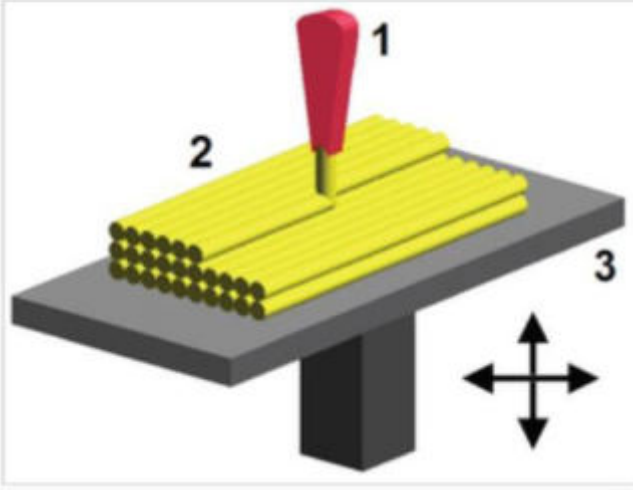

From this method, any complex or dissimilar or small-sized irregular geometrical object can be manufactured. It is mainly used in prototype Manufacturing were to create the actual material without any Subtractive Manufacturing methods. Because the cost of manufacturing only one or two materials in Subtractive Manufacturing will cost higher than Additive Manufacturing.So this method is preferred for Proto Type manufacturing. The Substrate material for Additive Manufacturing includes (PLA, ABS, Nylon, HIPS, PETG, ASA), etc. But top preferred materials are only chosen to study and one material is Additive Manufactured in form of Nuts and Bolts for further Testings and research purposes.

2. Experimental

We wish to study and compare the hardness of PLA and Steel manufactured. So, we designed to Additive Manufacture some pairs of nuts and bolts.

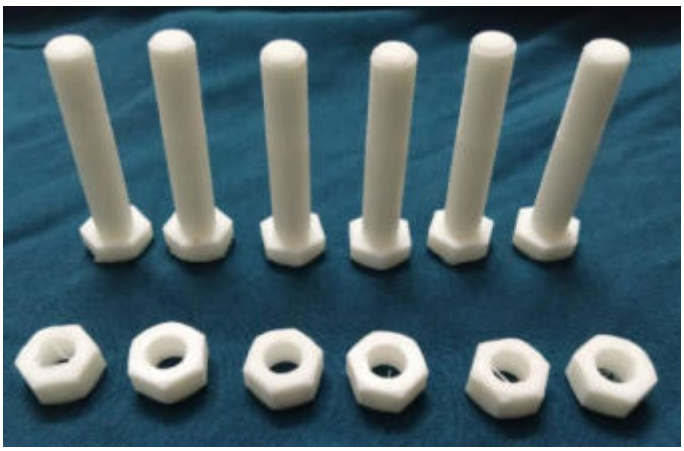

The above image is Additively Manufactured PLA based nuts and bolts. The make charges are Rupees One Thousand Five Hundred. It took nearly 6 days to complete manufacturing from scrap and the printer we used to print is a MAKERBOT type printer. We observed that the nut and bolt physically have good strength and a good hardness surface on nut and bolt. This shows that it will have a good resistance in Tear and Wear. The weight of our nut and bolt is 6gms. We instead of 3D Designing the object downloaded an STL file on the Thingiverse website. (i.e) an open-source website that has thousands of STL files for DIY printers and projects.

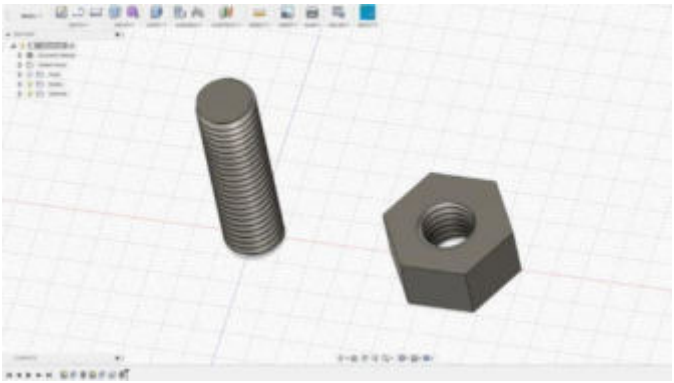

This is the 3D STL file that we chose for Additive Manufacturing. The color of PLA material we chose is White so that we can easily detect any grease or oil leakages. We also tested its

melting temperature to be 205^0 C approximately. We planned to take some comparisons from PLA to Stainless Steel material.

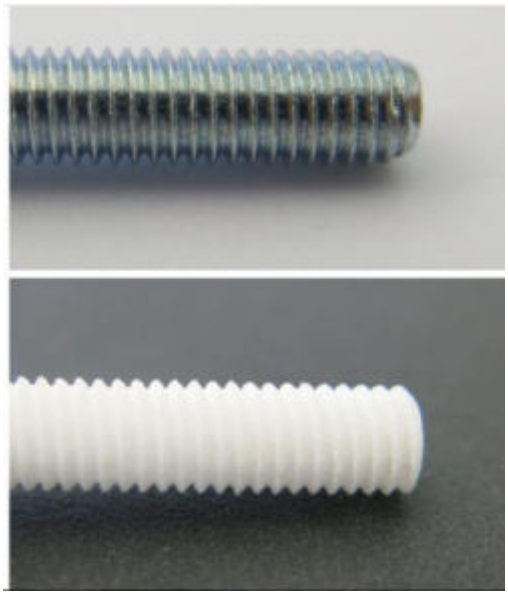

Although PLA could not be used instead of even Mild Steel in industries, as it is degradable. We tried to compare the Hardness values of both PLA and Stainless Steel material.

3. Results and Discussion

We plan to make the Shore Hardness test to our sample and identifies the hardness value of both nuts and bolts. As they gave a good strength output, even still they are biodegradable. So they cannot be replaced instead of Stainless Steel or Mild Steel. We found that our PLA based nut and bolt's properties matched with the standard PLA based Hardness value during Hardness experiments we performed.

Sample obtained to test	**Observed Values**
PLA Nut	76 – 78
PLA Bolt	76 – 78

From the Shore Hardness test, we can identify that in terms of Durometer our PLA comes under the category of SOFT typed. It has given an impact load of 0.822 kg with a resulting force of 8.064 N. Commonly the foot for indentation used will be made from Hardened Steel Rod with a diameter of 1.1 mm to 1.4 mm. Similarly, it also has a truncated cone of 35^0 . The diameter of this ball ranges from 0.79 mm.

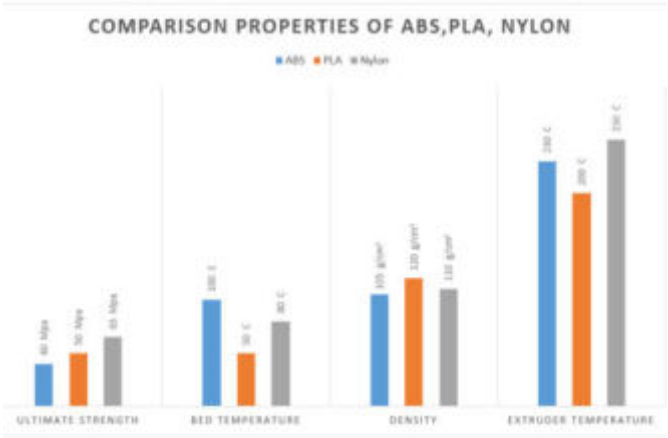

When we observe its degradable properties, we can identify that PLA can be easily decomposed with a time period of 50 days in Industrial Composters and 48 months in water. Where ABS is non-biodegradable, it can only be recycled. So, PLA is preferred in 3D Printing applications that include food, medical industries, etc.

Parametres	PLA	ABS	Nylon
Ultimate Strength	65 Mpa	40 Mpa	40 – 85 Mpa
Stiffness	7.5 / 10	5 / 10	5 / 10
Density	1.24 g/cm^3	1.04 g/cm^3	1.10 g/cm^3
Extruder Temperature	190 – 220^0 C	220 – 250^0 C	220 – 270^{0}C
Durability	4 / 10	8 / 10	10 / 10

4. Conclusions

It is observed that PLA is playing a major role in Additive Manufacturing. Because of its properties, it is used in Food, Medical industries specifically. The fabricated PLA material is implied for testing and the readings are discussed with a comparative study of ABS and Nylon. It is also identified that the nut and bolt we manufactured gave results that are similar to the standard data of PLA records. Further tests are also discussed in this journal. The fabrication analysis has given a complete view of PLA in Additive Manufacturing. We hope that this journal will help in providing deep knowledge of Additive Manufacturing to people who view this.

References

1. Canessa et al., 2013, Lowcost 3D Printing For Science Education Sustainable Development, ISBN – 92-95003-48-9
2. D. Christopher et al., Adventures in 3D Printing
3. H. Smith et al., 2013, Aviation to grow better fuel nozzles using 3D printing.3D Printing News and Trends.,http://3dprintingreviews.blogspot.co.uk/2013/06/ge-aviation-to-grow-better-fuel-nozzles.html
4.H. Smith., 2013, Who is right about 3D printing? Foxconn or GE?3D PrintingNews and Trends.http://3dprintingreviews.blogspot.com/2013/07/who-is-right-about-3d-printing-foxconn.html

Excess Thermodynamic and other Allied Parameters in the Binary Mixtures of N – Propylaminewith Benzyl Benzoate

J.Nageswara Rao[1,4], S.L.SrinivasaRao[2], G.Srinivasa Rao[3]
[1]Department of Physics, Government Degree College, Chintalapudi, W.G.Dist.
[2]Bhavans New Science College, Hyderabad.
[3]Department of Physics, Andhra Loyola College, Vijayawada.
[4]Krishna University, Machilipatnam.
E-mail : schoolofphysics.47@gmail.com

Abstract
Density, viscosity and Ultrasonic velocity have been measured in binary mixture of n-propyl amine with benzyl benzoate at 30^0C and 40^0C. From the measured data, thermodynamic and other allied parameters have been computed and the intermolecular interactions are estimated in the light of the excess parameters. The experimental kinematic viscosity values are correlated with empirical and semi empirical equations Tamura-Kurata (TK), Hind et al (Hind) and Auslaender (Aus). In the mixture of n-propyl amine with Benzyl benzoate Strong AB interactions besides dipole-dipole type interactions are suggested.
Keywords: Binary mixtures, n-propyl amine, Benzyl benzoate, Velocity, Viscosity and Molecular interactions.

1. Introduction
Thermo acoustic, volumetric and viscometric studies are much useful in understanding the molecular interactions in liquids and liquid mixtures. Ultrasonic velocities, densities and viscosities of liquid mixtures are essential in industrial applications. Even though number of binary mixtures have been studied [1 – 8] with at least one component as n-propyl amine or benzyl benzoate, the mixture of these two components not at discussed in ultrasonic study to the best of my knowledge. These two components have much importance in industrially and chemically.

Benzyl benzoate is used as antiparasitic insecticide and as a food additive in artificial flowers. N-propyl amine is used in making textile designs, pesticides and drugs. In which theoretical viscosity equations such as Tamura-Kurata, Hind et al. and Auslaender are compared with experimental viscosities of a binary mixture of Benzyl benzoate with n-propylamine.

2. Experimental
Benzyl benzoate and n-propyl amine are fine grade with accuracy of 99% purchased from Loba Chemicals Private Limited, Mumbai. The ultrasonic velocity was measured using ultrasonic interferometer with frequency 2 MHz supplied by Mittal enterprises, New Delhi with an accuracy of 0.05%. The viscosities of a binary mixture over the entire decomposition range measured with Ostawald viscometer with an accuracy of0.1%. Thedensity has been measured using pycknometer with an accuracy of 2 path in10^5. In this experiment temperature was measured using digital thermometer with least count of 0.1 K. All the instruments are calibrated with double distilled water.

3. Results and discussion

Ultrasonic velocity, density and viscosity of a binary mixture over the entire composition range of n-propyl amine with benzyl benzoate at temperatures 303.15 and 313.15 K at atmospheric pressure. Deviation in isentropic compressibility, excess free length, excess molar volume and deviation in viscosity have been computed using velocity, density andviscosity using the following equations

$$\text{Isentropic compressibility } \kappa s = \frac{1}{\rho u^2}$$

Where ρ is the density of the liquid or liquid mixture and u is the velocity of sound

$$\text{Excess molar volume} V_m^E = \frac{x_1 M_1 + x_2 M_2}{\rho} - \left(\frac{x_1 M_1}{\rho_1} + \frac{x_2 M_2}{\rho_2}\right)$$

The intermolecular free length was calculated using Newton-Laplace equation

$$\text{Inter molecular free length } Lf = \frac{K}{u\rho^{\frac{1}{2}}}$$

Where K is the temperature dependant Jacobson's constant , and $K= (93.875+0.375T) \times 10^{-8}$

$$\text{Excess free length } L_f^E = L_f-(x_1L_{f,1}+x_2L_{f,2})$$

$$\text{Deviation in kinematic viscosity } \Delta\eta = \eta_{mix}-(x_1\eta_1+x_2\eta_2)$$

The experimental viscosity is talliedwith the theoretical viscosity using equations of Hind et al. using following semi empirical equation

The expression for viscosity of binary mixture of Hind et al. is

$$\eta = x_1^2\eta_1+x_2^2\eta_2+2x_1x_2H_{12}$$

Where H_{12} is interaction term

As shown in table 1 and figure 1 ultrasonic velocity, density and viscosity increases with the mole fraction of benzyl benzoate. But decreases with temperature. As shown in figure 2 experiment viscosity tallied with calculated theoretical viscosities such as Tamura-Kurata (TK), Hind et al(Hind) and Auslaender (Aus)using their semi-empirical equations.

The excess molar volume is negative throughout whole composition range. Negative excess molar volume indicates the reduction in volume of a binary mixture than the individual molecules. This shows the formation of hydrogen bond, which is stronger interaction.

The division in isentropic compressibility is also negative over the whole composition range. The negative variation in isentropiccompressibility is due to decrease in free volume in the mixture as compared with the pure components due to rupture of n-propyl amine molecule with the addition of Benzyl benzoate.

Table 1.Experimental values of ultrasonic velocity (u), density (ρ) and kinematic of benzyl benzoate and n-propylamine mixture at 303.15 and 313.15 K

Mole fraction	Ultrasonic Velocity (u/ms^{-1})		Density ($\rho/kg.m^{-3}$)		Kinematic Viscosity (η/mPa.s)	
(X_1)	303.15 K	313.15 K	303.15 K	313.15 K	303.15 K	313.15 K
0.0000	1192.5	1149.4	707.22	697.40	0.3472	0.3125
0.0467	1198.45	1156.85	751.56	743.50	0.7123	0.5825
0.0993	1208.45	1169.15	795.78	788.25	1.1221	0.8719
0.1589	1224.58	1186.52	839.55	832.12	1.5716	1.2159
0.2271	1246.15	1209.25	882.98	875.22	2.0923	1.6112
0.3059	1274.15	1239.05	925.76	917.97	2.6685	2.0655
0.3980	1309.24	1275.89	967.85	960.14	3.3082	2.5665
0.5070	1352.02	1320.85	1008.62	1001.15	4.0153	3.1056
0.6381	1402.25	1372.52	1047.75	1040.57	4.7855	3.6785
0.7987	1452.89	1426.06	1084.59	1077.65	5.5921	4.2656
1.0000	1506.899	1471.44	1119.35	1109.75	6.5325	5.0211

Table 2.Experimental and calculated values of kinematic viscosity of Tamura-Kurata (TK), Hind et al(Hind) and Auslaender (Aus) for the binary mixtures of benzyl benzoate with n-propylamine mixture at 303.15, 313.15 and 323.15 K in mPa. s

Mole fraction x_1	Exp	TK	Hind	Aus	Exp	TK	Hind	Aus
	303.15 K				313.15 K			
0.0000	0.3472	0.3472	0.3472	0.3472	0.3125	0.3125	0.3125	0.3125
0.0467	0.7123	0.7389	0.7219	0.7211	0.5825	0.6029	0.5918	0.5793
0.0993	1.1221	1.1559	1.1341	1.1315	0.8719	0.9129	0.8990	0.8817
0.1589	1.5716	1.6025	1.5882	1.5833	1.2159	1.2464	1.2381	1.2242
0.2271	2.0923	2.0857	2.0909	2.0839	1.6112	1.6092	1.6147	1.6126
0.3059	2.6685	2.6141	2.6495	2.6416	2.0655	2.0081	2.0344	2.0523
0.3980	3.3082	3.1991	3.2719	3.2668	2.5665	2.4521	2.5041	2.5475
0.5070	4.0153	3.8560	3.9662	3.9719	3.1056	2.9534	3.0310	3.0997
0.6381	4.7855	4.6070	4.7404	4.7737	3.6785	3.5298	3.6230	3.7061
0.7987	5.5921	5.4834	5.5984	5.6917	4.2656	4.2063	4.2862	4.3548
1.0000	6.5325	6.5325	6.5325	6.5325	5.0211	5.0211	5.0211	5.0211

Table 3. Excess molar volume (V_m^E) , excess free length (L_f^E), excess compressibility (ΔK_s) and excess viscosity ($\Delta\eta$) of benzyl benzoate and n-propylamine mixture at 303.15, and 313.15 K

Mole fraction x_1	Excess molar volume ($V_m^E/10^{-6}$ m^3mole^{-1})		excess free length (L_f^E/ Å)		Variation In isentropic compressibility (Δk_s /10^{-10} Pa^{-1})		Variation in kinematic viscosity ($\Delta\eta$/ mPa. s)	
	303.15 K	313.15 K	303.15 K	313.15 K	303.15 K	313.15 K	303.15 K	313.15 K
0.0000	0.000	0.000	0.000	0.000	0.000	0.000	0.000	0.000
0.0467	-0.367	-0.610	-0.266	-0.446	-0.078	-0.134	0.076	0.050
0.0993	-0.722	-1.053	-0.479	-0.806	-0.136	-0.234	0.161	0.091
0.1589	-1.039	-1.402	-0.723	-1.110	-0.198	-0.310	0.242	0.155
0.2271	-1.331	-1.671	-0.940	-1.358	-0.247	-0.363	0.340	0.229
0.3059	-1.565	-1.913	-1.136	-1.612	-0.285	-0.412	0.430	0.313
0.3980	-1.736	-2.101	-1.295	-1.810	-0.310	-0.441	0.499	0.380
0.5070	-1.759	-2.159	-1.376	-1.925	-0.313	-0.444	0.532	0.406
0.6381	-1.562	-2.002	-1.310	-1.830	-0.282	-0.399	0.492	0.362
0.7987	-1.000	-1.470	-0.823	-1.307	-0.167	-0.268	0.304	0.193
1.0000	0.000	0.000	0.000	0.000	0.000	0.000	0.000	0.000

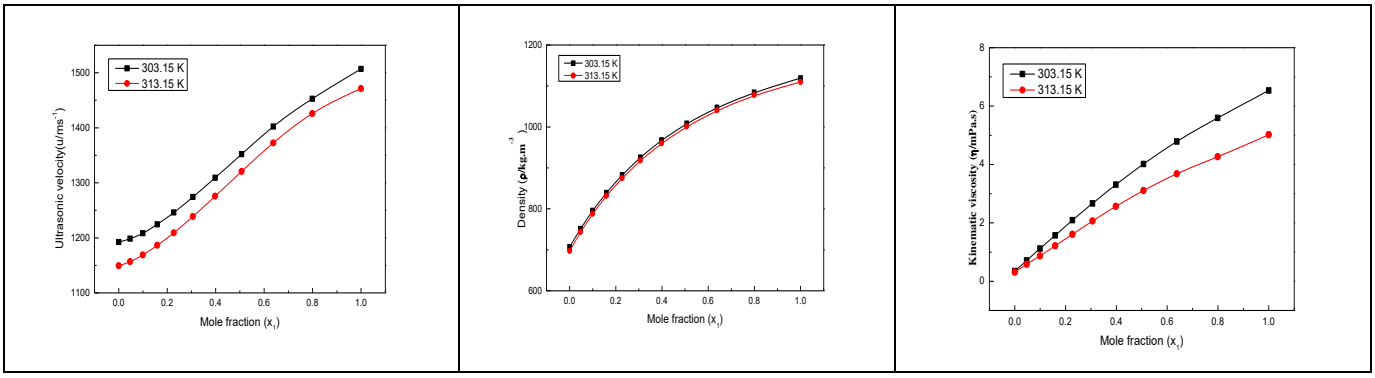

Fig.1 . Ultrasonic viscosity, density and kinematic viscosity of a binary mixture of n-propylamine with benzyl benzoate

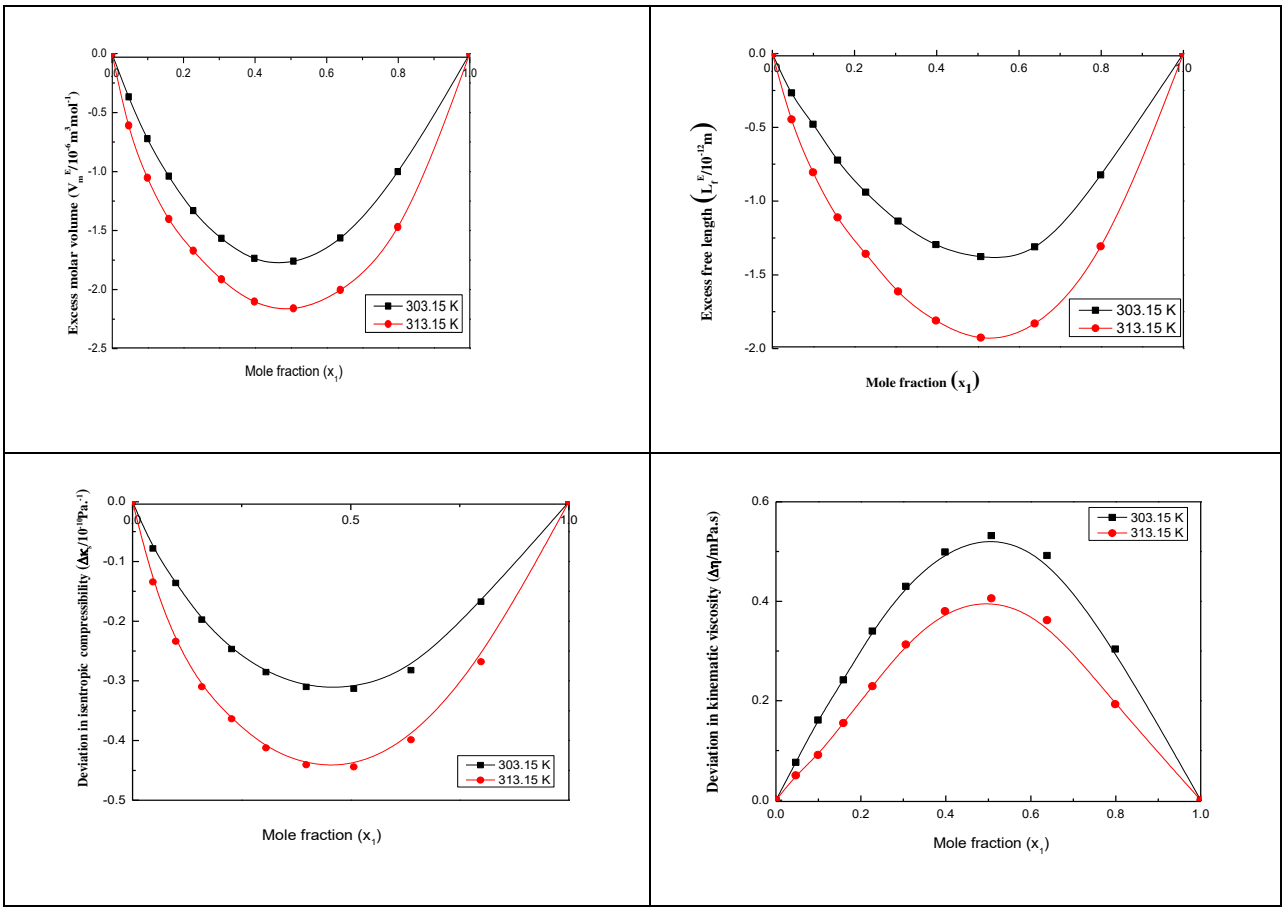

Fig.2. Excess molar volume, excess free length, deviation in isentropic compressibility and deviation kinematic viscosity of a binary mixture of n-propylamine with benzyl benzoate

The excess value of free length is also negative in the binary mixture of n-propyl amine with benzyl benzoate at temperature303.15 and313.015 K over the entire composition range.
But the deviation in viscosity is positive over the whole composition range in this binary mixture at temperatures 303.15 and 3.15K. The positive values of deviation in viscosity shows the specific interaction between unlike components such as dipole-dipole interaction or hydrogen bonding or charged transfer complex.

When temperature increases excess molar volume, Access free length and deviation inisentropic compressibility increases, but in deviation of viscosity decreases.All this predicts the strong molecular interactions between unlike molecules in a given binary mixture of n-propyl amine with benzyl benzoate.

4. Conclusion

Ultrasonic velocity, density and viscosity have been measured in pure and binary mixture of n-propyl amine and benzyl benzoate at temperatures303.15 and 313.15 K over the entire composition range. Calculatedexcess or deviated parameters using experimental values of velocity, density and viscosity.Using these excess parameters it is predicted strong molecular

interactions between unlike molecules of n-propyl amine and benzyl benzoate binary mixture. When temperature increases the strength of molecular interaction is also increases.

References

1. N. Jaya madhuri et al., E-Journal of Chemistry., 2011, **8** (1), 457-469.
2. Sk. MdNayeem et al., Journal of Thermodynamics., 2014, **2014**, ID 487403,1-13.
3. P. Ramesh et al., Invertis.J. Sci&Technol., 2011, **4** (1), 14-30.
4. Sk. MdNayeem et al., J. Mole. Liq., 2016, **218** (2016), 676–685.
5. A. Nagarjuna et al., Materials Today: Proceedings., 2018, **5**, 26322–26328.
6. Deepti Gupta et al., Asian Journal of Chemistry., 2008, **20**(6), 4234-4238.
7. A. Shakila et al., J. Mole. Liq., 2019, **285**, 279–287.
8. P Murali Krishna et al., Ind. J. Pure & Appl. Phys., 2009, **47**, 576-581.

Experimental Study on Mechanical Properties of AA7075, Al_2O_3 and Graphite Metal Matrix Composite

Mr. Ch. Naveen Reddy*, Mr. L. Sandeep Raj, Mr.GouravTiwari
Assistant Professor, VNR VignanaJyothi Institute of Engineering and Technology
Corresponding authors email: chnaveenreddy316@gmail.com

Abstract
Aluminum alloys are extensively used in very large number of applications including automobiles, aerospace and defense industries due to the concept of its high strength to low weight ratio. In this study, Aluminium alloy 7075 is chosen as specimen to examine the various mechanical properties after alloying. The aluminium metal matrix composite has been fabricated by using stir-casting technique at a temperature of 850 °C. TheAA7075 (Aluminium Alloy 7075) is strengthened with Al_2O_3(Alumina) and graphite particles. These particles were included into aluminium alloy to improve its properties. Two different compositions of specimens were made. One composition is of Al-7075, added with graphite (2.5 wt.%) and 5 wt.% of Al_2O_3. And the other with Al-7075, 5 wt.% of Al_2O_3. With these compositions of specimens determine the Impact, Hardnessand Tensile properties. Upon addition of alumina, the tensile strength of the materialincreased by 11% and the impact strength of the material increased by 15% compared to base material. Upon addition of graphite, the hardness decreased but it is 1% greater than the base material and the impact strength is equal to that of the base material. Due to casting defects and irregular distribution of particles, the tensile strength of the material decreased.
Keywords*:*Aluminium metal matrix composite, graphite particles, Mechanical Properties, Casting defects

1. Introduction
Most of the components that are used today are made up of alloys due to their improved mechanical properties. Even the metals such as steels are replaced by metals like aluminium as aluminium alloys provide strength as that of steel and also are lighter than steels. The mostly used materials are aluminium alloys and other metal alloys depending upon the requirement. There are many applications of aluminium alloys. Aluminium alloys are most widely used in aircraft industry. Among all the alloys of aluminium, AA7075 has almost the strength of steel. Baradeswaran and Elaya [1] have prepared the Aluminium metal matrix by stir casting technique. AA 7075taken as the base material and various percentages of graphite particles (i.e in 5, 10, 15and 20 weight percentages) were added into molten metal. Wear test, hardness and flexural strength were conducted. The hardness of the material keeps on decreasing with increase in graphite content and this is less significant at 5% (by weight) of graphite. The flexural strength reduces with increasing graphite and this effect was less at 5% (by weight) of graphite. Baradeswaran and Elaya [2] have investigated the influence of graphite on the wear behavior of Al 7075/Al_2O_3/5 wt.% graphite hybrid composite.The Al 7075/Al2O3/graphite hybrid composite was prepared with 5 wt.% graphite particles addition and 2, 4, 6 and 8 wt.% of Al2O3. The hardness, tensile strength, flexural strength and compression strength of the Al 7075–Al_2O_3–graphite hybrid composites are found to be increased by increased weight percentage of ceramic phase. Anandbabu and Deeapkkumar[3] has investigated that particulate reinforcements are predominantly added to the Al7075 Alloy for improving its properties and as a result the properties are altered when it is subjected to reinforcement. Mohanavela and Rajan [4] have fabricated aluminium metal matrix composite with varying mass fraction of graphite particulates by using stir casting technique. AA6351 was taken as base material. The variation of graphite composition was from 0% to 12% in a

stage of 4%. Tensile test and hardness was performed.After study of few research papers, it is noted that upon addition of Aluminium oxide and Graphite up to certain percentages, the flexural strength, and compression strength of the MMC (metal matrixcomposite) have been increased.The material exhibited superior wear properties. So as to study the mechanical properties of the material at different percentage composition, this project is carried out.

2. Materials and Methods

The test material selected is an aluminium alloy. It is a 7^{th} series aluminium alloy whose primary alloying element is zinc (5% to 6% by weight). Among all the 7^{th} series alloys, this alloy i.e AA7075 has strength almost equal to that of steel. It has lower resistance to corrosion than many other aluminium alloys but has remarkably better corrosion resistance than the 2000 alloys. The major application part of this alloy is in aircraft industry. AA7075 is less corrosive resistant. To enhance the corrosive resistance of the alloy, Aluminium oxide is added. It is quite difficult in machining, the alloy. It shows poor to average machinability properties. To enhance the machinability of the alloy, graphite is added which is a dry lubricant. Aluminium oxide: It is also called as alumina. It is mostly used to produce aluminium metal. As it is hard, it acts as an abrasive. Due to its high melting point temperature, it can also be used as a refractory. Graphite:It is a naturally occurring form of carbon. It is extremely soft and has a low specific gravity.

3. Results and Discussions

The hardness tests were carried out according to ASTM E-10-07 standards using Brinell hardness testing machine with a 10 mm ball indenter and 500 kg load for 30 s. The test was conducted at room temperature (30°C) and the measurement of hardness was taken at five different places on each sample to obtain an average value of hardness.As per the ASTM E-08-8 standard, the tensile strength was evaluated on the cylindrical rod of casted composites. Charpy V-notch test were carried out according to ASTM E-23 is a standardized high strain rate test which determines the amount of energy absorbed by a specimen during fracture.Mechanical properties of fabricated metal matrix composites as summarized in the table 1.The comparative charts for Impact Strength, Hardness and Tensile Strength of Fabricated Metal Matrix Composites are presented in fig. 1

Table 1 : Mechanical Properties of Fabricated Metal Matrix Composites

Composition	Tensile Strength (MPa)	Hardness	Impact Strength (J/mm^2)
Al7075	220	60	0.13
Al7075+Al2O3	195.32	67	0.15
Al7075+Al2O3+ Graphite	202.41	61	0.12

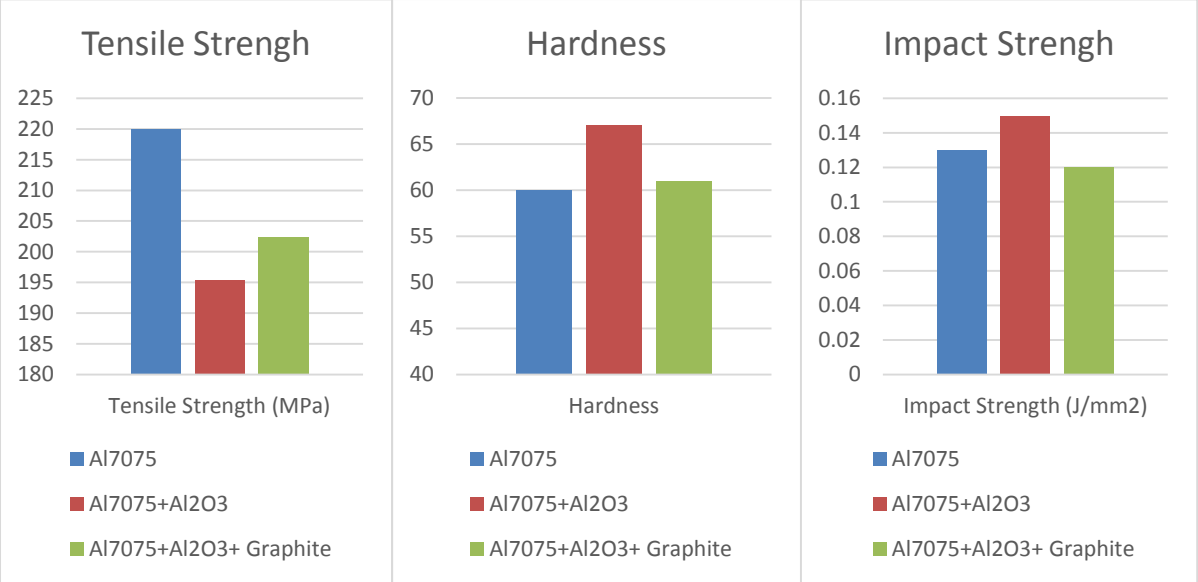

Fig.1 Impact Strength, Hardness and Tensile Strength of Fabricated Metal Matrix Composites

4. Conclusions

The effect of Al_2O_3 and graphite addition on the hardness of the hybrid composites results in the increased with increasing Al_2O_3 ceramic particulates. The tensile strength of AA 7075 is 220MPa. But due to the casting voids, and coagulation of particles the obtained strength values are less than the base materials. Upon addition of alumina to the base material, the tensile strength of the material reduced by 11%, and upon addition of graphite, the strength increased by 3% when compared to the alumina mixed with AA7075. When compared to base material, the strength decreased by 8%.

The impact strength of AA7075 is 0.13J and the toughness is about 0.0035J/mm3. Upon addition of Alumina, the impact strength increased by 15% compared to base material. Upon addition of Graphite, the impact strength of the specimen is almost equal to that of the base material.

The hardness value of AA7075 is 60 HRB. In Rockwell Hardness test, upon the addition of Alumina, the hardness of the alloy increased by 11%. Upon addition of graphite, the hardness of the material decreased by 8% when compared to the composition mixed with alumina i.e AA7075+Alumina as graphite has HCP structure. The hardness of the alloy combined with graphite, is 1% greater than the base material.

References

1. A. Baradeswaran et al., Composites Part B: Engineering., 2014, **56**,472-476.
2. A. Baradeswaran et al., Composites Part B: Engineering., 2014, **56**, 464-471.
3. S. S.Anandbabu et al., International Conference on Systems, Science, Control, Communication, Engineering and Technology 2016 [ICSSCCET 2016].
4. Mohanavela et al., Materials Today: Proceedings., 2018, **5** (1), 2945-2950.

Removal of corrosion and passivation of iron using cooking material as the electrolyte

Asma S. Al-Namaani, Pradeepkumar Krishnan*
*Mechanical and Industrial Engineering, National University for Science and Technology**
Corresponding author's email: pradeepkrishnan@nu.edu.om

Abstract
In nowadays, the institutions of water control either desalination companies, water distribution companies, or even water treatment companies spend huge sums which are specified to maintenance to aim repair or replace the rusted part produced from the corrosion problem. For this purpose, there is an increasing demand for metals treatment methods used recovering rusted pieces working hand to hand with traditional corrosion control methods. Electrolysis cleaning is one from featured methods that have high efficacy in removing the rusted iron and recovering rusted pieces with less number of residues generated at low cost. This study aims to study the abilities of cooking material when it used as an electrolyte of the electrolysis cell in the removal of rust iron from the submersible pump component. That done by fabrication of electrolysis cell by use cubic glass container, cylindrical iron, and stainless steel electrodes as anodes, five types of cooking material electrolyte, and electrical circuit with the electrical current regulator and by the help of support equipment such as measuring devices and fixation tools. The types of electrolytes, types of anodes, temperature, concentration, and current intensity, control the electrolysis cleaning process. The experiment applied by used to identify desired value and the main result was obtained is the saltwater is the best of electrolytes tested in the removal the rust, Stainless steel the best anodes tested, 50w/v the best concentration tested,40C best temperature tested and 3A best electrical current tested. The command application of electrolysis cleaning in metal industrial and metal recycle companies.
Keywords: Electrolysis, Anodes, Concentration, Stainless Steel, Iron, Treatment

1. Introduction
The corrosion problem and passive iron are some of the common problems for all human sectors due increase using metal because of its likable features of it, which is make it's used everywhere. The corrosion problem takes attention everywhere metal used although of the corrosion problem produce from effects by other liquid or gas in metal. The institutions of water control either desalination companies, water distribution companies, or even water treatment companies, for example, the problem occurs especially with the component that which it with direct contact with liquid such as a pump in general and in submersible pump in specific. This type of pump used in these companies used significantly in different applications such as pumped water from well, lake, and use in water overflow protective system. This type of pump has an old history with rust and corrosion problems that occur in a submersible pump which is from type centrifugal outfitted with an electrical engine that can work sunken under the fluid and the engine, for the most part, occupies the under part of the pump. The cup(cover) of the submarine pump is fabricated by using cast iron which regular rusted due to present iron parts like casing, cover packaging, and impeller of the submersible pump .This sort of cleaning commonly use utilized in the metal industry to evacuate contaminants clung to metal surfaces. The Objective of work To removal rust iron from iron part of submersible pump to reuse it and increase lifetime of pump with reduce the cost of replace or cost other method of treatment [1 – 9].

2. Experimental

The components of fabrication electrolysis cell are glass containers with the specification with dimension 344mm length, 344mm width 194mm height, 6mm thickness of the glass and it has in each corner 2 pores with 5mm diameter to aim to connect the container an electrical circuit. The four anodes used has a cylindrical tube shape from iron and stainless steel. The electrical circuit consists of an ammeter, current regulator, switch, and wire with used another support equipment such as fixation wood, level measuring roller, electrolyte preparation equipment, and measuring devices such as weight balance and thermometer. The fabrication of an experiment done by fixation the anodes in four corners of container and fixation the material to be treated in the center of container with the help of fixation wood. The anodes connect by the wire with an ammeter and electrical switch to the positive side of the current regulator and the material to be treatment connected to the negative side of the electrical current regulator. The fabrication of electrolysis cell The electrolysis cleaning is carried out by place the anodes to be studied iron or stainless steel in corner of a container and catholic material to be cleaned was installed in the center of the container by used fixation wood with knowing the initial weight of material to be cleaned, then both of anodes and cathodes were immersed in an electrolytic solution. The electrolyte solution used is made from five types of cooking material with a variable concentration and connected to a power source with the variable current intensity. The five parameters, which were studied to provide the optimum cleaning results, were the concentration of the electrolyte, Type of electrolyte, type of anodes material, temperature, and the current intensity. For each variable selected five-level were tested. Initially, the experiment is run to identify the best type of electrolyte than by using a best electrolyte, the concentration variable is studied, Next, by using the best electrolyte and the best concentration, the temperature is studied and then-current intensity is studied. The type of anodes is studied with all repetition of the experiment. The kind of electrolyte utilized saltwater, lemons juice, potato juice, preparing pop, and vinegar. The focus fluctuated from 20%,30%,50,60%, and 75%. Current power: shifted from3 Amperes, 2.5 Ampere, 2Ampere1.5Ampere and 1 Ampere. The temperature shifted from 20°C,25 °C,30ºC, 35°C and 40 ºC. The treatment time recorded for all redundancy.

3. Results and Discussion

The studying parameter was done in 25 days. Each variable studied separately except the type of anodes and to ensure the accurate result the experiment was recur for a single variable more one time. The time of the studied parameter is fixed within 60 minutes as a constant variable and according to the result of the previous parameter, the studied is set. The result collected for each variable as following

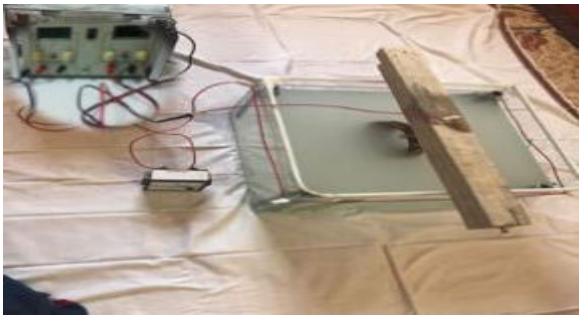

Figure 1: Fabrication o electrolysis cell experiment

1. Type of electrolyte

The type of electrolyte used in the electrolysis cell has a direct effect in in the amount of cleaning where was used different types of cooking material where was selected contingent to dependent on its notional ability in transmission electron when electrical current passing through it. The main reason for its electrical conductivity back to it has the aptitude to break down in water to the positive and negative charge due to the ionic component of its structure what makes it a different degree of conductive materials .The result obtained is showing in below tables and figure Figure 3 and Figure 4 hows the result of testing five kind electrolytes of cooking material of electrolysis cell with iron tubes or stainless steel as anodes of the cell where the result obtained from testing of different type electrolytes were saltwater was the best electrolyte in

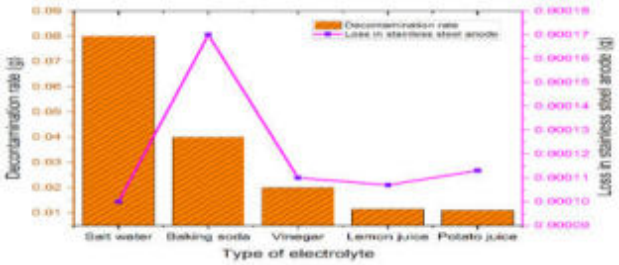

Figure 2: Study Type of electrolyte with Stainless Steel anodes

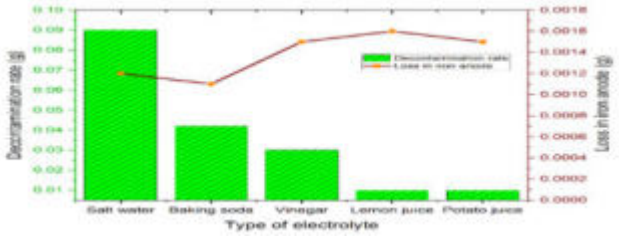

Figure 3: Study Type of electrolyte with Iron anodes

removing the rust frommaterial within the value 0.09g when test with iron anodes and 0.08g when test with stainless steel anodes. The cooking materials arrange dependent on its ability to remove rust as following salt water, baking soda, vinegar, lemon juice, and potato juice where was observed less amount of removal with potato juice within value 0.01g when test with iron anodes and 0.011g when test with stainless steel anodes .by potato juice, vinegar lemon juice, and saltwater was the saltwater show less measure of loss in anodes.

3.2. Concentration of electrolyte

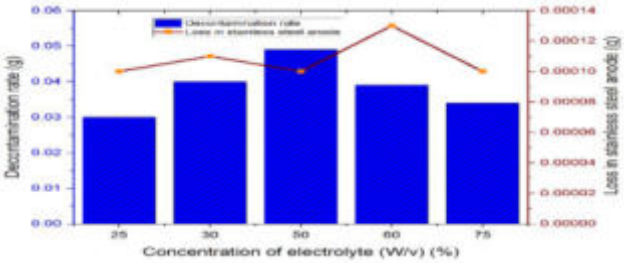

Figure 5: Study Concentration with Stainless Steel anodes

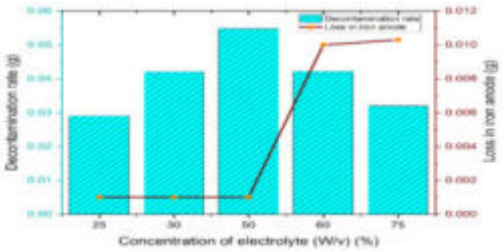

Figure 4: Study Concentration with Iron anodes

The concentration of electrolyte used in electrolysis cleaning was considered ones from important parameters that have highly effective in the quantity of rust removal where it was with the change of concentration of electrolyte the number of ions present in electrolyte increases or decreases dependent to that change. To study that variable was selected the best electrolyte in removing rust from the first repetition of the experiment which was saltwater. The result obtained is showing in below tables and figure. Figure 5 and Figure 6 show the result of the test five values of concentration with used iron anodes in and stainless steel anodes where it was the result of the test shows the concentration of 50% is the best concentration in iron rust removal of from material to be cleaning which was removed around 0.0548g with iron anodes and around 0.049g with stainless steel anodes. The normal arrangement of concentration, the amount of removal increase with the increased value of concentration until reach to 50% w/v which was concede as optimum concentration than the value of removal decrease with increasing concentration. The arrangement of concentration descending in the amount of removal 50% highest most decontamination rate in cleaning rate(g)then 60%,30%,75% and 25%.

3.3 Temperature change

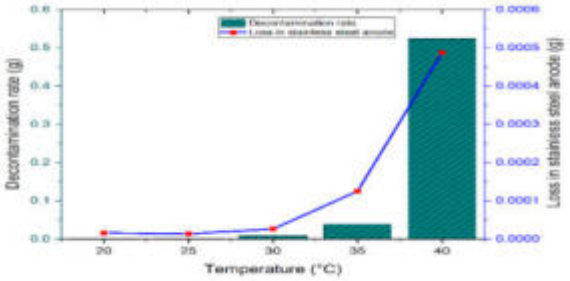

Figure 6: Study temperature effect with Stainless Steel anodes

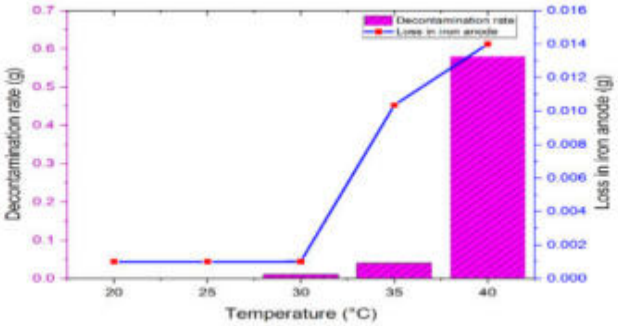

Figure 7: Study temperature effect with iron anodes

The temperature is a variable that was studied due to its theory effect in the amount of removal of rust from iron material where theoretically there is for each treatment material optimum value of removal. As indicated by the outcome from the first and second repetitions of the experiment, saltwater with 50% (w/v) concentration was used for studied temperature variables. The result obtained is showing in below tables and figures . Figure 7 and Figure 8 showing the result of testing the five values of temperature within iron anodes in Table 5 and stainless steel anodes with Table 6 where rust obtained was the maximum amount of removal rust within temperature 40 °C around 0.058g within iron anodes and 0.0524 g then 35°C 30,25°C and 20°C respectively where 20°C shows the lower estimation of removal rate with range 0.002g within iron anodes and 0.001g with stainless steel anodes. The relation between the temperature and measured value of rust removal rate was an immediate relationship where is by increasing temperature, the values of rust removal rate increase.

3.4 Type of anodes

The types of anodes used in electrolysis cleaning have direct effect in electrolysis cleaning were the result of testing two types of anodes iron and stainless steel of electrolysis cell .The result obtained the iron anodes are the best anodes in removal rust compare iron anodes but the amount of loss iron anodes very large compare stainless steel which makes stainless steel anodes more economical save but it required stronger procedure of safety to avoid toxic production.

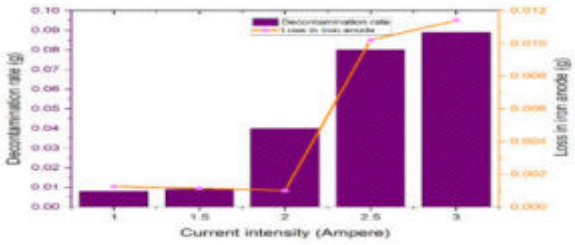

Figure 8:study current intensity with iron anodes

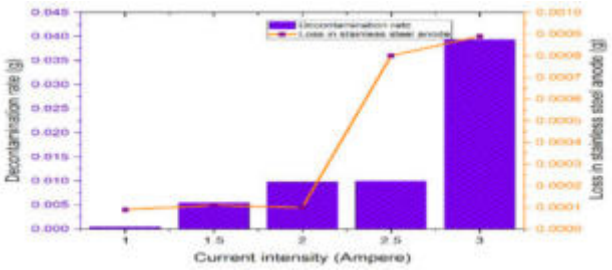

Figure 9: study current intensity with Stainless Steel anodes

3.5 Current intensity

The electrical current intensity is referred to as the amount of electrical current passes through the circuit in unit of time where is considered one from the parameter effect in electrolysis cleaning. According to first, the second and third repetitions of the experiment to studied electrical intensity parameter used saltwater with concentration 50%(w/v) and 40 °C temperature. The result obtained is showing in below tables and figure. Figure 9 and Figure 10 shows the result of testing five values of current intensity where the result obtained shows the maximum value of removal found with 3A value within 0.089g within iron anodes and 0.0394g with stainless steel anodes and then 2.5,2,1.5 and 1which has obtained the minimum amount of removal with 1 A with value 0.008 g with iron anodes 0.0005 g with stainless steel anodes which mean increase current intensity will causing increase amount of rust removal

4. Conclusions

In conclusion, The variable most effective in the decontamination rate of rust iron removal was the temperature which provided highly affected in the decontamination rate in the experiment carried out but additional experiments are recommended to evaluate the efficiency of using the higher temperature from 40°C to evaluate its an effect in removing rust and investigation from the relation between temperature and decontamination rate. Moreover, the availability of temperature 40°C, current intensity 3Ampere , electrolyte concentration 50(w/v) saltwater electrolyte, and iron anodes at the same time producing in the maximum amount of rust removal and best values in electrolysis cleaning to remove rust. In addition, using stainless steel anodes is more economical but it using requiring a high level of safety procedure. All values from all repetitions of the experiment were obtained values to measure in one hour so there are extra recommended by increase time of electrolysis to studied the time consumed in cleaning all cover of the submersible pump. The experiment was studied the five common variables which may affect in electrolysis cleaning but the other parameter such as pressure , the distance between anodes and cathodes , effect shape of the container in transfer electrons and relation of another electrolyte with the various variable is not studied which it may be studied it in future.

5. Acknowledgement

The authors thank the National University of Science and Technology, Sultanate of Oman for providing support through analytical facilities and equipment.

References

1. S. Urréjola et al., European Journal of Sustainable Development., 2016, **5(3)**, 197-206.
2. B. Rani and B. Basu, International Journal of Corrosion, 2011, **2012**, Article ID 380217, 1-15, doi:10.1155/2012/3802172012.

3. R. Rosliza., Improvement of Corrosion Resistance of Aluminium Alloy by Natural Products (Chapter), 2012, DOI: 10.5772/32952.
4. T.Runyan and M.Herrmann, J. Chem. Educ., 1993, **70 (10)**, 843-852
5. I.Chaves et al., Corrosion, 2015, **71(7)**, 811-818.
6. Y. Cheng et al., Journal of Materials Science, 2010, **45**, 562–565.
7. J. Alcantara., Materials, 2017, **10(4)**, 406, doi:10.3390/ma10040406
8. D. Davial and G.Burstein, Corrosion, 1980, **36(8)**, 416-422.
9. V. Duradjiz and K.Kaputki, J. Electrochem. Soc., 2016, **163**, E43–E48.

Soft Magnetic Properties of Fe-based Bulk Metallic Glass System Containing Niobium and Copper

Ch. Anjaneyulu[a*], B.S. Murty[b]
[a]Department of Physics, Bapatla Engineering College, Bapatla, India
[b]Department of Metallurgical & Materials Engineering, Indian Institute of Technology Madras, Chennai, 600036, India
***Corresponding author's email: chanjaneyulu9@gmail.com**

Abstract:
The alloy ingots with three different nominal compositions were prepared and investigated with SEM, XRD technique. BMG rods were then prepared by conventional suction casting through copper mould [1-2]. The XRD pattern of glassy rods exhibit few crystalline phases in all the alloy samples. The suppression of crystalline peaks to a reasonable extent is evident from respective XRD pattern of amorphous rods. Good extent of GFA was achieved with three alloy samples. However the GFA of Fe_1 sample is better than remaining two, but its saturation magnetisation is very poor. Fe_3 sample give better saturation magnetisation I_s and its GFA is moderate. Good GFA of Fe_1 sample correlates with higher squareness ratio of the same. The Percentage relative change of density and squareness ratio have same trend of variations. However these three samples exhibit very low squareness ratio. The magnetic properties of Fe_4 sample were intermediate between Fe_1 and Fe_3 samples. Hysteresis loss is found to be least for Fe_1 sample. Hence low Hysteresis loss and good GFA were correlated during this study. It was also observed that saturation magnetisation is high for the sample containing 3mol% of Nb.
Key words: GFA, Hysteresis Loss, Squareness ratio, Percentage relative change of density.

1. Introduction

Bulk metallic glasses (BMGs) are relatively new materials possessing a glassy structure. The critical cooling rate to produce BMGs is around 10^5 to 10^6 Ks^{-1}. These materials have an exciting combination of properties such as high mechanical strength, good thermal stability, large supercooled liquid region, low corrosion and potential for easy forming. The chief use of BMGs were obtained from their increased corrosion resistance, wear resistance and reduced eddy current losses in ferromagnetic ribbons as compared to the crystalline alloys of identical compositions[1-4]. The alloy compositions (with respective codes in bracket) supposed to study for present project are given as follows,

1. $[(Fe_{75}\text{-}Co_{10}\text{-}Ni_{15})_{70}\text{-}Zr_{10}\text{-}B_{20}]_{96}\text{-}Nb_3\text{-}Cu_1$ (Fe_1)
2. $[(Fe_{70}\text{-}Co_{10}\text{-}Ni_{20})_{70}\text{-}Zr_{10}\text{-}B_{20}]_{95}\text{-}Nb_4\text{-}Cu_1$ (Fe_3)
3. $[(Fe_{75}\text{-}Co_{10}\text{-}Ni_{15})_{70}\text{-}Zr_{10}\text{-}B_{20}]_{98}\text{-}Nb_1\text{-}Cu_1$(Fe_4)

2. Experimental method

The master alloy ingots of about 25 grams with nominal compositions as shown above were prepared by melting these pellets in Ti-gettered and high purified argon atmosphere in vacuum arc melting furnace facility at Department of Metallurgical and Materials Engineering, IITM, Chennai. A DC current of 100 to 140A was used to establish arc during the experiment.The XRD pattern of these as cast alloy ingots were shown in Fig [1]. Glassy rods of 3mm diameter were prepared by suction casting method using a copper mould.As cast rods were then examined by XRD method to understand their glassy nature. The XRD pattern of as cast rods is shown in Fig [2]. The density 'ρ' was measured by Archimedes'

method separately for as cast rough ingots and alloy rods. A small piece of about 0.5g was cut from three alloy rods and examined with Vibration Sample Magnetometer (VSM, Lake Shore, 7410 model, USA) at room temperature. Measured magnetic properties like Magnetization (M_S), Coercivity (H_C) and Retentivity (M_r) were summarised in Table [1]. M-H loop diagrams (VSM) of as cast rods at room temperatures were shown in Fig [3]. Variation of magnetic properties was shown in Fig [4].

3. Result & Discussion

All Fe-based alloys have the mixture of the glassy + α-Fe composite structure. This structure with α-Fe phase dispersed in glassy matrix (with an average grain size of 10nm) can have good soft magnetic properties like high saturation magnetization, low coercivity, and high electrical resistivity [**5-9**]. Percentage relative change of density %Δρ may be calculated by the following relation.

$$\%\Delta\rho=\frac{\rho(crystalline)-\rho(ascastrod)}{\rho(as\ cast\ rod)}x100$$

The value is nearly equal to 0.5% for three alloy samples. These α-Fe phases retained even after the preparation of bulk glassy rods by suction casting method. Hexagonal B_2Zr_1 crystalline phases were also seen with these samples particularly with Fe_3. However Fe_4 sample didn't show any such peaks. GFA is poor for Fe_3 as comparing with other samples concern this study. GFA is better with Fe_4 alloy as it has very minor crystallisation peaks. Hence this ingot is considered along with Fe_1 and Fe_3 samples to synthesize suction casting rods of 3mm diameter and to study their magnetic properties. CoercivityH_c is nearly same for all the three samples.Fe_3 sample exhibit the highest I_s value as it contain only 6 mol% of Ni, where as remaining two have nearly 13mol% of Ni. It has been reported that the replacement of Zr by Nb decreases I_s from 0.96T at 0% of Nb to 0.61T at 10% of Nb through 0.75T at 2at% of Nb, while H_c shows low values of 1.1-2.0 A/m and does not have appreciable compositional dependence. In the present study Nb content is decreasing 4at% to 1at% through 3at%, but $I_s$is found to be maximum with 3at% of Nb. Hysteresis loss may be given by the following relation

$$W=\int_0^M HdM\ {}^{erg}/_{cm^3}$$

Here 'M' is in emu/cm^3. The work done in magnetisation is simply the area M and H curves or closed M-H loop. In the present study this loss is significant with Fe_3 sample. Both squareness ratio (I_r/I_s) and percentage relative change of density have same trend of variation from Fe_1 to Fe_4 through Fe_3. The squareness ratio is relatively high for Fe_1 sample.

Table1:

Sample	Coercivity (H_c) kA m^{-1}	Retentivity (M_r) Tesla	Saturation Magnetisation (J_s) Tesla	Hysteresis Loss (kJ m^{-3})	Density(ρ) (g cm^{-3})		%Δρ	(I_r/I_s)
					As-cast rods	As-cast ingots		
Fe_1	19.8387	0.025	0.3997	91	6.8171	6.8514	0.5032	0.0625
Fe_3	20.2884	0.048	1.2162	217	6.8924	6.9270	0.5020	0.0395
Fe_4	20.4094	0.030	0.8583	114	6.7819	6.8159	0.501	0.034

							3	9

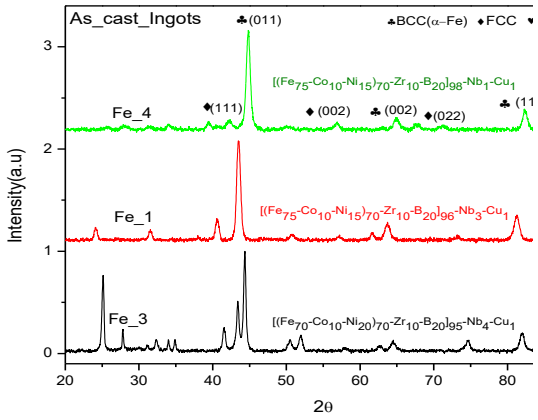

Fig1: XRD graph of as cast ingots

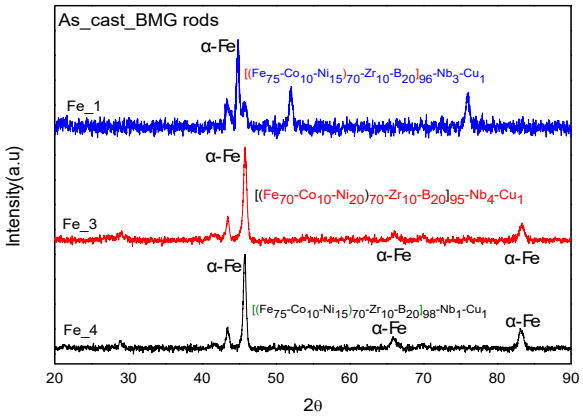

Fig2: XRD graph of as cast rods

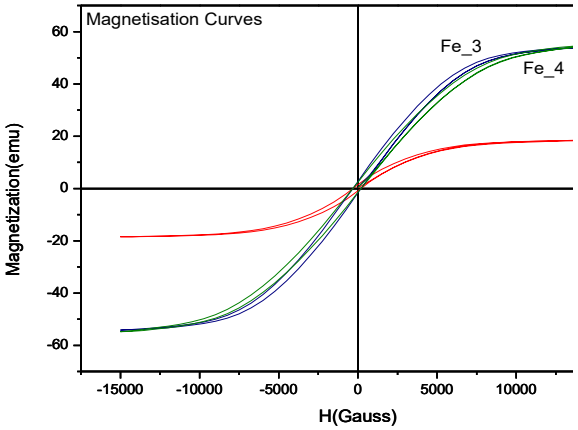

Fig3: Hysteresis loops(VSM) of rods

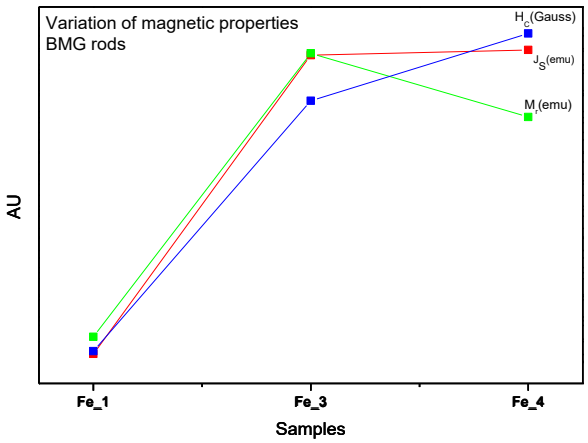

Fig4: Variation of magnetic properties of rods

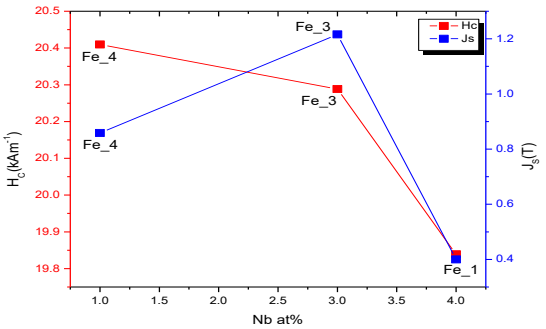

Fig5: Variation of coercivityvsNb concentration

4. Conclusions

As evident from XRD pattern glass forming is found to be incomplete for all the three samples. However suppression of crystalline peaks to a reasonable extent is evident from respective XRD pattern of amorphous rods.The GFA of Fe_1 sample is better than remaining two, but its saturation magnetisation is very poor. Fe_3 sample give better I_s

value and its GFA is not too bad. Good GFA of Fe_1 sample correlates with higher squareness ratio of the same. The Percentage relative change of density and squareness ratio have same trend of variations. Good GFA of Fe_1 sample may also be attributed to 4at% of Nb concentration in that sample. The variation of coercivity and saturation magnetisation with Nb concentration was shown in Fig [5]. From figure it is obvious that saturation magnetisation is high for 3at% of Nb. However these three samples exhibit very low squareness ratio. The magnetic properties of Fe_4 sample were intermediate between Fe_1 and Fe_3 samples. Hysteresis loss is found to be least for Fe_1 sample. Hence low Hysteresis loss and good GFA were correlated during this study[9]. It was further planned to compare the thermal properties like glass transition and crystallisation temperatures of these samples and to prepare melt spun ribbons with expectation of better soft magnetic properties to get more structural information and better GFA [10].

5. Acknowledgement

This work was supported by Indian Academy of Sciences, Bangalore, Indian National Academy of Sciences, New Delhi and The National Academy of Sciences, Allahabad in the form of summer research fellowship (PHYT22) to author 1. First author gratefully acknowledge the continuous encouragement and guidance of author2 and technical support of Chinmoy Chattopadyaya, Guru Vidhyardhi, AnirudhaKarati, Sk.Adiland ManwendraTripati during these experiments.

References

1. C. Suryanarayana et al., Boca Raton, FL, 2nd Edition, CRC Press, 2017.
2. K. P, Gopinathan et al., TRAnantharaman (Ed.), TransTech Publications, Stafa-Zurich, Switzerland, 1984.
3. Inoue et al., Materials Transactions., 1995, JIM **36** (9), 1180-1183.
4. J. Torrens-Serra et al., J. Non-Cryst.Solid., 2013, **367**, 30-36.
5. J. Torrens-Serra et al., J. Non-Cryst. Solid., 2013, **367**, 30-36.
6. K. Mondal et al., J. Non-Cryst. Solid., 2005, **351**(16-17), 1366-1371.
7. B. S. Murty et al., Appl. Phys.Lett., 2000, **77** (8), 1102-1104.
8. B. Rao et al., Intermetallics., 2013, **35**, 73-81.
9. I. Bakonyi et al., J.Magn.Magn.Materials., 2012, **324** (22), 3961-3965.
10. C. W. Shih et al, J. Appl. Phys., 2015, **117**(17), 17B736.

Physical and dc Electrical Properties of Vanadium doped Mixed Alkali Bismuth Borate Glasses

M.Subhadra [1*] ,K.RajGopal[2], Y.Srinivasa Reddy[1]and P.Kistaiah[3](Retd Professor)
[*1]Department of Physics, ChaitanyaBharathi Institute of Technology, Gandipet, Hyderabad – 500075, Telangana State, India.
[2]Department of Biotechnology, Chaitanya Bharathi Institute of Technology, Gandipet, Hyderabad – 500075, Telangana State, India
[3]Department of Physics, Osmania University, Hyderabad – 500044, Telangana State, India.
***Email: drsubhadra.pyaruka@gmail.com**

Abstract
Mixed alkali borate glasses of composition $xLiO_2$-(30-x) K_2O-10Bi_2O_3-55B_2O_3:5V_2O_5 with x=5,10, 15,20 and 25 mol% are prepared using melt quenching technique. Characterization of the samples is done by X-ray diffraction and DSC techniques. Physical parameters such density, molar volume, OPD and Tg have been calculated. DC conductivity measurements have been carried out in the temperature range373-623 K by two terminal method. Conductivity data has been analysed in the light of Mott's small polaron hopping model. The conductivity and activation energy are found to exhibit non-linear variation with x showing a maximum/minimum at around x=15mol%. It is found that the electrical conductivity is found to increase with increasing temperature and is due to ion conduction. Various polaron hopping parameters such as average separation, polaron radius and transition metal ion density etc., are calculated. These parameters are found consistent with Mott's model of phonon-assisted polaronic hopping.
Key words: alkali borate glasses, density, electrical conductivity, small polaron hopping

1. Introduction

The research on transition-metal oxide (TMO) doped inorganic glasses are continuing since long time because of their technological applications in electrochemical, electronic and electro-optical devices [1]. The oxidation state of transition metal ions (TMIs) changes as a result of reactions in the molten state involving the gain or loss of oxygen. The electron-phonon interaction in these glasses is strong enough to form small polaron, and the electrical conduction process occurs by the hopping of small polarons between different valence states as proposed by Austin and Mott [2]. Glasses containing Li^+, K^+, and Na^+ ions exhibit significant ionic conductivity at ordinary temperatures. An interesting aspect of electrical conduction in ionic glasses is the so called mixed alkali effect. Mixed alkali doped glasses exhibit lower electrical conductivity compared to that of single alkali composition, for the same total ionic concentrations [3]. The general understanding of ion transport in glasses is based on the assumption that cations jump from one position to another similar position while the negatively charged centers remain fixed in position in the glass matrix [4]. The mixed alkali effect has not been completely understood mainly due to the difficulty in determining the conduction pathways for the mobile ions [5]. Ion conducting glasses have technological applications for electrochemical devices such as solid-oxide fuel cells, solid statebatteries and chemical sensors [6].

In our earlier studies [7], we have reported the mixed alkali effect in the optical properties of mixed alkali bismuth borate glasses doped with vanadium (LK-series). Keeping in view of underlying physics and applications of MAE and changeover of conduction mechanism, the following system have been selected for density, glass transition temperature, and dc conductivity studies.

xLi_2O-(30-x) K_2O-10Bi_2O_3-55B_2O_3:5V_2O_5 with x = 5, 10, 15, 20, and 25mol%, --LK-series
The objective of the present investigation is to study the physical and electrical properties in these glass systems wherein both TMI and two different alkali ions are present and to look for the possibility of MAE in the direct current electrical conductivity of LK-series glass system.

2. Experimental

The glass system (LK-series) was prepared by the melt quench techniqueand annealed at 573K for 8h. The obtained glasses were lapped and two opposite sides were polished to be suitable for the use in the conductivity measurements.
X-ray diffraction patterns were recorded to check the non-crystallinity of the prepared glass samples using a Philips X-ray diffractometer PW/1710 with Ni-filtered Cu-Kα radiation powered at 40 kV and 30 mA. The patterns (not shown) revealed a broad hump, a characteristic of amorphous materials and did not reveal any discrete or sharp peaks. The density "d" of the glasses was determined at room temperature using Archimedes principle with xylene as an inert immersion liquid. The molar volume V_m of each glass sample was calculated. The thermal behavior of the glass samples was investigated using a differential scanning calorimeter (DSC) using DSC 821e Mettler Toledo model thermal instrument. The details of the determination of density, molar volume and glass transition temperature were given elsewhere [7].
For measuring dc conductivity, samples in the forms of discs of nearly 1mm thickness were chosen. Colloidal silver paint was used as an electrode material. The temperature of the samples was measured using a chromel–alumel thermocouple. To verify reproducibility and minimize errors the experiment was repeated and collected over sever experimenters has been averaged. The conductivity was determined as per, $\sigma = (1/\rho)$ where resistivity, $\rho = (RA/t)$, t is the thickness, R is resistance and A is cross-sectional area of the sample. Conductivity measurements were made by the standard technique, that is, two terminal method over a temperature range from about 373 – 623K, first by increasing the temperature and then by decreasing it. A constant voltage of 1.5 V was applied across the sample and the current was measured by using a Keithley 614 electrometer. To minimize the polarization effects, the d.c. voltage was applied for a very short period (<30s at a time) across the samples and the polarity of the applied d.c. voltage was also reversed at the time of measurement. The relative error in the measurement of conductivity (σ) and activation energy (W) was found to lie in the range 2 – 3%. Conductivities were measured very near to the glass transition temperatures at which the samples either deformed under the load of the springs on the electrodes or crystallized, rendering further measurements inaccurate.

3. Results and Discussion

3.1 Density, molar volume and glass transition temperature

The values of density (d), molar volume (Vm) and glass transition temperature (Tg) of all the glass samples have been calculated as explained earlier and their values are presented in Table 1.

Table 1 Physical parameters of LK series glass systems

Sample	Density (g/cc) ±0.01	Molar volume (cc/mol) ± 0.02	T_g (ºC) ± 1ºC
LK-5	3.27	36.43	418
LK-10	3.30	35.08	378
LK-15	3.36	33.47	375
LK-20	3.44	31.84	383
LK-25	3.43	30.94	390

The variation of the logarithm of d.c. conductivity σ, as a function of inverse temperature (T) for the the present glass system, LK-series is shown in Fig.1.

Fig.1 D.C. conductivity plots

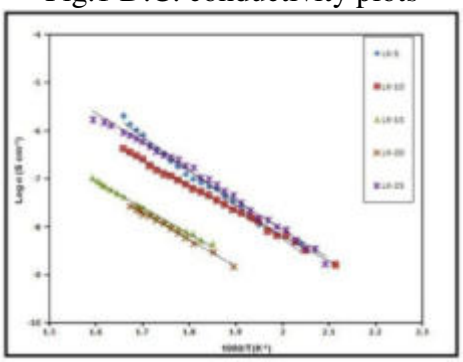

It is observed that σ increases with increasing temperature, indicating temperature dependent activation energy, W, a characteristic of a SPH conduction mechanism in TMO glasses [8].
According to Mott's small polaron hopping model (SPH) [8] the electrical conductivity in adiabatic regime is expressed as

$$\sigma = \sigma_0 \exp(-W/kT) \quad \ldots (1)$$

Where W is the activation energy and σ_0 is the pre-exponential factor given by
$\sigma_0 = \nu_0 Ne^2 R^2 C(1- C)\exp(-2\alpha R)/kT$, ($\nu_0 = \eta_D k/h$ is the optical phonon frequency [9] and h is the Planck's constant), $\eta_D = 2T_D$ is the Debye temperature and T_D is the temperature at which the deviation from linearity takes place, N is the concentration of TMI, R is mean spacing between the TMI given by $R = (1/N)^{1/3}$, α is the tunneling factor and C is the fraction of reduced TMI concentration to that of total TMI concentration,($C= V^{4+}/V_{total}$).
The density of total vanadium ion, "N" in each glass is estimated using the relation [10]

$$N = 2\left[\left(\frac{dm}{M}\right)N_A\right] \quad \ldots (2)$$

Where d is the density of the glass, m is the mole fraction of V_2O_5, M is molecular weight of V_2O_5 and N_A is the Avogadro number. The plots are found to be linear at high temperatures. It is observed that the conductivity increases with increase in the temperature for all the samples. The d.c. conductivity 'σ'of the present glasses vary between 10^{-9} - 10^{-7} S cm^{-1}. The activation energy W and the pre-exponential factor $\sigma_0$were obtained from the slope and the intercept of the least squares straight line fit of the conductivity plot. The values of conductivityσ, activation energy W for the the system is tabulated in Table2. The activation energy for conduction of the present glasses varies from 1.08 to 1.40eV. The errors in activation energies are found to be ± 0.002 eV. The activation energies of the present glasses are in agreement with other mixed alkali borate glasses [3]. The estimated values of N, R for the present glasses are presented in Table2.

3.2 Parameters associated with polaron hopping

Considering a strong electron-phonon interaction, Austin and Mott [8] proposed the following equation for the activation energy,

$$W = W_H + \frac{W_D}{2} \text{ for } T > \eta_D/2 \quad \ldots (3)$$

$$W \approx W_D \text{ for } T < \eta_D/4 \quad \ldots (4)$$

Where W_H is the polaron hopping energy and W_D is the disorder energy arising from the energy difference of the neighbours between two hopping sites. The polaron hopping energy W_H is calculated using the formula [11]:

Table 2Polaron hopping parameters for LK-series glass system

Sample	X (mol%)	σat 583K (S cm^{-1})	W (eV)	Logσ_0	N ($10^{21}cm^{-3}$)	R (nm)	r_p (nm)	ε_p	W_H (eV)	N(E_F) ($10^{21}eV^{-1}m^{-3}$)
LK-5	5	5.2 x10^{-7}	0.98	5.869	1.09	0.973	0.392	0.651	0.585	0.19
LK-10	10	1.84 x10^{-7}	1.04	2.293	1.10	0.969	0.390	0.616	0.649	0.25
LK-15	15	1.9 5x10^{-8}	1.08	1.667	1.12	0.963	0.388	0.597	0.645	0.25
LK-20	20	2.75 x10^{-8}	1.05	2.315	1.14	0.957	0.386	0.616	0.627	0.26
LK-25	25	4.76 x10^{-7}	1.02	5.439	1.14	0.957	0.386	0.635	0.609	0.27

$$W_H = \frac{W_p}{2} = \frac{e^2}{4\epsilon_p}\left(r_p^{-1} - R^{-1}\right) \quad \ldots (5)$$

Where W_p is the polaron binding energy, ϵ_p is the effective electric permittivity, which can be determined from the relation [12], $\epsilon_p = \frac{e^2}{4Wr_p}$ … (6)

and the small polaron radius [13], $r_p = \frac{1}{2}\left(\frac{\pi}{6N}\right)^{1/3}$ … (7)

$N(E_F)$ is the density of states at Fermi level expressed in terms of 'W' as given by [14]:

$N(E_F) = 3/4\pi R^3 W$ … (8)

The polaron hopping parameters W_H, ϵ_p, r_p and $N(E_F)$ are given in Table2.

In LK-series glass system, it is interesting to observe that the conductivity and activation energy vary non-linearly with lithium content exhibiting a mixed alkali effect (MAE). In this case the content of TMI i.e., vanadium ion is fixed as 5 mol%. The foundation of MAE in glasses containing TMI's as well as alkali ions of two different types depends upon the type and concentration of TMI's in the glass network, the type of the host glass matrix, and the types and concentrations of the alkali ions. These factors govern how the relative mobilities of alkali ions and polarons can suppress one another.

From Table 2 it is observed that the variation in the values of polaron hopping parameters around the vanadium ion is very small which may be due to the variation of alkali ion concentration. They make no detectable contribution to the total conductivity that is considered to be polaronic in nature. The variation of W and logσ_0 with lithium content (x) is shown in Fig. 2.

It is clear from the Fig. 2 that the variation of W and log$\sigma_0$is found to be non-linear with the increasing content of lithium. The compositional variation of σ at different temperatures is shown in Fig.3 and MAE is present at all these temperatures.

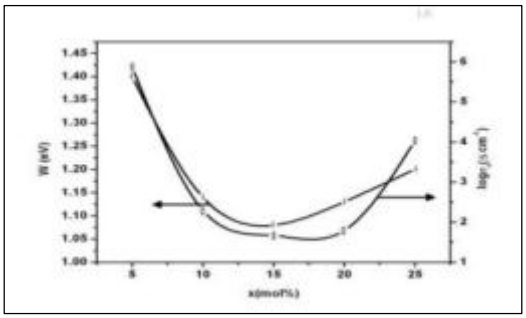

Fig.2 $\log\sigma_0$ and W vs. *x* plots

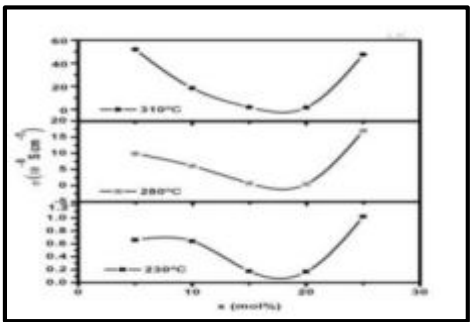

Fig.3 Isotherms of conductivity vs. x

4. Conclusions

Mixed alkali bismuth borate glasses doped with vanadium prepared by melt quench technique were studied through d.c conductivity measurements. Density of these samples is found to increase with the increasing content of the respective ions whereas molar volume is found to decrease due to the contraction of the glass matrix. In the present glass system (LK-series),the glass transition temperature exhibited non-linear variation indicating MAE.It is observed that the conductivity in these glasses increases with the increase in the temperature and with the composition of the respective ions. The values of conductivity lie in the range 10^{-9} S cm^{-1} to 10^{-7} S cm^{-1}.In the present system (LK-series) the conductivity of the glasses varies non-linearly with increasing Li_2O content exhibiting MAE. No appreciable change is observed in the polaron hopping parameters in LK- series and the conduction in these glasses is mainly due to the mobility of the respective ions.

5. Acknowledgements

One of the authors Dr.M. Subhadra thanks UGC, New Delhi, India for financial assistance through merit fellowship (RFSMS). The authors thank Prof. M.N. Chary, Dept of physics, O.U for providing D.C conductivity measurements.

References

1. Y.Sakurai et al., J. Electrochem. Soc., 1985, **132**, 512-513.
2. A. Mogus-Milankovic et al., Phys. Chem. Glasses., 1999, **40**, 69-74.
3. Y. Gao et al., Phys. Chem. Glasses., 2005, **46**,182-186.
4. I. W. Arpad et al., J. Non-Cryst. Solids., 2004, **333**, 231-239.
5. J. Swenson et al., Phys. Rev. Lett., 2003, **90**, 15-17.
6. F. Berkemeier et al., J. Non-Cryst. Solids., 2005, **35**, 3816-3825.
7. M. Subhadra et al., J. Alloys and Comp., 2010, **505**, 634-639.
8. I. G. Austin et al., 1969, Adv. Phys., 1969. **18**, 41-97.
9. H. Sakata et al., Phys. Rev. B., 1999, **60**, 3230-3236.
10. E. Mansour et al., Phys. Chem. Glasses., 2002, **43**, 80-86.
11. M. Pal et al., Phys. D: Appl. Phys., 2001, **34**, 459-464.
12. N. F. Mott et al., J. Non-Cryst. Solids., 1968, **1**, 1-17.
13. K. Sega et al., J. Mater. Sci., 1998, **33**, 1303-1308.
14. N. F. Mott et al., Electronic processes in Non-Crystalline Materials, Clarendon, Oxford, 1979.

Characteristic study on Geo-polymer based self-compacting concrete containing quartz as an alternative of natural river sand

M.Akhila, Nithish Kalwa, Challa Poojitha, Dr.B.Narendra Kumar*
VNR Vignana Jyothi Institute of Engineering and Technology,Hyderabad, India.
*E-mail: narendrakumar_b@vnrvjiet.in

Abstract

In current research Geo-polymer self-compacting concrete is an excellent substitution of conventional ordinary Portland cement-based concretes. The Technology of geopolymer self-compacting concrete also has the greatly minimize the CO_2 emissions which produces by the manufacturing of cement industries. In the present work we chosen an eco-friendly alternative material that is Ground Granulated Blast Furnace Slag (GGBS) for cement and as river sand is in crisis and natural depletion of resources, we replaced completely with Quartz Sand. In this paper we have tested fresh properties of concrete for various mixes by performing V-Funnel, V-Box and L-Box tests to determine fresh properties such as flow time, passing and filling ability of fresh concrete and we have tested mechanical properties of concrete i.e., compressive strength, flexural strength, split tensile strength at the age of 7 days , 28 days and 90 days for all the concrete mixes.

Index terms - Self compacting, Sodium hydroxide, Sodium silicate, GGBS, Quartz sand, Fly ash.

1.Introduction: In this paper we chosen an eco-friendly alternative that is GGBS for cement and as river sand is in crisis we replaced it with Quartz Sand. In this paper we have tested fresh properties of concrete for various mixes by performing V-Funnel, V-Box and L-Box tests to determine fresh properties such as flow time, passing and filling ability of fresh concrete and we have tested mechanical properties of concrete i.e., compressive strength, flexural strength, split tensile strength. This can be referred as a short guide for rest of the experiment [1 – 4].

2.Experimental:

2.1 Materials used: Fly-ash, GGBS (Ground granulated blast-furnace slag, Quartz sand, Sodium silicate, Sodium hydroxide, River sand, Coarse aggregate(CA) are the materials which we have used in our project.

2.2Mixingprocedure*:*

Initially we took all the materials in proportional quantities according to the mix design. Firstly, we have taken oven dried CA and to that Fine aggregate(FA) is added, after that GGBS is added to that mixture according to their mix design. Then Fly Ash and Quartz powder are added to the GGBS and everything is mixed thoroughly. While rotating the mixer we have added 50% of water into it. Later, we have added NaOH solution, Sodium Silicate solution and Super plasticizer into the mixer and continued to rotate it for 2-3 minutes. At last, we added the remaining 50% of the water and continued to rotate the mixer for another 2-3 minutes. Finally, after preparing the mixture we have casted the mixture into moulds. For further mixes we need to change ratios of Fine aggregate and Quartz sand, accordingly the strengths will be varied.

3.Results and Discussion

Mix	Fly-ash kg/m^3	GGBS (kg/m^3)	Quartz powder (kg/m^3)	River sand kg/m^3	Quartz sand (kg/m^3)	Coarse aggregate (kg/m^3)	Sodium silicate (kg/m^3)	Sodium hydroxide (kg/m^3)	Super plasticizer (%)
Mix1	400	100	100	925	0	805	125	50	1.8
Mix2	400	100	100	740	185	805	125	50	1.8
Mix3	400	100	100	555	370	805	125	50	1.8
Mix4	400	100	100	370	555	805	125	50	1.8
Mix5	400	100	100	185	740	805	125	50	1.8
Mix6	400	100	100	0	925	805	125	50	1.8

Table1: Mix proportions of various mixes of concrete

Fresh Properties: The fresh properties of various Mix designations are determined by performing V-Funnel, V-Box and L-Box and are listed in the below table.

Table2: Fresh properties of the six concrete mixes

Mix designations	Flow table		V-Funnel	L-Box (H_2/H_1)
	Diameter(mm)	T_{50}(seconds)		
Mix1	750	4	8	0.96
Mix2	730	5	9	0.93
Mix3	710	5	9	0.92
Mix4	690	6	10	0.90
Mix5	660	6	11	0.88
Mix6	640	7	12	0.84

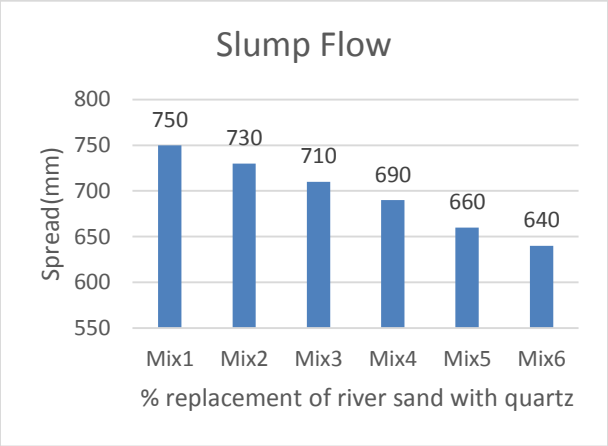

Fig1: Variations of slump flow for various mixes

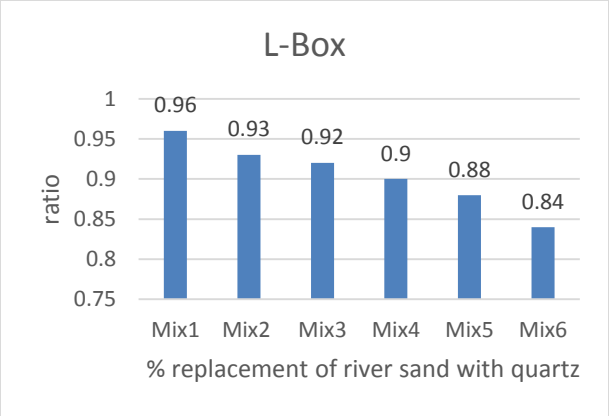

Fig2: Variations of L-Box for various mixes

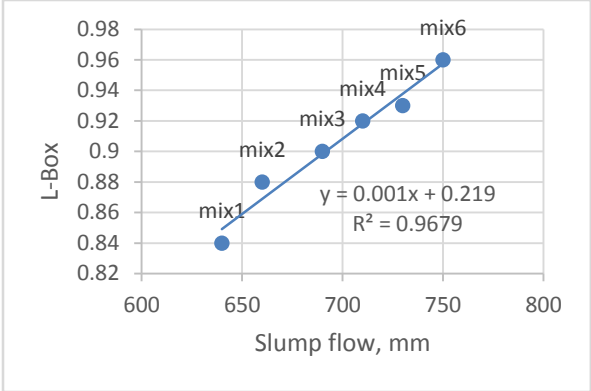

Fig4: Graph between slump flow and L-Box values for various mixes

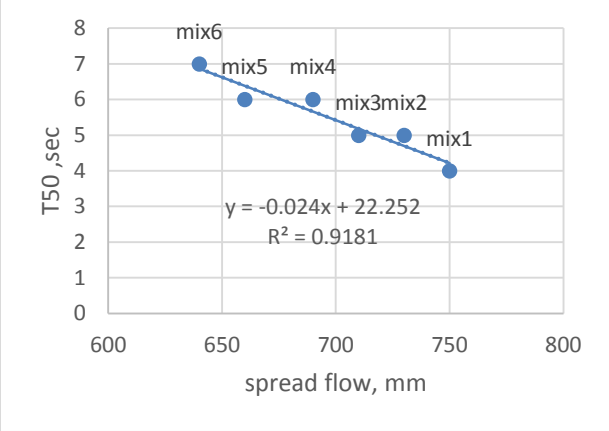

Fig3: Plot of slump flow vs T_{50} for various mixes

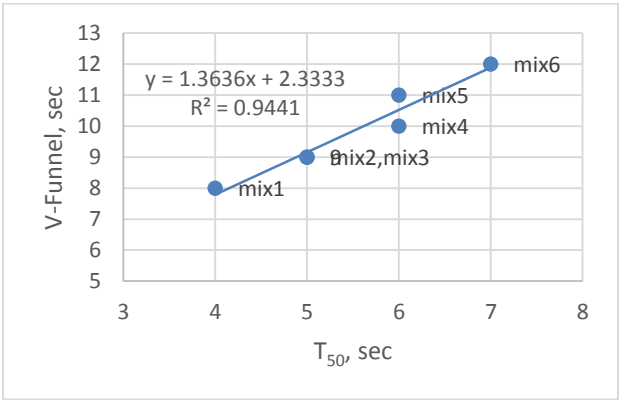

Fig5: Graph between T_{50} and V-Funnel values for various mixes

Compressive strength: This table gives the compressive strength values of concrete of the six mixes at 7day, 28day and 90day of time period.

Table3: Compressive strength

Mix	Compressive strength (MPa)		
	7day	28day	90day
Mix1	34.42	38.84	40.19
Mix2	36.81	40.14	43.41
Mix3	38.26	42.92	45.91
Mix4	40.12	44.80	47.32
Mix5	42.19	46.89	49.99
Mix6	45.52	48.92	51.25

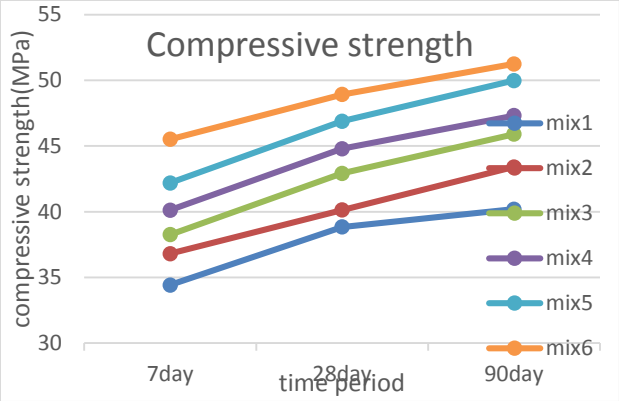

Fig6: Compressive strength of mixes

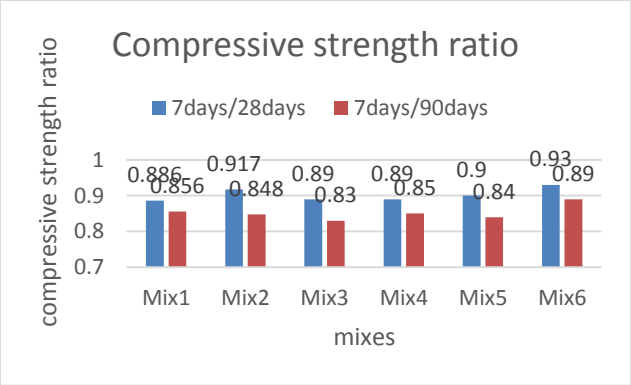

Fig7: Compressive strength ratio of mixes

Split tensile strength: This table gives the Split tensile strength values of the six concrete mixes at 7day, 28day and 90day of time period.

Table4: Split tensile strength

Mix	Split Tensile strength (MPa)		
	7day	28day	90day
Mix1	1.92	2.01	2.73
Mix2	2.63	2.47	2.97
Mix3	2.92	2.94	3.12
Mix4	2.98	3.02	3.68
Mix5	3.01	3.40	3.94
Mix6	3.22	3.52	4.12

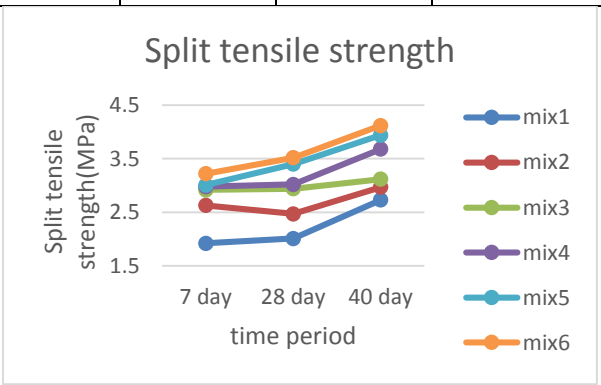

Fig8: Split tensile strength

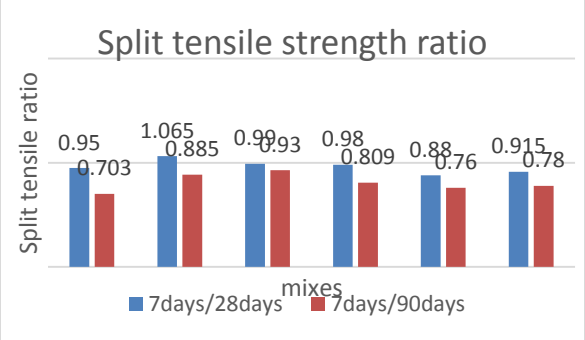

Fig9: Split tensile strength ratios of mixs

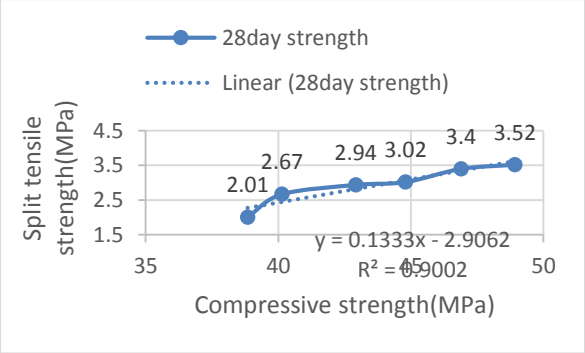

Fig10: Graph between split tensile strength and compressive strength

Flexural strength: This table gives the Flexural strength of concrete of the six mixes at 7day, 28day and 90day of time period.

Table5: Flexural strength

Mix	Flexural strength (MPa)		
	7day	28day	90day
Mix1	4.24	4.49	4.68
Mix2	4.32	4.68	4.77
Mix3	4.38	4.77	4.9
Mix4	4.56	4.92	4.97
Mix5	4.74	4.98	5.16
Mix6	4.86	5.10	5.32

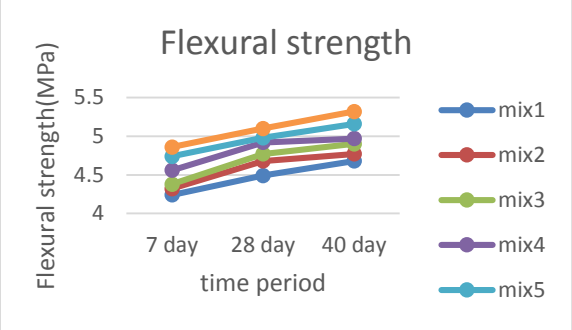

Fig11: Flexural strength of mixes

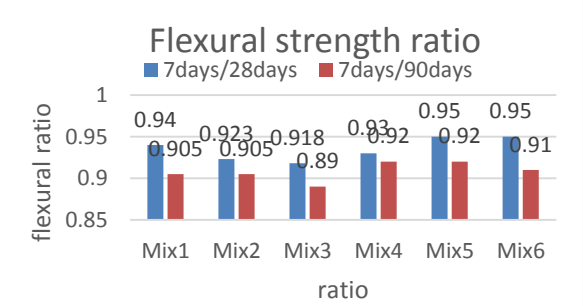

Fig12: Graph representing flexural strength ratios of mix

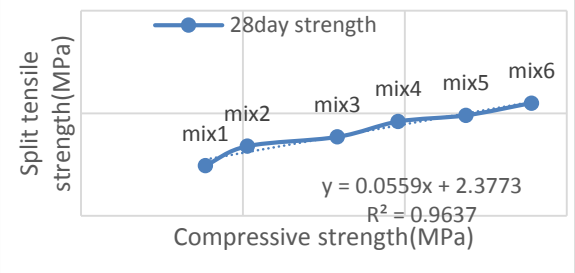

Fig13: Graph between compressive strength and Flexural strength

Discussion of test results: Study was conducted on optimization of mix proportions of SCGPC by substituting quartz sand in the place of river sand and by increasing dosages of quartz sand.

A. Fresh Properties of SCGPC: It can be observed from table that with increasing dosages of quartz sand there is decline in the fresh properties of concrete. It can be observed that there is a perfect relation between different fresh properties of quartz sand-based SCC.

B. Mechanical Properties of SCGPC: It can be observed that compressive strength, split tensile strength and flexural strength of concrete in increasing by increasing the amount of quartz sand in the place of river sand.

Table6: %increase in mechanical properties of concrete at 100% substitution of quartz sand in place of river sand

No. of days of curing	% increase in mechanical properties of concrete at 100% substitution of quartz sand in place of river sand		
	Compressive strength	Tensile strength	Flexural strength
7	32.5	67.71	14.62
28	25.95	75.12	13.59
90	27.65	50.92	13.67

4.Conclusion:

There was increase of 32.25%, 25.95%, 27.65% in compressive strength at the end of 7days,28days and 90days respectively for 100% substitution of quartz sand in place of river sand. There was increase of 67.71%, 75.12%, 50.92% in Tensile strength at the end of 7days,28days and 90days respectively for 100% substitution of quartz sand in place of river sand. There was increase of 14.62%, 13.59%, 13.67% in Flexural strength at the end of 7days,28days and 90days respectively for 100% substitution of quartz sand in place of fine aggregate.It can be finalized that with 100% substitution of Quartz sand in place of river sand is advantageous with respect to Fresh properties and Mechanical properties point of view. Fresh properties and Mechanical properties of all the six mixes of concrete for different dosages of quartz sand could satisfy EFNARC specifications.

Reference:

1. S. Ahmed et al., 2014, Int. J. Civil & Struct. Engi., 4(3).
2. Amit Mittal et al., 2004, The Indian Concrete Journal, PP 30-34.
3. Amit Mittal et al., 2005, International Conference on Advances in Concrete, Composites and Structures, SERC, Chennai, 441-449.
4. Anirwan Senguptha et al., 2006, 31st Conference on Our World in Concrete & Structures held At Singapore, 353-359.

Correlation of Optical Properties of Waveguide in Nano Scale

Alla Srivani, Nagarathnamaiah, Praveen and Mr Suneel

Vasireddy Venkatadri Institute of Technology

Corresponding Author Mail-id: vaniraghava2751982@gmail.com

Abstract: Optical properties are measured in wave guides in both Air medium 50 nm to 1000 nm and water medium 50 nm to 1000 nm and correlated between micro scale and Nano scale. Wave length is measured between 50 nm to 1000 nm and observed symmetry between core thickness in micro scale, cladding refractive index and layer thickness in nano scale**.**

Keywords: Wave length, Core thickness, cladding thickness, layer thickness, micro scale and nano scale ranges, air medium and water medium.

1. Introduction: The makes use of of waveguides for transmitting indicators have been recognized even before the term was once coined. The phenomenon of sound waves guided through a taut wire have been known for a lengthy time, as properly as sound via a hole pipe such as a cave or clinical stethoscope. Other makes use of of waveguides are in transmitting electricity between the components of a machine such as radio, radar or optical devices [1,2]. Waveguides are the quintessential precept of guided wave testing (GWT), one of the many strategies of non-destructive evaluation. Specific examples: Optical fibers transmit light and signals for long distances with low attenuation and a large usable vary of wavelengths. In a microwave oven a waveguide transfers power from the magnetron, where waves are formed, to the cooking chamber. In a radar, a waveguide transfers radio frequency energy to and from the antenna, the place the impedance needs to be matched for efficient electricity transmission. Rectangular and Circular waveguides are usually used to connect feeds of parabolic dishes to their electronics, either low-noise receivers or power amplifier/transmitters. Waveguides are used in scientific gadgets to measure optical, acoustic and elastic homes of substances and objects.

2. Experimental Methodology: Waveguides used at optical frequencies are normally dielectric waveguides, constructions in which a dielectric material with excessive permittivity, and for that reason excessive index of refraction, is surrounded by means of a fabric with decrease permittivity. The structure guides optical waves by means of whole internal reflection. An instance of an optical waveguide is optical fiber [3,4]. Other sorts of optical waveguide are additionally used, together with photonic-crystal fiber, which guides waves through any of countless wonderful mechanisms. Guides in the structure of a hole tube with a tremendously reflective inner floor have additionally been used as light pipes for illumination applications. The inner surfaces may additionally be polished metal, or may additionally be blanketed with a multilayer film that guides mild via Bragg reflection. One can additionally use small prisms around the pipe which mirror mild via complete internal reflection such confinement is always imperfect, however, seeing that whole inner reflection can never genuinely guide mild inside a lower-index core.

3. Results & Discussion

Air Medium:

1) Wavelength Range 50 nm-100nm

Wavelength Nm	Core thickness µm	Cladding Refractive index	Layer Thickness nm
50	1.1	1.1	27.24
60	1.2	1.2	22.59
70	1.3	1.3	21.05
80	1.4	1.4	20.40
90	1.5	1.5	20.11
100	1.6	1.6	20.00

Graph:-1

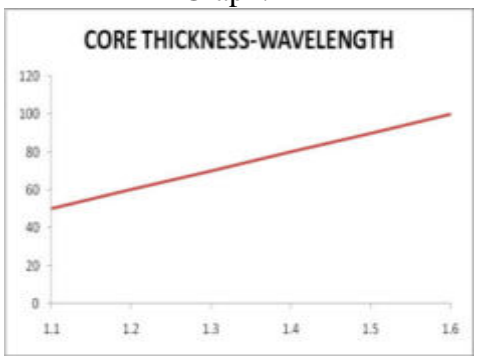

Graph-1 explains Wavelength increases linearly with Core Thickness.

Graph-2

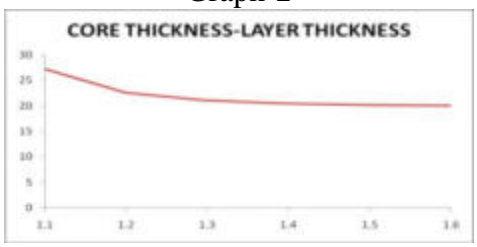

Graph-3

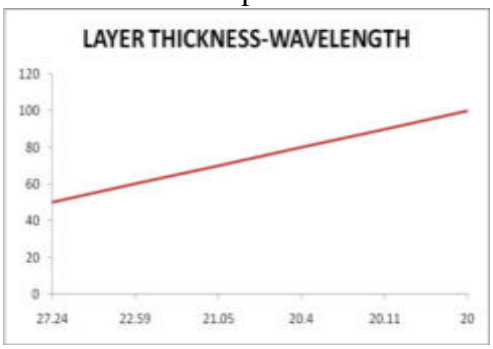

1) Wavelength Range: 200 nm To 500 nm

Table 2 explains about wave length (nm) from 200nm to 500nm range, core thickness from 1.1 µm to 1.4 µm, cladding refractive index from 1.1 to 1.4 and layer thickness from 27.24 nm to 20.40 nm

Wavelength Nm	Core thickness µm	Cladding Refractive index	Layer Thickness nm
200	1.1	1.1	27.24
300	1.2	1.2	22.59
400	1.3	1.3	21.05
500	1.4	1.4	20.40

.

Graph-4:

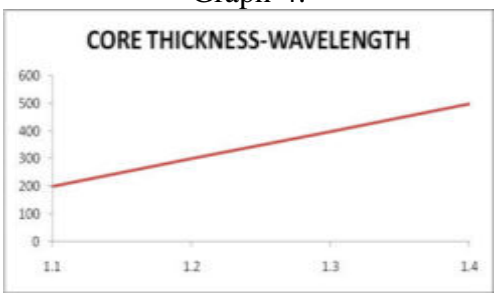

Graph-5:

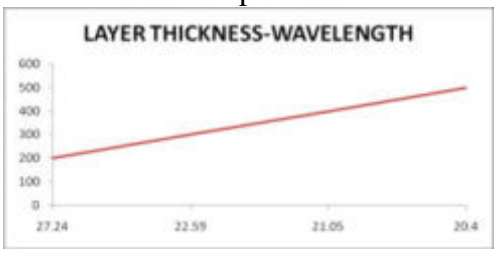

Graph-6:

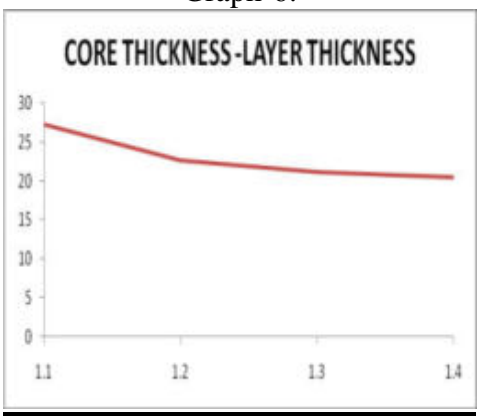

Graph-6 Explains Linear Relationship between Core Thickness and Layer Thickness.

2) Wavelength Range: 600 nm to 1000 nm

Table 3 explains about wave length (nm) from 600 nm to 1000 nm range, core thickness from 1.6 µm to 2.0 µm, cladding refractive index from 1.6 to 2.0 and layer thickness from 118.76 nm to 142.85 nm.

Wavelength nm	Core thickness µm	Cladding Refractive index	Layer Thickness nm
600	1.6	1.6	118.76
700	1.7	1.7	125.88
800	1.8	1.8	132.1
900	1.9	1.9	
1000	2.0	2.0	

Graph-7:

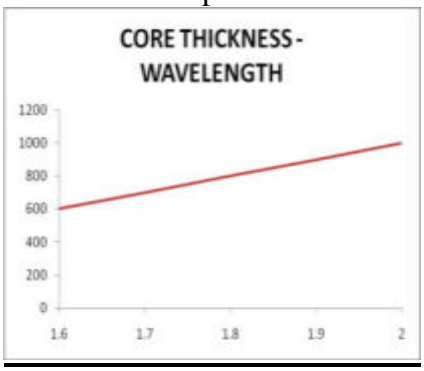

Graph-8:

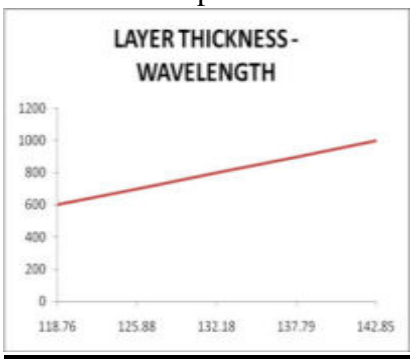

Graph-9

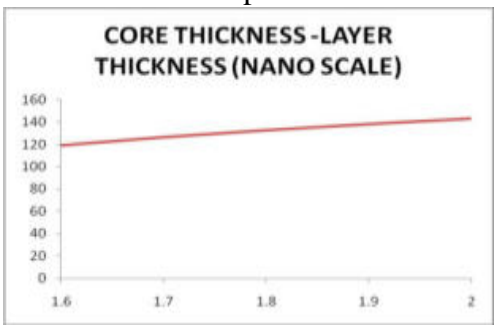

3) <u>Water Medium</u>:
Wave Length Range: 50-90 nm

Table 4 explains about wave length (nm) from 50 nm to 90 nm range, core thickness from 1.1 µm to 1.5 µm, cladding refractive index from 2.6 to 3.0 and layer thickness from 5.59 nm to 8.36 nm

Wavelength nm	Core thickness µm	Cladding Refractive index	Layer Thickness Nm
50	1.1	2.6	5.59
60	1.2	2.7	6.38
70	1.3	2.8	7.10
80	1.4	2.9	7.76
90	1.5	3.0	8.36

.

Graph-10:

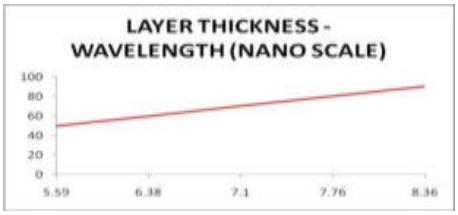

4) Wavelength range: 100 - 500nm

Wavelength nm	Core thickness µm	Cladding Refractive index	Layer Thickness nm
100	1.6	3.1	8.92
200	1.7	3.2	17.17
300	1.8	3.3	24.82
400	1.9	3.4	31.99
500	2.0	3.5	38.58

Graph-11:

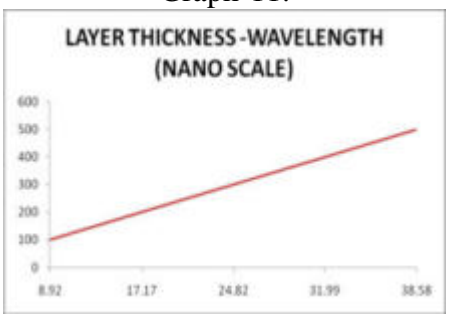

5) Wavelength range: 600 nm to 1000nm

Wavelength nm	Core thickness µm	Cladding Refractive index	Layer Thickness nm
600	2.1	3.6	44.79
700	2.2	3.7	50.63
800	2.3	3.8	56.11
900	2.4	3.9	61.29
1000	2.5	4.0	66.17

Graph-12:

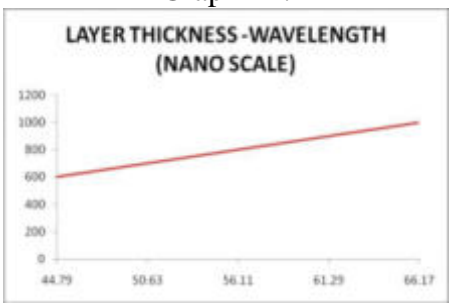

4. Conclusion

1) Water medium:

Wavelength range: 50 nm to 90nm

Wavelength nm	Core thickness µm	Cladding Refractive index	Layer Thickness nm
50	1.1	2.6	5.59
60	1.2	2.7	6.38
70	1.3	2.8	7.10
80	1.4	2.9	7.76
90	1.5	3.0	8.36

Graph-13:

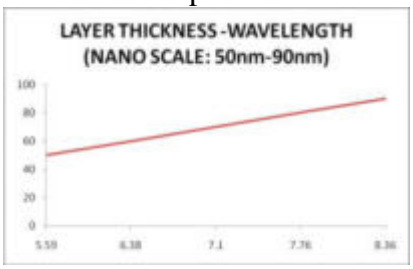

Wavelength nm	Core thickness µm	Cladding Refractive index	Layer Thickness nm
100	1.6	3.1	8.92
200	1.7	3.2	17.17
300	1.8	3.3	24.82
400	1.9	3.4	31.94
500	2.0	3.5	38.58

Graph-14:

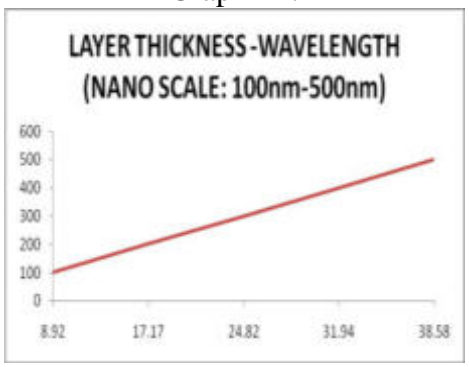

Table 9: Wavelength range: 600 nm to 1000nm

Wavelength nm	Core thickness µm	Cladding Refractive index	Layer Thickness Nm
600	2.1	3.6	44.79
700	2.2	3.7	50.63
800	2.3	3.8	56.11
900	2.4	3.9	61.29
1000	2.5	4.0	66.17

Graph-15:

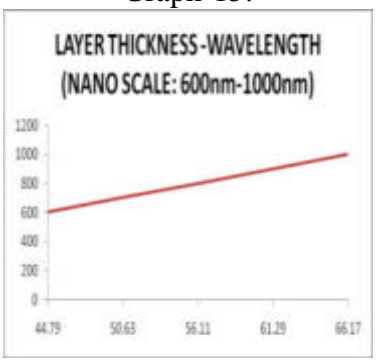

Applications in Modern Technology:

The utilization of nanotechnology in medication offers some energizing prospects. A few methods are just envisioned, while others are at different phases of testing, or really being utilized today. Nanotechnology in medication includes utilizations of nano particles right now being worked on, just as longer range research that includes the utilization of fabricated nano-robots to make fixes at the cell level. Whatever you call it, the utilization of nanotechnology in the field of medication could reform the manner in which we recognize and treat harm to the human body and ailment later on, and numerous procedures just envisioned a couple of years back are gaining wonderful ground towards turning out to be real factors. One use of nanotechnology in medication as of now being created includes utilizing nano particles to convey drugs, warmth, light or different substances to explicit sorts of cells. Particles are designed with the goal that they are pulled in to infected cells, which permits direct treatment of those cells.

Acknowledgement: My Sincere Thanks to my family for giving support in all my Research Activities.

5. **References**:

1. R. A. Freitas et al., Nanomedicine: Basic Capabilities. Austin, TX: Landes Bioscience. ISBN 978-1-57059-645-2, 1999.

2. V. Wagner et al., Nature Biotechnology., 2006, **24** (10), 1211–7.

3. R. A. Freitas et al., Nanomedicine., 2005, 1 (1), 2–9.

4. R. R. Coombs et al., Dev. Nano-technol., Gordon & Breach. ISBN 978-2-88449-080-1, 1996.

Synthesis, Characterization and Dielectric Studies of Polyvinyl alcohol/Cadmium oxide Nanocomposites

Chivukula Srikanth
Govt.College (Autonomous), Kalaburagi
***Corresponding author's email: chivukulasrik@gmail.com**

Abstract
Cadmium oxide nanoparticles have been synthesized by using Low Solution Combustion method. The Polyvinyl alcohol/Cadmium oxide nanocomposites were prepared by solutioncasting technique. The prepared composites were characterized by X-ray diffraction and Scanning Electron Microscopy. The crystallite size of these nanoparticles is found to be ~27.2 nm. The SEM analyses show an average grain size of 114-234 nm and 40-85 nm in PVA film and CdO respectively. The value of ac conductivity is found to increase by 33% for PVA/2% CdO nanocomposite compared to pure PVA at 700 kHz. The dielectric permittivity, dielectric loss of PVA/CdO nanocomposites decreased with increase in frequency values.
Keywords: Polyvinyl alcohol, Nano Cadmium oxide, ACconductivity, Dielectric permittivity , Dielectric loss.

1. Introduction

The polymer–nanocomposites in last few decades have become the subject of worldwide research interest. To exploit the full potential of the technological applications of these materials, it is very important to endow them with good processability. Polyvinyl alcohol (PVA) is a polyhydroxy polymer generally obtained by the hydrolysis of poly (vinyl acetate). Its good film forming nature, hydrophilicity and good chemical resistivity [1] have been used to develop inorganic-organic nanocomposite hybrids. Cadmium oxide (CdO) crystallizes in a cubic rock salt lattice like anion centres [2].It is an n-type semiconductor [3] with a band gap of 2.18 eV [4] at room temperature. In recent years, researchers have focused on cadmium oxide due to its potential applications specifically in the field of optoelectronic devices such as solar cells [5,6] , photo transistors [7] ,diodes [8] , transparent electrodes and gas sensors [9]. Many different research groups have investigated the structural, optical, thermal and electric properties of PVA containing different dopants. The previous investigations by different researchers have established the fact that PVA/CdO nanocomposites are scientifically challenging materials exhibiting a wide range of fascinating properties that can lead to a great variety of physical interests and technological applications. Although there exists a few brief reports on the investigations of PVA doped with CdO but there exists so far no detailed studies on the dielectric properties of these nanocomposites. We, therefore, prompted in the present study to undertake scientific investigations on these nanocomposites. We plan in our study to prepare CdO nanoparticles using combustion method and the PVA/CdO nanocomposite films using solution casting method. The prepared samples were characterized using X-Ray Diffraction (XRD) and Scanning Electron Microscopy (SEM) and studied their dielectric properties.

2. Experimental

Polyvinyl alcoholof analytical grade is obtained in the powder formfrom Nice Chemicals Pvt. Ltd. Cochin, with the average molecular weight of 1,25,000 g/mol (98% hydrolyzed) and Cadmium nitrate [$Cd(NO_3)_24H_2O$] is purchased from Molychem Ltd. Low Solution Combustion (LSC) technique is employed for the preparation of nano cadmium oxide [10].The pure PVA film and PVA/CdO nanocomposite films with different wt% (1,2,3,4)

were prepared by the solution casting method[11]. Powdered PVA of about 2.5g is dissolved in 50ml of double distilled water by stirring. The solution is then warmed up to 333K and thoroughly stirred, using a magnetic stirrer, for about 1hr until the polymer became completely soluble. By removing the trapped air bubbles, the solution is poured onto a levelled clean glass plate and left to dry at room temperature for about 48 hrs. The dried films were peeled off from the glass plate and cut into suitable pieces for measurements [12].

3. Results and Discussion

The X-ray diffraction pattern of CdO and PVA/CdO nanocomposite filmsare shown in Figure 1.The CdO nanoparticles have shown good crystallinity because of the existence of sharp peaks in the XRD pattern. The (111), (200), (220), (311) and (222) reflections are clearly seen and closely match the reference patterns for CdO (ICDD) File No. (05-0640)[13-15]. The crystallite size of the synthesized CdO nanoparticles which is calculated using Scherer's formula is found to be ~27.2 nm.The peak positionsfor all PVA/CdO nanocomposites show that diffraction angleappears around $19^{o} \leq 2\theta \leq 20^{o}$ for PVA.In the XRD pattern, different lines are attributed to the (111), (200), (220), (311) and (222) planes; by comparing the XRD pattern of the composite and CdO, it is confirmed that CdO has retained its structure even though it is dispersed in PVA matrix.

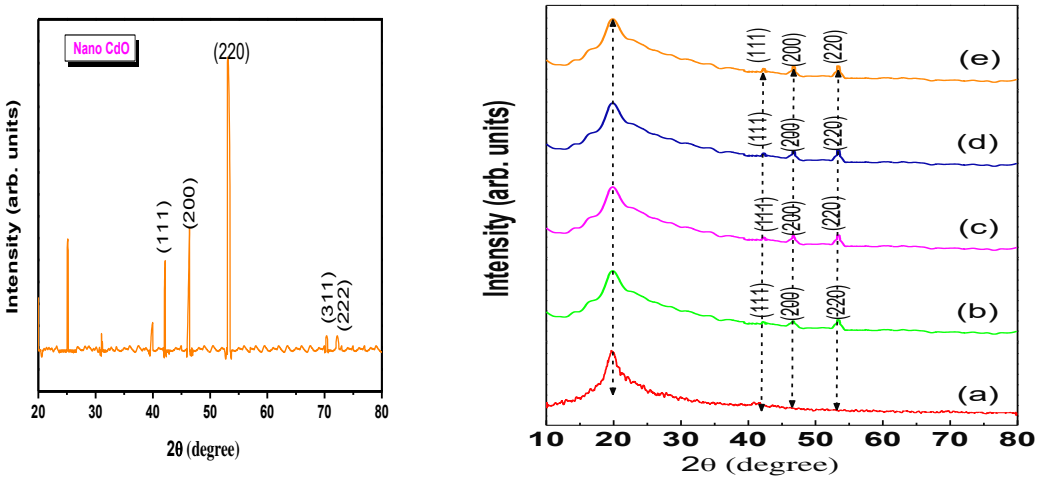

Figure 1: XRD pattern of CdO and (a) pure PVA (b) PVA/1% CdO (c) PVA/2% CdO (d) PVA/3% CdO and (e) PVA/4% CdO

The scanning electron micrographs of PVA film, nano CdO and PVA/2% CdO are shown in Figure 2.

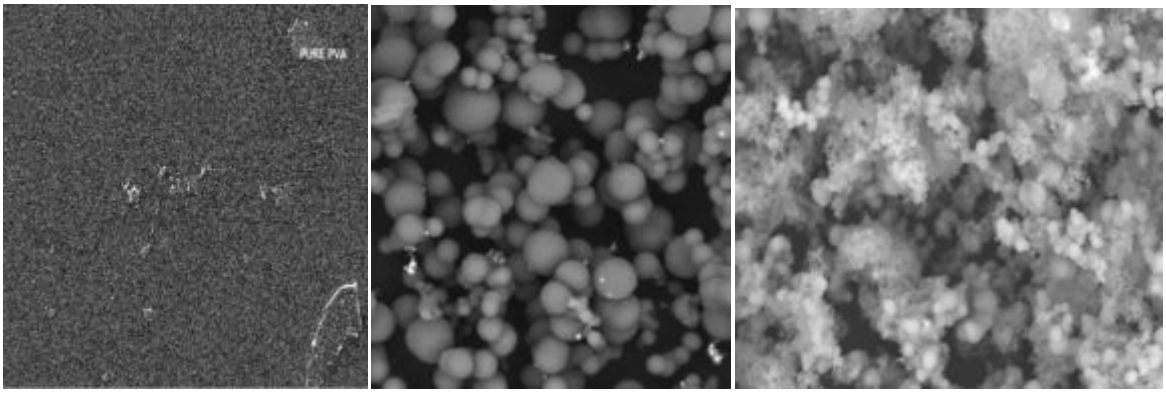

Figure 2: SEM image of pure PVA, nanoCdO and PVA/2%CdO

The SEM image of pure PVA shows uniformly processed smooth PVA matrix and the semi-crystalline nature of PVA supporting the observations of XRD analysis.The average grain size is found to be 114 nm to 234 nm.Also the CdO nanoparticles show spherical shape grains like morphology [16] having an average grain size from 40 nm to 85 nm. The crystallinity of the CdO is seen to decrease with the addition of PVA in it. The average grain size is found to be 70 nm to 150 nm.

3.1. Dielectric Studies

The *ac* conductivity of PVA/CdO nanocomposites at different frequencies is shown in Figure 3 at room temperature.

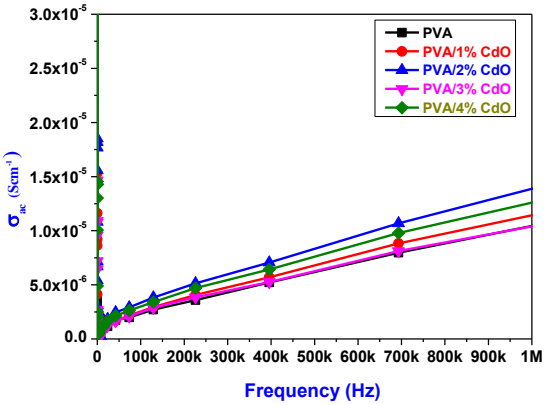

Figure 3: AC conductivity of PVA/CdO nanocomposites

At lower frequencies, the risein conductivity is negligible. In fact up to a frequency of 10^5 Hz, *ac*conductivity values were almost the same for all thenanocomposites. However, at higher frequency values, asharp rise in the conductivity values is observed. Also as the CdO concentration is increased upto 2 wt%, the inorganic filler molecules start bridging the gap separating the two localized states and lowering the potential barrier between them, thereby facilitating the transfer of charge carrier between two localized states and hence *ac* conductivity increases [17].

The dielectric permittivity (ε') anddielectric loss ε'' of PVA/CdO nanocomposites at different frequencies is shown in Figure 4at room temperature. The dielectric permittivity of PVA/CdO nanocomposites decreases with increase in frequency.

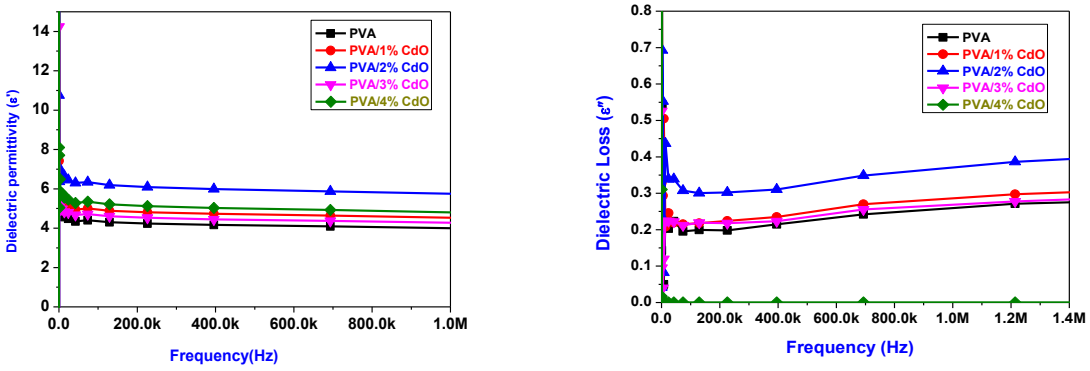

Figure 4: Dielectric permittivity and dielectric loss of PVA/CdO nanocomposites

At higher frequency above 10^5 Hz, ε′ remains almost constant throughout frequency region. On the other hand, the high value of ε′ at low frequencymight be due to the electrode effect and interfacial effect ofthe sample [18].

It can be seen that the dielectric loss decreases with increasing frequency. The dielectric loss has low value at higher frequency which may be due to the motion of free charges through the nanocomposites and above 10^5 Hz, ε''remains almost constant throughout the frequency region. It is observed that PVA/2% CdO show high dielectric loss, hence exhibits higher conductivity compared to that of other weight percentage. The dielectric constant is ε′= C d/$\varepsilon_{\circ}$Awhere d-thickness, A-area, $\varepsilon_{\circ}$-permittivity of free space, C-capacitance. The dielectric loss is ε″=σ/$\varepsilon_{\circ}$ω whereσ-ac conductivity,ω-frequency given by 2Πf.

The loss tangent of PVA/CdO nanocomposites at different frequencies is shown in Figure 5 at room temperature.

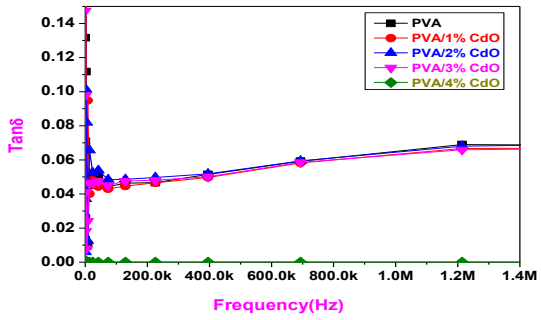

Figure 5: Loss tangent of PVA/CdO nanocomposites

The behaviour of loss tangent with respect to frequency follows the same trend as that of pure PVA at frequencies beyond 100 KHz as shown in Figure 5. At higher frequencies, these nanocomposites exhibit almost zero dielectric loss which suggests that these composites are low-loss materialsat frequencies beyond 1MHz. The loss tangentspectrum show relaxation process for all PVA/CdOnanocomposites considered and as the content of CdO increases, the magnitude of the relaxation peak decreases [19] and the breadth increases [20]. The values of tanδ are found to be below 1, indicating that the dielectric phenomenon is predominant in these nanocomposites. Loss tangent is calculated by using tan δ = c″(ω) / c′(ω) = ε″(ω) /

ε′(ω).From the plots it is clear that, the value of loss tangent for PVA/2% CdO is more compared to other weight percentages of CdO, which suggests higher electrical conductivity.

4. Conclusions

The results and conclusions drawn from the investigations on PVA/CdO nanocomposite films are the following.The XRD pattern of pure PVA shows a characteristic peak for an orthorhombic lattice centered at 20° indicating its semicrystalline nature. The XRD pattern of synthesized CdO nanoparticles shows good crystallinity. The crystallite size of these nanoparticles is found to be ~27.2 nm for (220) plane. The XRD pattern of PVA/CdO nanocomposites confirmed that CdO has retained its structure even though it is dispersed in PVA. The SEM analyses show an average grain size of 114-234 nm and 40-85 nm in PVA film and CdO respectively. The crystallinity of the CdO is seen to decrease with the addition of PVA in it and its average grain size is found to be 70-150 nm. The value of *ac* conductivity is found to increaseby 33% for PVA/2% CdO nanocomposite compared to pure PVA at 700K. The dielectric permittivity, dielectric loss of PVA/CdO nanocomposites decreased with increase in frequency values. The behavior of loss tangent with respect to frequency follows the same trend as that of pure PVA at frequencies beyond 100 KHz. At higher frequencies, these nanocomposites exhibit almost zero dielectric loss.

5. Acknowledgement

Author would like to thank Prof Vikas Patil, School of Physical Sciences, Solapur University, Solapur for providing lab facility to do dielectric studies.

References

1. M.Krumova et al., Polymer., 2000, **41**, 9265– 9272.
2. A. F. Wells et al., Oxford: Clarendon Press, 1984.
3. T.L. Chu et al., J. Electro. Mat., 1990, **19** (9), 1003–1005.
4. S. K. VasheghaniFarahani et al., Appl. Phys. Lett., 2013, **102** (2), 022102.
5. K. Sravani Reddy et al., J. Solar. Energy. Soc. India., 1996, **1**, 6.
6. L. M. Su et al., Electron. Lett., 1984, **20**,716.
7. R. Kondo et al., Jpn. J. Appl. Phys., 1971, **10**, 1547.
8. F. A. Benko et al., Solid State Commun., 1986, **57**, 901.
9. A. Shiori et al., Jpn. Patent No.7,909, 1997.
10. T. Mimaniet al., Mater. Phys Mech., 2001, **4**, 1.
11. H.N. Chandrakala et al., J. Mater. Sci., 2012, **47**, 8076.
12. Hemanth Kumar et al., Polymer., 2004, **45**, 5407–5415.
13. R. Kauretal., J.Non-Cryst. Solids., 2006, **352**, 2335.
14. R. R. Salunkheetal., Mater.Res. Bull., 2009, **44**, 364.
15. R. B. Waghulade et al., Talanta., 2007, **72**, 594.
16. K. Kesavan, et al., Nano Vision., 2013, **3** (3), 209-214.
17. M. H. Harun et al., Malay. Poly.J., 2008, **l3** (2), 24-31.
18. R. Singh et al., J. Appl. Phys., 1991, **69** (4), 2504.
19. T. Blyte et al., Electrical properties of polymers, Cambridge University Press, Cambridge , 2005,480.
20. K. C. Kao et al., Elsevier Academic Press, SanDiego, 2004, 112.

Band gap determination by Absorption Spectrum Fitting (ASF) method and Structural analysis of Bismuth based Glasses

Ch. Srinivasu
Department of P&C, MGIT, Gandipet, Hyderabad, India.
E-mail address: cholleti@mgit.ac.in, +91 9885476782

Abstract
Glasses having composition 10LiF-40Li_2O-20RO-30Bi_2O_3 where R= Mg, Ca, Sr & Ba have been prepared by the conventional melt quenching technique. The optical absorption spectra of the prepared glasses have been recorded in the wavelength range 200 to 800nm. Using the Tauc model, the absorption spectrum fitting method (ASF) was employed to obtain the optical band gap which is depend on the glass composition. Also, some physical parameters such as density, glass transition temperature and refractive index of prepared glasses were evaluated. It was found that, the densities of the glass increased in the order of MgO<CaO<SrO<BaO as expected from the relative masses of the alkaline-earth ions and the optical band gap (E_{opt}) values decreased with the replacement of RO oxides in the glass matrix.
Key words: Absorption; Composition; MDSC; Alkaline earth Oxides.

1.Introduction
In recent times, glasses based on HMO (TeO_2, GeO_2, Bi_2O_3, WO_3, PbO, Ag_2O, etc.) are promising materials for IR technologies, nonlinear optics and design of laser devices [1-4]. Bi_2O_3 is not a classical glass former, due to its high polarizability and small field strength of Bi^{3+}ions, in the presence of conventional glass formers, it may build a glass network of [BiO_n] (n = 3, 6) pyramids [5]. The properties of Bi_2O_3glass can often be altered by the addition of network modiiers. The most commonly used network modiiers are the alkali (Li2O, Na2O, and K2O) and alkaline earth oxides (MgO, CaO, SrO, and BaO). However, the structural role played by Bi_2O_3 in glasses is complicated and poorly understood. This is because the [BiO_n] polyhedra are highly distorted due to the lone pair electrons. The aim of the present work is determining of the optical band gap and tailing states and also discuss about some of the structural properties of 10LiF-40Li_2O-20RO-30Bi_2O_3 where R= Mg, Ca, Sr & Ba glasses such as density and glass transition temperature.

2.Experimental
The appropriate mole concentrations were weighted and grounded in a mortar. These materials were taken in porcelain crucible and placed in an electrically heated furnace maintained at 950°C. These mixtures took nearly 40–50 minutes to melt congruently; further, these mixtures were stirred occasionally to achieve homogeneity. The melt was then quenched by pouring it on to a preheated (around 250°C) stainless steel plate and pressing with another steel plate. The glasses formed were clear, transparent, bubble free with light blue tint. These glasses were annealed at that temperature to relieve the mechanical stresses. The thicknesses of the glass samples were around 0.5 to 1 mm. The compositions (in mol%) of the glasses studied in the present investigation were presented in Table 1.
XRD measurements were carried on an advance powder XRD (PANalytical X-pert PRO model with Cu-K Alpha radiation of wavelength 1.54048 Å) was usedwith Cu-Kα radiation with angle 2θ ranging from 10 – 80 . The optical absorption measurements were carried on polished glass samples using Shimadzu UV-1800 spectrophotometer in the wavelength region 200–800 nm at room temperature. Density measurements were carried out at room temperature using the Archimedes method with xylene as the immersion liquid. The density values were reproducible to ±0.02 g/cm^3.

3.Results and Discussions

The x-ray diffraction pattern of the reference glass (LiF-Li2O-20SrO-30Bi2O3) is given in the Figure 1 and the diffraction spectra of the present glass samples did not show any peaks. The peak free X-ray diffractograms indicated amorphous nature of the glass samples.

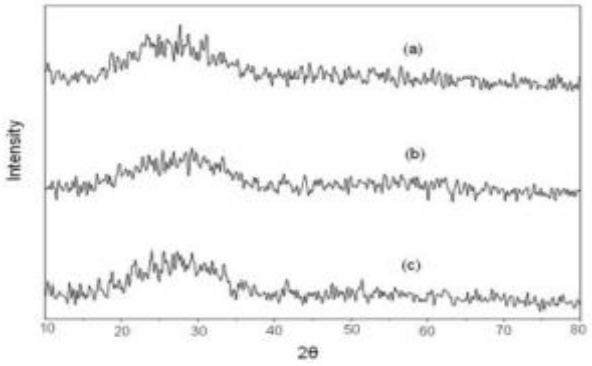

Figure 1. X-ray diffraction spectra

The room temperature density (ρ) of the samples was determined by the Archimedes principle. xlene was used as an immersion liquid. The densities were calculated by using the formula

$\rho = a^* 0.86 / (a-b)$ (1)

Where a is the weight of the sample measured in air, **b** is the weight of the sample measured in xylene (density of xylene at room temperature is 0.86 g/cc).The uncertainty in density measurement is ±0.001 g/cc. The molar volume of the glass samples was calculated using the formula

$V_m = M / \rho$(2)

Where M is the average molecular weight of the glass and ρ is its density. From the density data, oxygen packing density was calculated by using the formula

Oxygen packing density = (ρ/M)× number of oxygen atoms per formula unit. (3)

The variation of measured densities (ρ) of the present glasses along with evaluated values of molar volume (V_m) as function of alkaline earth element content is presented in in Table 1. Figure 2shows the variation of density of $10LiF\text{-}40Li_2O\text{-}20RO\text{-}30Bi_2O_3$ glasses, (where R= Mg, Ca, Sr and Ba). From the figure, the densities of the glass increased in the order of MgO<CaO<SrO<BaO as expected from the relative masses of the alkaline-earth ions. Similar results have been reported on $RO\text{-}Na_2O\text{-}Al_2O_3\text{-}P_2O_5$ glass system (where R= Mg, Ca, Sr and Ba).

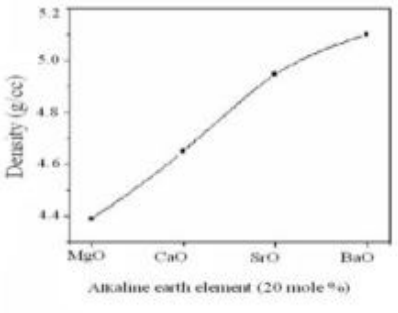

Figure 2. Density as a function of alkaline earth element (RO) in $10LiF\text{-}40Li_2O\text{-}20RO\text{-}30Bi_2O_3$ glasses

Figure 3 illustrates the MDSC thermograms of the $10LiF\text{-}40Li_2O\text{-}20RO\text{-}30Bi_2O_3$ glass system. Thermodynamical parameters such as glass transition temperature T_g, change in the transition temperature ΔT_g and specific heat capacity difference ΔC_pvalues were determined for all the glass samples and are presented in Table 1.

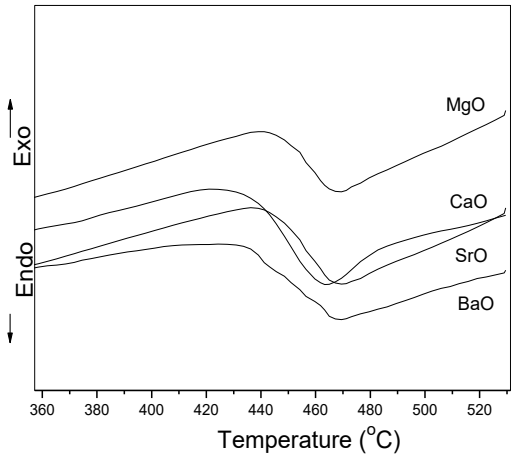

Figure 3. MDSC thermo grams

Figure 4plots the variation of glass transition temperature as function of alkaline earth element in $10LiF\text{-}40Li_2O\text{-}20RO\text{-}30Bi_2O_3$ (R= Mg, Ca, Sr and Ba).There is a difference of T_g about 28 ºC when MgO is replaced by BaO. The glass transition temperature decreased in the order of MgO>CaO>SrO>BaO. The decrease in T_g is attributed mainly to the lower field strength of the BaO compared to MgO.

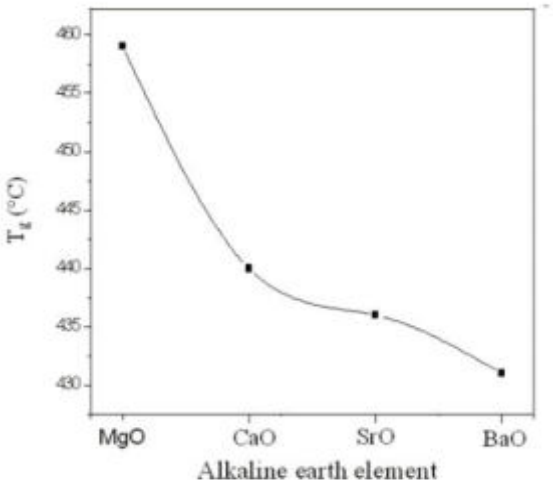

Figure 4. Glass transition temperature as function of alkaline earth element (20 mole %) in $10LiF\text{-}40Li_2O\text{-}20RO\text{-}30Bi_2O_3$ glasses

Table 1. Various physical parameters of present glasses

Glass Composition	Density (g/cc)	V_m (cc/mol)		λ_c(nm)	E_o(eV)	E_g^{ASF}
$40Li_2O$ -10LiF - $50Bi_2O_3$	4.98	49.70	421	413	3.01	3.0
$40Li_2O$- 10LiF -20MgO- $30Bi_2O_3$	4.38	36.34	459	431	2.88	2.90
$40Li_2O$ -10LiF- 20CaO - $30Bi_2O_3$	4.65	34.91	440	427	2.90	2.89
$40Li_2O$- 10LiF- 20SrO - $30Bi_2O_3$	4.82	36.30	436	420	2.95	2.94
$40Li_2O$ -10LiF- 20BaO - $30Bi_2O_3$	5.10	35.64	431	417	2.97	2.97

4. **Optical absorption spectra**

The absorption spectrum fitting (ASF) model [9, 10] has been applied to calculate the optical energy band gaps E_g^{ASF} for the investigated glasses using the measured UV absorption spectra. This method is characterized by the calculation of the optical gap energy of the prepared glasses can be achieved without needed to thickness measurement. The calculation mainly only depends on an absorbance data of the samples. Mott and Davis [6] have modified formula [7] for the optical absorption coefficient to be written as

$$\alpha(\omega)\,\hbar\omega = K(\hbar\omega - E_g^{ASF})^m \quad (4)$$

Beer–Lambert's law is used to calculate α(ω), K, ħω, and E_g^{ASF} are a constant, the incident photon energy, and the band gap energy. The optical transition type can be characterized by the power (m), where m =0.5 and 2, respectively, for allowed direct and indirect transitions [8]. Alarcon et al. [9], Souri and Shomalian [10] have expressed for the optical gap energy E_g^{ASF} as a function of incident photon wavelength E_g^{ASF} as

$$E_g^{ASF} = \frac{hc}{\lambda_c} = \frac{1239.83}{\lambda_c} \quad (5)$$

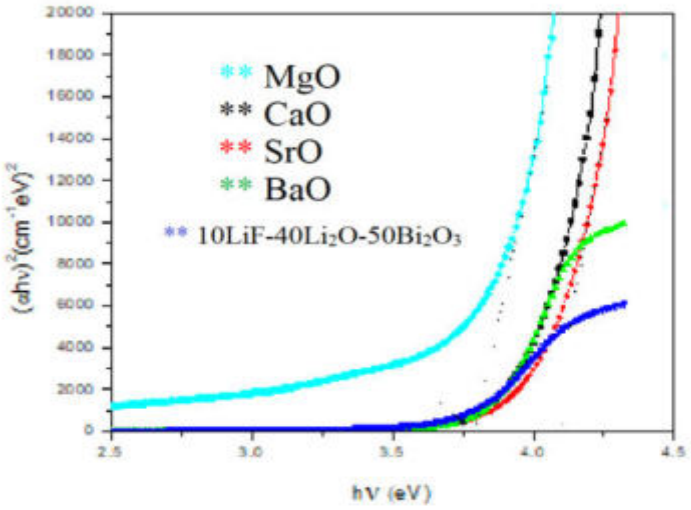

Figure 5.Tauc's plot

For ASF plots in between $(abs/\lambda)^2$versus $(1/\lambda)$ measured in $(nm)^{-1}$ for direct allowed transitions. and indirect allowed transition ASF plots are drawn between $(abs/\lambda)^{1/2}$ versus $(1/\lambda)$ measured in $(nm)^{-1}$. The values of E_g^{ASF} for direct or indirect transitions can be evaluated from the ASF plots by extrapolating the linear region of plotted data points, where $(A/\lambda)^m = 0$ and substituting in Eq. (6).E_g^{ASF}results for indirect and direct transitions are given in Table 1 and Figure 5 shows the Tauc's plots for the present glasses.

It is seen that E_g^{ASF} results of present glasses decrease with the content of alkaline earth conent. It is noticed that the direct E_g values are higher than the indirect allowed E_g. These values are close to which obtained by using Tauc's model.

4. Conclusions

In summary, our study gained new important data on glass formation, the glass transition temperarture and optical characteristics of the glasses based on the 10LiF-40Li_2O-20RO-30Bi_2O_3 (where R= Mg, Ca, Sr &Ba) multicomponent systems, which is useful for target synthesis of new glassy materials. The most suitable matrices for rare earths are glasses containing heavy metal oxides. Because of this, doping the glasses under study with rare earth oxides will give a possibility to extend their application range including the use as for optical fibre and optical devices application. Moreover, it can be used for optoelectronic and nonlinear optical devices.

5. Acknowledgement

The author would like to thank to Principal and Head of Department of Physics& Chemistry Mahatma Gandhi Institute of Technology, Gandipet, Hyderabad.

References

1. C.E. Stone et al., Phy Chem. Glasses., 2000, **41**, 409–412.
2. H. Hasu et al., J. NonCryst. Solids., 1996, **204** (1), 78.
3. P. Becker et al., Cryst. Res. Technol., 2003, **38** (1), 74.
4. D. Ehrt et al., Phys. Chem. Glasses., 2006, **47** (6), 669.
5. W.H. Dumbaugh et al., Phys. Chem. Glasses., 1986, **27**,119.
6. N. F. Mott et al., Electronic Processes in Non-Crystalline Materials. Clarendon Press, Oxford, 1979.

7. J. Tauc et al., Amorphous and Liquid Semiconductor. Plenum Press, New York, 1974.
8. C. Gautam et al., ISRN. Ceram., 2012, 1–17.
9. L. E. Alarcon et al., Appl. Surf. Sci., 2007, **254**, 412–15.
10. D. Souri et al., Journal of Non-Crystalline Solids., 2009, **355**(31-33):1597-1601

A Review on Carbon Based Heat Sink Materials

Sreekumar E.N, M.S Senthil Saravanan
Department of Mechanical Engineering
Sree Buddha College of Engineering, Pattoor
Corresponding Author Mail-id: sreekumar.rit@gmail.com

Abstract
Ever since the discovery of electronic devices excess heating was a major reliability concern. Recently many Thermal Management solutions are used to improve the performance of electronic devices and prevent their premature failure. Carbon/Graphene based Thermal Interface Materials (TIM) used as heat sinks in electronic devices are an on-going research interest as they enhance the thermal conductivity. In the present article, a detailed review on the recent developments in the area of Thermal Management of electronic devices is reported.

Keywords: Thermal Management, Thermal Interface Materials, Heat Sink, Thermal conductivity

1. Introduction

Over the years, electronic devices have undergone a significant reduction in its size, but on the contrary the power density still goes on increasing. According to Moore's law, which is an empirical observation that is used to predict the performance of Integrated Circuits (ICs) observed that the performance of ICs doubles in every two year [1]. As the performance increases, the amount of heat generated called Thermal Design Power (TDP) also increases. It became a major concern for heat dissipation in ICs. Research is going on to lower the heat generation or increase the heat dissipation in electronic devices. This can be achieved by either finding new materials or by heat transfer analysis. One major area is developing new materials with improved thermal conductivity. The development of new materials is attracted by most of the engineers and carbon based materials find much attraction in this area. This review aims to provide details about the synthesis of carbon based materials and thermal management ability of such materials.

2. Carbon based materials used for heat sink application

Conventional heat dissipaters are typically made up of materials like aluminum and copper which are quite heavy. So nowadays carbon based materials are used in different forms and compositions as they enhance the thermal conductivity. Graphene, Carbon Nano Tubes (CNTs) and theircombinations are widely used.

2.1.Graphene based composite materials

Grapheneis made up of single layer of carbon atoms arranged in a two dimensional honeycomb lattice, is a commonly used material for heat sink. They possess thermal conductivity in the range of 3000-5000W/mK at room temperature. They can be synthesised by Mechanical exfoliation [9], Chemical Vapour Deposition (CVD) [10]etc.

2.1.1. Graphene –Aluminum composite

Aluminum/graphene composite prepared by powder metallurgy method was used to enhance the heat dissipation and other mechanical properties. Enhancements have been observed in thermal conductivity by 15.4%, specific heat capacity by 9.1%, hardness by 21.1%, and compressive strength by 25.6% with an addition of 0.3 wt. % graphene into pure aluminum[2].

2.1.2. Graphene –Copper composite

A series of graphene nano sheets (GNs)/carbon nano tubes (CNTs) / copper (Cu) composite film was used for heat dissipation. The Laser flash and infrared thermal analysis showed that the thermal conductivity could be enhanced with GNs/CNTs composite film [3].

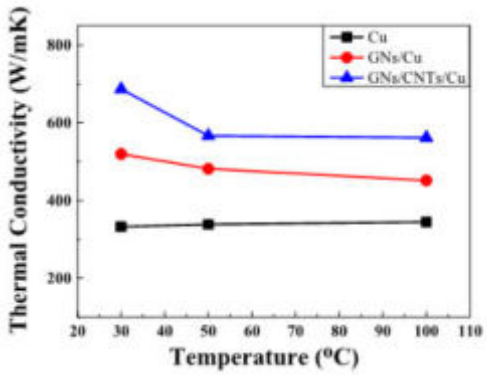

Figure 1.Thermal conductivity as a function of temperature [3].

Experimental studies demonstrated that Graphene- Cu-graphene heterogeneous film enhance the thermal conductivity as compared to Cu and annealed Cu films.CVD of a single atomic plane of graphene on both sides of a 9 μm thick Cu films increases their thermal conductivity by up to 24% near room temperature [4]. It was also observed that the enhancement of thermal properties was resulted from the changes in Cu morphology during graphene deposition than graphenes action as a heat conducting channel.

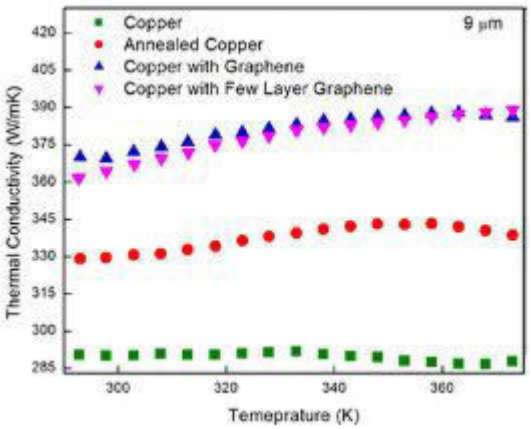

Figure 2.Thermal conductivity of reference Cu film, annealed Cu, Cu with CVD graphene, and Cu with CVD FLG[4].

The heat sink performance of Cu nanoparticle coated graphene sheets showed a thermal conductivity of 1912 W/mK at 50^0C.Simulation revealed that the graphene/Cu composite film exhibits more efficient thermal transport ability compared to Cu and graphene films [5].

2.1.3. Graphene –Multilayer Graphene Nano-composites

A mixture of graphene and multilayer graphene (MLG), produced by the liquid-phase-exfoliation(LPE) technique, can lead to an extremely strong enhancement of the cross-plane thermal conductivity of the composite. The laser flash measurements revealed a record-high enhancement of thermal conductivity by 2300% in the graphene-based polymer at a filler loading fraction of 10 vol. % [6].

Table 1. Thermal Conductivity Enhancement (TCE) in TIM Composites [6]

Filler Material	TCE	Fraction	Base Material	Method
Graphite	1800 %	20 wt. %	epoxy	laser flash
Graphene - MLG	2300 %	10 vol. %	epoxy	laser flash
Ni	566 %	<30 %	epoxy	laser flash

p-SWNT	350 %	9.0 wt. %	epoxy	laser flash

2.1.4. Carbon Nano tubes –Graphene Nano-sheets

The thermal conductivities ofheat sinks using CNTs and GNs within a temperature range of 323–373 K was extracted by experimentation. A homogenizing method was used to prepare three-dimensional CNT/GN framework, offering the higher thermal conductivity value as compared with CNTs and GNs. The thermal conductivity values of CNT/GN-based heat sink could attain as high as 1991 W/m K at 323 K. This enhanced thermal conductivity could be attributed to the fact that the hierarchical heat sink provided a three-dimensional thermal conductive network combining with point, line, and plane contact, leading to an efficient heat transport [7].

3. Conclusions

- From the review it is clear that graphene and its composites play an inevitable role in the field of Thermal Management. Carbon may be used in multiple forms to enhance the heat dissipation.
- Graphene based metal composites shows a major enhancement in heat dissipation.
- It was also observed that the thermal conductivity of copper may get enhanced with GNs-CNT film addition.

4. References

1. S. E. Thompson et al., Materials Today., 2006, **9**, 20-25.
2. L. Zhang et al., Journal of Alloys and Compounds., 2018, **748**, 854-860.
3. Y. L. Cheng et al., Journal of Alloys and Compounds., 2019, **790**, 156-162
4. Goliet al., Nano Letters., 2014,**14**, 1497-1503
5. T. h. Chienet al., Materials Chemistry and Physics., 2017, **197**, 105-112
6. M. F. Khan et al., Nano Letters., 2012, **12**, 861 − 867
7. C. Hsieh et al., Nano scale., 2015, **7**, 18663–18670.
8. Y. Fuet et al., 2D Materials.**,** 2019**, 7**, 1–42.
9. M Y Zigang Shen et al., Journal of Materials Chemistry A., 2015, **5**, 11700–11715.
10. C. Matter et al., Journal of Materials Chemistry., 2011, **21**, 3324 −3334.

Synthesis and Characterization of Corrosive Resistant Gelatin-Iron Zirconia Biocomposite

K.Saravanadevi [1*], R.Prabaharan [2]

[1] Assistant Professor of Chemistry, St.Mary's college (Autonomous), Thoothukudi, Tamilnadu, India

[2] Assistant Professor of Mechanical Engineering, Francis Xavier Engineering college, Tirunelveli, Tamilnadu, India

Corresponding author's email: whiterose.saravana@gmail.com

Abstract

Gelatin-iron zirconia nanoparticles were synthesized using co-precipitation method. The precipitation method was performed by adding ammonia solution to the aqueous solution of zirconium oxychloride, ferric chloride and gelatin by heating at 60°C. The surface morphology, size of the synthesized powders were structurally characterized by UV-Vis, FT-IR, EDAX, AFM, XRD and SEM. The UV-visible spectrum was noticed and the band gap is around 4.5 eV. The average particle size was calculated as 20nm with Body centered cubic crystals using scherrer's equation. The spherical shaped morphology were confirmed through the SEM analysis. From electrochemical impedance studies the prepared Gelatin-iron zirconia nanocomposites exhibit Corrosion resistance behaviour.

***Keywords**:* Gelatin, Zirconia, Co-precipitation, Corrosion resistance, Bio composite

1. Introduction

The interest in biocomposites is rapidly growing in terms of industrial application (automobiles, railway coach, aerospace, military applications, construction, and packaging) and fundamental research, due to its great benefits (renewable, cheap, recyclable, and biodegradable). Zirconium is mainly used as a refractory, opacifier and are corrosion resistant and biocompatible, and therefore can be used for body implants. In this study, we mainly synthesize gelatin-iron zirconia nanoparticles by chemical co-precipitation method and characterised using various techniques. The Nanoparticle is used in Corrosion resistance materials and it is Proved by Cyclic votametry.

2. Experimental

Gelatin-Iron zirconia nanoparticle was prepared by conventional co-precipitation method . The chemicals of zirconium oxychloride and ferric chloride was dissolved in 50ml of distilled water. To this 1g of gelatin was dissolved and 50ml of water was added. To this solution few mL of NH_4OH was added slowly and heated at 60°C. After cooling the color of the solution changes to brown indicating the formation of Gelatin -Iron zirconia nanocomposite.

Figure 2.1 Prepared Gelatin-Iron zirconia nanoparticle

3. Results and Discussion

3.1. Ultraviolet visible spectroscopy:

The UV-Visible spectrum(Fig 3.1 a) shows that the absorption band at 275 nm is observed. The blue shift is attributed to the smaller size of nanoparticles. This indicates the synthesized particles are in small size. The energy gap is 3.50852 eV (Fig 3.1 b)

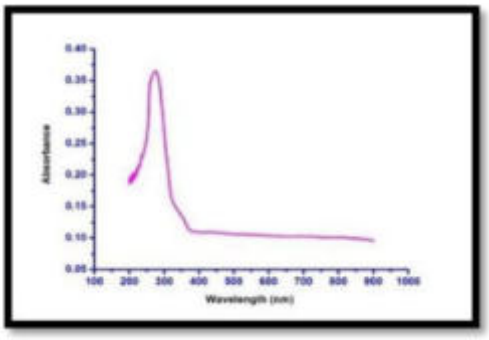

Fig:3.1(a)UV-Visible spectra Absorbance Vs wavelength

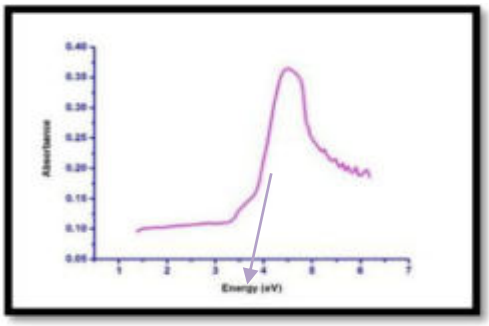

Fig:3.1(b) UV-Visible spectra Absorbance Vs Energy

3.2. FT-IR Studies:

The FT-IR spectrum of Gelatin-Iron zirconia composite was shown in the Fig3.2. In the spectrum the common band of protein appeared from 1743 cm^{-1} to 1512 cm^{-1} corresponding to the stretching vibration of C=O bond, N-H bond and C-N bond. The presence of gelatin-Iron zirconia nanocomposites can be confirmed by strong absorption band of (Zr-O) stretching at 632 $cm^{-1}$and 594 cm^{-1} [2,3]. The (Fe-O) stretching can be seen at 2360 cm^{-1} and 2322cm^{-1}. The sharp band around 3741 cm^{-1} shows the O-H stretching vibration.

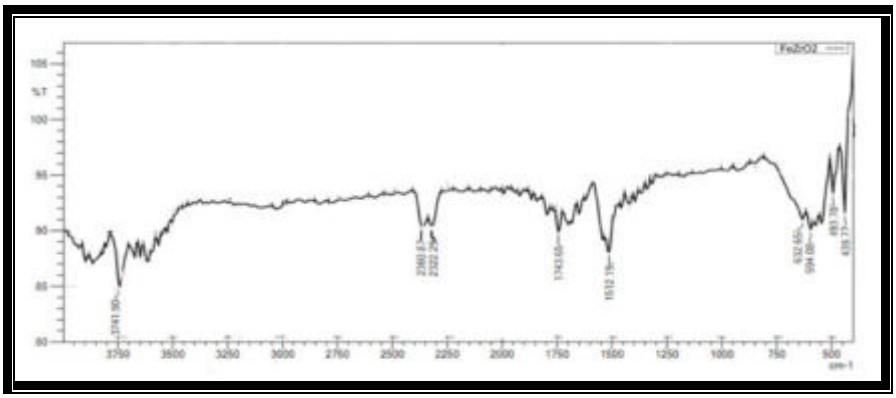

Fig.3.2 FT-IR Spectrum of Gelatin-iron zirconia composite

3.3.X-ray diffraction (XRD):

The structure of Gelatin-iron zirconia nanocomposites corresponds to body centered cubic structure which is confirmed by the crystalline lattice planes (210), (211), (222), (411) [4]. The average crystalline size of Gelatin-iron zirconia nanocomposites was found to be 20nm. The lattice value for the synthesized nanocomposites was found to be 5.9740 Å using Debye-scherrer formula.

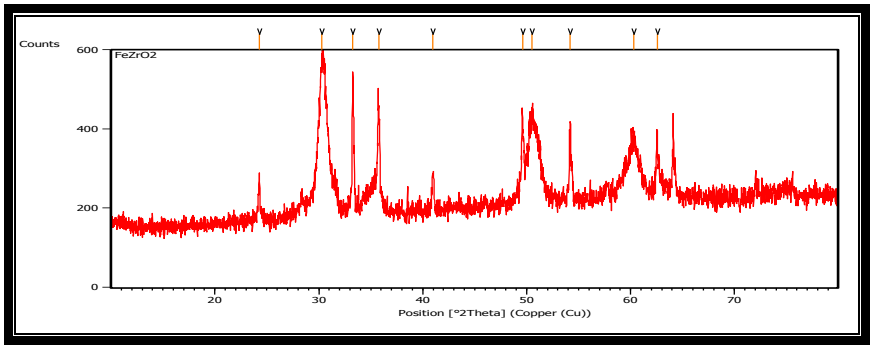

Fig3.3 XRD Spectrum of Gelatin-iron zirconia nanocomposites

3.4. Scanning electron microscope (SEM):

The morphology and size distribution of the synthesized gelatin-Iron zirconia nanoparticles ranges from 50 µm -1µm and they look like a rocks, nanoflakes and nano rods. The particle can be seen like spherical and hexagonal in shapes.

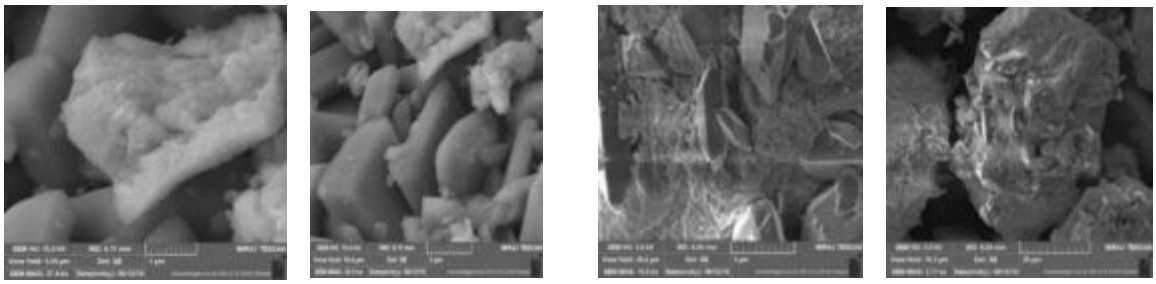

(a) (b) (c) (d)

Fig.3.4. a,b,c,d SEM image of Gelatin-iron zirconia magnified at 1µm,2µm,5µm, 20 µm

3.5. Energy dispersive x-ray analysis (EDAX):

The elemental analysis of gelatin-iron zirconia nanocomposites was carried out using EDAX. The energy dispersive x-ray analysis was used to confirm the elemental composition of the co-precipitation synthesized gelatin-iron zirconia nanoparticles. The Figure: 3.5 shows the zirconia,iron and oxygen elements present in synthesized gelatin-iron zirconia nanoparticles.

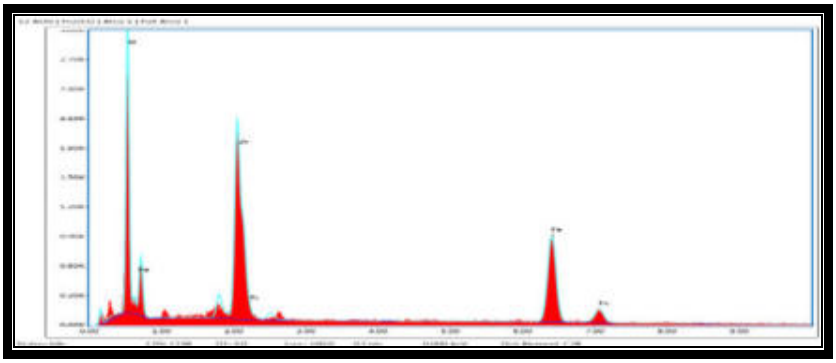

Fig:3.5.5 EDAX spectrum of Gelatin-iron zirconia nanocomposites

3.6. AFM analysis of gelatin-iron zirconia nanoparticles

Fig **5.6** shows the AFM spectral image of gelatin-iron zirconia nanoparticle synthesized using co-precipitation method with the scanning area of 9.842 pm^2 between 0 m X 3.13 µm and 0 m Y 3.13µm. . The size is in the range of 497nm to -328 nm. 3D view shows that the nanocomposites are triangular in shape.

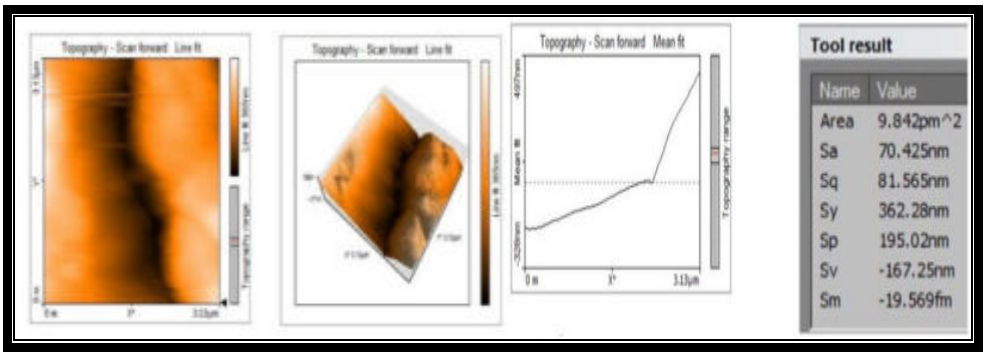

Fig : 3.6 AFM spectrum of gelatin-iron zirconium nanoparticles

3.7 Cyclic voltammetric behavior:

3.7.1 Polarization measurements and impedance studies:

Polarization measurments for Gelatin -ironzirconia nanocomposites on Glassy carbon recorded in 1% HCl solution. The protection efficiency (P.E%) of the coating was calculated using the following formula as 40% in 1% HCl. **P.E.% = (I_{corr} – I'_{corr}) × 100/ I_{corr}** [5,6]

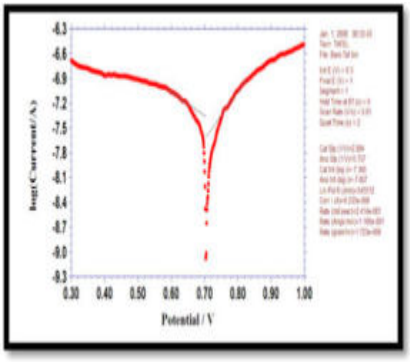

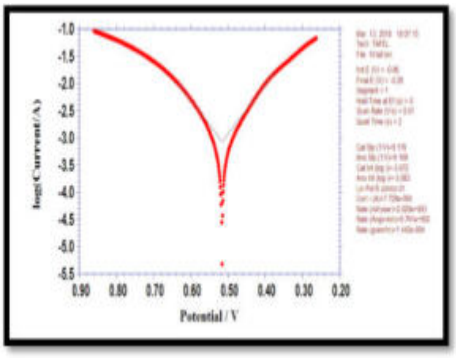

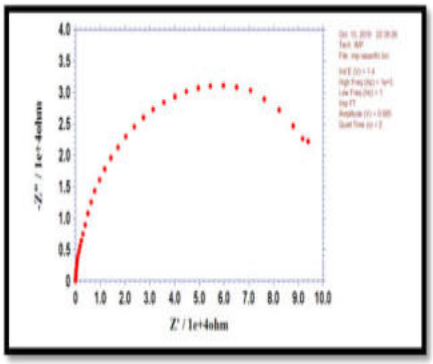

Fig: 3.7.1 Tafel plot for uncoated GC Fig: 3.7.2 Tafel plot for coated GC
Fig.3.7.3.Electrochemical impedence spectra for Gelatin-Iron zirconia nanocomposite

The corrosion current and corrosion rate is also less than bare for Gelatin-Iron zirconia nanocomposite coated GC Electrode. It makes the coating more corrosion resistant at lower concentration. Gelatin-iron zirconia nanocomposite powder shows an improved specific capacitance of 471 F g^{-1} in pH 1 buffer which is greater value at the current density of 1 A g^{-1}.

4. Conclusions

- Gelatin-iron zirconia nanoparticles was successfully synthesisted by using co-precipitation method.
- The surface morphology of the gelatin-iron zirconia nanoparticles was characterized by SEM analysis and suggested different morphological structure. It was a spherical and hexagonal in shape.
- The energy dispersive x-ray analysis was used to confirm the elemental composition of the co-precipitation synthesized gelatin-iron zirconia nanoparticles.
- Tafel curves shows that the protective action of the metal nanocomposites promotes a change of corrosion potential to more positive cathodically.
- From electrochemical impedance studies the prepared Gelatin-Iron zirconia nanocomposites exhibit corrosion resistance behaviour also.

5. Acknowledgement

I acknowledge the management of St.Mary's college (Autonomous), Thoothukudi, Tamilnadu Francis xavier engineering college(Autonomous),Tirunelveli, Tamilnadu DST-FIST sponsored PG & Research department of V.O.Chidambaram college, Thoothukudi, Tamilnadu for their Kindly support and encouragement to done this work.

6. References

1. M Fazeli, *et al.* Composites Part B: Engineering, 2018**,** 163, 207-216,
2. M Fazeli, *et al.* Int. Journal of Biological Macromolecules, 2018, 116, 272-280.
3. K Saud *et al.* Journal of Applied Polymer Science. 2017, 46, 134
4. G S. Brady *et al.* Materials Handbook (15thed.).McGraw-Hill Professional, 2011,1063
5. H. R. Sahu *et al.* Bull. Mater. Sci., 2000, 23(5) 5, 349- 354.
6. A. Powers *et al.*, Inorg. Chem, 1973**.** 12 (11), 2721-2726,

Influences of Nano Materials on the Rheological Properties of Self Compacting Concrete

Somasri.Madhavarapu[1] , Dr.Boppana.Narendra Kumar[2]
[1]PG Student, VNR VJIET, Bachupally, Hyderabad- 500090, India
[2]Professor, VNR VJIET, Bachupally, Hyderabad- 500090, India
Email: somasri.m96@gmail.com

Abstract

Now a day's maximum utilizable and considerable material in improving strength and durability performance of cement composites are Nano materials. But, noticeably still inclusion of Nano materials in cement compounds is in developing stage, one such Nano material in Graphene oxide (GO). This paper investigated the influence of GO on rheological properties of cement compounds. Furthermore, it shows how GO is prepared in the laboratory and how it improves the properties of cement composites. This paper also discusses about the practical problems involved in the GO incorporated cement composites. However, adopting this advanced material not only improves the existing properties but also brings new properties into existence. Incorporation of GO in various fields made outstanding progress where as extensive research still has to be done in the field of construction materials. Rheological properties of concrete are obtained for 0, 0.02, 0.04, 0.06, 0.08, 0.1 wt% Graphene Oxide.

Keywords*:* Graphene Oxide; Concrete; Cement composites; Cementitious Materials; Mechanical Strengths.

1. Introduction

Nanomaterials are characterized as a lot of particles where in any event one of its measurement is under 100nm. At this scale exceptional properties emerge and these have incredible effects in medication, developments and different fields. A portion of the Nano materials utilized in the development field are Nano silica, Fullerene, Carbon Nanotubes, Graphene oxide and so forth.

In this examination Graphene oxide is utilized to create HSSCC by changing the miniature structure of the concrete. When GO is added to solidify, Pore structure is refined when bloom like gems are shaped by nucleation of concrete hydrate and calcium silica hydrate gel. With increment in GO content in concrete, glasslike structure improves and makes pore structure more minimized. Mechanical properties are additionally improved because of the filling activity of GO experiencing significant change zone, nucleation of concrete hydrate and calcium silica hydrate and attachment among solidify and GO.

2. Experimental

Flow properties of the fresh concrete with and without graphene oxide are determined. The values are tabulated in Table.1 as follows

Table.1 Flow properties of concrete with and without GO

Mix designation	GO %	L-Box	Slump flow (mm)	T_{50}	V-Funnel (Seconds)	T_{5min}
HSSCC 1	0	0.84	600	16	24	24
HSSCC 2	0.02	0.87	605	15	19	23
HSSCC 3	0.04	0.90	612	15	18	22
HSSCC 4	0.06	0.92	620	14	20	22
HSSCC5	0.08	0.93	652	12	19	21
HSSCC6	0.1	0.94	670	11	18	20

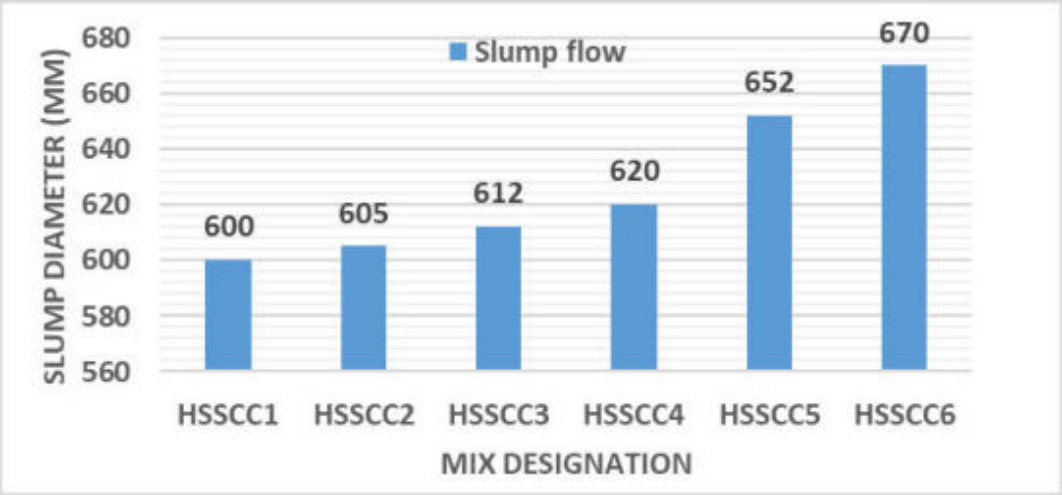

Figure1. The graph showing the variation of slump diameter with mix designation

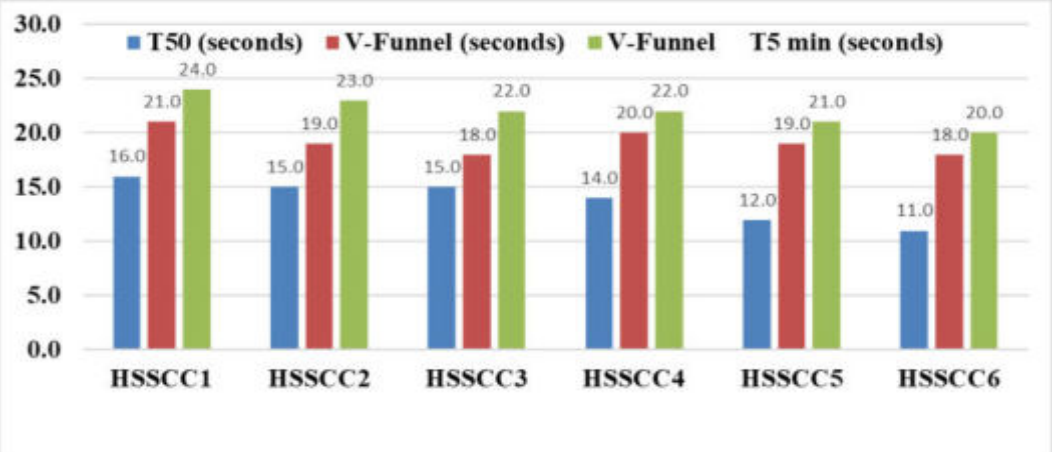

Figure2. The graph showing the variation of flow with mix designation.

3. Conclusions

- It was observed that there is significant increase in the flow properties with the increase in the amount of Graphene oxide in HSSCC.
- Mixes HSSCC1-HSSCC6 relative to the addition of GO in 0, 0.2, 0.04, 0.06, 0.08 and 0.1 wt. % of cement. Rheological properties are presented in Table 1. Fig 1- 2 represents the graph of the variations fluidity properties for different dosages of Graphene oxide.
- . It can be concluded that 0.1% is yielding best fresh properties.

4. References

1. C. S. R Indukuri, Construction and Building Materials, 2019, 229, 116863
2. S. C. Devi *et al.,* Journal of Building Engineering, 2020, *27*, 101007.
3. A. Mohammed *et al.* Australian Journal of Civil Engineering, 2017, 15(1), 61-71.
4. Y. Shang *et al.* Construction and Building Materials, 2015, 96, 20-28.
5. M. Chen *et al*. Construction and Building Materials, 2018, 189, 601-611.
6. L. Lu *et al*. Construction and Building Materials, 2018, 189, 33-41.

The Structural Elucidation of Lead Doped Transition Metal Oxide Nano Particles

D. Sudhakara Rao[1] and Dr. Y. Lakshman Kumar[2*],
[1]*Department of Physics, Tellakula Jalayya Polisetty Somasundaram College, Guntur-522 006, India.*
[2]*Department of Chemistry, QIS Institute of Technology, Ongole, India.*
Email: [1]physicstjpsc@gmail.com and [2]ylakshmankumar@yahoo.com*

Abstract

The intention of the explore was mainly focused on the blend of Pb doped transition metal oxide (ZnO) nanoparticle at room temperature. The section composition of the synthesized Pb doped ZnO nanoparticles were confirmed from powder x-ray diffractometer (XRD) and uv-vis spectra. In the current work we focused on the synthesis of Pb doped ZnO nanoparticles using coprecipitation method. From the xrd analysis, the crystalline size of Pb doped ZnO nanoparticles are calculated by debye scherrer's formula and found to each precursor was a hexagonal wurtzite zinc oxide structure with characteristic peak at 2θ=36.4. For uv-vis spectra of Pb dopped transition metal oxide (ZnO) nanoparticle the sharp absorption edge observed at 209 nm .

Keywords: Synthesis, XRD, UV-Vis, Pb doped ZnO.

1. Introduction:

All through the previous few years, synthesis of nano-structured oxide materials have been involved considerable awareness [1–3]. The metal oxides are tremendously important hi-tech materials for use in electronic and photonic devices and as catalysts in chemical industries. A range of physicochemical techniques have been employed to create nano-sized ZnO and MgO particles [4-6]. Quite a few techniques have been also developed to prepare nanocomposite of ZnO/MgO. This nanocomposite has attracted much attention because it has a superior band gap than ZnO [7]. On the other hand, most of the techniques need high temperatures and perform under a costly inert atmosphere. Our aim in this explore is to put forward an easy method to synthesize more porous and spongy nano-structured zinc oxide.The metal oxides nanocomposites are exceptionally vital technological materials for exercise in optoelectronic and photonic strategy and as catalysts in chemical industries. Zinc oxide (ZnO) is a large band gap n-type semiconductor with an energy gap of 3.37 eV at room temperature. It has been used very a large amount for its catalytic, electrical, optoelectronic, and photochemical properties [8]. MgO is typical wide band gap semiconductor; it possesses inimitable electronic, magnetic, thermal and chemical properties due to its quality structures [9]. These two oxides have been broadly used in almost the similar application areas. Upward a new composite material by combining them into one may perhaps open up a new track for research and applications. In recent years, researchers have paying attention more on the synthesis of nano amalgamated of ZnO/ MgO due to their application in sophisticated technologies.

The competence of ZnO nanoparticles, functionality and nanostructures can be enhanced by increasing and modifying their surface areas all the way through nanoscale addition of some dopants materials such as biomolecules and transition metals (Mn, Fe, Cr, Cu). This surface modification with biomolecules and transition metals confers new properties on ZnO nanoparticles so they can function as biosensors, antimicrobial, antioxidants, drug delivery systems and bioimaging materials. Manganese (Mn) is the metal of choice for doping of ZnO

nanoparticles because of the ready availability of its d electrons at t2g level, and also for the fact that these electrons can easily overlap with the valance bond of ZnO nanoparticles [10,11]. Different methods have been developed for the fabrication of un-doped ZnO and transition metaldoped ZnO nanoparticles [12]

2. Experimental:

2.1. Synthesis of Pb Doped ZnO Nano Particles

Zinc nitrate (Merck) lead nitrate $Pb(NO_3)_2$ is used as precursor prepare lead doped Zinc Oxide nano particles in chemical co-precipitate method, NaOH is used in the experiment as a precipitate. To prepare Lead doped zinc Oxide nano particles 100ml of (0.4M) NaOH is added drop wise into a mixture solution of 100ml (0.6M) Zinc Nitrate $Zn(NO_3)_2$ and 100ml of (0.01M) lead nitrate under constant stirring. Then the resulting solution was kept at the room temperature for 3 hours under constant stirring. The obtained precipitate is washed several times with distilled water and dried at 100ºC in oven for 3 hours. Finally The product was dried at 400ºC for 4 hours then grained into a fine particles. The dried precursor powder was to obtained the lead doped Zinc Oxide.

3. Results and Discussion:

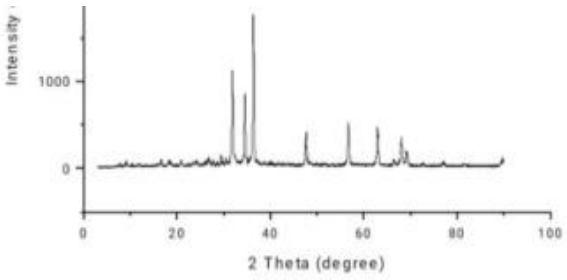

Fig 1 :-XRD pattern of synthesized Pb doped ZnO nanoparticle

3.1 Powder X-ray diffraction

The XRD pattern of synthesized lead doped zinc oxide nano particles as shown in fig. 1 for sample. The dominant peaks appears at 2θ~31.88, 2θ~34.56, 2θ~36.4, 2θ~47.68, 2θ~56.7, 2θ~63.0, 2θ~68.1, 2θ~69.16 corresponds to (100), (002), (101), (102), (110), (103),(112),(201) planes are in single phase with Hexagonal wurtzite structure. The diffraction peaks are well matched with the JCPDS card number:36-1451 for Hexagonal **wurtzite** structure of lead doped ZnO. The characteristic peaks dislocation and lattice strain for **sample A** are as shown in Table-1 the most intense peak is observed around **36.4nm** for **lead doped ZnO** nano particles which have a preferred growth orientation along **<< 101>>** direction.

These results shows that with increasing the amount of doping the particle size is decreasing continuously under the same reaction conditions and the same reaction temperatures.

Table-1: Lattice strain values of Pb doped ZnO nanoparticle

S.NO	SAMPLE CODE	POSITION (2θ)	FWHM (β)	CRYSTALLITE SIZE D(nm)	ATOMIC PLANES hkl	DISLOCATION DENSITY(δ) $\times 10^{-3}$Lines/m^2	LATTICE STRAIN (∈)
1	Pb doped ZnO	31.88	0.2697	30.64	100	1.0645	0.0041
2		34.56	0.2667	31.20	002	1.0266	0.0037
3		36.4	0.2687	31.13	101	1.0313	0.0035
4		47.68	0.2923	29.72	102	1.1314	0.0028
5		56.7	0.3901	23.15	110	1.8656	0.0031
6		63	0.3641	25.60	103	1.5255	0.0025
7		68.1	0.4323	22.19	112	2.0307	0.0027
8		69.16	0.4234	22.80	201	1.9235	0.0026

S.NO	SAMPLE CODE (Pb doped ZnO)	POSITION (2θ)	FWHM (β)	CRYSTALLITE SIZE D(nm)	ATOMIC PLANES (hkl)	DISLOCATION DENSITY(δ) $\times 10^{-3}$Lines/m^2	LATTICE STRAIN (∈)
1	sample A	36.4	0.2687	31.13	101	1.0313	0.0035

3.2 UV-Visible absorption spectroscopy

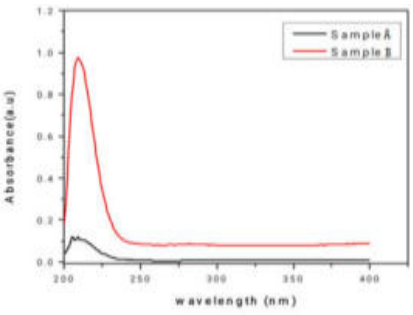

Fig 2 :- UV-Vis spectra of Pb doped ZnO nanoparticles

The optical study of Pb doped ZnO nanoparticles was carried at a room temperature using Shimadzu. UV-Vis is 1800 spectrophotometer in the wavelength ranging from 200 nm to 400 mm. The absorbance spectrum of the aligned Pb doped ZnO nanoparticle indicated that it has high UV-Vis absorbance properties at wavelengths below 400 nm. The sharp absorption edge observed around 207nm,209 nm for sample A and 209nm for sample B for the Pb doped ZnO annealed at 400^0C was decreased by increasing the temperature up to 500^0C. It corresponds to direct transition of electrons between the edges of the valance band and the conduction band.

4. CONCLUSION

The Lead doped ZnO Nanoparticles are prepared by Chemical precipitation technique, Lead doped ZnO the Nano particles are calcined at 400^0C for 4 hours. XRD, UV-Vis studies are made to determine the structural properties. XRD pattern of synthesized Pb doped ZnO nanoparticle is shown in fig 1, XRD peak confirms that the formation of Pb doped ZnO nanoparticles from each precursor was a Hexagonal Wurtzite zinc oxide structure with

characteristic peak at 2θ=36.4 for sample A. From the UV-Vis Spectra, Pb doped ZnO nanoparticle the sharp absorption edge observed around 207nm, 209 nm for sample A.

References

1. F. Nastase *et al.* , Prog. Solid State Chem. 2006, 34, 191-96.
2. S.H. Yoon *et al.* , Curr. Appl. Phys. 2006, 6, 154-59.
3. Y.Q. Huang, *et al.* Mater. Sci. Eng. B, 2001, 86, 232-238.
4. Y. Yang *et al.* J. Cryst. Growth, 2004, 263, 447-52.
5. B.Q. Xu *et al.* , Catal. Today, 2001, 68, 217-21.
6. M. Purica *et al.* Thin Solid Films 2002, 485, 403–404
7. M Ohtomo, *et al.* Appl. Phys. Lett. 1998, 72, 2466-74.
8. K. Pauporte *et al.* Chimica Acta., 2000, 45(20), 3345–53.
9. K. Ramanujam, *et al.* J Photochem Photobiol, B 2014, 141 296–300.
10. A B Djuisic *et al*. Appl Phys Lett 2004, 84(14) 2635- 37.
11. K M Reddy *et al.* Appl Phys Lett, 2007, 90, 2139021-23.
12. XX Yan *et al.* Physica B 2009, 404(16), 2377-2381.

Facile Hydrothermal Synthesis of Zinc Cobaltite Microspheres for High Performance Supercapacitors

G. Rajasekhara Reddy[1] G. Nataraju[2] and B. Deva Prasad Raju[3, *]
[1]Department of Instrumentation, Sri Venkateswara University, Tirupati – 517502, India
[2] Department of Physics, Chaitanya Bharathi Institute of Technology (A), Hyderabad-500075, India
[3]Department of Physics, Sri Venkateswara University, Tirupati – 517 502, India
Corresponding author's email: drdevaprasadraju@gmail.com

Abstract

The electrochemical performance of zinc cobaltite–based nano/micromaterial depends on its shape and morphology. Here we report on the electrochemical performance of zinc cobaltite ($ZnCo_2O_4$) material synthesized via a facile hydrothermal method. The synthesized material was characterized by X-ray diffraction (XRD), scanning electron microscopy (SEM) analysis. It was found to be a single-phase zinc cobaltite material with a cubic spinel crystal structure. The electrochemical performance of the synthesized zinc cobaltite microstructure material was evaluated by cyclic voltammetry, cyclic chronopotentiometry and electrochemical impedance spectroscopy. The zinc cobaltite microspheres material displayed a high specific capacitance of 600.37 F g^{-1} at a current density of 1 A g^{-1}. Such electrochemical performance may qualify the zinc cobaltite microspheres material as a potential electroactive material in supercapacitors.

Keywords*:* Hydrothermal; $ZnCO_2O_4$; microsphere; specific capacitance

1. Introduction

Supercapacitors, also known as electrochemical capacitors, have been considered as some of the most promising energy storage devices because of their many advantages, including high power density, faster charge and discharge processes, and longer lifespan, and hold great potential as power sources for applications in electric vehicles and hybrid electric vehicles [1]. Mixed transition metal oxides, typically binary metal oxides with two different metal cations, have received a lot of interest recently on account of their promising roles in many energy related fields [2]. Recently, binary $ZnCo_2O_4$ has been widely investigated as a high-performance electrode material for energy storage (including lithium-ion batteries and supercapacitors) due to its low cost, environmentally benign nature, natural abundance and high theoretical capacitance. Moreover, $ZnCo_2O_4$ possesses much better electrical conductivity and higher redox activity compared to nickel oxide and cobalt oxide, which originate from the co-existence of the Zn and Co species [3]. Herein, we present a two-step facile strategy involving a hydrothermal method and subsequent thermal annealing treatment to fabricate $ZnCo_2O_4$ microspheres. When evaluated as electrode materials for supercapacitors, the $ZnCo_2O_4$ microspheres show a high specific capacity of 600.37 F g^{-1} at 1 A g^{-1}, as well as good cycle stability.

2. Experimental

2.1 Synthesis of $ZnCo_2O_4$ microspheres

All chemical reagents were of analytical purity and were used without further purification. In a typical procedure, 20 mmol of $Co(Ac)_2.4H_2O$, 10 mmol of $Zn(Ac)_2.4H_2O$, 0.5g of urea and 0.8g of CTAB were dissolved in a 70 mL of DI water by constant stirring, and the mixture was stirred to form a pink solution. Then, the solution was transferred to a Teflon-lined stainless-steel autoclave and heated at 150 ℃ for 4 h. After naturally cooling down to room temperature, the resulting precipitates were collected by centrifugation,

washed several times with absolute ethanol and dried at 80 ºC in an oven. To obtain $ZnCo_2O_4$ microspheres, the precipitates were calcined at 400 ºC for 4 h.

2.2 characterization

The powder X-ray diffraction (XRD, PANalytical X'Pert Pro) patterns of the prepared samples were recorded using Cu Kα radiation (λ=1.540 Å) at a voltage of 40 kV and a current of 30 mA. The morphology of the samples was analyzed by field emission electron microscopy (FE-SEM, S-4800, Hitachi, Japan). Electrochemical measurements were conducted at room temperature using a typical three-electrode system, where an Ag/AgCl electrode was used as the reference electrode and platinum wire as the counter electrode. For all experiments, KOH (6M) was used as the active electrolyte. Cyclic voltammetry (CV), galvanostatic charge-discharge cycling (CD), and electrochemical impedance spectroscopy (EIS) were used to examine the electrochemical performance of the samples using a commercial instrument CHI 760E, CH Instruments, USA. The specific capacitance (*C*) was determined using the CD curves according to the following equation [4] :

$$C_s = \frac{2I\int V dt}{mV^2\Big|_{V_i}^{V_f}}$$

where C_S is the specific capacitance of the electrode (F g^{-1}); *I* is the discharge current (A); *m* is the mass of the active material (g); $\int Vdt$ is the area under the discharge curve and (V_f-V_i) is the voltage window (V).

3. Results and Discussion

The crystalline phase and purity of the as-synthesized sample was determined by powder XRD, as shown in Figure 1a. All the XRD peaks matched well with the standard AB_2O_4 type pattern of the cubic spinel structure (JCPDS No: 23-1390) [5]. All the characteristic peaks at 19.03°, 31.18°, 36.78°, 38.60°, 44.66°, 55.57°, 59.20°, 65.27°, 74.11°, and 77.11° 2θ were assigned to the (111), (220), (311), (222), (400), (422), (511), (440), (620), and (533) planes of cubic spinel $ZnCo_2O_4$, respectively. The XRD peaks were quite intense and sharp, indicating good crystallinity of the as-prepared $ZnCo_2O_4$ sample. In addition, no other XRD peaks were detected, confirming the absence of any contaminants and/or impurities. The morphology of the $ZnCo_2O_4$ products were carefully observed by means of SEM. The typical SEM images of the pure $ZnCo_2O_4$ products (Figure 1b) show that they are composed of microspheres with irregular diameters, very rough surface and comprised small nanoparticles.

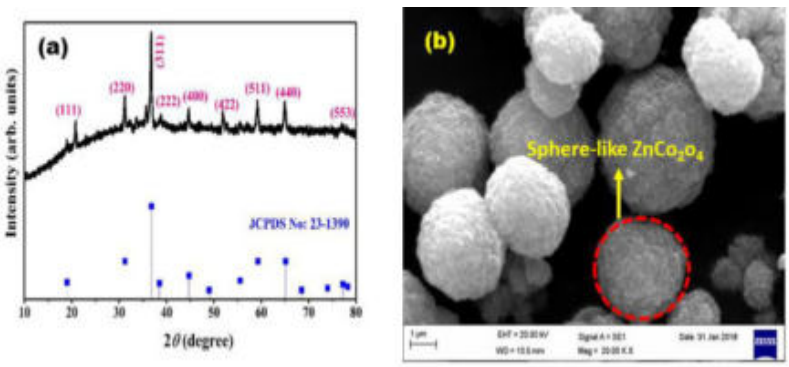

Figure 1. XRD pattern (a) and SEM image (b) for $ZnCo_2O_4$

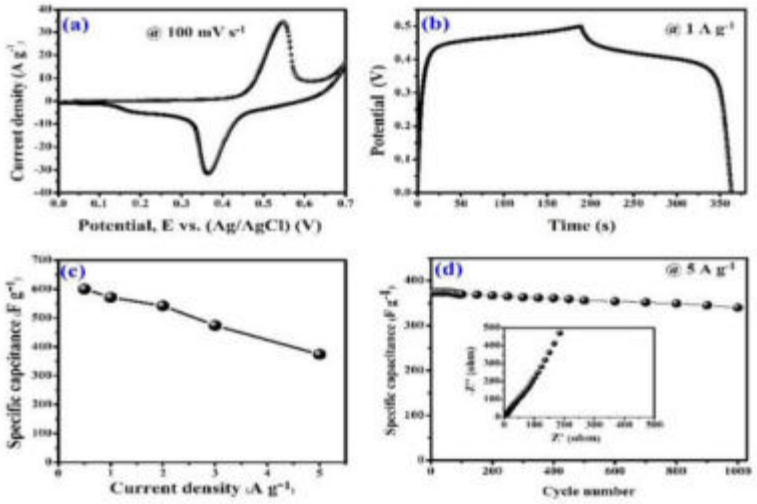

Figure 2. Electrochemical performance of $ZnCO_2O_4$ microspheres (a) CV (b) CD (c) Current density Vs. Specific capacitance (d) Cyclic performance and Nyquist plot (inset)

CV and CD were carried out to evaluate the electrochemical performance of porous $ZnCO_2O_4$ microstructures as a supercapacitor electrode material in a three-electrode system using a 6 M aqueous KOH solution as the electrolyte. Figure. 2a shows the typical CV curves of the $ZnCo_2O_4$ microstructures at 100 mV s^{-1} over the potential window of 0 to 0.7 V (vs. Ag/AgCl). The entire CV curves do not have a rectangular shape, inferring a pseudocapacitance (exhibits a pair of well-defined redox peaks) other than the electrochemical double-layer capacitance [6]. To further evaluate the potential applications of the $ZnCo_2O_4$ microstructures as an electrode material for electrochemical supercapacitors, CD measurements were carried out between 0 and 0.5 V at current density of 1 A g^{-1} (Figure 2b). The specific capacitance of the $ZnCO_2O_4$ microspheres electrode were estimated to be 600.37, 571.56, 542.41, 474, and 374.16 F g^{-1} at current densities of 0.5, 1, 2, 3 and 5 A g^{-1}, respectively, as shown in Figure 2c. The long-term cycle performance and stability are of great importance for practical applications of electrochemical supercapacitors [7]. The cycling performance of the $ZnCO_2O_4$ microspheres was examined by CD at a current density of 5 A g^{-1} for 1000 cycles over the potential region of 0 to 0.5 V. The capacitance of the $ZnCo_2O_4$ microspheres retained more than 90%, even after 1000 cycles, indicating good electrochemical cycling stability. To understand the outstanding electrochemical performance of the $ZnCO_2O_4$ microspheres, EIS measurements were further carried out. Inset of the Figure 2d exhibits the Nyquist plots of the $ZnCO_2O_4$ microspheres and exhibits a lower internal and charge-transfer resistance [8]. All of the results indicated the good electrochemical activity of the $ZnCo_2O_4$ microspheres electrode for energy storage.

4. Conclusions

- Zinc cobaltite microspheres material was synthesized by an economically facile hydrothermal process.
- The synthesized material displayed excellent electrochemical performance, which favoured electrolyte ion transport.
- It exhibits a high specific capacitance of 600.37 F g^{-1} at 1 A g^{-1}, a remarkable long-term cycling stability (90% of the maximum capacitance is retained after 1000 cycles at 5 A g^{-1})
- The synthesized zinc cobaltite microspheres material may prove to be promising electroactive material for applications in supercapacitors.

5. References

1. Y. Gai *et al.* RSC Adv, 2017, 7, 1038–1044.
2. Y. Xie *et al.* Angew. Chem. Int. Ed. 2014, 53, 1488-1504.
3. G.R. Reddy *et al.* Appl. Surf. Sci., 2020,529,147123.
4. L. Xu *et al.* Energy.,2017, 123, 296–304.
5. G.R. Reddy *et al.* Nanomaterials, 2020, 10, 1206.
6. F. Bao *et al.* RSC Adv., 2014, 4, 2393
7. V. Kumar *et al.* ACS Omega., 2017, 2, 6003–6013.
8. H. Chen *et al.* Ceram. Int.,2019, 45,8577 –8584.

Optical Properties of Annealed Spray Pyrolyzed Zinc Oxide Thin Films

Ayana A[1*] and B V Rajendra[1]
[1]Department of Physics, Manipal Institute of Technology, Manipal, India-576104
*Corresponding Author: aayana12345@gmail.com

Abstract

Metal oxide semiconductor of Zinc Oxide (ZnO) thin films are getting considerable attention in the earlier decades due to its extensively wide variety of applications in various fields. In this work, ZnO films have deposited at 450 ^{o}C on a chemically cleaned glass substrate through a conventional chemical spray pyrolysis technique. The precursor solution is prepared by adding zinc acetate dihydrate with double distilled water. The deposited samples were annealed at different temperatures for 2 hours. Optical transmission in the visible region were maximum for the sample annealed at 450 ^{o}C. The energy band gap increased with annealing temperature due to the enhancement of grain size in the deposits. The refractive index(n) and extinction coefficient(K) values of the samples were estimated for different wavelengths. The decrease in Urbach energy with an increase of annealing temperature indicates the improvement of the crystallinity of the sample.

***Keywords**:* spray pyrolysis, optical bandgap, urbach energy

1. Introduction

Nanostructured semiconductors of Zinc Oxide (ZnO) has attracted extensive research for the last several years owing to their several properties, such as wide direct band gap(3.37eV), a large band strength with large excitonic binding energy(60meV), the broad range of radiation absorption, etc.[1-4]. The simultaneous low resistivity and high optical transmittance characteristics of ZnO make it an obvious choice for optoelectronic applications. These properties make ZnO as a suitable material for many applications such as solar cells[5], UV detectors[6], piezoelectric nanogenerators[7], gas sensors[8], light-emitting diodes[9], etc. It is an n-type II-VI semiconductor owing to the presence of native defects. ZnO thin film is a common nanostructure, which has the advantage of depositing in almost all non-conventional methods, including sol-gel[10], chemical vapor deposition[11], sputtering[12], pulse laser deposition[13], and spray pyrolysis[14]. Based on its simplicity and economical equipment, the spray pyrolysis is exclusively used method due to its possible wide-area depositions and easy control of film thickness. The present report provides the effect of annealing on optical properties of ZnO thin film deposited on glass substrate using 0.05M concentration precursor solution of Zinc acetate through the spray pyrolysis method.

2. Experiment

ZnO thin films were deposited on a chemically cleaned glass substrate at 450 ^{0}C using a low-cost spray pyrolysis method. Zinc acetate dihydrate of 0.05M concentration (supplied by sigma Aldrich>99%) and double distilled water were used to prepare the solvent. The solution stirred continuously for getting a homogeneous and transparent solution. The spray nozzle to substrate temperature and pressure of carrier gas fixed at 28 cm and 5 kg/cm^2,

respectively. The solution rate was maintained as 2ml/min, and the process was carried out in the atmospheric condition. The prepared films were annealed at various temperatures for 2 hr. The thickness of the film was in the range of 500-550 nm calculated by a profilometer. Transmission spectra of the annealed samples were measured using schimadzu -1800 UV-VIS spectrophotometer operated at a resolution of 1nm from 300 nm to 800 nm.

3. Results and Discussion

The transmittance of the annealed samples was about 80-85% in the visible region [fig.1]. The figure shows that optical transparency in the visible region is higher for the sample annealed at 450^0c. The slight increase in transparency with temperature may be due to the improvement of the film structure. The sharp change at the absorption edge indicates the prepared samples suitable for optoelectronic devices.

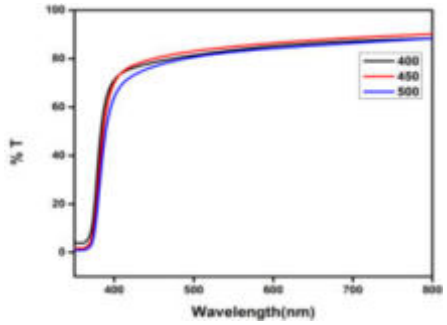

Figure 1: Variation of transmittance with wavelength of ZnO film annealed at various temperatures.

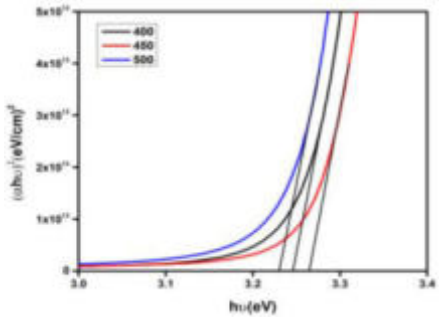

Figure 2: Variation of $(\alpha hv)^2$ with hv of ZnO film annealed at various temperatures.

The energy band gap (E_g) values estimated from transmission measurements using Tauc's relation,

$$\alpha h\upsilon = A\left(h\upsilon - E_g\right)^n \quad \text{-------- (1)}$$

Where hυ is the energy of the incident photon, and E_g is the energy gap between the conduction and valence band. A is a constant depending upon the transition probability for the direct transition, and n is a constant which is equal to ½ if the transition is allowed or 3/2 if the transition is forbidden, α is the optical absorption coefficient. Variation of $(\alpha h\upsilon)^2$ upon incident photon energy (hυ) used to calculate the optical band gap E_g. Here optical bandgap increased for samples annealed at 400 and 450 ^oC. At ambient temperature, there are only fewer charge carriers present in the ZnO samples. But, as the temperature increases, the electronically active carriers will also increase, this will lead to the creation of excess charge carriers in the conduction band. The rise in charge carriers is due to thermal excitation, which increases the conductivity of the films. The decrease in the optical band gap at an annealing temperature of 500°C may be due to defects created in the deposited samples. Also, there is a chance to remove oxygen vacancies at higher temperatures, which may reduce the carrier concentration and, consequently, the band gap, which may be due to the Burstein-Moss shift

[15]. The ZnO thin film with annealing temperature at 450 °C has a higher band gap energy [table 1].

The extinction coefficient and refractive index values play an essential role in the analysis of optical materials. The extinction coefficient and refractive index value vary with annealing temperature, as shown in Figures 3 & 4. The refractive index value is less for the sample annealed at 450 °C. This may be due to an increase in energy bandgap, which causes lattice expansion and the grain size to grow and decreases the defect. The decrease in K value with an increase in wavelength shows the decrease in absorbance, and it is less for the sample annealed at 450 °C. Furthermore, the optical absorption edge can be seen clearly for three samples.

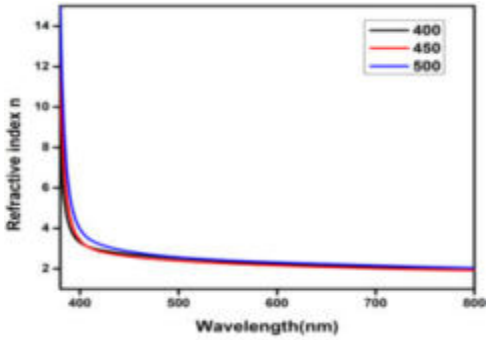

Figure 3: Variation of refractive index with wavelength of ZnO film annealed at various temperatures

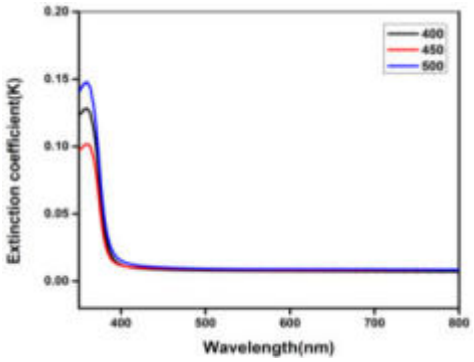

Figure 4: Variation of extinction co-efficient(K) with wavelength of ZnO film annealed at various temperatures.

The Urbach energy can be calculated by using the following equation,

$$\alpha = \alpha_0 \, exp\left(\frac{h\nu}{E_u}\right) \quad \text{----------(2)}$$

where α_0 is a constant and E_u is Urbach energy. The plot of lnα versus photon energy hν of ZnO thin films annealed at different temperatures is shown in figure 5. The decrease in Urbach energy within increase of annealing temperature indicates the improvement of crystallinity of the deposits.

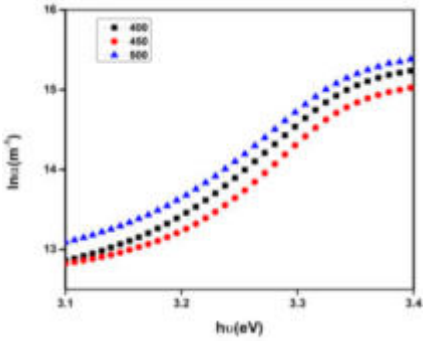

Figure 5: Variation of ln (α) with hν of ZnO film annealed at various temperatures.

Table 1: Energy gap, Urbach energy of ZnO films annealed at different temperatures

Temperature (°C)	Band Gap (eV)	Urbach energy (meV)
400	3.246	103.388
450	3.264	95.278
500	3.231	97.381

4. Conclusions

- Highly transparent zinc oxide films were deposited on the glass substrate at 450^0C using the spray pyrolysis method.
- The energy band gap increased with annealing temperature of the samples due to the enhancement of grain size in the deposits.
- The refractive index and extinction coefficient of the samples were estimated for different wavelengths.
- The decrease in Urbach energy with an increase of annealing temperature indicates the improvement of crystallinity of the deposits.

Acknowledgment
Authors are grateful to Maipal Institute of Technology, Manipal, for providing instrumentation facility and financial support to carry out research work.

References

1. R. Bomila *et al.* J. Supercond. Nov. Magn., 31, 3, 855–864, 2018.
2. A. Bougrine *et al.* Mater. Chem. Phys., 80, 2, 438–445, 2003.
3. R. Zamiri *et al.* J. Asian Ceram. Soc., 5, 1, 1–6, 2017.
4. A. Manikandan *et al.* J. Alloys Compd., 723, 1155–1161, 2017.
5. K. Keis *et al.* Sol. Energy Mater. Sol. Cells, 73, 1, 51–58, 2002.
6. J. Cheng *et al.* J. Cryst. Growth, 310, 1, 57–61, 2008.
7. A. Khan *et al.* Appl. Phys. Lett., 101, 19, 2012.
8. M. W. Ahn *et al.* Appl. Phys. Lett., 93, 26, 91–94, 2008.
9. Y. Ryu *et al.* Appl. Phys. Lett., 88, 24, 2006.
10. D. Bao *et al.* Thin Solid Films, 312, 1–2, 37–39, 1998.
11. S. T. Tan *et al.* J. Appl. Phys., 98, 1, 2005.
12. Y. M. Lu *et al.* Mater. Chem. Phys., 72, 2, 269–272, 2001.
13. L. Zhao *et al.* Appl. Surf. Sci., 252, 24, 8451–8455, 2006.
14. R. Ayouchi *et al.* J. Cryst. Growth, 247, 3–4, 497–504, 2003.
15. M. M. Aghgonbad and H. Sedghi, “PT US CR,” Chinese J. Phys., 2018.

Influence of Pr^{3+} Ions on Structural and Photoluminescence Properties of Barium Yittrium Phosphate Phosphors

K. Anila[1], B. Prasanna Lakshmi[1], K. Rajeswari[1], B. Deva Prasad Raju[1] and G. Nataraju[*,2]
[1] Department of Physics, Sri Venkateswara University, Tirupati -517502
[2] Department of Physics, Chaitanya Bharathi Institute of Technology (A), Hyderabad-500075
[*]Corresponding author email: gnataraju_physics@cbit.ac.in

Abstract

Currently the development of red-emitting phosphor is still an ongoing challenge. Here in the structural and photoluminescence properties of Pr^{3+} ions doped barium yttrium phosphate phosphors, with composition of $6NH_4H_2PO_4+6BaCO_3+Y_2O_3+xPr_6O_{11}$ to get $Ba_3Y_{(1-x)}(PO_4)_3$ compound where (x = 0, 0.01, 0.05, 0.1, 0.15 and 0.2), have been prepared by solid-state reaction method. These phosphors are characterized by X-ray diffraction, FTIR analysis, and photoluminescence studies. The dopants of Pr^{3+} ions occupied the Y^{3+} sites with high inversion symmetry in the host matrix. The average crystallite size is estimated by using the Scherrer's equation and is approximately 63.8 Å. The luminescence spectra consist 468, 473, 482, and 492, 602, 643 and 691 nm corresponding to the $^3P_1 \rightarrow {}^3H_4$, $^1I_6 \rightarrow {}^3H_4$, $^3P_0 \rightarrow {}^3H_4$ and $^3P_0 \rightarrow {}^3H_4$, $^1D_2 \rightarrow {}^3H_4$, $^3P_0 \rightarrow {}^3F_2$, and $^1D_2 \rightarrow {}^3F_5$ transitions results in blue and red regions respectively. When this is compensated with green light it emits white light. Based on the above results, the 0.15mol% Pr^{3+} doped $BaY(PO_4)_3$ phosphors may be used for the white LED applications. The obtained CCT values show that the $Ba_3Y(PO_4)_3$: Pr^{3+} phosphors can serve as potential phosphors for warm white LEDs.

Keywords: Phosphate phosphor; solid-state reaction; photoluminescence; color coordinates

1. Introduction

The increasing demand for phosphors has promoted the researchers to develop types of phosphors for their applications as luminescence materials. Phosphors are composed of an inert host lattice and an optically excited activators, typically 3*d* or 4*f* electron metal ions, which are capable of exhibiting high photoluminescence efficiency, stability and high absorption cross sections [1]. On the other hand, lanthanide ions have been widely used as the activators in different host materials. The unique luminescence properties of lanthanide ions hosted in different matrices have form technologically important applications in optoelectronic devices such as plasma panels, flat panel displays, luminescent lightning and IR windows [1,2]. The development of display devices has always been accompanied by improvement in the usage of phosphors. For example, the advent of color television was based on the development of efficient red phosphors [3].

In this study, we aimed to explore the efficiency of $La_2Hf_2O_7$:Pr^{3+} NPs as a potential candidate material for use in lighting and scintillators materials. Therefore, we have synthesized $La_2Hf_2O_7$ NPs with various Pr^{3+} doping concentrations.

2. Experimental

$BaCo_3$, Y_2O_3, $(NH_4)_2HPO_4$ and Pr_6O_{11} according to the stoichiometric ratio of $Ba_3Y_{(1-x)}(PO_4)_3:xPr^{3+}$ (x = 0, 0.01, 0.05, 0.1, 0.15 and 0.2) were accurately measured and placed in ceramic mortar. First, the precursors were ground with a proper amount of acetone, until the powder was mixed evenly. $Ba_3Y_{(1-x)}(PO_4)_3:Pr^{3+}$ phosphor was prepared by the high temperature solid state reaction method.

The structure of prepared samples has been checked by recording the XRD pattern using PANalytical benchtop X-ray diffractometer with Cu-K_β radiation to identify the possible phases in the sample. Fourier-transform infrared transmission spectra was measured using Bruker Alpha – II FTIR spectrometer with a spectral resolution of 0.5-0.6 cm^{-1}. The excitation and emission spectra measurements were made by a FLS 980 spectrofluorometer.

3. Results and discussions:

1. XRD analysis:

X-ray diffraction pattern of $Ba_3Y(PO_4)_3:Pr^{3+}$ phosphors were shown in Figure 1a. The XRD patterns of phosphors after heating at 1100^0C were well agreed with the standard JCPDS code 00-044-0318 [4]. The orthophosphate $Ba_3Y(PO_4)_3$ is a host material of the active Pr^{3+} ions belong to the large family of eulytile type compounds. $Ba_3Y(PO_4)_3$ contains three possible different orientations of the PO_4 tetrahedron within the $(Ba, Y)_8$ basisphenoids corresponding the three sets of partially occupied oxygen positions [4]. It means the Y^{3+}/Ba^{2+} pairs of cations are disordered on a single crystallographic site while the oxygen atoms of the phosphate groups are distributed over three partially occupies sites. This disorder involves statistical cell. This can be associated with the mixed occupancy of the metal site and short-range disorder of this sub-lattice. The intrinsic structural disorder in both oxygen and metal sub-lattices should be reflected in spectroscopic properties of the material.

$Ba_3Y(PO_4)_3$ has a cubic structure with space group of I-43d and lattice parameters a = b = c = 10.46 Å and V=1146.5 Å. The Y^{3+} ions occupies a distorted octahedron of oxygen ions due to three short and three long Y − O distances. Therefore, we can predict that the Y^{3+} ions occupy non-inversion centrosymmetric sites. Considering the effect of ionic sizes of cations and valence numbers, Pr^{3+} ions replace Y^{3+} more easily than Ba^{2+} ions. Because the ionic radius of Pr^{3+} ions (0.99 Å) is very close to ionic radii of Y^{3+} (1.019 Å) than Ba^{2+} (1.42 Å). The crystalline size of the phosphors is calculated by using Scherrers equation and the crystallite size value is 63.8 Å.

3.2 Photoluminescence properties

The excitation spectrum of $Ba_3Y_{(1-x)}(PO_4)_3:xPr^{3+}$ was monitored at emission wavelength of 602 nm corresponding to the transition $^1D_2 \rightarrow {}^3H_4$. It produces a strong excitation band in the region of 375 to 550nm. This spectrum is mainly composed of three peaks at 444,470 and 482 nm respectively. The excitation peaks are originated from the transitions $^3H_4 \rightarrow {}^3P2$, $^3H_4 \rightarrow {}^3P_1$ and $^3H_4 \rightarrow {}^3P_0$ respectively within the $^4f2$ configuration. When electrons are excited to $^3P_{0,1,2}$ levels, they may either relax to $^3P0$ state and recombine to ^3H_J and ^3F_J states or non-radiatively relax to $^1D_2$ state and recombine to lower levels following selection rules. Among all the excitation peaks, the peak corresponding to the

transition $^3H_4 \rightarrow ^3P_2$ (444 nm) is more intense and is used as an excitation wavelength to record the emission spectra for all the phosphors in the present study. The excitation spectra of $Ba_3Y_{(1-x)}(PO_4)_3:xPr^{3+}$ was shown in Figure 1b.

Figure 1. XRD patterns (a) Excitation spectrum (b) Emission spectra (c) CIE chromaticity diagram (d) of $Ba_3Y(PO_4)_3:Pr^{3+}$ phosphors

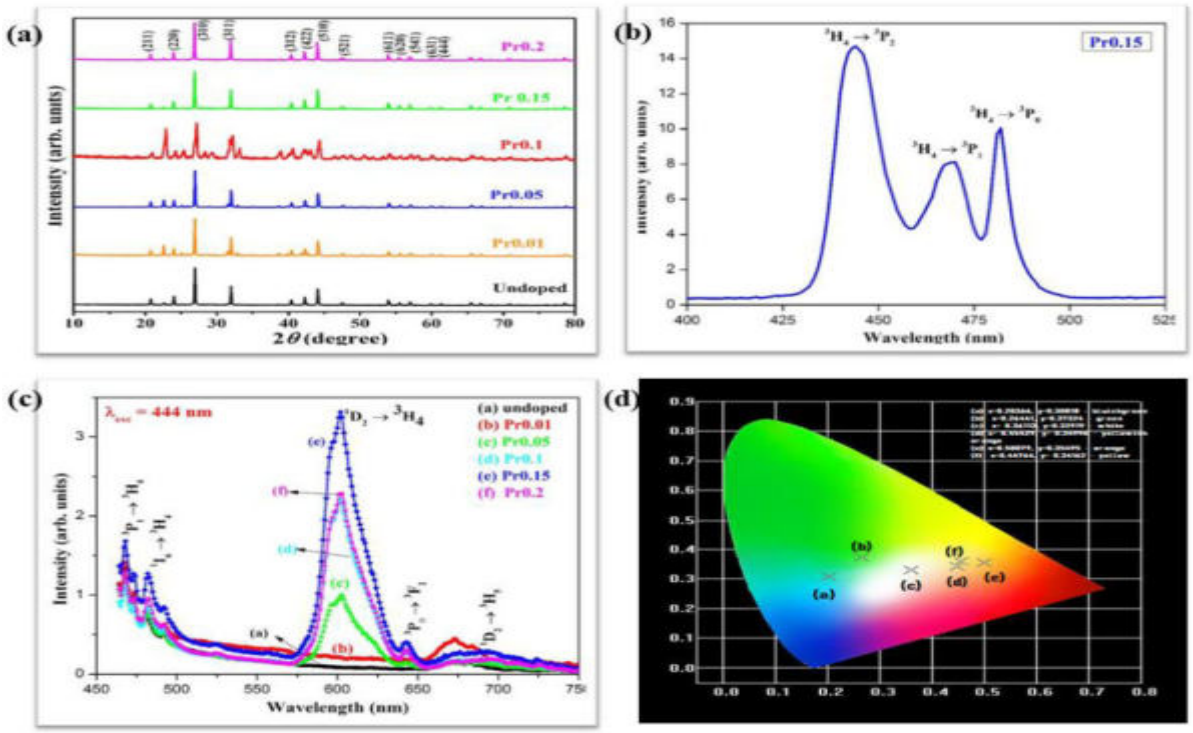

The emission spectra of $Ba_3Y_{(1-x)}(PO_4)_3:xPr^{3+}$ was monitored at excitation wavelength 444nm ($^3H_4 \rightarrow ^3P_2$). This emission spectrum is separated into two emission bands. First is blue emission band with four peaks at 468, 473, 482 and 492 nm. These peaks are corresponding to the $^3P_1 \rightarrow ^3H_4$, $^1I_6 \rightarrow ^3H_4$, $^3P_0 \rightarrow ^3H_4$ and $^3P_0 \rightarrow ^3H_5$ transitions. Second is red emission band with three peaks at 602, 643 and 691 nm which are originated from $^1D_2 \rightarrow ^3H_4$, $^3P_0 \rightarrow ^3F_2$ and $^1D_2 \rightarrow ^3F_5$. The transition $^1D_2 \rightarrow ^3F_4$ shows very close energy difference because in principle, this transition is spin forbidden and only become partially allowed by the Judd-Ofelt mechanism. The characteristic emission peaks of Pr^{3+} ions mainly originate due to the transition probabilities of different energy levels of Pr^{3+} ions and among all the transitions, $^1D_2 \rightarrow ^3H_4$ transition at 602 nm is the more intense one.

The intensity of the luminescence increases as the concentration increase but the intensity decreases with the further increase of concentration of dopant and this is known as concentration quenching effect. The optimal concentration of the emission spectra of $Ba_3Y_{(1-x)}(PO_4)_3:xPr^{3+}$ is 0.15mol% and concentration quenching takes place at this concentration. The emission spectra of $Ba_3Y_{(1-x)}(PO_4)_3:xPr^{3+}$ (x = 0, 0.01, 0.05, 0.1, 0.15 and 0.2) phosphors are shown in Figure 1c.

3.3 CIE Parameters:

Usually, the color purity of phosphors is examined by CIE chromaticity coordinates (x, y). To examine the potentiality of the $Ba_3Y_{(1-x)}(PO_4)_3:xPr^{3+}$ phosphors, the CIE in 1931 chromaticity coordinates are to be calculated. The chromaticity coordinates for the

$Ba_3Y_{(1-x)}(PO_4)_3:xPr^{3+}$ phosphors are calculated from the corresponding emission spectra and are shown in figure 1d. The evaluated CIE chromaticity coordinates are found in the different regions corresponding to bluish green (x = 0), green (x = 0.01), white light (x = 0.05), yellowish orange (x = 0.1), orange (0.15), yellow (x = 0.2). When $Ba_3Y_{(1-x)}(PO_4)_3$ is doped with 0.05% Pr^{3+} ions, we will get exact white light emission which is widely used in white LED applications. In order to further examine the quality of white light, the color correlated temperature values are calculated using McCany empirical formula and is expresses as

$$CCT= -449n^3=3525n^2-6823n+5520.33$$

where $n = (x-x_e)/(y-y_e)$ is the inverse slope line and $x_e = 0.332$ and $y_e = 0.186$

The evaluated CIE chromaticity coordinates (x, y) for the $Ba_3Y_{(1-x)}(PO_4)_3:xPr^{3+}$ phosphors were summarized in table 1

Table 1. CIE chromaticity coordinates (x, y) for the $Ba_3Y_{(1-x)}(PO_4)_3:xPr^{3+}$ phosphors

$Ba_3Y_{(1-x)}(PO_4)_3:xPr^{3+}$	**Color Coordinates**		**CCT**
	x	y	
x = 0	0.2037	0.3082	17102.22
x = 0.01	0.2644	0.3732	8463.74
x = 0.05	0.3611	0.3200	4274.42
x = 0.1	0.4543	0.3499	2206.03
x = 0.15	0.5008	0.3549	1774.39
x = 0.2	0.4476	0.3416	2215.77

Correlated color temperature is the temperature of a blackbody whose chromaticity most nearly resembles that of a light source. Low CCT value implies warmer light, while the high CCT appears to be colder. The CCT values around 2700K refers to a warm light, moving to neutral white at around 4000K, and to cool white at 5000K or more. which can be regarded as a cool white light for commercial applications.

4. Conclusion

- In summary, the phosphors $BaY_{(1-x)}(PO_4)_3:Pr^{3+}$ (x = 0, 0.01, 0.05, 0.1, 0.15 and 0.2) with a cubic structure were successfully prepared by the solid-state reaction method.
- The dopants Pr^{3+} ions occupied the Y^{3+} sites with high inversion symmetry in the host matrix. The average crystallite size by the Scherrer equation is estimated approximately 63.8 Å.
- The structural properties for Pr^{3+} doped $BaY(PO_4)_3$ have been analyzed through FTIR. Upon 444 nm excitation, the blue emission at 468, 473, 482 and 492 nm and red emission at 602, 643 and 691 nm which are corresponding to *f-f* transitions have been observed.
- Based on the above results, it is concluded that 0.05mol% Pr^{3+} doped $BaY(PO_4)_3$ phosphors emit white light and they may be used for the white LED applications.

5. References

[1]. J. McKittrick *et al*., Diplays, 1999, 19, 169.

[2]. T. Justel *et al.* Angew, Chem. Int.Ed. 1998, 37, 3084

[3]. A.K. Levine *et al.* Appl. Phys. Lett. 1964, 5, 118.

[4] G. Engel *et al.* Allg. Chem.1972, 387 22–30.

Green Route to Synthesize Zinc Oxide Nanoparticles Using Leaf Extract of Hibiscus and Their Antibacterial Activity

*M Mohamed Ibrahim, M Anujency, Betty Anna Thomas, P U Anusha, A Pandiaraj and R Ranjithkumar
Department of Physics, Kongunadu Arts and Science College, Coimbatore-641 029, India.

*Corresponding author: mibrahim27@gmail.com

Abstract
Biological synthesis of zinc oxide nanoparticles were synthesized by co-precipitation method using the leaf extract of hibiscus. Zinc acetate dehydrate was used as a precursor. The leaf extract of hibiscus was used as reducing as well as capping agent. X-ray diffraction analysis (XRD) was carried out to determine the structural properties of the synthesized samples. The average grain size of the samples was determined by using the Debye-Scherer's equation. The existence of functional groups of the samples was confirmed by Fourier transform infrared (FTIR) spectroscopy. The direct and indirect band gap energy of pure and doped samples was calculated using UV-visible analysis. Also the antibacterial studies of the as synthesized nanoparticles showed sensitivity to both gram positive and gram negative bacteria and analysed in this report.

Keywords: Co-doped ZnO Nanoparticles, XRD, FTIR, Antibacterial activities.

1. Introduction

In recent years ZnO NPs have drawn attention of countless researchers' foe their unique optical and chemical behaviors which can be easily coordinate by changing the morphology. Within the enormous family of metal oxide NPs ZnO NP has been various cutting edge applications like electronics, communication, sensor, cosmetics, environmental protection, biology and medicinal industry. Additionally, ZnO NP has an overwhelming potential in biological applications like biological sensing, biological labeling, gene delivery, drug delivery and Nano-medicine together with its antibacterial, antifungal and anti-diabetic activities [1-15].

Zinc oxide nanoparticles have currently been well studied and used as a potential antimicrobial principle. Nanoparticle synthesis within the size range of 10-100nm have evolve into an extensive research and concern due to their potential applications as it can act as catalyst which is useful in reduction or elimination of the toxic hazardous chemicals from the environment. Some of the metal oxide nanoparticles like, $FeSO_4$, TiO_2, CuO and ZnO are thoroughly been investigated for their differing biological activity. This study it can be come to an end that lemon extracts can be effectively used for synthesizing Zn nanoparticles. This study also submits that green synthesized Zn nanoparticles can be used as an alternative to existing antimicrobial agents.

2. Experimental

2.1. Preparation of plant extract

Hibiscus leaves were washes with running tab water and soaked in a 300 ml of titration flask. The extract was taken, the extract was allowed to cool to room temperature, filtered through filter paper, and the filter was stored for further experimental use.

2.2. Synthesis of ZnO NPs

1 Mm Zinc acetate dehydrate [(CH_3COO) Zn.2 H_20] was dissolved in 50ml deionized water and kept in stirrer for 2 hours respectively. Then, Addition with 1mL, 2 mL, 3 mL, and 4 mL

of leaf extract of hibiscus was added into the Zink acetate solution after the 1 hour of stirrer and 20 mL of NaOH solution was added with pH value is 12. The precipitate was separated from the reaction solution by centrifugation at 2500 rpm for 5 min and pellet was collected. Pellet was dried using a hot air oven operating for 1hour and maintained in air-tight bottles for further studies.

2.3. Characterization

Optical properties of ZnO NPs were characterized based on UV absorption spectra with the wavelength range of 300-500 nm. The crystalline structure of prepared ZnO nanoparticles was determined using XRD technique.. ZnO nanoparticles were identified using FTIR. FTIR spectral reading was carried out in the range from 500 to 4000 cm^{-1} at a resolution of 4 cm^{-1}. The crystalline structure of prepared ZnO nanoparticles was determined. Finally, antibacterial activities found the gram-positive and gram-negative bacteria are more active of doped samples [2].

2.4. Antibacterial activity

The antibacterial activity of the nanoparticles was determined by agar well diffusion method against both gram negative and gram positive microorganisms. Once the medium was solidified, a suspension of each sample of the bacteria was diluted prior to 10^{-1}, 10^{-2} and 10^{-3} (1 ml of 108 cells/ml) and was spread on a solid agar medium in petri plates. The wells were prepared by using sterile cork borer (6 mm). Each well was filled with different concentrations of nanomaterial ranging from 10-50 mg/ml. the plates were incubated at 37°C for 24 hours. The zone incubated was measured with mean SD values.

3. Results and Discussion

3.1. UV-visible analysis

The conformation of presence of zinc nanoparticles in colloidal solution was done using UV-spectral analysis. The samples were than analyzed by UV-spectral analysis (300- 500 nm). It was observed that all the four sample extracts showed an optical absorption band peaking at 360 nm and gradually decreasing at higher wavelengths. Zinc oxide nanoparticles have been reported to exhibit a characteristic broad absorption peak between 360-400 nm. Thus optical absorption band peaking at 400 nm confirms the synthesis of zinc nanoparticles by using leaf extract of hibiscus.

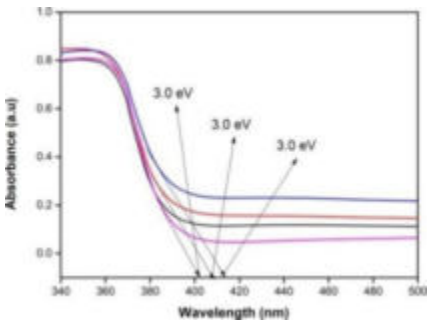

Fig 1: UV spectrum of ZnO nanoparticles

3.2. XRD

XRD spectra provide an insight about the crystallinity of nanoparticles. (figure. 2) represents XRD spectra of ZnO NPs synthesized using lemon extract. Size of the nanoparticle was calculated using Debye- Scherrer equation. X-ray diffraction peaks obtained at 31.9$^{\theta}$, 37.2$^{\theta}$, 48.3$^{\theta}$, 56.8$^{\theta}$, and 68.7$^{\theta}$ corresponded to the lattice plane of (1 0 0), (1 0 1), (1 0 2), (1 1 0), (2 0 1) suggesting the face centered cubic (FCC) crystal structure of the nanoparticle. Average size of the synthesized was found to be 32.76 nm [3].

$$D = \frac{K\lambda}{\beta Cos\theta}$$

Where, D- particle size in nm, λ- X-ray wavelength, β- FWHM, θ-Bragg's angle of reflection.

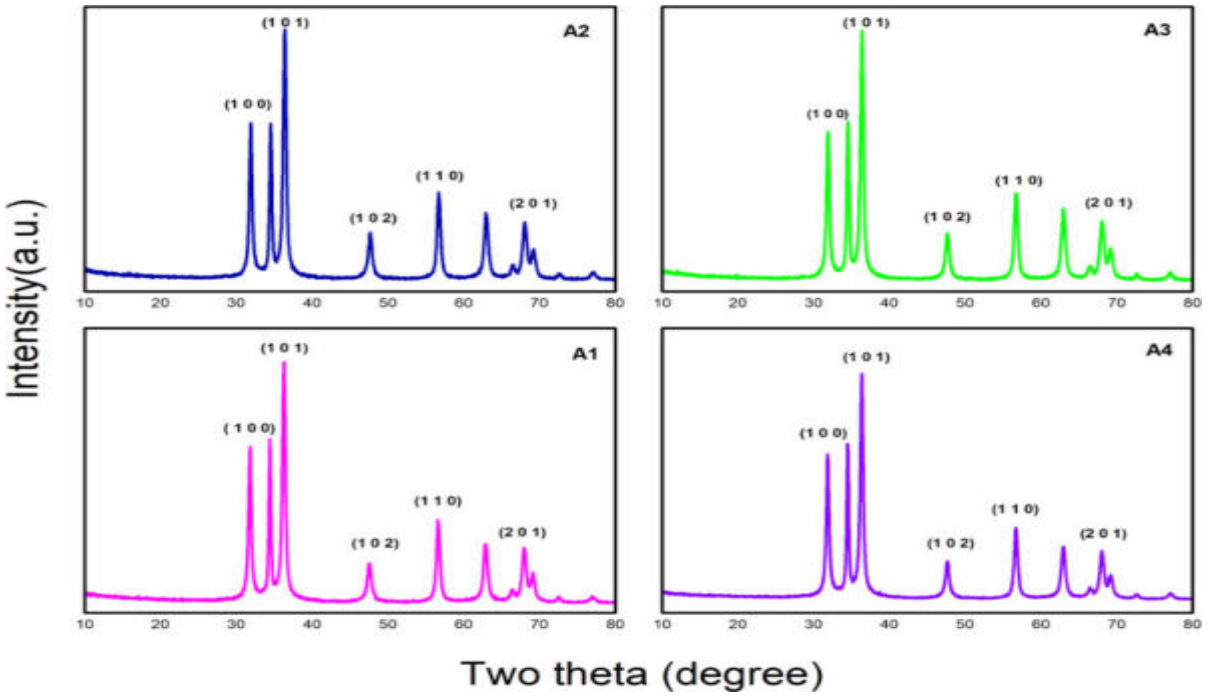

Figure 2: XRD Spectrum of ZnO Nanoparticles.

Table 1: Parameter calculation for average size calculation for nanoparticle.

Pos. [°2Th.]	Height [cts]	FWHM Left [°2Th.]	d-spacing [Å]	Rel. Int. [%]
31.8448	2171.66	0.2676	2.81020	74.18
34.5168	2498.46	0.1840	2.59853	85.35
36.4256	2927.40	0.1338	2.46662	100.00
47.6169	554.81	0.3346	1.90977	18.95
56.5950	964.98	0.3346	1.62628	32.96
62.9025	794.82	0.3346	1.47753	27.15
66.3656	113.35	0.6022	1.40859	3.87
68.0298	671.73	0.3011	1.37813	22.95
69.1011	331.06	0.4684	1.35936	11.31
72.6069	66.58	0.5353	1.30212	2.27
77.0259	75.22	0.6691	1.23807	2.57

3.3. FTIR

FTIR spectra of prepared nanoparticles were shown in figure 3. In the FTIR spectrum, there is a band present at 402, 416, and 420cm^{-1}, which is a characteristic signal of the Zn—O bond, confirming that the material is indeed zinc oxide. Meanwhile, the bands at 958, 1384 are attributed to the aromatic rings. 2354 and 2973 cm^{-1} attributed to O–H stretch vibrations of

phenols and their functional groups present in the organic compounds in theextract.

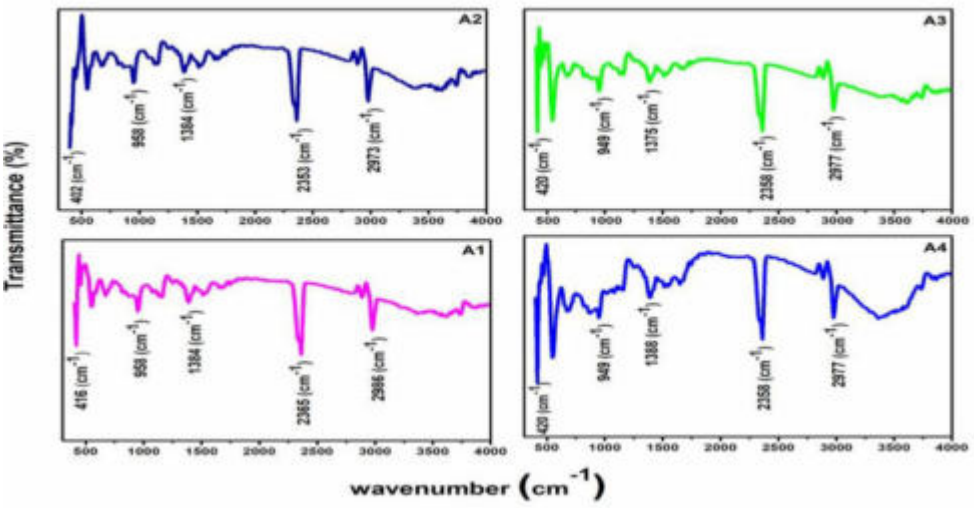

Figure 3: FT-IR Spectrum of ZnO Nanoparticles.

3.4. Antibacterial activity

The antibacterial activity of zinc oxide nanoparticles was tested against gram negative bacteria E. coli(MCC-2412), P. vulgaris (MTCC-426) and gram positive bacteria S. aureus (MCC-2408) and S. mutans (MTCC-497) by agar well diffusion method. In fig.4 antibacterial activities of zinc oxide nanoparticles at different concentrations 10 mg/ml, 20 mg/ml, 30 mg/ml, 40 mg/ml, 50 mg/ml against both gram negative and gram positive bacteria were shown. The diameter of inhibition zones around each well is measured in millimeters and represented in table 2. Results have indicating that the degree of zone of inhibition (with mean±SD values) was more against gram negative bacterial strains E. coli (31±0.20 mm) and Proteus vulgaris (30±0.45 mm) when compared to the gram positive bacteria (Staphylococcus aureus with 24±0.35 mm and Streptococcus mutans with 23±0.30 mm). As well as differences in structural organization between both gram classes of bacterial cell wall i.e. due to the presence of thicker peptidoglycan layer in gram positive bacteria, they are less prone to nontoxicity of ZnO nanoparticles when compared to gram negative bacteria. This is might be the reason for the obtained results that indicates high degree of inhibition zone in the case of gram negative bacteria compared to gram positive bacteria.

Organism	Zone of inhibition (mm)				
	10mg/ml	20mg/ml	30mg/ml	40mg/ml	50mg/ml
E. coli	7±0.25	14±0.30	21±0.25	28±0.30	31±0.20
P. vulgaris	6±0.25	11±0.35	18±0.45	23±0.25	30±0.45
S. aureus	6±0.35	10±0.15	14±0.10	19±0.15	24±0.35
S. mutans	4±0.25	9±0.35	13±0.35	18±0.35	23±0.30

Number of experiments n=2, mean SD

Table 2: Antibacterial activity of ZnO nanoparticles by agar well diffusion method

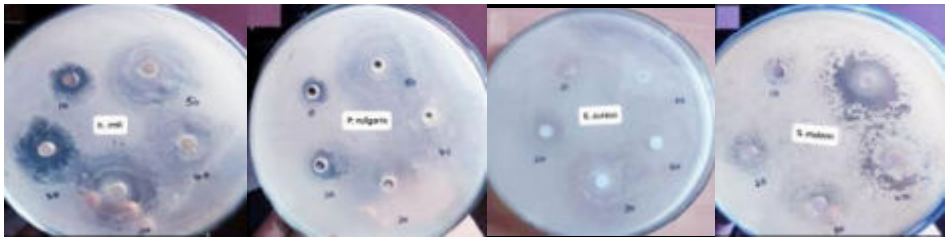

Figure 4: Antibacterial activities of zinc oxide nanoparticles at different concentrations 10 mg/ml, 20 mg/ml, 30 mg/ml, 40 mg/ml, 50 mg/ml against both gram negative and gram positive bacteria.

4. Conclusions

Green synthesis of nanoparticles used in this experiment is found to be eco-friendly, non-toxic and less usage of chemicals. The leaf extract helps in the synthesis of metal oxide nanoparticle by inducing oxidation and reduction reaction. As a preliminary confirmation, the rapid synthesis of ZnO NP was measured using the UV- Visible spectroscopy at a maximum absorbance of 380 nm. Further the XRD analysis proved the crystalline nature of the ZnO NP, and the bands formed in FTIR attributes to O-H stretch vibrations of phenols and their functional group present in the organic compounds in the different concentrations of the same extracts which is a characteristic signal of the Zn-O bond, confirming that the material is indeed zinc oxide. Based on the results, it can be concluded that gram negative organisms have exhibited more sensitivity when compared to gram positive organisms to metal oxide nanoparticles. The difference in the activity of both gram negative and gram positive bacteria might be due to structural and compositional variations of the cell membrane. Gram positive bacteria have thicker peptidoglycan layer when compared to gram negative bacteria due to this kind of difference in structure, it is tough for nanoparticles to penetrate into embrace resulting in a low bacterial action.

Acknowledgement

The authors would like to Avinashilingam Institute for Home Science and Higher Education for Woman for providing the laboratory facilities where some of the experiments were carried out.

References

[1]. N Bala *et al.* RSC Adv., 2015, 5, 4993-5003.
[2]. K M Ezealisij *et al.* International Nano Letters, 2019, 9, 99–107.
[3]. J. Santhoshkumar *et al.*, Resource-Eff. Tech 000 (2017) 1-7.
[4]. O.J. Nava *et al.* Journal of Molecular structure, 2017, 1147, 1-6.
[5]. D Bharathi *et al.* Int. Journal of Biological Macromolecules, 2019,29, 989-996.
[6]. Y.Z. Chen *et al.*, J. Colorants Interface, 2014, 422, 226-230.
[7]. A. Nicolaev *et al.* Sol. Energy Mat. Sol. Cells, 2016, 158, 92, 202-208.
[8]. F. Davar *et al.*, J. Am. Ceram. Soc. 2015, 98 (6), 1739-1746.
[9]. C. Vidya *et al.,* Environ. Nanotechnology. Monit. Manag. 2016, 6, 134-138.
[10]. A. Di Mauro *et al.* Appl. Catal. B, 2016, 186, 68-76.
[11]. R. Aladpoosh *et al.* Carbohydr. Polym. 2015, 126, 122-129.
[12]. T. Tian *et al.,* Ceram. Int., 2015, 41, S774-S778.
[13]. L. Fu *et al.* Biotechnol. Adv., 2013, 31 (2), 346-356.
14]. J. Fowsiya *et al,* J. Photochem. Photobiol. B, 2016, 162, 395-401.
[15]. A.K. Mittal *et al.* J. Mol. Struct., 2017, 1134, 121-125.

Biochar Loaded Membrane for Microbial Fuel Cell Applications

Harsha Nagar[1], Vineet Aniya[2]
[1]Assistant Professor, Department of Chemical Engineering, Chaitanya Bharathi Institute of Technology, Hyderabad 500075, India
[2]Scientist, Department of Process Engineering and Technology Transfer, CSIR- Indian Institute of Chemical Technology, Hyderabad, 500007, India
Corresponding author's email: harshanagar_chem@cbit.ac.in

Abstract

Treatment of wastewater along with generation of energy from the renewable resources attracts a great attention. In this aspect, biochemical systems such as microbial fuel cell (MFC) appears as a novel energy-producing technology that generates electrical energy with the aid of microbial activity that degrades the organic waste present in the wastewater. The dual functionality of electricity generation with simultaneous treatment of both domestic as well as industrial wastewater enhances their wide applicability. Membrane is the foremost component for the MFC system with their dual functionality of proton conduction and a selective barrier. The DuPont manufactured Nafion membrane is widely accepted as membrane for MFCs, but its high cost, oxygen crossover, substrate loss, cation transport and accumulation, low stability and hydration at higher temperatures confines its applicability and thereby creates a demand for the search of an alternative membrane. Therefore, in the present work biochar loaded sulfonated polysulfone membrane is synthesized using NMP as a solvent through solution casting and solvent evaporation method. Further the synthesized membrane is characterized to understand their physio-chemical modifications using FTIR, XRD and SEM studies. Finally, the membrane performance is estimated using single slice MFC unit.

Keywords*:* Microbial fuel cell, Biochar loaded membrane, Membrane characterization, Wastewater treatment

1. Introduction

The huge generation of wastewater due to the industrialization and urbanization requires the technology that treat the wastewater in eco-friendly manner. In this prospect microbial fuel cell (MFC) appears to be potential one due to its advantageous feature of simultaneously treating wastewater with electricity generation. MFC work on the principle of redox reaction wherein microbial activity degrades the organic compounds present in the wastewater and generate electricity. MFC is composed with electrode and membrane, membrane is the foremost component of MFC with their dual functionality of barrier and proton transporter. Generally, the commercial membrane has a certain setback like high oxygen crossover, low proton conductivity, low stability and high cost that restricts the MFC commercialization. Therefore, in the present work synthesis of biochar loaded membrane was proposed which is prepared by solution casting and solvent evaporation method using n-methyl 2 pyrrolidine solvent. Biochar was prepared through pyrolysis of chicken feather biomass and characterized by particle size analyser for their particle size estimation. The synthesized membrane was further characterized by SEM, FTIR to understand their physiochemical modification. Finally the membrane properties like ion exchange capacity (IEC), water sorption and polarization curves is determined.

2. Experimental

Chicken feathers were bought at local shop. PSf (Polysulfone) and NMP (N-methyl pyrrolidone) chemicals were bought from Sigma Aldrich. Concentrated H2SO4 and aniline were used for sulphonation and membrane synthesis. Naoh (Sodium hydroxide) pellets were used for IEC estimation. Glassware like petriplates, conical flasks was used. Nutrient agar

and Nutrient broth were purchased from Sigma Aldrich for inoculum preparation. All the chemicals obtained were of analytical reagent grade.

Chicken feathers were washed with distilled water and dried at 60°C for 24 hrs. Pyrolysis process was done where chicken feathers were heated at 550°C.The process was done for 1 hr. Biochar was produced after pyrolysis process. Biochar particle size was later reduced to micro size by filtrating it with ethyl acetate and later vacuum dried it. Dried biochar particles were finely grounded and passed through 63µm sieve

The structural illustration, surface morphology of synthesized biochar loaded membrane is studied using FTIR and SEM respectively. The water sorption (%) and IEC of the membranes are investigated using water sorption and classical acid base titration method, respectively. The 2×2 cm membrane sample was dipped in water for 24 h to estimate the wet weight Ws. The water uptake capacity was estimated using eq.1 with dry weight (W_d) of the membrane. In the case of IEC, a titrimetric method using phenolphthalein indicator with H_2SO_4 and NaOH was carried out as described in our previously reported work [1, 2].

3. Results and Discussion

Particle size of the prepared biochar is shown in Fig. 1 and found be 1676 nm. The FTIR spectrum of the biochar loaded sulfonated Psf membrane is shown in Fig. 2. The pristine PSF membrane has a sulfone group that has characteristics peak at 1149 cm^{-1} whereas the peak at 2904 cm^{-1} represents the CH_3 groups of polysulfone and the main aromatic ring of PSF polymer peak at 3443 cm^{-1}. The appearance of the new peak at 1013 cm^{-1} corresponding to sulfonic group symmetric stretching that clearly indicates the successful modification with H_2SO_4. Compatibility between the polymer and biochar was confirmed by SEM analysis by showing homogeneous uniform surface as shown in Fig.3. The properties of the membrane are presented in Table 1, which shows that addidtion of biochar till 10 wt % provide the high proton conductivity with sufficient mechanical stability. Table 2 shows the membrane performance of pristine SPsf and biochar loaded membrane in terms of COD removal and power density. The highest power density of 200 mW/cm^2 and 92 % COD removal efficiency was achived by the biochar loaded membrane.

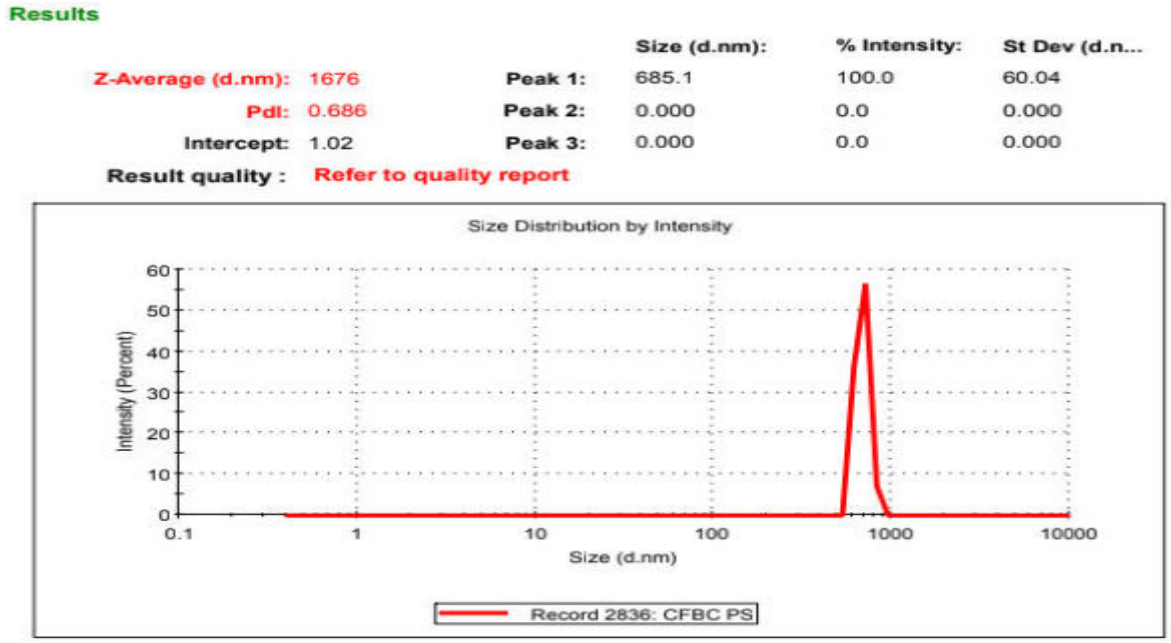

Fig.1 Particle Size of biochar

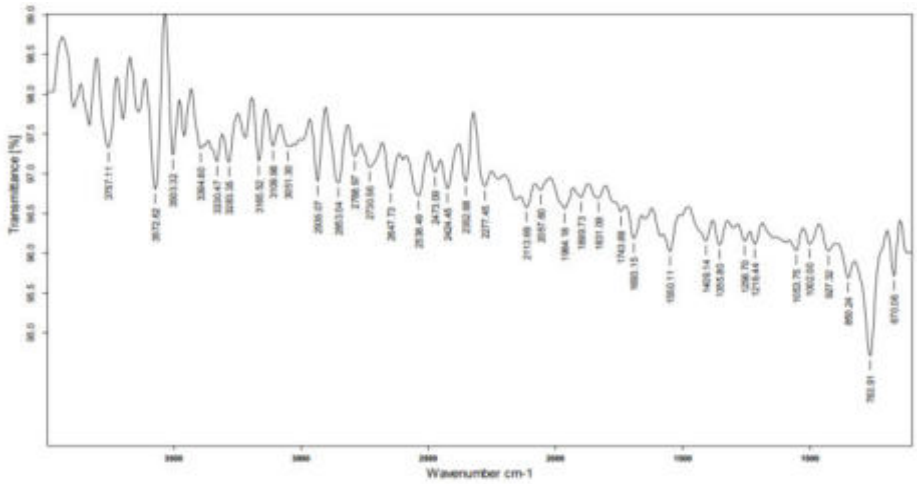

Fig.2 FTIR Spectra of biochar loaded membrane

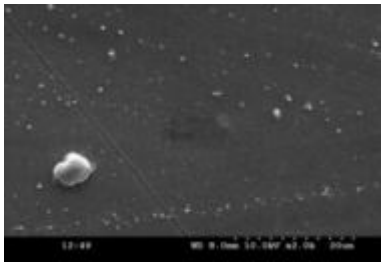

Fig.3 SEM image of biochar loaded membrane

Table 2 Properties of different synthesized membranes.

Membrane	IEC (meq/gm)	Water Sorption (%)	Proton conductivity (S/cm)	Tensile strength (MPa)
SPsf	0.78	25	0.042	30
M1	0.62	27	0.072	32
M2	0.98	29	0.092	35
M3	0.52	28	0.087	37
Nafion 117	0.89	28	0.067	26

Parameters	Initial Parameter	SPsf	M2	Nafion 117
TDS (ppm)	1500	1250	1100	1150
Turbidity (FAU)	52	48	40	46
COD Removal (%)	-	83	92	85
Oxygen diffusivity (cm2/s)	-	6.39×10^{-8}	7.12×10^{-7}	8.39×10^{-9}
Power density (mW /cm2)	-	170	200	160
OCV (mV)	-	0.87	0.92	0.85

- The biochar filler concentration of 10 wt% provided high ion exchange capacity, water sorption, and stability, and therefore chosen for detailed studies.

- The higher power density of 200 mW cm^{-2} with substantial COD removal (92%) was achieved with the indigenous membrane during kitchen wastewater treatment as compared to both pristine SPsf and Nafion 117 membranes.

Acknowledgement
Authors would like to thank CSIR- Indian Institute of Chemical Technology, Hyderabad, 500007, India for providing facilities.

References

1. P. Boguslaw, Environmental Biotechnology, 2008, 4, 60–64.
2. Harsha Nagar *et al.*, Materials Chemistry and Physics, 2019, 224, 175–185.

Insertion-Type Electrodes for Li-Ion Batteries

D.Saritha
Department of Chemistry, Chaitanya Bharathi Institute of Technology (A), Hyderabad, Telangana, 500075, India
Corresponding author's email: dsaritha_chm@cbit.ac.in

Abstract

Li-ion battery research enormously spotlight on progression in the fabrication, optimization, and categorization of electrode resources. They became popular as energy storage resources particularly owing to energy and power densities, life span, price and protection. The brisk expansion of electronic devices and electric vehicles stress a great energy density. Consequently, metals, alloys and transition-metal oxides have been employed as anodes for Li-ion batteries. Transition-metal oxide anodes further organized into alloying-category, conversion-category insertion-category materials. The extensive enlightenment on contemporary comprehension of insertion-type resources as anodes for Li- ion batteries will be offered in this paper with few instances.

Keywords*:* Insertion, electrode, Li-ion battery, anodes

1. Introduction

The research society is currently paying interest on well-organized energy storage approaches intended for the progress of optional energy for the substitution of fossil fuels [1]. Electric vehicles replaced by gasoline driven transport vehicles reduces the release of greenhouse gases. Li-ion batteries take part in a major task owing to their superior energy, power density, extensive cycle existence and small self-discharge [1]. These batteries are employed in several versatile devices as cellular phones, laptops and digital electronics [2]. The enhancement of Li-ion battery energy density can be accomplished by advancing either superior capacity anode and cathode electrode resources. The novel anode materials can be categorized into three chief types supported on their reaction procedure 1) Insertion/de-insertion materials with few instances carboneous materials, Li4Ti5O12,TiO2, etc; 2) Alloy/de-alloy materials with few instances Si, Ge, Sn, Al, Bi, SnO2, etc; 3) Conversion materials with few instances transition metal oxides, metal sulphides etc. The insertion

process is shown in Figure.1.The current paper is discussed on the insertion-type materials and its significance.

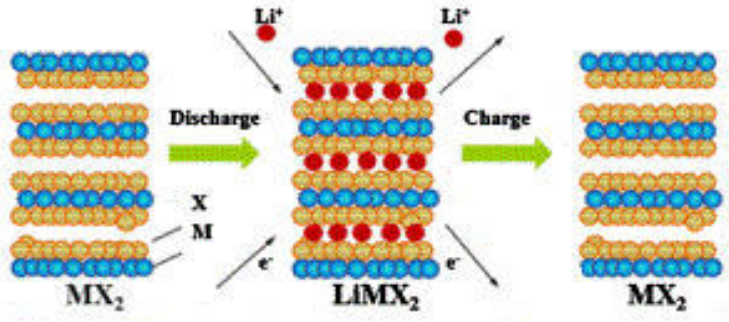

Figure.1. Insertion reaction mechanism [2].

2. Inserion-type materials

2.1 Carboneous materials

Graphite is the superior anode material owing to the insertion of Li into the gap among the layers [3]. The process is taking at less than 0.25 V versus Li^+/ Li with a reversible capacity of 372 $mAhg^{-1}$[1]. Low capacity was the disadvantage of Graphite. As a result, the progresses of carbonaceous materials are required to attain superior outcomes. These materials offer further gap among the layers to accommodate the Li and acquire privileged capacity. Carbon nanotubes, nanofibers and graphene are immensely explored as option to graphite owing to better surface area in addition to greater electron conductivity [4].

2.2 Spinel structured $Li_4Ti_5O_{12}$

Graphite is the preferred anode in Li-ion batteries. Solid electrolyte interface (SEI) layer is created on the exterior of graphite which is due to the low working potential (0.25V) [5]. SEI and dendrite formation is diminished in $Li_4Ti_5O_{12}$ due to its high operating potentional [6].As a result, utilizing graphite as anode can be avoided by employing spinel structured $Li_4Ti_5O_{12}$ [7]. $Li_4Ti_5O_{12}$ has a spinel structure in which Li reside in the entire tetrahedral 8a sites, Li/Ti with an atomic ratio of 1:5 dwell in the octahedral 16d sites and oxygen atoms dwell in the 32e sites, correspondingly. 3Li ions at the 8a sites jointly go to the empty 16c sites allocating the conversion of the spinel structure to a rock salt structure $Li_7Ti_5O_{12}$ at 1.55 V during lithiation and this is a two-phase reaction process [5]. The volume connected with this phase change is incredibly little. Accordingly, $Li_4Ti_5O_{12}$ is eminent as a zero-strain material and recommend enormously extensive cycle existence. Lithium insertions into $Li_4Ti_5O_{12}$ direct to the creation of rock salt type $Li_7Ti_5O_{12}$ and it will preserve the spinel symmetry during extraction [5].Low diffusion of Li and electronic conductivity are the issues originated in

$Li_4Ti_5O_{12}$.Two strategies have been applied to conquer these concerns. One approach is to employ surface treatments to boost the electronic conductivity and other approach is by downscale the $Li_4Ti_5O_{12}$ to the nanoscale. Effortless combustion technique was employed to produce nanocrystalline $Li_4Ti_5O_{12}$ (20-50nm size) in tiny time span [8]. The achieved theoretical capacity value was170 $mAhg^{-1}$at 0.5C rate and the obtained capacities were 140 and 70 $mAhg^{-1}$ at 10C and 100C rate correspondingly. Doping is one of the eminent procedures to boost electrical conductivity of $Li_4Ti_5O_{12}$. The electrical conductivity of $Li_4Ti_5O_{12}$ can be enhanced by growing these nanowires on titanium foil and confirmed by XPS studies [9]. It displayed advanced rate performance and achieved capacity was173 $mAhg^{-1}$ at 0.2C rate. Even at 30C rate, it exhibited a capacity of 121 $mAhg^{-1}$at 30C rate.

2.3 Titanium dioxide (TiO_2)

Titanium-based oxides gained significance as alternatives to graphite anode from the security perspective. Structural variety, abundance, low price, low toxicity, chemical steadiness, oxidation ability and superior electro activity are the benefits of TiO_2 which makes it as excellent anode resource [1]. Hence, several researchers have been dedicated to working on insertion-based anode materials [10-11]. The theoretical capacity of TiO_2 is 330 $mAhg^{-1}$ which can insert 1Li/Ti [12]. The familiar allotropic forms are anatase, rutile and brookite. 300 nm sized rutile TiO_2 demonstrated a constant capacity of 50 $mAhg^{-1}$ over 20 cycles at 0.05 Ag^{-1}. As the size of the particle reduced from 300 nm to 15nm and exhibited capacity was 200 $mAhg^{-1}$ [12].30 nm sized anatase TiO_2 displayed superior capacity of 71 $mAhg^{-1}$ over 20 cycles at 0.1 C rate where as the corresponding 6 nm size TiO_2 exhibited 200 $mAhg^{-1}$ respectively due to the enhanced diffusion of Li and short path length [13].Anatase TiO_2 nanotube with length 100-300nm, diameter 8-10 nm and thickness 2-3nm was formed by hydrothermal route [14]. The revealed capacity was 250 $mAhg^{-1}$ over 100 cycles and exhibited excellent cycling existence. Mesoporous TiO_2(B) with 12nm size was produced by Brown et al. as anode at various C rates [15]. The excellent capacity achieved was 120 $mAhg^{-1}$ even at 60 C rate owing to the rapid kinetics.TiO_2/Graphene composite was formed by using hydrothermal process. The attained composite consist of 10 nm diameter TiO_2 nanotube fabricated on a graphene layer [16]. The achieved capacity was 300 $mAhg^{-1}$ and it confirmed excellent cycling consistency over few thousand cycles. These gifted outcomes were feasible owing to the morphology of nanotube and the electronic connections among the components.

3. Conclusions

- The insertion materials including carbonaceous, $Li_4Ti_5O_{12}$ and TiO_2 materials were discussed as anodes.
- Structural stability after several cycles is the major benefit of the insertion materials
- It is crucial to design nanoscale interfacial materials for commercial applications.

4. References

1. S. Goriparti *et al.* Journal of Power Sources, 2014, 257,421-443.
2. J. Lu *et al.*, Electrochemical Energy Reviews, 2018, 1, 35-53.
3. D.Saritha, *et al.,* Materials Today: Proceedings, 2019, 19, 726-730.
4. R. Raccichini *et al.,* Nature Materials, 2015, 14, 271–279.
5. P. Roy *et al.,* J. Mater. Chem. A, 2015, 3, 2454–2484.
6. R. A. Huggins, Springer Science & Business Media, New York, USA, 2009.
7. E. Ferg *et al.,* J. Electrochem. Soc, 1994, 141, L147-L150.
8. A.S. Prakash *et al.,* Chem. Mater, 2010, 22, 2857-2863.
9. L. Shen *et al.,* Adv. Mater, 2012, 24, 6502-6506.
10. D. Saritha, Material Science and Engineering B, 2018, 228, 218-223.
11. D.Saritha, Advanced Science Letters, 2018, 24(8), 5593-5597.
12. C. Jiang *et al.,* Electrochem. Solid-State Lett, 2007, 10A127-A129.
13. A.K. Rai *et al.,* Electrochim. Acta, 2013, 90,112-118.
14. V. Gentili *et al.,* Chem. Mater. 2012, 24, 4468-4476.
15. H. Liu *et al.,* Adv. Mater, 2011, 23, 3450-3454.
16. J. Wang *et al.,* Electrochim. Acta, 2013, 88,847-857.

Synthesis and Characterisation of Fluorescent Ion Imprinted Polymers for Selective Recognition of Nickel (II)

Pallavi Bhardwaj, Kuldeep Kaur*
Department of Chemistry, Mata Gujri College, Fatehgarh Sahib, Punjab, India-147002
*e-mail: shergillkk@gmail.com

Abstract

Novel Ni (II) ion-imprinted fluorescent polymers (Ni-IIP) were prepared by using Ni(II) ion-quercetin complex as the template molecule, 3-(aminopropyl)triethoxysilane as monomer, tetraethoxyorthosilicate as cross linker and ammonia as catalyst. The synthesized polymer particles were characterized by using infrared spectroscopy (IR), UV-Visible spectrophotometry and fluorescence spectrophotometry. The fluorescent IIPs were found to show emission signal at 520 nm when excited at 290 nm. The binding of Ni(II) to imprinted cavities was followed by monitoring the fluorescence changes occurring in the fluorescence spectra of IIP as a result of binding by Ni(II). An enhancement in the fluorescence emission intensity of IIPs signal on the addition of Ni(II) ion solution of different concentrations was observed. The enhancement was found to be proportional to concentration of Ni(II) ions. The synthesized IIPs can selectively recognize Ni(II) ions as a result of imprinted cavities. These can be further used for effective identification of water soluble ions, especially heavy metal ions.

Key words: Ion imprinted polymers, fluorescence, selective recognition, nickel ion, quercetin

1. Introduction

Molecularly Imprinted Polymers are three-dimensional cross-linked polymers with template-specific interaction sites or cavities within the polymer structure and capable of recognizing the template molecule specifically [1]. Ion imprinted polymers (IIP) target to recognize ions especially metal ions while retaining the unique virtue of molecularly imprinted polymers such as structure predictability and application versatility [2]. Typically, IIPs are stable and robust due to polymeric nature formation from cross linked materials [3]. Ion imprinted polymers offer many advantageous features such as being light and inexpensive, allowing easy shaping, high reusability, extensive applicability, and high selectivity towards the target ion. MIIPs can carry out effective identification of water soluble ions, especially heavy metals and radioactive elements [4]. The development of IIPs capable of performing metal recognition in aqueous systems has important scientific significance and application value [5].

The effect of toxic heavy metals on human health and environment is an issue of great concern worldwide [6]. Exposure to higher concentrations of heavy metals like nickel can have detrimental effects on human health such as allergy, cardiovascular and kidney diseases, lung fibrosis, lung and nasal cancer [7]. This calls for development of simple, effective analytical tools to determine nickel ion in various samples. Numerous techniques such as atomic absorption spectroscopy [8], inductively coupled plasma mass spectrometry [9], spectrophotometry [10], colorimetry [11] and voltammetry [12] have been reported for determination of Ni(II) ion in environmental samples. However, many of these methods still suffer from sensitivity and selectivity issues. Fluorescent ion imprinted polymers combine high selectivity of imprinted materials with high sensitivity of fluorescence analysis thus

enabling label free sensitive detection of metal ions with reduced interferences from similar substances [13].

The present work reports the synthesis of a novel Ni (II) ion-imprinted fluorescent polymer for detection of Ni(II) ions in water samples. The fluorescent IIP was synthesized using (3-aminopropyl)triethoxysilane (APTES) as monomer, tetraethoxyorthosilicate (TEOS) as cross linker, ammonia as catalyst and Ni-quercetin complex as template. The synthesized polymer was found to be fluorescent and was able to selectively bind Ni(II). The fluorescent IIPs can be used to identify and determine Ni(II) ions in the real water samples.

2. Experimental

2.1 Apparatus and Reagents

All fluorescence spectra were recorded using Shimadzu RF-5301 PC spectrofluorometer with slit widths of 5 nm. UV-Vis absorption spectra were obtained by a Shimadzu UV-Vis 1800 spectrophotometer. Infra-red spectra were recorded in KBr disc on Perkin Elmer FTIR-spectrometer (Panjabi University, Patiala). All reagents were of analytical grade and used as received. Double distilled water was used for preparation of all the solutions. All the chemicals were purchased from Avra and all solvents were purchased from Loba Chemie.

2.2 Procedure

Dissolved quercetin (1mmol) and $NiCl_2.6H_2O$ (2 mmol) in 100mL methanol solution. Then added APTES (2mmol) as functional monomer, stirred for 30mins and stored at 4°C in dark for 6h, then added TEOS (10 mmol) as cross linking agent and aqueous ammonia (5mL, 14%) as catalyst. The mixture was then stirred on a magnetic stirrer at room temperature for 2 hours and then aged by stirring at 60°C for 6h to obtain high cross linking structure. The resultant IIPs were collected by centrifugation (20,000rpm for 30min) and then rinsed with methanol for three times to remove the residues. The template Ni(II) was removed from IIPs by several sequential elution steps with 0.5 M HCl under vigorous stirring. The final Ni(II) concentration in aqueous solution was determined by atomic absorption spectrometry. In the same way, the non-imprinted polymer (NIP) was prepared in the similar manner but without the addition of the imprint ion.

For studying recognition of Ni(II) by IIPs, 5 volumetric flasks (5mL) having fixed volume of 2mL of above prepared IIP solution and different concentrations of Ni(II) solution with concentrations varying from 0 to 1 mL of 100 ppm were prepared and the volume was made upto 5 mL with methanol. The fluorescence spectra were recorded 15 minutes after the addition of reagents to stabilize the intensity. The addition of buffer solution of different pH values was found to have no major effect on intensity of fluorescence emission. So buffer solution was not added.

3. Results and Discussion

The prepared IIPs and NIPs were characterized by FTIR spectral analysis, fluorescence analysis and UV-Vis spectroscopy. The results obtained are discussed below.

3.1 FTIR Analysis

The FTIR spectra of the prepared IIPs were recorded in the range of 400-4000 cm^{-1}. The bands positions obtained for NIP, unleached IIP and leached IIP are shown in Table 1. The broad bands observed in the range of 3214-3243 cm^{-1} are assigned to O-H stretching vibrations of O-H groups present in quercetin. The bands in the range of 1366-1611 cm^{-1} are assigned to C=O stretching vibrations of the ketonic group present in the quercetin structure. The strong bands observed in the region from 1061-1070 cm^{-1} belong to Si-O stretching vibrations while the band observed in all the three spectra at 937 cm^{-1} belongs to Si-OH bond vibrations. The strong sharp bands at 795 cm^{-1} and the shoulder bands observed in the range of 776-781 cm^{-1} belong to Si-O-Si vibrations. These assignments prove the formation of

silica matrix from the precursors by sol-gel method. The ν(O-H), ν(C=O) and ν(C-OH) vibrations are observed at lower wavenumbers in unleached IIP as compared to leached IIP indicating breakdown of H-bonds due to metal chelation in unleached IIP.

Table 1. The wave numbers and intensity of selected bands from FT-IR spectra of studied compounds.

Range (cm^{-1})	NIP ν(cm^{-1})	Unleached IIP ν (cm^{-1})	Leached IIP ν (cm^{-1})	Assignment
3214-3243	Not marked	3214.94 (wb)	3243.01(wb)	O-H stretching
1607-1611	1607.9(w)	1599.08(ws)	1610.50(ws)	C=O aryl ketonic stretching
1497-1485	1497.6 (w)	1484.9(w)	Very weak	C-OH vibrations
1366	1366.1(vw)	Very weak	Very weak	C-OH vibrations
1061-1070	1061.12(ws)	1060.30(ws)	1070.11(s)	Si-O stretching
942-948	942(w)	937.75(w)	947.68(ws)	Si-OH bond vibrations
795	795(s)	795.16(s)	795.17(s)	Si-O-Si bending vibrations
776-781	776.5(w)	772.34(w)	780.82(w)	Si-O-Si bending vibrations

w-weak, vw-very weak, s-strong, b-broad.

3.2 UV-Vis Analysis

The UV-Vis spectra of leached IIP are shown in Fig.1. The UV-Vis spectra of quercetin shows two absorption bands in methanol, one at 275 nm and other at 395 nm. However in the absorption spectrum of IIP (Figure 1), instead of two bands only one band was obtained at an emission wavelength of 325 nm indicating change in absorption properties of quercetin on its integration in the IIP matrix.

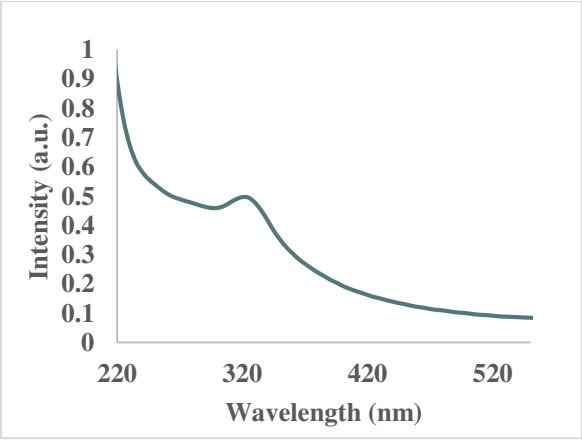

Figure 1. UV-Vis spectra of Ni(II) imprinted IIP ($1x10^{-3}$ M) in methanol

3.3 Fluorescence Analysis

The fluorescence spectra of quercetin in methanol solution was recorded with the help of a spectrofluorimeter. For quercetin, the best excitation wavelength was found to be 290 nm and the fluorescence emission was obtained at 525 nm. The fluorescence emission spectra of the leached IIP was also recorded using an excitation wavelength of 290 nm and maximum fluorescence emission was obtained at 362 nm (Figure 2).

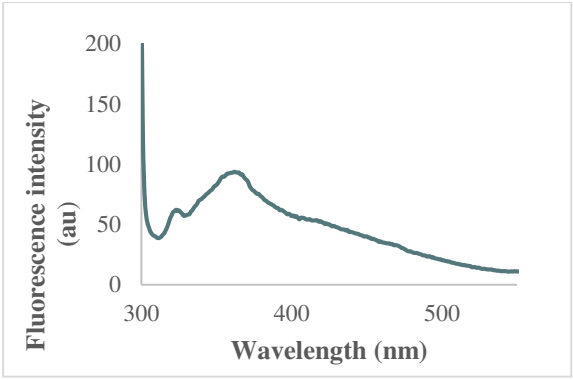

Figure 2. The fluorescence emission spectra of Ni (II) imprinted IIP ($1x10^{-3}$ M)

3.4 Recognition Studies

The studies on recognition of Ni(II) by the leached IIP were carried out in methanol solution. The spectra obtained are shown in Fig. 3. On addition of increasing amounts of Ni(II), the fluorescence emission intensity of MIP was found to increase along with shift to lower wavelength. While IIP emission was found to be at 362 nm, it shifted to 345 nm on addition of Ni(II). The increase in the value of the intensity of the leached IIP on addition of different concentrations of nickel was found to be proportional to concentration of Ni(II). The recognition studies were also carried out with NIPs. No obvious red shift was obtained in case of NIP. The selectivity studies were also carried out in presence of other metal ions namely Zn(II), Cd(II) and Co(II). Though these metal ions were found to interfere to some extent in the determination of Ni(II), the effect was more pronounced at higher concentrations. However, the binding affinity of Ni(II) was found to be much higher than other metal ions.

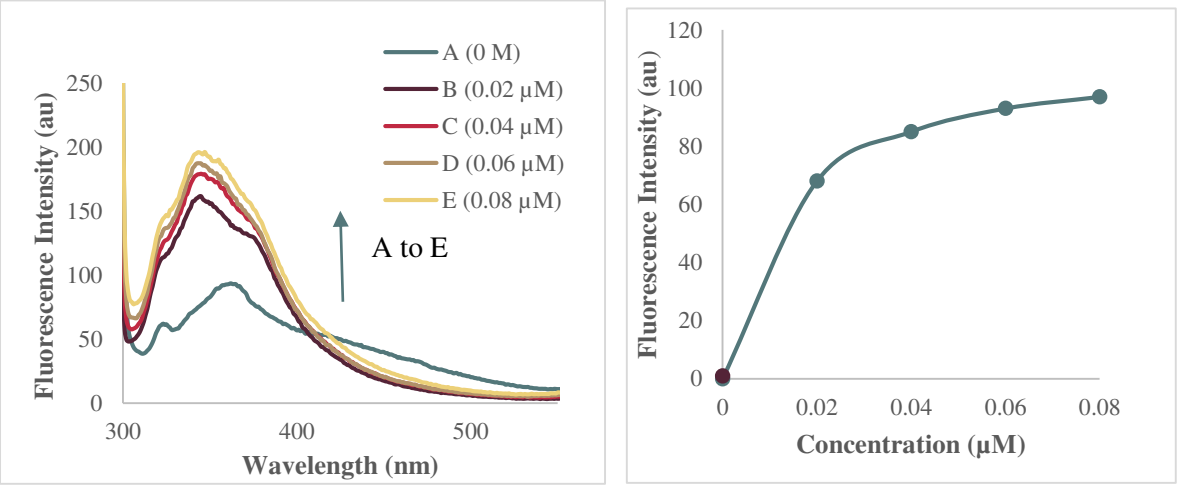

Figure 3. a) The fluorescence emission spectra of IIP on addition of increasing amounts of Ni (II). B) The non-linear fit of the experimental data

4. Conclusions

In this research work, ion imprinted polymers were prepared for nickel ion (II). The Ni(II)-quercetin complex was used as template ion and silica precursors were used to form the MIP. The IIPs were found to be fluorescent due to incorporation of fluorescent quercetin molecule in the structure. The fluorescent IIPs were able to recognize Ni(II). The binding of Ni(II) to imprinted cavities was followed by monitoring the fluorescence changes occurring in the fluorescence spectra of IIP as a result of binding by Ni(II). An enhancement in the fluorescence emission signal of IIPs was observed on addition of Ni(II) ion solution of

different concentrations. The enhancement in fluorescence was found to be proportional to the concentration of Ni(II) ion. The formed IIPs can carry out effective identification of Ni(II) ion in water samples and can be further used for other water soluble ions, especially heavy metals ions.

Acknowledgements

The authors are thankful to Mata Gujri College, Fatehgarh sahib, Punjab for providing necessary lab facilities.

References

1. M. Irshad et al., Nanomaterials, 2013, 3, 615-37.
2. S. Xu *et al.* Journal of Hazardous Materials, 2012, 237–238, 347–354.
3. M. M. Yusoff *et al.,* Journal of Rare Earths, 2017, 35, 177–86.
4. J. Fu *et al.,* Journal of Material Chemistry A, 2015, 3, 13598–627.
5. T.K. Biswas *et al.,* Separation Science and Technology, 2019, 0, 1-10.
6. M.A. Momodu *et al.,* Research Journal Environmental and Earth Sciences, 2010, 2, 39-43.
7. G. Genchi *et al.,* Int J Environ Res Public Health, 2020, 17, 679.
8. M.S. Bidabadi *et al.,* Journal of Hazardous Materials, 2009, 166, 291–96.
9. S. Thangavel *et al.,* Talanta, 2015, Vol No. 131, 505-9.
10. B.N. Kumar *et al.,* International Journal of Modern Science, 2016, 2, 239-50.
11. S. Mathpal *et al.,* E-Journal of Chemistry, 2009, 6, 445-48.
12. S. Kanchi *et al.,*Arabian Journal of Chemistry, 2016, 2, 239-50.
13. F.A. Aly *et al.,* Analytical Methods, 2018, 10, 3851–58.

Effect of Interlaminate Shear Strength Properties on E-Glass Fabric/Epoxy Composites

Balu Maloth [1*], N.V.Srinivasulu [2], R.Rajendra[3]

[1] Research Scholar,Deapartment of Mechanical Engineering, College of Engineering ,Osmania University,O.U, Hyderabad, India

[2] Professor, Department of Mechanical Engineering, Chaitanya Bharathi Institute of Technology, Hyderabad, India

[3] Professor, Department of Mechanical Engineering, ,College of Engineering ,Osmania University,O.U, Hyderabad, India

Corresponding author's email: balu.1703@gmail.com

Abstract

Polymer glass fabric reinforced composites are major application in the aerospace and structural applications, in this research work fabrication of composites by using vacuum bagging method and mechanical characterization of glass fabric reinforcement epoxy composites which contains E-Glass fabric and matrix filled with TiO_2/ATBN.The effect of TiO_2/ATBN in modifying the mechanical properties of ILSS of the glass fabric epoxy composites are improved with the incorporation of filler materials. The results of the ILSS properties more in case of ATBN.

Keywords: E-Glass fabric polymer composites, TiO_2/ATBN, Vacuum bagging method, polymer matrix composites, ILSS.

1. Introduction

Now a day, E-Glass 8 mill fabric reinforced polymer matrix (EGFRP) composite has one of the important significant composite materials for structural and aerospace application. EGFRP composite is main centre of attraction for aerospace and structural research, because of its diversified application. However the changing mechanical properties of these GFRP composites are still being modified for different applications. The challenge for most engineers is the creating of new E-Glass fabric polymer matrix composites materials. Composites depend on epoxy have considerable potential to replace traditional metal structures. Changing of the new polymer matrix composites is one of the ways to develop the new polymer matrix composites. In all kind of engineering applications, E-glass fabric particulate incorporated fabric reinforced polymer matrix composites (FPMCs) are employed to increase in advanced polymer matrix, hybrid polymer matrix composites are still undergoing significant research and development today. Filler and/or fabric -reinforced polymer composites (FRPCs) are at present used in aero-space and automobile industries; because of it has unique properties such as high strength, high rigidity lightweight, and resistance to corrosion wear. [1]. Fiber reinforced polymer composite is an important material for structural application. In this work we have modified the epoxy by Al_2O_3, SiO_2 and TiO_2 micro particles in glass fabric /epoxy composite to improve the mechanical properties. The laminate is prepared by vacuum bagging method. It is observed that mechanical properties like flexural strength, flexural modulus and ILSS are more in case of SiO2 modified epoxy composite compare to other micro modifiers [2]. The influence of micro/nanoalumina

(Al_2O_3) on the mechanical properties of epoxy/jute fiber (J)/glass fiber (G) laminates was studied. All the composites are fabricated by the hand layup technique. The flexural strength and tensile strength of the epoxy/hybrid laminates were increased profoundly in the presence of micro/nano-Al_2O_3. The epoxy + GJGJ + 4 wt% nano-Al_2O_3 composites showed better flexural results when compared with the epoxy/glass fiber composites, whereas epoxy + GJJG + 4 wt% nano-Al_2O_3 composites show better tensile results [3]. The filler materials are Al_2O_3, TiO_2, fly ash and clay in nano and micro nano scale. The influence of filler size (nano and micro scale) and applied load values on the mechanical properties of epoxy composites were studied. Tensile, three points bending and hardness were carried out. The results show, the large influence of filler size and type on the performance of the epoxy composite. [4]. Composites were fabricated with different proportions of nano-modified micro-composite fillers in epoxy matrix at as much possible filler loadings. Results revealed that nano-modified SiO_2/Al_2O_3 micro-composite fillers enhanced inter-particle network and offer benefits like homogeneous microstructures and increased thermal conductivity. Epoxy composites attained thermal conductivity of 0.8 W/mK at 46% filler loading. Mechanical strength and bulk hardness were reached to higher values on the incorporation of nano-modified fillers. Tribology study revealed an increased specific wear rate and decreased friction coefficient in such fillers [5]. The effect of nano Al_2O_3 filler and cross head velocity on mechanical properties of glass fiber reinforced polymer composite (GFRP). Nano Al_2O_3 filler of 3 wt% of epoxy is dispersed into the epoxy matrix through temperature assisted magnetic stirring followed by sonication for a time period of 60 min. GFRP composites are fabricated by hand-lay-up techniques. It is observed that flexural strength about 14 % and interlaminar shear strength (ILSS) about 11 % improved in nano Al_2O_3 filled GFRP composite as compared to control GF composites. Further, ILSS is evaluated as a function of volume fraction of glass fiber and at different cross head velocity (1, 50, 100, 500 and 1000 mm/min). The results revealed that ILSS values increases with cross head velocity from 1 to 100 mm/min and decreases further increase in cross head velocity [6]. This research is intended to attain better understanding on the effect of particle sizes and geometry of fillers with different ratios of composition on the thermal and mechanical properties of hybrid composite system. It investigates the effect of combining polygonal aluminum oxide (Al_2O_3) and boron nitride (BN) platelets to enhance the thermal conductivity of epoxy composite. The surface of the two fillers was functionalized with aminopropyltriethoxysilane (KH550), thereby reducing the thermal interfacial resistance between filler and matrix. It was observed that there is no significant difference in the thermal and mechanical performance between $BN_{1\mu m}$ and $BN_{5\mu m}$ filler-filled composites. However, at filler loading of 30 wt%, the Al_2O_3 and $BN_{1\mu m}$ hybrid filler system (ratio 5:5) provided significant enhancement of maximum thermal conductivity of 0.57 $Wm^{-1}\,K^{-1}$ compared to 0.17 $Wm^{-1}\,K^{-1}$ that of neat epoxy. This synergistic effect results from the bridging of BN platelets between the Al_2O_3 particles facilitating the formation of effective thermal conductance network within the epoxy matrix. [7]. Experimental study has been carried out to study the effect of addition of fly ash at different weight percentage i.e. 3wt%, 6wt%, 9wt% and 12wt% on the mechanical properties of epoxy composites. Mechanical properties such as Impact strength, Flexural strength, and Flexural modulus and Fracture toughness are studied as per ASTM standards. Specimens are prepared using open

mould casting. The results shows the enhancement in Impact strength, fracture toughness, Flexural strength and Flexural modulus is by 100% and 50.96%, 73.5% and 19% at 12wt% of graphite in epoxy composites as compared to pure Epoxy. [8]. the surface-treated micro- and nano-silicas were mixed with epoxy resin and polyester-modified polydimethylsiloxane (PEM-PDMS) by using an ultrasonicator. Transmission electron microscope (TEM) was used to observe the even dispersion of nano-silica in an epoxy/micro-silica composite and it was found that the nano-silica was well dispersed. The electrical breakdown strength of the epoxy/micro-silica (60 wt%)/nano-silica (1 phr)/PEM-PDMS (0.5 phr) system was 60.0 kV/2 mm, which was 13.6% higher than that of epoxy/micro-silica (60 wt%)/PEM-PDMS (0.5 phr) system, 52.8 kV/2 mm. The contact angle of neat epoxy was 77°, which was 132% higher than that of epoxy/micro-silica (60 wt%)/nano-silica (1 phr)/PEM-PDMS (0.5 phr) system, 101.6°.[9].The mechanical properties were evaluated by means of static tensile test and Charpy impact strength method. The thermal stability was investigated by thermo gravimetric analyses in inert and oxidizing atmospheres. Results showed that combining basalt fibers with basalt powder improves stiffness and thermal resistance of the epoxy composites. The new hybrid composites are more resistant to temperature changes than the reference sample as proven by dynamic mechanical thermal analysis. [10]. The mechanical and dynamic mechanical thermal properties on this hybrid composite were found by means of tensile test, flexural test, Charpy impact strength method and dynamic mechanical thermal analysis. In this gaze, results show that the reinforcing of glass fiber with basalt powder heightens the strength of the epoxy composites.

2. Experimental

2.1 Materials

In this work, E-glass 8 mill fabrics is used as the reinforcement material, epoxy resin and ATBN (amine terminated butadiene- acrylonitrile) are used as matrix in the polymer matrix composites. E-Glass fabric composite are the most common of all polymer matrix composites (PMCs) reinforcing fibers. Low cost, high tensile strength, good chemical resistance and excellent insulation properties are the key advantages of E-glass fabric.

2.2. Filler materials

Composites of polymer matrix are used in the greatest variety due to their lower cost, ease of processing, higher specific strength, simplicity of design and light weight. The reinforcement of the polymer matrix with glass fiber results in a general improvement in mechanical properties. In general, filler materials are inert materials used in composite materials to minimize material costs, enhance mechanical properties and in a number of cases to enhance process capability. In this work, Titanium dioxide or titanium (TiO_2) and ATBN metallic fillers is selected for use in this polymer composites prepared for this study as particulate fillers in predetermined proportions.

(a) Epoxy resin LY556 (b) hardener

(c)E-Glass 8 mill fabric (d) ATBN (e) TiO_2

Figure 1: Matrix and reinforcement materials for composites

2.3. Composites fabrication

Most of the researchers have used the hand lay-up process to develop polymer matrix composites. It will reduce the strength of the composites. So, in this research vacuum bagging method is used to develop the composites. Vacuum bagging is a procedure used in the course of its cure process to build mechanical pressure over a composite. There are quite a few functions of this methods and the first and most important function is to pressurize a composite lamination to remove the air in it. Second, it increases the attraction between fiber layers for effective fiber adhesion for the transmission of force and reduces the orientation of fiber shifting throughout cure. Third, it is minimize the humidity. At last, the vacuum bagging method minimizes the parts of composite in terms of fiber-to-resin ratio. In the last two decades, these enhanced benefits in the aerospace and racing industries to make the most of the mechanical and physical characteristics of glass fiber reinforced polymer matrix composites.

The description and composition of epoxy resin, ATBN, E-glass 8 mill fabrics, fillers and hardener are revealed in Table 1.The development of the composite is completed by vacuum bagging technique. As per the recommendation, the minimum temperature curing LY-556 (epoxy resin) and subsequent HY951 (hardener) are assorted in a ratio of 10 to 1 by weight. The fillers are mixed scrupulously with the epoxy resin before it will apply over the E-glass. Each E-glass fiber is of in the dimension 300 × 300 (mm) and 5 samples are developed with the same combinations of the materials. After developing the composite, it will cure at room temperature. The final size of the polymer fiber reinforced composite is 300 × 300 × 4 (mm).

Table. 1. Materials and their ratios in grams

Materials	Weight
Epoxy Resin(LY-556)	600 grams
Hardner (HY-951)	135 grams

ATBN(amine terminated butadiene acronitrile)	10% of Epoxy Resin(60 grams)
E- Glass 8 Mill Fabric	460 grams
TiO_2	10% of Epoxy Resin(60 grams)
	Ratio.100:23

2.4. Specimen preparation

The E-Glass 8 mill fabric reinforced particulate filled epoxy composite is removed from mould. Based on ASTM standard, the test specimens are extracted from the composite for mechanical characterization (i.e. ILSS test). For tensile test, the test specimen was cut as per ASTM D2344 A (ILSS) is used to develop the sample for Interlaminate shear strength test. The developed composite and the extracted sample specimen for ILSS are shown in Fig.2.

(a)Composites (ATBN) (b) Composite ((TiO_2) (c) ILSS test (ATBN) (d) ILSS test (TiO_2)

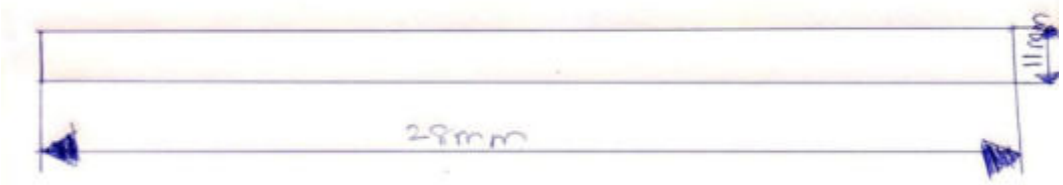

(e)ASTM standard specimens

Fig.2. developed composites and ILSS specimens

The developed composites and sample specimens are extracted from the composites are displayed in Fig.2.

Interlaminate shear strength test: The ILSS tests were carried out on the specimens using computerized Universal Testing Machine (UTM) of 30 tons capacity. Experiments could be conducted at normal temperature and each experiment was conducted until a rupture take place. During the test for measuring stress and strain, the applied shear load and extension were reported. The experiments were conducted by maintaining strain rate is constant and at the rate of 10 mm/min. The gauge length of the specimen was chosen as 165 mm. For each experiment, five samples pieces were experienced. The specimen used in experiments and the tested specimens are depicted in Figure 3.The results of the ILSS test are shown in Table 2.

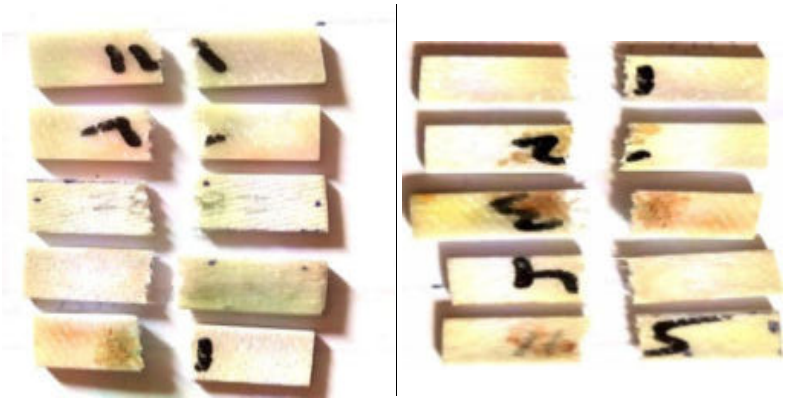

(a) ILSS test(ATBN) (b) ILSS test(TiO_2)

Figure 3: Tested specimens

3. Results and Discussion

3.1. Mechanical characterization

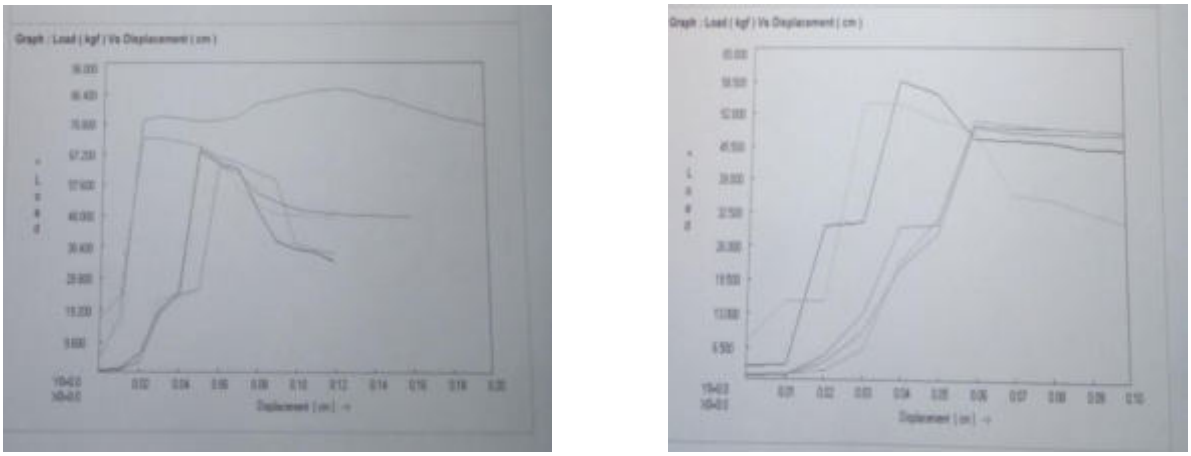

(a) ILSS(ATBN) (b) ILSS (TiO_2)

Figure 4: Graph of inter laminate shear strength test

The characterization of the developed composites reveals that addition of particulate filler has influenced strongly on the ILSS properties of nano-filled E-glass 8Mill fiber reinforced composites. The result and graph of interlaminate shear strength of the developed E-glass fabric reinforced composites are shown in Table 2 and Fig. 4. The interlaminate shear strength is varied from 255.591 Kgf/cm^2 to 316.336 Kgf/cm^2 (ATBN). The average inter laminate shear strength of the E-glass fabric reinforced composite is 272.193 Kgf/cm^2 (ATBN). It shows that the average of inter laminate shear strength is nearly equal to the inter laminate shear strength of the fiber (282.234 Kgf/cm^2). The interlaminate shear strength is varied from 240.825 Kgf/cm^2 to 201.62 Kgf/cm^2 (TiO_2). The average inter laminate shear strength of the E-glass fabric reinforced composite is 205.882 Kgf/cm^2 (TiO_2). It shows that the average of inter laminate shear strength is nearly equal to the interlaminate shear strength of the fabric (282.234 Kgf/cm^2). The interlaminate shear strength is more in case of ATBN.

Table 2: Result of Interlaminate shear strength (ILSS) test for five samples

Sample No	ILSS test(ATBN) (Kgf/cm^2)	ILSS test(TiO_2) (Kgf/cm^2)
1	316.336	201.62
2	263.768	225.703
3	277.377	156.441
4	247.625	204.837
5	255.591	240.825

4. Conclusions

This work was conducted to determine the effect of nano-filler material and ATBN on E-glass 8mill fabric composites. Five samples are developed by vacuum bagging method to find the interlaminate shear strength of the E-glass fabric reinforced composites. The finding of this analysis was summarized as: 1. The average interlaminate shear strength of the composite is 272.193 Kgf/cm^2 and this value is nearer to the maximum interlaminate shear strength of the fiber (E-Glass 8 mill fabric composites).The interlaminate shear strength test result reveals that addition of TiO_2 filler and ATBN has influenced strongly on the interlaminate shear strength of the composites. It is proved that the ATBN values are increased the interlaminate shear strength of the composites and interlaminate shear strength is equal to the ILSS of the fiber (282.234 Kgf/cm^2) 2. The average interlaminate shear strength of the composite is 205.882 Kgf/cm^2. It is proved that the interlaminate shear strength of TiO_2 are decreased compared to interlaminate shear strength of ATBN.

Acknowledgement

I am very thankful to my Supervisor **Dr.N.V.Srinivasulu** , Professor in Mechanical Engineering Department, CBIT, HYD, for his encouragement and guidance to complete this Research work successfully. I am very thankful to my Co-Supervisor **Dr.R.Rajendra**, Professor in Mechanical Engineering Department, O.U, HYD, for his encouragement and guidance to complete this Research work successfully. I sincerely thankful to Chaitanya Bharathi Institute of Technology, Hyderabad, India for extending all facilities to carry out this Research work.It's my great pleasure to thank **Dr.V.Murali Krishna,** Professor & Head of the Department, Mechanical Engg Dept, CBIT, Hyderabad, giving me an opportunity to carry out the Research work in Chaitanya Bharathi Institute of Technology, Hyderabad. I offer heart full thanks to **Mr. R. Srinivas Rao,** Chief Executive Engineer, R.R Industries, Hyderabad, India for his invaluable guidance and precious suggestions to complete the Research work successfully.

References

[1] R K Nayak *et al.,* materials science, 2014, 6, 1359-1364.
[2] G Raghavendra *et al.,* materials science, 2014, 27(3), 342-351.
[3] A Mimaroglu *et al.,* journal of Industrial Engineering Research, 2015, 61(10), 601-609.
[4] S Sadasivan *et al.,* Polymer for advanced technologies, 2016, 27(7), 905-914.
[5].R K Nayak *et al.,* International Journal of Plastics Technology, 2016, 20(2), 334–344.

[6]. P Anithambigai *et al.,* Journal of Materials Science, 2016, 51(16), 7415–7426.
[7]. B Hrushikesh *et al.,* International Journal of Advanced Engineering Research and Studies E-ISSN2249–8974, Int. J. Adv. Engg. Res. Studies/VI/I/Oct.-Dec,2017/01-05.
[8] J Jun *et al.,* IEEE Transactions on Dielectrics and Electrical Insulation, 2017, 24 (6), 3794-3800.
[9] D Matykiewicz *et al.,* Composites Part B, 2017, 125, 157-164.
[10] S Mahesh Babu *et al.,* Journal of the Chinese Advanced Materials Society, 2018, 6(3), 311-328.

Comparative Study of Structural and Electrical Conductivity Studies of Pure PVA and PVA Doped with Malonic and Succinic Acid Polymer Electrolytes

K. Alakanandana[a], A.R.Subrahmanyam[b] and J. Siva Kumar[c]

[a]Department of BS, G. Narayanamma Institute of Technology & Science, Hyderabad, Telangana, India

[b]Department of S&H, MVSR Engineering College, Hyderabad, Telangana, India

[c]Department of Physics, Osmania University, Hyderabad, Telangana India

Corresponding author email ID: alakanandana@gmail.com

Abstract

Conducting polymers, particularly the soluble derivatives are attractive in Organic electronics due to their conductivity with ease of fabrication. Novel proton conducting solid polymer electrolytes based on Poly vinyl alcohol (PVA) with Malonic acid and PVA with Succinic Acid as dopant are prepared by solution cast technique with varying doping concentrations up to 40 wt.%. XRD is used to examine the complexation of PVA polymer with Malonic acid and Succinic acid. The results of XRD reveal that with the increase of Malonic acid and Succinic acid concentration, the amorphous nature of PVA polymer matrix increases. FTIR spectra studies for pure and complexed polymers reveal the vibrational changes that occur due to the presence of dopant salt in the polymer. Also, the presence of O-H, C-H and C-C groups is indicated when FTIR spectrum of pure PVA is compared with the spectra of complexed polymers. The DC conductivity measurements have been taken on the polymer samples in the temperature range 303 K to 373 K. From these measurements it is observed that the conductivity is found to increase with the concentration of dopant as well as temperature. Thus the results obtained are presented.

Key words: XRD, FTIR, polymer electrolyte, conducting polymers, composite PVA, Oxalic acid, Malonic acid.

1. Introduction

Polymers find potential applications in permanent and temporary data storage devices or as a basic material for the fabrication of active & passive light guides. Ion doped organic polymers are highly efficient in holographic recording [1]. Very few Vinyl polymers are soluble in water and Poly Vinyl Alcohol is recognized as one among them. By virtue of environmental sensitivity of PVA it finds extensive applications in textile wrap sizing, adhesives, paper sizing agents, ceramic binders. It is also used in cosmetics, pharmacy and electronic industry.

Polymer complexes with suitable inorganic and organic acids are known as polymer electrolytes which play an important role in the development of various electrochemical devices such as fuel cells, batteries, photo electron chemical cells, electrochemical displays, smart windows etc. Very conducive mechanical properties, ease of fabrication into thin films of

desirable sizes and their ability to form proper electrochemical devices are some of the important advantages of polymer electrolytes.

The aim of the present work is to study the structural and electrical properties of PVA based polymer electrolytes. These are synthesized by doping dicarboxylic acids such as Malonic acid and Succinic acid into PVA in different proportions (weight). The study is carried out using XRD, FTIR techniques and by obtaining the dc conductivity of PVA composite polymer systems.

2. Preparation of polymer electrolyte films

Pure PVA (Mw 1, 40,000 from AR chemicals) complexed with Malonic acid and Succinic acid in various compositions (90:10), (80:20), (70:30) & (60:40) by wt% ratio, are prepared using the solution caste technique. PVA & Malonic acid, PVA & Succinic acid are dissolved in double distilled water; the solutions obtained are thoroughly stirred for 10-12 hrs. to get homogeneous mixture. The stirred solution is caste onto polypropylene dishes and allowed to evaporate slowly at 50˚C. After one or two days solid polymer layers are formed as thin electrolytes with nearly 100 microns thickness at the bottom of dishes. These electrolytes are dried in vacuum (10^{-3} torr) to eliminate the residual traces of water then carefully separated from the dishes and stored in evacuated desiccators.

The X-ray diffraction (XRD) patterns of the electrolytes are made with PHILIPS PW 3710 X-ray diffractometer in the range 10^0-80^0. Fourier transform infrared (FTIR) spectra of these systems are recognized using JASCO FTIR- 5300 spectrometer. The measurements are taken over a wave number range of 400-4000cm^{-1}. D.C. conductivity is measured using indigenously built instrument in the temperature range 300-373K with Keithley programmable electrometer (modelNo.196). Thickness of the films is measured by Mitutoyo thickness gauge (no.7301, range 0.01mm to 10mm.

3. Results and discussion

3.1. XRD Analysis

The X-ray diffraction patterns of pure PVA and PVA complexed with Malonic acid and pure PVA and PVA complexed with Succinic acid are as shown in fig.1a and fig.1b.respectively. A few differences are identified between the diffraction patterns of PVA complexed electrolytes and that of pure PVA. Above Figs. shows that the pure PVA has a characteristic peak corresponding to an orthorhombic lattice centered at 20° indicating its semi crystalline nature [2]. The peak becomes less intense as the content of Malonic and Succinic acid is increased. This could be attributed to the disruption of crystalline structure of the PVA by the addition of acid. The pattern pertaining to pure Malonic/Succinic acid contains very sharp peaks. Absence of such sharp peaks corresponding to the presence of these acids in the patterns of polymer complexes indicates the dissolution of Malonic/Succinic acid in the polymer matrices.

As the Malonic/Succinic acid content is increased in the polymer, the diffraction peaks become less intense, suggesting the decrease in the degree of crystallinity and simultaneous increase in the amorphousness of those polymer electrolyte films. The intensity of XRD pattern of PVA decreases as the amorphous nature increases [3]. No sharp peaks were observed for higher concentrations of Malonic/Succinic acid in the polymer, suggesting the dominant presence of amorphous phase [4]. The amorphous nature results in greater ionic diffusity with

high ionic conductivity which can be obtained in amorphous polymers that have flexible back bone [5].

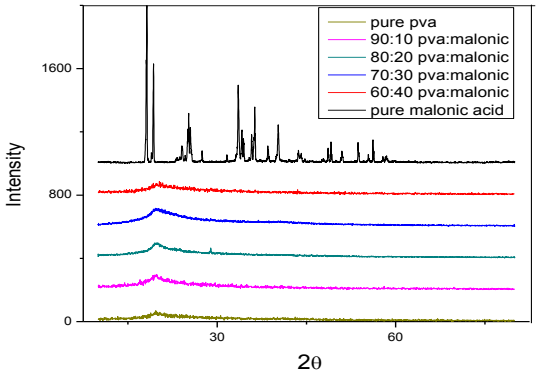

Fig.1a : X-ray diffraction patterns of pure PVA and PVA and PVA complexed with Malonic acid

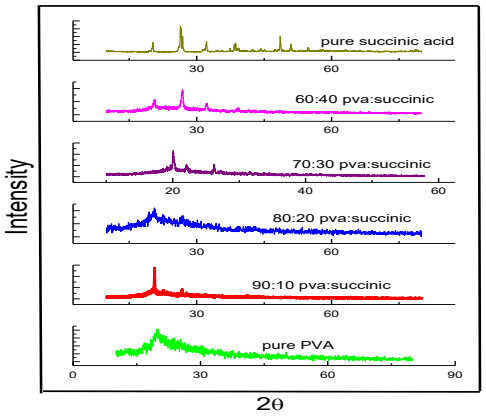

Fig.1b: X-ray diffraction patterns of pure PVA PVA complexed with succinic acid

3.2.FTIR Analysis

Fig.2a. shows the FTIR spectra pertaining to pure PVA, PVA complexed with different compositions of Malonic acid and pure Malonic acid. The following changes in the spectral features have been observed after comparing the spectrum of complexed PVA with that of pure PVA & Malonic acid. The absorption band in the region 3550-3114 cm^{-1} is due to inter molecular hydrogen bonded O-H stretching frequency of PVA which is shifted to 3592-3092, 3613-2739,3624-2676, 3603-2853 cm^{-1} in the 10, 20, 30 & 40 % acid complexed PVA films respectively. In addition to this, the C-H bond stretching of CH_2 showed an absorption band at 2947 cm^{-1} in pure PVA and is shifted to 2968 cm^{-1} , 2739 cm^{-1}, 2635 cm^{-1} , 2624 cm^{-1} respectively. The C-H bending of CH_2 in pure PVA exhibited absorption at 1453 cm-1 and it is shifted to 1464, 1464, 1453 &1464 cm^{-1} in the complexed films respectively. Deformation is coupled to C-H wagging gives rise to a peak at 1438 cm^{-1} in pure PVA and it is shifted to 1468,1448,1458 & 1470 cm^{-1} in 10,20,30& 40% of complexed PVA with Malonic acid films respectively. In pure PVA, the C-C stretching occurs at 948 cm^{-1} and it is shifted to 937, 925, 914 & 925cm^{-1} in complexed films of PVA polymer electrolyte respectively. The complexation of PVA and Malonic acid clearly indicates the changes in the FTIR spectra. The FTIR spectra pertaining to pure PVA, PVA complexed with different compositions of Succinic acid and pure Succinic acid are shown in Fig.2b. The following changes in the spectral features have been observed after comparing the spectrum of complexed PVA with that of pure PVA & Succinic acid. The absorption band in the region 3551-3114 cm^{-1} is due to inter molecular hydrogen bonded O-H stretching frequency of PVA which is shifted to 3561-3086, 3593-2966, 3519-2873 and 3585-2892 cm^{-1} in the 10, 20, 30 & 40 % acid complexed PVA electrolytes respectively.

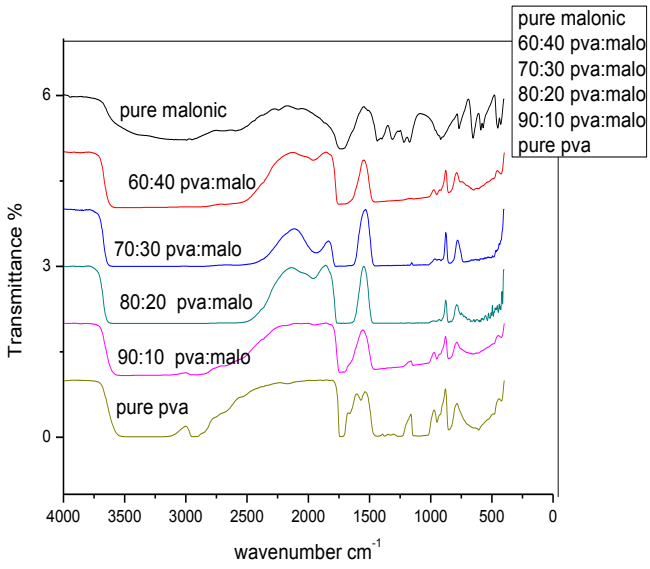

Fig.2a: FTIR spectra of PVA & PVA complexed with complexed Malonic acid polymer electrolytes

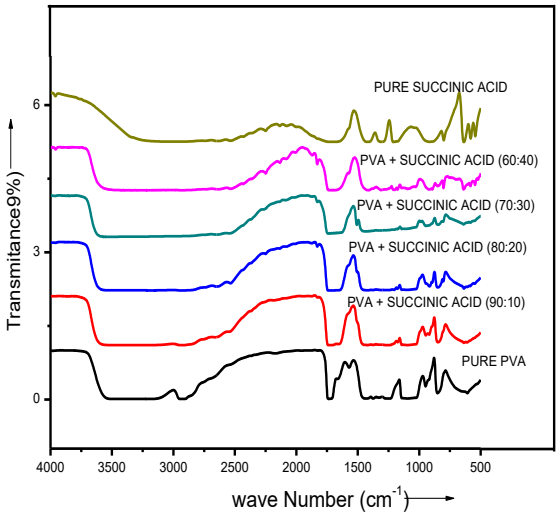

Fig.2b: FTIR spectra of PVA & PVA complexed with Succinic acid polymer electrolytes

In addition to this, the C-H bond stretching of CH_2 showed an absorption bend at 2947 cm^{-1} in pure PVA and is shifted to 2980 cm^{-1}, 2874 cm^{-1}, 2798 cm^{-1} , 2724 cm^{-1} respectively . The C-H bending of CH_2 in pure PVA exhibited absorption at 1453 cm^{-1} and it is shifted to 1461, 1467, 1473 & 1455 cm^{-1} in the complexed electrolytes respectively. In pure PVA, the C-C stretching occurs at 948 cm^{-1} and it is shifted to 942, 923, 954 & 929 cm^{-1} in complexed electrolytes of PVA polymer electrolytes respectively.

3.3.Electrical properties

Conductivity of polymer electrolytes depends on the actual concentration of conducting species and their mobility.
The conductivity (σ) varies with temperature (T) according to the equation

$$\sigma = \sigma_0 \exp (E_a/kT)$$

where σ_0 is pre exponential factor, E_a is activation energy, k is Boltzmann constant and T is absolute temperature.

The conductivity was found to increase with the increase in temperature in pure PVA as well as all the compositions of polymer electrolytes. The conductivity versus temperature follows Arrhenius behavior throughout. The conductivity values do not show any abrupt jump with temperature, which indicates that, these electrolytes exhibit amorphous nature [6]. This type of behavior is observed in a number of PVA based electrolyte systems [7, 8].

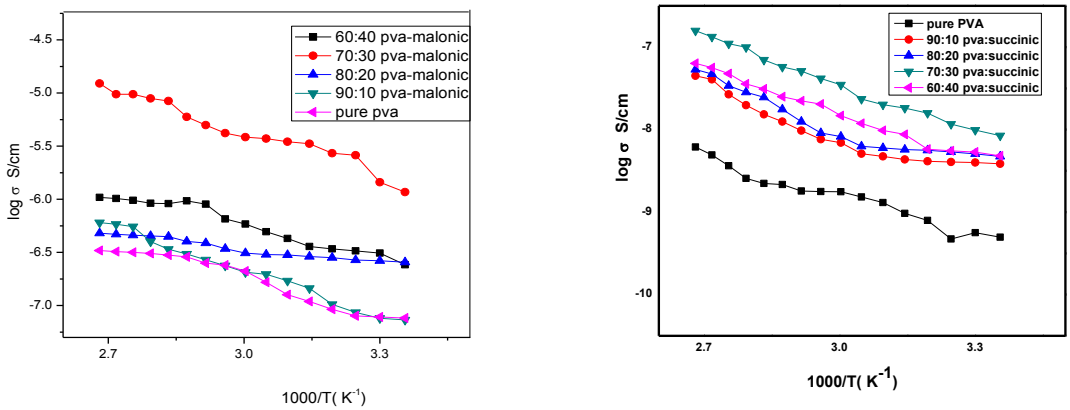

Fig.3: Electrical conductivity as a function of temperature and compositions of PVA-Malonic acid and PVA-Succinic acid.

Fig. 3 shows the variation of electrical conductivity as a function of temperature for pure PVA and for different compositions of Malonic/Succinic acid doped polymer electrolytes in the temperature range 303K-373K. These are also shown in the table-1 & table -2. Quite interestingly, it is observed that the conductivity values are highest for 70:30 PVA: Malonic acid & 70:30 PVA : Succinic acid electrolytes.

Table 1: Conductivity of PVA and PVA: Malonic acid electrolyte films.

Polymer electrolyte	**Conductivity (σ) S/cm at 303K**	**Conductivity (σ) S/cm at 373K**
PVA	5.62×10^{-10}	6.15×10^{-9}
PVA: Malonic acid 90:10)	7.33×10^{-8}	3.73×10^{-7}
PVA: Malonic acid (80:20)	2.56×10^{-7}	4.796×10^{-7}
PVA: Malonicacid (70:30)	1.17×10^{-6}	1.23×10^{-5}
PVA: Malonic acid (60:40)	2.42×10^{-7}	1.04×10^{-6}

Table2: Conductivity of PVA and PVA: Succinic acid electrolytes.

Polymer electrolyte	**Conductivity (σ) S/cm at 303K**	**Conductivity (σ) S/cm at 373K**
PVA	5.62×10^{-10}	6.15×10^{-9}
PVA: Succinic acid (90:10)	3.98×10^{-9}	4.49×10^{-9}
PVA: Succinic acid (80:20)	5.07×10^{-9}	5.35×10^{-8}
PVA: Succinic acid (70:30)	9.87×10^{-9}	1.58×10^{-7}
PVA: Succinic acid (60:40)	5.34×10^{-9}	6.36×10^{-8}

The increase in conductivity with temperature is due to decrease in viscosity and increase in chain flexibility and mobility [9]. The conductivity- temperature data obey Arrhenius relationship, the nature of cation transport is quite similar to that in ionic crystals, where ions

jump into neighboring vacant sites and increases the ionic conductivity [10]. The increase in conductivity may be due to the transition from semi crystalline phase to amorphous phase. Due to this phase change conductivity shows an increasing trend with temperature and this can be interpreted as hopping mechanism between coordinating sites, local structure and segmental motion of the polymer [11]. As the amorphous region increases, the polymer chain acquires faster internal modes in which bond rotations produce segmental motion. This in turn favors hopping inter-chain and intra-chain movements and thus increases in the conductivity of the polymer.

4. Conclusions

- The complexation of PVA polymer with Malonic acid and with Succinic acid is confirmed with XRD and FTIR studies.
- The conductivity of pure PVA is about $5.62x10^{-10}$ & $6.15\ x10^{-9}$S/Cm at room temperature & at 100^0C and this value increases to $1.17x10^{-6}$ & $1.23x10^{-5}$ S/Cm when PVA complexed with Malonic acid (70:30). This particular sample of PVA complexed with Malonic acid (70:30) has provided the maximum conductivity compared to other samples.
- The conductivity of pure PVA is about $5.62x10^{-10}$ & $6.15\ x10^{-9}$S/Cm at room temperature & at 100 ^{0}C and this value increases to $9.87x10^{-9}$& $1.58\ x10^{-7}$ S/Cm when PVA complexed with Oxalic acid (70:30). This particular sample of PVA complexed with Oxalic acid (70:30) has provided the maximum conductivity compared to other samples.
- Among the two types of PVA complexed polymer electrolytes, due to relatively high conductivity, PVA complexed with Malonic acid (70:30) electrolyte could be a promising electrolyte for applications in electrochemical cells.

Acknowledgements

The authors thank the Head the department of physics, Osmania University and Chairman Board of studies in physics, Osmania University for their constant encouragement and providing facilities. Also the author thanks the coordinator SAP department of physics for providing the necessary facilities, Principal, G. Narayanamma Institute of Technology and Science for his constant encouragement.

References

1. G. Filoti *et al.,* Journal of Radioanalytical and Nuclear Chemistry, 190, 2, 315-320.
2. M Kurumova *et al.,* Polymer, 2000, 41:925-9272.
3. R M Hodge *et al.,* Polymer, 1996, 37:1371
4. V Madhu Mohan, Master Chem Phys, 2004, 94:177
5. A A Mohamad *et al.,* Solid State Ionics, 2003, 156:171
6. MS Michael *et al.,* Solid State Ion, 1997, 98:167
7. Ch V Subba Reddy *et al.,* Polymer, 2006, 47:1318
8. A Bhide *et al.,* J Power Sources, 2007
9. S S Sekhon *et al.,* Solid State Ionics,1996
10. J L Souquet *et al.,* Solid State Ionics, 1994, 70-71,337.
11. K K Maurya *et al.,* J Phys. Soc Jpn, 1994, 1, 1709.

r-Regular Integers Modulo n^r

M. Ganeshwar Rao
Chaitanya Bharathi Institute of Technology,
Gandipet, Hyderabad
e-mail: ganeshwararao_maths@cbit.ac.in

Abstract

Introducing the notion of a r-regular integer modulo n^r we obtain some basic properties of such integers and arithmetic properties of certain functions related to them.

***Key words*:** *r*-regular integer modulo n^r, unitary divisor, *r*-free integer, *r*-gcd of two integers.

1. INTRODUCTION

Let *r* be a fixed positive integer. A positive integer *a* is said to be *r-regular modulo* n^r if there is an integer *x* such that $a^{r+1}x \equiv a^r \left(\mathrm{mod}\, n^r\right)$. The case $r=1$ gives the notion of *a regular integer modulo n*, introduced by J. Morgado ([6] and [7]) who made an investigation of their properties.

Clearly $a=0$ is *r*-regular modulo n^r for every $n \geq 1$. Also if $a \equiv b\left(\mathrm{mod}\, n^r\right)$ then *a* and *b* are *r*-regular modulo n^r simultaneously. Further, if *a* and *b* are *r*-regular modulo n^r then so is *ab.*

For positive integers *a* and *b* their greatest r^{th} power common divisor is denoted by $(a,\ b)_r$ and is called the *r-gcd of a and b*. Note that $(a,\ b)_1 = (a,\ b)$, the gcd of *a* and *b.*

We recall the notions given in ([5], *p* 42–43):

A complete set of residues modulo n^r is called a $(n,\ r)$*-residue system.* $C_{n,\,r} = \left\{a : 1 \leq a \leq n^r\right\}$ is the minimal $(n,\ r)$-residue system. The set of all *a* in an $(n,\ r)$-residue system such that $\left(a,\ n^r\right)_r = 1$ is called *a reduced* $(n,\ r)$*-residue system.* $R_{n,\,r} = \left\{a \in C_{n,\,r} \ :\ \left(a,\ n^r\right)_r = 1\right\}$ is the minimal reduced $(n,\ r)$-residue system.

V.L. Klee [3] defined a generalization φ_r of the Euler's function by $\varphi_r(n) = \#\left\{a : 1 \leq a \leq n \text{ and } (a,\ n)_r = 1\right\}$ and proved that

$$\varphi_r(n) = \sum_{d \mid n} \mu_r(d).\frac{n}{d}, \tag{1}$$

where μ_r is the *r*-analogue of the Mobius function μ given by

$$\mu_r(n) = \begin{cases} 1 & \text{if } n = 1 \\ (-1)^t & \text{if } n = \left(p_1 p_2 \ldots p_t\right)^r \text{ where } p_1 < p_2 < \ldots < p_t \text{ are primes} \\ 0 & \text{otherwise} \end{cases}$$

Note that $\mu_1 = \mu$ and that $\varphi_r\left(n^r\right) = \#R_{n,\,r}$.

Let $\mathrm{Reg}_r\left(n\right) = \left\{a \in C_{n,\,r}\text{: } a \text{ is r-regular modulo } n^r\right\}$ and $\rho_r\left(n^r\right) = \#\mathrm{Reg}_r\left(n\right)$.

Observe that any $a \in R_{n,\,r}$ is in $\mathrm{Reg}_r\left(n\right)$. In fact, if $a \in R_{n,\,r}$ then $\left(a,\, n^r\right)_r = 1$ so that $\left(a,\, n^r\right) = 1$ and therefore there is an integer x_0 such that $a\,x_0 \equiv 1\left(\mathrm{mod}\, n^r\right)$ which gives $a^{r+1}x_0 \equiv a^r\left(\mathrm{mod}\, n^r\right)$ showing $a \in \mathrm{Reg}_r\left(n\right)$. Hence $\varphi_r\left(n^r\right) < \rho_r\left(n^r\right) \le n^r$ for every $n > 1$, with $\rho_r\left(n^r\right) = n^r$ if and only if n is squarefree.

Recently Laszlo Toth [4] has studied several properties of the function $\rho\left(n\right) := \rho_1\left(n\right)$.

In this paper we prove some basic properties of the integers in the set $\mathrm{Reg}_r\left(n\right)$ and also certain arithmetic properties of the function $\rho_r(n^r)$

2. INTEGERS IN $\mathbf{Reg}_r\left(n\right)$

In all that follows $n > 1$ be of the canonical form:

$$n = p_1^{\alpha_1} p_2^{\alpha_2} \ldots p_t^{\alpha_t}, \tag{2}$$

where $p_1 < p_2 < \ldots < p_t$ are primes and α_i are integers ≥ 1.

Theorem A. For an integer $a \ge 1$ the following are equivalent:

(i) $a \in \mathrm{Reg}_r\left(n\right)$

(ii) for every $i \in \left\{1,\ 2,\ \ldots,\ t\right\}$ we have either $p_i \nmid a$ or $p_i^{\alpha_i r} \mid a^r$

(iii) $\left(a,\, n^r\right)_r \,\|\, n^r$,

($d \,\|\, m$ means that $d \mid m$ and $\left(d,\, \dfrac{m}{d}\right) = 1$, in which case d is called a *unitary divisor* of m)

(iv) $a^{\varphi_r\left(n^r\right)+r} \equiv a^r\left(\mathrm{mod}\, n^r\right)$

(v) There is an integer $k \ge 1$ such that $a^{k+r} \equiv a^r\left(\mathrm{mod}\, n^r\right)$.

Proof: Suppose $a \in \mathrm{Reg}_r\left(n\right)$ so that $a^{r+1}x_0 \equiv a^r\left(\mathrm{mod}\, n^r\right)$ for some integer x_0. Therefore for each $i\left(1 \le i \le t\right)$, $p_i^{\alpha_i r} \mid a^r\left(ax_0 - 1\right)$. Since $\left(a,\, ax_0 - 1\right) = 1$ we have $\left(a^r,\, ax_0 - 1\right) = 1$, we have either $p_i \nmid a$ or $p_i \mid a^r$ for each i, and in the later case it follows $p_i^{\alpha_i r} \mid a^r$. Thus (i) $\Rightarrow$ (ii).

Assume (ii). That is, a is an integer ≥ 1 such that either $p_i \nmid a$ or $p_i^{\alpha_i r} \mid a^r$. We have to show $a \in \mathrm{Reg}_r\left(n\right)$.

In case $p_i \nmid a$ then $\left(a,\ p_i^{\alpha_i r}\right)=1$ so that there is an integer x_i with $a\,x_i \equiv 1\left(\mathrm{mod}\ p_i^{\alpha_i r}\right)$ and hence $a^{r+1}x_i \equiv a^r \left(\mathrm{mod}\ p_i^{\alpha_i r}\right)$.

In case $p_i^{\alpha_i r} \mid a^r$ then for any integer x, $a^{r+1}x \equiv a^r \left(\mathrm{mod}\ p_i^{\alpha_i r}\right)$ holds. Thus $a^{r+1}x \equiv a^r \left(\mathrm{mod}\ p_i^{\alpha_i r}\right)$ is solvable for $1 \le i \le t$ and hence $a^{r+1}x \equiv a^r \left(\mathrm{mod}\ p_1^{\alpha_1 r}.p_2^{\alpha_2 r}....p_t^{\alpha_t r}\right)$ is solvable, showing $a \in \mathrm{Reg}_r\left(n\right)$. Thus (ii) $\Rightarrow$ (i).

Note that (ii) holds $\Leftrightarrow a^r = a_0.d^r$, where $d^r = \prod_{p_i \mid a} p_i^{\alpha_i r}$ and $\left(a_0,\ n\right)=1$

$\Leftrightarrow \left(a^r,\ n^r\right)=d^r$, which is a unitary divisor of n^r

$\Leftrightarrow \left(a,\ n^r\right)_r = d^r \,\|\, n^r$, since $\left(a^r,\ n^r\right)=\left(a,\ n^r\right)_r$. Thus (ii) $\Leftrightarrow$ (iii).

(ii) $\Rightarrow$ (iv). If $p_i^{\alpha_i r} \mid a^r$ then $a^{\varphi_r\left(n^r\right)+r} \equiv a^r \left(\mathrm{mod}\, n^r\right)$ is obvious. If $p_i \nmid a$, then by Euler-Fermat Theorem, $a^{\varphi\left(p_i^{\alpha_i r}\right)} \equiv 1\left(\mathrm{mod}\ p_i^{\alpha_i r}\right)$ so that

$$a^{\varphi_r\left(n^r\right)} = \left[a^{\varphi\left(p_i^{\alpha_i r}\right)}\right]^{\varphi_r\left(n^r\right)/\varphi\left(p_i^{\alpha_i r}\right)} \equiv 1\left(\mathrm{mod}\ p_i^{\alpha_i r}\right),$$

since

$$m := \frac{\varphi_r\left(n^r\right)}{\varphi\left(p_i^{\alpha_i r}\right)} = \frac{\varphi_r\left(p_1^{\alpha_1 r}\right)\varphi_r\left(p_2^{\alpha_2 r}\right)...\varphi_r\left(p_t^{\alpha_t r}\right)}{\varphi\left(p_i^{\alpha_i r}\right)} = \left(\prod_{j \ne i} \varphi_r\left(p_j^{\alpha_j r}\right)\right)\frac{\varphi_r\left(p_i^{\alpha_i r}\right)}{\varphi\left(p_i^{\alpha_i r}\right)}$$

$$= \left(1 + p_i + ... + p_i^{r-1}\right).\ M \text{ where } M = \prod_{j \ne i} \varphi_r\left(p_j^{\alpha_j r}\right) \text{ so that } m \text{ is an integer.}$$

Thus $a^{\varphi_r\left(n^r\right)+r} \equiv a^r \left(\mathrm{mod}\ p_i^{\alpha_i r}\right)$ for $1 \le i \le t$, giving (iv)

(iv) $\Rightarrow$ (i). If $a^{\varphi_r\left(n^r\right)+r} \equiv a^r \left(\mathrm{mod}\, n^r\right)$ then $a^{r+1}.x_0 \equiv a^r \left(\mathrm{mod}\, n^r\right)$ where $x_0 = a^{\varphi_r\left(n^r\right)-1}$ showing $a \in \mathrm{Reg}_r\left(n\right)$.

(iv) $\Rightarrow$ (v) is immediate with $k = \varphi_r\left(n^r\right)$. Also if $a^{k+r} \equiv a^r \left(\mathrm{mod}\, n^r\right)$ for some $k \ge 1$ implies $a^{r+1}.x_0 \equiv a^r \left(\mathrm{mod}\, n^r\right)$, where $x_0 = a^{k-1}$, showing $a \in \mathrm{Reg}_r\left(n\right)$. Thus (v) $\Rightarrow$ (i).

3. THE FUNCTION $\rho_r\left(n^r\right)$.

In this section we study the function $\rho_r\left(n^r\right)$ and its relation with $\varphi_r\left(n^r\right)$. Also we express the sum $S_r\left(n\right)$ of the *r*-regular integers modulo n^r in terms of $\rho_r\left(n^r\right)$ (Theorem D).

Theorem B. For every $n \geq 1$, $\rho_r\left(n^r\right) = \sum_{d^r \| n^r} \varphi_r\left(d^r\right)$.

The function $\rho_r\left(n^r\right)$ is multiplicative and $\rho_r\left(p^{\alpha r}\right) = p^{\alpha r} - p^{(\alpha-1)r} + 1$, for any prime p and integer $\alpha \geq 1$.

Proof: We give two proofs for the first part.

First Proof: Let $a \in \mathrm{Reg}_r(n)$.

If $p_i \nmid a$ for $1 \leq i \leq t$ then $(a, n) = 1$ so that $\left(a, n^r\right)_r = \left(a^r, n^r\right) = 1$ and the number of such a's is $\varphi_r\left(n^r\right)$.

Suppose ${p_i}^{\alpha_i r} \mid a^r$ for exactly one i so that $\left(a, p_j\right) = 1$ for $j \neq i$ and $a = b.{p_i}^{\alpha_i r}$ where $1 \leq b \leq \dfrac{n^r}{{p_i}^{\alpha_i r}}$ and $\left(b, \dfrac{n^r}{{p_i}^{\alpha_i r}}\right) = 1$; the number of such a's is $\varphi_r\left(\dfrac{n^r}{{p_i}^{\alpha_i r}}\right)$.

Suppose ${p_i}^{\alpha_i r} \mid a^r$ and ${p_j}^{\alpha_j r} \mid a^r$ for $1 \leq i < j \leq t$; and for $k \notin \{i, j\}$ $\left(p_k, a\right) = 1$. Then $a = C.{p_i}^{\alpha_i r}.{p_j}^{\alpha_j r}$, where $1 \leq C \leq \dfrac{n^r}{{p_i}^{\alpha_i r}{p_j}^{\alpha_j r}}$ and $\left(C, \dfrac{n^r}{{p_i}^{\alpha_i r}{p_j}^{\alpha_j r}}\right) = 1$; and the number of such integers is $\varphi_r\left(\dfrac{n^r}{{p_i}^{\alpha_i r}.{p_j}^{\alpha_j r}}\right)$; and so on. Thus

$$\rho_r\left(n^r\right) = \varphi_r\left(n^r\right) + \sum_{1 \leq i \leq t} \varphi_r\left(\frac{n^r}{{p_i}^{\alpha_i r}}\right) + \sum_{1 \leq i < j \leq t} \varphi_r\left(\frac{n^r}{{p_i}^{\alpha_i r}{p_j}^{\alpha_j r}}\right) + \ldots + \varphi_r\left(\frac{n^r}{{p_i}^{\alpha_i r}{p_2}^{\alpha_2 r}\cdots{p_t}^{\alpha_t r}}\right)$$

$$= y + \sum_{1 \leq i \leq t} \frac{y}{y_i} + \sum_{1 \leq i < j \leq t} \frac{y}{y_i y_j} + \ldots + \frac{y}{y_1 y_2 \cdots y_t}$$

.

where $y_i = \varphi_r\left({p_i}^{\alpha_i r}\right)$ and $y = y_1 y_2 \ldots y_t$.

Therefore

$$\rho_r\left(n^r\right) = \left(y_1 + 1\right)\left(y_2 + 1\right)\ldots\left(y_t + 1\right)$$

$$= \left(\varphi_r\left({p_1}^{\alpha_1 r}\right) + 1\right)\left(\varphi_r\left({p_2}^{\alpha_2 r}\right) + 1\right)\ldots\left(\varphi_r\left({p_t}^{\alpha_t r}\right) + 1\right)$$

$$= \sum_{d^r \| n^r} \varphi_r\left(\frac{n^r}{d^r}\right) = \sum_{d^r \| n^r} \varphi_r\left(d^r\right).$$

Second Proof: Group the integers $a \in C_{n,r}$ according to the value $\left(a, n^r\right)_r = d^r$.

Note that $\left(a,\ n^r\right)_r = d^r \Leftrightarrow a = j.d^r$ where $1 \le j \le \dfrac{n^r}{d^r}$ and $\left(j,\ \dfrac{n^r}{d^r}\right)_r = 1$. Hence the number of a's in $C_{n,\,r}$ with $\left(a,\ n^r\right)_r = d^r$ is $\varphi_r\left(\dfrac{n^r}{d^r}\right)$. Thus $\rho_r\left(n^r\right) = \sum\limits_{d^r \| n^r} \varphi_r\left(\dfrac{n^r}{d^r}\right) = \sum\limits_{d^r \| n^r} \varphi_r\left(d^r\right)$.

Now
$$\rho_r\left(n^r\right) = \sum_{D \| n^r} \varphi_r(D).\chi_r(D), \tag{3}$$

where $\chi_r(m) = 1$ or 0 according as m is the r^{th} power of an integer or not.

Therefore $\rho_r\left(n^r\right) = \left(\varphi_r \chi_r \circ I\right)\left(n^r\right)$, where $I(n) \equiv 1$ for all n and $\circ$ is the unitary convolution of arithmetic functions discussed by Eckford Cohen [2]. Since unitary convolution preserves multiplicativity, we get $\rho_r\left(n^r\right)$ is multiplicative, because φ_r, χ_r and I are all multiplicative.

Also $\rho_r\left(p^{\alpha r}\right) = \varphi_r\left(p^{\alpha r}\right) + 1 = p^{\alpha r} - p^{(\alpha-1)r} + 1$, completing the proof of Theorem B.

Theorem C. $\sum\limits_{\substack{a \in C_{n,\,r} \\ \left(a,\ n^r\right)_r = 1}} a = \dfrac{1}{2} n^r.\varphi_r\left(n^r\right)$ for $n > 1$.

Proof: First observe that for positive integers a and b, $\left(a,\ b\right)_r = 1$ if and only if $\left(a,\ b\right)$ is r-free (Recall that an integer not divisible by the r^{th} power of any prime is said to be *r-free*). Let $q_r(m) = 1$ or 0 according as m is r-free or not. Then it is well-known ([1], problem 6, *p*.47) that

$$q_r(m) = \sum_{t^r \mid m} \mu(t), \tag{4}$$

where μ is the Mobius function.

Now, by (4) and (1), we get

$$\sum_{\substack{a \in C_{n,\,r} \\ \left(a,\ n^r\right)_r = 1}} a = \sum_{1 \le a \le n^r} a.q_r\left(\left(a,\ n^r\right)\right)$$

$$= \sum_{1 \le a \le n^r} a \left\{ \sum_{\substack{t^r s = a \\ t^r \mid n^r}} \mu(t) \right\}$$

$$= \sum_{\substack{t^r s \le n^r \\ t^r \mid n^r}} t^r s\mu(t)$$

$$= \sum_{t^r \mid n^r} \mu(t) t^r \left\{ \sum_{s \le \frac{n^r}{t^r}} s \right\}$$

$$= \sum_{t^r \mid n^r} \mu(t) t^r . \frac{1}{2} . \frac{n^r}{t^r} \left(\frac{n^r}{t^r} + 1 \right)$$

$$= \frac{n^r}{2} \sum_{t^r \mid n^r} \mu(t) \frac{n^r}{t^r} + \frac{n^r}{2} \sum_{t^r \mid n^r} \mu(t)$$

$$= \frac{n^r}{2} . \sum_{t_* \mid n^r} \mu(t_*) \frac{n^r}{t_*} + \frac{n^r}{2} \sum_{t^r \mid n^r} \mu(t)$$

$$= \frac{n^r}{2} . \varphi_r\left(n^r\right),$$

since $\sum_{t^r \mid n^r} \mu(t) = 0$ for $n > 1$.

Remark 1. The case $r = 1$ of Theorem C is the well-known formula:

$$\sum_{\substack{1 \le a \le n \\ (a,\, n)=1}} a = \frac{n\varphi(n)}{2} \text{ for } n > 1. \text{ (For example see [1], Problem 16, } p.48)$$

Theorem D. If $S_r(n) := \sum_{a \in \mathrm{Reg}_{r(n)}} a$ then $S_r(n) = \frac{1}{2}\left[\rho_r\left(n^r\right) + 1\right]$ for $n \ge 1$.

Proof: We have, by Theorem A, that $a \in \mathrm{Reg}_r(n) \Leftrightarrow \left(a,\, n^r\right)_r = d^r \,\|\, n^r$.

Therefore

$$S_r(n) = \sum_{\substack{a \in C_{r,\,n} \\ \left(a,\, n^r\right)_r \,\|\, n^r}} a = \sum_{d^r \,\|\, n^r} \sum_{\substack{\left(a,\, n^r\right)_r = d^r \\ a \in C_{r,\,n}}} a$$

$$= \sum_{d^r \,\|\, n^r} d^r \sum_{\substack{j \in C_{\frac{n^r}{d^r},\, r} \\ \left(j, \frac{n^r}{d^r}\right)_r = 1}} j,$$

since $\left(a,\, n^r\right)_r = d^r \Leftrightarrow a = j.d^r$ where $1 \le j \le \frac{n^r}{d^r}$ and $\left(j,\, \frac{n^r}{d^r}\right)_r = 1$.

Now, in view of Theorem C and Theorem B, for $n \ge 1$ we have

$$S_r(n) = n^r + \sum_{\substack{d^r \| n^r \\ d^r < n^r}} d^r . \frac{1}{2} . \frac{n^r}{d^r} . \varphi^r \left(\frac{n^r}{d^r} \right)$$

$$= n^r + \frac{n^r}{2} \sum_{\substack{d^r \| n^r \\ d^r < n^r}} \varphi^r \left(\frac{n^r}{d^r} \right)$$

$$= n^r + \frac{n^r}{2} . \left[\rho_r \left(n^r \right) - 1 \right]$$

$$= \frac{n^r}{2} \left[\rho_r \left(n^r \right) + 1 \right],$$

proving the theorem.

REFERENCES

[1] T. M. Apostol., Springer International Student Edition, Naroso Publishing House, New Delhi, 1998.

[2] C. Eckford., Math. Zeitschr., 1960, 74, 66-80.

[3] V. L. Klee., Amer. Math., 1948, 55, 358-359.

[4] T. Laszlo., Annals Univ. Sci. Budapest., Sect. Comp., 2008, 29, 263-275.

[5] P. J. McCarthy., Springer-Verlag, New York, 1985.

[6] J. Morgado., Gazeta de Mathematical (Lisboa)., 1972, 33(125-125), 1-5.

[7] J. A. Morgado., Portugal. Math., 1974, 33, 185-191.

Effect of Heating Rate on Paper Waste Residues of Municipal Solid Waste Composition

Samit Kumar Singh[1] and Sadanand A Namjoshi[1*]

Madhav University, Pindwara, Rajasthan, India

Email: [1]samit.meet@gmail.com and [1*]namjoshisadanand@yahoo.co.in

Abstract

The growth of municipal solid waste (MSW) and handling of MSW are two parallel activities observed now-a-days. The conversion of MSW into energy either incineration or gasification or pyrolysis are the three thermochemical conversion options which are available. In case of any thermochemical conversion process, reactor design plays a vital role. The reactor design is based on kinetic studies and these studies are associated with heating rate. The objective of present work focuses on the effect of heating rate at 10 and 20 ^{0}C/min on the residues of newspaper, printing paper, glossy paper and cardboard waste existing in MSW composition obtained after thermal decomposition in case of Thermogravimetric Analysis (TGA).

***Keywords**:* Municipal Solid Waste, Kinetic Studies, Heating Rate, Thermogravimetric

1. Introduction

'War on waste' is common phrase nowadays because of waste generation increases at faster rate. Fulfilment of energy demand and simultaneously to find proper solution of MSW from economical, social and environmental point of view waste-to-energy is the best option; also the energy crisis is the new challenge in the front of world to push the economy in the progressive direction and simultaneous global warming and efficient use of energy are also challenging tasks.

With high GDP rises in all over the world the MSW generation also increases and the per capita MSW generation in developed countries varies from 0.5 to 2.0 kg while for under developed countries these figures lies on average in the range of 0.4 to 0.8 kg by considering towns to metro cities. The handling of MSW is social, economical and environmental problem and to convert MSW into useful energy is really the challenging task and the energy extraction from MSW is hard assignment because the MSW is mixture of various MSW constituents, and it consists of bio degradable and non-combustibles. The 1 % increment MSW creates so many issues in the today's modern world.

Energy demand is increasing worldwide and efficient use of energy is also equally important to justify any thermal conversion system design efficiently is one of the important parameters but the thermal conversion system where heat exchanges the design is more critical. The pyrolysis is one of the good options of thermal degradation out of available methods of waste handling and disposal in the deficiency of oxygen. The outcome of pyrolysis is synergy gas, char and pyrolytic oil; it means three types of fuels are available. The significance of pyrolysis is also due to the decomposition of polymers into fuels which are not easily degradable and contaminant atmosphere heavily when throw as a waste at open places. The products of pyrolysis process having good energy content for alternative energy source. S L Kuen et al. [1] gained results kinetics results of Residual Derived Fuel (RDF) and focused on the constituents on its pyrolysis process. Reaction kinetics of RDF was carried out using (TGA). Ch. Pasel et al. [2] concentrated on pyrolysis of shredder waste for purpose of chemical recycling of plastic wastes and satisfy industrial requirements. The consideration for reactor design and process development is inclined by heating rate, residence time, temperature are parameters in scale-up considerations. L. Sorum et al. [3] studied in detailed evidence on the pyrolysis and chemical reaction kinetics of most useful constituents of MSW. TGA comprising estimation of kinetic parameters is performed at a heating rate of 10^0C/min in inert atmosphere. The lignocellulosic of MSW was considered three independent parallel reactions describing degrading of hemicellulose, cellulose and lignin. J.M. Encinar et al. [4] estimated the kinetics of polymers has been carried out in presence of nitrogen atmospheres with heating rates 5–30 K min^{-1}. N. Miskolczi et al. [5] studied pyrolysis of plastics obtained from agricultural and packaging sectors in a small reactor in presence of nitrogen atmosphere up to 520 ^{0}C with employment of ZSM-5 catalyst. The design of pyrolyser is based on kinetics studies which correlate the mass loss with respect to time and temperature (Heating); and which represents space or in other word volume requirement of fuel (Municipal Solid Waste) as well as pyrolytic products with respect to time temperature. The quantities of yield products also depend on available space otherwise temperature gradient will exist and conduction losses increases. Ayhan Demirbas [6] studied non-catalytic pyrolysis of different polymer waste to determine kinetic parameters. The pyrolysis of plastic wastes covers a whole spectrum of hydrocarbons. J P Lin et al. [7] focused on kinetics of a rubber mixture by a dynamic TGA reaction system with heating rates of 3, 5 and 7 K/min, in a nitrogen atmosphere, over the temperature limit of 400 to 950 K. I W Park et al. [8] suggested a new method for estimation of kinetics parameters for polymers at heating rates between 10 and 50^0C/min. David et. al [9] described pyrolysis of cardboard on the basis of a series of TGA

experiments. The research work includes the estimation of kinetics parameters for cardboard. This research work focuses on pyrolysis phenomenon for cardboard with series of TGA experiments and observations are compared the results of graphical method with numerical results too. Miranda et al. [10] studied thermal degradation behaviour of textile waste by TGA at various heating rates with the help of semi-batch pyrolysis. The DTG curves shows three peaks; the first peak was of hemicellouse and second one might be of cellouse while third might be of synthetic polymer.

2. Experimentation

The elemental analysis of residues of all lignocellulosic waste materials (newspaper, cardboard, printing paper, glossy paper) are carried out with the help scanning electron microscope (JEOL 5610LV) (SEM) using Energy Dispersive Spectroscopy (EDS). EDS is an analytical technique in which x-rays that are emitted from the sample when attacked by the electron beam to recognize the elemental composition of the specimen. The elemental analysis of residue is carried out with the help of scanning electron microscope at two heating rates of 10 and 20^0C/min have been carried out. This elemental analysis clearly shows the effect of heating rates on presence of elements in the residue.

3. Results and Discussion

Figures 1 to 16 represents the photographs and elemental spectrums of all paper constituent residues at heating rate of 10 ^{0}C/min and 20 ^{0}C/min respectively. The importance of this study is to explore the effect of heating rates on end products and elements presence in the residues of all papers constituents and also its impact on environment [6]. The elemental results of all paper residues are represented below out of total 16 EDS results.

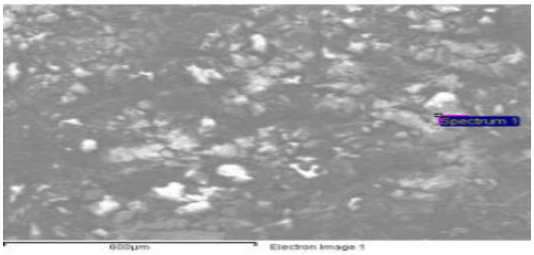

Fig. 1. Glossy Paper Residues (10 ^{0}C/min)

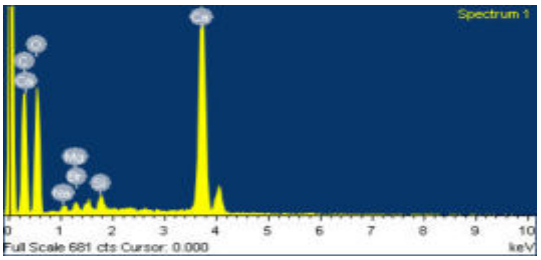

Fig. 2. Elemental Spectrum

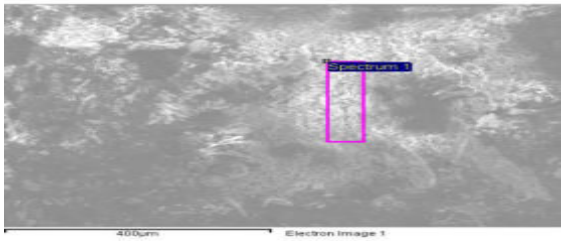

Fig. 3. Glossy Paper Residues (20 ^{0}C/min)

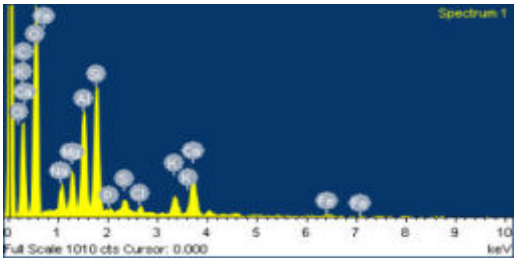

Fig. 4. Elemental Spectrum

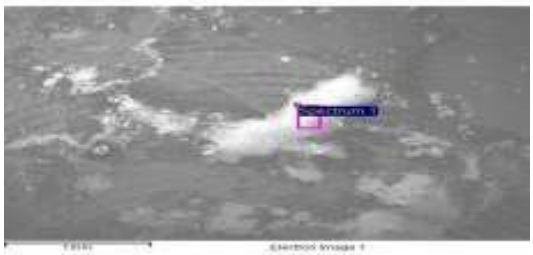

Fig. 5. Printing Paper Residues (10 ^{0}C/min)

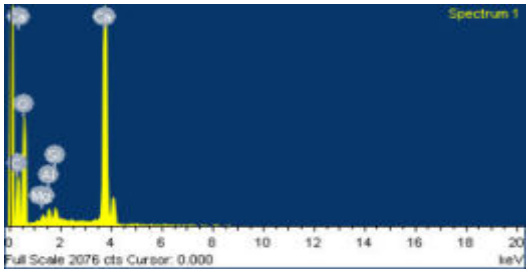

Fig. 6. Elemental Spectrum

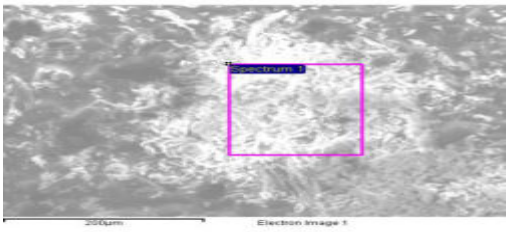

Fig. 7. Printing Paper Residues (20 ^{0}C/min)

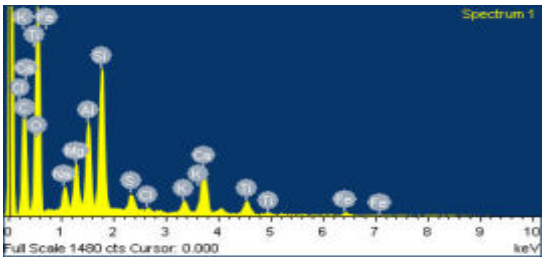

Fig. 8. Elemental Spectrum

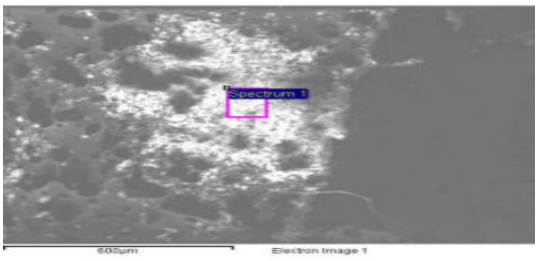

Fig. 9. Newspaper Residues (10 ^{0}C/min)

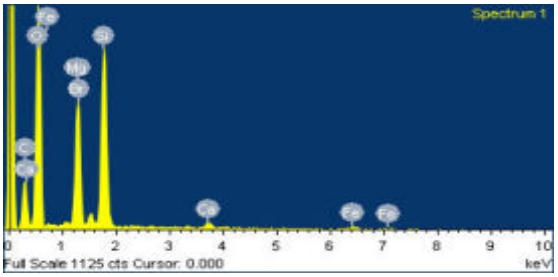

Fig. 10. Elemental Spectrum

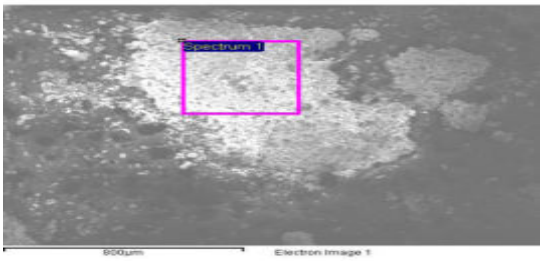

Fig. 11. Newspaper Residues (20 ^{0}C/min)

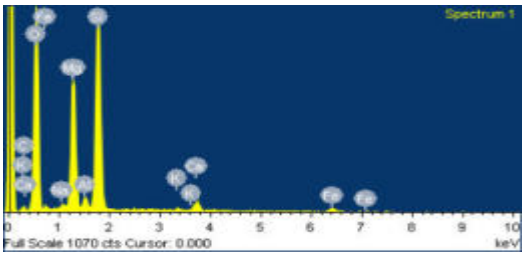

Fig. 12. Elemental Spectrum

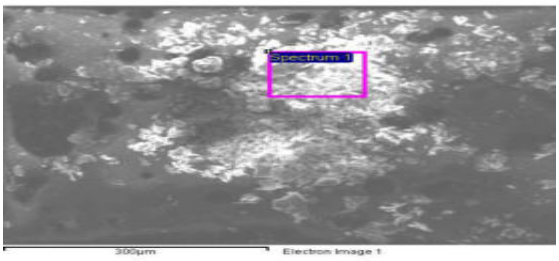

Fig. 13. Cardboard Residues (10 ^{0}C/min)

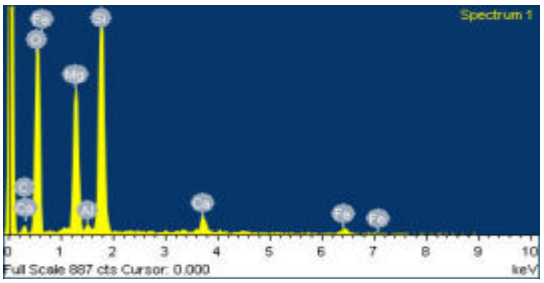

Fig. 14. Elemental Spectrum

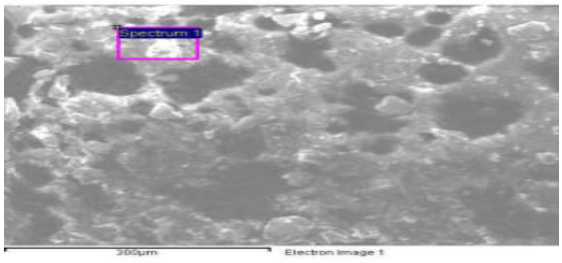

Fig. 15. Cardboard Residues (20 ^{0}C/min)

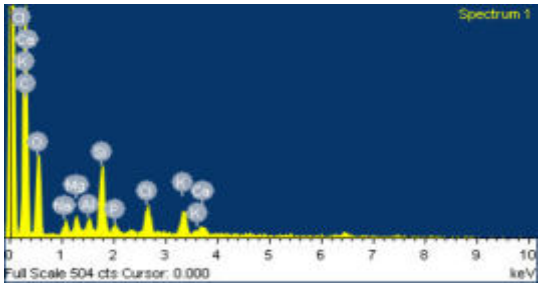

Fig. 16. Elemental Spectrum

Table 1 displays the effect of heating rate on different elements presents in glossy paper, printing paper, newspaper and cardboard residues.

Glossy Paper														
Heating Rate	Element	C	O	Na	Mg	Al	Si	P	S	K	Br	Ca	Cl	Total
10^{0}C/min	Weight%	24.78	45.28	0.65	0.62	0.0	0.94	0.0	0.0	0.0	1.16	26.38	0.0	100
20^{0}C/min	Weight%	12.5	49.72	0.0	0.54	0.93	1.00	0.0	0.0	0.0	0.0	35.31	0.0	100
Printing Paper														
Heating Rate	Element	C	O	Na	Mg	Al	Si	P	S	Br	Fe	Ca	Cl	Total
10^{0}C/min	Weight%	22.8	50.1	0.0	9.28	0.0	14.21	0.0	0.0	1.51	1.18	0.84	0.0	100
20^{0}C/min	Weight%	44.68	52.69	0.0	1.19	0.0	1.44	0.0	0.0	0.0	0.0	0.0	0.0	100
Newspaper														
Heating Rate	Element	C	O	Na	Mg	Al	Si	P	S	Cl	K	Ca	Fe	Ti	Total
10^{0}C/min	Weight%	29.25	45.33	2.07	2.19	5.38	7.55	0.33	0.77	0.67	1.88	3.91	0.66	0.0	100
20^{0}C/min	Weight%	30.86	43.80	1.63	2.42	4.12	7.44	0.0	1.01	0.28	1.16	4.31	0.95	2.03	100
Cardboard														

Heating Rate	Element	C	O	Mg	Al	Si	Ca	Fe	Na	P	Cl	K	-	Total
10^0C/min	Weight%	6.85	50.36	13.79	0.52	22.84	2.82	2.82	0.0	0.0	0.0	0.0	0.0	100
20^0C/min	Weight%	59.59	27.58	0.84	0.59	3.84	0.90	0.0	0.92	0.63	2.49	2.62	0.0	100

Table 1. Elements Present in Different Residues

From Table 1, it is observed that as heating rate increases, the carbon percentage rises in all papers except glossy paper where presence of chemical composition resist heat penetration. As a result, more ash remains in case of glossy paper (Fig 1 and Fig 3). The second interesting observation which can be observed in case of all papers some common elements like Ca, Si and Mg have been found which directs that when all papers gets converted into fuel using any appropriate technology possible residues with their quantities can be predicted in advance.

4. Conclusion

The elemental analysis carried out with SEM show that as rises in the heating rate the percentage of elements present in the residue changes. The significance of this analysis is to know the possible elements existing in the residue and how they will affect the environment from pollution point of view in later stage.

References

1. K S Lin *et al.,* Fuel Processing Technology, 1999, 60, 103–110.
2. Ch Pasel *et al.,* Fuel Processing Technology, 2003, 80, 47– 67.
3. L Sorum, *et al*., Fuel, 2001, 80, 1217-1227.
4. J M Encinar *et al.,* Fuel Processing Technology, 2008, 89, 678 – 686.
5. N Miskolczi *et al.,* Fuel Processing Technology, 2009, 90, 1032-1040.
6. A Demirbas, Journal of Analytical and Applied Pyrolysis, 2004, 72, 97–102.
7. J P Lin *et al.,* Journal of Hazardous Materials, 1998, 58, 227–236.
8. I W Park *et al.,* Polymer Degradation and Stability, 2000, 67, 535-540.
9. C David *et al,* Journal of Analytical and Applied Pyrolysis, 2003, 67, 307- 323.
10. R Miranda *et al*., Journal of Analytical and Applied Pyrolysis, 2007, 80, 489-495.

Natural Background Gamma Radiation Levels in few dewllings of Rajanna Sircilla district, Telangana State, India

G. Srinivas Reddy[2], K. Vinay Kumar Reddy[3], M. Sreenath Reddy[1] B. Linga Reddy[3], B. Sreenivasa Reddy[3]

[1]Department of Physics, Osmania University, Hyderabad-500007, India
[2]Department of Physics and Chemistry, Mahatma Gandhi Institute of Technology, Hyderabad -500 075, India
[3]Deprtment of Physics, Chaitanya Bharathi Institute of Technology, Hyderabad-500075, India

Abstract

Natural background gamma radiation has been of radiological significance in the environs of locations with various types of geological rock formation and high granitic concentration. The locations of study area in Rajanna Sircilla district of Telangana have been partially spread in the Karimnagar Granulitic Terrain (KGT) which is identified as a radiological significat location with the the occurrence of high grade uraniferous rocks as established in the studies by Atomic Minerals Directorate for Exploration and Research, Hyderabad (AMDER). The interest in the study is to varify the influency of geological formation on the variation of gamma radiation. An attempt has been to estimate gamma radition levels in about 13 dwellings over period of one year on quaterly basis using a portable μR-survey. The annual average of estimated natural gamma ration in the district was to be 2280±297 $\mu Gy^{-}1$. The ratio between indoor tooutdoor gamma radition levels is observed to vary between 1.01 and 1.22 against world average of 1.2. A deatiled analysis of the radiation levels with building characteristics and seasonal variation will be discussed.

Keywords: Natural background gamma radiationlevels, Karimnagar Granulite terrain, μR-survey meter

1. Inroduction

A continuous exposure to ionizing background gamma radiation is of most significant environmental research activity. In the recent past many attempts have been made to assess radiation levels. The radiation levels of various magnitudes have been araising from natural sources. Natural background gamma radiation can be cauesd in two ways extra terristrial and terristrial. The radiation originating from the cosmic rays from the sun and radionuclides presents in earth's crust and building materials [1,2]. The phinominon of decay series is the source for radiation. Potasium element can also be a significant source for gamma radiation. The radiation at different levels can due to the radionuclides available at different concentration which varies from place to place depending on the geological features [3, 4]. There are two possibilities of exposure of human being to ionizing radiation: internal and external. The external exposure can be one in which the naturak background gamma ration which directly incident on the human body leads to the cause of external radiation, internalexposure cab due to inhiation of air into the the human body and entry radon and thoron through the food taken by the human being. The ionizing radiation causes lungs cancer with interaction of biological tissue. The estimation of gamma radition in the indoor atmosphere is of most significant activity as the human being gets exposed continuously to the radiation emitted from the radiotrace elements present in the building materials. The

level of exposure is depedent factor of concentration or content of radioelements. The variation of concentration of radiotrace elments is due to the the various factors such as lithological and geological features, types building materials and local geological features of rock formation and soil characteristics. Building characteristics can also be a significant factor as the exposure of levels of radiation can be effectively influenced [5, 6].

The data acquired in the measurements in the study concludes facts of interpretation when the data have been processed. The information in the invistigation through the interpretation of various facts related to the radiaoactive phinominon with the behaviour of the data in the process of analysis can be retrieved. The statistical methods generally are potential to derive the the information burried in the data set acquired in the experimental measurements.

2. Study location

The estimation of natural background gamma radiation ia attempted in few dwellings of Rajanna Sircilla districts,one among the northen districts of Telanagana state. In view of geological aspects some of the locations are partially under geological zone of Karimnagar Granuilite Terrain (KGT). The earlier studies conducted by Atomic Mineralisation and Exploration direactorate in the locations nearby Sircilla town have established the some rocks formation leads to radioactive anomaly which may cause an effective radioactivity in the environment [4].

3. Methods of measurements

The measurements of radiation is carried out in almost 10 to 13 dwellings by Microsurvey meter on quaterly basis covering all the seasons anf different types of dwellings. At each location of measurements nearly 12 to 15 readings have been acquired for 30 to 40 minutes at each visit in the season. A detailed methodology is discussed in the earleir invistigations [2].

4. Results and discussion

The natural background gamma radiation at diiferent locations have been measured and statistical techniques of gauusian or normal distribution is applied to the data. The indoor and outdoor natural background gamma radiation is found to be respectively 2336 ±844 $\mu Gy^{-1}$and 2178 ±614 μGy^{-1}.

The table.1 gives the summery of the measured data corresponding to floor and roof materials in the dwellings under the study area. It is observed in the table that the values of gamma radiation recorded at granite stones and cement floor dwellings represents relatively higher values which attributes due to the prsence of considerable concentration radionuclides in granite stones and flyash content in cement.

Table 1. Natural background gamma radiation levels in building materials

	Mean (μGy^{-1})	SD*
Roof		
Tiled	2400	163
Asbestos	2390	143
Stones	2377	112
RCC	2505	134
Floor		

Cement	2485	203
Limestone	2105	116
Granite stones	2741	194

SD* Standard deviation

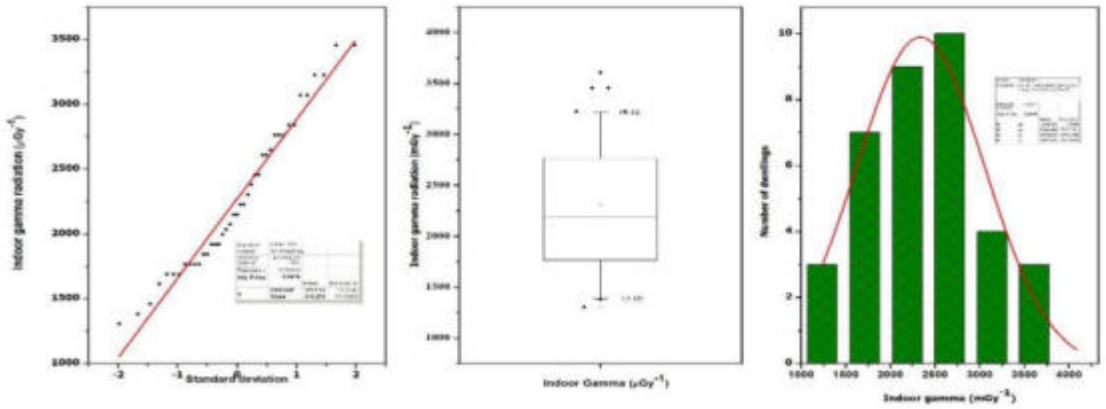

Figure 1. Indoor natural background gamma radiation (μGy^{-1})

The indoor gamma gamma radition levels were depicted in **figure 1**. The normal quantile plot, box plot which minimum, maximum, mean and outliers obtained in the entire measurements of indoor environments of dwellinghs of study area. In the quantile normal conforms that the majority of data points in the measurements have been normally distributed across the mean but the outliers in quantile plot which represnts the ends points in histogram convey statical anamoly which interpret the significant influence of environmental facts at those locations which enable the behaviour of the data points to be deviated from normal distribution.

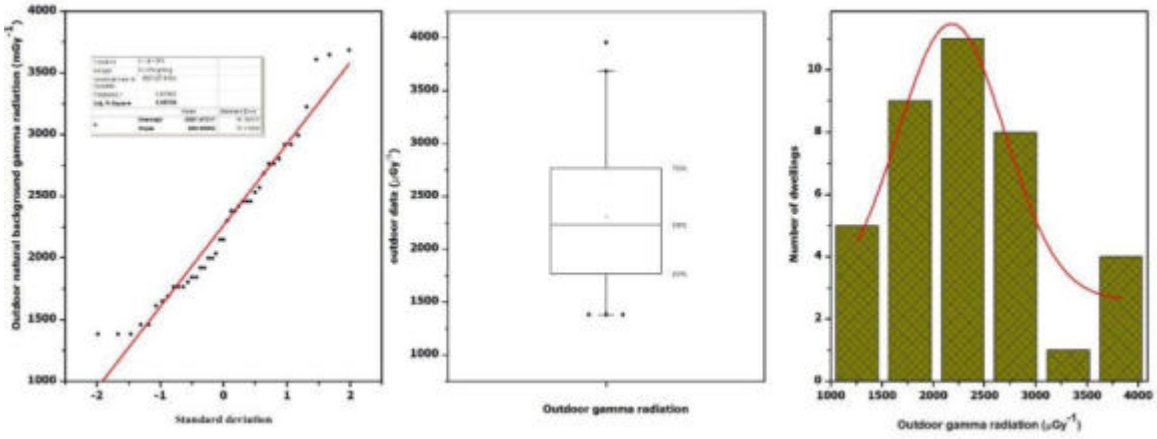

Figure 2. Outdoor natural background gamma radiation (μGy^{-1})

The figure 2 represents the data obtained in outdoor measurements and it is noted that the three points exhibit abnormal stastical deviation which can be the evidence that the influencing factors in outdoor environment effectively alter the normal distribution of those particular locations.

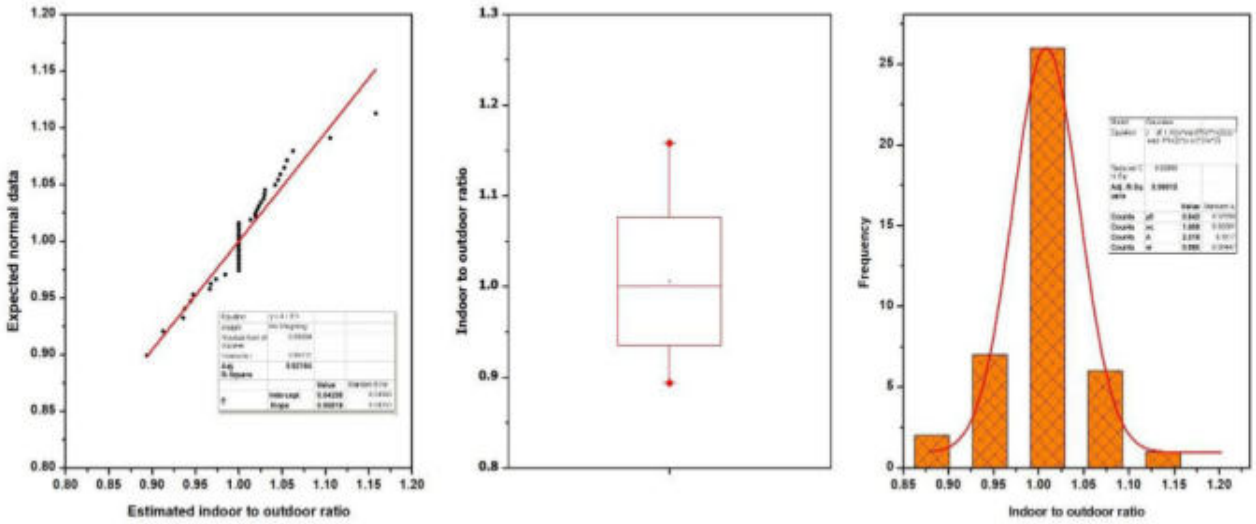

Figure 3. Estimated and expected normal data of indoor to outdoor ratio

The data of indoor to outdoor ratio of expected in the normal distribution and estimated in the investigation has been shown in the **figure 3**. The indoor to outdoor ratio is found to vary from 1.01 to 1.22 against world average of 1.2. It is observed from figure 3 that indoor to outdoor ratio is appximately 1.02 and obeys the normal distribution with some statistical deviation corresponding to indoor and outdoor data influenced by the environmental influencing factors. There seems to be no significant changes in seasonal variation of gamma radiation levels in the study [2].

References

1. UNSCEAR, 2000. United Nations Scientific Committee on the Effects of Atomic Radiation, Ionizing Radiation: Source and Effects of Ionizing Radiation. United Nations, New York.
2. K. Vinay kumar Reddy *et al.,* Indoor built Env, 2020, 29(7).
3. Thuruganur *et al.,* Rad Pro,Dos., 2020, 188(4).
4. S Anjan Som *et al.,* J. Geol. Soc. India., 2010, 76, 247-250.
5. M Sreenath Reddy *et al.,*, Andhra Pradesh, India, 2010, 48(11):778-781
6. B Sreenivasa Reddy *et al.,* Radiat. Prot. Environ., 2015, 28, 301-303.

The Force Constants Tetrahedral Site and Octahedral Site of Nd^{3+} Ions Substituted Ni-Zn Nano Ferrites from Infrared Spectroscopic Analysis

G.V.Nagesh, K.V.Ramesh
1. Department of Physics, LENDI Institute of Engineering and Technology, Vizianagram
2. GITAM Institute of Science, GITAM University, Vishakhapatnam
Email: vnganti83@gmail.com

Abstract:
The IR spectroscopy of Nd^{3+} doped in Nanocrystalline Ni-Zn ferrites ($Ni_{0.5}Zn_{0.5}$ $Nd_xFe_{2-x}O_4$) with 'x' is ranging (x=00, 0.05 and 0.10,) have been synthesized by the nitrate citrate gel auto combustion method. for as prepared samples recorded in the range of frequency 300-1000 cm^{-1} All the sample illustrate the existence of the two absorption bands ν_1&ν_2, where ν_1 is the high frequency band from 559cm^{-1} to 568 cm^{-1} is assigned to intensity vibration of A site coordination where ν_2 is the lower frequency band from 374 cm^{-1} to 429 cm^{-1} is assigned to intensity vibration. The structural studies were reported from FTIR. On doping of Nd^{3+}ion in Ni-Zn ferrites the Infrared Spectroscopic Analysis the shift of ν_2 towards ν_1 which indicates that the occupancy of Nd^{3+} on B site. The force constants on both sites can be determining the strength of bonding at lower and higher vibration frequencies the method proposed by Waldron for both tetrahedral (K_A) and octahedral (K_B) sites and are considered by means of this equivalence.

Keywords: Ni-Zn-Nd ferrite, Citrate gel auto-combustion process, IR spectroscopy, force constants tetrahedral site (K_A) and force constants octahedral site (K_B).

1 Introduction:

The applications of electronic devices were enhanced due to smart technology. The spinel ferrite plays an important role in various applications in electromagnetism over the years. As compared with bulk system nanoparticles show remarkable structural and magnetic properties. The Ni-Zn ferrites are investigated by reason of abnormal properties of their like prominent initial permeability, high magnetic saturation, elevated electrical resistivity, Swirl current losses and etc.

The scientific and researchers community was fascinated in the direction of the study of ferrites because of the novel properties and technology applications in particular when the size of the particle approaches to nano scale. Ferrites are made of ferric oxide Fe_2O_3, commonly known as Magnetite; combine with one or other divalent metal oxides. The general formula of magnetite written as [$Fe^{2+}O^{2-}.Fe_2^{3+}$, O_3^{2-}].generally the mixed oxides of ferrites are in the form of [M^{2+} $Fe_2^{3+}O_4$] or $M^{2+}.O.Fe_2^{3+}O_3$. Where M^{2+} indicates suitable metal divalent ions, as Ni, Zn, Co, Mg, Cu or Cd. By replacing M^{2+} divalent metal ions a mixed ferrites are formed [1,2]. Ferrites have outstanding features in electrical and magnetic fields. At high frequencies there will be low eddy loss in current noted with iron due to very high resistivity in ferrites. No other magnetic materials are replaceable with ferrites due to such terrific combinations of magnetic conductor and electrical insulator. Day by day they require for soft magnetic materials enhance along with

advances technological in different areas [3] . The properties of ferrite material are entirely dependent on several routes of preparation [4] and sintering conditions [5]. Several researchers are enhancing to synthesize of Ferrites materials with different methods such as ,double Sintering [6,7] , Solid state reaction [8] ,Co-precipitation [9,10] , Classical method [11] , Ceramic method [12] , Refluxing method [13] , Egg-White precursor [14] , Hydrothermal process [15,16] , Emulsion method [17] , Reveres Micelle technique [18] , Sol-gel process [19,20] , Citrate gel auto-combustion process [21,22]. The conventional ceramic process involving high temperature suffers many defects and this method takes a long time to synthesize nano powder. For preparation of nano ferrite the sol-gel technique is the best method [23]. This method is engaged to get hold of improved powder characterization. Several reports are available on the structural and physical properties of nano crystalline. Over all the wet chemical methods broadly used in synthesis of ferrites, the citrate gel auto combustion method is getting good consideration since single phase ferrite establishment, homogenous ferrite powders with a very thin grain growth and uniform grain size distribution.

2 Experimental details:

the structural properties in substitution of rare earth ion (Neodymium) in Nickel Zinc nano ferrite with the change in chemical composition. A Series of samples having chemical formula $Ni_{0.5}Zn_{0.5}$ $Nd_xFe_{2-x}O_4$ with(x=0.00, 0.05and0.1) were prepared through nitrate citrate auto combustion technique. Using AR grade iron nitrate, Neodymium nitrate, Nickel nitrate and Zinc nitrate are starting materials. The elements were weighted in a design stoichiometric process and the composition was dissolved in a minimum amount of distilled water according to the molecular waves, citric acid was added into the solution with the ratio 1:1. Now keep stirring all the nitrates for an hour separately on a magnetic stirrer. Then add citric acid to the mixture of nitrate solution under vigorous stirring. And now these aqueous (salt) solutions are mixed and made homogenous, while increasing the temperature gradually. Slowly these solutions are heated and all the water molecules get evaporated from the mixture and thus the gel substance is formed and it thickens continuously and it develops a dense layer. Then gel gets ignited and burns with glowing flints and gives rise to a dried brown color dry massy residue was formed [24]. From the examination of Infrared Spectroscopic the shifts of v_2 towards v_1 which signify the occupancy of Nd^{3+} on site B.

3. Result and Discussion

Dielectric constant as a function of frequency:

The IR spectroscopy of $Ni_{0.5}Zn_{0.5}$ $Nd_xFe_{2-x}O_4$ with(x=0.00, 0.05 & 0.1) for as prepared samples recorded in the range of frequency 300-1000 cm^{-1} were observed in Figure 1. All the sample illustrate the existence of the two absorption bands v_1&v_2, where v_1 is the high frequency band from 559cm^{-1} to 568 cm^{-1} is assigned to intensity vibration of A site coordination where v_2 is the lower frequency band from 374 cm^{-1} to 429 cm^{-1} is assigned to intensity vibration of octahedral [25]. The force constant, which is the succeeding derivative of potential energy has been predictable by the method proposed by Waldron for both tetrahedral (K_A) and octahedral (K_B) sites and are considered by means of this equivalence,

$$K_A = 7.62 \times M_1 \times v_1^2 \times 10^{-3} dynes \cdot cm^{-1}$$

$$K_B = 10.62 \times \frac{M_2}{2} \times v_2^2 \times 10^{-3} dynes \cdot cm^{-1}$$

On substation of Nd^{3+} ions the band ($Fe^{+3} - O^{-2}$) shift towards higher frequency side has been observed, as Nd^{3+} concentrate increases replacement of Fe^{3+} ions and consequently the bond length of B-site increases and lattice distortion takes place. The variation of intensities and band intensities are dependent on the replacement of the ions.

The enlarged in peaks of the bands which shift v_2 towards v_1 indicates that the occupancy of Nd^{3+} on site B [26]. The Table 1. shows the variant of force constant on replacement of content of Nd^{3+} ions. This confirms that as neodymium content increases in nano ferrites the octahedral force constant enhances. This type of character shows the strengthening of the anion and inter-ionic bonding can be bounced at enormous internuclear separation [27].

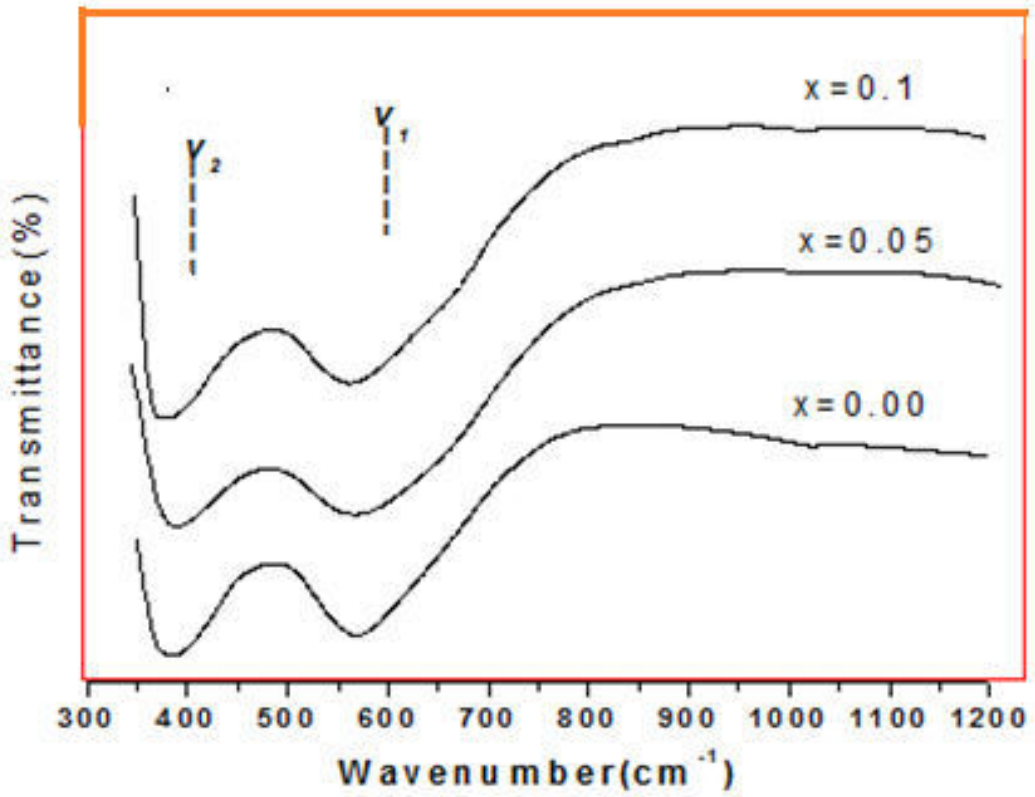

Fig.1.IR spectroscopy of $Ni_{0.5}Zn_{0.5}Nd_xFe_{2-x}O_4$ with(x=0.00, 0.05 & 0.1) for as prepared samples

Table 1. IR Parameters of $Ni_{0.5}Zn_{0.5}Nd_xFe_{2-x}O_4$ with(x=0.00, 0.05 & 0.1) for as prepared samples

Composition(x)	v_1(cm^{-1})	v_2 (cm^{-1})	v^2_1	v^2_2	Kt(dyne/cm)	Ko(dyne/cm)
0	567.1	374	321602.4	140033.1	148543.7	84114.05

0.05	564.2	421	318321.6	177628.5	147028.4	110865.6
0.1	563.24	408	317239.3	166431.4	146528.5	107782.2

4. Coclusions:

i. It is observed that the force constant of B-site enhances with increases of Nd^{3+}ion concentrate in Ni-Zn ferrite which represents the strengthening of inter-ionic bounding and anion can be bound at large internuclear separation.

References:

1. S. Hilpert, Ber. Disch. Chem. Ges. 1909, 42, 2248.
2. P.N.vasudvca, Fundamentals of magnetisem and electricity by page; 460, S.Chand &compom pvt.ltd.
3. R Nasrabadi *et al.,* J. Mater. Sci. Mater. Electron., 2015, 26, 9776–9781.
4. Alex Goldman, "Modern Ferrite Technology" Van Nosttrand Reinhold New York, 1990.
5. M.M.Barakat *et al.,* J.Thermal Analysis, 1991, 37, 605-611.
6. Q Wei *et al.,* J.Materials Characterization, 2001, 47, 247-252.
7. Muthafar.F.Al-Hilli *et al.,* J,Magn ,Magn ,Mate, 2012, 324, 873-879.
8. Ying Zhang *et al.,* Materials Chemistry and Physics, 2012, 13, 575-580.
9. Jacob.J and Khadar .M.A,J Appl.Phys, 2010, 107, 114310.
10. R.V.Upadhyay *et al.,* J , Magn ,Magn Mate, 1999, 201, 129-132.
11. N.Rezlescu *et al.,* J.Phys.Condensed Matter, 6, 29.
12. S.K. Sharma *et al.,* J. Phys.: Condens. Matter, 2008, 20, 235214–235221
13. Y.Y.Meng *et al.,* J.powder Technology, 2012, 229, 270-275.
14. M.A.Gabal *et al. J* ,Magn Magn Mater, 2012, 324, 2258-2264
15. S.Basu *et al.,* 978-1-4673-0074-2/110(20011) IEEE.
16. C.Upadhyay *et al.,* J. Magn. Magn. Mater, 2007, 312, 271.
17. Hua Yang *et al.,* J ,Magn ,Magn ,Mate, 2004, 271, 230 -236.
18. S Thakur *et al.,* J. phys .Chem .C, 2009, 113, 20785-20794.
19. M.T.Farid *et al.,* Dig. Joun. of Nanomaterials and Biostructures, 2015, 10 (1), 265-275.
20. Smita Thankachan *et al.,* Phys . Scr , 2013, 87, 025701.
21. Venkatesh N, Goud S, Hari Kumar N, Aravind G, Ravinder D, Veera Somaiah P., IOSR Journal of Applied Chemistry (IOSR-JAC), 8(5)(Ver. II), (2015), 22-27.
22. B.Rajesh, M.S.R.Prasad, K.V.Ramesh, Y.Purushotham ,Material Chemistry and Physics 148 (2014) 585-591.
23. Li, X. and Wang, G., J. Magn. Magn. Mater. Vol.321, pp.1276–1279, (2009).
24. M. Siva Ram Prasad , B.Rajesh babu ,K.V.Ramesh and K.Trinadh J. Magn. Magn.Mater.323, (2011) 2115
25. Mohd.Hashim, Alimuddin, Shalendra Kumar, Sagar E.Shirsath, R.K.Kotnala, Jyoti Shad, Ravi Kumar.j.Ceramint.39 (2013) 1807-1819.
26. Ying Zhang,Dijiang Wen/Materials Chemistry and physics 131(2012) 575-580.

27. Smita Thankachan, Binu P Jacob , Sheena Xavier and E.M Mahammed, Phys . Scr , 87 (2013) 025701.

Impact of Sodium Dodecyl Sulphate on Structural Properties in Cobalt Nano Ferrite

Devy.K [1] M Murugan[1*] GSVRK Choudary[2] M C. Verma[3] A. Patrick Prabhu[4]

[1] Department of Physics, Government Arts College (Affiliated to Bharathidasan University) Tiruchirappalli, 620022, Tamil Nadu, India

[2] Department of Physics, Bhavan's Vivekananda College of Science, Humanities and Commerce, Sainikpuri, Secunderabad , 500094 Telangana, India

[3] Department of Physics, GIT, GITAM University, Vishakapatnam, Andhra Pradesh 530045, India

[4]Department of Physics, St.Joseph's college, Tiruchirappalli, Tamil Nadu 620002, India

*Corresponding author. Mobile: (+91) 9488688327, E-mail: manickmurugan68@gmail.com

Abstract

Influence of sodium dodecyl sulphate (SDS) on structural properties of cobalt nano ferrites synthesized by reverse micelles method was investigated in the present study. Samples with different cobalt to SDS ratio (Co: SDS = 1: 0.33, 1: 0.5, 1 : 0.66) were employed and were subjected to XRD, DTA, FTIR, and TEM studies to elucidate the impact of SDS on structural properties. All the samples exhibited single phase spinel structure with crystalline size in the range 29 to 35 nm. Increase in SDS content resulted slight decrease in crystallite size. The average particle size has been estimated from volume averages of number of TEM pictures for a particular sample by fitting the particle size distribution with a gauss function.

Keywords : Reverse micelles, Crystallite size, Particle size

1. Introduction

The properties of ferrites are highly sensitive to the method of processing and amount of additives present in the ferrite system [1-2]. The particle size is a key parameter in altering the properties as each property is interrelated to characteristic length scale.

Cobalt ferrite is a hard-magnetic material with high coercivity (4.3KOe) and a high curie temperature (T_C 520°C). The material is also incredibly chemically stable and is resistant to wear, an electrical insulator and is easily synthesized. The unique physical and mechanical characteristics of cobalt ferrite ($CoFe_2O_4$) have led to many important applications in nano medicines. Such impressive properties have led to cobalt ferrite being regarded as a promising candidate for a large variety of different medical applications including magnetic drug delivery, radio frequency hyperthermia and Magnetic Resonance Imaging [3-7]. Several methods such as sol–gel, co-precipitation, microemulsion, etc. have been reported for ferrite synthesis [8-10]. Hence, the control of particle size in ferrites is required by exploiting a suitable preparation method, heat treatment and compositional effect in order to achieve the best tradeoff between the various parameters.

For present investigations cobalt ferrite ($CoFe_2O_4$) is selected and synthesized in reverse micelles method with varying SDS concentration.

2. Experimental Details

2.1 Materials and Methods

The materials used were of analytical grade and used without further purification. Cobalt nitrate hexahydrate [Co $(NO_3)_2.6H_2O$], Iron nitrate hexahydrate [Fe $(NO_3)_2.6H_2O$], Dodecyl sulphate sodium salt (SDS), n-Hexane (99%), 1-Butanol were procured from HIMEDIA.

Cobalt ferrite has been processed through reverse micelles methods. Precursor solution is formed by mixing Cobalt (II) Nitrate and Iron (III) Nitrate in required proportions in deionized water and then stirred for an hour to improve the homogeneity. Two micro-emulsion systems consisting of water, SDS, 1butanol and n-hexane were prepared and left until a clear transparent solution was obtained [11]. The precursor solution is dissolved in one of the micro-emulsion system while in another micro-emulsion, 20 ml NaOH of 5molar was added. The two micro-emulsions were mixed together and subjected to a rapid magnetic stirring for an hour. Cobalt ferrite precipitate formed due to reverse micelle process was washed with distilled water and then dried in an electric oven at 90 °C for 6 hour. The dried powder (as-prepared sample) was mixed homogeneously in an agate mortar and pestle for 10 minutes for further study. Samples with different cobalt to SDS ratio (Co: SDS = 1: 0.33, 1 : 0.5, 1 : 0.66) were employed to investigate the impact of SDS.

XRD, DTA, FTIR and TEM techniques were utilized for structural analysis of the samples. The dried powder (as-prepared) was structurally characterized by irradiating with Cu-K_α radiation (λ = 1.5406 Å) using a Bruker advanced 80 X-ray diffractometer. The dried powder was made in the form of a pellet using potassium bromide (KBr) for recording the room temperature infrared spectrum using Perkin Elmer 5DX 1650 FTIR spectrometer in the range from 400 cm^{-1} to 4000 cm^{-1}. The dried powder was also examined under transmission electron microscope (TEM, model JOEL JEM 200CX) at the electron accelerating voltage 120 kV.

3. Results and Discussion

Figure 1. XRD Pattern of as prepared cobalt ferrite.

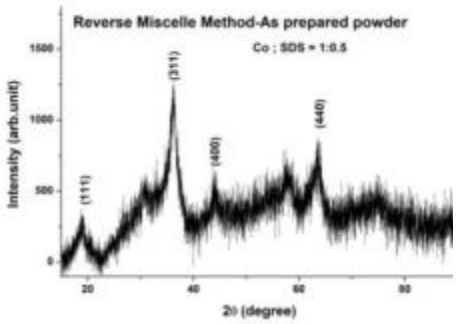

Figure 2. TGA & DTA pattern of as prepared cobalt ferrite

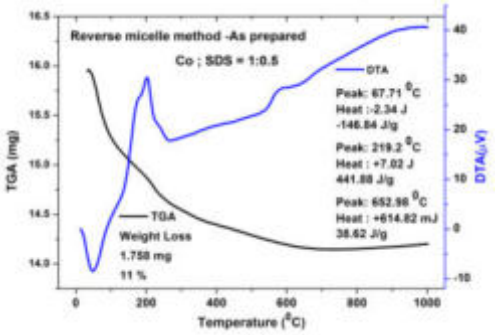

Sample with Co to SDS ratio 1:0.5 was subjected to X-Ray diffraction to ascertain that intended material is obtained. From the above XRD pattern (figure 1), the peaks obtained show commencement of ferrite formation and suggest that there is a need for improvement of crystallization process thus requiring further heat treatment. To identify the temperatures for further heating, the samples were subjected to DTA & TGA studies. From figure 2, we find one exothermic peak at 68°C and two endothermic peaks centered at 219°C and 652°C. From this information, the sample were heated at 250°C and 500°C and then subjected to XRD, DTA, FTIR and TEM studies.

Figure 3. FTIR Spectra of cobalt ferrite samples for as prepared and annealing temperature of 250^{o}c and 500^{0}c with Co : SDS ratio (a) =1:0.33 (b) =1:0.5 (c) =1:0.66

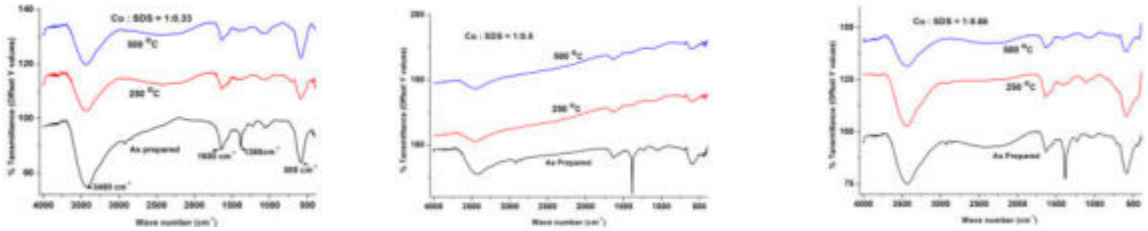

On inspection of the above FTIR spectra, we observe a peak at approximately 3400 cm^{-1}. In reference with characteristic IR absorption peaks, we can say that the peak was due to the presence of moisture (water) that was later reduced after heating. We observe another peak at around 1600 and 1380 cm^{-1} corresponding to the asymmetric ν_{as} (COO^-) and symmetric ν_s (COO^-) stretching vibrations of the COO^- group respectively that was also reduced after heating.

Figure 4. X-ray diffraction patterns of cobalt ferrite at annealing temperature of 250^o and 500^{0}c with Co : SDS ratio (a) =1:0.33 (b) =1:0.5 (c) =1:0.66

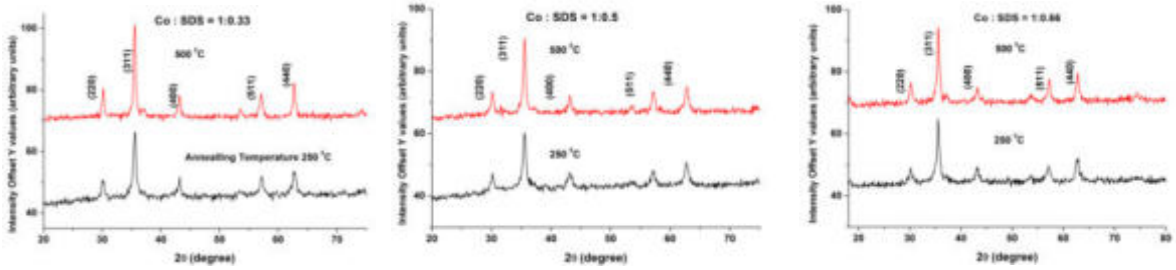

X-ray diffraction patterns of all the samples showed the spinel structure. The plane indices (hkl) are assigned to each peak in X-ray diffraction patterns by comparing the measured d-values with standard d-values of the spinel structure. Lattice constant '*a*' and Nelson-Riley function has been calculated for each peak of the X-ray pattern and reported in table 1. Crystallite size was determined by Scherer equation [12]. Crystallite size obtained from the FWHM of a diffraction peak represents contributions from crystallite size and the effects of micro strain and instrumental broadening. The contributions of the micro strain and instrumental effects can be separated in a straight forward fashion if the peaks are Lorentzian or Gaussian shaped. Williamson-Hall method [13-14] is one of the simpler approaches in analyzing the size and strain broadenings. From the Williamson-Hall plots for all the samples, crystallite size was estimated and are given in the following table 1.

Table 1. Lattice constant values (in A°), crystallite size and particle size for cobalt ferrite with different Co : SDS ratio at different annealing temperatures.

Co: SDS ratio	Annealing temperature (°C)	Lattice constant a (Å)	Crystallite size (nm)		Particle Size (nm)
			D_{XRD}	$D_{Scherer}$	
1:0.33	250	8.3705	29	27	12.0
	500	8.3725	38	34	17.7
1:0.5	250	8.3709	28	23	11.5
	500	8.3722	36	29	14.5
1:0.66	250	8.3702	27	21	10.4
	500	8.3723	35	26	13.0

3.1 Particle Size

Figure 5,6,7 shows Transmission electron micrographs (TEM) of cobalt ferrite with different Co : SDS ratio at different annealing temperatures where fine and uniform particles have been observed. The average particle size has been estimated from volume averages of number of TEM pictures for a particular sample by fitting the particle size distribution with gauss function.

Figure 5. TEM images and histograms of particle size distribution Cobalt ferrite with Co: SDS =1:0.33 at annealing temperature of 250°c and 500°c

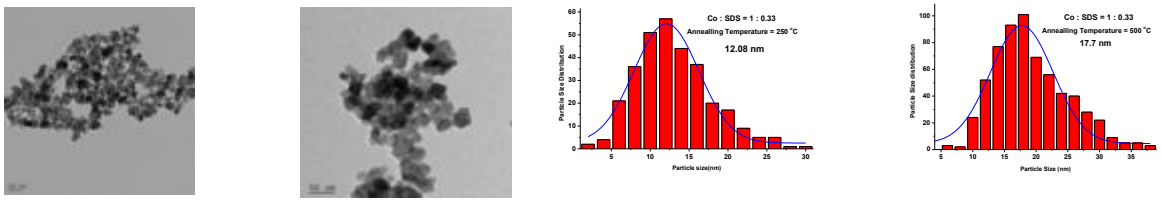

Figure 6. TEM images and histograms of particle size distribution of Cobalt ferrite with Co: SDS =1:0.5 annealing temperature of 250°c and 500°c

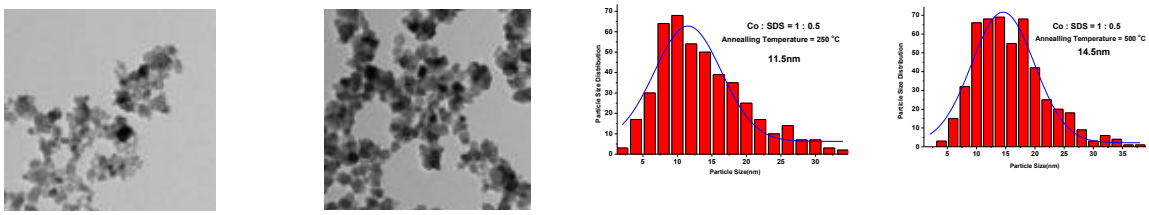

Figure 7. TEM images and histograms of particle size distribution of Cobalt ferrite with Co: SDS =1 : 0.66 annealing temperature of 250°c and 500°c


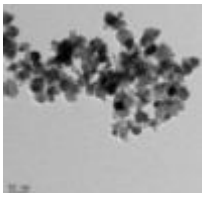
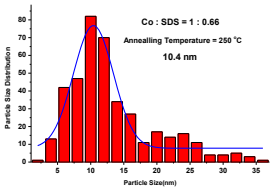

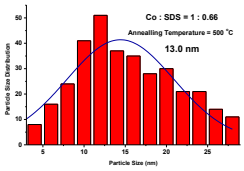

Average particle size (table 1) has been observed to increase with increase in temperature and decreases with increase in the SDS content.

4. Conclusion

The above work is a preliminary search for the appropriate amount of the surfactant required to prepare highly crystalline cobalt ferrite. The purpose of using ionic surfactant is to create spin distortions in the system and study the impact on structural properties in such case. The as prepared cobalt ferrite material suggest there is a need for improvement of crystallization process. From the information obtained from TGA/DTA studies, the samples were heated at 250^{o}C and 500^{o}C. The interplanar spacing (d-values) for different hkl values of cobalt ferrites, and lattice constants obtained in XRD studies were in agreement with reported values[JCPDS 22-1086].The average particle size estimated from volume averages of number of TEM pictures has been observed to increase with increase in temperature and decreases with increase in the SDS content.

Acknowledgements

Dr GSVRK Choudary is very thankful to UGC-SERO, Hyderabad for sanctioning financial assistance through Minor Research Project No. FMRP-6812/2017-18 (SERO/UGC). Devy.K acknowledges the support from the management of St. Francis College for Women, Hyderabad, for this research study.

References

1. S Gyergyek *et al.*, Journal of Nanoparticle Research. 2010, 12(4), 1263-73.
2. M A Ahmed *et al.*, Nanotechnology. 2008, 19(6), 065603.
3. M.A. Ahmed *et al.*, Journal of Magnetism and Magnetic Materials, 2009, 321, 1959–1963.
4. S. Rana *et al.*, Materials Chemistry and Physics, 2010, 124, 264–269.
5. S.Ayyappan *et al.*, Journal of Physical Chemistry C, 2010, 114, 6334–6341.
6. S.B. Darling *et al.*, Journal of *Materials Chemistry, 2005, 15, 4189.*
7. M.H.Yousefi *et al.*, Materials Research Bulletin, 2010, 45, 1792–1795.
8. B G Toksha *et al.*, Solid State Communications, 2008, 147(11-12), 479-83.
9. Y Zhang *et al.*, Journal of Magnetism and Magnetic Materials, 2010, 322(21), 3470-5.
10. N Moumen *et al.*, Journal of Physical Chemistry, 1996, 100(5), 1867-73.
11. S T Hussain *et al.*, Journal of Alloys and Compounds, 2012, 544, 99-104.
12. L B Patle *et al.*, AIP Conference Proceedings, 2018, 1953, 030045.
13. M L Meier, Department of Chemical Engineering and Materials Science, University of California. 2005.
14. G K Williamson *et al.*, Acta Metallurgica, 1953, 11, 22-31.

Green Synthesis of Zinc Oxide Nanoparticles Using Azadirachta Indica Leaf Extract and its Antibacterial Activity

*Singam.Shylaja
Assistant Professor of Chemistry, Vignana Bharathi Institute of Technology, Ghatkesar, Medchal, Telangana 501301.

Email: singam.shylaja@vbithyd.ac.in

Abstract

The present study mainly focuses on the synthesis of Zinc Oxide nanoparticles from the leaves of Azadirachta indica using zinc nitrate hexahydrate, as a precursor material. This green method of ZnO nanoparticles synthesis is simple, economic and eco friendly. The average crystallite size of nanoparticles was confirmed by XRD (X-Ray Diffraction) analysis. The morphology and elemental composition was characterized by SEM (Scanning Electron Microscope) and EDAX (Energy Dispersive X ray Spectroscopy). Thus confirmed ZnO nanoparticles were applied to study antibacterial activity against Escherichia coli, gram-negative bacteria by agar well diffusion method. It was observed that the ZnO nanoparticles have shown an efficient antibacterial activity.

***Keywords**:* ZnO Nanoparticles, Azadirachta indica, Escherichia coli, Antibacterial Activity.

1. Introduction

Nanoparticles are the particles with at least one dimension measured in the range of 1 -100 nm. These nanoparticles possess characteristic physical and chemical properties such as size, morphology, electrical and thermal conductivity, chemical stability, photo stability, wide range absorption etc because of its larger surface to volume ratio in comparison to bulk materials [1, 2]. Due to their remarkable properties, they are extensively used in the field of Medicine, Electronics, Agriculture, Fuel cells, Solar cells, Batteries, Water purification, Chemical Sensors, Cosmetics etc [2,3, 4].

Among various synthesized metal oxide nanoparticles such as CuO, CeO_2, Fe_3O_4, TiO_2 [4], ZnO nanoparticles have established tremendous applications in the medical field. ZnO nanoparticles can be synthesized by different methods like Chemical co-precipitation, Sol-gel, Hydrothermal, Chemical Vapor Deposition, Biological and Green methods .Green and Biological methods for the synthesis of nanoparticles could be eco-friendly than conventional methods [5, 6].

In the present study, we developed green method for the synthesis of ZnO nanoparticles using the leaf extract of Azadirachta indica (neem) and zinc nitrate hexahydrate as a precursor material. Leaf extract of neem is used as reducing agent. Leaves of neem mainly yield quercetin (flavonoid) and nimbosterol (ß- sitosterol) as well as number of liminoids (nimbin and its derivatives). Quercetin (a polyphenolic flavonoid) is known to have

antibacterial and antifungal properties [7]. This may perhaps account for the curative properties of leaves for sores and scabies. The plant phytochemical with antibacterial properties accountable for the preparation of metal oxide nanoparticles. Thus the average crystallite size and structure of the ZnO nanoparticles were confirmed by XRD. Morphology and elemental composition were detected by SEM and EDAX respectively. Moreover, the antibacterial activity of the nanostructured materials was evaluated by using the agar well diffusion method on gram negative bacteria, Escherichia coli.

2. Experiment

Green synthesis of ZnO nanoparticles

2.1 Preparation of neem leaf extract:

Some fresh leaves of Azadirachta indica were collected from the premises of VBIT. Then the leaves were cleaned with deionised water to remove the dust particles and air dried. Later 40 grams of leaves were weighed and added to 250 ml deionized water taken in a 500ml beaker. After that, the mixture was boiled at 80^0C for one hour until the colour of the solution changes to light yellow. Thus, the prepared leaf extract was cooled down to the room temperature. Then the extract was thoroughly filtered and refrigerated for further use [8].

2.2 Zinc Oxide Nanoparticles preparation:

For synthesizing ZnO nanoparticles, 50 ml of leaf extract was taken and boiled for 15 minutes at 80^0C.Later, 5 grams of zinc nitrate hexahydrate(A.R grade, Finar chemicals) was added to the solution. Then the mixture was continued to boil until light yellow color paste is obtained. Thus formed product was transferred to ceramic crucible and heated at 800^0C for two hours. After heating at the temperature mentioned, the paste turned into white colored powder. The powder was stored for further characterizations.

2.3 Antibacterial study

The agar diffusion method was performed to study the antibacterial property of synthesized ZnO nanoparticles against E. coli. Nutrient agar media was prepared and poured into petriplates. After solidification of the media, E.coli bacteria was spread uniformly using a sterile spreader. Then ZnO nanoparticles and ampicillin (control) was placed in the wells, prepared in the media and incubated at 37^0C for 24 hr. After the incubation period zone of inhibition was measured.

3. Result and Discussion

3.1 XRD Studies of ZnO nanoparticles:

The average crystallite size of green synthesized nano ZnO samples were characterized by powder XRD (instrument xperto pro PHILIPS) with CuKα radiation = 1.5418Å with 2θ ranging from 10 – 90 degrees at 40 kV, 30 mA .

ZnO nanoparticles(Fig 1) shows the XRD pattern distinctively at 2θ values of 31.52, 34.21, 36.02, 47.33, 56.37, 62.69, 66.16, 67.76, 68.90, 72.55, 76.79 with planes (100), (002), (101), (102), (110), (200), (112), (201), (004), (202).The peak positions have shown good agreement with the existing values (JCPDS -36- 1451) [9] and the existence of zinc oxide nanoparticles was confirmed. By using Debye Scherrer equation D=K λ/(βcosθ), Where, λ is the wavelength of X-ray source (Cu-Kα line0.1541 nm), β is the full width at half maximum (FWHM) in radians and θ is Bragg's diffraction angle. Thus average crystallite size of zinc oxide was found to be 28nm.

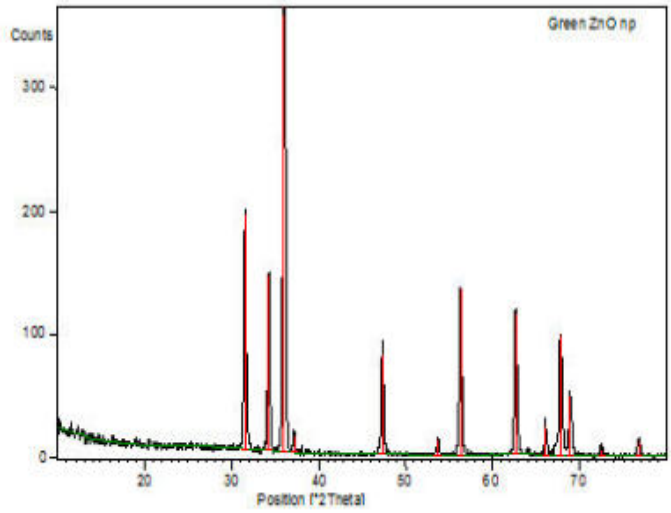

Fig .1: XRD of ZnO nanoparticles

3.2 SEM Analysis:

SEM (recorded from Zeiss EVO 18) gives the surface image of the sample. From (Fig. 2) it reveals that the particles are spherical shaped and are present as agglomerated structure.

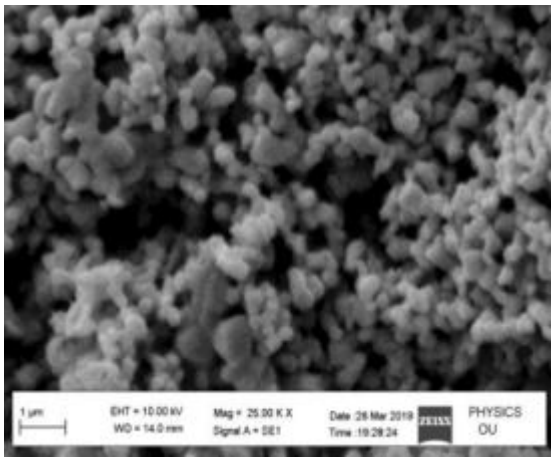

Fig.2 SEM image of ZnO nanoparticles

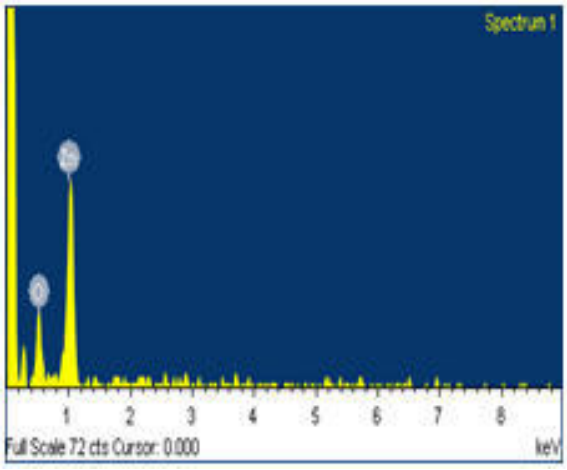

Fig.3 EDX composition of ZnO nanoparticles

3.3 EDAX Analysis:

The elemental composition of ZnO nanoparticles was done by EDAX. (Fig. 3)ZnO nanoparticles reveals the elemental composition of zinc and oxygen as 72.82 % and 27.18 %.This states that nanoparticles are pure and extent of impurities are negligible. The synthesis of ZnO nanoparticles from neem leaf extract would be simple, ecofriendly and effective for large scale production.

3.4. Antibacterial activity

Synthesized ZnO-NPs were tested on Gram-negative bacteria E. coli, by agar well diffusion method. Ampicillin was used as a control. (Fig.4) Results clearly demonstrate that the nanoparticle showed anti- bacterial effect with maximum zone of inhibition of 10.33 mm comparatively (zone of inhibition was seen as smear)[9,10,11]. ZnO nanoparticles prepared via green route using neem leaf extract showed excellent antimicrobial activity against E.coli.

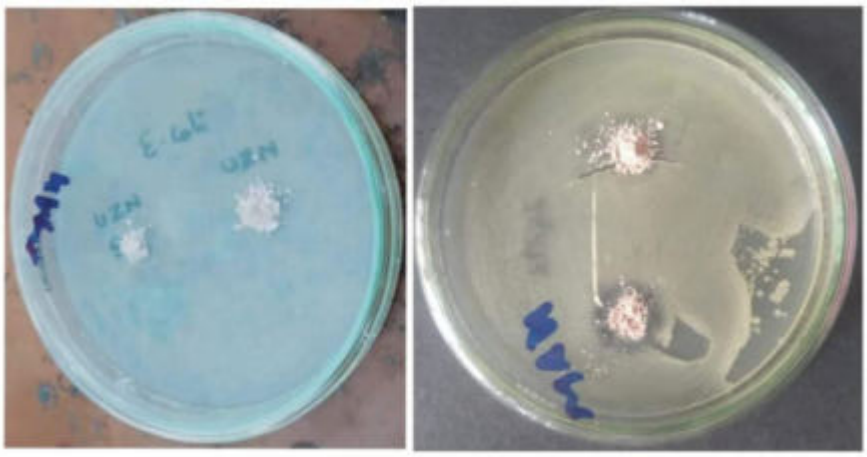

Fig.4 Anti bacterial activity of ZnO against E.coli

4. Conclusion

The zinc oxide nanoparticles were synthesized successfully by simple, environmental friendly green method. The average crystallite size of ZnO nanoparticles was found to be 28nm. Morphology and elemental composition of ZnO nanoparticles was confirmed by SEM and EDAX. We have reported that the synthesized ZnO nanoparticles were highly active as antibacterial agent against pathogenic bacteria.

Acknowledgement:

Author acknowledges the management of VBIT for their support.

References

1. H Reza *et al.*, Journal of Chemistry, 2015, 31(2), 1219-1221

2. S Sabir *et al.*, The Scientific World Journal, 2014, Article ID 925494, 8.

3. N B Singh *et al.*, J .Nanoeng.Nano, 2013, 3, 353-364.

4. I Hussain *et al.*, *Biotechnol Lett* , 2016, 38, 545–560

5. P Malik *et al.*, Journal of Nanoparticles, 2014, Article ID 302429, 14 pages.

6. R. Tamileswari *et al.*, IJERT, 2015, ISSN:2278-0181,Vol.4 (04).

7. R Subapriya *et al.*, Curr Med Chem Anticancer Agents, 2005, 5(2), 149 - 156

8. S Singam *et al.*, IJITEE, 2019, ISSN: 2278-3075, 8(10), 1824-1829.

9. A. M. Awwad *et al.*, Chemistry International, 2020, 6(3), 151-159.

10. J. Santhosh kumar *et al.*, Resource-Efficient Technologies, 2017, 3(4), 459-465.

11. M. Gupta et al., Front. Microbiol., 2018, https://doi.org/10.3389/fmicb.2018.02030

Photocatalytic H_2 Production from Glycerol-Water Mixtures Over Fe and Ag-Loaded Tio_2 Composite Systems

Gullapelli Sadanandam[a,b] *, Mike S. Scurrell[b] , Kumaraswamy Gullapelli[c]
[a] Energy & Resource Management Division, CSIR-National Environmental Engineering Research Institute, Nagpur, India
[b] Department of Civil & Chemical Engineering, University of South Africa, Florida, 1710,
Johannesburg, South Africa
[c] Department of Physics & Chemistry, Mahatma Gandhi Institute of Technology, Hyderabad-500075.

Corresponding author Email: sadaiict@gmail.com

Abstract
Fe-TiO_2 and Ag-TiO_2 photocatalysts prepared by impregnation method and characterized by various catalyst characterization techniques. DRS studies clearly show the expanded photo response of TiO_2 into visible region on impregnation of Ag and Fe ions on surface layers of TiO_2. Maximum hydrogen production of 2820 µmol/h/g is observed on 2wt% Fe-TiO_2 catalysts in glycerol-water mixtures under solar irradiation. A significant improvement in hydrogen production is observed in glycerol-water mixtures and maximum hydrogen production of 4,500 µmol/h/g is obtained over 1wt% Ag-TiO_2. Compared with Fe-TiO_2, Ag-TiO_2 composite exhibited an approximately 1.5 times enhancement of hydrogen production. Thus, the enhancement and in H_2 production can be attributed to the synergetic effects of silver-loaded TiO_2 heterojunction with highly photoactive Ag_2O-Ag phase.
Keywords: H_2 Production, Ag-TiO_2, Fe-TiO_2, Solar light, Glycerol-water mixtures.

1. Introduction:

Photocatalytic hydrogen production represents a very promising but challenging contribution to clean, sustainable and renewable energy system. Hydrogen is considered by many as an ideal future energy carrier and so the photocatalytic hydrogen production from water splitting becomes an important aspect for the storage and conversion of solar energy [1]. To date, metal oxides have been recognized as most promising photocatalytic materials due to their excellent corrosion resistance in aqueous solution. TiO_2 semiconductor photocatalytic systems because of their many desirable properties, appear to be the most attractive option for energy conversion and environmental purification [2,3]. The only drawback of the TiO_2 semiconductor is that it absorbs in the UV region (band gap energy of $TiO_2 \approx 3.2$ eV). Hence, in order to harvest maximum solar energy, it is essential to shift the absorption threshold towards the visible region. Transition metal loading proved to be one of the possible methods for dealing with this issue. Although many materials have been developed, the enhancement of photo-to-hydrogen efficiency remains challenging as a result of limited light absorption efficiency in the visible region of interest due to the large band-gap of metal oxides [4,5]. In order to address these issues, our main aim is to develop best photocatalyst system which is produce more hydrogen with long-term stability and recyclability. In our earlier studies, we have effectively demonstrated the Cu, Co and Ag doped nano TiO_2 and Ni/Al_2O_3 modified with TiO_2 visible light sensitive photocatalysts for hydrogen production [6–10]. The present investigation, we initially prepared Fe and Ag loaded TiO_2 by an impregnation method. Lower photocatalytic H_2 production was observed on Fe-loaded TiO_2 and more H_2 production efficiency was achieved with using of Ag-loaded TiO_2 composite under solar light irradiation.

A mechanism of the enhanced H_2 production activity under solar light irradiation was proposed**.**

2. Experimental

2.1 Preparation of Fe-loaded TiO_2 (FeT) and Ag-Loaded TiO2 (AgT)

Ferric nitrate equivalent to 0.5, 1, 2, 3 and 5 wt% of Fe was loaded on TiO_2 (P-25) and Silver 0.5, 1, 2, 3 and 5 wt% was loaded on TiO_2 (P-25) by impregnation. For each Fe and Ag modified sample, the required amount of TiO_2 was dispersed in ferric nitrate and silver nitrate solutions in distilled water. Excess water was evaporated to dryness under constant stirring with slow heating. The samples was dried at 100 ºC and calcined at 450ºC/4h. The catalysts with 0.5, 1, 2, 3, and 5 wt% of Fe-loaded TiO_2 are labelled as 0.5FeT, 1FeT, 2FeT, 3FeT and 5FeT, and 0.5, 1, 2, 3, and 5 wt % of silver-loaded TiO_2 are labelled as 0.5AgT, 1AgT, 2AgT, 3AgT and 5AgT, respectively. The experimental procedures involving the basic concepts of spectroscopic techniques like XRD, SEM, TEM, BET Surface area, UV-Vis DRS, FT-IR, Raman, and XPS etc. The reaction setups, experimental conditions adopted in evaluation of hydrogen production from glycerol water mixtures and techniques used for identification of products such as GC (TCD) have been briefly discussed in our earlier reports [7,9].

3. Results and discussion

The UV-Vis diffuse reflectance spectra of TiO_2, Fe-loaded TiO_2 and Ag-loaded TiO_2 samples are shown in Fig. 1. The DRS spectrum of TiO_2 consists of a broad intense absorption around 384 nm (corresponding to a band gap energy of 3.2eV calculated from $\lambda = 1239.8/ E_{bg}$) [6]. The diffuse reflectance spectra of P-25, Fe-loaded TiO_2 and Ag-loaded TiO_2 samples are shown in Fig. 1a and b and these showed a red-shift. An increase in the concentration of Fe^{+3} and Ag^{+1} ions on TiO_2 resulted in a significant change or shift of the band edge from the UV to the visible region. However, the absorption peaks were gradually shifted towards longer wavelengths with increasing amount of Fe and Ag [8,11]. The UV-Vis DRS spectra of 1AgT and 1AgTU (used in solar light) photocatalysts are compared and shown in Fig. 1c. The absorption value of 1AgTU shifted to higher wave lengths compared to 1AgT catalysts. In addition, 1AgTU a broad absorption in the range of 440-560 nm with a peak about 482 nm, which is correspond to the surface plasma resonance of Ag (0) particles and the appearance of these bands confirm some of the metallic silver formed in used catalysts [8].

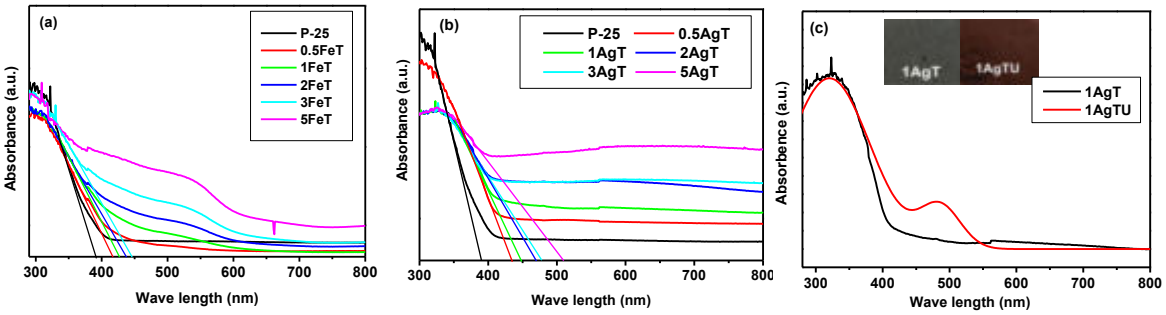

Fig. 1. DRS analysis of (a) Fe-loaded TiO_2 catalysts, (b & c) Ag-loaded TiO_2 catalysts

Photocatalytic activities:

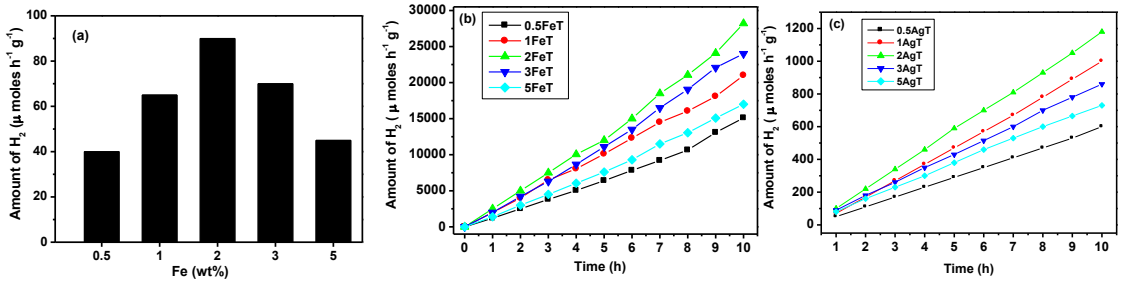

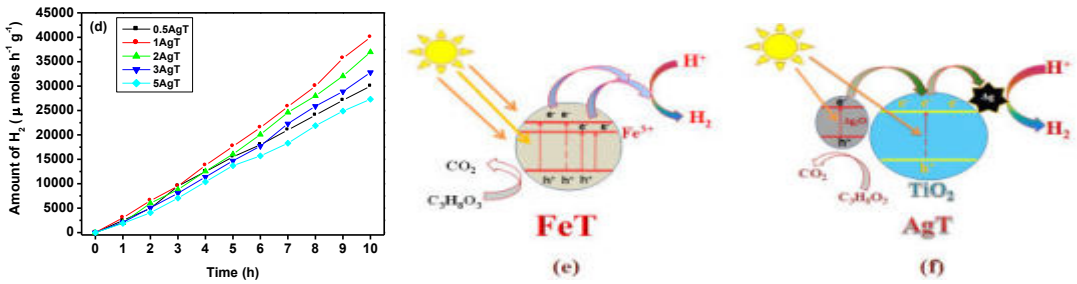

Fig. 2. Fe and Ag loading vs hydrogen production activity under solar light (a & c) in pure water (b & d) in glycerol: water mixtures, (e & f) photocatalytic mechanisms of Fe-loaded TiO_2 and Ag-loaded TiO_2.

Photocatalytic hydrogen production from pure water splitting is carried out over Fe-loaded TiO_2 and Ag-loaded TiO_2 photocatalysts under solar light irradiation. Fig. 2a and c shows the hydrogen production from pure water over Fe-loaded TiO_2 and Ag-loaded TiO_2 photocatalysts and maximum hydrogen production of 90 µmol $h^{-1}g^{-1}{}_{cat}$ is observed on 2wt% Fe-loaded TiO_2 and 120 µmol/h/g_{cat} is observed on 2wt% Ag-loaded TiO_2 catalysts respectively. Fig. 2b and d shows the H_2 evolution over Fe-loaded TiO_2 and Ag-loaded TiO_2 catalysts from glycerol: water mixtures under solar light irradiation. The activity increases with the amount of Fe-doping and reaches an optimum value at 2wt% Fe-doping, and the amount of hydrogen production over this catalyst is about 2820 µmol/h/g_{cat}. With further increase in the Fe-doping the activity decreases. The activity increases with the amount of silver doping and reaches an optimum value at 1 wt% Ag_2O-doping, and the amount of hydrogen production over this catalyst is about 4000 µ mol h^{-1} g^{-1} cat. With a further increase in the silver doping level, the activity falls. In summary, at 2 wt% Fe loading on TiO_2 and 1 wt% Ag loading on TiO_2, the light-harvesting capacities as well as the minimization of e^-/h^+ recombination are satisfied. Hydrogen production activity Ag-loaded TiO_2 is more than Fe-loaded TiO_2 because after few hours of reaction the loaded Ag_2O converted to the highly active and stable Ag_2O-Ag phase and in this phase Ag_2O acting as visible light sensitizer and metallic Ag acting as an electron sink. The photogenerated electron–hole pairs are effectively separated in presence of Ag_2O-Ag phase [8]. The photocatalytic mechanisms of Fe-loaded TiO_2 and Ag-loaded TiO_2 heterojunction are proposed in Fig. 2e and f.

4. Conclusions:

- Fe-loaded TiO_2 and Ag-loaded TiO_2 showed extended absorption in the visible region.
- Maximum hydrogen production of 2820 µmol/h/g is observed on 2wt% Fe-TiO_2, 4,500 µmol/h/g is obtained over 1wt% Ag-TiO_2 catalyst.
- Ag-loaded TiO_2 catalysts shows more hydrogen production due to the presence of Ag_2O-Ag phase structure.

Acknowledgments:
The authors sincerely thank to University of South Africa for technical and financial support.

References:

[1] R.M. Navarro *et al.* , Energy Environ. Sci. 2009, 2, 35–54.
[2] Y. Ma *et al.*, Chem. Rev. 2014, 114, 9987–10043.
[3] A. Kubacka *et al.*, Chem. Rev. 2012, 112, 1555–1614.
[4] X. Li *et al.*, J. Mater. Chem. A, 2015, 3, 2485–2534.
[5] T. Seadira *et al.*, Rev. Chem. Eng. 2017, 34, 695–726.
[6] K. Lalitha *et al.*, J. Phys. Chem. C, 2010, 114, 22181–22189.
[7] T.W.P. Seadira *et al.*, Appl. Catal. B Environ. 2018, 222, 133–145.
[8] G. Sadanandam *et al.*, Int. J. Hydrogen Energy. 2017, 42 (2017) 807–820.

[9] G. Sadanandam *et al.*, Int. J. Hydrogen Energy. 2013, 38, 9655–9664.
[10] S. Gullapelli *et al.*, Int. J. Hydrogen Energy. 2017, 42, 15031–15043.
[11] G. Sadanandam *et al.*, J. Renew. Sustain. Energy. 2018, 10 034703(1–13).

XRD and FT-IR Studies of Cu^{2+} doped Zinc Aluminium Lithium Borate Glasses

Tirumala Rao. B[1] and Sandhya Cole[2*]

[1]Department of Basic Science, Vishnu Institute of Technology, Vishnupur, Bhimavaram-534202, Andhra Pradesh, India.
[2]Department of Physics, Acharya Nagarjuna University, Guntur-522510. Andhra Pradesh, India.

*Corresponding e-mail: btrao2006@gmail.com

Abstract

Zinc Aluminum Lithium borate (ZALB) glasses of different compositions doped with Cu^{2+} ions have been prepared using conventional melt quenching technique. X-Ray diffraction and Fourier transform infrared studies have been carried out for ZALB glasses. The physical properties have been measured and it is one of the tools to reveal the degree of structural changes of the glass network with composition. The FT-IR studies indicate that these glasses are made up of [BO_3] and [BO_4] basic structural units.
Keywords: Borate Glasses, XRD and FT-IR Spectroscopy

1. Introduction:

The preparation and investigation of oxide glasses are getting significant attention due to their structural peculiarities and properties like good transparency, excellent corrosion resistance [1]. In these glasses borates have high refractive index and low dispersion characteristics. Due to these unique properties borates have been extensively used for phosphors, optical lenses, glass discharge tubes and solar energy technologies [2]. The chemical durability of glasses has improved due to the introduction of modifier cum network former Zinc, Lithium is an important alkali cation and Aluminum is an important metal ion. Zinc lithium aluminum system has interest in recent years due to their significant applications in industry and science. Borate glasses containing zinc-aluminum-lithium have many technological applications as batteries and microelectronic packing [3]. In the present work, an attempt has been made to undertake Fourier Transform InfraRed (FTIR) Spectroscopy.

2. Experimental

The raw materials Boric Acide, Lithium Carbonate, Zinc Oxide, Aluminum Oxide and Copper Oxide of A.R grade reagents were obtained from Loba Cemia Company. Required amounts of chemicals were weighed by using an electric balance with an accuracy of 0.001g. The composition was thoroughly mixed and melted in a porcelain crucible in a temperature range of 800-1050 ^oC for about 30 min until a bubble free liquid was formed. The melt was then poured on a brass plate and annealed at 300^oC for about 3 hours to avoid breaking the sample through residual internal strain. The obtained glass samples were polished with cerium oxide to obtain maximum flatness. The compositions of the present glass samples are given in Table1.

Table 1: Compositions of the glass samples (mole %)

Glass	Composition
TGC1	$10ZnO+5Al_2O_3+19.8\ Li_2O+65B_2O_3+0.2CuO$
TGC2	$10ZnO+5Al_2O_3+19.6\ Li_2O+65B_2O_3+0.4CuO$
TGC3	$10ZnO+5Al_2O_3+19.4\ Li_2O+65B_2O_3+0.6CuO$
TGC4	$10ZnO+5Al_2O_3+19.2\ Li_2O+65B_2O_3+0.8CuO$

3. Results and Discussion

The FTIR spectra of ZALB series of glass samples are shown in Figure 1. The fundamental infrared absorption peaks of borate vibrational modes are present in ZALB series of glasses. The bands at about 1250 cm^{-1} are assigned to =B-O-B≡ linkage with one of the boron in tetrahedral coordination. The bands at 1040 cm^{-1} are attributed to the B-O stretching vibration of BO_4 units in tri-tetra and pent borate groups [4]. The bands at 990 cm^{-1} may be due to vibration of boron atoms attached to NBO's in the form of BO_4 vibrations [5]. The nonexistence of band at around 800 cm^{-1} in all the recorded glass samples indicates the absence of boroxol ring in glass network [6]. This indicates that ZALB glass structure consists of BO_3 and BO_4 groups. The band at 700 cm^{-1} is assigned to the bending vibration of B-O-B linkage in borate networks [7]. The vibrational modes observed at 580 cm^{-1} are due to bending mode of Zn–O vibrations and bands at 550 cm^{-1} are attributed to the vibrations of Li^+ cations against their network. The addition of CuO breaks boroxol rings (B_3O_6) and more and more BO_3 and BO_4 groups are formed [8]. The intensity of bands increases with 0.6%, 0.8% of CuO and further decreases with 1% of CuO content. With change of composition there is no much variation in peak position and band shapes. With a gradual increase in the concentration of the dopant CuO in the ZnO-Al_2O_3-Li_2O-B_2O_3 glass, a successive change in the intensity of the bands due to symmetrical borate structural units is observed at the expense of bands due to asymmetrical groups. The Physical properties, Optical and FTIR observations clearly suggest that an increasing rigidity (or) a decreasing disorder of the glass with increasing CuO concentration.

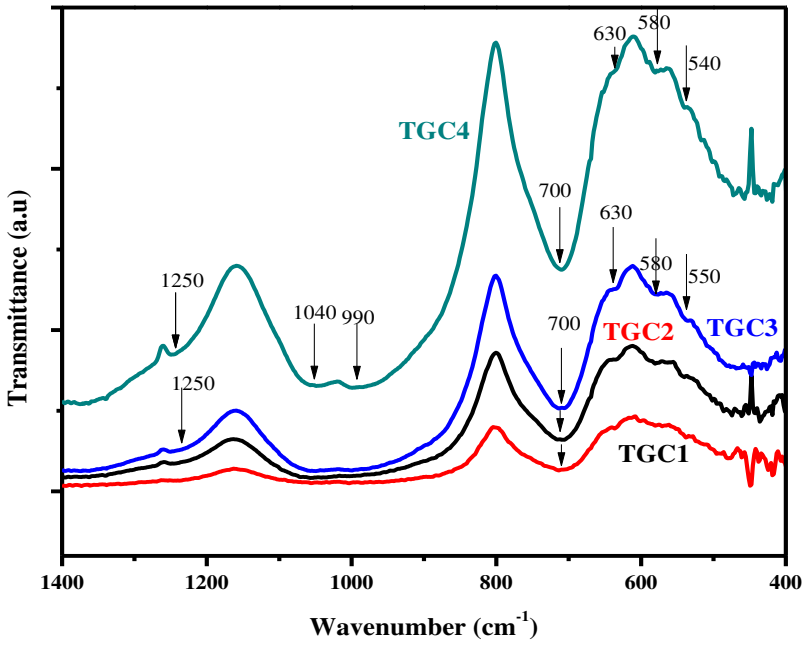

Figure 1 FTIR spectra of ZnO-Al_2O_3-Li_2O-B_2O_3: CuO glasses

4. Conclusion

An increase in copper oxide causes composition of B_2O_3 by breaking the bonds and allowing the formation of BO_4 units, in this way increase the density and reduces the band gap of ZnO-Al_2O_3-Li_2O-B_2O_3 glasses. FTIR spectra showed that the increment of copper oxide caused the breaking of B-O-B bonds and by creating new and more bonds.

Acknowledgements

Authors are thankful to Dr. Sandhya Cole, Associate professor, Department of Physics, Acharya Nagarjuna University, Guntur, for her valuable suggestions and providing FTIR recordings. Authors are thankful to the Principal, Vishnu Institute of Technology, Bhimavaram and college management for giving support and encouragement.

References

1. R.K. Brow *et al.*, Journal of the American Ceramic Society,1997, 80, 239.
2. G. Pal Singh *et al.*, Physica B, 2011, 406, 1890.
3. Z.A. Talib *et al.*, Journal of Physics and Chemistry of Solid, 2008,69,1969.
4. M Arora *et al.*, Nuclear instruments and methods, 2009, 267, 817.
5. I. Ardelean *et al.*, Material Letters, 2004, 58, 3499.
6. A.H. Verhoef *et al.*, Journal of Non-Crystalline Solids, 1992, 146, 267.

7. G. Fuxi *et al.*, Shaghai Scientific Technical Pub., Springer-Verlag, Shanghai, 1987, 32.
8. W. Soppe *et al.*, Journal of Non-Crystalline Solids, 1987,93, 142.

Synthesis and thermal expansion of Yttrium doped Ceria based nanomaterials for SOFC

Prashanth Kumar Vaidya[1,*], Y.S.Reddy[2], and C.Vishnuvardhan Reddy[3]

[1]Department of Physical Sciences, Kakatiya Institute of Technology & Science, Warangal, Telangana, India

[2]Department of Physics, Chaitanya Bharathi Institute of Technology, Hyderabad, Telangana, India

[3]Department of Physics, Osmania University, Hyderabad, Telangana, India

***Email:** pv.pss@kitsw.ac.in

Abstract

A kind of electrolyte materials for intermediate temperature solid oxide fuel cells (IT-SOFCs) were prepared by sol-gel method. Thermal expansion of the yttrium based electrolytes was studied by dilatometry. Thermal expansion measurements on the sintered samples were carried out from room temperature (RT) to 1000^0C. The average linear thermal expansion coefficient range was found to increase with increasing Y. The thermal expansion curves for all values of x displayed rapid increase in slope at high temperatures.

***Keywords**:* Solid Oxide Fuel Cells, Sol-gel, Electrolytes, Thermal Expansion

1. Introduction

The solid oxide fuel cell (SOFC) is an electrochemical device that can be used for either stationary or mobile generation of electrical energy as a clean, reliable and flexible power production [1]. SOFC is regarded as a highly efficient power-generation system with future application. A typical high-temperature SOFC uses 8 mol% Yttria-Stabilized Zirconia (YSZ) as the electrolyte, which is usually operated at temperatures as high as 800^0C–1000^0C. However, such high temperatures will lead to reaction between the components, thermal degradation, or thermal expansion mismatch [2, 3]. In order to reduce the operation temperature from 1000^0C to 800^0C or even lower, doped ceria has been considered as the solid electrolyte for moderate temperature solid oxide fuel cells [4, 5]. Gadolinium Doped Ceria (GDC) is an intermediate temperature material used in SOFCs [6]. It has great potential for replacing the more common YSZ as the electrolyte [7].

Recently, we have started investigations on growth, structure and electrical and thermal properties of GDC electrolyte materials synthesized by sol-gel technique. In this paper, we mainly describe the synthesis process thermal expansion of GDC.

2. Experimental

The $Ce_{0.8}Gd_{0.2-x}Y_xO_3$ electrolyte materials were prepared by sol–gel method. Cerium nitrate, yttrium nitrate, and gadolinium oxide were used as starting materials [8]. Cerium nitrate and yttrium nitrate were dissolved in water and the desired amount of gadolinium oxide was dissolved in nitrate solution. The individual solutions were mixed together and an aqueous solution of citric acid corresponding to every mole of metal atom was added. The amount of citric acid used was necessary to bind all the metals present in the solution. The pH value of the mixed solution was adjusted to ≈7 with ammonia solution under continuous stirring at 80^0C and homogeneous sol was formed. With the evaporation of water, sponge-like gel was obtained, which was calcined at 600^0C to get the final composition powder. Then the dried powders were ground in an agate mortar and then pallets were made using hydraulic press. The pellets were sintered finally at 1300^0C in air for four hours.

Thermal expansion measurements were performed in air from room temperature to 1000^0C on rectangular samples of 25 × 6× 6 mm^3 using Netzsch 402PC dilatometer calibrated to a

Alumina standard. Heating and cooling rates amount to 3^0C/min, with annealing time half an hour at maximum temperature [9].

3. Results and Discussion

The thermal expansion characteristic of $Ce_{0.8}Gd_{0.2-x}Y_xO_2$ (x = 0, 0.05, 0.1) obtained during the heating in air are shown in Fig.1. The thermal expansion depends on the electrostatic forces within the lattice, which depend on the concentration of positive and negative charges and their distances within the lattice [10]. The thermal expansion increases if the attractive forces decrease. The thermal expansion of a lattice with a certain structure and fixed oxygen to metal stoichiometry is characterized by a steady thermal expansion coefficient, α, caused by the thermal lattice vibrations. The thermal expansion coefficients (TEC) are calculated from the curves and the value increases with increasing Yttrium content.

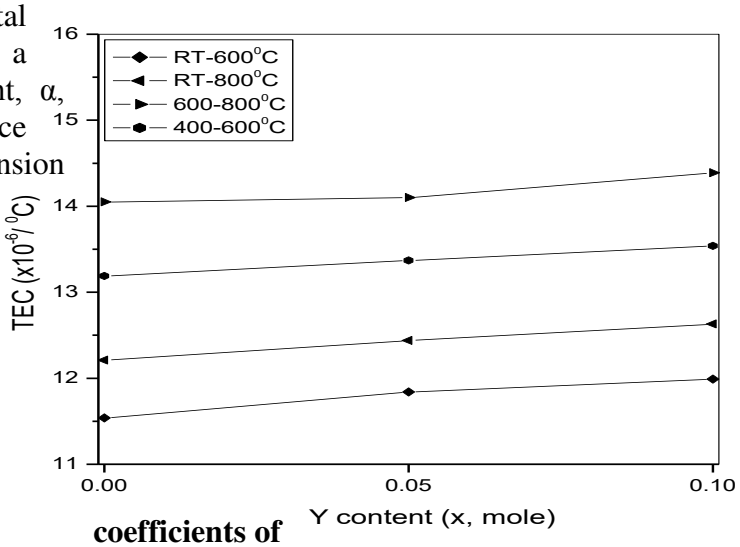

Fig.1: Average linear thermal expansion coefficients of $Ce_{0.8}Gd_{0.2-x}Y_xO_2$ (x=0-0.1)

The thermal expansion characteristic curves are linear and have two slopes. The temperature, at which the change of slope occurs, decreases with increasing temperature and this is called onset temperature. The value of onset temperature is located at approximately 380^0C, 350^0C and 290^0C for x=0, 0.05 and 0.1, respectively. The slope of the curves is slightly increased with increasing the yttrium content at high temperatures. These increases were found to be reversible in subsequent heating and cooling cycles at a rate of 3^0C/min in air. The lattice expansion observed at high temperatures in these oxides may be attributed to the loss of lattice oxygen and the formation of oxygen vacancies. The increasing of TEC is accompanied by the decreasing of the unit cell parameter [11, 12]. The values of average linear TEC with Y dopant are shown in Table 1. This is in good agreement with the previous reports and same trends are also observed for orthoferrites and cobaltites [13].

Table 1: The average thermal expansion coefficients of $Ce_{0.8}Gd_{0.2-x}Y_xO_2$

Composition (x)	Average TEC RT to 600^0C ($x10^{-6}/\ ^0$C)	Average TEC RT to 800^0C ($x10^{-6}/\ ^0$C)	Average TEC 600 to 800^0C ($x10^{-6}/\ ^0$C)	Average TEC 400 to 600^0C ($x10^{-6}/\ ^0$C)
0.0	11.54	12.21	14.05	13.19
0.05	11.84	12.44	14.10	13.37

0.1	11.99	12.63	14.39	13.54

4. Conclusions

- Nano size rare-earth co-doped $Ce_{0.8}Gd_{0.2-x}Y_xO_2$ (x=0-0.1) materials were prepared by the sol–gel method.
- The slope of the thermal expansion curves is slightly increased with increasing the yttrium content at high temperatures.
- The TEC values of all the compositions are in the range 11-14X$10^{-6}/^0$C

5. Acknowledgement

One of the authors, Prashanth Kumar Vaidya, thanks to Defence Research & Development Organization (DRDO) and Council of Scientific and Industrial Research (CSIR), New Delhi, India for the financial assistance.

6. References

1. Haizhen Wei et al., Advances in Colloid and Interface Science., 2010, **161**, 181–194.
2. M. Godickemeier et al., J. Electrochem. Soc., 1997, **144**, 1635-1646.
3. Yen-Pei Fu et al., Int. J. hydrogen energy., 2010, **35**, 745–752.
4. N.Q. Minh et al., J Am Ceram Soc., 1993, **76**, 563–88.
5. S. Ramesh et al., Solid State Ionics., 2010, **181**, 86–91.
6. H. Inaba et al., Solid State Ionics., 1996, **83**, 1-16.
7. B.C.H. Steele et al., Solid State Ionics., 2000, **129**, 95-110.
8. B. Jafee et al., Academic Press., 1971.
9. R.D. Shannon et al., Acta Crystallogr. Sect., 1976, **A32**, 751-767.
10. V. Venkatesh et al., Advances in Materials Physics and Chemistry., 2012, **2**, 5-8.
11. G.Ch.Kostogloudis et al., Solid State Ionics., 2000, **135**, 537-541.
12. Xueqing Sha, et al., J. Alloys Compd., 2006, **424**, 315-321.
13. V. Prashanth Kumar et al., International Journal of Modern Physics B, 2012, **26**, 1250174.

Storage of Visible Light for Persistence Luminescence in Chromium Activated Zinc Gallate Ceramic Material

Neeraj.Kr. Mishra and Kaushal Kumar

Optical Material and Bio-imaging Research Laboratory, Department of Physics, Indian Institute of Technology (Indian School of Mines), Dhanbad - 826004, India

Corresponding author: kumar.bhu@gmail.com

Abstract

The chromium activated zinc gallate ($ZnGa_2O_4$) phosphorwas successfully synthesized through conventional solid state reaction method. The structural and morphological study of the prepared sample was done through powder X-ray diffraction method (XRD) and FE-SEM respectively. The photoluminescence characteristics of the prepared samples were inspected systemically. The emission spectra of the sample consists of various lines generated through the electronic transition of Cr^{3+} between the levels $^2E(^2G) \rightarrow {}^4A_2\,(^4F)$. The band gap of sample $ZnGa_2O_4:Cr^{3+}$ was calculated by using Kumbelka-Munk equation (tauc plot) and it was found 4.5eV. The color purity of the sample was observed by CIE color chromaticity diagram. It was observed that there is no significant change in CIE co-ordinate when different excitation wavelengths 410 nm, 550nm were used. The prepared red color producing phosphor material could be used in solid state lighting,optoelectronic devices and bio-imaging applications

***Keywords*:**Persistence luminescence, Zinc gallate, CIE Diagram, Kumbelka-Munk equation, XRD.

1. Introduction

Persistence luminescence also known as long lasting luminescence or Afterglow, is the optical phenomenon in which luminescent materials emits radiations for long time even after the removal of excitation source [1]. Such luminescent materials have prodigious research interest due to its wide range of applications such as identification markers, safety sign, medical diagnostics, and fibre optics thermometer. However the noteworthy research have been done in the area of persistent phosphor but still the research and enlargement of persistent phosphor materials needed due its rising demands for the applications in the field of solid state lighting and bio imaging[2]. Persistence luminescence or long lasting luminescence of luminescent materials is depends on thetemporary storage of radiations as a trapped electrons and holes, followed by radiative recombination and detrapping of the charge carriers.

Zinc gallate $ZnGa_2O_4$ is a semiconductor compound with spinel structure in which $Zn^{2+}$and Ga^{3+} ions occupy tetrahedral and octahedral sites respectively. It shows slightly inversion character wherein few percent of Zn^{2+} occupy octahedral sites and few percent of Ga^{3+} occupy tetrahedral sites. The defects introduced due to such inversion character are known as antisite defects. The $ZnGa_2O_4$ material is considered as self-activated blue color emitting phosphor without any doping. While it emits green color on the doping of Mn^{2+} and emits red color on the doping of Cr^{3+} ions. The $ZnGa_2O_4$ host material is one of suitable host material for Cr^{3+} ions as the ionic radius of Cr^{3+} (0.62Å) similar to one of Ga^{3+}(0.62Å) in octahedral sites. When the Cr^{3+} activated $ZnGa_2O_4$ excited with visible light (410nm, 550nm) it shows a broad emission spectrum ranging from 650nm to 750nm peaks at 696nm. This wavelength domain is suitable for vivo imaging as this range of wavelength have maximum transmission for the biological tissue [3].

In this work, we report the successful synthesis of $ZnGa_2O_4$;1.0%Cr^{3+} via high temperature solid state reaction method. The structural, morphological and optical study of

the synthesised sample has been done through X-ray diffraction method (XRD), Field Emission Scanning Electron Microscope (FE-SEM) and photoluminescencerespectively.

2. Experimental

2.1 Materials and Method

The sample was prepared by solid state reaction method by using the composition;

$ZnO + (100-x)$ mol% $Ga_2O_3 + x$ mol% Cr_2O_3

The starting materials were ZnO (99.99%, Merck), Ga_2O_3 (99.99%, Alfa Asear) and Cr_2O_3(99.99%, Otto). All the starting materials were taken in stoichiometric proportion and grinded for 2 hr in agate mortar pastel using acetone as mixing agent. The obtained mixture was placed in alumina crucible and then heated in furnace at 1250℃ in open atmosphere for 6 hr. Further, the obtained compound was again grinded to obtain fine powder sample.

2.2 Structural and Morphological Study

The structural and phase purity study of the synthesised sample was confirmed by X-ray diffractometer (XRD). Fig1.(a) shows the XRD pattern of prepared chromium activated Zincgallate sample. The diffraction pattern of sample shows that it possess spinel cubic structure with single phase having Fd3m space group which well matched with the standard data of ICSD NO. 01-071-0843. On the doping of Cr^{3+} there is no significant change in the diffraction peaks of sample it may be due to very less concentration of dopants. The crystallite size of the sample were calculated by using Debye Scherrer Formula and was found to be in the range of 15nm to 28 nm. Fig. 1 (b) shows the FE-SEM image of the synthesised sample. The image shows that particles are in round shape. The average grain size of the sample were calculated by using *ImageJ software* and it was 20-50μm.

Fig1(a). XRD patterns of Synthesised $ZnGa_2O_4$;1.0%Cr^{3+} Fig1(b).FE-SEM image of $ZnGa_2O_4$;1.0%Cr^{3+}

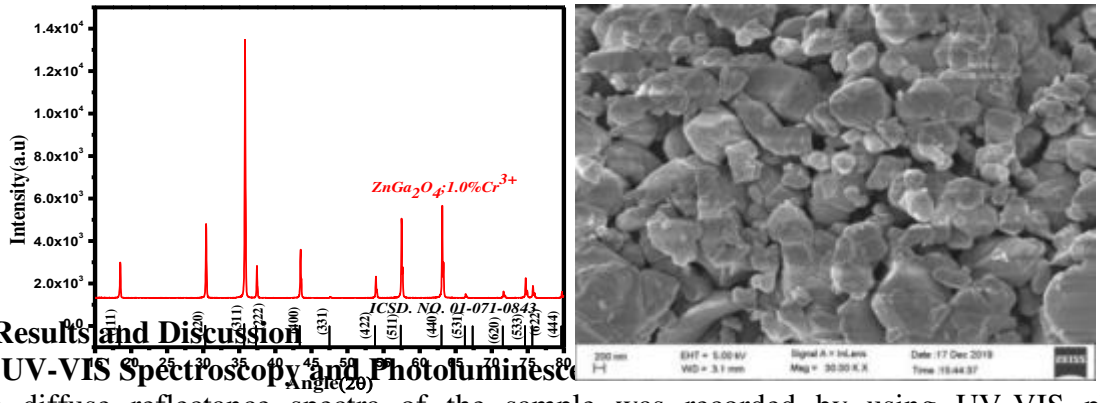

3. Results and Discussion

3.1 UV-VIS Spectroscopy and Photoluminesc

The diffuse reflectance spectra of the sample was recorded by using UV-VIS photo spectrometer, which is shown in the Fig.2(a). From the recorded spectrum the optical band gap of the sample was calculated by using Kumbelka Munk equation. By the Tauc plot it was found that prepared sample have direct band gap of 4.55eV. The diffuse reflectance spectra shows two absorption band at 410 nm and 550nm, which are attributed to the electronic transitions of Cr^{3+} ions from $^4A_2(^4F) \rightarrow ^4T_1(^4F)$ and $^4A_2(^4F) \rightarrow ^4T_2(^4F)$ respectively. The photoluminescence excitation (PLE) and photoluminescence spectra (PL) spectra of the sample are shown in the Fig.2(b) and Fig.2(c) respectively. The PLE spectra was recorded at the emission wavelength of 696nm and two excitation bands were observed as in the case of diffused reflectance spectra.The PL spectra were recorded at the excitation wavelength of 410 and 550nm. The Cr^{3+} activated $ZnGa_2O_4$ shows broad emission band ranging from 625nm to 725nm. This peculiar emission arises due to electronic transition of Cr^{3+} ions between the levels of $^2E(^2(G) \rightarrow ^4A_2(^4F)$ [4].Fig.2 (d) shows the decay curve of the sample. The photoluminescence decay ofthe sample was recorded at emission wavelength 696nm and

excitation wavelength of 410nm and it was found that decay curve is bi-exponential in nature. The calculated average decay time is 8.58ms

Fig.2(a) Diffuse Reflectance Spectra of $ZnGa_2O_4$;1.0%Cr^{3+} *Fig.2(b) Excitation Spectra of $ZnGa_2O_4$;1.0%Cr^{3+}*

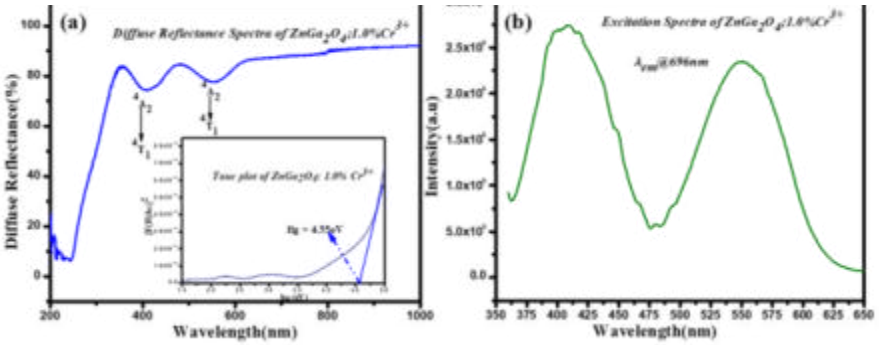

Fig.2(c) Emission Spectra of $ZnGa_2O_4$;1.0%Cr^{3+} *Fig.2(d) Decay Spectra of $ZnGa_2O_4$;1.0%Cr^{3+}.*

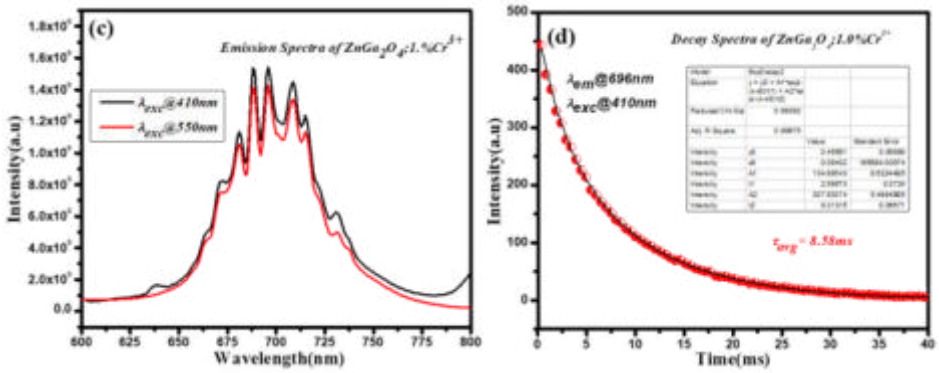

3.2 CIE Chromaticity Diagram

The color purity of the synthesised sample was confirmed by the CIE chromaticity diagram, which is shown in the Fig3. The obtained CIE coordinatesare (0.68, 0.32) at 410nm and (0.66, 0.34) at 550nm which are close to red color.

Fig 3. CIE Chromaticity diagram of $ZnGa_2O_4$;1.0%Cr^{3+}

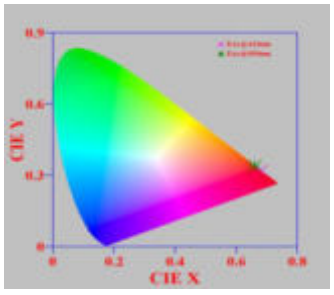

4. Conclusions

- Chromium activated Zincgallate sample was synthesised successfully.
- The structural, morphological and optical property of the synthesised sample was inspected.
- The color purity of the sample was investigated by CIE chromaticity diagram.

5. Acknowledgement
The authors would like to acknowledge Indian Institute of Technology(ISM), Dhanbad for providing infrastructure and research facility. One of the author Neeraj would like to acknowledge MHRD, Government of India for providing financial support in the form of institute fellowship.

6. References

1. Aurelie Bessiere et al., Chem. Mater., 2014, **26**, 1365-1373.
2. Hongbin Chen et al., Material Science and Engineering C., 2017, **79**, 372-381.
3. Amba Mondal et al., Physica B: Condensed Matter., 2019, **569**, 20-30.
4. B. Bhupedra et al., Chem. Commun., 2015, **51**, 7372-7375.

Synthesis, Characterization and Studies on the Biological Applications of Novel Amide Based Mixed Ligand Cu(II) Complexes

S. Kathiresan[a,b] and J. Annaraj[b]*
[a]Department of Chemistry, Kongunadu College of Engineering and Technology (Autonomous), Trichy - 621 215, Tamil Nadu, India.
[b]Department of Materials Science, School of Chemistry, Madurai Kamaraj University, Madurai - 625 021, Tamil Nadu, India.
E-mail: annaraj.chem@mkuniversity.org

Abstract
A new amide based mixed ligand copper(II) complexes have been successfully synthesized and characterized by several spectroscopic and spectrometric methods of UV-Vis, ^{1}H ,^{13}C NMR and ESI–MS. Their interactions with HS-DNA have been studied through emission spectral method. The results indicated that Cu(II) complexes showed moderate binding affinity towards HS-DNA through partial intercalation mode. The absorption and fluorescence techniques are explored that, complexes underwent a static quenching mechanism with bovine serum albumin (BSA).

Keywords: *Amide ligand, Cu(II) complexes, DNA interaction, BSA binding.*

1. Introduction

The transition metal complexes with Schiff bases have played an important role in the development of coordination chemistry. Multi-dentate Schiff bases ligands have been generally used, because they can be easily attached to metal ions due to the formation of highly stable coordination compounds [1-2]. Since it is commonly accepted that DNA and proteins are considered as the main molecular targets in the action of drugs, and many compounds wield their drug effects through binding to DNA or proteins, which is the basis of designing and discovering new and more efficient metal based drugs, the studies on syntheses and interactions of metal complexes with DNA and proteins have been an active field of research [3-6]. Thus, much interest in the design and synthesis of new amide-based drugs with target-specific, less-toxic and non-covalent DNA binding. Among these non-covalent binding modes, the intercalation attracts considerable attention due to its strong binding ability and various applications in cancer therapy and molecular biology [7-9].

2. Experimental

2.1. Materials and Methods

All reagents, chemicals and solvents used were of analytical reagent grade. ^{1}H & ^{13}C NMR spectra were measured on a Bruker 300 MHz spectrometer in $CDCl_3$ solution using TMS as the internal standard. Electrospray Ionization Mass Spectrometry (ESI-MS) analysis was performed in both positive and negative ion modes on a liquid chromatography-ion trap mass spectrometer (LCQ Fleet, Thermo Fisher Instruments Limited, USA). Electronic absorption spectra were recorded using an Agilent 8453 UV-vis Spectrophotometer in the range 190-1100 nm. Emission spectra were recorded with Agilent Cary Eclipse fluorescence spectrophotometer.

2.2. Synthesis of ligand (L)

Picolinic acid (0.5 g, 4.06 mmol) was dissolved in $CHCl_3$ (10 mL) and kept for stirring, to this solution CDI (1,1'-carbonyl diimidazole, 0.72 g, 4.47 mmol) was added slowly for 15 min at RT. After 1 hr the activation of the acid was checked by TLC and to confirm the activation of acid,

2-amino benzothiazole (0.61 g, 4.06 mmol) was added to the above solution and allow stir for further 10 hr. Then the progress of the reaction completion is checked by TLC and the reaction solution is quenched with water. The obtained crude product is extracted with ethyl acetate, on evaporating the organic layer, the desired solid is obtained as light grey color and dried in *vacuo*. Yield: 84%; color: gray; ^{1}H NMR (300 MHz, $CDCl_3$) δ 11.36 (s, 1H), 8.68 (t, *J* = 9.8 Hz, 1H), 8.32 (d, *J* = 7.8 Hz, 1H), 8.02 – 7.81 (m, 3H), 7.61 – 7.52 (m, 1H), 7.47 (t, *J* = 7.7 Hz, 1H), 7.34 (t, *J* = 7.7 Hz, 1H). ^{13}C NMR (75 MHz, $CDCl_3$) δ 162.90, 157.73, 149.15, 147.91, 138.18, 132.79, 127.91, 126.64, 124.42, 123.38, 121.75.UV-vis (CH_3OH, λmax, nm): 248 and 307. ESI-MS: Found *m/z* = 278.05 $[M+Na]^+$ (Calcd *m/z* = 255.05).

2.3. Synthesis of metal complexes

2.3.1 Synthesis of [Cu(L)phen] (1)

Complex **1** was prepared by the addition of ethanolic solution (3 mL) of a mixture of 1,10-phenanthroline (39 mg, 0.19 mmol) and L (50 mg, 0.19 mmol) to a solution of copper(II) nitrate trihydrate (47 mg, 0.19 mmol) in ethanol (2 mL) and then refluxed for 4 h. The green color solid was obtained and washed with small amounts of cold ethanol and diethyl ether and then dried in *vacuo*. Yield: 74%; color: green; Anal. calcd for $C_{25}H_{16}CuN_5OS$: C, 60.29; H, 3.24; N, 14.06 Found: C, 60.14; H, 3.35; N, 14.11. UV-vis (CH_3OH, λmax, nm): 266, 330, 394 and 652 (d-d transition). ESI-MS: Found *m/z* = 497.20 $[Cu(L)phen]^+$ (Calcd *m/z* = 497.04).

2.3.2. Synthesis of [Cu(L)bpy] (**2**)

Complex **2** was prepared by addition of ethanolic solution (3 mL) of a mixture of 2,2- bipyridyl (31 mg, 0.19 mmol) and L (50 mg, 0.19 mmol) to a solution of copper(II) nitratetrihydrate (47 mg, 0.19 mmol) in ethanol (2 mL) and then reflux for 4 h. The dark green color solid was obtained and washed with small amounts of cold ethanol and diethyl ether and then dried in *vacuo*. Yield: 69%; color: dark green; Anal. calcd for$C_{23}H_{16}CuN_5OS$: C, 58.28; H, 3.40; N, 14.77 Found C, 58.19; H, 3.34; N, 14.72. UV-vis (CH_3OH, λmax, nm): 272, 326, 396 and 667 (d-d transition). ESI-MS: Found *m/z* = 473.15 $[Cu(L)bpy]^+$ (Calcd *m/z* = 473.04).

2.4. DNA/ Protein binding Studies

The DNA (EtBr fluorescence displacement assay) and protein (UV-Vis and fluorescence spectra) binding experiments procedure in previous methods [10-11].

3. Results and Discussion

3.1. Characterization of Synthetic Compounds

The electronic spectra of the ligand showed two bands 248 and 307 nm which corresponds to the π-π* and n-π* transitions respectively. The spectra of Cu(II) complexes exhibit four bands, three bands appeared in the around 266-272, 336-330, 394-396 nm corresponds to intra-ligand transitions and another one band in d-d transition (652-667 nm). The observed one singlet ^{1}H NMR spectrum of L at 11.36 ppm is amide (N-H) proton. In the ^{13}C NMR spectrum of L, the signal at 162.90 ppm due to carbonyl carbon (C=O). The ESI-MS spectra of L and complexes were recorded in methanol. The ligand showed a peak at *m/z* 278.05 $[M+Na]^+$ and complexes **1** and **2** showed their characteristic molecular ion peaks at *m/z* 497.20 $[Cu(L)phen]^+$ and 473.15 $[Cu(L)bpy]^+$.

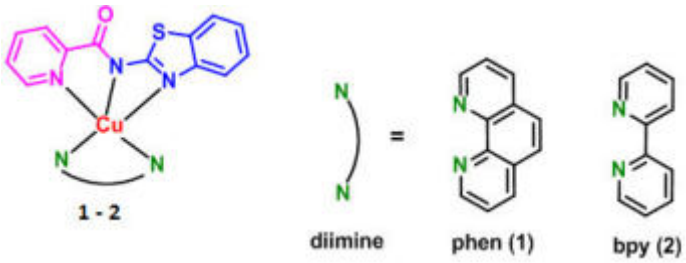

Scheme 1 Synthesis of mixed ligand Cu(II) complexes.

3.2. DNA Interaction Studies

3.2.1 EtBr fluorescence displacement assay

The synthesized mixed ligand Cu(II) complexes have not been fluorescence property at room temperature in solution or in the presence of CT DNA. So the binding affinity of the Cu(II) complexes with HS-DNA could not be directly predicted through the emission spectroscopy [12]. Hence, in order to EtBr fluorescence displacement assay was done to understand the mode of DNA interaction with the complexes. EtBr is a cationic dye it emits an intense fluorescence in the presence of HS-DNA around 610 nm due to its strong intercalation between the adjacent base pairs of the double helical DNA**.** The incremental concentration (0-150 µM) of Cu(II) complexes leads to significant decrease in the binding spots of DNA with EtBr, thus decreasing the fluorescence intensity of the EtBr bound with HS-DNA complex, which indicates that their significant efficiency for the partial displacement of EtBr from the EtBr-DNA complex (Figure1). The fluorescence quenching constant has been calculated from the Stern-Volmer equation $I_o/I = K_{SV}$ [Q] + 1 [13]. The quenching constant (K_{SV}) value has been derived from the slope of the plot I_o/I versus [Q] and are 4.36×10^5 M^{-1} and 4.17×10^5 M^{-1}. The apparent DNA binding constant (K_{app}) values were calculated by using the equation K_{EtBr} [EtBr] = K_{app}[complex]. Where, [complex] is the value at 50% decrease in the fluorescence intensity of EtBr, K_{EtBr} (1.0×10^7 M^{-1}) is the DNA binding constant of EtBr and [EtBr] is the concentration of EtBr (10 µM). The K_{app} values for complexes **1** and **2** is 1.72×10^6 M^{-1} and 1.65×10^6 M^{-1}.

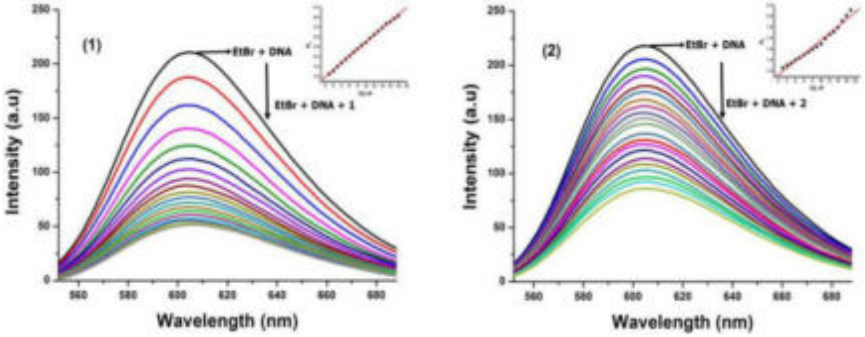

Figure: **1** Fluorescence quenching spectra of EtBr bound to DNA by complexes **1–4.** [DNA] = 5 µM, [EtBr] = 10 µM and [complex] = 0**-**150 µM. Inset: Stern-Volmer quenching curve.

3.3. Protein binding studies

3.3.1. Absorbance and fluorescence studies

The interaction between Cu(**II**) complexes with BSA was monitored by fluorescence quenching measurements with the addition of increasing concentration of Cu(**II**) complexes and the fixed concentration of fluorescence emission of BSA. The typical fluorescence emission band at 348 nm of BSA was quenched in a consistent manner as the increasing concentration of these

complexes, along with a hypsochromic shift around 2-6 nm (Figure 2b). The complexes can interact hydrophobically with proteins, which is evident from the observed hypochromism [14]. These results suggest a strong interaction has been occurred between the copper(II) complexes and BSA protein. The protein quenching constant (2.35×10^5 M^{-1} (**1**), 1.97×10^5 M^{-1} (**2**)) and binding constant (2.12×10^6 M^{-1} (**1**), 2.01×10^6 M^{-1} (**2**)) can calculated from Stern–Volmer and Scatchard equation.

Furthermore, absorption spectra of BSA were also recorded in the presence of these Cu(II) complexes, The observed electronic spectra indicated that the absorption intensity of BSA was enhanced upon the increment addition of Cu(II) complexes along with a very slight blue shift (Figure 2a). It exposed that the static interaction between Cu(II) complexes and BSA [15].

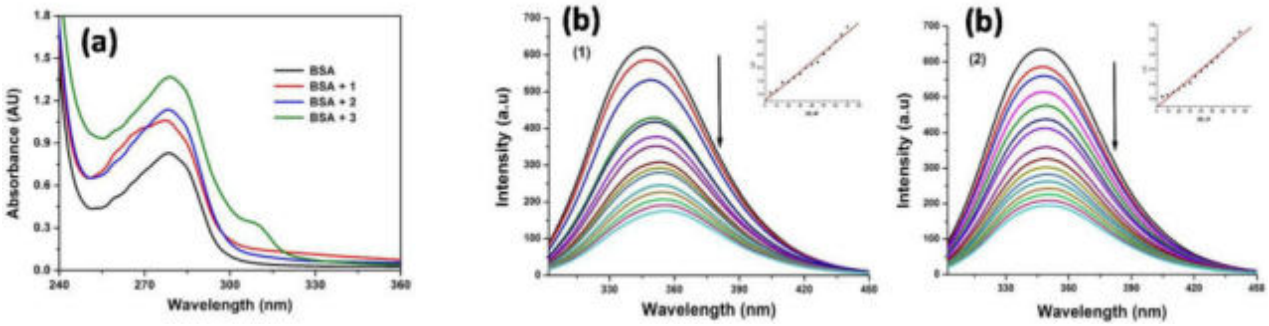

Figure: **2** (a) Absorption spectra of BSA (10 μM) and BSA with **1**-**2** (5 μM). (b) Fluorescence quenching curves of BSA in the absence and presence of **1** and **2**. [BSA] = 1 μM and [complex] = 0-50 μM.

4. Conclusions

- In this work, new mixed ligand Cu(II) complexes have been synthesized and characterized by spectral and analytical data.
- The interaction between the complexes to HS-DNA and BSA has been investigated by UV-vis absorption and fluorescence analysis. The observed results indicate that interaction of the Cu(II) complexes with HS-DNA through non-covalent intercalation.
- The good protein binding ability of the Cu(II) complexes was exposed from fluorescence measurement.
- Future work could be extended to investigate the anticancer activity of the isolated compounds.

5. Acknowledgement

The authors Dr J. A and S. K gratefully acknowledge Department of Science and Technology (DST), New Delhi [Grant No: SB/FT/CS-175/2011] and the UGC, New Delhi [F.No.42-247/2013 (SR) dated 12-03-2013] for financial support.

6. References

1. L.P.Lu et al., Journal of Inorganic Biochemistry., 2003, **95**, 31–36.
2. S.Dhar et al., Inorganic Chemistry, 2003, **42**, 2483–85.
3. C.G.Hartinger et al., Organometallics., 2012, **31**, 5677–85.
4. G.Sava et al., Dalton Transactions., 2012, **27**, 8226–34.
5. N.P.Barry et al., Chemical Communication., 2013, **49**, 5106–31.
6. V.Rajendiran et al., Dalton Transactions., 2008, **1**, 148–163.

7. F.H.He et al., New Journal of Chemistry., 2012, **36**, 2078–87.
8. F.Xue et al., Journal of Inorganic Biochemistry., 2012, **115**, 78–86.
9. P.R.Chetana et al., Polyhedron., 2014, **68**, 172–179.
10. S.Kathiresan et al., RSC Advances., 2016, **6**, 1810–25.
11. S.Kathiresan et al., New Journal of Chemistry., 2017, **41**, 1267–83.
12. R.K.Gupta et al., Inorganic Chemistry, 2013, **52**, 13984–96.
13. R.Raj Kumar et al., RSC Advances., 2015, **5**, 46760–73.
14. D.Senthil Raja et al., European Journal of Medicinal Chemistry, 2011, **46**, 4584–94.
15. D.Senthil Raja et al., Inorganic Chemistry, 2011, **50**, 12852–66.

Recent Advances in the Fabrication of ZnO Based Nanostructures for Opto-Electronic Devices

Santhosh Kumar A*, G. Nataraju, Y. Srinivasa Reddy and B. Linga Reddy*
Department of Physics, Chaitanya Bharathi Institute of Technology

*corresponding author email: saanthosh.phy@gmail.com

Abstract
In recent years, there has been increasing interest in ZnO nanostructures due to their variety of shapes and availability of simple and cost effective processing. While there are still unanswered questions concerning fundamental properties of this material, in particular those related to defects and visible luminescence lines, great progress has been made in synthesis methods and device applications of ZnO nanostructures. In this review, we will provide a brief overview of synthesis methods of ZnO nanostructures, with particular focus on the growth of oriented arrays of nanorods/nanoarrays which are of interest for optoelectronic device applications.

***Keywords**:* ZnO, Nanostructures, Fabrication, Opto-electronics, DSSC

1. Introduction

Semiconducting oxide nanostructures such as ZnO, TiO_2, SnO_2, CuO_2 and so on are the focus of current research efforts in nanotechnology due to their special shapes, compositions, chemical, and physical properties. They have now been widely used in the fabrication of energy saving and harvesting devices such as solar cells [1, 2], Lithium ion batteries, fuel cells, transistors, Light emitting devices (LEDs), hydrogen production by water photolysis and its storage, water and air purification by degradation and adsorption of organic pollutants and toxic gases, environmental monitoring by their applications in the fabrication of gas, humidity and temperature sensors, UV screening, and photodetectors [1-3]. Instead of these they have also fabulous applications inbiological and medical sciences such as drug delivery, cancer treatments, fluorescentimaging and bio-labeling etc.

Among the semiconducting oxides, ZnO based nanomaterials have revolutionized the nanomaterials research because of the possibility of soft chemical synthesisbesides tremendous application potential. UndopedZnO ZnO with a Wurtzite structure naturally becomes an n-type semiconductordue to the presence of intrinsic or extrinsic defects, which have been generally attributedto native defects, such as the Zn-O antisite, the zinc interstitial, O vacancy.The highest room temperature electron mobility for a bulk ZnO single crystal grown byvapor-phase transport method is reported to be about 205 cm^2/Vs with a carrier concentrationof 6.0 x $10^{16}cm^{-3}$[4]. ZnO is a soft material, witha hardness of s 5 GPa at a plastic penetration 300 nm. The thermal conductivity (k)of a semiconductor is an important property when considering high-power/high temperaturedevices. It is a kinetic property influenced by the vibrational, rotational andelectronic degrees of freedom, and is predominantly limited by phonon-phonon scatteringin a pure crystal. ZnO, like most other semiconductors, contains a large number ofpoint defects, and these have significant effect on the thermal conductivity. The values typically fall in the range 0.6 - 1 $Wm^{-1}K^{-1}$[4]. In this review, we will provide a brief overview of synthesis methods of ZnO nanostructures, with particular focus on the growth of perpendicular arrays of nanorods/nanoarrays which are of interest for optoelectronic device applications.

2. Growth methods of ZnO nanostructures

As a technologically important material, ZnO has attracted many researchers due to its unique properties (semiconducting, piezoelectric, magnetic etc.). A variety of methods has been used

for the synthesis ZnO films and nanostructures. For consolidation, methods have been categorized as either vapor or chemical routes.

2.1.Vapor routes

Vapor phase synthesis methods are probably the approach most extensively studied in the fabrication of ZnO nanostructures [5]. A typical vapor phase synthesis is carried out in a closed chamber with a gaseous environment. Vapor species are produced first by evaporation, chemical reduction, and gaseous reaction. After that, the species are transferred and condensed onto the surface of a solid substrate. In general, the vapor phase synthesis process is carried out at higher temperatures (500^{o}C to1500^{o}C) to produces high-quality ZnO nanowires. The typical vapor phase synthesis methods include vapor-liquid-solid (VLS) growth, chemical vapor deposition (CVD), metal organic chemical vapor deposition (MOCVD), physical vapor deposition (PVD), molecular beam epitaxy (MBE), pulsed laser deposition (PLD), and metal organic vapor phase epitaxy (MOVPE). Several vapor phase synthesis methods are introduced below.

(i) VLS method:

Among the vapor phase techniques, VLS method is a simple and low cost process, and is advantageous for growing ZnO on large wafers. This process is widely used for the growth of 1D nanostructures such as nanowires and nanorods. The nanosized liquid metal droplets are used as catalysts (Cu, Au, Ni, Sn and etc.) in a typical VLS process. ZnO nanowires have been successfully grown on sapphire, GaN, AlGaN, and AlN substrates through the VLS process [6]. The quality and growth behavior of the ZnO nanostructures are strongly affected by the chamber pressure, oxygen partial pressure, and thickness of the catalyst layer [6]. In 2012, well-aligned ZnO nanowires were synthesized by Chu et al. using VLS mechanism on Si substrate with chamber temperature varying from 600 to 950 ^{o}C and pressure from 0.75 to 3 torr. They showed that ZnO nanowires with high aspect ratio grew vertically on the Si substrate at 700 to 750 $^{\circ}$C [7].

(ii) Catalyst-free MOCVD

Catalyst-free MOCVD is another important synthesis method to grow ZnO nanostructures on solid substrates. The catalyst-free method eliminates the possible incorporation of catalytic impurities and produces high-purity ZnO nanostructures. Moreover, the growth temperature of catalyst-free MOCVD is lower compared to typical VLS growth temperature [8]. In 2005, Zeng et al. fabricated highly-aligned ZnO nanowires on Si substrate using catalyst-free MOCVD. In their fabrication process, high-purity zinc diethyl (99.99%) and nitrous oxide (99.99%) were used as zinc and oxygen sources, respectively, and N_2 as the carrier gas. The working pressure and base pressure of the reactor chamber were maintained at 50 and 10^{-5}torr, respectively. At the beginning they have been grown a thin nucleation layer of ZnO at a low substrate temperature of 400 ^{o}C. After annealing the nucleation layer, ZnO nanowires were grown on the nucleation layer at the substrate temperature of 650^{o}C [9].

(iii) Physical vapor deposition

Various physical vapor deposition (PVD) techniques such as evaporation deposition or thermal evaporation, electron beam physical vapor deposition, sputtering (magnetron and DC/RF sputtering), cathodic arc deposition and pulsed laser deposition etc have also been used to fabricate ZnO nanostructures. The PVD techniques have the following advantages: (1) composition of products can be controlled, (2) free of pollution (drain water, discharge gas, and waste slag) and (3) simple process. The PVD process usually is direct thermal evaporation and oxidation of Zn powder at a high temperature and then deposition on the solid substrate to form the final product. In 2009, Zhang et al. demonstrated the growth of ZnO nanowirearrays on Si substrates by PVD method at a relatively low temperature of about 500 ^{o}C. In their process of synthesis, high-purity Zn powder was placed in a ceramic boat located at the center of a horizontal tube furnace. The Si substrates were placed on top of the

boat to collect the products. The system was quickly heated to 500 ^{o}C under 50 cm^3 /min N_2 flowing at a pressure of about 1 m.Torr for 60 min and then cooled down to room temperature [10].

2.2. Chemical routes

Compared with these vapor routes, more and more researchers have started to utilize soft solution methods to obtain the aligned ZnO nanorod arrays, due to their simplicity, large scale production, high product yield and low energy consumption. Several solutions based on chemical synthesis methods are introduced below,

(i) Chemical bath deposition

Chemical bath deposition (CBD) technique produces a solid structure in a single immersion through a control of the formation kinetics of the solid, normally without changing the metals oxidation states. ZnO nanorods can be produce by CBD at a temperature as low as 60^{o}C. Vayssiereset al. used this method to grow ZnO nanorods in 2001 [11]. ZnO seeds are required to initialize the oriented nanowires growth. The solution containing zinc nitrate hexahydrate (Zn $(NO_3)_2.6H_2O$) and hexamethylenetetramine (HMT) is used. The deposition rate is mainly dominated by HMT decomposition rate, which is strongly temperature dependent. Therefore, by adjusting reaction temperature and time, ZnO nanostructures with different features can be obtained. The normal reaction temperature range is ranging from 60 ^{o}C to 200 ^{o}C [11]. ZnO nanostructures such as nanorods, nanowires [11-14], nanoplates, and nanospheres can be produced by varying the reaction temperature, time, solution pH value, Zn salt type, basic reagents, and additives. However, the ZnO nanostructures produced by this technique normally do not have good adhesion to the substrate.

(ii) Sol-gel method

Compared with other techniques, sol-gel process provides the great potentiality for the production of materials with homogeneous chemical composition [3-6]. ZnO thin films, nanorods [6] with preferred crystallographic orientation have been synthesized using the sol-gel method. The term sol is referred to a colloidal suspension. The formation of sol will develop inorganic networks, and as the networks form in a continuous liquid phase, it becomes gel. The precursors for synthesizing these colloids consist of a metal/metalloid surrounded by various reactive ligands. However, a number of factors such as pH of gel, temperature and time of reaction, reagent concentrations, catalyst nature and concentration, aging temperature and time, and drying have impacts on the characteristics and properties of a particular sol-gel inorganic network by affecting the rate of hydrolysis and condensation reactions. For example, ZnO nanorod and plate like structures on the SiO_2/Si substrate are grown using sol-gel approach employing zinc nitrate hexahydrate ($Zn(NO_3)_2.6H_2O$) as zinc precursor, deionized water as solvent and methylamine ($C_6H_{12}N_4$) as stabilizing agent. The zinc precursor and$C_6H_{12}N_4$ solution were used in equi-molar (0.01 mol/L) concentrations. After making homogeneous precursor solution using magnetic stirring at 60 ^{o}C for 2h, it was aged for 24h at room temperature to obtain homogeneous clear gel. Neutral (pH=7) and acidic (pH=6, by adding HNO_3) gel precursors were used to get different zinc oxide nanostructures. The cleaned and etched Si substrate was immersed in the gel precursor and heated in the oven at 90^{o}C for 2h. Thereafter Si was removed from the gel precursor and dried in the oven at 108^{o}C followed by annealing in the quartz tube at 500^{o}C for 4h under oxygen flow. Neutral solution (pH=7) produces rods, while acidic (pH=6) generates rods as well as plate like structures. Huang et al. reported a template-free sol-gel technique for controlled growth of ZnO nanorod arrays [16].

3. Opto-electronic applications of ZnO nanostructures

Zinc oxide nanostructured material has numerous potential applications in photonics, electronics, optoelectronics, sensors, energy storing and harvesting device fabrications etc. Zinc oxide has excellent transparency in the visible, while good absorbance in the UV region

therefore, used as window and sunscreen material. Instead of high transparency it has several other favourable properties such as high electron mobility, wide bandgap, strong room-temperature luminescence, etc. These properties are already used in emerging applications for transparent electrodes in liquid crystal displays and in energy-saving or heat-protecting windows, and electronic applications of ZnO as thin-film transistor and light-emitting diode. Here, a few potential optoelectronic applications of ZnO are discussed under the following sections.

(i) Photo detector

Photo detection is another promising opto-electronic application of ZnO nanowires. The UV detector utilizes the electric potential of the ZnO nanowires changed under UV irradiation. In 2009, Chenget al. constructed a UV photo detector by contacting a circular spiral structure ZnO nanowire with 30 nm IrO_2 electrodes. The current (I) -voltage (V) measurement showed that the photo-generatedcurrent reaching $5.1x10^{-7}$A, under a bias voltage of 5 V, and the photocurrent being 2 orders of magnitude larger than the dark curve [17]. Li et al. proposed ZnO bridging nanowire structures for nanowatt UV detection. The device exhibited drastic current changes (10 -10^5 times) under a wide range of UV irradiance (10^{-8} - 10^{-2} Wcm^{-2}). Moreover, the detector showed fast response (rise and decay times of the order of 1s) to UV illumination in air [18]. Yang et al. fabricated a simple self-assembled lateral growth ZnO nanowire photo detector with the photocurrent of the ZnO nanowires under UV illumination being twice as larger as the dark current with a bias voltage of 5 V [19]. Lin et al. reported that loading of Ag particles in ZnO nanowires produces an enhanced photo response [20]. Chang et al. combined the ZnO nanorods with grapheme enabling the visible blind UV sensor to reach 22.7 A W^{-1} [17].

(ii) Solar Cell

Various forms of ZnO morphologies and sizes significantly contribute to the novel characteristics of the devices. ZnO arrays are considered promising photo anode material for 3rd generation solar cells (Dye solar cells, Quantum dot solar cells) because of their highly controllable 1D single-crystalline nanoscale morphology which can provide direct electron transport pathways for photo-generated electrons [1,2]. In order to improve the DSSC/QDSSC efficiency, much work has been reported on modifying ZnO by doping with various dopants such as Sn, Al, Ga, F, In and Cu. In 2010 Lupanet al. electrodeposited the well-aligned arrays of ZnO on ITO-coated glass for dye-sensitized solar cells. The maximum overall photovoltaic conversion efficiency was 0.66% at 100 mW-cm^{-2} [21]. In 2008, Cheng et al. fabricated DSSCs using solvothermally grown branched ZnO nanowires. The short-circuit current density and the energy conversion efficiency of the branched ZnO nanowire DSSCs are 4.27 mA-cm^{-2} and 1.51% [22]. Sudhagar et al. reported branched jacks-like ZnO nanorods architecture as a photo anode in dye-sensitized solar cells and the result exhibited a higher conversion efficiency of η = 1.82% (Voc= 0.59 V, Jsc = 5.52 mA-cm^{-2}) than that of the branch-free ZnO nanorods electrodes (η =1.08%,Voc =0.49 V, Jsc = 4.02 mA-cm^{-2})[23]. In 2012, Ameen et al. synthesized tin (Sn) doped zinc oxide (ZnO) nanostructures by the hydrothermal method and the photovoltaic performances of Sn doped ZnO derived photo anodes were studied. The DSSC with Sn-ZnO photo anode yields the highest power energy conversion efficiency (solar-to-electricity conversion efficiency) of ~1.82% with short circuit current (JSC) of 5.1 mA-cm^{-2} , open circuit voltage (VOC) of 0.786 V and fill factor (FF) of 0.45, which was higher than that of DSSC with ZnO photo anode [24]. Wang et al. examined the effects of Sn element on the characteristics and electrochemical properties of ZnO spherical particle used as dye sensitized solar cells (DSSCs) photo anode. They observed that the efficiency of dye-sensitized solar cells increased with the addition of Sn element and the SZO4 (Sn:Zn = 4 wt.%) based DSSC had the highest power energy conversion efficiency of 0.80%, which is greatly increased compared to that of the DSSC based on ZnO (0.28%) [25].

Jian Chang et al. (2018), Co–Ni/carbon aerogel composite with a unique three-dimensional network structure and high specific surface area was prepared through simple ion exchange and carbonization of low-cost sodium alginate supramolecular hydrogels. Using this metal/carbon aerogel composite as the counter electrode of ZnO-based DSSCs, a photoelectric conversion efficiency (PCE) of 5.08% was obtained [26].

4. Conclusions

Zinc oxide is one of the best wide bandgap semiconductors materials with advanced technological applications in the development of semiconductor laser diodes, light emitting diodes, transistors/FETs, Solar cells for energy harvesting, Lithium ion and fuel cells for energy storage, sensors (Physical, biological as well as chemical), hydrogen generation and its storage, environmental pollution monitoring and biological/medical applications. It provides material for laser diodes with broad spectral coveragefrom deep UV to near IR, white as well as colored LEDs. As the highest conversion efficiency of zinc oxide based DSCs have reached upto 5-8% yet, which is too lower than that based on the titanium dioxide base DSSCs, but it is expected that zinc oxidemay be used to replace Si based costly solar cells with high efficiency. Instead of technological and biological applications it has also tremendous industrial applications. There is large number of cheap and simple available physicaland chemical, solution and vapor phase routes for the synthesis of wide morphology ofzinc oxide nanostructures with great optoelectronic, electronic, spintronic and optical properties, which makes it more popular amongst the researchers.

Acknowledgement

Dr. Santhosh Kumar A wants to acknowledge SERB-NPDF project (PDF/2016/004094).

References

1. Colodrero et al., Adv. Mater., 2009, **21**, 764–770.
2. M. Gratzel et al., Nature., 2001, **414**, 338–344.
3. Mehrabianet al., Physica E: Low-dimensional Systems and Nanostructures, 2011, **43**, 1141–1145.
4. JagadishChennupatiet al., 2006, Zinc Oxide Bulk, Thin Films and Nanostructures: Processing, Properties, and Applications. Elsevier
5. Yi et al., Semicond. Sci. Technol., 2005, **20**, S22.
6. Wang et al., J. Am. Chem. Soc., 2005, **127**, 7920–7923.
7. Chu et al., Nanoscale., 2012, **4**, 1471–1475.
8. Huang et al., Adv. Mater., 2001b, **13**, 113–116.
9. Zeng et al., Appl. surf. sci., 2005, **250**, 280–283.
10. Zhang et al., Sci. China. Ser. D., 2009, **52**, 883–887.
11. AS Kumar et al. ElectMateLett, 2014, **10** (4), 753-758.
12. AS Kumar et al. Journal of Optoelectronics and Advanced Materials, 2014, **16** (43987), 547-553.
13. AS Kumar et al. IOP Conference Series: Materials Science and Engineering, 2015, **73** (1), 012077
14. Vayssieres et al., J. Phys. Chem., B, 2001, **105**, 3350–3352.
15. Greene et al., Inorganic chemistry., 2006, **45**, 7535–7543.
16. Huang et al., Appl. Surf. Sci., 2011, **257**, 6026 – 6033.
17. Chang et al., Nanoscale., 2011, **3**, 258–264.
18. Lu et al., Semicond. Sci. Technol., 2009, **24**, 075005
19. Yang et al., Thin Solid Films., 2010, 518, 328–7332.
20. Lin et al., 2009, Appl. Phys. Lett., 94:172103–172103
21. Lupanet al., J. Photochem. Photobiol. A., 2010, **211**, 65–73.
22. Cheng et al., J. Phys. Chem. C., 2008, **112**, 16359–16364.

23. Sudhagar et al., Mater. Res. Bull., 2011, **46**, 1473–1479.
24. Ameen et al., Chem. Eng. J., 2012, 187, 351–356.
25. Wang et al., ElectrochimicaActa., 2013, **111**, 797–801.
26. Jian Chang et al., New J. Chem., 2018, **42**, 16329-16334

Geochemical Aspects of Groundwater Bearing and Petrological Infulence on Souhern Parts of Nalgonda, Telangana

Musini Venkateshwarlu[1], K. Suresh[1] and Y S Reedy[2]
[1]Department of Civil engineering, CMR College of Engineering & Technology (A), Kandlakoya (V), Medchal Road, Medchal District, Hyderabad -501401. Telangana. India.
[2]Department of Physics, Chaitanya Bharathi Institute of Technology (A), Gandipet, Hyderabad 500075, Telangana State, India

Corresponding Author: venkatmusini@gmail.com

Abstract

This paper intends to assess domestic, drinking agricultural usage water quality of region. The area is a part of the stable peninsular shield and is a granitic terrain underlined by unclassified crystalline of Precambrian age. The ground water quality data were used to study chemical parameter hardness, sodium absorption ratio, sodium percentage sodium carbonate, magnesium ratio corrosivity ratio,chloro alkaline indices and permeability index found to be based on evaluation of the chemical parameters quality of water is fit for drinking, industrial and agriculture uses, except in a few isolated locations. According to Gibbs diagram most of the sample fields in rock dominance. Wilcox's diagram indicates that less than 50% of samples fall in excellent to good and good to permissible types.

Keywords: Hydro geochemistry, Groundwater quality, Nalgonda, Telangana

1. Introduction

India holds for 2.2% of the global land and 4% of water resources and has 16% of the population. It is estimated that, one third of world's population uses groundwater for drinking purpose [1]. Geochemical study of major ions in groundwater of wailpali area, Nalgonda district of Telanagana State had been carried out in addition to fluoride ion distribution. Low Fluoride water (less than 0.6 mg/lit) causes dental problems and high fluoride (greater than 1.2 mg/lit) results in fluorosis [2, 3]. In India about 62 million people are affected with dental, skeletal and/or non skeletal fluorosis [4]. There are more studies in literature on the fluoride occurring minerals associated with granitic gneiss and charnockites in different parts of Andhra Pradesh [5,6]. An attempt has been made to investigate the fluoride ion distribution in the groundwater of study area to demarcate the safe zones and unsafe zones with references 25 groundwater samples fluoride content.

Study area located in the western part of Nalgonda district and lies between latitudes $17^0$00` - $17^0$10` N and longitudes $78^0$48' – $79^0$00' E covering Survey of India top sheet 56 K/16.Study area is underlain by Archaean Group of rocks represented by older Group of rocks and Peninsular Gnessic Complex. Older rocks include hornblende schist biotite schist and amphibolites, while peninsular gneissic complex is represented by pink and porphyritic granite gneisses, pink granites and injuctions of quartz, pegmatites and epidote veins. Dolerites mark the last phase of igneous activity in the area and they cut across all the above rocks. The integrated groundwater prospects maps are preferred by using different geochemical studies [7].

2. Materials And Methods

25 samples were taken from study area located in and around Wailpalli area, Nalgonda District of Telangana, Samples were analyzed for major ions by employing standard methods (APHA, 1985). pH and Electrical conductivity (EC) were measured using pH and conductivity meters. Total Dissolved Solids (TDS) were computed by multiplying the electrical conductivity by a factor (0.55 – 0.75) depending on the relative concentration of ions. Fluoride was analyzed by Spectrophotometer by Zirconium Alizarin Red S method. Total alkalinity (TA) were estimated by titrating with H_2SO_4, Total hardness (TH) as $CaCO_3$ and Calcium (Ca^{+2}) were analyzed titrimetrically, using EDTA. Magnesium was computed taking the difference between TH and Ca^{+2} values. Sodium and Potassium were analyzed by Flame Photometer. Chloride ion was estimated by standard $AgNO_3$ titration. All the parameters are expressed in milligrams per liter (mg/l) except pH.

3. Results And Discussions

The analytical results of groundwater samples are presents in (table1). Groundwater has pH in the range of 7.2 to 8.36 indicating acidic to alkaline nature. The Total hardness varies from 90 to 820 mg/l .Hardness of these samples were correlated with standard values [8].This results shows that 75.86 % of samples belongs to hard category. Carbonate and bicarbonate ions in groundwater of the study area vary from 0 to 45 mg/l. and 134 to738 mg/l respectively (table-1). It is observed that bicarbonate in all the groundwater samples of the area are in desirable limits of 1000 mg/l. The Concentration of Sodium varies from 18 to 438 mg/lit and in within the prescribed limit of 200 mg/lit for drinking water [3], Potassium concentration various from 0 to mg/lit to 2.1 mg/lit are within the acceptable limit of 10 mg/lit to 15 mg/lit and the calcium concentration varies from 26 mg/lit to 62 mg/lit which is again within the prescribed limit of calcium in drinking water is 75 mg/lit [9]. It is observed that 79.37% of samples are within prescribed limit. The magnesium varies from 1 mg/lit to 177 mg/for lit. The prescribed limit of magnesium in drinking water is 30 mg/lit.[9] and it is observe that 56.89% of the samples are in the study area exist the desirable limit prescribed for drinking purposes. . The concentration of fluoride varies from 1 to5.8 mg/lit (table-1). It is observed that fluoride in the ground water samples of the area of investigation are in desirable limits of 1.5 mg/lit for drinking purposes [10]. The SAR values lies between 0.60 to 6.65 in the water samples collected from the study area. Electrical conductivity values and SAR values, show that 80% of the total groundwater. RSC values lies between 0 to 3.4 meq/liter from the water samples taken (Table-1). In the present study, half of the water samples shows values less than 1.25 meq/liter. The Magnesium ratio are found to be more than the permissible limit in most of the water sample.Corrosivity ratio values of groundwater of the study area are given (table 1).The positive values of base exchange reaction are signs of chlore-alkaline dis-equilibrium. Gibbs is found that most of the water parameters in the study area falls under the rock dominance.

Table 1: STATISTICALPARAMETERS OF GROUND WATERSAMPLES

STATISTICALPARAMETERS OF GROUND WATERSAMPLES													
statistical analysis	**PH**	**EC**	**TH**	**Ca**	**Mg**	**Na**	**K**	**CO_3**	**HCO_3**	**CL**	**SO_4**	**NO_3**	**F**
Mean	7.929	1110.8	295.6	43.28	45.48	119.29	2.12	0	433.56	106.48	35.048	32.72	3.036
Median	7.96	968	235	42	33	99	0.66	0	438	60	19	20	3

Mode	8.12	1150, 820	235	44, 60, 32	33	161, 21, 35	0.27	0	317, 445	60	12, 26	14	4, 2
Standard deviation	0.311	685.66	140.3	10.45	34.75	94.83	6.73	0	147.05	142.03	38.98	34.46	1.23
skewness	-0.67	1.86	1.91	0.29	1.99	1.6	4.55	0	0.22	2.68	1.79	2.47	0.07
Range	1.11	1524	730	36	176	420	2.1	0	604	642	134	154	4.8
Minimum	7.25	526	90	26	1	18	0	0	134	14	10	8	1
Maximum	8.36	2050	820	62	177	438	2.1	0	738	666	144	166	5.8

4. Conclusion

Groundwater is having fluoride concentration associated with high sodium and low calcium. Present study on groundwater quality with reference to fluoride ion concentration in Wailpalli area indicates that the groundwater is acidic to alkaline in nature. Increase of fluoride content in groundwater. Few samples of the fluoride content are higher than the optimal limit. Gibbs diagrams most of the sample fields in rock dominance. Wilcox's diagram indicates that less than 50% of samples fall in excellent to good and good to permissible types. The geochemical character of ground water is reflecting the nature of the rocks in which it was occurred.

Acknowledgements

We express our thanks to Ch. Gopal Reddy, Secretary, CMRGI, Principal and HOD, CMR College of Engineering &Technology (A), Hyderabad, for providing necessary Laboratory facilities, for help and encouragement to publish this paper.

References

1. R Nickson *et al.* Appl Geochem , 2005, 20:55–68
2. WHO. (1996). "Guidelines for Drinking Water Quality". 2nd edition. Health criteria and supporting information Geneva. 231-237
3. WHO. (2004). "Guidelines for Drinking Water Quality". 3rd edition Geneva.
4. A K Susheela, current Sci., 1999, 77: 1250- 1256,
5. Ramamohan Rao *et al.,* India.Envron.Geol.1993, 21: 84-89.
6. Subba Rao *et al.,* J. Environ. Hydrol., *1998.* 6: 1-5.
7. M. Venkateshwarlu *et al.*, Indian J. Environmental protection, 2020, 40(8), 887 -891.
8. Sawyer, C.N. and Mc carty, P.L. (1967). "Chemistry for pamtary engineers". *Ind. D. Mc Graw hill,* New York", 518 p
9. ISI (1983): Indian standard specification for drinking eater. IS10500. New Delhi
10. BIS (2003), Drinking water Specification, Bureau of Indian Standards, New Delhi IS: 10500, 11.

Assessment of Water Quality Index and Monitoring of Pollutants by Physico-Chemical Analysis in Water Bodies

Musini Venkateshwarlu[1], Y. S. Reddy[2], B Prasad[1] and A.P. Ravi Chandra[1]
[1]Department of Civil engineering, CMR College of Engineering & Technology (A), Kandlakoya (V), Medchal Road, Medchal District, Hyderabad -501401. Telangana. India.
[2]Department of Physics, Chaitanya Bharathi Institute of Technology (A), Gandipet, Hyderabad-500075, Telangana State, India

Abstract

Groundwater is a major source for domestic, drinking and irrigation purposes in Kistapur village, Medchal, Telangana. 22 samples were collected through bore wells in the surrounding areas of kistapur and tested for pH, acidity, alkalinity, DO, BOD, COD, EC, Turbidity, Ca^+, Mg^+, Na^+, Total hardness, K^+. The test results are favourable and are in permissible limits which can be used for drinking, domestic and irrigation purposes. This tests showed that the compositions of $Ca^+ > Mg^+ > Na^+ > K^+$. The groundwater is polluted due to effluents from factories nearby the study area. After selecting some important water quality parameters, the calculation of Water Quality Index (WQI) was done. Hence the use of waters of open wells in and around the industrial area to determine the quality of groundwater. Investigations of location of points & distribution of groundwater is done by using GIS and are interpolated using inverse distance weighted (IDW may cause health hazards to nearby inhabitants. So it is necessary to control the contaminant transportation and ground water pollution in and around study area.

Keywords: Physico-chemical analysis, Groundwater, IDW, WQI, GIS, Kistapur, Medchal, Telangana.

1. Introduction

Water is the most important source for livelihood in nature. As there is rapid growth in urbanisation, irrigation techniques, living standard of life, industrialisation, there is a need of excess quantity of water for various purposes. As water from many sources such as rivers, lakes, ponds etc are being used excessively and are contaminated due to wastes from factories, improper usage of water [1, 2]. Due to inadequate supply, they are depending on groundwater which is the primary source for domestic and irrigation in many parts of India. Knowledge of quality parameters result in knowledge of different characteristics which may affect health conditions of people living in the area [3]. The results which are obtained after testing are compared with the standard results given by the WHO and Water Quality Standards (IS 10500-2012.) [4].

The study area falls in between latitude 17.6295^{o}N and longitude 78.5072^{o}E. It is 3 Km from Medchal located in Telangana. Its study area falls in the Survey of India topo sheet E44M10 and E44M5. Average annual rainfall is 833 mm in which July is the wettest month of the year and June to September contributes a rainfall of 652mm. Geomorphology of the area indicates that the present-day landforms are the products of different geomorphic processes such as erosion, deposition, crustal movements coupled with climatic changes operating on the surface.

The study area consists of mainly pink granites which are highly weathered and fractured. Number of intrusive like dolerite dykes, pegmatite veins and quartz reefs/veins are common in this area [5, 6]. Groundwater Quality studies with reference to drinking and irrigation purposes in different regions were carried out by [7, 8, 9, and 10].The integrated groundwater prospects maps are preferred by using different geochemical studies [11].

2. Materials and Methods:

21 samples were collected from underground through borewells, dug wells at different locations in Medchal, Telangana. They were stored in polyethylene bottles and stored at temperature of 15-20^{o} C. The samples were tested for parameters like pH, Electrical Conductivity (EC), Total Dissolved Solids (TDS), Alkalinity, Acidity, Dissolved Oxygen, BOD, COD, Turbidity, Calcium ($Ca^{+)}$, Magnesium (Mg+), Sodium (Na+), Total Hardness (TH), Potassium (K+). PH, EC, TDS were measured using pH/EC/TDS meter immediately after bringing the samples from the locations in bottles. Ca+, TH were measured using standard EDTA solution using Eriochrome Black T-Indicator. Na+ and K+ were measured using the technique of emission flame photometry. CO_3^{-2}, HCO_3 were measured using titration method using phenolphthalein as indicator. Alkalinities, Acidity were measured by titration method using phenolphthalein, methyl orange indicators using NaOH, H_2SO_4 solutions. DO was measured using titration method by Winkler. Turbidity was measured using Nephelometric turbidimeter. BOD and COD were measured using titration method in which Phosphate buffer, Magnesium sulphate, Calcium chloride, Ferric Chloride were the reagents used and Sodium thiosulphate was the titrant used.

Calculation of Water Quality Index

The Weight arithmetic water quality index meth has been used for calculation of WQI

The overall WQI is determined by using Equation:

$$WQI = \Sigma Qi\ Wi / \Sigma Wi$$

Unit weight was calculated as following

$$Wi = Wi / \Sigma Wi$$

Where, Wi is the relative weight, Wi is the weight of each parameter and Σ Wi is the sum of weights of all parameters.

Quality rating Qi was calculated as below:

$$Qi = (Vi / Si)\ X100$$

3. Results and Discussion

The minimumium, maximum, mean median and standard deviation values generated from the analysis of the samples are presented in table The pH indicates the acidity or alkalinity material present in the water. The pH values of the groundwater vary from 8-10 with a mean pH of 8.6 which is alkaline in nature and it tastes bitter. The permissible limit for drinking water should be in the range of 6.5-8.5. The groundwater shall be treated before consuming as its value is above the permissible limit. Acidity of water is the capacity to neutralize bases. The Acidity of the Groundwater samples varies from 20-150 mg/l with a mean value of 71.42 mg/l. The limit for drinking water should be Alkalinity of water is the capacity to neutralize

acids. The Alkalinity of the Groundwater samples vary from 20-128 mg/l and mean value was 68.85 mg/l. The permissible limit of drinking water should be less than 250 mg/l and the samples are safe for drinking purposes. The TDS is a sum of cations and anions in the water. It consists of Inorganic salts and some organic salts. The Groundwater samples have a TDS value varying from Conductivity is the capacity of water to carry an electrical current. The Groundwater samples have an EC values varying from 0.89-13 µS/m with a mean value of 2.6 mS. the permissible value of EC is 1500 mS/cm[12]. The Groundwater Samples are safe for drinking purposes. Amount of Dissolved Calcium and magnesium in water represents the TH of water. The Groundwater samples have a TH varying from 72.56-915.82 mg/l with a mean value of 465 mg/l. The permissible limit of TH in drinking water is 600 mg/l. hence the groundwater samples can be used for drinking purposes. Calcium concentrations vary from 80.2-150 mg/l with a mean value of 125.5 mg/l. The permissible value of calcium is 200 mg/l and the samples are found to be safe for drinking purposes. Magnesium concentrations vary from 36-108 mg/l with a mean value of 70.7 mg/l and the permissible value for magnesium is 30 mg/l [13]. Which are not safe for drinking purposes? Due to relative abundance in rocks the values of calcium exceed the magnesium values. Sodium and magnesium concentrations are due to mineralogical origin of soils and Soluble Na^+ and K^+ are results from weathering of feldspar. Na^+ values vary from 15-51 mg/l with mean value of 34.28 mg/l. The permissible value of Sodium in water is 45 mg/l. K^+ values vary from 2-26 mg/l with mean value of 5.21 mg/l. The permissible value of potassium in water is 10mg/l. Both sodium and potassium are in the range and Groundwater samples can be utilised for drinking purposes. Carbonates of water samples vary from 24-66 mg/l with mean value of 36.48 mg/l and Bicarbonates values vary from 79.31-292.84 mg/l with mean value of 167.28 mg/l.BOD is the most widely used test to establish the concentration of organic matter in waste water samples[14,15]. It is based on the principle that if sufficient oxygen is available, aerobic biological decomposition by microorganisms will continue until all waste is consumed. The Groundwater samples have a BOD value varying from 50.6-487.6 mg/l with a mean value of 210 mg/l. COD is the alternative test to BOD for establishing the concentration of organic matter in wastewater samples. The PH exhibits positive correlation with BOD (R2= 0.5) in fig.1.COD test can be completed within few hours compared to BOD. The Groundwater samples have COD values varying from 50.72-260 mg/l with a mean value of 80 mg/l. It is observed that the PH positive correlation BOD (R2=0.23), COD (r2=0.02) in fig.1 -3.The water can be safely discharged into streams and this water samples cannot be utilised for drinking as organic matter is very high. The amount of oxygen present in the water in dissolved state is DO. The Groundwater samples have DO values varying from 6-25 mg/l with mean value of 15.5 mg/l. Therefore, the water contains sufficient amount of DO for growth of aquatic life. This water samples can be used for drinking. The presence of dissolved solids in water may affect taste. Water with extremely low concentrations of TDS may also be unacceptable due to its flat, insipid taste. The Groundwater samples collected from locations have a TDS value varying from 637-8450 mg/l with a mean value of 1691.90 mg/l. Though some values have TDS values which are permissible for drinking purposes the samples S-14 & S-15 have a high TDS value of 8450 mg/l which are unacceptable for drinking purposes. The amount of suspended particles in the liquid. The Groundwater samples have a value of 2-18 NTU with a mean value of 5.2 NTU. The WQI of the groundwater ranged between87.2 to 396.5 that indicates the pollution level is very high [16, 17].

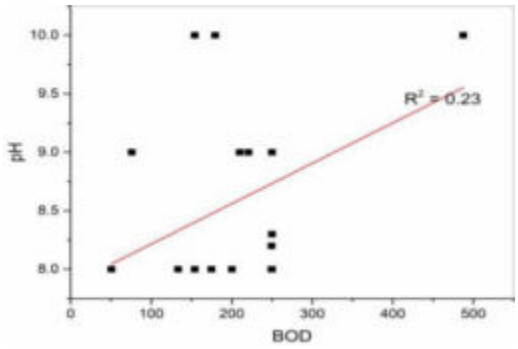

Fig 1.Scatter diagram of P^H Vs BOD Vs BOD

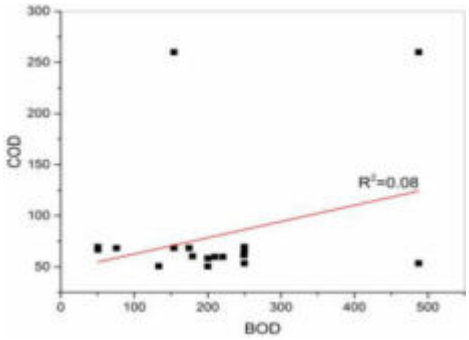

Fig 2. Scatter diagram of COD

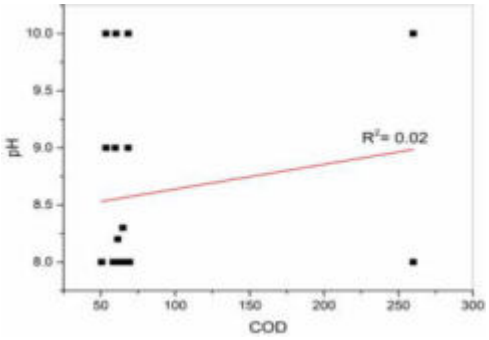

Fig 3.Scatter diagram of P^H Vs COD Vs BOD

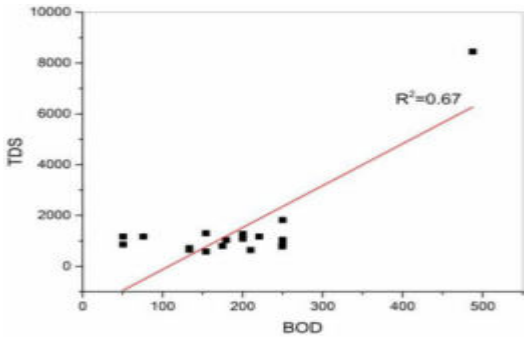

Fig.4. Scatter diagram of COD

Table 1 .Descriptive Statistics of Physico- Chemical Quality of Ground water

Sl. No.	Water Quality Parameter	W.H.O. standards in ppm		I.S.I. standards in ppm		Analysis of the area investigated	
		Min.	Max.	Min.	Max.	Min.	Max.
1	pH	6.5	8.5	6.5-8.5	6.5-9.2	8	10
2	EC	500	2000	500	1500	0.89	13
3	Ca	75	200	75	200	80.2	195
4	Mg	50	150	30	100	36	108
5	Na	-	200	-	200	15	53
6	K	-	12	-	12	2	26
7	HCO_3	500		-	-	79.37	292.84
8	TDS	-	500			637	8450

9	TH	-	200		300	120.7	915.8
10	Alkalinity	20	128			20	128
11	acidity	20	150			20	150
12	BOD	30				50.6	457.6
13	COD	250				50.3	260
14	DO					6	15.4
15	Turbidity		5		5	2	18

4. Conclusion

The groundwater sources in and around Kistapur area, Medchal district of T.S., have been evaluated for their chemical composition and suitability for drinking and irrigation purposes. In the study area malignity of groundwater samples are within permissible limits prescribed for drinking water. The source of chloride is more due to the weathering of minerals present in the rocks of the study area. The addition to the TDS content in increased due to natural sources, domestic sewage and industrial effluents. The BOD/COD found in all cases as less than 0.50, which indicate the poor biodegradability of the waste, need more attention in the treatment processes and to be treated before its final disposal. The WQI values for 88% locations are higher exceeding 100, the upper limit for drinking water. From the result it is concluded that the WQI for Groundwater water in all locations were founds unsuitable for drinking purpose.

Acknowledgments

We express our thanks to Ch. Gopal Reddy, Secretary, CMRGI, Principal and HOD, CMR College of Engineering and Technology Hyderabad, for help and encouragement to publish this paper.

References

1. N Aghazadeh and A Mogassem, Environmental Monitoring and Assessment, 2010, doi: 10.1007/S10661-0101574-4.
2. Z Ahmad and A Qadir, Environmental Monitoring and Assessment, 2011, 175(1-4), 9.
3. D Alexakis, Environmental Monitoring Assessment, 2011, doi: 10.1007/S10661-011-1884-2.
4. WHO (2004). Guidelines for drinking water quality. Geneva: world Health Organization.
5. R M Garrers, (1967), Genesis of some ground waters from igneous rocks .In: Ahelson ph.D Researches in Geochemistry, Wiley, New York, 405.
6. V K Garg *et al.* Environmental Geology, 2009, 58, 1329.
7. E Craig, and M P Anderson, The effect of Urbanization on Groundwater Quality – A case study. Groundwater, 1979, 17, 5, 456-462.

8. S N Davis and RJM Dewiest (1966), Hydrogeology, New York, Wiley, 463.
9. R M Garrers, (1967), Genesis of some ground waters from igneous rocks .In: Ahelson ph.D Researches in Geochemistry, Wiley, New York, 405
10. V K Garg *et al.*, Environmental Geology, 2009, 58, 1329.
11. M. Venkateshwarlu *et al,* Indian J. Environmental protection, 2020, 40 (8), 887 -891.
12. APHA (1992), Standard Methods for the Examination of Water and Wastewater, Washington D.C: American Public Health Association.
13. BIS (2003), Drinking water Specification, Bureau of Indian Standards, New Delhi IS: 10500, 11
14. WHO (2004). Guidelines for drinking water quality. Geneva: world Health Organization.
15. WHO (1983). Guidelines for drinking water quality. Geneva: world Health Organization.
16. Mihaiescu Tania, Mihaiesu radu, Varban Dan, Varban rodica, Mihaiescu Mihnea. Water quality assessment of the Nadas River in terms of NSF water quality index. Analele universitapii din Oradea, facicula protecpia mediului, xxi 2013.
17. C Chaterjee and Raziuddin, Environmental and Pollution technology, 2002, 1 (2), 181-189.

Laser-induced breakdown spectroscopy: a potential tool for depth-profiling of quartz

Sonali Dubey[1], Abhishek K. Rai[2], Rohit Kumar[3], Jayanta K. Pati[2], Awadhesh K. Rai[1]
[1]Department of Physics, University of Allahabad, Prayagraj-211002, India
[2]Department of Earth and Planetary Sciences, Nehru Science Centre, University of Allahabad, Prayagraj-211002, India
[3]Department of Physics, CMP Degree College, University of Allahabad, Prayagraj-211002, India
Email: sonalidubey193.sd@gmail.com

Abstract

In this work, the capability of depth profile analysis of Laser-induced breakdown spectroscopy has been demonstrated. The composition of the surface , as well as matrix elements of quartz using LIBS have been evaluated. Quartz is arguably the most abundant mineral on the earth. It is the mineral form of SiO_2, stable at low temperatures and pressures. Quartz is known to contain small but variable amounts of structurally substituted or interstitial ions. It formed under particular environmental conditions might be anticipated tocontaina reasonably constant and characteristic level of foreign matter. It can havetrace amounts of aluminium, alkalis, and transition elements. LIB spectra of quartz recorded in the wavelength range 230-850 nm reveals the presence of elements, Ca, Mg, Si, and O. The variation of elements from the surface to depth is subtle for visual inspection, but delicate observation of persistent line of elements in the spectra shows intensity variations in-depth profiling.

***Keywords**:* LIBS, Quartz, Multi-elemental profiling, Depth profile analysis

1. Introduction

Laser-induced breakdown spectroscopy technique has manifested its analytic potentialin the area of environmental analysis, space exploration, plants, nuclear materials, geological materials[1-2]. It is a rapidly growing technique for last few decades. LIBS gained wide attention from the geological world because of its simple, real-time, minimal destructive, field-portable nature. C. Liu*et al*. has used LIBS technique for Cd detection in the 12 soil samples [3].LIBS study of a meteorite sample from Dergaon, India by A. Rai *et al.*shows the presence of Ni, Cr, Co and Ir in the sample [1].

Natural quartz is a pure form of SiO_2 mineral, and it is rare. It can be found in various colours depending on the presence of minor mineral inclusions, crystal defects or colour centers. Amethyst, smoky quartz, rose quartz *etc.* are some varieties of coloured quartz. Some studies showed that trace element concentration of quartz might be used as geological indicators [4]. S. Klemme*et al*. have performed electron microprobe and oxygen isotope of quartz and said that the green colour of quartz was due to theacicular amphibole inclusions, whereas traces of Fe may be responsible for the purple colour of amethyst [5]. LIBS, in conjunction with discriminate function analysis, has been used for the qualitative analysis of five different quartz samples[6]. K. G.Suastika*et al.*analysed four different coloured amethyst using LIBS technique and detected Al, Ca, K, Fe, Gd, Ba, Si, Be, H, O, N, Cl and Pu with various emission intensities.

Quartz is unaffected by weathering and temperature changes due to its hard-crystalline structure. Previous studies demonstrated the presence of the small but variable amount of foreign elements in quartz, which motivated this work. In the present work, LIBS has been used for the analysis of major as well as minor elements of a pale green quartz

crystal. The point detection capability of LIBS has been used for the depth profiling of quartz.

2. Experimental

A quartz sample is provided by one of us (J.K. Pati). No sample preparation has been done.A detail about the experimental setup used for recording the LIBS spectra of quartz samples may be obtained from our previousworks [1-2]. It consists of an Nd-YAG laser source (Continuum Surelite III-10) with maximum deliverable energy 390mJ and a maximum repetition rate of 10 Hz. A convex lens of focal length 15 cm was used for focusing the laser on the surface of the sample. Emitted photons from plasma was collected by collection optics (CC52 collimator,Andor Technology) and fed to the Mechelle spectrograph(ME5000, Andor Technology) equipped with an ICCD camera (iStar334, Andor Technology). Gate delay and gate width were optimized to 1μs and 5μs, respectively, for better signal to noise ratio.LIBS spectra were recorded for 1st laser shot, 2nd lased shot, 3rd laser shot up to tenth laser shots by focusing the laser beam at the same spot/point of the sample surface, and the resulting spectra are analyzed to find the variation in the concentration of the elements from the surface to matrix(inside).

3. Results and Discussion

3.1 qualitative analysis

LIB spectra of quartz samples have been recorded in the wavelength range 200-850nm.For the surface analysis,the sample was continuously moving with the help of the sample stage such that every laser shot faces a new spot.

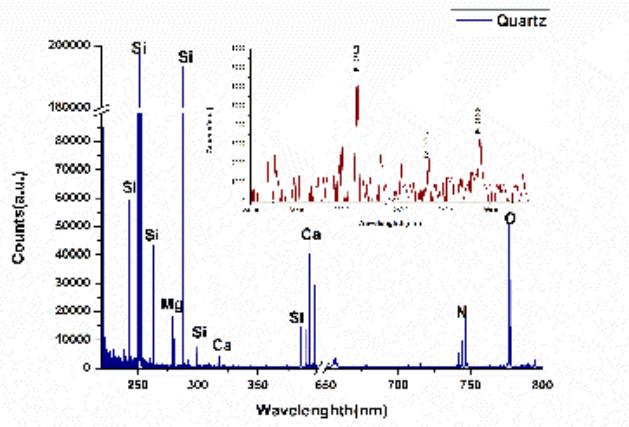

Figure 1: LIB spectra of quartz sample in the wavelength range 220-800nm showing the presence of Fe.

Accumulation of hundred laser shots has been taken for one LIB spectra, and an average of ten such spectra was used for the analysis of elements present on the surface of the sample.Spectral lines have been identified using the National Institute of Standards and Technology atomic spectroscopic database.

LIB spectra of quartz samples (Figure1) demonstrate the presence of spectral lines of Si, O, Ca, N, H, Mg. Quartz is a mineral form of SiO_2, elements other than Si and O may be impurity elements on the surface. Previously reported work found that the green colour of quartz is due to the presence of Fe on the interstitial site of the quartz structure [8]. Figure 1 showing the presence of the persistence line of Fe at 238.2, 259.3 and 259.9nm, which depict the presence of iron in green quartz.

3.2 Depth profile analysis

Depth profile analysis has been performed to ensure the presence of impurities inside the quartz sample. We focused our study on the presence of Ca and Mg, whether it is on the surface or in the matrix of quartz. Interference-free lines of Mg, Ca and Si at 279.5, 393.3 and 390.5nm, respectively chosen to check the shot to shot spectral intensity variation. LIB spectra of 1st, 2nd, 5th and 10th laser shot have shown in Figure 2. It depicts that Mg and Ca lines have maximum intensity in the first laser shot and decreasing with an increase in laser shots. In contrast, the intensity of the spectral lines of Si is increasing with increasing laser shots and it is maximum in tenth laser shot. Since quartz is found in metamorphic and volcanic rock, the constituent of the host rock may be found on the surface of the quartz. [9]

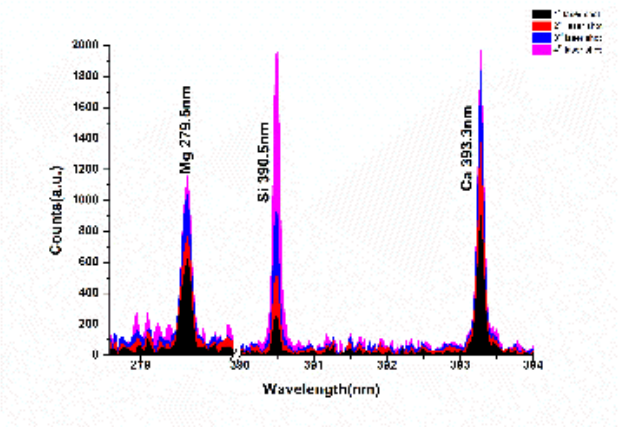

Figure 2: Comparison of LIB spectra of quartz sample for different laser shots

3.2 Matrix element analysis

The variation of intensity of different spectral lines of constituents of quartz has also been studied. The integrated intensity of Ca (422.6nm), Mg (279.5 nm), Si (288.1nm), O (777.7nm) spectral lines have calculated, and a graph is ploted between integrated intensity and the successive laser shots.

Figure 3: Variation of the intensity of elements in the LIB spectra of quartz with a successive laser shot

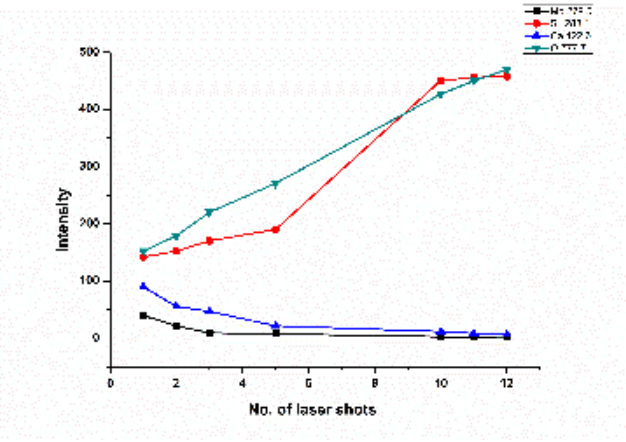

Figure 3 clearly shows that the intensity of Ca and Mg decreased continuously and became almost zero after the 10th laser shot. The spectral line intensity of Si and O, was increasing with successive laser shot and became almost constant to 10th laser shot. The impurity elements on the surface of quartz disappear after 10th shot, so it may be concluded that after 10th shot laser reaches the matrix of quartz, which is made up of SiO_2. At the same

time, impurity elements Ca and Mg on the surface of quartz becomes zero due to the removal of the impurity on the surface.

4. Conclusions

- In the present paper, identification of elements presents in the quartz has been performed using LIBS.
- LIB spectra containthe spectral signature of O, Mg,Si, Ca, Fe.
- The colour of pale green quartz may be due to the presence of Fe on the interstitial site of the structure.
- The study revels that Ca and Mg present on the surface of quartz as an impurity. These elements are constituents of the host rock
- Si and O are matrix elements of quartz with Fe as a substitute element on the interstitial site.

Acknowledgment

One of the authors, Ms. Sonali Dubey, is thankful to the UGC for the D. Philfellowship.

References

1. A. K. Rai *et al.,* Molecules., 2020, **25** (4), 984
2. R. Kumar *et al.,* Spectroscopy Letters., 2014, **47**, 554
3. C. Liu *et al.*, Appl. Phys. B., 2020, **126**, 153
4. M.R. Ackerson et al., Geochemistry, Geophysics, Geosystems., 2015, **16**, 1894
5. S. Klemme *et al*., Minerals., 2018, **8** (11), 487
6. A. Ali et al., J. Spec., 2016, **7**
7. K. G. Suastika *et al*., J.Phy. S. Indonesia, 2019, **1**(1), 9
8. U. Henn *et al.,* J. Gemmol., 2012, **33**, 29
9. W. H. Dennen *et al.*, Geological Society of America Bulletin, 1964, **75**, 241

Sustaining the Environment using Vermicomposting Green Technology

G. Subbulakshmi

Assistant professor, Department of Chemistry, Jain University, Bangalore, India

Email: g.subbulakshmi@jainuniversity.ac.in

Abstract

Increasing population, urbanization and industrialization have led to an everlasting generation of wastes there by polluting the environment. Disposal and environmental friendly management of these wastes are becoming a serious global problem A newer branch of biotechnology called 'Vermiculture Technology' is emerging by the use of earthworms to solve various environmental problems. Vermicomposting has been identified as one of the potential methods of solid waste management as it is cost effective, eco-friendly technology and it is free from toxic chemicals. The process of vermicomposting helps in replenishment of plant nutrients, maintains soil health, reduces the pollution problem and creates employment opportunities therefore it can be recognized as a strategy for sustainable organic farming. The present study has been carried out by the production of vermicompost from solid wastes using earthworm species and also to determine the rate of vermicompost on the growth and better yield of plants.

Keywords: Solid Biomass, Earthworm, Vermicompost, Plant growth

1. Introduction

Vermicompost Technology (Vermitechnology) through Earthworm is indigenous, economic and easy technology to convert all biodegradable waste into best quality organic manure. Wastes are nothing but misplaced resources. A large volume of organic matter is generated from agricultural activities, dairy farms and animal shelters which are usually dumped in corners where it putrefies, usually emanating foul smell. These Renewable resources turn into valuable wealth product by using Vermicomposting technology [1,2]. This approach reduces pollution and provides a valuable substitute for chemical fertilizers. This process is profitable at any scale of operation, provided proper process parameters are maintained. Vermi compost is a valuable input for sustainable agriculture and wasteland development [5,6]. It was proved that the Vermicomposting of floral waste with cow dung at 50:50 and 60:40 appears to be the most promising high value bio-fertilizer. This not only increases the plant growth (as seen in tomato plant) and productivity by nutrient supply but also it is cost effective and pollution free. A novel approach technology called vermicomposting method [3]. Encourages environmental sustainability by converting a waste to a usable product that improves our environment. The important characteristics such as N, P, and K, Ratio exhibited the increasing order in the entire composting bin. Both vermicompost and its body liquid (vermiwash) are proven to be growth promoters & protectors for crop plants [4].This project is Eco-friendly and one stroke solution of most of the burning problems like pollution, unemployment, upliftment of rural poor, poor soil fertility, wasteland development, poor health, declining yield, more use of chemical fertilizers and pesticides etc. So, we can solve these problems by establishing Vermicomposting concept in

a particular region and thereby total biodegradable wastes can be converted into money i.e. best quality organic manure, employment to unemployment youth.

2. Materials and Methods

Before composting Segregation process of vegetable biomass should be done. Composting can be done in pits under shade, in a prominent level, to prevent water stagnation in pits during rains. Make small holes on the side of pits to connect outlet PVC Pipe for collecting vermiwash. Soil should be kept as bedding material at the bottom of the Pit. Followed by a layer of soil to a total thickness of 6-7 cms. Pits was filled by organic waste (4- 5 cm length). Cattle dung (dry) are then scattered over the soil and covered with a 10cm layer of hay. Introduce earthworms (1kg) and cover the pits with jute cloth cover and wire mesh to protect earthworm from birds, moles, and shrews. Water is sprayed till the entire set up is moist but not wet. Less water kills the worms and too much water chases them away. Provide a shed over the compost to prevent entry of rainwater and exposure to direct sunshine. Sprinkling of water should be stopped when 90 % bio-wastes are decomposed. Maturity could be judged visually by observing the formation of granular structure of the compost at the surface of the tank. Normally after 60 days, organic refuse changes into a soft, spongy, sweet smelling; dark brown compost will be ready for collection. Harvest the Vermicompost by scrapping layer wise from the top of the tank and heap under shed. This will help in separation of earthworms from the compost. Sieving may also be done to separate the earthworms and cocoons. The temperature and moisture content were maintained by sprinkling adequate quantity of water at frequent intervals.

3. Result and discussion

Many Researchers have recognized the capability of using earthworms as a management technique for numerous wastes into valuable fertilizer. Vermicomposting results in the bioconversion of the waste into three useful products, vermicompost, earthworm biomass and vermiwash .Vermicomposting done for six weeks and sample were collected from the pit and analysed for their nutrient composition.

Table 1: Parameter analysis

S.No	Parameters	Instruments Used
1	pH	pH meter
2	Electrical conductivity	Digital EC meter
3	Total Kjeldahl Nitrogen (TKN)	Micro Kjeldahl method
4	Total Phosphorus (TP)	spectrophotometrically
5	Total Potassium (TK)	Flame Emission Technique
6	Total organic carbon (TOC)	Walkey and Black’s method

Reduction in pH is due to microbial decomposition during the process of composting. The lowering of pH due to productions CO_2 which was an acidic gas and when it came in contact with water it might have formed carbonic acid, due to which pH had decreased [7]. The EC was

reduced owing the loss of weight of organic matter and release of different mineral salts in available form. The low value Electrical conductivity shows the greater the decomposition rate. The decrease in organic carbon could be appropriate to respiration and assimilation of microorganism and earthworm. A large fraction of organic matter in the initial substrates was lost as CO_2 by the end of the vermicomposting period. Increased Nitrogen content in vermicompost possibly will be due to the release of nitrogenous products of earthworm metabolism through their cast (excreta) and urine. Moreover, the earthworm bodies which contain protein of 65% are organic nitrogen sources in vermicompost. The passage of organic residue through the gut of earthworm discharges phosphorus.

Table 2: Physicochemical analysis of Vegetable Biomass based Vermicompost

S.No	Parameters	Initial value (%)	Vermicompost Values In Percentage (%)
1	pH	6.3	4.2
2	Electrical conductivity	3.21	2.89
3	Total Kjeldahl Nitrogen (TKN)	1.71	2.57
4	Total Phosphorus (TP)	1.01	1.12
5	Total Potassium (TK)	0.97	1.04
6	Total organic carbon (TOC)	19.6	4.6
7	Carbon Nitrogen Ratio (C:N)	44.2	11.23

Increase in Phosphorous content during vermicomposting is possibly through mineralization and Mobilization of phosphorus by bacterial and faecal phosphatase activity of earthworms. Increase in the amount of phosphorus in the vermicompost with the progress of time. Due to the metabolic activity of microorganisms present in earthworms gut. Solubilization of inorganic sodium and potassium in organic wastes by microorganisms through acid production. Microbes in compost digest carbon as an energy source and ingest nitrogen for protein synthesis. The proportion of these 2 elements should approximate 30 parts carbon to 1 part nitrogen by weight. C: N. ratio range should be 25:1 to 30:1 for vermicomposting. This is because the bacteria involved in composting digest carbon twenty five to thirty times faster than they digest nitrogen. The C: N ratio indicates the degree stabilization of a waste, as carbon is lost as CO_2 during vermicomposting whereas nitrogen content is enhanced during this process and these factors contributes to the lowering of C: N ratio.

4. Conclusion

Environmental Hazards are compounded by accumulation of organic waste from different sources like domestic, agricultural and industrial wastes that can be recycled by improvised and simple technologies. Vermicompost could be effectively used for the cultivation of many crops and vegetables, which could be a step towards sustainable organic farming. Such technologies in organic waste management would lead to zero waste techno farms without the organic waste

being wasted and burned rather then would result in recycling and reutilization of precious organic waste bringing about bioconservation and biovitalization of natural resources.

References:

1. M.Babita Devi *et al.*, International Journal of Current Microbiology and Applied Sciences., 2017, **6** (2), 82-85.
2. T.Meera Sose *et al.,* Journal of Research in Engineering and Technology., 2017, **6** (2), 22-23.
3. Nitesh *et al.*, International Research Journal of Engineering and Technology., 2017, **4** (7), 3461-3421.
4. Priyanka Ashiya *et al.,* International Journal of Agriculture & Environmental Science., 2017, **4** (2), 8-13.
5. Nisha Jain *et al.*, International Journal of Environmental & Agriculture Research., 2016, **2** (7), 89-94.
6. T.Ravimycin *et al.,* International Journal of Advanced Research Applicable in Biological Sciences., 2016, **3** (6), 91-98.
7. P.Porkodi *et al.,* Journal of Environmental Science, Toxicology and Food Technology., 2014, **8** (12), 78-82.

Photodegradation of Methylene Blue Dye by Hydrothermally Synthesized Zinc Oxide Nanorods

I. Reeta Mary[a,b], A. Yuvarani[b], R. Vaideeswaran[b], D. Mangalaraj[a], C. Viswanathan[a] and N. Ponpandian[a*]

[a] Department of Nanoscience and Technology, Bharathiar University, Coimbatore
[b] Department of Physics, Government Arts College, Coimbatore
*corresponding author mail.id: ponpandian@buc.edu.in

Abstract

The rapid increase of textile industries causes a threatening environmental and health issues for the past few decades. Most of the textile industries use azo based dyes, Methylene blue (MB) is one among them. Dye degradation of textile residues has been considered as the primary concern in wastewater treatment due to their complicated constituents and high chemical stability. Nowadays, nano-photocatalysts are used for degradation of such dyes which breaks the organic dye molecules into H_2O, CO_2 and mineral acids that further reduces the secondary pollution. Owing to the vast number of structural geometries, metal oxide nanoparticles have been used as heterogeneous nano-photocatalysts. Zinc Oxide (ZnO), a non-toxic and eco-friendly material is one among them with wide range of applications like elimination of hazardous materials, drug delivery, biomolecular detection, etc. Hence, an attempt has been made to synthesis ZnO nanoparticles by facile hydrothermal technique to explore its photocatalytic activity against MB dye. The structural property was confirmed by X-Ray Diffraction (XRD) technique. The surface morphologies of ZnO nanorods were depicted by Field Emission Scanning Electron Microscopic (FESEM) analysis. The optical studies were carried out by UV-Visible (UV-Vis) Spectroscopic technique. Further, the photodegradation of Methylene Blue dye by Zinc Oxide nanorods under UV irradiation was also investigated.

Keywords: Environmental, methylene blue, nano-photocatalysts, ZnO, UV irradiation

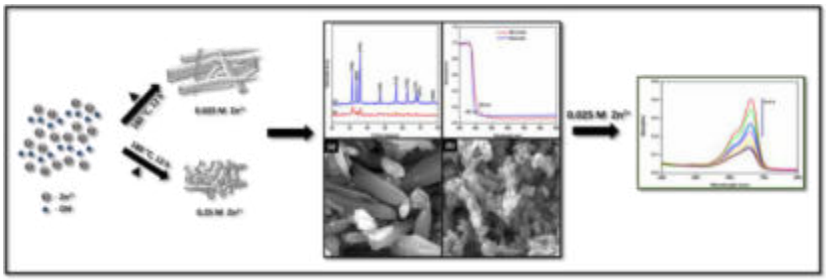

1. Introduction

Majority of textile industries use azo based dyes to manufacture their fabrics and discharge huge amount of colored effluents in various water bodies. These dyes retard biological activity of aquatic environment and cause harmful effects on humans. Hence, it is essential to eliminate hazardous dye from wastewater before it pollutes the environment [1]. In the past few decades, researchers have been developing several methods to eliminate organic dye molecules from wastewater [2]. Photodegradation is one of the methods in which molecules are degraded by absorbing a photon of wavelength particularly in the ultraviolet and visible regions. Photocatalysis is one of the photodegradation processes in which photo induced reaction is accelerated in the presence of a catalyst. In this process, electron-hole pairs are created by the absorption of incident light that leads to a redox reaction. Nowadays, nano-photocatalysts are used for degradation of dyes that breaks the organic dye molecules into H_2O, CO_2 and mineral acids that further reduces the secondary pollution [3]. Due to the electronic structure of semiconductors, ZnO, ZnS, TiO_2, etc., act as nano-photocatalysts [4]. Owing to its eco-friendly nature, low-cost and high catalytic ability, ZnO nanostructures have been used as prominent photocatalysts for the degradation of organic pollutants in wastewater [5, 6]. Diverse synthesis methods have been employed for the preparation of ZnO nanoparticles. Among them, synthesis of ZnO nanoparticles with various morphologies can be obtained via simple hydrothermal method by tuning the reaction parameters [7]. In this work, we report a facile hydrothermal approach to synthesize Zinc Oxide mico/nanorods by varying the precursor concentration. The crystallite structure and phase of the prepared ZnO nanostructures were confirmed by using X-Ray Diffractometer (XRD) and the optical absorption peak was found by using UV-Visible spectrophotometer. The surface morphologies were inferred from Field Emission Scanning Electron Microscope (FESEM). Further, the photocatalytic activity of the prepared ZnO nanorods was investigated against methylene blue (MB) dye under UV irradiation.

2. Experimental section

2.1. Materials

Zinc nitrate hexahydrate [$Zn(NO_3)_2.6H_2O$] and sodium hydroxide [NaOH] of analytical grade were procured from HIMEDIA, India and were used as received.

2.2. Synthesis of ZnO nanostructures

The required amount of zinc nitrate hexahydrate (0.025 M) was dissolved in 60 ml of distilled water and stirred for 30 min in a magnetic stirrer. Then, sodium hydroxide solution was added drop wise till the pH of the solution become 12 and was stirred for 30 min to obtain a homogenous mixture. The resultant solution was treated hydrothermally at 180 °C for 12h. The final precipitate was washed and dried at 100 °C to obtain Zinc Oxide nanostructures. The same reaction was carried out for the precursor concentration of 0.25M.

2.3. Characterization of ZnO nanostructures

The synthesized ZnO nanoparticles were structurally, optically and morphologically characterized by using Bruker ECOD 8 Advance X-Ray Diffractometer, Shimadzu UV-Visible Spectrophotometer and Bruker Field Emission Scanning Electron Microscope respectively.

2.4. Experimental procedure for photodegradation

An appropriate amount of as-prepared ZnO nanorods were mixed well with 50 ml of MB solution and was illuminated by a UV source. The photodegradation ability of ZnO nanorods was evaluated by measuring the absorption intensity of MB dye for regular intervals of time.

3. Results and Discussion

3.1. Structural and Optical properties

The XRD pattern of the synthesized ZnO nanostructures is illustrated in Fig. 1(i). All the samples were well crystallized and the diffraction peaks were in accordance with the standard JCPDS (#36-1451) of ZnO. The lattice constants for hexagonal crystal structured ZnO were found to be a = b = 3.253 Å and c = 5.213Å. The crystallite size was calculated from Debye Scherrer formula as 20 and 24 nm for 0.025 and 0.25 M respectively. The increase in crystallite size for higher concentration of Zn precursor might be due to the change in the growth of different crystallographic planes [8, 9].

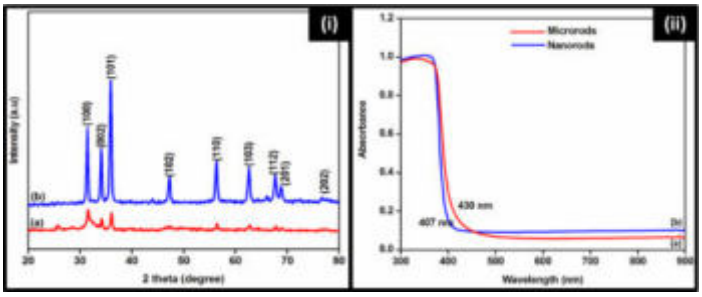

Fig. 1 (i) XRD pattern and (ii) UV-Vis absorption spectrum of ZnO
(a) 0.025 M and (b) 0.25 M

The absorption spectrum of ZnO nanostructures is shown in Fig. 1(ii). The absorption edge wavelength was observed at 430 and 407 nm for micro and nanorods respectively. The blue-shift might be due to the decrease in particle size that could be attributed to the confinement effect [10].

3.2. Surface morphological properties

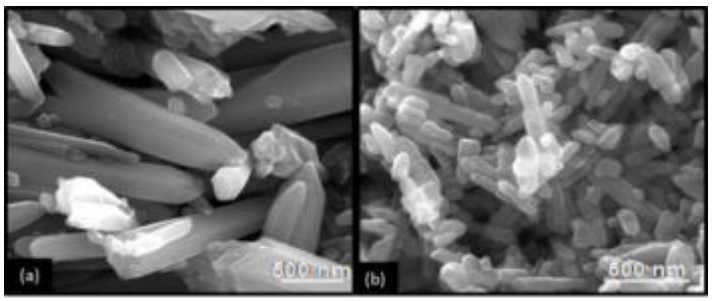

Fig. 2 FESEM images of ZnO (a) 0.025 M and (b) 0.25 M

FESEM images of ZnO nanostructures are shown in Fig.2. The formation of microrods was observed for 0.025M of Zn^{2+} concentration (Fig. 2(a)) whereas for 0.25M, formation of nanorods was noticed (Fig. 2(b)). The decrease in the particle size of the rods for 0.25 M of Zn^{2+} ions in the precursor solution was due to the increased nucleation rate than the growth rate of ZnO nuclei [11].

3.3. Photocatalytic Activity

Photocatalytic degradation of Methylene Blue dye using Zinc Oxide nanorods as photocatalyst under UV irradiation is represented in Fig. 3. The removal of MB dye by ZnO nanorods was evident from the gradual decrease in intensity of the absorption peak of MB at 663 nm (Fig. 3(i)). The infinitesimal photodegradation of MB dye under UV irradiation in the absence of nano-photocatalyst might be due to the photo-induced self-sensitized photolysis (Fig. 3(ii)). The enhanced photodegradation after the inclusion of ZnO nanorods was due to its high adsorption capacity. The linear plot of degradation rate indicated that the degradation of MB follows first-order kinetics. The increased degradation rate of ZnO nanorods (0.0502 min^{-1}) was due to its high surface area to volume ratio that provides more photocatalytic reaction centers for adsorption of dye molecules. At the same time, the large surface area of ZnO nanorods is beneficial for UV irradiation to promote electron-hole pair generation [5] which is responsible for degradation process and hence Zinc Oxide nanorods can be effectively used as an efficient nano-photocatalyst for the degradation of Methylene Blue dye under UV irradiation.

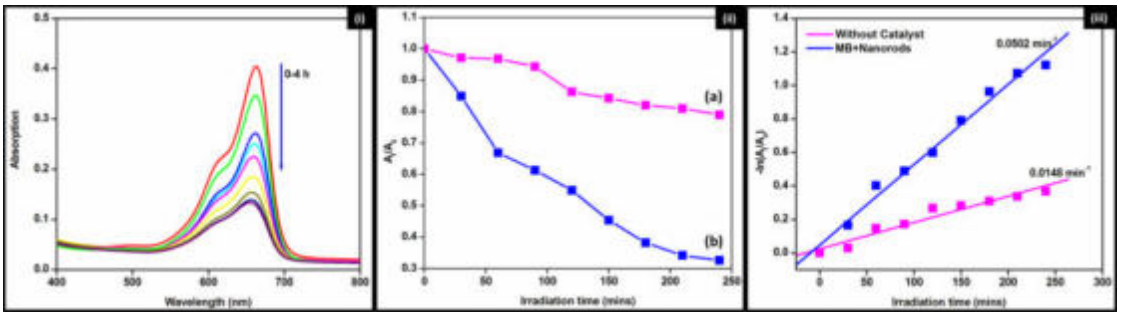

Fig. 3 (i) Photocatalytic degradation of MB dye by ZnO nanorods (ii) Photodegradation efficiency (a) without photocatalyst (b) with ZnO nanorods and (iii) Photodegradation rate

4. Conclusion

- Zinc Oxide micro and nanorods have been successfully synthesized via a facile hydrothermal method by varying the precursor concentration under mild reaction conditions
- The structural properties and optical absorption wavelength were evaluated by X-ray diffractometer and UV - Vis spectrophotometer respectively
- The surface morphology was depicted by using Field Emission Scanning Electron Microscope
- The enhanced photocatalytic activity of the synthesized Zinc Oxide nanorods was investigated for the degradation of Methylene Blue dye

Reference

1. D. A. Yaseen *et al.*, International Journal of Environmental Science and Technology., 2019, **16**, 1193–1226.
2. Rummi Devi Saini *et al.*, International Journal of Chemical Engineering Research. 2017, **9**, 121-136.
3. Sunandan Baruah *et al.*, Nanoscience & Nanotechnology-Asia., 2012, 90-102.
4. Alex Omo Ibhadon *et al.,* Catalysts., 2013, **3** (1), 189-218.
5. Swee-Yong Pung *et al.*, International Journal of Inorganic Chemistry., 2012, **2012**, 1-9.
6. S. Sakthivel *et al.*, Solar Energy Materials and Solar Cells., 2003, **77**, 65-82.
7. K. Byrappa *et al.,* Progress in Crystal Growth and Characterization of Materials., 2007, **53**, 117-166.
8. P. M. Aneesh *et al.*, Nanophotonic Materials – IV., 2007, **6639**, 66390J.
9. A.Shaker *et al.*, Physica E: Low-dimensional Systems and Nanostructures., 2017, **88**, 169-173.
10. M.K. Debanath *et al.,* Materials Letters., 2013, **111**, 116-119.
11. G. Amin *et al.*, Journal of Nanomaterials., 2011, **2011**, 1-9.

APPLICATION OF PIXE TO NANO MATERIALS - AN OVERVIEW

R.Venkateswara Rao[1,*] and K.SrinivasaRao[2]

[1]. *Department of Physics, Lendi Institute of Engineering & Technology, Vizianagaram, A.P, India.

[2]. Department of Physics, ANITS, Sangivalasa, Visakhapatnam A.P, India.

Corresponding author's email: rvrao.venkat999@gmail.com

Abstract

With the advent of Nano particles produced in high quantities and employed in different products or processes, the need to evaluate their potential effects is necessary. Hence a brief description of the various available techniques that are employed in characterization of Nanomaterials is presented. Ion beam-based techniques such as Particle-Induced X-ray Emission (PIXE) technique for the analysis of Nanomaterials is described in the present work. An overview of various Nanomaterials analyzed by the PIXE technique and the significance of the studies was described. The present paper discusses the importance of nano materials in several fields and their analysis by analytical techniques. This study also emphasizes the usage of PIXE in the field of nanotechnology.

Keywords: PIXE, Nanomaterials, elemental analysis, Ion beam techniques.

1. Introduction

Nanotechnology is an interdisciplinary research field in which many physicists, chemists, biologists, materials scientist and other specialist's are involved. Nanotechnology is considered to be the technology of the future; it is perhaps today's most advanced manufacturing technology and has been called "extreme technology", because it reaches the theoretical limit of accuracy which is the size of a molecule or atom. When measuring properties of a material on a nanoscale, there is a strong correlation between the dimensionality of the material and the physical or chemical properties. For example, a small change in the size of quantum dots (~ 5 nm) can shift their luminescence from the red end of the visible light spectrum to the blue end. Therefore, the precision required controlling the dimensionality within a few nanometers or less is necessary for the development and use of nanomaterials. Nanotechnology is a platform technology that is finding more and more applications daily.

There are several methods to characterize nanomaterials and structure of materials at nanoscale such as SEM, TEM, STM, XRD, etc. Apart from above mentioned techniques there are certain analytical techniques like INAA, AAS, XRF, RBS and PIXE to identify the elements and their concentrations (elemental purity of the sample). In this context, one has to adopt suitable analytical technique to examine the elemental purity of the nanomaterials. Some of the analytical methods are destructive, so that the samples cannot be used for further studies; some of the techniques give information on one element only or require sample preparation before analysis. In comparison, PIXE has some distinctive features of being non destructive and quick, allowing multi elemental determination and requiring little or no sample preparation. PIXE is a relatively simple, yet powerful analytical technique that can be used to identify and quantify trace elements in a sample [1-5]. PIXE is a nuclear analytical technique for rapid analysis of a wide range of trace elements with ppm sensitivity. Use of protons offers a good sensitivity even at lower atomic numbers due to the fact that bremsstrahlung caused by protons is low compared to electron excitation. PIXE technique

has rapidly gained acceptance as a valuable analytical tool because of the ever-increasing need for elemental analysis of very small amounts of sample, as in the case of nano materials. In the present work the authors reviewed the role of PIXE in analyzing the nano materials.

2. Experimental details of PIXE

The PIXE experiment was performed using a 3 MV Pelletron accelerator facility. This accelerator has been regularly used for carrying out material analysis using the PIXE technique [6]. A 3 MeV proton beam was used to excite the samples. The samples were suspended on an aluminium sample holder. Then the target holder was loaded into the PIXE chamber and the irradiation was carried out in vacuum conditions. A collimated proton beam of 4 mm diameter was made to fall on the target. The beam current was kept at 20 nA. The targets on the aluminium holder were positioned in the scattering chamber at an angle of 45° with respect to the proton beam. With respect to that beam, an energy dispersive Si (Li) detector (with 160 KeV FWHM resolutions at 5.9 KeV) recorded the characteristic X-ray spectra at 90°. For each sample, the total charge collected and the average beam current were noted. The spectra were gathered for a sufficiently long time in order to obtain good statistics. Spectra were recorded by using a Canberra series MCA. The concentrations of different elements were estimated in each sample using GUPIX software package.

3. Results & Discussions:

Some of the nano materials (Fe, Ni & Fe_2O_3) analyzed by the PIXE technique are discussed and presented in this paper. Chanda et al [9] analysed the nanocrystals by PIXE investigation for elemental analyses at Institute of Physics, Bhubaneswar. The PIXE spectra for these samples were shown in Figs. 1-3.

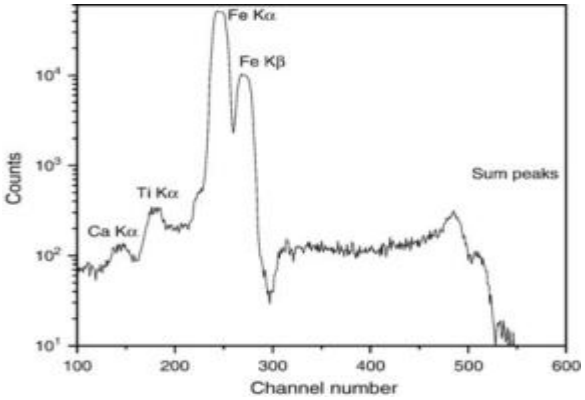

Fig.1: PIXE spectrum of α-iron with peaks representing the small amount of Materials

Table 1: Concentrations of various elements in α-Fe nanocrystals

Element	Concentration	Statistical error (%)
Ca	1502 ppm	13
Ti	1550 ppm	10
Fe	99.6%	0.1

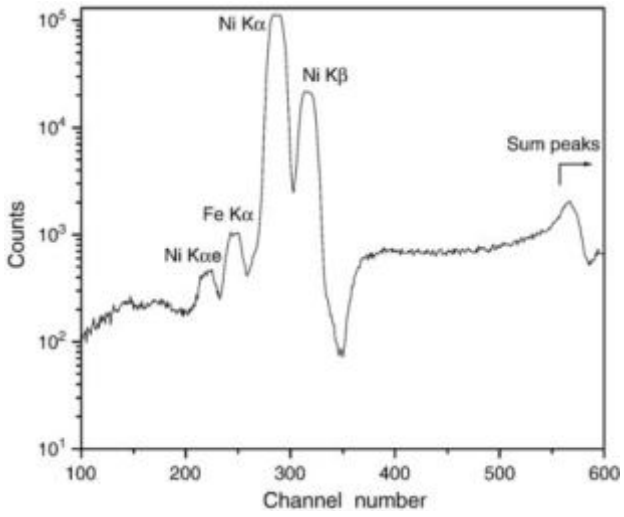

Fig:2 PIXE spectrum of Ni with a characteristic peak

Table 2: Concentrations of various elements in Ni nanocrystals

Element	Concentration	Statistical error (%)
Fe	32727.1ppm	21
Ni	99.6%	0.1

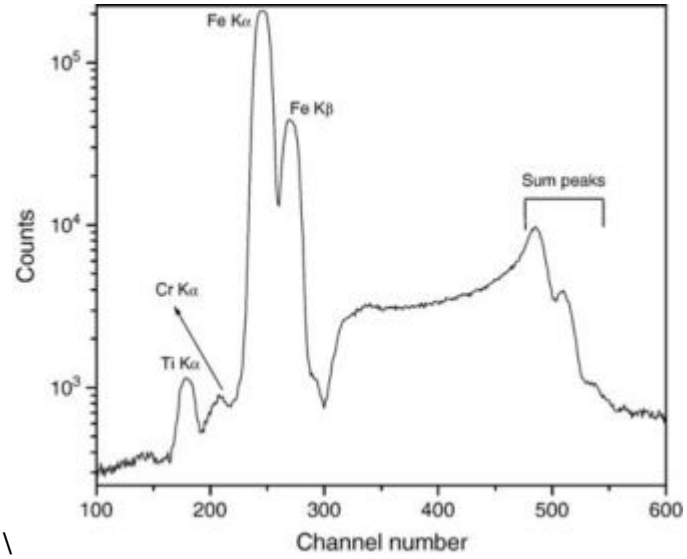

\

Fig:3 PIXE spectrum of α-ferric oxide compared to other materials peaks.

Element	Concentration	Statistical error (%)
Ti	403.2 ppm	27
Cr	275.8 ppm	81
Fe	69.5%	0.1

The Fe, Ni & Fe_2O_3 are found pure except foreign element in ppm order. Fe is α-Fe type and Fe_2O_3 is α- Fe_2O_3 as consultation with α-Fe and α- Fe_2O_3 spectrum. The analysed PIXE results obtained by using GUPIX were presented in Tables 1–3 for α-Fe, Ni and α-Fe_2O_3, respectively. It can be observed from Table 1 that the prepared α-Fe nanocrystals are having 99.6% purity with contaminants like Ca and Ti in trace level. Fig.1 is the PIXE

spectrum of Fe-nanocrystals dominated by X-ray lines of iron. However contaminants like Cu, Zn and Pb were not present.

The Table-2 and Fig.2 indicate that Ni nanocrystals having Fe as major trace contaminant. Table 3 presents only two contaminants in very low concentrations, i.e., Ti and Cr are present in α- Fe_2O_3 nanocrystals, which is well evidenced from Fig. 3. However, we would further like to mention here that although the trace contaminants like Cu, Zn, Pb and other elements have not been observed in spectra, the characteristic x-ray lines in the energy region of the pile-up continua may be present, and could not be estimated due to increase in minimum detection limit of the respective elements. The importance of effective suppression of the pile-up continuum is obvious in terms of limit-of-detections of trace level contaminants. The pile-up continua of major elements like Fe and Ni may overlap the X-ray lines of trace elements, then the limit-of-detections for those elements are significantly worse. However, as the residual concentration is only within some thousands of ppm then these individual elements must be in very less concentration, if present, and may not affect the purity of the materials significantly. So the PIXE results confirm the effectiveness of our nanocrystals preparation procedure. SS Kumar et al [7] used the PIXE technique to study the purity of ZnO-nanoparticles.

4. Conclusions:

- Ion beam-based techniques such as Particle-Induced X-ray Emission (PIXE) technique for the analysis of Nanomaterials is described in the present work.
- An overview of various Nanomaterials analyzed by the PIXE technique and the significance of the studies was described.
- The present paper also discusses the importance of nano materials and their analysis by analytical techniques.
- This study also emphasizes the usage of PIXE in the field of nanotechnology.

5. Acknowledgement:

The authors are thankful to the College Administrators of Lendi Institute of Engineering & Technology & ANITS for granting necessary permissions and time to undertake this sophisticated work.

6. References

1. S.R.Ryan *et al.,* Nuclear Instruments and Methods in Physics Research B., 1985, **10** (11)**,** 645 - 649.
2. W. Maenhaut *et al.,* Nuclear Instruments and Methods in Physics Research B., 1987, **22**, 138.
3. M.Uda *et al.,* Nuclear Instruments and Methods in Physics Research B., 1993, **75**, 476
4. R.Venkateswara Rao *et al.*, International Journal of Physics and Applications., 2010, **2**, 123-134.
5. S.C. Chanda *et al.,* Materials Letters., 2007, **61**, 5059-5062.
6. V. Vijayan *et al.,* Int. J. PIXE., 1995, **5**, 211-219.
7. S.Siva Kumar *et al.,* Int. Nano letters., 2013, **3**, 30.

Conductive granular graphite as alternate electrode material for efficient bioelectricity generation in Microbial fuel cells

C. Nagendranatha Reddy*, Y. Rajasri, Bishwambhar Mishra, Y. Vineetha, A. Shalini

Department of Biotechnology, Chaitanya Bharathi Institute of Technology, Hyderabad-500075, Telangana, India

***Corresponding author:** E-mail: nagendranath_biotech@cbit.ac.in,

Telephone: +91 40-24193276 Ext: 163

Abstract

Global waste disposal and energy crisis requires a multifaceted solution in today's world to achieve efficient method that holds great promise for waste remediation and energy generation. Recovering maximum possible energy by treating complex waste in an integrative strategy by utilizing Microbial fuel cell (MFC) technology can be part of the bioenergy solution. In this research, dual chambered MFC was used with granular graphite rods as electrodes and graphite granules as packed substratum to form biofilm in anode. Experimental operation was carried out in two stages. In the first stage, evaluation of biocatalyst for initial optimization (bioanode) using designed synthetic wastewater (DSW) followed by real field acidogenic reactor effluent collected from a upflow anaerobic sludge blanket (UASB) reactor in the second stage. All the parameters that may act as bottlenecks to the reactor were optimized to enhance the bioelectrogenic activity along with simultaneous COD removal. Among the various flowrates, COD concentrationsand applied resistances, optimum operating conditions of 0.6 ml/min (Flowrate), 9 g/l (COD Conc.) and 22 Ω (resistance) depicted maximum stable voltage of 0.43 V, power density (0.4 W/m^2), current density (1.79 A/m^2), COD removal (94%) and currents generation (0.042/-0.018 A OC/RC) using designed synthetic wastewater as carbon source. By considering the optimum parameters, the MFC fed with real field wastewater (UASB Effluent) operated with food waste depicted voltage of 0.358 V with COD removal of 89.2 %. The present study proposed and demonstrated a method for enhanced bioelectricity production by utilizing the food waste operated UASB effluent.

Keywords: Microbial fuel cell (MFC), Conductive granular graphite, upflow anaerobic sludge blanket (UASB) Effluent, Bioelectricity, COD removal

1. Introduction

Development of alternate sources of energy is considered to be essential in the realm of shortage of non-renewable energy sources and its associated pollution problems. MFC is being considered as a potential and sustainable alternative source of renewable energy which gains power by utilization of variety of substrates including wastewater. This technology provides dual benefits of wastewater treatment and provides access to cheap and environmental friendly energy [1]. However, lower power yield is the major and persistent limitation existing with the MFC operation due to inherent electron losses during its transfer from biocatalyst to working electrode especially with systems containing wastewater as anolyte. These losses occur either due to the inefficiency of electrode material to capture electrons or due to high internal resistance in the system that limits the transfer of electrons from the biocatalyst to the anode surface and subsequently to cathode. Little is known about the influence of electrodes on the structure and functions of the microbial community. The mechanism for the enhancement of exoelectrogenic microorganisms in the microbial

communities with electrodes placement needs to be specifically focused to improvise the process efficiencies which can directly improvise productivity at industrial scale [2]. The understanding of mechanism aspects and microbial community structure on electrode influence helps in enhancing the specific products output. The application of potential to microbial community is another scientific factor that needs to be focused for specifically deriving a biobased product from the organic substrate. The limitations on efficient bioelectricity production from MFC is leading to search for alternate and efficient electrode materials with minimal losses in a controlled manner and consumed on demand. Understanding the electron transfer capability with different electrode materials or configurations by varying different parameters helps in overcoming a few of the major bottlenecks during up scaling process. Therefore, an attempt was made in this study to investigate the functional role of conductive granular graphite as alternate electrode material in enhancing the electrogenic activity of MFC. To enumerate the variation in electron transfer mechanism, the results were compared with the performance of MFC under various parameters (substrate flowrates, COD concentrations and resistances). System performance was analyzed and compared based on electrogenic activity, electron losses, bio-electrochemical behavior, and electron discharge pattern and substrate degradation.

2. Materials and Methods

2.1 Bioreactor Construction

The MFC reactor was constructed by assembling two equal rectangular 'perspex' plates (designated as anode and cathode) with working volume of 100 ml each. A Proton exchange membrane (PEM; Nafion 117) was sandwiched between two electrodes to allow the passage of protons. Initially, the bioreactor was operated in batch mode for parameters optimization and then the feed will be continuously fed. The chambers filled with conductive granular graphite will be used as both the anode and cathode electrodes and the contact between the external circuit and the granular graphite will be made using graphite rods. The reactors will be operated as a three-electrode system coupled to a power supplier. AD effluent will be used as the anodic substrate for anode of MFC reactor under continuous flow and while Potassium ferricyanide (50mM) will be used as the terminal electron acceptor in the cathodic chamber (abiotic).

2.2 Biocatalyst and Wastewater

Anaerobic sludge obtained from local wastewater treatment plant will be used as the inoculum source to start up the anodic compartment of MFC bioreactor. Prior to inoculation, parent inoculum was sieved to remove the clumps and large sized particles to avoid blocking of tubes and establish fine biofilm in the anode chamber. Culture was inoculated into the anode by re-suspending through feed to facilitate the initial adaptation and stabilization of the microorganisms. The wastewater in the anode chamber was recirculated by employing peristaltic pump. The upflow anaerobic sludge blanket (UASB) reactor operated with food waste as substrate was used as source for effluent. The bioreactor was operated with a cycle period (HRT) of 24 h for periodic effluent which would be replaced immediately. UASB effluent (pH, 4.9; chemical oxygen demand (COD), 23 g/l) was used as substrate. Prior to loading effluent in anode chamber, the pH and COD was adjusted to 7 ± 0.1 and 9 g/l respectively.

2.3 Experimental Operation

Initially, the anode chamber alone was optimized to form biofilm under various operating parameters. In anode, designed synthetic waste followed by anaerobic digestion effluent was used while in cathode, potassium ferricyanide was recirculated. The K_3FeCN_6 will act as

terminal electron acceptor to form water molecules. The various substrate flowrates, COD concentrations and resistances were optimized to obtain maximum bioelectrogenic activity along with simultaneous COD removal. The three bioreactors were operated simultaneously and the average data is plot in graphs. The bioreactors were analyzed for voltage with resistance, current, cyclic voltammetry, pH, VFA, ORP, electrical conductivity, COD removal efficiency and polarization.

3. Results and Discussion

3.1 Optimization of various Flowrates

After stable biofilm formation and reaching a steady state, the anode chamber was fed with 3g/l COD concentration. Throughout the experiments, both anolyte and catholyte were recirculated at a rate of 0.3, 0.6, 1.0 and 2.0 ml/min to maintain uniform distribution and avoid concentration gradients at the corners of the bioreactor and clogging of the granular matrix during continuous operation. The anodic COD concentration was maintained at 3 g/l in all the flowrates varied at 22 Ω resistance. The anode chamber was provided with 3g/l COD concentration to meet the requirements of biocatalyst present in working electrode chamber. The higher COD removal was observed with 0.6 ml/min (87.4 %) followed by 1.0 ml/min (83.2 %), 2.0 ml/min (79 %) and 0.3 ml/min (73 %) respectively. The bioelectrogenic activity of biocatalyst will be achieved by utilizing the carbon source. The bioelectrogenic analysis depicted maximum voltage with 0.6 ml/min (0.313 V) followed by 1.0 ml/min (0.25 V), 2.0 ml/min (0.21 V) and 0.3 ml/min (0.15 V). The 0.6 ml/min was able to provide sufficient time for the biocatalyst to utilize COD from the wastewater

3.2 Optimization of various COD concentrations

One of the important parameters that affect the MFC operation is COD concentration in anode chamber. The COD concentration is thus varied at 3, 6, 9 and 12 g/l and its removal was investigated. The higher COD removal was observed with 9 g/l COD conc. (93.5 %) followed by 12 g/l (91.8 %), 6 g/l (90.7 %) and 3 g/l (87.4 %) respectively. The bioelectrogenic analysis depicted maximum voltage with 9 g/l COD conc. (0.429 V) followed by 12 g/l (0.381 V), 6 g/l (0.35 V) and 3 g/l (0.306 V) respectively. The results obtained by varying various COD concentrations depicts that 9 g/l is the optimum substrate concentration for enhancing the activity of microorganisms towards higher substrate removal and bioelectrogenic activity

3.3 Optimization of various Resistances

With the optimized flowrate (0.6 ml/min) and COD concentration (9 g/l), the resistance is varied to evaluate the biocatalyst activity in terms of CV profiles and bioelectrogenic activity. Resistance plays an important role in biocatalyst functioning by regulating the electron flow. The varying resistances showed variation with COD removal. The COD removal of 93.5 % was observed with 22 Ω followed by 89.1, 84 and 79.4 % with 47, 100 and 5 Ω resistance The voltage profile also followed the same pattern depicting the higher activity of biocatalyst by varying resistances. The 100 Ω resistance depicted higher voltage of 0.537 V followed by 47 Ω (0.48 V), 22 Ω (0.43 V) and 5 Ω (0.355 V) respectively.

The overall activity of MFC bioreactor at optimum operating conditions of 0.6 ml/min (Flowrate), 9 g/l (COD Conc.) and 22 Ω (resistance) depicted 0.43 V of stable voltage, 0.4 W/m^2 of power density, 1.79 A/m^2 of current density, 93.5 % of COD removal and currents generation of 0.042/-0.018 A OC/RC.

3.4 MFC operation using UASB effluent

After optimizing various parameters viz., flowrate, COD concentration and resistances, the bioreactors were fed with real field wastewater (UASB Effluent) operated with food waste.

This integration of MFC bioreactor using effluent from a UASB reactor paves a way towards sustainable and economic way to treat wastewater and generate bioelectricity as a value added product. The COD removal of MFC operated with UASB effluent showed decrement due to presence of high VFAs concentration and other TDS, VS etc. may have a negative impact on the performance. The activity reduced a bit initially and later showed stable performance of 89.2 %. The voltage profile also followed the same pattern of decrement with real field effluent operation in MFC bioreactors. The MFC bioreactors showed activity of 0.358 V with real filed wastewater while the voltage was 0.43 V with synthetic media operation. Though there is decrement in the voltage generation at initial stages, it regained in the latter stages of operation and depicted stable performance. During polarization, the maximum power density and current density of 0.28 W/m^2 and 1.65 A/m^2 was observed with 22 Ω followed utilizing UASB effluent [3]

Table 1: COD removal (%) and Voltage (V) corresponding to various parameters optimization

Designed synthetic wastewater (DSW)		COD Removal (%)	Voltage (V)
Flow rate (ml/min)	0.3	73	0.15
	06	87.4	0.313
	1.0	83.2	0.25
	2.0	79	0.21
COD Conc. (g/l)	3	87.4	0.306
	6	90.7	0.35
	9	93.5	0.429
	12	91.8	0.381
Resistance (Ω)	5	79.4	0.355
	22	93.5	0.43
	47	89.1	0.48
	100	84	0.537
Real Field wastewater			
UASB Effluent	0.6 ml/min (Flowrate), 9 g/l (COD Conc.) and 22 Ω (resistance)	89.2	0.358

4. Conclusions

- The present study proposed and demonstrated a method for enhanced bioelectricity production by utilizing the food waste operated UASB effluent.
- The operating conditions were varied and evaluated for optimum parameters for enhancing activity of biocatalyst which in turn can be used for supporting other systems like MEC.

5. Acknowledgement

The authors thank the management of CBIT for constant support and encouragement in carrying out this work.

6. References

1) S.Venkata Mohan *et al.*, Biosens. Bioelectron., 2009, **24**, 2021-2027.
2) Y.A Gorby *et al.*, Proc. Natl. Acad. Sci. USA., 2006, **103**, 11358-11363
3) A.E.Tugtas *et al.*, Bioresource Technology., 2013, **128**, 266-272

Effect of Poly ethylene glycols for the Conversion of Organic acids to β – nitrostyrenes under conventional and Non-conventional Conditions.

K. Ramesh[1*], K. C. Rajanna[2]
1 Department of Chemistry, Chaitanya Bharathi Institute of Technology (A), Gandipet, Hyderabad-500075, Telangana (India)
2 Department of Chemistry, Osmania University, Hyderabad -500001, Telangana (India)
Corresponding author's email: kramesh_chm@cbit.ac.in

Abstract
Poly ethylene glycols (PEG-200, 300, 400, 600, 4000 and 6000) supported reactions were conducted with certain α, β-unsaturated acids in presence of metal nitrates under solvent free (solid state) and mineral acid free conditions. The reactants were ground in a mortar with a pestle for about 30 minutes. The aromatic acids underwent nitro decarboxylation and afforded β-nitro styrene derivatives in very good yield while α, β-unsaturated aliphatic carboxylic acids gave corresponding nitro derivatives. Addition of PEG accelerated rate of the reaction enormously. Reaction times substantially decreased from several hours to few minutes followed by highly significant increase in the product yield. Among the several PEGs, PEG-400 has been found to be much more effective than other PEGs.

Keywords: Poly ethylene glycols (PEG); rate accelerations; α, β-unsaturated acids; metal nitrates; solvent free (solid state); β-nitro styrene derivatives; α, β-unsaturated aliphatic acids; nitro derivatives.

1. Introduction

During the past two to three decades, there has been green revolution in the field of chemical research all over the world to prevent environmental pollution and the use of non volatile solvents, which are essential ingredients in a large number of Organic synthesis protocols [1, 2]. More specifically removal of organic solvents in chemical synthesis is important in the drive towards benign chemical technologies. Reactions performed under solvent - free conditions have gained much attention because of their enhanced selectivity, mild reaction conditions and associated ease of manipulation [3, 4]. Since more than a decade our group is also actively working on exploiting the use of a variety of eco friendly materials such as metal ions and surfactants as catalysts and non-conventional energy sources (such as microwave and ultra sound) to assist organic transformations such as Vilsmeier –Haack , nitration and Hunsdiecker reactions[5,6].

Polyethylene glycol such as PEG-400 is a biologically acceptable inexpensive polymer and an eco-friendly reagent [7], which is widely used in many organic transformations in recent past [8- 10] to accelerate the reactions. Encouraged by these results, Polyethylene glycols (PEGs) have been applied here as efficient additives in these reactions under solvent free conditions.

2. Experimental Details

Cinnamic acid, metal nitrates, nitric acid and polyethylene glycols were obtained from SD Fine Chemicals or Loba. Substituted Cinnamic acids were prepared by Perkins reaction as cited in literature.

2.1. General Procedure for PEG mediated synthesis of β – nitro styrenes in MeCN medium.

In a typical solid state synthesis, Cinnamic acid (0.01mol), PEG (0.02 mmol) and metal nitrate (0.12 mmol) are placed in a clean two necked R. B. flask and stirred for certain time.

Progress of the reaction is periodically monitored by TLC. After completion, the reaction mixture is treated with 2% sodium carbonate solution, followed by the addition dichloromethane (DCM) or dichloroethane (DCE). The organic layer was separated, dried over Na_2SO_4 and the solvent is recollected by distillation using Rotavapor. The resultant compound is further purified with column chromatography using ethyl acetate: hexane (3:7) as eluent to get pure product. Hexane and ethyl acetate are also separated using Rotavapor according to standard procedures [11-12].

2.2. General Procedure for the synthesis of β – nitro styrenes under solvent free condition.

In a typical solid state synthesis, Cinnamic acid (0.01mol), PEG (0.02 mmol) and metal nitrate (0.12 mmol) are placed in a clean mortar and ground with a pestle for about 30 to 60 minutes until the mixture is homogeneous, the particles are no longer getting smaller. Progress of the reaction is periodically monitored by TLC. After completion, the reaction mixture is treated with 2% sodium carbonate solution, followed by the addition dichloromethane (DCM) or dichloroethane (DCE). The organic layer was separated, dried over Na2SO4 and evaporated under vacuum, purified with column chromatography using ethyl acetate: hexane (3:7) as eluent to get pure product.

3. Results and Discussion

All the reactants (α, β- unsaturated acid, PEG, and metal nitrate) are taken in a clean mortar and ground with a pestle and solution phase for about till the reaction is completed, as ascertained by TLC. The reactions with aromatic carboxylic acids such as cinnamic acids afforded β - nitro styrenes, while the aliphatic carboxylic acids such as crotonic acid afforded nitroalkenes in good yield of products with high regioselectivity. Initially the reactions are conducted with cinnamic acid, metal nitrate, and different PEGs are to select the best PEG. The observed results are presented in table-1 & table-2. The products were characterized by IR, 1H-NMR, Mass spectra and physical data with authentic samples and found to agree well with earlier reports [13-14].

Table-1: Effect of Additive PEG on Metal Nitrate mediated Nitro decarboxylation of Cinnamic Acid in MeCN medium.

Entry	$Fe(NO_3)_3$		$Mn(NO_3)_2$	
	RT (hrs)	Yield (%)	RT (hrs)	Yield (%)
PEG-200	1.75	84	1.75	80
PEG-300	2.25	86	2.25	80
PEG-400	1.40	88	1.40	85
PEG-600	1.65	86	1.65	84
PEG-3000	2.60	80	2.60	75
PEG-6000	2.75	82	2.75	80

Table-2: Effect of Additive PEG on Metal Nitrate mediated Nitro decarboxylation of Cinnamic Acid under Solvent free conditions.

Entry	$Fe(NO_3)_3$		$Mn(NO_3)_2$	
	RT (min)	Yield (%)	RT (min)	Yield (%)
PEG-200	45	90	45	88
PEG-300	60	86	60	83
PEG-400	30	88	30	87
PEG-600	30	86	30	85
PEG-3000	60	76	60	80
PEG-6000	35	88	30	87

To check the generality of the reaction an array of substituted Cinnamic acids are also used as substrates under present reaction conditions, as shown in **Scheme - 1**.

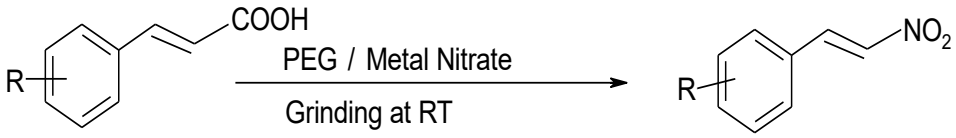

Scheme-1: PEG = PEG-200,300, 400, 600, 3000 and 6000

Metal Nitrate = $Fe(NO_3)_3$, $Mn(NO_3)_2$

Effect of Structure on Reactivity: Data presented in Table – 3 and figure - 1, revealed that the reaction times and yield of reaction products under different conditions, the reaction is sensitive to the structural variation of cinnamic acid, when the nitro decarboxylation reaction is conducted with aromatic acids underwent nitro decarboxylation and afforded β-nitro styrene derivatives in very good yield while α, β-unsaturated aliphatic carboxylic acids gave corresponding nitro derivatives in presence of PEG-400 and metal nitrates reaction rates accelerated with the introduction of electron donating groups and retarded with electron withdrawing groups.

Table -3: Nitro decarboxylation of Cinnamic Acids in presence of PEG-400 and metal nitrates under Solvent free conditions.

Entry	$Fe(NO_3)_3$		$Mn(NO_3)_2$	
	RT (min)	Yield (%)	RT (min)	Yield (%)
CA	30	88	30	87
4-ClCA	60	86	60	83
4-OMeCA	30	88	30	87

4-MeCA	30	86	30	85
4-NO_2CA	60	76	60	80
4- OHCA	30	92	30	88
AA	30	80	30	78
CRA	60	78	60	78
3-PhCRA	30	76	30	80
2-ClCA	60	82	60	70

Figure-1: Fe(III) Nitrate mediated Nitro decarboxylation of different Cinnamic Acids in presence of PEG-400 under Solvent free conditions.

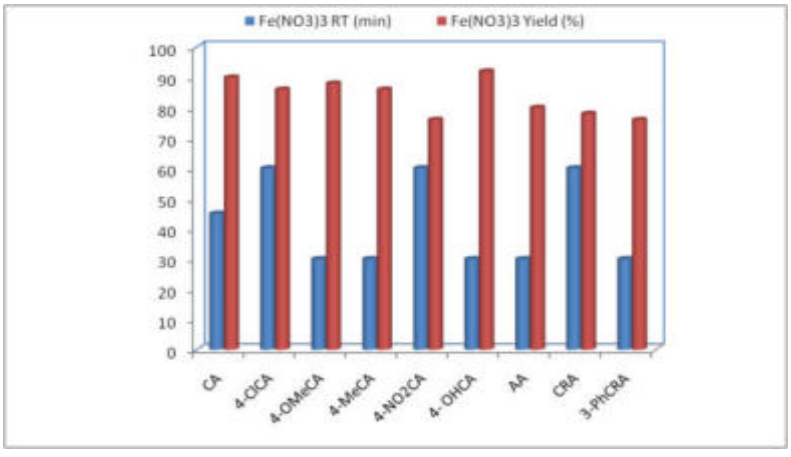

4. Conclusions

In summary, we have accomplished Poly (ethylene glycol) supported Fe(III) nitrate and Mn(III) nitrate as efficient reagents for the synthesis of β-nitro styrenes from α, β-unsaturated carboxylic acids in MeCN medium and under solvent-free conditions using cost-effective grind-stone technology. The reactants were ground in a mortar with a pestle till the reaction is completed. The reaction time is generally about 30-60 minutes. The present finding has advantages such as the use of economically cheap and readily available desktop

Fe(III) and Mn(III) nitrates, PEGs, and unsaturated acids. Addition of PEG accelerated the rate of the reaction enormously. Reaction times substantially decreased from several hours to few minutes followed by highly significant increase in the product yield. Among the several PEGs, PEG-400 has been found to be much more effective than other PEGs.

Acknowledgement

The authors thank the Management of C.B.I.T, Hyderabad for constant encouragement and support.

References

1. L. El Kaïm *et al.*, Green Chem., 2003, **5**, 477-499.
2. G. R Desiraju *et al.*, Reactivity of Solids: Present, past and future, V.V. Boldyrev Ed; Blackwell Sciences, London., 1995, 223.
3. G. W. V Cave *et al.,* Chem Commun., 2001, 2159-2169
4. J.L.Scott *et al.,* Green Chem., 2000, **2**, 123-126.
5. M. M.Ali *et al.,* Synlett., 2001, **2**, 251-253
6. S.Ramgopal *et al.,* TetrahedronLett.,. 2007, **48**, 4043-4045.
7. T. J Dickerson *et al.,* Chem. Rev., 2002, **102**, 3325-3344.
8. B. Das *et al.,* Tetrahedron Lett., 2006, **47**, 8471- 8473.
9. S. Chandrasekhar *et al.,* Tetrahedron., 2006, **62**, 338-345.
10. J-H.Li *et al.,* Tetrahedron., 2006, **62**, 31-38.
11. M. J. Thompson *et al.,* Tetrahedron., 1989, **45** (1), 191-202.
12. D. Gaudea *et al.*, Synth. Com., 1986, **16**, 63-68.
13. J. P. Das *et al.,* Organic. Lett., 2002, **4**(18), 3055–3058.
14. J. M. Rao et al., Tetrahedron Lett., 2005, **46** (47), 8141-8143.

Cu^{2+} Ions in Sodium-Alkali Fluoroborate Glasses Studied by Optical Absorption and EPR Techniques

V. Rajashekar Reddy and P. Kistaiah*

Department of Physics, University College of Science, Osmania University, Hyderabad-500007.

Corresponding author: vrsreddy07@gmail.com

Abstract

Optical absorption and EPR spectroscopic studies were carried on 30NaF-10AF_2-59B_2O_3-1%CuO, (A=Ca, Sr, Ba) glass system to understand the effect of Ca, Sr and Ba alkaline earth metals. Optical absorption results shows typical spectra of Cu^{2+} ions in distorted octahedral sites and the various optical parameters such as, optical bandgap (E_{opt}) and Urbach energy (ΔE) calculated. Optical bandgap (E_{opt}) values increasing from 3.05 to 3.23 eV and Urbach energy (ΔE) values are varying from 0.55 to 0.48 eV. From observed EPR spectra are representative of Cu^{2+}ions in octahedral sites with tetragonal distortion. By correlating the EPR and optical data, the molecular orbital coefficients have been evaluated.

Key words: Alkali fluoroborate glasses, Optical absorption, EPR technique.

1. INTRODUCTION

Inorganic glasses are studied widely using spectroscopic techniques to understand the structural and optical properties. Transition metal ions are implanted into glasses to probe local structure through optical absorption, electron paramagnetic resonance techniques etc.The study of optical absorption of transition metal ions (TMI) doped glasses are an attractive area of research both from the fundamental and technological view point [1-5]. The TM ions can be used to probe the glass structure, since their outer d-electron orbital functions have rather broad radial distributions and their response to surrounding cations is very sensitive [6-8]. Transition metal ions have been frequently used as paramagnetic probes for exploring the structure and properties of vitreous systems. Studies of the coordination, bonding characteristics and covalency state of TM ions in glasses are very useful in understanding the structure of the materials in glassy state [9-10].

In recent years the intrest in inorganic glasses contaning transition metal ions has grown because these glasses have properties of technological importance in electronics, tunable solid state lasers and fiber optic communication systems. Alkali fluorobarate glasses are extensively used in phosphors, solar energy converters, solid state batteries and many electronic devices.

2. EXPERIMENTAL

2.1 Glass preparation

Analar grade chemicals were used to prepare the glass samples according to the molecular formula 30 NaF-10 AF_2 - 59 B_2O_3 – 1%CuO (A=Ca, Sr, Ba). Below table lists the batch composition in mol% of glasses studied in the present work. Analar grade reagents NaF, SrF_2, H_3BO_3, CuO, BaF_2 and CaF_2 were taken in appropriate proportions in accordance with the above formula and ground together to constitute a 10g batch. The ground mixture was taken in porcelain crucibles. The melt was held at temperature of about 1000°C for 2 hours until homogeneous glasses were obtained and the melts were quenched in air by pouring on to a preheated steel mold plate to avoid breaking of the samples due to thermal strains and pressing it quickly with another steel plate. These glasses were then immediately transferred to another furnace kept at 300°C and annealed for 5 hours to remove thermal strains and cooled to room temperature. These glass samples were labelled as NCBC, NSBC and NBBC for convenience.

Glass composition	Glass code
30NaF-10CaF_2-59B_20_3 -1CuO	NCBC
30NaF-10SrF_2-59B_20_3 -1CuO	NSBC
30NaF-10BaF_2-59B_20_3 -1CuO	NBBC

2.2. Glass characterization

The glass formation was confirmed by X-ray measurements using Philips X-ray diffractometer PW/1710 with Cu-K_α radiation (λ=1.5406 Å) powered at 40kV and 30mA. The diffractograms have been recorded in the Bragg's angle region $20° \leq 2\theta \leq 80°$ and are shown in **Figure 1**.

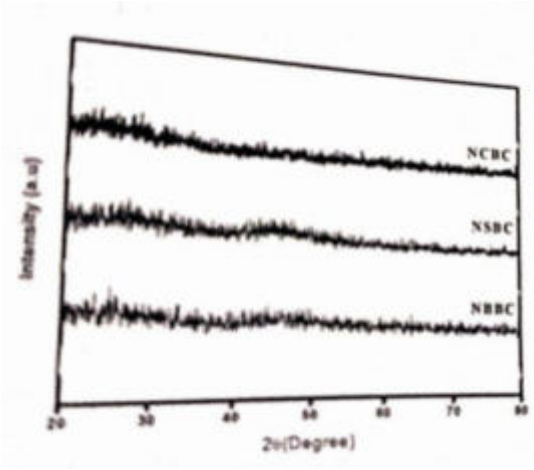

Fig. 1

The glass transition temperature (T_g) was measured in all the glass samples using Modulated Differential Scanning Calorimeter (TA Instruments, DSC 2910). All the samples heated at the rate of 10°C/min in aluminum pans in the temperature range 250 - 550°C. **Figure 2** shows the glass transition temperature of all the samples.

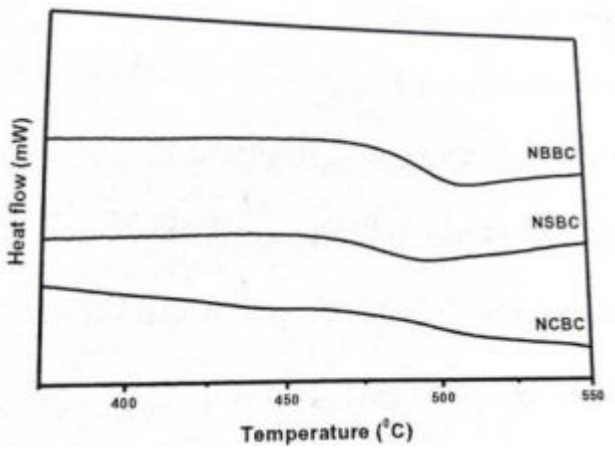

Fig. 2

3. RESULTS AND DISCUSSION

3.1 *Optical band gap and Urbach energy*

The study of optical absorption particularly the absorption edge is useful method for the investigation about the band structure and energy gap in both crystalline and non-crystalline materials. The principle of the technique is that a photon with energy greater than the band gap energy will be absorbed. There are two kinds of optical transitions at the fundamental absorption edge: direct and indirect transitions, both of which involve the interaction of an electromagnetic wave with an electron in the valence band. The absorption coefficient $\alpha(\upsilon)$ can be determined near the edge using the relation [11].

$$\alpha(\upsilon)=(1/d)\ \ln(I_0/I) = 2.303(A/d) \qquad \textbf{(3.1)}$$

where the factor $\ln(I_0/I)$ is the absorbance 'A' at a frequency υ and d is the thickness of the sample. For amorphous materials the optical absorption at higher value of $\alpha(\upsilon)$ ($\geq 10^4$ cm^{-1}) above the exponential tail follows a power law given by Davis and Mott, which in the most general form is given by

$$\alpha(\upsilon)=B(h\upsilon - E_{opt})^n / h\upsilon \qquad \textbf{(3.2)}$$

where B is an energy independent constant and n takes values of 1/2 and 2 for direct allowed and indirect allowed transitions respectively. For the direct transitions from the valance band to the conduction band it is essential that the wave vector for the electron be unchanged. In the case of indirect transitions the interactions with lattice vibrations

(phonons) take place, thus the wave vector of electron can change in the optical transition and the momentum change will be taken or given up by phonons.

Using the above equation, by plotting $(\alpha h\upsilon)^{1/2}$ and $(\alpha h\upsilon)^2$ as a function of photon energy $h\upsilon$. **Figure 3** and **Figure 4** shows the corresponding $(\alpha h\upsilon)^{1/2}$ and $(\alpha h\upsilon)^2$ vs. $h\upsilon$ graph for the all glass samples. The respective values of E(opt) are obtained by extrapolating to $(\alpha h\upsilon)^{1/2} = 0$ for indirect transitions and $(\alpha h\upsilon)^2 = 0$ for direct transitions and are given in **Table 3.1**.

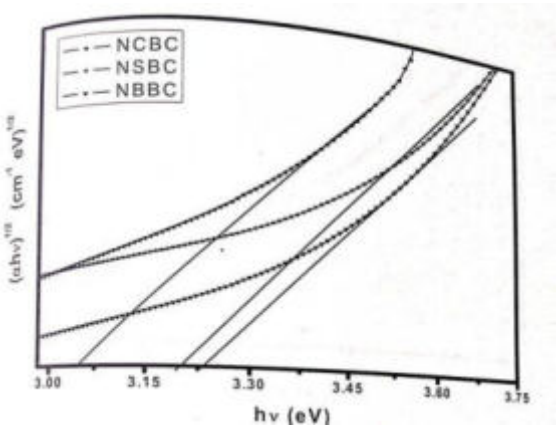

Fig. 3

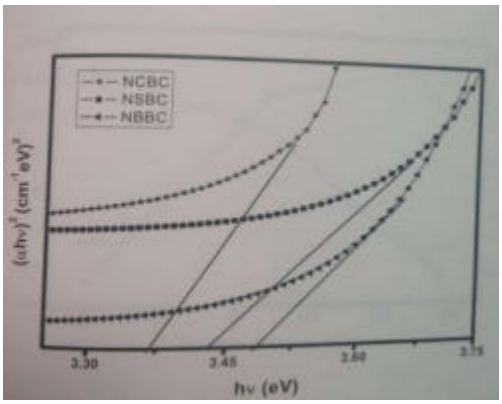

Fig. 4

The variation of ln(α) with $h\upsilon$ is found to be non-linear near UV absorption edge. This indicates the exponential behavior of absorption coefficient near the edge given by

$$\alpha(\upsilon) = B \exp(h\upsilon/\Delta E) \qquad \textbf{(3.3)}$$

Where ΔE is the Urbach energy and is found as the inverse slope of ln (α) vs. $h\upsilon$ plot [15] shown in the **Figure 5**. Urbach energy, which corresponds to the width of localized states, is used to characterize the degree of disorder in amorphous and crystalline systems. Materials with larger ΔE would have greater tendency to convert weak bonds into defects. The values of ΔE of the present glass system is in the range 0.55-0.48 eV (**Table 3.1**) for all the glasses. It can be observed that the decrease in Urbach energy with the substitution of alkaline-earth metals due to decreased defects.

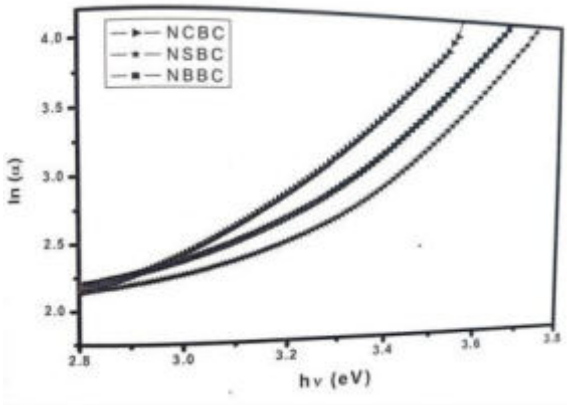

Fig. 5

3.2. *Optical absorption spectra*

The optical absorption spectrum is influenced by the host structure into which the TM ions are incorporated. In oxide glasses, the TM ions mostly form coordination complexes with doubly charged oxygen as the ligands. However Cu^{2+}, being as d^9 ion, experiences a strong Jahn-Teller distortion, which leads to the splitting of energy levels and causes predominantly an elongated octahedral coordination with four short in plane bond lengths and longer axial bond lengths. Accordingly three transitions, viz $^2B_{1g} \longrightarrow {}^2A_{1g}$, $^2B_{1g} \longrightarrow {}^2B_{2g}$ and $^2B_{1g} \longrightarrow {}^2E_g$ are expected. However, only a single optical absorption band was observed in most of the cases. The absorption spectra of copper doped glass samples (**Figure 6**) show that Cu^{2+} single broad band is centered at 813, 763 and 756 nm corresponding to the transition $^2B_{1g} \longrightarrow {}^2B_{2g}$ in NCBC, NSBC and NBBC respectively [12-15].

The values of cut off wave length, optical band gap energy and The Urbach energy are given**.** The oxide ion polarizability and optical basicity values are given in **Table 3.1.**

Table 3.1.

Glass	Cut off wavelength (λc) (nm)	Cu^{2+} peak (nm)	Optical band gap energy (eV)		Urbach energy (ΔE) (eV)	α_{o2-} ($Å^3$)	Λ (E_{Opt})
			indirect	direct			
NCBC	387	813	3.05	3.37	0.55	3.92	1.24
NSBC	337	763	3.20	3.42	0.53	3.29	1.16
NBBC	328	756	3.23	3.47	0.48	2.44	0.98

3.3. *EPR Spectroscopy of Cu^{2+} ions*

Electron paramagnetic resonance is used to characterize the local structure of a para-magnetic centre. EPR can interpret observed transitions among various energy levels, structural and chemical environment about the metal ion. An EPR signal was observed for all the glasses containing Cu^{2+} ions. The EPR spectra of present glass samples are shown in **Figure 7.** Cu^{2+} ion with S=1/2 has a nuclear spin I=3/2 for both ^{63} Cu (natural abundance of 69%) and ^{65}Cu (natural abundance of 31%) and therefore (2I+1) i.e, four parallel and four

perpendicular hyperfine (hf) components would be expected. In the present work, three weak parallel components are observed in the lower field region and the fourth parallel component is overlapped with the perpendicular component. However, the perpendicular components are not resolved (due to the width of the individual components exceeding the $A_\perp$ separation) leading to an intense line in the high field region. It can be observed that the high field side of the spectrum is more intense than low field side. The EPR spectra of all the glasses doped with Cu^{2+} ions exhibit resonance signals similar to those reported for Cu^{2+} ions in glass systems [16-19]. The EPR spectra of copper ions in all the glass samples have been analyzed using an axial spin-Hamiltonian [20] in which the quadrupole and nuclear Zeeman interaction terms are ignored.

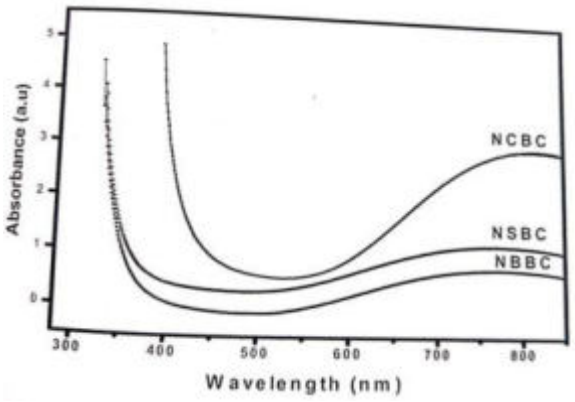

Fig. 6

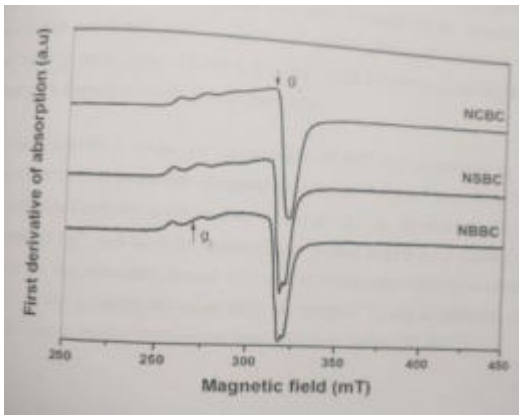

Fig. 7

Spin Hamiltonion equation is

$$H = g_\parallel \beta H_z S_z + g_\perp \beta (H_x S_x + H_y S_y) + A_\parallel I_z S_z + A_\perp (I_x S_x + I_y S_y) \quad \textbf{(3.4)}$$

where $g_\parallel$ and $g_\perp$ are the parallel and perpendicular components of the g tensor and $A_\parallel$ and $A_\perp$ are the parallel and perpendicular components of hyperfine tensor A.

The solution to the spin-Hamiltonian gives the expressions for the peak positions related to the principal values of g and A tensors as [21] for the parallel and perpendicular hyperfine peaks respectively.

$$h\upsilon = g_\parallel \beta H + mA_\parallel + (15/4 - m^2)\ A_\perp^{\,2} / (2\, g_\parallel \beta H) \quad \textbf{(3.5)}$$

$$h\upsilon = g_\perp \beta H + mA_\perp + (15/4 - m^2)\ (A_\parallel + A_\perp) / (4\, g_\perp \beta H) \quad \textbf{(3.6)}$$

Here 'm' is the nuclear magnetic quantum number of the copper nucleus and 'υ' is the microwave frequency at resonance. Using the above equations the spin-Hamiltonian parameters of all the glasses have been evaluated. The observed "*g"* values are characteristic of Cu^{2+} coordinated by six ligands, which form an octahedron elongated along z-axis. From the shape of the EPR spectra it can be observed that the "*g*" values are $g_\parallel > g_\perp > g_e$ (2.0023) and it can be inferred that the ground state of Cu^{2+} ions in all the samples under present study is d_{x2-y2} orbital ($^2B_{1g}$ state) and the site symmetry around Cu^{2+} ion is tetragonally distorted

octahedral sites.Moreover, $g_{\parallel}$, $g_{\perp}$ and $A_{\parallel}$, $A_{\perp}$ values are increasing with respect to the progressive substitution of alkaline earth metals from calcium to barium [22,23].

The values of spin Hamiltonion parameters of the present glass system 30NaF-10AF_2-59B_2O_3 -1CuO glasses (A= Ca, Sr, Ba) agree with this relationship and are close to those of similar copper complexes reported in the literature [53-56]. It is, therefore, confirmed from Table 4.10 that the copper ions in alkali fluoro borate glasses exist as Cu^{2+} ions in tetragonally elongated octahrdral sites and the ground state is d_{x2-y2} orbital ($^2B_{1g}$ state). The line width of parallel hyperfine lines increases in order of m (the nuclear magnetic quantum number of the copper nucleus with values 3/2, 1/2, -1/2 and -3/2). This broadening may be attributed to the micro environmental fluctuations around Cu^{2+} ion, which is intrinsic to the glassy state. The structural variation in glass causes fluctuation in ligand field and in turn, it is reflected in the variation of the spin-Hamiltonian parameters are presented in **Table 3.2**.

Table 3.2 Spin Hamiltonion parameters of Cu^{2+} ions.

Glass	$g_{\parallel}$	$A_{\parallel}$ x 10^{-4} (cm^{-1})	$g_{\perp}$	$A_{\perp}$ x 10^{-4} (cm^{-1})
NCBC	2.366	123	2.088	62
NSBC	2.340	154	2.087	92
NBBC	2.315	184	2.068	123

3.4.Bonding parameters of Cu^{2+} ions

Optical absorption spectra of Cu^{2+} ions in these glasses show broad absorption band whose peak ranges from 813 to 756 nm. This absorption can be assigned to the $^2B_{1g} \longrightarrow {}^2B_{2g}$ transition of Cu^{2+} ion in octahedral symmetry with an elongated tetragonal distortion. The EPR results are consistent with this assumption. The EPR and optical absorption spectral data can be correlated to understand the environment of Cu^{2+} in present glass system, in this connection the bonding parameters are evaluated using EPR and optical data by the following equations [24].

$$g_{\parallel} = 2.003\ [1 - 4\ \lambda\ \alpha^2\ \beta_1^2\ /\ \Delta E_{xy}] \quad \textbf{(3.7)}$$

$$g_{\perp} = 2.003\ [1 - \lambda\ \alpha^2\ \beta^2\ /\ \Delta E_{xz,yz}] \quad \textbf{(3.8)}$$

where the terms ΔE_{xy} and $\Delta E_{xz,yz}$ are the heights of the predominantly d_{xy} and $d_{xz,yz}$ molecular orbital levels above the ground state $d_{x^2-y^2}$ respectively and λ is the spin-orbit coupling constant (= -828 cm^{-1}) and bonding coefficients α^2 β_1^2 and β^2 (= 1.00) characterize respectively, the in-plne σ bonding with the d_{x2-y2} orbital, in-plane π bonding with the d_{xy}

orbital and out-of-plane π bonding with the d_{xz} and d_{yz} orbital of the Cu^{2+} complex in the glasses. In the present glasses the bonding parameters α^2, β_1^2 and β^2 were evaluated.

The normalized covalency of Cu^{2+}-O in-plane bonding of σ and π symmetry is expressed by [25].

$$\Gamma_\sigma = 200(1\text{-}S)\,(1-\alpha^2)\,/\,(1\text{-}2S)\ \%\ \text{and} \qquad \textbf{(3.9)}$$

$$\Gamma_\pi = 200\,(1-\beta_1^2)\ \% \qquad \textbf{(3.10)}$$

where S is the overlap integral ($S_{oxy} = 0.076$).

The calculated values of α^2 for the glasses (**Table 3.3**) suggest that the in plane σ bonding in the glasses is moderately covalent in nature. The values of the molecular orbital coefficient parameter β_1^2 obtained for various glasses indicate that the in-plane π bonding is significantly ionic in nature. All the above observations indicate a gradual transformation of Cu^{2+} ions from covalent environment in present glass system.

Table 3.3. The peak positions and covalency parameters of Cu^{2+} ions

Glass	Cu^{2+}peak (nm)	ΔE_{xy} (cm^{-1})	α^2	β_1^2	β^2	Γ_σ(%)	Γ_π(%)
NCBC	813	12,300	0.785	0.856	0.979	46.85	28.8
NSBC	763	13,106	0.844	0.787	0.911	33.99	42.6
NBBC	756	13,227	0.895	0.696	0.859	22.88	60.8

4. CONCLUSION

- The absence of sharp peaks in the X-ray diffraction pattern, the existence of glass transition temperature Tg in the differential scanning calorimetric traces indicate that the samples prepared were amorphous in nature.
- From the optical and EPR spectra of cu^{2+} ions in sodium fluoroborate glasses, it is found that the Cu^{2+} ions occupied octahedral sites with tetragonal distortion.
- The optical absorption of these samples show single broad band due to cu^{2+} ions distorted octahedral sites.

- Increasing of α^2 is observed in this system, which can be attributed to increase in its ionic character.

5. ACKNOWLEDGEMENT

One of the author Dr. V.Rajashekar Reddy thanks to Dr. V. Raghavender Reddy UGC- DAE, Indore center and Hyderabad Central University for providing experimental facilities.

6. REFERENCES

1. Gan Fuxi *et al.*, Optical and Spectroscopic Properties of Glass, Springer-Verlag., 1992.
2. L.David Pye *et al.*, Borate glasses: Structure, Properties and Applications, Plenum Press., 1978.
3. B.P. Dwivedi *et al.*, J. Phys. Chem. Solids., 1993, **54** 621.
4. H.G. Hecht *et al.*, J. Chem. Phys., 1967, **46,** 23.
5. V.P. Seth *et al.*, J. Non-Cryst. Solids., 1993, **162**, 263.
6. S. Khasa *et al.*, Mater. Chem. Phys., 2001, **72**, 366.
7. K.J. Rao *et al.*, Structural Chemistry of Glasses, Elsevier publisher., 2002.
8. N.J. Kreidl *et al.*, J. Non-Cryst. Solids., 1990, **123**, 377.
9. E.I. Kamistsos *et al.*, J. Mol. Struct., 1991, **247**, 1.
10. G.W. Anderson *et al.*, J. Appl. Phys., 1969, **39**, 1634.
11. E.A.Davis *et al*., Philos.Mag., 1970, **22**, 903.
12. H.Kawazoe *et.al,* J.Non Cryst.Solids., 1979, 33, 103.
13. V. Kamalakar *et al.*, Ind Journal of Pure and Appl Physics., 2010, **48**, 709-715.
14. P.G.Prakash et al., Journal of Material Science., 2004, **39,** 193-200.
15. Swapna, *et al*., Ind Jour of Pure and Appl Phys., 2004, **42,** 560-564
16. R.P.Sreekanth Chakradhar *et al.*, Journal of Alloys and Compounds., 1998, **265,** 29.
17. G.Ramadevudu *et al.*, J. Non Cryst.Solids., 2000, **278**, 205.
18. S.Suresh *et al.*, Phys. Chem. Glasses., 2005, **46**, 27.
19. P. Nageshwara Rao *et al.*, Mater. Chem. Phys., 2005, **91**, 381.
20. A.Abragam *et al*., Proc.Roy.Soc. London.Ser.A., 1951, **205**, 135.
21. B.Bleany *et al.*, Proc. Roy. Soc. London-A., 1955, **228**, 147.

22. R. H. Sands *et al.*, Phys. Rev., 1955, **99**, 1222.

23. H.Imagawa *et al.*, Phys. Status Solidi., 1968, **30**, 469.

24. A.Klonkowski *et al.*, Phys. Chem. Glasses., 1983, **24** (2), 116.

25. H.Kawazoe *et al*., J. Non-Cryst, Solids., 1978, **29**, 173.

An Experimental Investigation on New Engineered Nano Materials on the properties of High Strength Self Compacting Concrete

V.Rajesh[1*], Boppana Narendra Kumar[2]

[1]PG student, Dept. of Civil Engg., VNR VJIET, Hyd.
[2]Professor, Dept. of Civil Engg., VNR VJIET,Hyd, India.

*e-mail: rajeshceiiit@gmail.com

ABSTRACT

There are many recent studies on a newly produced nano materials in cement composites, Graphene Oxide is one among such materials, utilization of Graphene Oxide in self compacting concrete is the moto of this work, the main objective of this project is to make a high strength self-Compacting concrete by using Graphene Oxide which increases the strength of the concrete, in this present work the Graphene Oxide was tried with self - compacting concrete by adding in 0.01%, 0.02% 0.03 % 0.04 %and 0.05% to the weight of the cement to get maximum strength, the mix was done for M40 grade concrete, and in this concrete the cement was replaced with 20% with Fly-ash, and fresh properties test like Slump flow and V- funnel test were performed before casting, this casted specimens were cured for the duration of 7 and 28 days before testing, and the hardened concrete test like Compression, Split tensile and Flexural Strength test were performed at both 7 and 28 days, and the maximum strengths were obtained at 0.05% addition of Graphene Oxide to the concrete.

Keywords: Slump Flow, Graphene Oxide, Compressive Strength, Split Tensile Strength

1. Introduction

As the cement is the mostly used binding material in concrete and as well as in mortar, the usage of cement has rapidly increased in the field of construction, due to the greater demands there are many producers in the market, these cement manufacturers produces 8% of CO_2 among the all other carbon dioxide producers, this leads to global warming and which makes a huge impact on living and non-living being, approximately 3.0 tonnes of raw materials which includes materials like silica, alumina, calcium, iron and fuel are required to produce 1.0 tonne of Portland cement.

Concrete is the material which provides a rock like massive substance on hardening, this concrete consists of materials like fine aggregate (sand & rock dust) and coarse aggregate (gravel) which are bonded together by a cementitious material especially like cement, this cement when mixed with coarse aggregate, fine aggregate and water forms a fresh concrete, the concrete strength increases with increase in its age and becomes constant at a point.

This concrete is mainly divided it in to three parts according to the Indian standards, the first one is the Ordinary concrete (M10 to M20 grade), the second one is the Standard Concrete (M25 to M55 grade), and the third one is the High strength concrete (M60 to M80 grade).

As there are many difficulties being faced in the field of construction because of conventional concrete which requires a mechanical vibrators to remove voids and to occupy the complete shuttering space, in order to avoid this self compacting concrete is developed [1].

2. Materials Used

The constituents material which are used for the development of High Strength SSC are Ordinary Portland Cement 53 Grade (binder-1), Fly-ash (binder-2), River Sand (fine aggregate), Gravel (coarse aggregate), water (as hardener), Master Glenium ACE 30 (super plasticizer), Graphene Oxide (additive).

3. Methodology

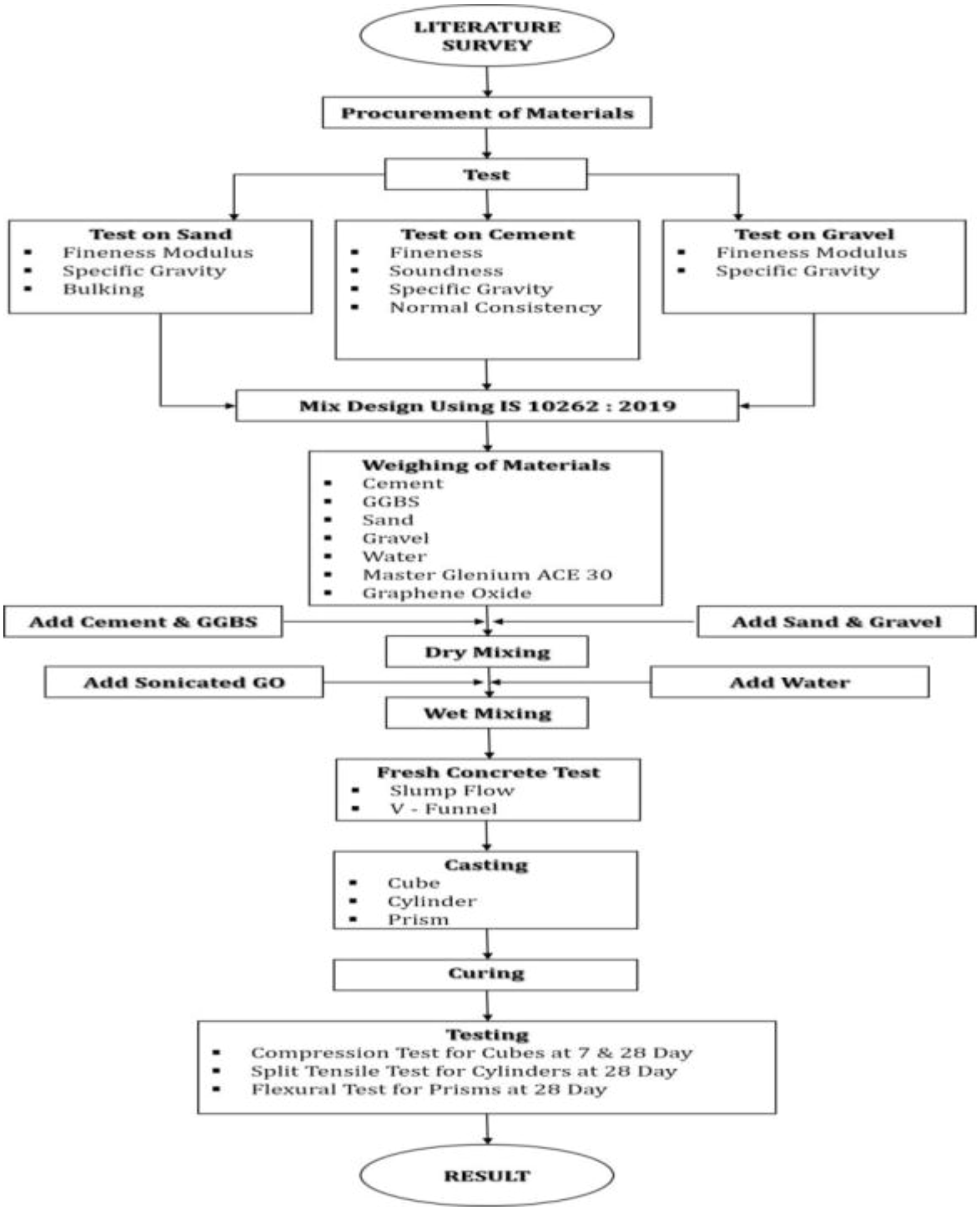

4.Ingredients of Concrete

To make a Self- Compacting Concrete the material required are follows:

a)	BINDER	:	OPC 53grade cement and fly ash
b)	FINE AGGREGATE	;	River Sand
c)	COARSE AGGREGATE	:	Gravel
d)	HARDENER	:	Water
e)	SUPER PLASTICIZER	:	Master Glenium ACE 30
f)	ADDITIVE	:	Graphene Oxide (GO)

5. Trial Mix Proportions

During the first stage the GGBS was been optimised with the cement content based on fresh and hardened properties of concrete and in second stage the properties were to be improved by adding Graphene Oxide additive in various percentages and to be confirmed whether improves the fresh and hardened properties[2].

6. Experimental Programme

6.1 Batchingor Weighing

In this process the instruments which are used for measuring were checked for their accuracy, later the cement, GGBS, sand, gravel and Super Plasticizer were done in proportioning which was given by the Mix Design procedure and were weighed and then later transferred to the mixing pan[3], the graphene oxide was weighed with a greater accuracy instrument and the and the water was measured in volume.

Fig 1: Batching or Weighing

6.2 SONICATION

Sonicator uses sound waves to disperse additive material particles in a solution, and it alters an electrical signal into a physical vibration to break substances apart, these disruptions can mix solutions, accelerates the dissolution of a solid into a liquid, and removes dissolved gases from liquids, the Graphene Oxide is to be added in to the water in mentioned quantity any to be sonicated for 30 minutes at 30°c.

Fig 2 Sonication

6.3 Compression Test

Compression Test plays a vital role among the all other hardened properties which provides a compressive strength value, in this test the cubes of 150 mm in sizes are used, and this cubes are generally cured for the duration of 1,7,14 and 28 days and then tested in a compression testing machine in which the load is applied uniformly increasing manner.

Fig 3: Compressive Testing

6.3.1 Procedure for Compressive Testing

- The cubes whose strength is to be found is taken out from the curing tank and placed at room temperature for 1 hour, later the cube is cleaned with cloth.
- This cube whose strength is to be found is termed as specimen which will be placed in a platens of compression testing machine.
- Before placing the cube in between platens, the surfaces of the plates must be checked whether its clean or not, or else the surface of the plates must be cleaned.
- The cube must be placed properly in the centre of the plates.
- The load on the cube must be applied without any jerks and the rate of apply of load must be uniform.

- The point at which the cracks would be observed on the surface of test specimen and the specimen tends to fail, during this failure the highest applied load is to be recorded.

7. Experimental Investigation

7.1: Slump Flow Test Results

The below bar graph shows the slump flow of M60 grade concrete on which five trials were performed by changing in percentages of Graphene Oxide like 0.01, 0.03 and 0.05%.

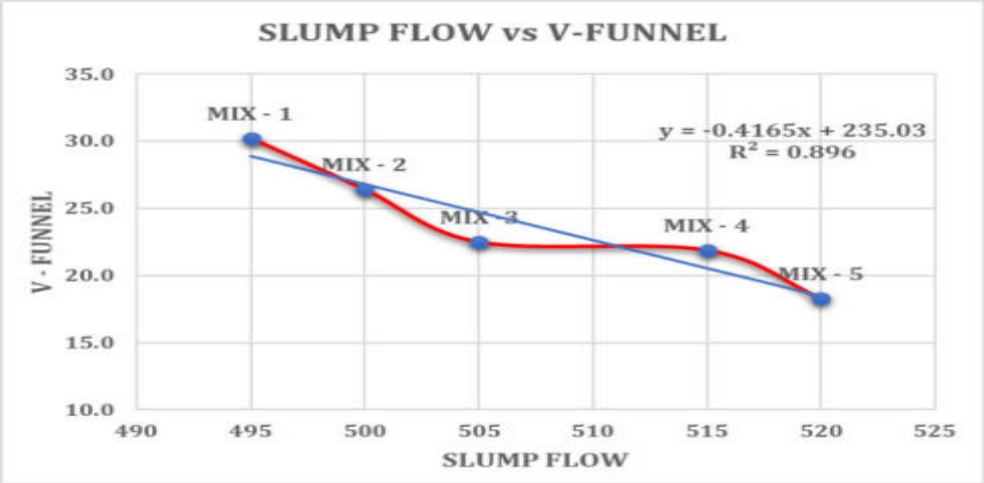

6.1.3 COMPRESSION TEST RESULT

The below graph shows the compressive strength results of the M60 grade concrete on which five mix trials were performed by changing in percentages of Graphene Oxide like 0.01, 0.03 and 0.05% and the test were conducted for both 7 and 28 days of curing.

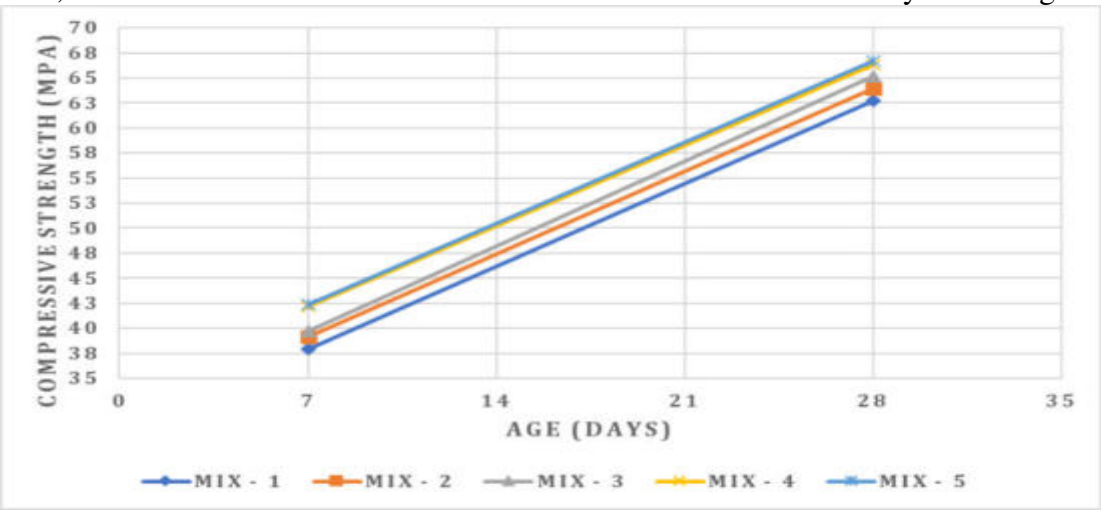

7. Conclusions

The following conclusions were made from the above test results:

The Research findings of this paper is , the compressive strength, the split tensile strength and the flexural strength values were improved when Graphene Oxide of 0.05% to the weight of cement content was been added to the self compacting M60 grade concrete.

References

1. Dimitar Dimov *et al.*, Advanced functional materials., 2018, **28**, 1705183.

2. Samuel Chuah *et al.*, Construction and Building Materials., 2014, **73** (30), 113-124.

3. S.C. Devi *et al.*, Journal of Building Engineering., 2020, **27**, 101007.

Interaction of Calcium Magnesium Alumino Silicate on Thermal Barrier Coating Materials at High Temperatures

Sophia Rani. I[1]*, Radha Kanta Satpathy[2] and Zafir Alam[2]

[1]Bharat Institute of Engineering and Technology, Mangalpally, Hyderabad, India
[2]Defense Research Metallurgical Laboratory, Kanchanbagh, Hyderabad, India
***Email:** sophiarani@biet.ac.in

Abstract

Ceramic thermal barrier coatings (TBCs) are deposited on turbine components of advanced aeroengines to reduce the requirement of the cooling systems. However, during operations at high temperatures, ingestion of airborne particles such as sand and ash leads to progressive infiltration of molten calcium magnesium alumino silicate (CMAS) glass into TBC structure leading to premature failure of the coating. Therefore, study of the corrosion mechanism of CMAS on advanced TBC materials is essential to develop durable coatings for futuristic aeroengines. In the present study, interaction of CMAS with the state-of- the-art TBC material namely yttria stabilized zirconia is presented. Further, interaction of CMAS with new TBC material namely lanthanum zirconate is also presented. Yttria stabilized zirconia destabilized after 1 hour of interaction with CMAS at 1450°C whereas lanthanum zirconate continued to be stable for 100 hours at the same temperature and conditions. The protective mechanism that restricts the damage of lanthanum zirconate based TBCs such as formation of stable rod-shaped apatite phases could be observed and confirmed by SEM and XRD. Thermal diffusivity and wettability studies were carried out to further study the failure mechanism of the TBCs while interacting with molten CMAS.

Keywords: Thermal barrier coating, Air plasma spray (APS), CMAS, yttria stabilised zirconia, freestanding coatings, thermal diffusivity.

1. Introduction

"CMAS attack" on hot end components, namely the high-pressure rotating turbine blades, is a major challenge faced by the gas turbine industries. Suitable thermal and environmental barrier coatings (TEBC) are currently in demand for protecting turbine engine components in high temperature combustion environments against CMAS attack [1]. Hitherto, yttria stabilized zirconia is extensively used as thermal barrier coating for turbine components. However, their resistance to CMAS attack needs to be evaluated in order to ensure protection of the underlying components at high temperatures. More over new coating materials with comparable coefficient of thermal expansion to that of yttria stabilized zirconia need to be explored and their resistance to CMAS are to be evaluated [2,3]. In the present work, free standing coatings of yttria stabilized zirconia and lanthanum zirconate were fabricated by atmospheric plasma spray deposition method. Their resistance to CMAS was studied systematically at 1450°C.

2. Experimental

2.1 Preparation of free standing coatings of 8-YSZ and LZ

Free standing coatings of 8- yttria stabilized zirconia (8-YSZ) and lanthanum zirconate (LZ) were fabricated by atmospheric plasma spray method. A Metco 9MB plasma torch gun was

used for coating deposition. Stainless steel substrates with a diameter of 12 mm and thickness of 5 mm were prepared using wire electrical discharge machining followed by mild grit blasting and the discs were cleaned thoroughly using ethanol. The clean substrates were then used as substrates for the coating deposition. Commercially obtained LZ and YSZ powders were used for coating deposition and a coating thickness of 200–250μm was maintained for both 8-YSZ and LZ coatings. The free standing coatings could be obtained by natural delamination of the coatings after certain period of cooling at room temperature due to thermal stresses between the ceramic coating material and the stainless steel substrate.

2.2: Slurry deposition of CMAS on the free standing coatings

The CMAS deposit is found as a brownish powder on the after-flight components, and was collected from HAL, Koraput. Slurry was prepared by dispersing CMAS in ethanol by manual stitring. The slurry was applied on to the entire top surface of the disks by a paint brush. The amount of slurry applied on the disks was kept constant at 10 mg/cm^2.

2.3: Isothermal high temperature exposure and further evaluation

The free standing coatings were subjected to isothermal exposure in air at 1450°C up to 100 hours. The microstructure, phase studies, thermal diffusivity studies and wettability studies were carried out systematically. Fig. 1a & 1c are the images of the as- prepared, free standing coatings LZ and YSZ coatings respectively. Severe reaction indicated by change in physical appearance after the heat treatment could be observed (Fig. 1e & 1f).

Fig. 1 (a) Free standing coating of LZ (b&c) LZ coating loaded with CMAS (c) free standing YZ coating (d) YZ coating loaded with CMAS (e) YSZ coating after reacting with CMAS (f) LZ coating after reacting with CMAS

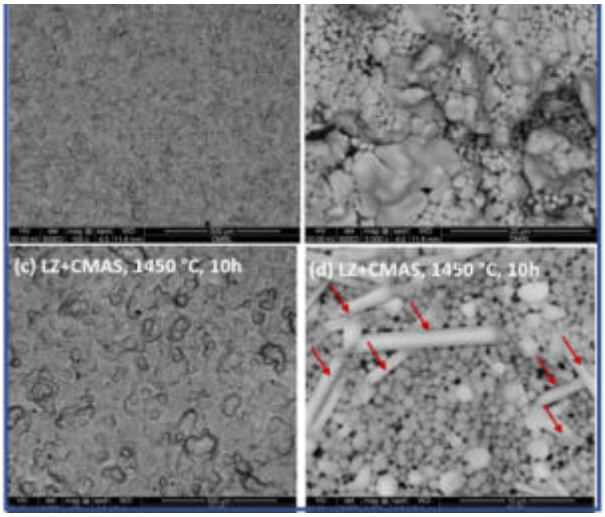

Fig.2.SEM images of free standing coatings after reaction with CMAS at 1450 °C for 10 hours. The red arrows indicate rod-like apatite phases.

3. Results and Discussion

3.1 Microstructural studies

The extent of reaction of calcium magnesium alumina silicate (CMAS) deposit on the surface of the free standing YZ and LZ coatings, treated at 1450 °C for 10 hours is shown in Fig. 2. The presence of granular precipitates on the CMAS loaded YSZ samples shows that YSZ has reacted and reprecipitated, presumably with lower yttria content. This phenomenon of leaching of yttrium from YSZ leads to the formation of monoclinic zirconia which is detrimental for the life of the coating. The presence of rod like precipitates on CMAS reacted

lanthanum zirconate coatings and the gradual densification of such reacted layer with respect to time is due to the formation of apatite phases and their densification on the surface the coating. Formation of apatite phases and densification is favourable to arrest further reaction and infiltration of CMAS that can actually happen during the flight of the component.

3.2 Phase evaluation studies

Fig. 3a shows the x-ray diffraction pattern for LZ and YSZ coatings before and after reaction with CMAS. A reaction product with the chemical composition of $La_2Ca_2(SiO)_4O_2$ was formed on the sample treated for 1 hour. The same reaction product was found to be present on the samples treated for 100 hours and it was found to be stable. The formation of this reaction product on the surface of LZ coating prevents further damage of the underlying component by the CMAS attack. In other words, the LZ coating acts almost as a sacrificial coating layer and spends its composition to react with CMAS. In case of YSZ coatings, the coating destabilized from tetragonal zirconia to monoclinic and cubic structures after thermal exposure for 1 hour. This indicates that 8-YSZ is not reliable as a TBC at 1400°C.

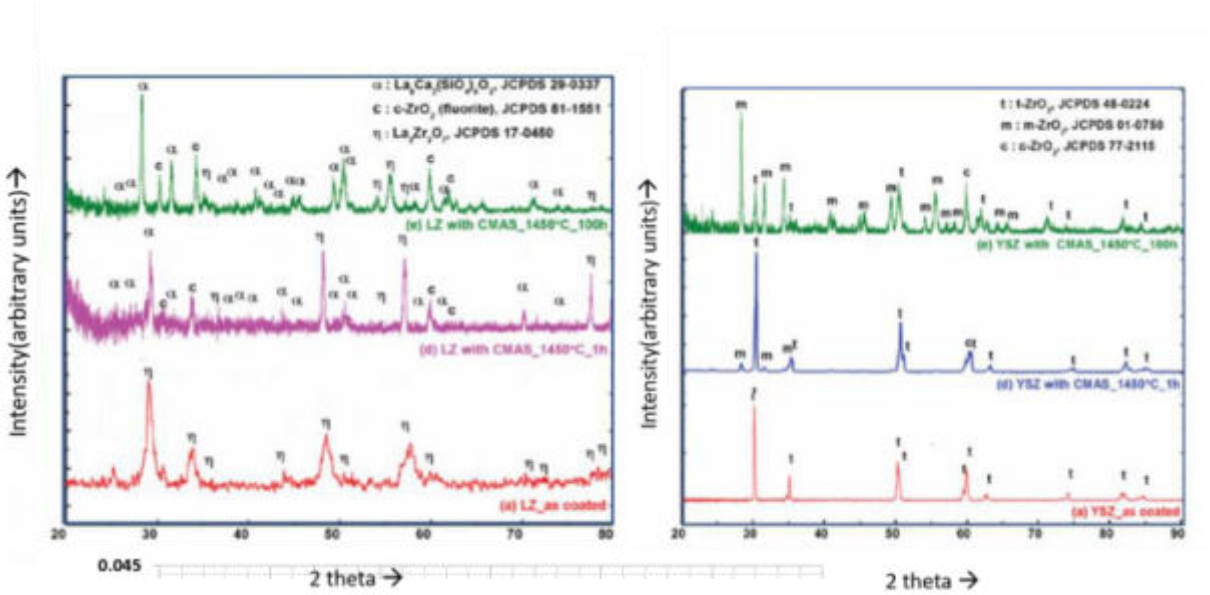

Fig.3 XRD of free standing coatings before and after reaction with CMAS at 1450 °C for 1 and 100 hours (a) LZ (b) YSZ.

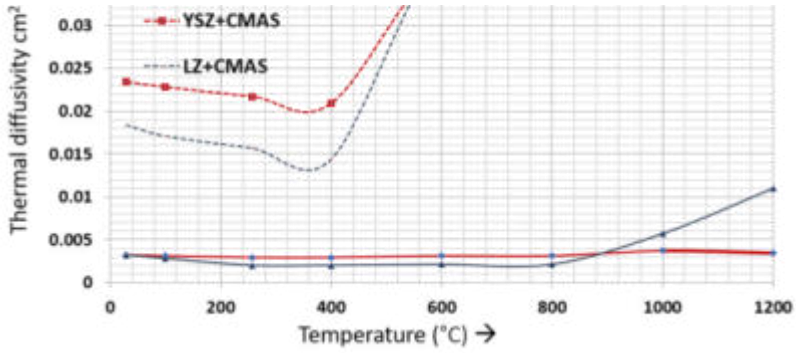

The YSZ coating treated up to 100 hours degraded further which is indicated by the presence of large fraction of monoclinic zirconia.

3.3 Thermal diffusivity studies

Thermal diffusivity plot for LZ and YSZ coatings is shown in Fig. 4. The coatings were stable up to 1200 °C as indicated by the plot. The coatings loaded with CMAS had a sudden rise of thermal diffusivity values at about 600 °C after which the diffusivity stabilized. The rise of diffusivity at about 600°C is presumably due to the closure of pores in the coating due

Fig. 4. Thermal diffusivity plot of free standing coating of LZ and YSZ with and without CMAS up to 1200 °C.

to the presence of CMAS. The closure of pores affects the basic function of thermal barrier coating to an extend and therefore CMAS attack is considered to be an important factor and suitable measures are to be adopted while employing LZ and YSZ TBCs, especially on vehicles that are to be deployed in CMAS rich environment.

3.4 Wettability studies

Table 1: Wettability study results of LZ and YSZ coatings

Sample	Radial Spread
LZ+CMAS	2.69 ± 0.7 mm
YSZ+CMAS	3.95 ± 0.5 mm

The CMAS powder was loaded on to the LZ and YSZ coatings as a blob with 2 mm diameter and then heat treated at 1250°C for 1 hour in air furnace. The extend of spreading of CMAS powder on the surface of the coating was carefully measured by an optical microscope. The measurements as indicated in table 1 imply that LZ coating held the CMAS powder on its surface without allowing large spread of the CMAS powder on the coating surface. The diameter of the CMAS blob was only 0.69 ± 0.7 mm higher than the original 2mm diameter of the blob. In case of YSZ the diameter of the CMAS blob increased by 1.95 ± 0.5 mm over the original CMAS blob of 2mm diameter. The CMAS spreaded readily which is an indication that YSZ doesn't react or form any reaction product and the spreading is mostly due to physical melting. As presented in previous studies, smaller spreading area is an indication of higher CMAS resistance [4, 5].

4. Conclusions

- Lanthanum zirconate coating was superior to 8-Yttria stabilized zirconia in terms of CMAS resistance of the coatings at 1450°C.
- The underlying mechanism for the superior CMAS resistance was found to be the formation of impenetrable apatite phase up on reaction with CMAS in case of lanthanum zirconate coatings
- The lanthanum zirconate coating was stable up to 100 hours at 1450°C
- The 8-yttria stabilized yttria coatings were destabilized to monoclinic and cubic phases after 10 hours of reaction with CMAS
- The thermal diffusivity of LZ is higher at high temperatures compared to YSZ in the presence of CMAS
- Wettability studies showed that lanthanum zirconate absorbed and spreaded the CMAS to a lower extent compared to yttria stabilized coatings
- Therefore, the effect of CMAS on coating degradation cannot be neglected [6] and further studies on multilayer composite and graded coatings are necessary to develop durable TBCs [7].

Acknowledgement
The authors thank Director, DMRL-Hyderabad, for his permission to pursue this research.

References

1. I. Webster Rebekah *et al.*, Journal of Materials Research., 2020, 1-15.
2. H. Zhao *et al.*, Surface and Coatings Technology., 2014, **251**, 74–86.
3. J. Zhang *et al.*, Surface and Coatings Technology., 2017, **323**, 18–29.
4. Zhang XF *et al.*, Ceramics International., 2016, **42**, 19349–19356.

5. W.E. Lee *et al.*, VII Int. Conf. Molten Slags Fluxes Salts, Cape Town: The South African Institute of Mining and Metallurgy., 2004**,** 309- 319.
6. G.Boissonnet *et al.*, Journal of the European Ceramic Society., 2020, **40**, 2042-2049.
7. X. Chena *et al.*, Journal of the European Ceramic Society.**,** 2020, **40**, 1424-1432.

Dielectric Studies of La^{3+} doped Cobalt Nano Ferrites Using Combustion Method

S. Abdul Khader[1*], Asiya Parveez[1], Chivukula Srikanth[2], Tanveer Fatima[3] and Devidas G. B[4]
[1]Department of Physics, Govt.Science College, Chitradurga-577501, Karnataka. India
[2]Department of Physics, Govt.College (Autonomous), Kalaburagi-585105, Karnataka.
[3]Department of Physics, Gulbarga University, Kalaburagi-585105, Karnataka, India.
[4]Department of Physics, Kuvempu University, Shimoga-577451. Karnataka, India.
***Author for Correspondence: khadersku@gmail.com**

Abstract
La^{3+} substituted cobalt ferrite nanoparticles with the chemical composition $La_xCoFe_{2-x}O_4$ (here, x=0, 0.05, 0.1, 0.15 and 0.2) were synthesized using auto-combustion method. Structural and morphological studies were probed using X-ray diffraction (XRD) and Field emission scanning electron microscopy (FESEM). X-ray diffraction studies confirms the single phase spinel cubic structure for the La^{+3} doped $CoFe_2O_4$. Average crystallite size (D) was found to be varying from 43.71nm to 55.37nm with the increase in La^{3+} concentration. Frequency dependent dielectric properties of synthesized samples were measured from 100 Hz to 1 MHz at room temperature using a precision HIOKI make LCR HI-TESTER. Dielectric dispersion was observed at lower frequencies for the synthesized samples.

***Keywords**: Combustion method, Ferrites, Crystallite Size, Dielectric Studies.*

1. Introduction
Materials in the nano-scale regime exhibit remarkably new properties compared to materials at their bulk counterpart. Nanomaterials appear in every industry from agriculture to service sector. Numerous applications of nano-technology find in wide range of industries enlarges day to day and a few of applications are transformer inductors, humidity sensors, drug delivery systems, electronic components, multilayer chip inductors, in enhanced photo catalytic performance, magnetic resonance imaging etc. [1-5]. Among the ferrites, spinel ferrites with nano-structure are most important. Ferrites comes under magnetic materials family and the spinel structure with molecular formula AB_2O_4(A^{2+} B_2^{3+} O_4^{2-}) where A is divalent metal ion e.g. Fe, Mg, Zn, Ni, Mn, Cu, Co, etc., and B is trivalent cation e.g. Fe^{3+}, Al^{3+} etc., and O=oxygen anion e.g. O^{2-} Metal cations, A and B are fitted at A-site (tetrahedral site) and B-site (octahedral site) and oxygen has face centred cubic(FCC) close packing structure [6]. Spinel ferrites are familiar dielectric materials with high resistivity and low hysteresis loss. An account of their peculiar magnetic, dielectric and electrical properties of spinel ferrites, they are used in high density information storage system, medical diagnosis, transformer cores, inductor coils, microwave devices, telecommunication, microwave absorbers, magnetic recording, biosensors, power transformers, radio electronics etc. [5,7-10].

Cobalt ferrites are a well-known fact that they are hard magnetic materials, which is studied in detail due to its high coercivity, high chemical stability, high saturation magnetization, mechanical hardness, high resistivity and good electrical insulator [11]. Various research studies explain the cobalt ferrites doped with divalent and trivalent metal ions such as Mn^{+2}, Mg^{+2}, Zn^{+2}, Ni^{+2}, La^{+3}, Ga^{+3} etc. are received increasingly attentiveness in many applications, especially for sensors and high frequency applications. Properties of cobalt ferrites can be altered such as by incorporating a dopant into its structure, sintering temperature and preparation methods. Consequently, based on their structural, optical, magnetic and electrical properties they can be used in many applications [12-14].

In this work, an in-expensive auto-combustion method is chosen as it provides good crystallinity, less power consumption, high purity, ease of sample preparation, stability etc. compared to other techniques like co-precipitation method, sol-gel, micro emulsion route, hydrothermal method [16-20]. Herein, La^{+3} is elected as dopant and substituted it into cobalt ferrite system. Effect of lanthanum (La^{+3}) substitution in $CoFe_2O_4$ can be studied on its structural, morphological, dielectric and hence electrical properties.

2. Experimental

Lanthanum (La^{3+}) doped nano cobalt ferrite powders were synthesized using auto-combustion method. This method is the simplest and reliable method for obtaining high purity nano-materials. To prepare $La_xCoFe_{2-x}O_4$ nano-powders, the precursors selected are, $La(No_3)_3.6H_2O$ (Lanthanum nitrate), $Co(No_3)_2.6H_2O$ (Cobalt nitrate), $Fe(No_3)_3.9H_2O$ (Ferric nitrate) and $C_6H_8O_7$ (Citric Acid). All the chemicals were procured from Sigma Aldrich; all are of 99.8% purity. Calculated stoichiometry molar amounts of lanthanum, cobalt, and ferric nitrates are added with distilled water and mixed thoroughly using a magnetic stirrer until metallic nitrates are dissolved completely at room temperature. While aqueous solution of citric acid was prepared and added slowly to the aqueous solution of corresponding metallic nitartes. Aqueous solution containing redox mixture was taken in a silica crucible and allowed in to a muffle furnace, which was already pre-heated to a temperature of 500^0C. Because of the auto-combustion reaction, aqueous mixture of metallic nitrates and organic fuel finally yields porous and fluffy voluminous powder. Fluffy material was well grinded to get ferrite powder. As-burnt ash was calcined at 900^0C for 4 hours to get better crystallization and homogeneous cation distribution in the spinel and finally grinded to get La^{+3} doped $CoFe_2O_4$ ferrite nano powders.

3. Results and Discussion

3.1 Phase confirmation studies: Phase confirmation of the prepared samples is done using Bruker AXE D8 Advanced diffractometer. Diffractogram of $La_xCoFe_{2-x}O_4$ (x=0, 0.05, 0.1, 0.15 and 0.20) powder nano-particles are shown in Fig 1. Obtained XRD data of La^{+3} substituted $CoFe_2O_4$ are compared with standard data (JCPDS PDF card No.22-1086).

Average crystallite size (D) was calculated using the Scherer – Debye Eq. (1) [20].

$$D = 0.9\,\lambda/\beta\cos\theta \quad \text{.....(1)}$$

Lattice parameter or lattice constant (a=b=c) is measured using Bragg'sequation for all LCF samples by the maximum intense peak (311) using Eq. (2) [20].

$$a = d_{311}\sqrt{h^2+k^2+l^2} \quad \text{.....(2)}$$

Where $d_{311}$is the inter-planar spacing for the (311) reflection plane and (h, k, l) are the corresponding miller indices.

Average crystallite size was found to be varying from 43.71nm to 55.37nm along with the increase in the La^{3+}concentration from 0.05 to 0.2. This might be because of the distortion caused in the structure with the substitution of rare earth La^{+3} concentrations. It is observed that the lattice constant increased from 8.37Å to 8.48Å with increasing the doping ratio of lanthanum, this is due to that La^{3+} has larger ionic radii 1.031Å replaces the Co^{2+}(0.74Å) and Fe^{3+}(0.64Å) ions having lower ionic radii in La-doped $CoFe_2O_4$ system. This kind of behaviour being caused by cation distribution between the two sites. Therefore, more energy is needed to get La^{3+} ions enter the spinel lattice to complete crystallization.

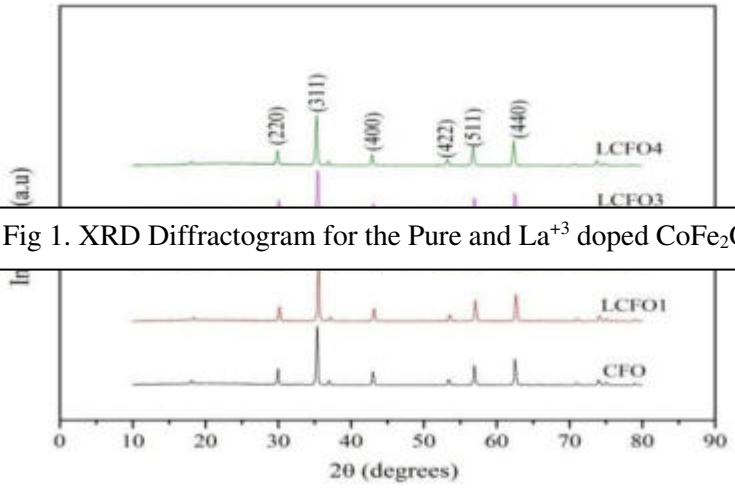

Fig 1. XRD Diffractogram for the Pure and La^{+3} doped $CoFe_2O_4$

Morphological Studies Surface morphology of the synthesized LCF nano-particles were analysed using FESEM (FEG-Quanta-250), indicates that homogeneous nature for the obtained nano-powders and are shown in Fig 2. Field emission scanning electron micrographs shows that the morphology of the particles regular distribution of nano-particles. FESEM micrographs further suggests that the samples consist of cubical shaped nano-particles with agglomeration. As the doping concentration of La^{+3} increases, the gain becomes more and more dense.

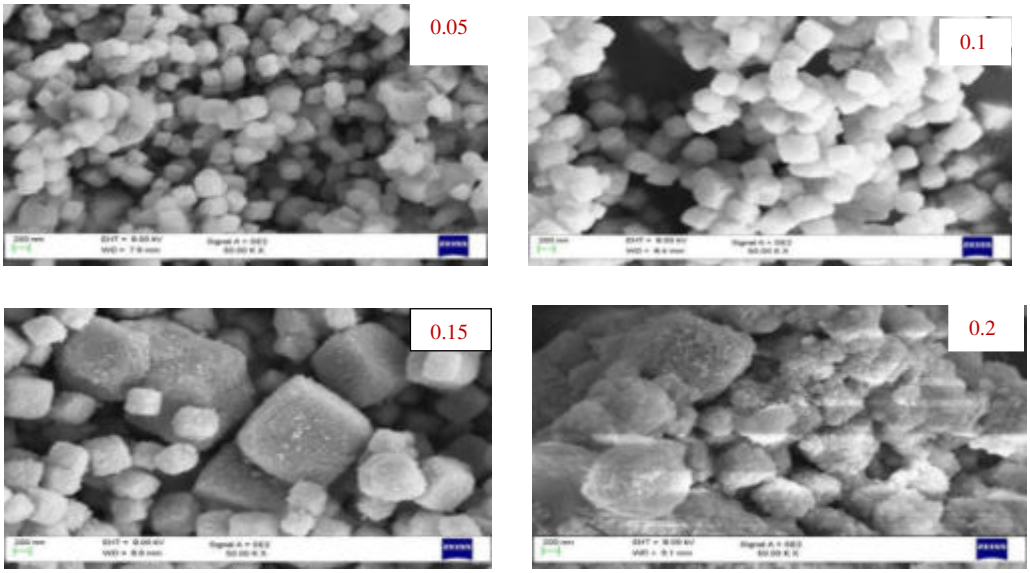

Fig. 2. Micrographs of the LCF samples with various doping concentrations.

3.2 Dielectric Studies

Variation of dielectric constant (ε'), and its imaginary counter-part (ε'') and ac conductivity (σ_{ac}) with frequency at room temperature for the pure cobalt ferrite and La^{+3} doped cobalt ferrite is shown in Fig.3 (a) to Fig.3 (d), it is clear that ε' decreases steeply at lower frequencies and remains constant at higher frequencies. The variation of dielectric constant with applied frequency is due to charge transport relaxation. This dielectric dispersion is attributed to Maxwell and Wagner type of interfacial polarization which is in agreement with Koop's theory, as the dielectric constant is a combined effect of dipolar, electronic, ionic and interfacial polarizations [20-24]

In order to understand the conduction mechanism and type of polarons responsible for conduction, ac conductivity, σ_{ac} were estimated as per $\sigma_{ac}= \omega\ \varepsilon_0\ \varepsilon''$, with ε_0 is the permittivity of free space and $\omega=2\Pi f$.

Variation of σ_{ac} with frequency, ω is shown in Fig.3(c) for all the samples. Obtained plots are linear for almost entire range of frequency except at very low frequencies. Linear variation of σ_{ac} with frequency indicates that the conduction occurs by the hopping of charge carriers between the localized states which confirms the small-polaron typeof conduction [24-26].

Fig3. Variation of ε^{I}, ε^{II} , $\ln(\sigma_{ac})$ with frequency $\ln(\omega)$ for the proposed samples

4. C
4.

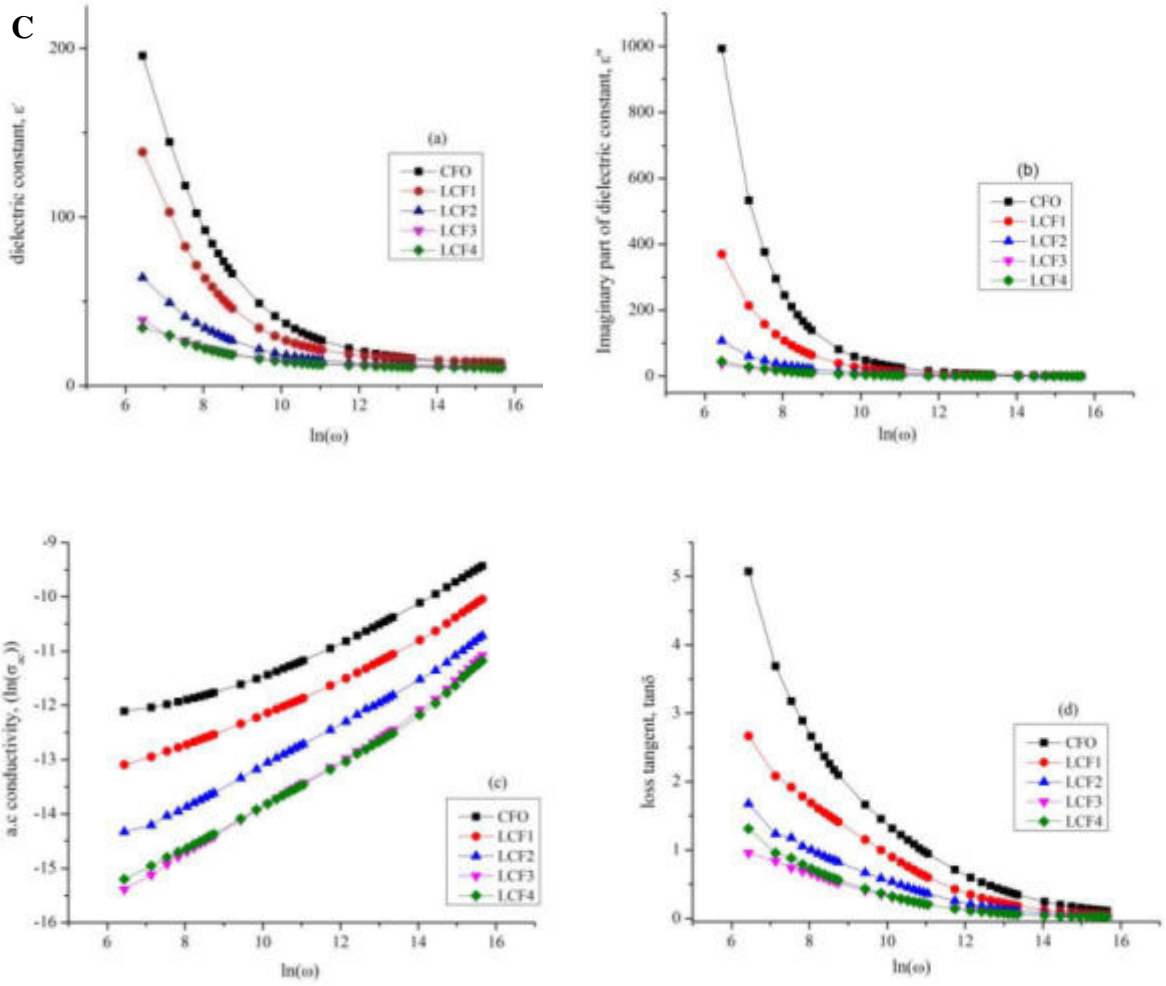

4. Conclusions

All the synthesized samples have single phase spinel cubic structure, without any secondary phases indicating the absence of any impurities. From the dielectric measurements, it is observed that the synthesized samples exhibited dielectric dispersion. Linear nature of AC conductivity measurements, confirms the conduction mechanism in the proposed samples is because of small-polarons.

References

1. P.Kumar *et al.*, J. Electro-ceramics., 2011, **27** (51), 9649-4.
2. T. Ramaprasad *et al.,* Mater.Res.Express., 2018, **5**, 095025.
3. P.Kumar *et al.*, Journal of Alloys and Compounds., 2010, **508**, 115-118.
4. Simona Burianova *et al.*, Journal of Applied Physics., 2011, **110**, 073902.
5. K.C. B Naidu *et al.,* Jour. Materials Chemistry and Physics., 2017, **187**, 164-176.
6. S. Sun *et al.*, J.Appl.Chem.Soc., 2004, **126**, 273-279.
7. K.C. B Naidu *et al*., Jour. Bulletin of Materials Science., 2017, **40**, 417-425.
8. C.B.Naidu Kadiyala *et al.*, Jour.Phase transitions., 2017, **90**, 847-862.
9. Yuksel koeoglu *et al.*, Ceramics International., 2012, **38**, 3625-3634.
10. U.Naresh *et al.*, Jour. Materials Chemistry and Physics., 2019, **236**, 121807.
11. A. Muhammad *et al*., Journal of Applied Phy., 2009, **111**, 013918.
12. M.Shyam *et al.*, IPCBEE, IACSIT Press, Singapore., 2012, **46**.
13. A.B.Shinder *et al.*, International Journal of Innovative technology and exploring engineering (IJITEE)., 2013, **3** (4).
14. M.Pawan kumar *et al.*, Jour. Integrated Ferroelectrics., 2012, **134**, 53-57.

15. Ragendran Indhrajothi, *et al.*, Ceramics international., 2012, **38**, 4771-4782.
16. Elina Manova *et al.*, Chem. Mater., 2004**, 16**, 5689-5696.
17. N. Suresh kumar *et al.*, Ceramic International., 2018, **44 (16),** 19408-19420.
18. Ragendran Indhrajothi., New J. Chem., 2015, **39**, 4601-4610.
19. P. Annie Vinosha *et al.*, Materials Science & Engineering., 2017.
20. Pawan kumar *et al.*, Jour. Integrated Ferroelectrics., 2012, **134**, 53-57
21. O.P. Verma *et al.*, Mater. Sci. Eng. B., 2005, **116**, 1–6.
22. X. Batlle *et al.*, J. Phys. D: Appl. Phys., 2002, **35**, 15–42.
23. A. Thakur *et al.*, J. Phys. Chem. Solids., 2007, **68**, 378–381.
24. Z. Beji *et al.*, Chem. Mater., 2010, **22**, 1350–1366.
25. T. Upadhyay *et al.*, Phys. Rev. B., 1997, 55, 5585–5588.
26. K. Raju *et al.*, Ceram. Int., 2014, **40**, 9337–9344.

Green Synthesis of Silver Nanoparticles Using Leaf Extract of Argyreia Nervosa and its Anticancerous Activity

Chittepu Obula Reddy*, Ananya Sangineni, Sana Thabassum, Sreya
Chaitanya Bharathi Institute of Technology, Hyderabad

Email: cobulreddy_biotech@cbit.ac.in

Abstract
Cancer is an abnormal mass of tissue which may be solid or fluid filled, cells divide more and do not die.Anticancer agents can be divided into alkylating agents, topoisomerase inhibitors. But all these have side effects like alopecia, myelo suppression, etc. Plants are the new economic and highly effective resources for drugs to treat the cancer. A. nervosa, belongs to family- Convolvulaceae. It is a woody climber and is also called by the name Elephant Creeper. It has wide range of pharmacological activities. Silver has been recognized as a nontoxic, safe inorganic antibacterial/antifungal agent used form many years. Silver shows a very high potential in a number of scientific applications, more particularly in the form of nanoparticles. Silver nanoparticles can be successfully used as antitumor agents due to their antiproliferative and apoptosis inducing properties. These are considered potentially ideal for cancer treatments. The present paper focuses on the evaluation of the invitro anticancer potential of the aqueous leaf extract of Argyreia nervosa and silver nanoparticles synthesized from it, on HeLa cell line. The cell growth inhibition was tested by using MTT assay.

Keywords: Green Synthesis, Nano particles, Anticancer, Argyeria nervosa

1. Introduction

Cancer is a heterogeneous group of related disorders with macroscopic features like metastatic spread, mass, abnormal and relentless growth [1]. Plant based systems have an essential role in the primary health care of 80% of the world's population including diseases like cancer [1]. There are various methods for the treatment of cancer but by using plants, there are none or very less side effects [1]. Nano science and technology along with the science of nanoparticles has been successfully applied in various fields [2]. Nanoparticles are used in treatment and diagnosis due to the shape, size and unique light and heat characteristics.

The metal nanoparticles due to their properties, are ideal for various biological applications. These properties are due to a ratio of size and raised surface area to the volume [2]. Main key is to achieve the most cost-effective treatment available to the humans [2]. Biological methods play a paramount role in the synthesis of metal nanoparticles [2]. Living organisms can also be utilized to produce these particles, like fungi, bacteria and plants [2]. The synthesis from plants provides an eco-friendly approach as free from the use of toxic and harmful and costly ingredients in medium for growth [2]. Few other advantages of nanoparticles synthesized from plant include swift synthesis, stable product and economical.

Objective of the proposed work: Synthesis of silver nanoparticles using aqueous leaf extract of *Argyreia nervosa andto* check its ant cancerous activity.

2. Experimental

2.1Preparation of *Argyreia nervosa* Leaves Extract for Nano synthesis:Healthy leaves of *A. nervosa* leaves were collected from a Herbal Garden located in Hyderabad, Telangana, India.The collected leaves were dipped in distilled water to remove surface-adhered dust

particles and was shade dried for 15 days.126 grams of cut leaves were mixed with 2.5L of distilled water and then boiled for 1.5 hr at 60 ^{0}C, cooled to room temperature, and filtered with Muslin cloth to obtain clear leaf aqueous extract (ANE).The prepared ANE was used for AgNPs (silver nanoparticles) synthesis. The reaction mixture was then shaken to ensure thorough mixing, and allowed to settle at room temperature. The color changed to dark reddish brown within 24hrs. The extracts were stored for further use.

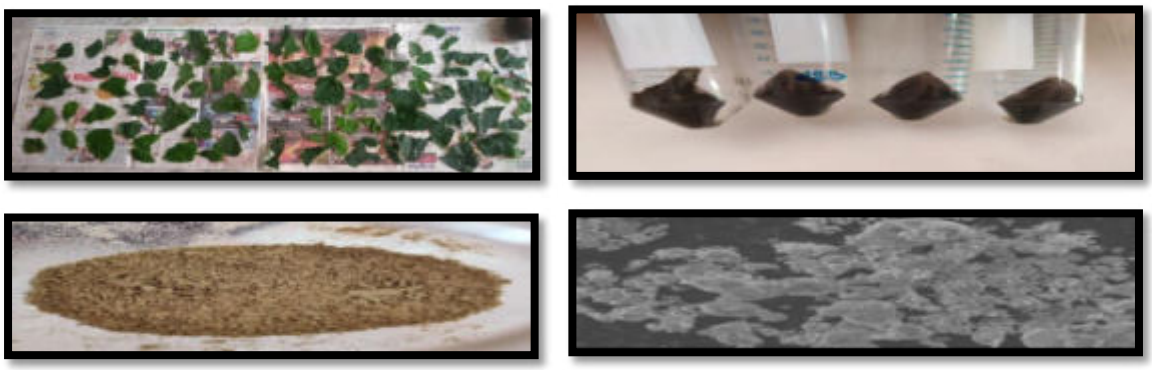

Fig1: Top left to Right (Drying of Plant leaves and Extraction of silver Nanoparticles)
Fig2: Bottom Left to Right (Powdered leaves and SEM characterization of Nanoparticles)

2.2 PURIFICATION: The obtained ANE-AgNPs were purified and separated from unreacted components by repeated centrifugation at 6000 rpm for 20min twice, followed by washing three times with in deionized water. Purified powder was obtained by rota evaporator and the dried ANE-AgNPs were used for further characterization.

2.3 CHARACTERIZATION:

SEManalysis: SynthesizedAgNPswere detected with Scanning electron microscopy (SEM) and particles are about approximately spherical in shape.

UV-Vis SPECTROMETRY- The spectrum of the sample was seen to be in the range of 250 nm to 550nm. The maximum wavelength was found to be at 490nm. This is due to Super plasmon resonance effect. This effect is exhibited only by silver nanoparticles

2.4 MTT Assay: Assay is to be performed on a cancer cell line: HeLa cell lines.

3. Results and Discussion

3.1 Preparation of A. nervosa Leaves Extract for Nano synthesis. The leaf concentrate (ANE) was prepared and 2 liters of extract was procured and stored for further use.

3.2 Purification of Silver Nanoparticles: The purified powder was obtained and the dried ANE-AgNPs were used for characterization.

3.3 Characterization by Scanning Electron Microscopy: Synthesized AgNPs were detected with Scanning electron microscopy (SEM) and particles are about approximately spherical in shape.

UV-VIS Spectroscopy: The spectrum of the sample was seen to be in the range of 250 nm to 550nm. The maximum wavelength was found to be at 490nm. This is due to Super plasmon resonance effect. This effect is exhibited only by silver nanoparticles.

3.4 MTT ASSAY: The cytotoxic effect of A.nervosa against Hela cell lines is to be seen as a direct dose response relationship .It is expected to show a minimum of 25 g/ml of silver nanoparticles cause 50% of cell mortality and 50 g/ml of silver nanoparticles is expected to inhibit the cell growth by more than 85%.The silver nanoparticles may induce reactive

oxygen species and cause damage to cellular components causing the death of the cells. The A. nervosa cytotoxicity may be due to the presence of bioactive compounds which act as capping agents in the synthesis of these nanoparticles.

Fig:1: Synthesis of silver Nanoparticles

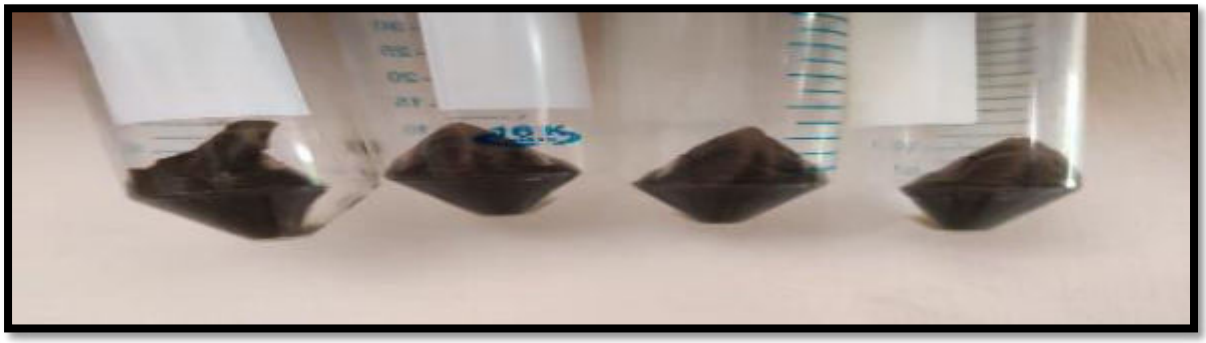

Fig:2: UV Spectrophotometer spectra for characterization of Silver Nanoparticles

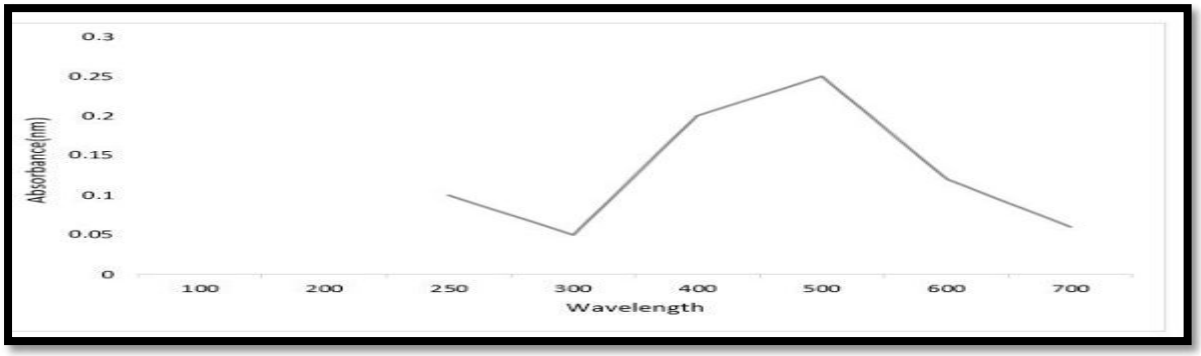

Fig3: MTT Assay Showing the cytotoxic effect of silver Nanoparticles on Hela cell line

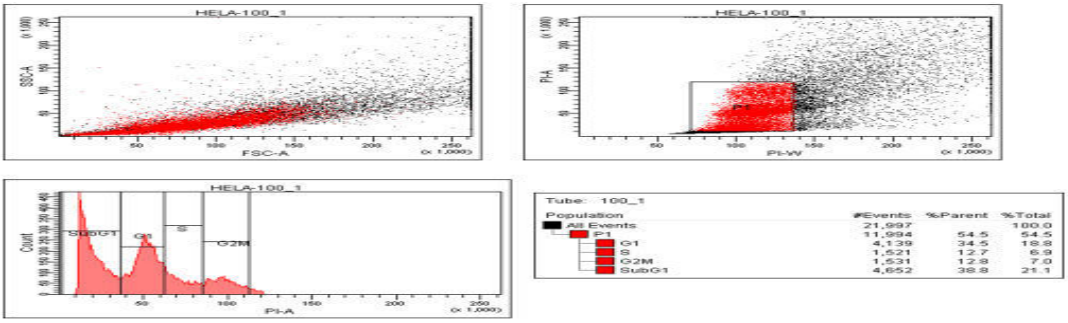

4. Conclusions

The cell cycle arrest on HeLa cell lines was found to be at Sub G 1 phase at a concentration of 50 g/ml of Silver Nanoparticles obtained from Argyria nervosa.It helps us to perform the cell cycle inhibition analysis of Argyria plant Nanoparticles on other cancer lines like Vero, MCF-7 cell lines and to prove it as Multi anticancerous agent.

Acknowledgement

Author thankful to Department of Biotechnology, CBIT, Gandipet, Hyderabad for funding the project.

References

1. A. Mukherjee *et al*., Current Medicinal Chemistry., 2001, **8** (12), 1467–1486.
2. T.Sen *et al.*, Advances in Biochemical Engineering/Biotechnology., 2014, 59–110.
3. Mascarenhas *et al.*, International Journal of Current Pharmaceutical Research., 2017, **9** (6), 94-97.

4. MilimitaPadhi *et al.*, Journal of Advanced Pharmaceutical Research., 2013, **4** (1), 23-32.
5. Abinash Kumar Sahu *et al.*, Ijppr.Human., 2019, **14** (3): 101-111.
6. Chaudhary *et al.*, Advanced Science Letters., 2017, **23**. 1781-1784.
7. T. Mosmann *et al.*, J. Immunol. Meth., 1983, **65**, 55– 63.
8. Thombre *et al.*, International Journal of Pharma and Bio Sciences., 2014, **5**, 114-119.
9. G. D. Saratale *et al.*, Journal of Cluster Science., 2017, **28** (3), 1709–1727.

Fuel Oil from Plastic Waste.

G.LokeshSai[1], I.ChaitanyaVamsi Krishna[2], P.Tharunesh[3].K.Prasad Babu[4]

[1].G.LokeshSai,3rdyear, Department of Chemical Engineering, Chaitanya Bharathi Institute of Technology, Hyderabad, Telangana, India
[2].I.Chaitanya Vamsi Krishna,3rdyear, Department of Chemical Engineering, Chaitanya Bharathi Institute of Technology, Hyderabad, Telangana, India
[3].P.Tharunesh,3rdyear, Department of Chemical Engineering, Chaitanya Bharathi Institute of Technology, Hyderabad, Telangana, India
[3]*.K.Prasad Babu,Assistant Professor, Department of Chemical Engineering, Chaitanya Bharathi Institute of Technology, Hyderabad, Telangana, India

*E-mail: kprasadbabu_chem@cbit.ac.in

Abstract:

In Earlier days PLASTIC is a revolutionary invention which brought many changes in industrial & daily activities. But now a days, it is being a major problem as it is increasing the landfills which is leading to more pollution because of its high degradation time & and no proper disposable way which may not affect the environment. As wastage of plastic is increasing day by day many engineering processes were found to produce alternative fuels.

Pyrolysis is the most useful and prominent method as it has a wide range of uses and helps in decreasing the large amount of waste plastic. Pyrolysis is process which converts the large hydrocarbon chains to small hydrocarbon chains by heating the plastic's at high temperature (350 – 400 C) & the products obtained are fuel oil & non- condensable fractions. The fuel oil can be used for heating purposes and non-condensable fractions to reduce air pollution. Polythene, Polypropylene are used as they are pure hydrocarbons and burnt cleanly. These fuels are used as industrial feedstock in many industries like petroleum refineries, alkene production etc.

We are now considering plastic as a waste product but upon reprocessing and application of new technologies can yield many valuable products which can lead us to a sustainable and healthy environment in future.

***Keywords*:** Pyrolysis, Polythene, alternative fuels, landfills.

1. Introduction:

PLASTIC, we call this period as the era of plastic since the material world is literally ruled by plastic. Plastic has become an engineering marvel in the field of material sciences from its inception and has shown its multi-faceted utility and versatile properties which give the plastic unique dominance over all other materials [1-3]. In each aspect plastic has shown a prominent role but now it has become one of the major reasons for contamination as the presence of it causes a variety of problems in environment because single used plastics does not biodegrade in landfills.

According to the various surveys, In India 13.4 million tonnes is produced per annum and nearly half of it is single used plastic and is expected to increase up to 20 million tons by 2020. Only 40% of the produced plastic is being recycled and the remaining is dumped into oceans and landfills which are creating environmental pollution. Single used plastic is mostly used in food sector and packing like straws, covers, and etc. Plastic has become a part of the day-to-day activities of every human being which is the major problem now the society is facing. On an average every house hold produces 1kg of plastic per month.

As wastage of plastic is increasing day by day many engineering processes were found to produce alternative fuels. These fuels are used as industrial feedstock in many industries like petroleum refineries, alkene production etc. Recycling the waste plastic produces very low-grade plastic which might be useful but creates lot of damage which made the researchers to produce other alternative products from waste through different process and one of its kinds is pyrolysis [4].

Pyrolysis is the most useful and prominent method as it has a wide range of uses and helps in decreasing the large amount of waste plastic. This process is carried out at temperature range of 300- 400^0c and major plastic materials used in it are polyethylene, polypropylene, polyethylene terephthalate, polystyrene. It is carried out in a batch and fluid bed reactor in laboratory purposes. This process can be carried out either by catalytic or non-catalytic reactions.

The presence of catalyst decreases the heat losses and the required reaction temperature when compared with the non-catalytic process. It also helps in producing the aromatic compounds for the production of gasoline (petrol). This paper deals with the comparison of properties of plastic pyrolysis oil with diesel and gasoline.

2. Materials and methods:

The raw materials used in this process is High density polyethylene (HDPE) like grocery bags, covers, HDPE bottles, caps, plates and Recycled plastic pellets. The waste plastic collected from household includes different types of plastics and they are segregated. Dust and other unwanted materials are removed and selected plastic materials are shredded into small pieces of size 3-5mm and the amount is weighed.

2.1 Equipment used:

(1) Triple neck round bottom flask-1000ml
(2) Round bottom flask heater.
(3) Collecting flask-500ml.
(4) Condenser.
(5) Vacuum bends.
(6) Thermal well.
(7) Thermometer.

2.2 Catalyst:

We chose Bentonite as our catalyst which is aluminum phyllosilicate ($Al_2H_2Na_2O_{13}Si_4$). This catalyst reduces the heating temperature of the process. The Oil yield is also increased when compared to non-catalytic process. On further detailed characterization and experiments economic viability of the process with catalyst can be decreased.

2.3 Procedure:

A flask with feed is placed in the heater which can attain a maximum temperature of 600 ^{0}C and the process is carried out under atmospheric pressure and a heating rate of 20 ^{0}C /min. At 130^0C, melting of plastic initiates and vapours are generated once the temperature reaches 300^0C.The Vapours are condensed in a condenser by cold water at 20 ^{0}C. The condensable vapours are collected in the collecting flask and non-condensable gases are either stored or allowed to pass through a bubbler and to the Bunsen burner. Temperature is

held until no gases are evolved. By-products like wax and grease are collected from the bottom of the flask and filtered. Process is concluded when there is no further formation of droplets of oil.

3. Results and discussion:

The end products obtained are fuel oil, flammable gases and by-products are char & wax and are shown in table1.

Table 1. Percentage composition of products is:

Products	F1	F2	F3	F4
Fuel oil (gm)	168.75	55.65	59.04	45.4
Gases(gm)	8.25	37.35	115.96	21.02
Wax (gm)	0	7	125	0
Carbon char(gm)	0	0	0	33
Grease (gm)	23	0	0	0
Conversion (%)	84	55.65	17	46.62

- Feed 1 (F1)- 200gms of HDPE pellets.
- Feed 2 (F2)-50gms HDPE pellets +50gms HDPE covers + 50gms catalyst.
- Feed 3 (F3)-300gms of HDPE covers.
- Feed 4(F4)- 100gmsHDPECovers +50gms Catalyst.

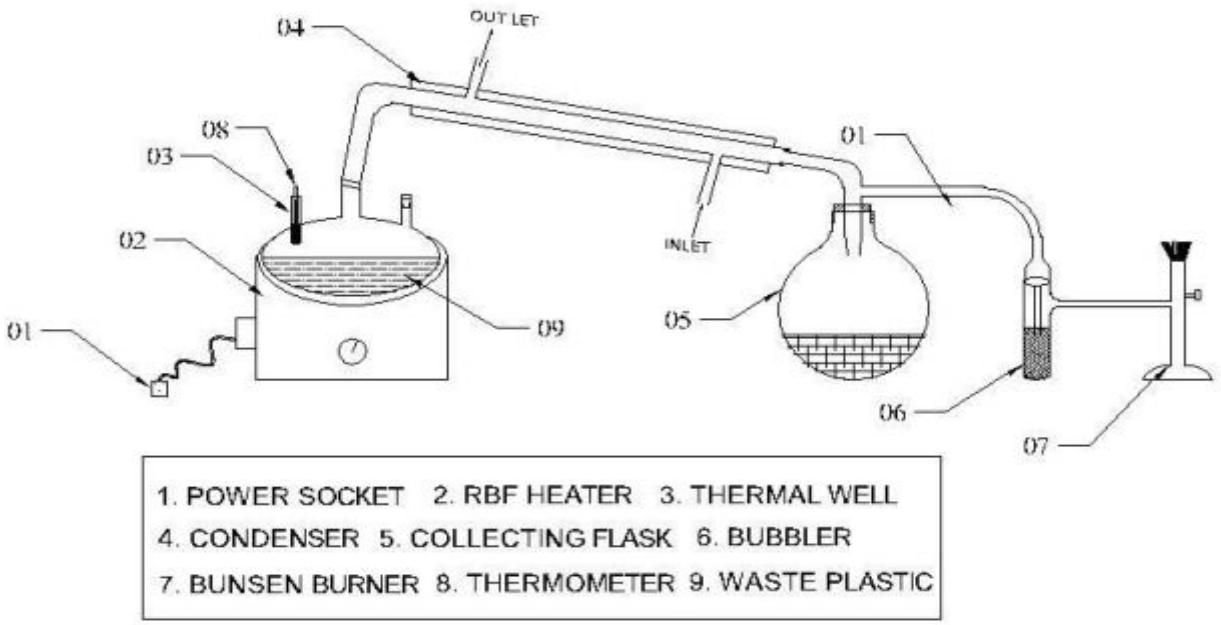

Fig1. Waste plastic to fuel oil production process

Table 2. Comparison of properties of fuel oil with other fuels:

Property	**Kerosene**	**PPO**	**Petrol**	**Diesel**
Density(kg/l)	0.83	0.749	0.747	0.85
Viscosity(cst)	2.71	1.43	0.93	2.12
Flash Point (℃)	36	16	-45	43
Fire Point (℃)	40	20	-40	45
Boiling Point (℃)	180	200	85	240
Gross Calorific value (MJ/Kg)	46.2	36.14	45.8	45.5

From the above table of comparison of properties, Plastic Pyrolysis oil (PPO) cannot be used as a conventional diesel but it is very much useful as industrial feed stocks.

3.1 Utilization of By-products:

By products such as char, wax and grease are produced from different feed in the processes [5,6]. Wax can be used as a non-conventional material for manufacture of candles which is shown in fig9. Grease can be used as a lubricant and we have used in our material unit operations lab for the moving parts of the machinery.

Fig6: Grease

Fig7: Char

Fig 8: Wax.

Fig 9. Candle.

3.2 CHNS Analysis:

This analysis helps to determine the percentage composition of Carbon(C), Hydrogen (H), Nitrogen (N) and Sulfur(S) in a given liquid sample [3,5]. In this method sample is burnt in the excess amount of oxygen, which produces the combustion products. By analyzing the quantity of the combustion products, we can determine the percentage of each element in the sample.

Table 4. Percentage composition of elements:

Nitrogen	0.57%
Hydrogen	10.57%
Carbon	61.35%
Sulfur	0.07%
Oxygen	1.46%

From the above results we can calculate the calorific value
G.C.V=33195C+144452.5(H-O/8) +96305S KJ.

The Value was found to be 8572.34 Kcal/Kg.

4. Conclusion:

Pyrolysis of plastic waste results in the production of fuel oil either by catalytic or non- catalytic conversion. GCMS and CHNS analysis shows the presence of high volatile compounds and the percentage composition of carbon, hydrogen, nitrogen, oxygen, Sulphur in the oil. The presence of hydroxyl groups can also be known by the GCMS analysis. The obtained properties of fuel oil are compared to other fuels which give an idea that it can be used as feedstock in industries. On conducting more experiments and characterization of fuel oil, this oil can be used in place of conventional fuels.

Acknowledgement:

The authors acknowledge the support of Dr B. Ganesh & K. Prasad Babu Assistant professor of Chemical Engineering in Chaitanya Bharathi Institute of Technology (CBIT).

References:

(1) "Applications acid treated kaolin clay for conversion of polymeric waste material into Pyrolysis diesel fuel" by Ali Waqas et al., ICESP., 2014, 0124.
(2) "A Comparison of the Use of Pyrolysis Oils in Diesel Engine" by C. Wongkhorsub, N. Chindaprasert.
(3) "Catalytic pyrolysis of polyethylene" by Ranbir Bagri, Paul T. Williams, Department of Fuel and Energy, The University of Leeds, Leeds LS2 9JT, UK.
(4) "Experimental study on the production of diesel-like fuel from waste high density polyethylene via non-catalytic pyrolysis" by Khalil KAHINE Lebanese university, IUT Saida, B.P.813.
(5) "Recycling of plastic waste via pyrolysis" byN. Kiran, E. Ekinci and C.E.Snape.
(6) https://www.hindawi.com/journals/jeph/2016/7869080/ - Pyrolytic Waste Plastic Oil and Its Diesel Blend: Fuel Characterization.

Measurements of thermodynamic and transport properties of binary liquid mixtures of sulfolane with some organic solvents at 303.15 K

Dr.P.Muralikrishna[1]*, Dr.G.Kumaraswamy[2] and G.Srinivas Reddy[2]
*[1]Chaitanya Bharathi Institute of Technology, Hyderabad
[2] Mahatma Gandhi Institute of Technology, Hyderabad
Email: pmuralikrishna_chm@cbit.ac.in

Abstract

An experimental determination of physical parameters of speed of sound propagation, density parameter and viscosity for the binary mixtures of various combination organic solvents (sulfolane + n-Butylacetate), (sulfolane + Butanone), (sulfolane + n-Butylamine) has been attempted at the temperature of 303.15 K. The thermodynamic properties of various liquids and their possible mixtures which are required for the purpose of design, storage of energy and other equipment processing have been measured. There has been a significant deviation exhibited by the various thermodynamic properties of binary mixtures which contains components that are of ability of being subjected to specific interactions. The deviations from established ideality have been in terms of fluctuations of molecular size and changes in structural shape. The data obtained in the experiment have been fitted to a polynomial equation of Redlich-Kister for estimating the coefficients along with standard deviations observed in measurements.

.

Keywords*:* Thermodynamics, Transport properties, Excess molar volume, Deviation in Isentropic Compressibility, Sulfolane, Intermolecular interactions.

1. Introduction

The attempt made in the present work aims at investigating the physical and chemical characteristics of the binary systems of n-butyl acetate, n-butylamine and sulfone with butanone. The behavior of molecular interactions in the system of binary liquid mixture can be analyzed through the studies of thermodynamic properties. The physical and chemical characteristics of mixtures play a Vitol role in the various processes of transport and structure of certain of aspects of the structures of the solutions in the design of chemical laboratory equipment [1-2]. Many of industrial and engineering systems implementations involve the various calculations in which the consideration of fluid flow or the process of mixing are influencing factors in relation to the applications such as mass transport and others.

Sulfolane (thiolane-1, 1-dioxide), which is a significant solvent having a potential physical and chemical characteristics, can be implemented in general on petroleum products in extracting monocyclic aromatic hydrocarbons. A similar solvent of Butanone is potential industrial solvent generally implemented in solid coatings with less quantity of solvent emissions. The process of drug manufacturing involve raw material of N-butylamine, which functions as plasticizer and has a thermoplastic behavior in various chemical processes such as polymer-processing industries and fragrance.

In most of practical applications and investigations of structural effects, the consideration of interactions among various carbonyl groups of ester, ketone and other solvents having polar groups like sulfone is of vital importance in the analysis and the structural studies. It is noted

that mixtures of sulfolane implemented with the other solvents is of notable interest in the investigations of the structural studies. The knowledge of mixing mechanisms of sulfolane with butanone, n-butylacetate and n-butylamine is required in establishing many engineering applications. There seems to no attempt made on the investigations of mixture of sulfolane with the solvents of n-butyl acetate butanone, n-butylamine at the temperature of 303.15K.
The present investigation made in the paper establishes a systematic data of measurements attempted on the properties of organic solvents [3-9]. An experiment executed in the present work will estimate density as well as the speed of sound through three pure liquid solvents of n-butylacetate, butanone and n-butylamine. The study of binary mixtures of three organic solvents with sulfolane at the pressure and temperature of 0.1MPa and 303.15K respectively has been attempted.

2. Experimental

An airtight bottle is used for preparation of binary mixtures by mass. An instrument of a Dhona 100 DS, India, single-pan analytical balance with a resolution of $0.01 \cdot 10^{-6}$ kg has been implemented for measurements of mass. The measurements of the properties of mixture have been made on the same day of mass measurements. The uncertainty in the measurements of mole fractions is found to be less than $\pm\ 1 \cdot 10^{-4}$. The density of pure liquids and their corresponding mixtures have estimated with $1 \cdot 10^{-5}$ m^3 double arm pycnometer [6].
It is well noted that there is reproducibility of density values obtained from triplication of replicating at different temperatures is observed within the limits of $\pm\ 2 \cdot 10^{-2}$ $kg \cdot m^{-3}$. The value of uncertainty in the measurements of density has been the value of $\pm$ 0.04 $kg \cdot m^{-3}$.
An ultrasonic interferometer [model M-82, Mittal Enterprises, India], at the range of at 2 MHz frequency was deployed for the measurements of sound. In the earlier study, the details of measuring speed of sound is clearly conveyed [3]. The temperature of solution is maintained at a constant value with circulation of water at a required level using a double-walled cell. In the process of measurements of all properties, a limit of ± 0.01 K in temperature through temperature bath [INSREF model IRI – 016 C, India] is maintained. Platinum resistance thermometer is used to monitor the temperature in the order of an accuracy of ± 0.001 K and an uncertainty of measurements is limited to ± 0.004 K. In order to enhance the accuracy and quality in measurements, sulfolane (99%) of the high purity grade which is furnished by Sigma-Aldrich chemicals (USA) has to be implemented.
To reduce the contact of the deliquescent reagent associated with moist air, it is needed to keep the product in a sealed bottle which is in a desiccator. The purity of the substances has to be carefully checked by GLC. Densities along with viscosities of pure substances with the values recorded in the literature values are presented in Table 1[11-16].

Table 1. Experimental densities (ρ) and speeds of sound (u) of pure components at 303.15K.

Component	$\rho 10^{-3}$ kg·m^{-3}		u m·s^{-1}	
	Expt	Lit	Expt	Lit
sulfolane	1.2639*	1.2640[11]	1588**	1588[12]
Butanone	0.8012*	0.8009[13]	1192	1192[14]
n-Butyl amine	0.72225	0.7239 [15]	1198.2	-------
n-Butyl acetate	0.8756*	0.8759[16]	1203*	1201[13]

*T=298.15K

** T=303.15K

3. Results and Discussion

The experimental values estimated in the present work for physical parameters as function of mole fraction have been calculated. The parameters have been measured at the temperature of 303.15K.

***Excess molar volume*:** The graph plotted as the function of values of excess molar volume (V^E) with estimated mole fraction (x_1) of sulfolane for n-butylacetate, butanone and n-butylamine at the temperature of 303.15 K is depicted in Fig.1.

The excess values of estimated molar volumes for all binary mixtures with sulfolane have been found to be negative. The values of V^E estimated in the study indicate the resultant forces of physical and chemical properties and they may be in general considered as: (i) The order of breaking of liquid on the process of mixing with the second organic solvent component; (ii) Interactions with Non – specific physical and unfavourable interactions between unlike molecules; (iii) Specific interactions which come across in the process where mixture among dissimilar molecules by hydrogen bond formation; and (iv) Specific interactions that appear in the mixture among components of solvent and co-solvent through the attachment of dipole-dipole interaction.

The first two factors influence the expansion of volume and the latter two factors cause the less volume. It is seen from Fig.1, that V^E curves drawn at 303.15 K denote role of domination of factors which reduce the volume and expansion factors are observed to be insignificant. The variations in the negative values of V^E are observed to obey the order as follows n-butylamine < butanone < n-butylacetate< 0.

An expansion in the volume of the mixture is resulted in due to the fact that dissociation of liquids structure occurs and amines are bonded with via H-bonding. The factor of volume reduction indicated with excess negative molar volumes plays a significant role among unlike molecules. Complex hydrogen bond formation has been revealed through factors of molar volumes. Therefore, the large negative values of V^E which are observed in the calculations denote the domination of -S=O·····HN- bonds formation over the breakage of bonds existing in the combination of pure sulfolane and n-butyl amine.

n-butyl amine is moderately polar solvent. Sulfolane is a dipolar aprotic solvent [17], because its high dipole moment (4.8 D) favours dipole-dipole interactions [17] in which negative end of the dipole has exposed. Hence, dipole-dipole interactions exist among unlike molecules of the four systems and cause the reduction in the value of volume. From the Fig. 1 it is observed that the specific interactions at a larger number exist among the mixtures of combinations of sulfolane and n-butylamine than sulfolane + butanone and sulfolane + n-butylacetate.

Figure 1. Plots showing the profile of the function of molar fractions at the temperature value of 303.15 K with the parameters of excess molar volume, V^E, of the combinations sulfolane (1) + Butanone, n-Butylamine and n-Butyl acetate (2) Δ, Butanone; ▲, n-Butylamine; □, n-Butylacetate; the symbols represent experimental values.

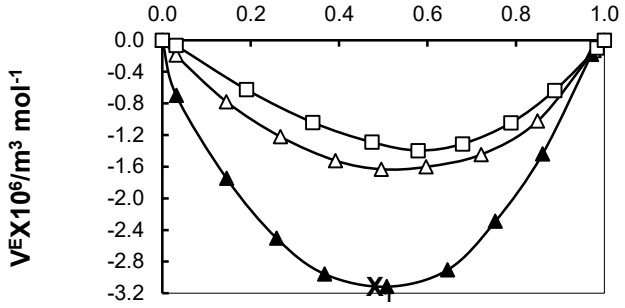

Deviation in isentropic compressibility-The profile of $\Delta\kappa_s$ with mixture (Φ_1 of sulfolane) is depicted in Fig. 2. From the isotherms, it is noted that $\Delta\kappa_s$ values were found to negative for all parameters in the study of present systems studied. The values of $\Delta\kappa_s$ observed in the study for the three systems which are at equimolar compositions are found to be in the order as follows

n-butyl amine < butanone < n-butyl acetate < 0.

Figure 2. Plots of deviation in isentropic compressibility, $\Delta\kappa_s$, of sulfolane (1) + Butanone, n-Butylamine and n-Butyl acetate (2) system as function of volume fraction at T=303.15 K; Δ, Butanone; ▲, n-Butylamine; n-Butylacetate; the symbols indicate respective values obtained in the experiment.

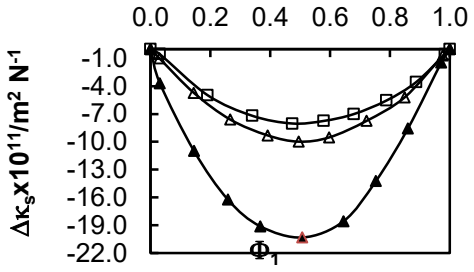

Sulfolane and n-butyl amine have been highly polar in their nature..The specific terms or factors of chemical forces – dipole-dipole interactions, formation of hydrogen bonding and physical forces – dispersion can express the behavior of various mixtures.

The earlier studies reveal that the increase in former factor causes the enhancement in intermolecular path lengths causing the increase in compressibility [18].The decrease in compressibility is caused with latter factor. The values obtained are dependent of relativity between the effects of two opposite factors of latter and former. The negative in the estimated values of $\Delta\kappa_s$ for the mixtures under study reveal the domination of the specific interactions on the dispersive interactions among molecules of unlike characteristics. The similarity in the behaviour exhibited by parameters of V^E and $\Delta\kappa_s$ is also an interesting finding in terms of same values and order.

4. Conclusions

- The estimation of parameters of density, viscosity and speed of sound for the binary mixtures of sulfolane with butanone, n-butylamine and n-butyl acetate at temperature of 308.15 K and with various compositions has been made.
- The estimated excess thermodynamic functions are observed to be correlated with values obtained in processing with curve fitting of the polynomial equation of Redlich-Kister.
- The magnitudes of quantities with the signs indicating positive and negative variations have been clearly analyzed with various terms of hydrogen bonding and dipole-dipole

interactions among the various combinations of the mixing organic solvents with components.

- The deviations found in the estimation of the parameters of isentropic compressibility, viscosity in the composition range of excess molar volume have been found to be at negative values.

References

1. M. R. Kula *et al.*, Advances in Biochemical Engineering: Berlin., 1982, **24**, 178.
2. C. M. Kinart *et al.*, *Pol. J. Chem*., 1993, **67**, 895-902.
3. R. K. Bachu *et al.*, J. Chem. Eng. Data., 2008, **53**, 2403-2407.
4. S. Boodida *et al.*, .J. Chem. Thermodyn., 2008, **40**, 1422-1427.
5. R.K.Bachu *et al.*, .Indian J. Chem., 2008**, 47A**, 1026-1031.
6. B. Sathyanarayana *et al.*, J. Chem. Thermodyn., 2007, **39**, 16-21.
7. S. J. Tangeda *et al.*, J. Chem. Thermodyn., 2006, **38**, 1438-1442.
8. S. Nallani *et al.*, J. Chem. Eng. Data., 2007, **52**, 405-409.
9. B. Sathyanarayana *et al.*, Indian J. Pure & Appl. Phys., 2006, **44**, 587-591.
10. O. Redlich *et al.*, Ind. Eng. Chem., 1948, **40**, 345-348.
11. J.A.Riddick *et al.*, Organic solvents; physical properties and methods of purification. Eds, John Wiley & Sons: New York., 1986.
12. M. Karvo *et al.*, J. Chem. Thermodyn., 1986, **18**, 809-813.
13. S. Prakash *et al.*, Can. J. Chem., 1980, **58**, 942-945.
14. B. Gonzalez *et al.*, J. Chem. Thermodyn., 2006, **38**, 707-716.
15. M. C. S Subha *et al.*, Indian J Chem., 2004, **43A**, 1876-1881.
16. M. I. Aralaguppi *et al.*, J. Chem. Eng. Data., 1999, **44**, 441-445.
17. A. Sacco *et al.*, J Chem Thermodyn., 1972, **4**, 191-197.
18. B. Jacobson *et al.*, J Chem Phys., 1952, **20**, 927-928.

Optical properties of lithium borate glasses co-doped with transition metal ions for Li-ion battery applications

B. Sai Charan[a], Ashok Bhogi[a*] and P. Kistaiah[b]
[a]VNR Vignana Jyothi Institute of Engineering and Technology, Hyderabad, Telangana, India.
[b]Department of Physics, Osmania University, Hyderabad, Telangana, India.
*corresponding author's Email: ashokbhogi@gmail.com

Abstract

Glasses with composition $15Li_2O$-25RO-(60-x) B_2O_3-0.5CuO-0.5Fe_2O_3 (R= Ca, Sr and Ba) have been prepared by traditional melt quenching technique and investigated by X-ray diffraction and Optical absorption techniques. The X-ray diffraction patterns of the prepared glass samples confirmed the glassy nature. In optical absorption spectra, two absorption bands are existing at around 452 nm and at around 750 nm and these are analogous to the $^6A_{1g}$ (S) → $^4A_{1g}$ (G); ^{4}Eg (G) transition of iron ions in octahedral symmetry and $^2B_{1g}$→ $^2B_{2g}$ characteristic transition of Cu^{2+} ions in the distorted octahedral sites. From ultraviolet absorption edges, the optical band gap and Urbach energies have been evaluated. The effect of alkaline earths on these properties is discussed.

Keywords*: Oxide glasses, XRD, Absorption edge and Urbach energy.*

1. Introduction

This work is devoted to the investigation of optical absorption studies of lithium borate glasses co-doped with various transition metal ions (CuO and Fe_2O_3). The oxide glasses such as Borate, Tellurite, Vanadate co-doped with transition metal ions have create substantial technological applications such as cathode materials for batteries, electrical switching devices, electronic circuit elements and gas sensors [1–3]. Among the various oxide glasses the borate (B_2O_3) glasses have been chosen in the present study. B_2O_3 acts as glass network forming oxide and the boron atoms can coordinate with oxygen to form BO_4 tetrahedral units and also BO_3 triangular units [4]. In such glasses, the anomalous effect i.e. the presence of multivalent states of two transition metal ions demonstrate semiconducting behavior and this conduction is attributed to polaron hopping from lower valance state of one transition metal ion site to higher valance state of another transition metal ion (TMI), for example Cu^+ and $Cu^{2+}$and Fe^{2+} and Fe^{3+}, etc.

In the present paper, the experimental results like XRD and optical absorption studies of lithium borate glasses in the composition, $15Li_2O$-25RO-(60-x) B_2O_3-0.5CuO-0.5Fe_2O_3 (R= Ca, Sr and Ba) are presented.

2. Experimental

The required amounts of reagent grade chemicals such as Boric acid (H_3BO_3), Li_2Co_3, $CaCo_3$, $SrCO_3$, $BaCo_3$, CuO and Fe_2O_3 were thoroughly mixed by manually grinding in an agate mortar then transferred to porcelain crucible (J-brand). This mix was heated to melting at 1050 °C in a high temperature electrical muffle furnace. When the homogenous transparent melt was obtained, the melt was rapidly quenched and the random sized samples formed were collected. The samples were subjected to annealing by heating them for an hour at a temperature of 300 °C and allowed to cool to room temperature over 24 h. The composition of the samples is $15Li_2O$-25RO-(60-x) B_2O_3-0.5CuO-0.5Fe_2O_3 (R= Ca, Sr and Ba) and are labelled as CLBCF55, SLBCF55 and BLBCF55 respectively.

The samples were subjected to X-ray diffraction studies. XRD patterns of the all the samples were taken at room temperature using Cu-K_α radiation of wavelength1.54056 Å in Phillips PW3710 diffractometer and in the diffraction angle region of 2$\theta$from 10^o to 80^o insteps of 0.02^o and 0.2 sec counting time per step.

The optical absorption spectra of prepared samples were recorded at room temperature on Shimadzu 8400S UV-VIS spectrophotometer in the wavelength range of 300 nm to 1000 nm in order to determine the cut-off wavelength (λ_c), Optical band gap energy (E_{opt}) and Urbach energy (ΔE) values.

3. Results and Discussion

3.1 XRD:

XRD patterns of all these samples depict a diffused peak confirming the amorphous phase of the glasses. The X-ray diffraction patterns of all the samples are shown in Figure 1.

3.2 Optical absorption:

The optical absorption spectra of the present glass system are shown in Figure 2. From this figure, it has been observed that the fundamental absorption edges are less sharp than that of crystalline materials which is a characteristic of the glassy nature [5].

In optical absorption spectra, two absorption bands are existing at around 447 nm and at around 750 nm and these are analogous to the $^6A_{1g}$ (S) → $^4A_{1g}$ (G); ^{4}Eg (G) transition of iron ions in octahedral symmetry and $^2B_{1g}$→ $^2B_{2g}$ characteristic transition of Cu^{2+} ions in the distorted octahedral sites. By the substitution of alkaline earths progressively this band is blue shifted. These fluctuations in the absorption band with fixed concentration of copper and iron indicate that these ions were affected due to the presence of different modifier oxides in the glass system. Such fluctuations may be due to the variation of energy separation between the6A1g(S) and 4Eg (G) and $^2B_{1g}$→ $^2B_{2g}$energy levels [5]. The fluctuations in the band position are due to the variations either in Fe-O bond length or in radial position of electron cloud or in both of them.

Figure 1.XRD patterns of prepared glasses. **Fig 2.**Optical absorption spectra of glasses

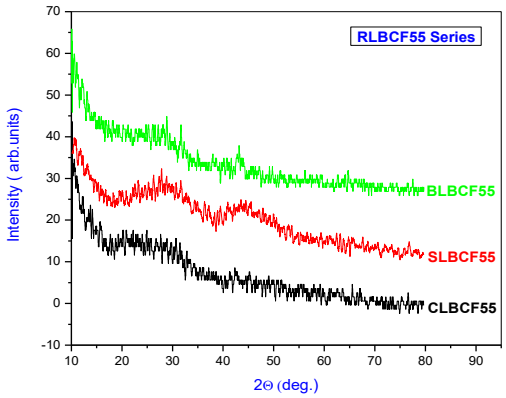

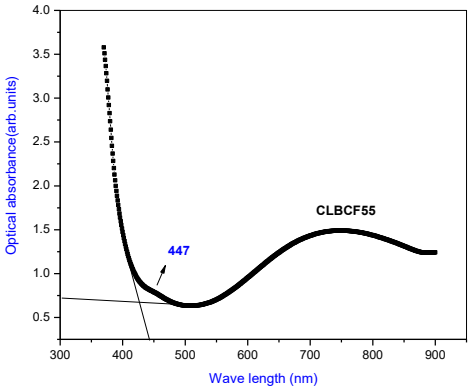

The Optical band gap and Urbach energies obtained in the present work. Figure 3 and Figure 4 represents the Tauc's and Urbach plots of prepared glass samples. The minimum Eg value is observed for SLBCF55 glass sample which suggesting the formation of large number of non-bridging oxygens (NBOs). The addition of SrO to B_2O_3 glass matrix undertakes web incorporations in the form of SrOnpolyhedron groups. The negative charge on the polyhedron pushes transition metals to form the bond within the network Thus the concentration of bridging oxygens (BO) is decreased. The decrease in band gapis also explained on the basis of color centers/defects in the iron doped glasses which provide energy states in the forbidden gap, derived from their outer orbitals. The minimum Urbach energy is observed forCLBFCF55 glass sample which indicates the least width of the tails among investigated samples. The increase in ΔE value with the substitution of SrO is due to the formation of defects like wrong bonds and fluctuations in bond angle distortions [6].

Figure 3. Tauc's plots of prepared glass system.**Figure 4.**hν vs lnα graph of glass system.

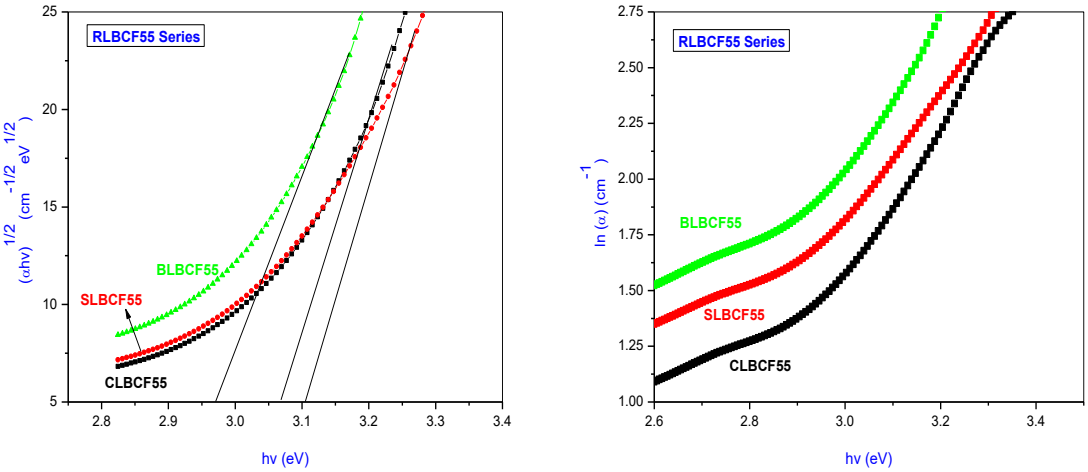

4. Conclusions

Amorphous nature of the samples is confirmed by the XRD patterns.

The optical absorption parameters have been evaluated.

Acknowledgement

The authors, B. Sai Charan and Ashok Bhogi thanks the management of VNR VJIET, Hyderabad, for their constant support and encouragement.

References

1. S. Chakraborthy *et al.*, J.Applied Physics., 1997, **82**, 5520-5525.
2. A. Ghosh *et al*., J. Applied Physics, 1988, **64**, 2652-2655.
3. M.R. Tripathy *et al.*, Materials Letters., 2007, **61**, 585-587.
4. R. Ashok Bhogi *et al.*, J. Non-Crystaline Solids., 2015, 426**,** 47-54.
5. E.A. Davis *et al.*, Phila. Mag. 1970, **22**, 903-909.

Study of Activated and Impregnated Rice Husks for Carbon Dioxide Adsorption

P.Kishore*[1], K.Subba Rao[1], B. N. Srinivas[1]
Department of Chemistry, Usha Rama College of Engineering & Technology,Vijayawada, India
email: *drkishorepalle@gmail.com

Abstract

Porous materials are being suggested as suitable adsorbents for CO_2 capture due to their highly developed porous structure. The rice husk activated carbons are mainly microporous. The increase in activation time results in a continuous steady rise of the mesopore area and volume, while the micropore and total pore area and volume reach a maximum at 3 h. The surface areas go through a maximum within creasing solid yields. The adsorption capacity of the rice husk activated carbons decreases with increasing adsorption temperature rapidly, probably due to the adsorption being a physisorption process. The activated carbon with the highest CO_2 adsorption capacity is the sample activated at 400 ^{0}C for 2 h, whose surface area was only 542 m^2/g, and the adsorbed amount of CO_2 was 64.8 mg-CO_2/ g-adsorbent. This is probably due to a relationship between micro porosity and CO_2 physisorption processes. Several surface treatment techniques, including NH_3 heat treatment and polyethylenimine (PEI) impregnation, were used to alter the surface properties of the activated carbons in an attempttoincrease their CO_2capturecapacityathighertemperatures.Thesurfacetreatmentmethods investigated change the porous structure and surface chemistry of the activated carbons, and therefore, affect their CO_2 adsorption capacities.

Keywords: Rice husk, Activation, CO_2 adsorption, Surface treatment, Pore structure, Functional group.

1. Introduction

Due to their well-developed porous structure, porous materials are recommended as suitable adsorbents for carbon dioxide adsorption. Although rice husks are known to provide activated carbons with high surface area, the application of activated carbons is very incompetent. As a result, high surface area activated carbons from rice husk were synthesized through steam activation in this research study and their carbon dioxide adsorption capacity was studied. The rice husk activated carbons are mainly micro-porous. The rise in activation time results in continuous steady growth of both the mesopore area and volume, whereas at 3 hours the micropore area and total pore volume reaches a maximum. With growing solid yields, the surface areas go through a highest level. The rice husk activated carbons adsorption capability reduces rapidly with growing adsorption temperature, probably due to the physisorption method being adsorption [1].

2. Materials and Methods

2.1 Preparation of Rice Husk Activated Carbon (RHAC) and Activation

Rice husk obtained from rice mill near Telaprolu, Vijayawada, India, was washed vigorously with distilled water for the removal of adhering soil and dust, and dried at 110^{0}C overnight. The temperature was programmed as 10^{0}C per minute and gas flow maintained at 40 ml per minute. The activation temperature was maintained between the range of 300-800^{0}C for intervals of 2–3.5 hrs. The feeding steam concentration is 65.8% and it was

balanced with nitrogen gas. Synthesized treated samples were labelled as RHAC-*a*-*b*, where *a* &*b* indicates temperature and time of the activation, respectively.

2.2 Surface Treatment

For two different surface treatment methods, the sample RHAC-600-3 (activated at 600°C about 3 hours) was chosen. A known quantity of sample was placed in a quartz tube in the center of a horizontal tube furnace for the ammonia treatment. Then NH_3 gas was carried, while the furnace was warmed to the temperature required for activation. The NH_3 gas was shifted to argon after the furnace was kept at the specified temperature for 90 minutes and the furnace was cooled down. At room temperature, the sample was separated from the furnace. The synthesized samples have been labeled as RHAC-600-3-NH_3-xxx, where the ammonia treatment temperature is indicated by the last three numbers of the sample title. As formerly represented for MCM-41 substantials [1], the RHAC-600-3 sample also taken for some other surface tending technique composed of impregnation with PEI in methanol solution. The sample was desiccated overnight in a vacuum oven at 75°C after impregnation with PEI. The following sample was labeled as RHAC-600-3-PEI and the loading of the PEI was 33.4 % weight.

2.3 Sample Characterization

The porosity of the specimens was characterized by studying nitrogen adsorption isotherms at 77 K using Quanta chrome adsorption device, Autosorb-1 Model ASIT. Total pore volume (V_t) measured from amount of vapour adsorbed at a relative pressure of 0.95, and the total surface area (S_t) was measured using multi-point BET formula at a relative pressure ranging of 0.05–0.35. Following the nomenclature of IUPAC [2], the pore sizes 2 nm and 50 nm were taken as the boundaries between micro-and mesopores and meso-and macropores. Barrett–Joyner–Halenda (BJH) was used to measure the mesopore size distribution.

2.4 CO_2Adsorption

The carbon dioxide adsorption capacity of the synthesized activated carbons was characterized by break through curve (BTC) values. Approximately 10 milligram of sample was placed in a small platinum pan in a typical adsorption study, heated to 100°C in nitrogen at a stream speed of 40 mL / min, and kept heat for 30 minutes. The temperature was then adapted to the required adsorption temperature and operated at a flow rate of 40 mL / min at 99.8 percentage bone-dry CO_2 adsorbate. The gas was shifted to 99.995 % natural N_2 gas at a flow rate of 40 mL/min after adsorption to conduct desorption at same temperature. Adsorption capability in milligram/gram (adsorbate/adsorbent) was used to assess the adsorbent.

3. Results And Discussion

3.1 Influence of Activation Time and Temperature on Activated Carbons Porous Structure

The time, activation conditions and temperature, and also the precursor's properties and structure have been well known to impact the porous structure of the resulting activated carbons [3, 4, 5].A parametric examination has therefore been performed to determine the impact of time and temperature on the porous framework of elevated carbons prepared from rice husk. Figure.1 represents the rice husk sample nitrogen adsorption isotherms activated at 300–800 ^{0}C for 2 hours. The isotherm of raw rice husk is also shown in Fig.1 for comparison. The enabled sample isotherms have considerably improved the adsorbed volume at small relative pressure compared to the pure sample isotherm before ignition. This remark shows that, as earlier stated [3, 6-9], the initiation method particularly advanced micropores in the rice husk. In all the activated rice husk samples, the ratio of micropore to total volume is

greater than 90 percent. By growing activation temperature, however particularly above 800^0C, the isotherm indicates a more open knee at small relative pressure, suggesting wider distribution of pore volume with bigger micropores and increasing mesoporosity.The isotherm adsorbed volume for lower activation temperature (300^0C) was very low, especially compared to the higher temperature activation isotherms (400–800^0C), and thus only high temperatures (above 400^0C) were chosen in this research to explore the activation period impact.

Figure1.Nitrogen adsorption isotherm models (77K) of the rice husk and their samples activated for 2 hours at various temperatures.

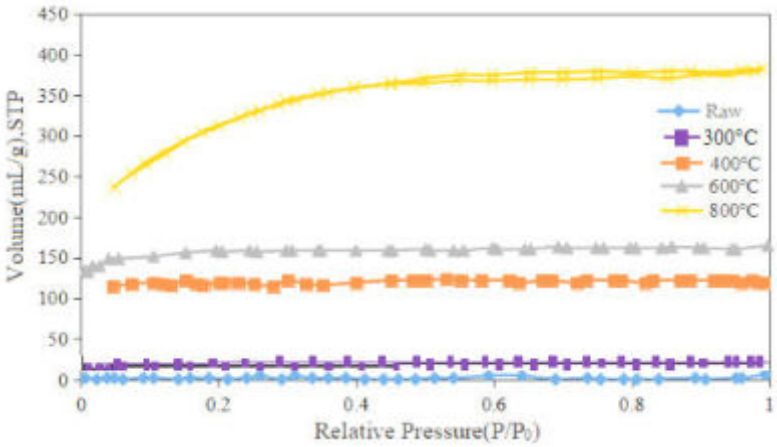

Figure.2 and Figure.3 represents the change in surface area and pore volume and total, micro and mesopore pore volume for a series of rice husk samples activated at 600^0C for different times, respectively. The variation of surface area and total pore volume of the rice husk activated carbon is mainly depends on the micropores.

Figure.2 Variation of the surface area for the activated carbons of rice husk at 600^0C for various times.

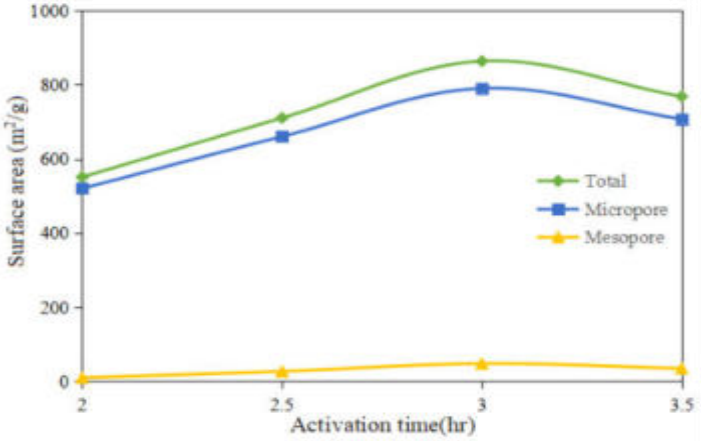

The total surface area of 863 m^2/g, micro and mesopore areas are 784m^2/g and 42m^2/g respectively for the sample activated at 600^0C for 3 hours shown in fig.5.9. Table1 represents the total surface area, micro and mesopore areas of samples activated at 600^0C for 3 hours. It should be noted that, by increasing the activation time, the mesopore area and volume continuously increased steadily, while the microporous and total pore area and volume achieved a maximum of 3 hours.

This is likely owing to prolonged gasification leading to enlargement of micropores and removal of pore wall. For the rice husk activated carbon (463 m^2/g and 0.36 mL/g combined), previous activation studies on the same rice husk sample (RH) revealed reduced surface area and pore volume[3]. However, these activation studies use large particlesize (1–

3 mm) and a fixed-bed reactor.

Table1: Total, micro and mesopore areas of rice husk activated at 600^{0}C for 3hrs

Time	Surface area (m^2/g)			Pore volume (mL/g)		
(hours)	Total	Micropore	Mesopore	Total	Micropore	Mesopore
2	556	524	12	0.26	0.24	0.01
2.5	714	663	28	0.37	0.30	0.03
3	863	784	42	0.46	0.41	0.04
3.5	773	710	34	0.43	0.37	0.04

Figure.3. Pore volume changes for the rice husk activated carbons at 600℃ for various times.

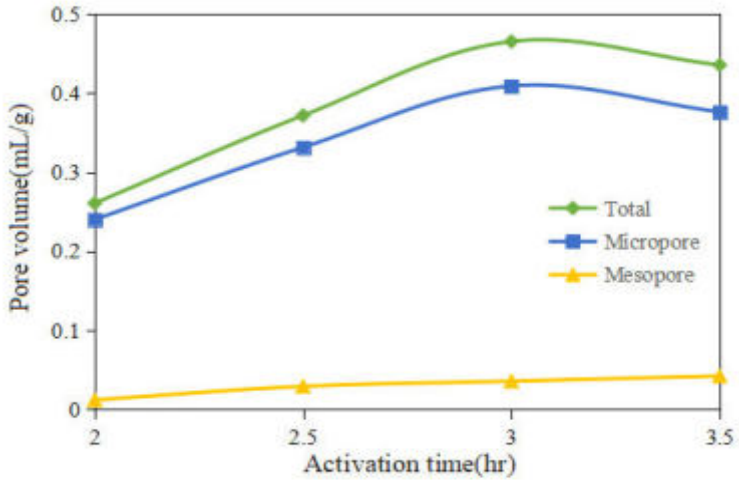

Figure.4 indicates the mesoporesize distribution of the rice husk samples activated at 600^{0}C for 2 to 3.5 hours, as measured by the BJH method. It was determined that for all the activated carbons produced from rice husk, there are 2 peaks in the mesopore range. The main peak is focused at around2nm and alittleadditionalpeakseemsat3.6–3.7 nm, related to that described for mesoporous activated carbons from fly ash carbons [4]. Both peaks become larger with increasing activation time, indicating enhancing mesoporosity. This was found accordant with Fig.2 and 4 that showed a continuous growth of the surface area and mesopore volume with time. For periods of 2–3.5 hours, a series of samples were activated at 400, 600 and 800^{0}C. Figure5 and 6, respectively, shows the variation of total pore size and surface area with varying application temperature and time. Both the volumes of the pore and the surface area increase with growing activation temperature when maintaining the activation period constant.

Table 2: Representation the total surface area and pore volumes of rice husk activated at different temperatures for different activation times.

Time (hours)	Surface area (m^2/g) at			Pore volume (mL/g) at		
	400°C	600°C	800°C	400°C	600°C	800°C
2	405	556	1072	0.18	0.26	0.57
2.5	507	714	1035	0.24	0.37	0.54
3	612	863	677	0.28	0.46	0.34
3.5	679	773	---	0.33	0.43	---

Figure.4. Mesopore size distribution of the raw rice husk activated carbon and its counterparts activated at 600 ^{0}C for different times.

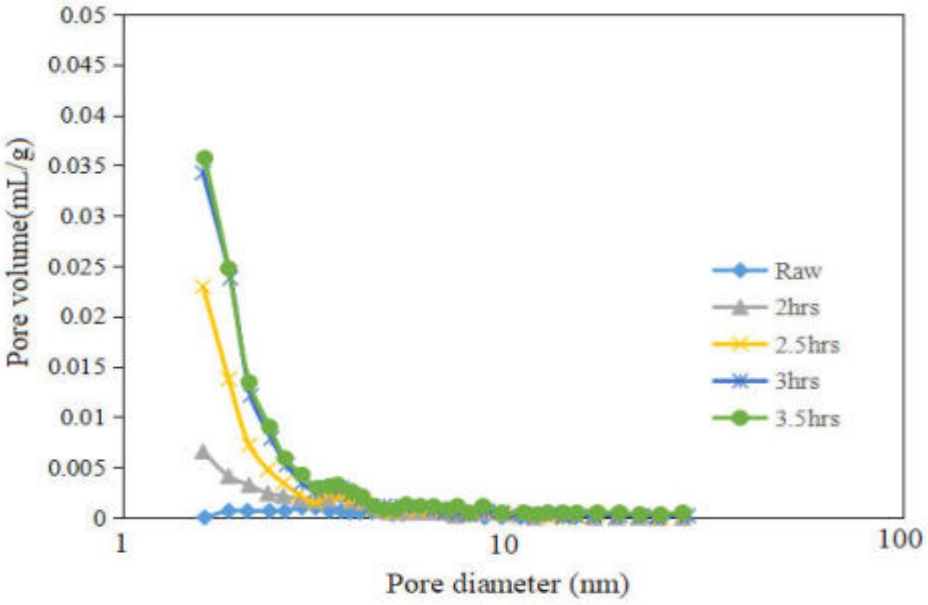

However, the sample synthesized at high temperature activation, i.e. 800^{0}C, has a lesser pore volume and surface area than the lower activation temperature (600^{0}C) when the activation period is 3hrs. The surface area and pore volume do not increase continuously with growing activation time for a specified activation rate (Figure 5 and 6). The activation time required attaining largest surface area and volume of pores changes to smaller as the temperature of activation raises.

Figure 5 and 6. Variation of the Surface area and Pore volume at different activation temperatures (400-800^{0}C) with activation time.

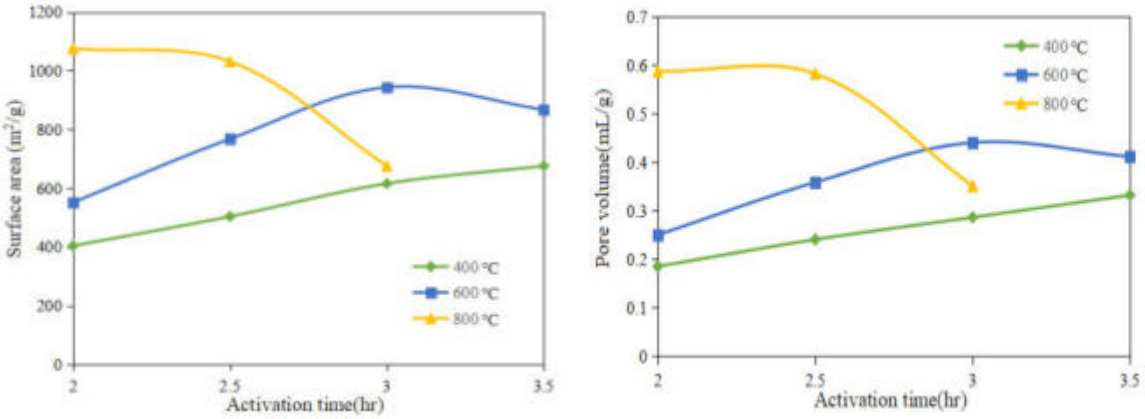

For instance, for activation studies at 800^{0}C, the surface area and pore volume will

reduce when the activation period is extended by more than 2hrs, while the surface area and pore volume will not reduce until the activation period is extended by more than 3hrs. Eventually, for the sample activated at 400^0C, increasing the activation time to 3.5 hrs results in a constant increase of both surface area and pore volume, and likely prolonged times are required before the surface area and pore volume begin to decrease.

Table-3 demonstrates the solid yield of activated carbon from rice husk under various circumstances (time and heat). Figure.7 demonstrates the connection between rice husk activated carbon surface area and solid yield. As expected, the solid yields lowering with risingactivation time and temperature. For example, the solid yield goes from 78 % for the 400^0C activation to 21% at 800 ^{0}C for the rice husk activated for 2hrs. Similarly, for a given activation temperature, the solid yield reduces with activation time. For example, for the rice husk activated at 600^0C, the solid yields for the 2 and 3.5 hours activation were 58% and 14% respectively. As represented when growing the activation time at a given temperature, the surface area does not growth continuously with diminishing solid yields.

Table.3 Rice husk activated carbons Solid yield (wt.%) under different conditions (time and temperature)

Temperature	**Solid yield (wt. %)**			
	2h	2.5h	3h	3.5h
400	78	75	65	52
600	58	44	33	14
800	21	17	4	0.01

Figure.7demonstrates that the surface areas go through a maximum value with growing solid yields. For example, for the activation at 600^0C, the surface area first increases with decreasing solid yield and reaches a maximal value at around 4 percent solid yield, later the surface area begin to decrease. This activity has been previouslydescribedfor rice husks activated using steam and carbon dioxide ,although the solid yield value at which the surface area peaks varies within these studies, it occurs due to the different activation conditions used [3,8].

Figure.7 Surface area variation as a function of solid yield.

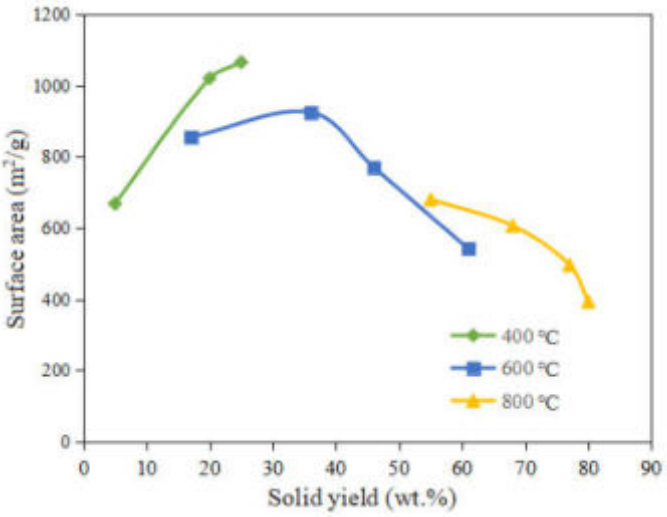

Firstly increase in surface area is mainly due to opening of pores and establishment of micropores, while the decrease in surface area for lower solid yields (<40%) is due to the enlargement of micropores and removal of pore wall. This is also consistent with the

variations mentioned for surface area and pore volume as a function of activation conditions (Figures2–6) demonstrated the development of the porosity with extended times and temperatures, and therefore, lower solid yields.

3.2 Influence of Surface Treatment on the Porous Structure of the Rice Husk Activated Carbons

Rice husk sample activated at 600 ^{0}C for 3hrs was chosen for the conduction of surface treatment with ammonia or impregnation with polyethyleneimine.The porous surface properties, as determined from the 77 K nitrogen isotherms, of the raw rice husk activated carbon and their surface treated samples are presented in Table 4. The ammonia treatment enhances activated samples surface area, particularly at lower temperatures (250^{0}C). For example, the surface area of the ammonia treated activated rice husks increased from 863 to 1054 and 954 m^2/g when treated at 250 and 400^{0}C, respectively. Maximum pores are mainly micropores (>91%) in the activated rice husk produced at 600^{0}C using different activation times.

The micro porosity (91%) of the activated rice husk can be maintained by lower temperature ammonia treatment. In comparison, the higher temperature ammonia treatment decreases the micro porosity ratio from 91% to 87% and grows up the pore size from 1.92 to 1.98 nm. The chemical impregnation resulted in a impressive decrease of the surface area of the rice husk activated carbon, where the surface area and pore volume of the RHAC-600-3-PEI are very small (0.96 m^2/g and 0.0094 mL/g, respectively). This is totally because of blockage of pores and coverage of surface by PEI, as earlier studies mentioned for MCM-41 materials with PEI impregnation [1].

Table 4: Properties of the porous structure of RHAC-600-3 and its treated samples

Sample	BET surface area(m^2/g)	Pore volume (ml/g)	Microporosity ratio(%)	Average pore diameter(nm)
RHAC-600-3	863	0.44	91	1.91
RHAC-600-3-NH_3-250	1054	0.52	92	1.92
RHAC-600-3-NH_3-400	954	0.46	87	1.98
RHAC-600-3-PEI	0.96	0.01	-	-

3.3 Carbon dioxide Adsorption of the Activated Rice Husks

3.3.1 Influence of Temperature on CO_2 Adsorption Capacity

Fig.8. Displays the CO_2 adsorption capacity of the rice husk activated at 600^{0}C at different temperatures of adsorption (30, 50 and 75 ^{0}C) for 2.5 hours. It can be seen that with growing adsorption temperature, the adsorption capability reduces quickly. This activity is typical of a physical adsorption method, where both the diffusion rate of molecule and surface energy of adsorption increase with increasing temperature. As a result, the gas adsorbed on the surface of the activated carbon turn to unstable, resultant in the desorption of adsorbed carbon dioxide molecules. In the present research study, rice husks carbon dioxide adsorptioncapacityactivatedat30^{0}C is about two–three times more than that at 75^{0}C (5.7 mmol/g vs. 2.6 mmol/g). This type of behavior was determined for all the rice husks activated carbonspreparedin this work and has been previously investigated for zeolite based adsorbents. Typical flue gas pressures, however, are typically up to 150^{0}C, so creating sorbents that can work at greater temperatures is essential. For effective CO_2 removal,

chemical adsorption procedures are scheduled for carbon dioxide trapping using high-surface area having materials. Previous research concentrated primarily on impregnating zeolite products and fly ash carbons. Especially, PEIimpregnatedMCM-41hasbeenreported for the production of adsorbents that can adsorption carbon dioxideatcomparatively high temperatures [1]. Consequently, in this study rice husk activated carbons were impregnated with PEI in an attempt to modify their carbon dioxide adsorption capacity, specially at higher temperatures.

Figure 8. Carbon dioxide adsorption capacities of the rice husk carbons RHAC-600-2.5 as a role of the temperature of adsorption.

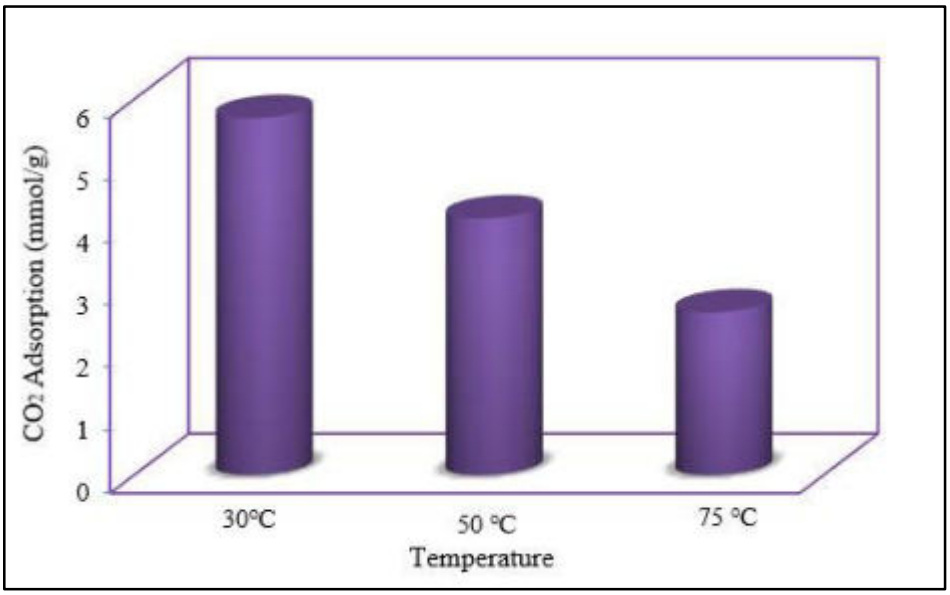

3.3.2 Influenceof Activation ConditionsonCarbon Dioxide Adsorption

Figure.8 illustrates the carbon dioxide adsorption capacity at 30^0C of the fresh and activated carbons of rice husk.The carbon dioxide adsorption capacity reduced with accelerating activation temperature and there is no clear relationship between surface area and carbon dioxideadsorption capacity. For instance, the rice husk providingthe highest surface area($1072m^2/g$,800^0C for2hours) has a carbon dioxide adsorptioncapability of only 3.9 mmol/g, while the rice husk with the highest CO_2 adsorption capacity 6.48 mmol/g has only a surface area of 612 m^2/g (400^0C for 3 hours). Figure.8.also demonstrated that the fresh rice husk together with the rice husks activated at lower temperature (300^0C) for 2 hours have amazingly high CO_2adsorptioncapacities (3.7 and 3.9 mmol/g, respectively),contempt of their low porosity.

Figure 9. Carbon dioxide adsorption capability at 30℃ of the fresh and activated carbons of rice husk.

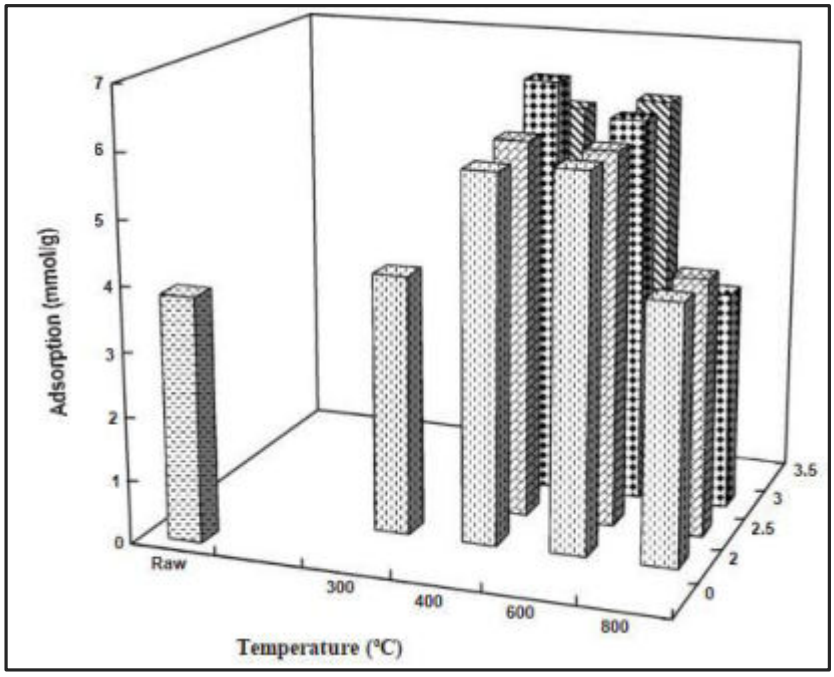

3.3.3 Influence of Surface Treatment on Carbon Dioxide Adsorption

The carbon dioxide adsorption capacities at 30 and 75^{0}C of the rice husk activated carbons RHAC-600-3 and their surface treatedmaterials (ammoniatreatment andpolyethylenimine impregnation) aredepictedinFigure.10. It can be seen that there are apparent changes in the carbon dioxide adsorption capacity of the samples with temperature of adsorption.When examinen the capacity for carbon dioxide adsorption at 30^{0}C, the adsorption of the fresh rice husk was somewhat more than that for the chemically treated samples, other than for the impregnated PEI sample, where it is more than that. Of all the treated samples, the carbon dioxide adsorption capacity at 75^{0}C was somewhat more than that of the raw rice husk. For example, at 75^{0}C, the carbon dioxide adsorption capacity was 2.14, 2.63, 2.34 and 2.59 mmol/g for RHAC-600-3, RHAC-600-3-NH_3-250, RHAC-600-3-NH_3-400 and RHAC-600-3-PEI, respectively. For theNH_3treatment at low temperature (250^{0}C) gives in reasonably more carbon dioxide adsorption capacities than the treatment at high temperature (400^{0}C).This is due to the change of micro porosity and the existence of functional groups, as discussed below. Moreover, lesser carbon dioxide adsorption capacities on activated carbons treated with ammonia at elevated temperatures have been reportable for commercially available rice husk activated carbons, because of blockageo f micropores by nitrogen containing groups [10]. For the Ppolyethylenimine impregnated samples, the carbon dioxide adsorption capacity enhanced with temperature, as expected from a chemical adsorption method.

Figure10. Carbon dioxide adsorption capacities for untreated and treatedRHACs at various temperatures

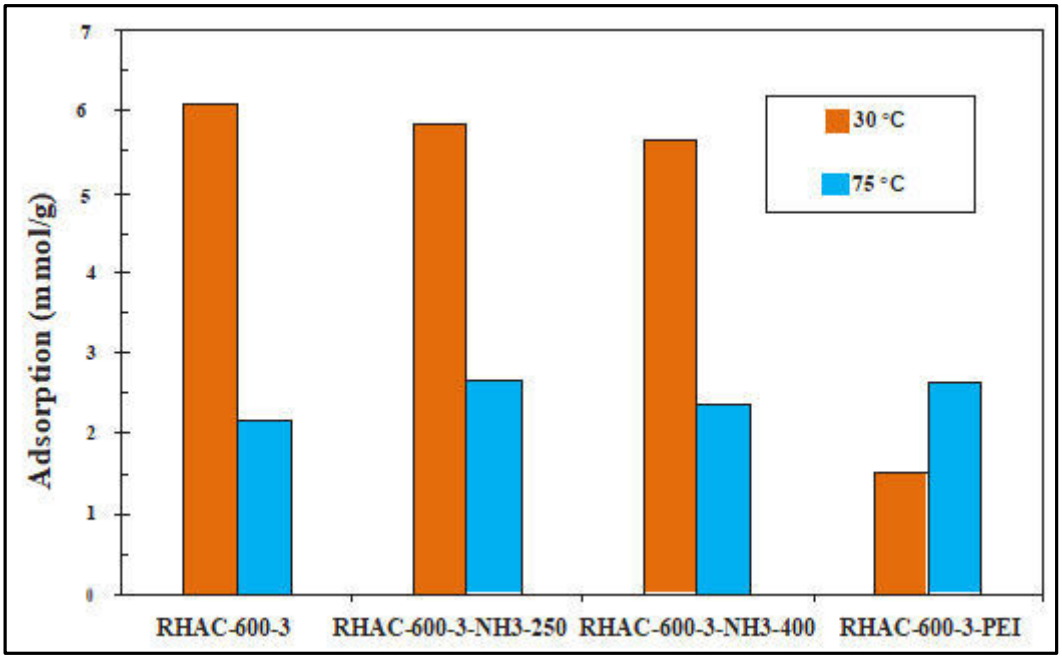

3.3.4 Factors Influenceing on theCarbon Dioxide Adsorptionof Rice Husk Activated Carbons

The samples with the great carbon dioxide adsorption capacity was the rice husk activated at 400°C for 3 hours with a surface area of 612 m^2/g and the adsorbed amount of carbon dioxide was 6.48 mmol/g from the above-mentioned carbon dioxide adsorption studies.Although, the rice husk with the higher surface area and pore volume(1072m^2/g and 0.574 ml/g, respectively) was that activated for two hours at 800^0C and its carbon dioxide adsorption capacity was merely 3.9 mmol/g. For instance, measured theoretical carbon dioxide adsorption capacity of the rice husk activated for 2 hours at 400^0C and also 2 hours at 800 ^{0}C are 23.16 mmol/g and 41.12 mmol/g, respectively. This shows that not all the surface area or the activated rice husk pore volume contributes to the carbon dioxide adsorption. The relationship between CO_2 adsorption and the micro porosity of the activated rice husks is presented in Figure11.The samples with the superior micro porosity appear to have the greatest ability for carbon dioxide adsorption. Earlier investigations have shown that only pore dimensions below five times that of the adsorbate's molecular size are effective for capturing of gas at atmospheric pressure.The molecular size of CO_2 is 0.209 nm, only pores less than 1.0 nm are effective towards CO_2 capture at atmospheric pressure. Therefore, it is desirable to tailor the pore size distribution of the activated carbons, especially in order to maximize the pores less than 1.0 nm, to optimize the physical adsorption of CO_2 on to the carbon surface.

Figure11. Variation of CO_2 adsorption capacities and micro porosity of the activated rice husks.

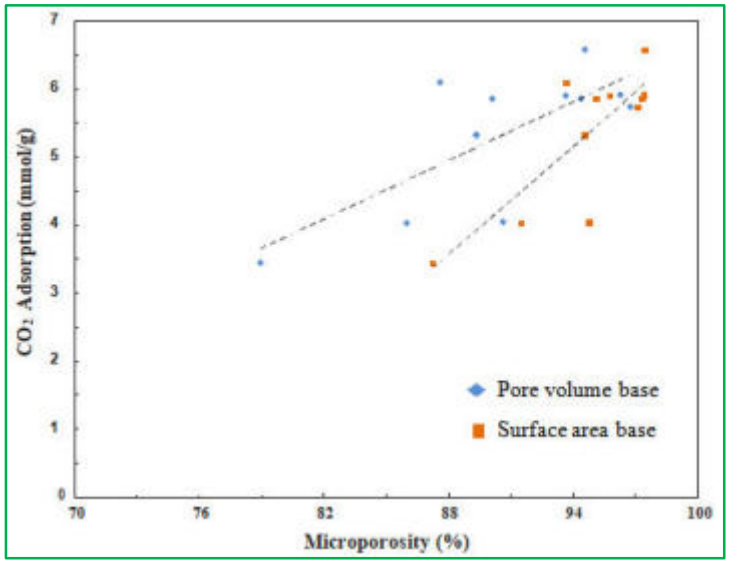

Because carbon dioxide is an acidic gas, active alkaline surface functional groups will promote CO_2 chemisorptions. Among all the surface functional groups investigated on the activated carbon surface, just a few nitrogen groups are alkaline. This is also why techniques of surface treatments are used to enhance the ability of sorbents for carbon dioxide adsorption by raising the content of nitrogen[9,11].

4. Conclusions

- High surface area activated carbons were prepared from rice husk sample (RHAC) by steam activation using fluidized bed reactor. N_2-77 K adsorption studies show that the activated rice husks are mainly microporous and the micro porosity decreased with increasing activation time and temperature.
- The maximum surface area and pore volume are 1052 m^2/g and 0.586 mL/g for the rice husk activated at 800 ^0C for 2 hrs. The surface areas go through a maximum with increasing solid yields. The initial increase in surface area is probably due to opening of porosity and formation of micropores, while the decrease in surface area for lower solid yields (less than 40%) is due to the enlargement of micropores and pore wall removal.
- The adsorption of CO_2 on the activated rice husk is mainly a physical adsorption process and the adsorbed amount decreased with increasing adsorption temperature. The CO_2 capture results do not show a linear relationship with the surface area. For example, the sample with the highest CO_2 adsorption capacity (64.8 mg-CO_2/g-adsorbent) was the rice huskactivatedat600^{0}C for 2hrs, whose surface area was only 540m^2/g. Similarly, the rice husk presenting the highest surface area (1052 m^2/g, 800 ^0C for 2 hrs) hasaCO_2 capacity of only 40 mg-CO_2/g-adsorbent. This is probably due to only certain size pores being effective for CO_2adsorption.
- Two surface treatment methods, including NH_3 heat treatment and polyethylenimine (PEI) impregnation, were used to modify the surface properties of the activated rice husks toincreasetheirCO_2capturecapacityathighertemperatures.
- TheNH_3treatmentincreases the surface area of the activated samples, especially at lower temperatures (250^0C). The chemical impregnation with PEI results in a dramatic decrease of the surface area of the activated rice husk, probably due to pore blockage and surface overagebyPEI.
- Both the treatment and PEIimpregnation can increase the CO_2capturecapacityoftheactivated rice husks at higher adsorption temperature, due to the introduction of alkaline nitrogen groups on the surface. Further studies are being

conducted to optimize the treatment of activated rice husks in an effort to maximize their CO_2 adsorption capacities.

Acknowledgement

The authors would like to thank the Chairman Sri Sunkara Ramabrahmam, Director Dr. K. Rajasekhara Rao, Principal Dr. G.V.K.S.V. Prasad of Usha Rama College of Engineering& Technology, Vijayawada for their continuous support during this work.

References

1. X.C. Xu *et al.*, Energy and Fuels., 2002, **16** (6) 1463-1469.
2. K. S. W. Sing *et al.*, Pure and Applied Chemistry., 1985, **57** (4), 603-619.
3. K. Gergova *et al.*, Energy and Fuels., 1993, **7** (5), 661-668.
4. Y.Z. Zhang *et al.*, Energy and Fuels., 2003, **17** (2), 369-377.
5. M. Turmuzi *et al.*, Carbon., 2004, **42** (2), 453-455.
6. J. J. Pis *et al.*, Fuel., 1998, **77** (6), 625–630.
7. M.M. Maroto-Valer *et al.*, Shanxi Science and Technology Press, Taiyuan, China, 1999, 909.
8. M. Mittelmeijer-Hazeleger *et al.*, Carbon., 1992, **30** (4), 695-709.
9. D. Spencer *et al.*, Fuel., 1976, **55** (4), 291-296.
10. J. Przepio´rski *et al.*, Applied Surface Science, 2004, **225** (1–4), 235-242.
11. M.L. Gray *et al.*, Separation and Purification Technology., 2004, **35** (1), 31-36.

Determination of Photon Interaction Parameters and Mass Attenuation Coefficients of Cerium Oxide and Praseodymium Oxide Using Gamma Ray Attenuation Method

[1]M.Ranga Rao*, [2]N.Gopikrishna, [3]S.Chandralingam
1 Dept. of Physics, Kavitha Memorial Degree and P.G College, Khammam-507002, Telangana, India
2 Dept. of Physics Kakatiya University, Warangal-506009, Telangana, India
3 Dept. of Physics, JNTUH Hyderabad-500085, Telangana, India
Email: mrraophysics@gmail.com

Abstract
This present paper is aimed to measure the mass attenuation coefficients (μ_m) of cerium oxide and praseodymium oxide and the determination of effective atomic number and related parameters using the radioactive sources ^{137}Cs and ^{60}Co with gamma photon of energies 662 KeV, 1173 KeV and 1332 KeV. Transmission experiments with narrow beam good geometry set up have been carried out to measure the incident and transmitted intensity to determine the attenuation coefficients. The gamma intensities have been measured with a high resolution NaI (Tl) detector. The photon interaction parameters viz., effective atomic number (Z_{eff}),linear attenuation coefficient(μ_l), total atomic cross- section (σ_t), electron cross-section(σ_e),electron density(N_{eff}) and photon mean free path(λ) were determined with semi-empirical relations using mass attenuation coefficients obtained experimentally and theoretically. The experimentally computed values in the present work and theoretical values obtained using mixture rule and X-com were compared and are found to be satisfactory.

Keywords: rare earth oxide, mass attenuation coefficient, effective atomic number

1. Introduction

Keeping in view of the extensive use of the radioactive sources in medicine, agriculture, industry etc., in recent years the study of photon atom interaction in different materials has gained importance. As these interactions involve various compounds with different compositions, that the effective atomic number of a material composed of several elements cannot be expressed by a single number, it can be concluded that it is an energy dependent parameter due to the different partial photon interaction processes with matter for which the various atomic numbers in the material have to be weighted differently. A number of investigations on effective atomic numbers for total and partial photon interactions have been reported in the literature. There are many scientific, technological, medical, industrial and commercial applications of rare-earth oxides [1-4]. A number of investigations on effective atomic numbers for total and partial photon interactions have been reported in the literature [5-14]. Lanthanide oxides have many applications in scientific, technological, medical and commercial fields. However, studies about lanthanide oxides on Z_{eff} are lacking. Lanthanide oxides are considered to be better shielding materials to the exposure of gamma radiation, hence the photon interaction parameters turn out to be useful. Thus the importance of these materials at high temperature nuclear applications prompted us to carry out the present work.

Mass attenuation coefficient is a useful parameter to derive many other photon interaction parameters. Theoretical methods are available to calculate mass attenuation

coefficients for elements and compounds/mixtures. Hubbel [15] reported mass attenuation coefficient values for 40elements and 45 mixtures and compounds. Most popular method for calculating the effective atomic number and related parameters is to obtain the mass attenuation coefficient of the material under study. Hence, it is of prime importance that the attenuation coefficients should be known with high accuracy, as atomic parameters are to be obtained from it. Berger et al [16] developed XCOM for estimating the mass attenuation coefficient at different energies for different elements/compounds/mixtures. Recently we reported effective atomic number and related interaction parameters of some oxides of lanthanides [17].

In the Present work, the results of experimental studies of mass attenuation coefficients and other estimated photon interaction parameters of cerium oxide (CeO_2) and praseodymium oxide (Pr_6O_{11}) at different photon energies of 662KeV, 1173KeV and 1332KeV are reported. The experimental values of photon interaction parameters of the materials in the present study at different photon energies are compared with the estimated theoretical values and the values of X-Com.

2. Materials and Method of measurement

2.1 Experimental

A good geometry narrow beam transmission experimental setup as shown in figure1 is used for measuring the incident and transmitted intensities of gamma photons for the determination of the mass attenuation coefficient. The gamma rays are well collimated using lead collimators. Each of the collimators has cylindrical shape and circular aperture.

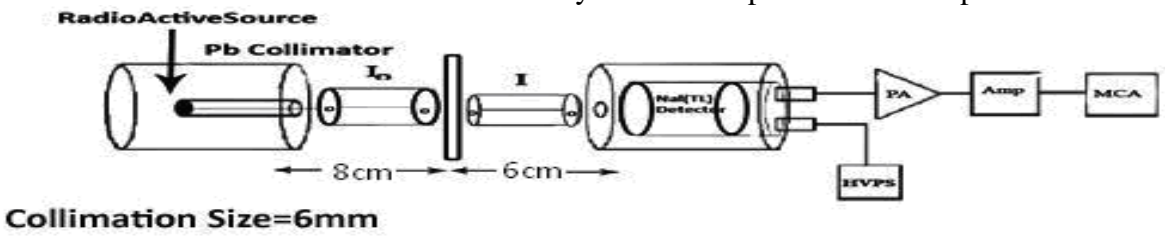

Figure 1: Schematic diagram of gamma ray absorption setup (not to scale)

High purity powders of CeO_2 and Pr_6O_{11} are compressed into pellets with 20mm diameter die set using hydraulic press, for making measurements. These are then firmly placed on the sample holder. The pellets in the sample holder are fixed between the source and the detector ensuring a proper alignment of sample with collimation 6mm either side. The samples are irradiated by the gamma photon of energies Cs (0.66MeV), Co (1.173MeV and 1.332MeV). Intensities of the transmitted photons were recorded and counted by using MCA (multichannel analyzer). Complete experimental details given in our earlier paper [18].

2.2 Analysis of data

The mass attenuation Co-efficient for the oxides of rare-earth at various photon energies are measured by performing the transmission experiments through the basic equation

$$I = I_o \exp(-\mu_m t) \qquad (1)$$

Where I_0 and I are the un-attenuated and attenuated photon intensities, $\mu_m = \mu / \rho$ (cm^2/g) is the mass attenuation coefficient, t g/cm^2 is sample mass thickness (the mass per unit area).

The total mass attenuation coefficient μ_m for any chemical compound or mixture of elements is given by mixture rule

$$\mu_m = \sum_i w_i (\mu_m)_i \qquad (2)$$

Where w_i is the weight fraction (the proportion by weight) $(\mu_m)_i$ is the mass attenuation coefficient of i^{th} element.

The effective atomic number Z_{eff} of the material is determined through the following relation,

$$Z_{eff} = \frac{\sigma_t}{\sigma_e} \quad (3)$$

Where the σ_t and σ_e are total atomic cross section and total electronic cross section.
The detailed procedure of analysis of data is discussed in our earlier paper [19].

3. Results and Discussion

Mass attenuation coefficients (μ_m) for cerium oxide (CeO_2) and praseodymium oxide (Pr_6O_{11}) are obtained experimentally for different gamma photon energies. The values obtained in the present work are compared with theoretical values calculated by using semi-empirical relations (2,3) and with the values of X-Com and found to be in good agreement as can be seen in the Table1 and Table2. The mass attenuation coefficient values decrease with increase in photon energy as seen from figure 2. The experimental values for cerium oxide (CeO_2) and praseodymium oxide (Pr_6O_{11}) are smaller than their theoretical values. This is because probability of absorption decreases with increasing incident photon energies. Linear attenuation coefficient (μ_l), total photon interaction cross-sections (σ_t and σ_e), effective atomic number (Z_{eff}), effective electron number (N_{eff}) and photon mean free path(λ) for rare-earth oxides at different photon energies are estimated by using experimental mass attenuation coefficients. Values obtained from theoretical, X-COM [16] and experimental values are given in Table 1 and Table 2. From the figures 3-5 it is observed that linear attenuation coefficient, total atomic cross section and total electronic cross section decrease with increase in photon energy. As seen from figure 6, figure7 the Z_{eff} and the N_{eff} remains constant and are found to be independent of photon energy. The agreement between the calculated values from semi empirical relations, X-Com and experimental results is good. However the presence of some impurities in these rare-earth oxides might create a different environment in CeO_2 and Pr_6O_{11} and this could bring about a change in the binding forces, chemical surroundings and distortions in crystallinity. Such changes in CeO_2 and Pr_6O_{11} by the impurities are not considered when the values of mass attenuation coefficients were computed by X-Com and empirical relations. But the influence of these effects, discussed above reflects in experimental measurements. The photon mean free path (λ) is found to be increasing with the photon energy as seen from the table 1 and 2 and figure 8.

Table1: Gamma photon interaction parameter values of cerium oxide (theoretical and experimental) at various photon energies

	m_m [10^{-3} m^2 kg^{-1}]	μ_l [m^{-1}]	σ_t [10^{-25} barn/atom]	σ_e [10^{-26} barn/atom]	Z_{eff}	N_{eff} [10^{23} electron/g]	λ [10^{-2} m]
0.662 MeV							
X- COM	7.99	57.69	7.61	2.78	27.32	2.86	1.73
EMP. VALUE	7.99	57.69	7.61	2.78	27.32	2.86	1.73
EXPT. VALUE	7.98	57.65	7.6	2.78	27.28	2.86	1.73
1.173 MeV							
X- COM	5.47	39.51	5.21	2.02	25.79	2.7	2.53
EMP VALUE	5.47	39.51	5.21	2.02	25.79	2.7	2.53
EXPT. VALUE	5.35	38.6	5.09	2.02	25.19	2.64	2.59
1.332 MeV							
X- COM	5.09	36.74	4.85	1.88	25.68	2.69	2.72

EMP. VALUE	5.09	36.74	4.85	1.88	25.68	2.69	2.72
EXPT. VALUE	5.01	36.21	4.78	1.88	25.31	2.65	2.76

Table2: Gamma photon interaction parameter values of praseodymium oxide (Pr_6O_{11}) (theoretical and experimental)at various photon energies

	μ_m [10^{-3} m^2 kg^{-1}]	μ_l [m^{-1}]	σ_t [10^{-25} barn/atom]	σ_e [10^{-26} barn/atom]	Z_{eff}	N_{eff} [10^{23} electron/g]	λ [10^{-2} m]
0.665 MeV							
X- COM	8.15	53	8.13	2.81	28.91	2.89	1.88
EMP. VALUE	8.15	53	8.13	2.81	28.91	2.89	1.88
EXPT. VALUE	8.14	52.92	8.12	2.81	28.86	2.89	1.88
1.173 MeV							
X- COM	5.54	36.02	5.52	2.02	27.23	2.73	2.77
EMP VALUE	5.54	36.02	5.52	2.02	27.23	2.73	2.77
EXPT. VALUE	5.52	35.88	5.5	2.02	27.13	2.71	2.78
1.332 MeV							
X- COM	5.15	33.51	5.14	1.89	27.12	2.71	2.98
EMP. VALUE	5.15	33.51	5.14	1.89	27.13	2.71	2.98
EXPT. VALUE	5.13	33.35	5.11	1.89	27	2.7	2.99

Figure2: variation of mass attenuation coefficient coefficient with photon energy

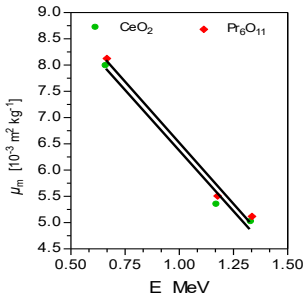

Figure3: variation of linear mass attenuation with photon energy

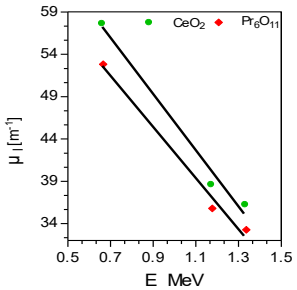

Figure4: variation of atomic cross-section with photon energy

Figure5: variation of total electronic cross-section with photon energy

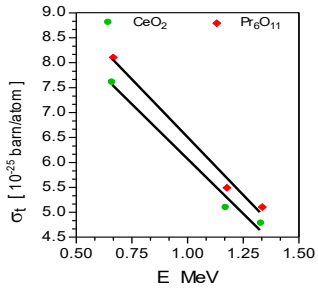

Figure6: variation of effective atomic number with photon energy

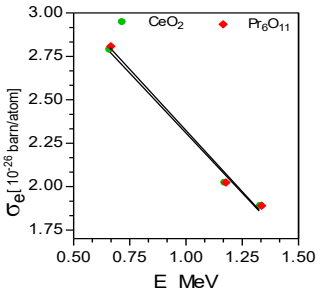

Figure7: variation of effective electron density with photon energy

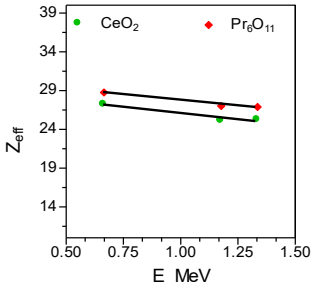

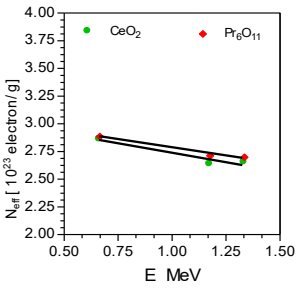

Figure8: variation of mean free path with photon energy

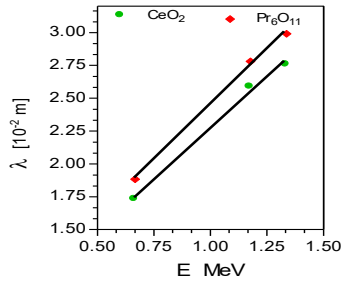

4. Conclusions

- Present experimental Study has been undertaken to determine effective atomic number (Z_{eff}) and related parameters (σ_t, σ_e, N_{eff} and λ) for rare-earth oxides (CeO_2 and Pr_6O_{11}) from mass attenuation measurements at different photon energies.
- The μ_m values of these rare-earth oxides in the present study decrease with increase in photon energy.
- Also, the variation of σ_t and σ_e with energy is identical to mass attenuation coefficient.
- The electron density is found to have the same qualitative energy dependence as effective atomic numbers for the samples.
- In all the cases the photon mean free path (λ) is found to be increasing with photon energy.
- The data on μ_m, μ_l σ_t, σ_e, Z_{eff}, N_{eff} and λ at different photon energies for CeO_2 and Pr_6O_{11} are reported in this communication.

Acknowledgement

The authors gratefully acknowledge the help extended by Prof. K. Gopalkishan Rao and Prof. C. Radhakrishnamurthy of Central Instrumentation Centre (CIC), Kakatiya University, Warangal.

References

1. M. P. Singh *et al.*, Radiation Measurements., 2018, **45**.
2. R. S. Niranjan *et al.*, Pramana journal of physics., 2012, **78**.
3. Gurinderjeet Singh *et al.*, Journal of Alloys and Compounds., 2015, **619**, 356-360.
5. G.S. Bhandal *et al.*, Appl. Radiat. Isotopes., 1993, **44**, 929.
6. G.S.Bhandal *et al.*, Appl. Radiat. Isotopes., 1993, **44**, 1231.
7. S. Gurmel *et al.*, Appl. Radiat. Isotopes., 1991, **42**, 509
8. Icelli *et al.*, J. Quant. Spectrosc. Radiat, Transfer., 2005, **91**, 485.
9. S. Gowda *et al.*, Nucl. Instrum. Methods in Phys. Res, B239., 2005, **361**.
10. S.S.Hiremath *et al.*, Ind. J. Pure Appl. Phys., 1993, **31**, 855.
11. D.V Krishna Reddy *et al.*, Can. J. Phys., 1985, **63**, 1421.
12. K. Parthasaradhi *et al.*, Ind. J. Pure Appl. Phys., 1968, **6**, 609.
13. A. Perumallu *et al.*, Can. J. Phys., 1984, **62**, 464.
14. S. Chandralingam et al., Ind. J. Phys., 1984, **A58**, 285.
15. J.H. Hubbell *et al.*, International Journal of Applied Radiation and Isotopes., 1982, **33**, 1269-1290.
16. M.J. Berger *et al.*, NBSIR, NIST., 1987, **87**, 3597.
17. M.Ranga rao, *et al.*, Journal of Emerging Technologies and innovative research., 2019, **6** (6)
18. Narender *et al.*, Research Journal of Physical Sciences., 2013, **1**(10), 1-5.
19. A.S.Madhusudhan Rao *et.al.*, Research Journal of physical sciences., 2013, **1**(6), 11-16.

MHD FREE CONVECTIVE COUETTE FLOW OF CU-WATER NANOFLUID

G. Jithender Reddy
Department of Mathematics, VNR Vignana Jyothi Institute of Engineering and Technology, Hyderabad, 500090, Telangana State, India
Corresponding author's email: jithendergurejala@gmail.com

Abstract
The unsteady MHD free convection heat transfer Couette flow of Cu-water nanofluid at viscous incompressible electrically conducting fluid was considered. A Finite Element Method (FEM) employed to find the numerical solutions of the dimensionless governing coupled equations for the profiles of primary, secondary velocity and temperature of Couette of Cu-water nanofluid with the effect of volume of particles of nanofluid, Grashof number for heat transfer, Magnetic, rotation parameter and Prandtl number. The primary, secondary velocity profiles are enhanced as an increase of Grashof number while fall down as an increase of magnetic parameter and Prandtl number.
***Keywords**: MHD, FEM, Coutte flow, Cu-water Nanofluid*

1. Introduction
In fluid dynamics, the Couette flow states to the laminar flow of a viscous fluid in a space among the two parallel plates, one of which changes relative to the other. This fluid flow is driven by virtue of viscous drag force acting on fluid and the practically pressure gradient is parallel to the plates. Das *et al*.[1] investigated the magnetic field effect on MHD free convective Couette flow between the horizontal plates which are parallel, with the presence of a rotating system. Sheikholeslami et.al[2] analyzed the nanofluid contains with the mixer of water and suspended Cu particles on a sheet which is stretched. Kalidas et. al [3] studied the characteristics of Cu-water nanofluid flow on a plate with various parameters and the plate is in upward direction. The authors are not explored the on Coutte flow of nanofluid with the effect of rotation fluid along with plates.

2. Formulation of Model
Consider the unsteady heat transfer flow of a viscous incompressible electrically conducting nanofluid containing water with suspended copper particles. The flow between two infinite parallel plates when the fluid and the plates rotate in unison with uniform angular velocity Ω' about an axis normal to the plates, shown in **Fig 1**. Let d be the distance between the two plates, where d is small in comparison with the characteristic length of the plates. The upper plate moves with a uniform velocity U in its own plane in the x'-direction, where the x'-axis is taken along the lower stationary plate. The z'-axis is taken normal to the x'-axis and the y'-axis is taken normal to the $x'z'$-plane, lying in the plane of the lower plate, and it is assumed that the flow is fully developed. Further, there is no applied pressure gradient as the flow is due to the motion of the upper plate. Also assume that initially i.e. at time $t' \le 0$, both the fluid and plates of the channel are in rest and these are maintained at a uniform temperature T_d'. At time $t' > 0$, plates starts moves in z' - direction with uniform velocity U in its own plane. and it is maintained at uniform temperature T_w' .Since the plates are infinitely long along the x'- and y'-directions, all physical quantities will be functions of z' and t' only. Here u' and w' are velocity components along the x' and y'-directions.

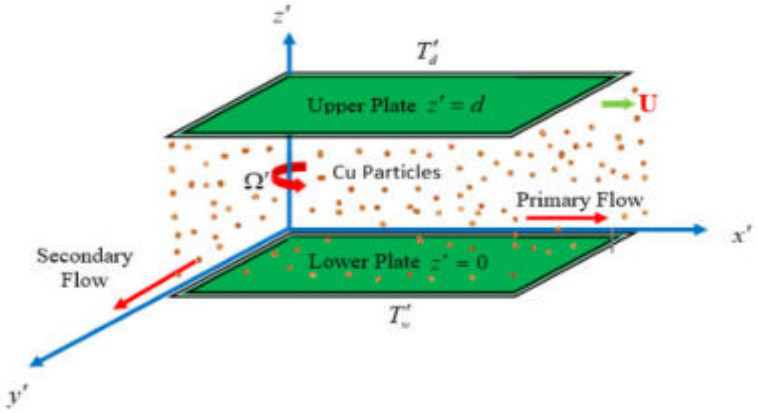

Fig 1. Geometry of the problem

The modelling equations of the nanofluid flow in a rotating frame of references are

$$\rho_{nf}\left(\frac{\partial u'}{\partial t'}\right)=\mu_{nf}\left(\frac{\partial^2 u'}{\partial z'^2}\right)+2\mu_{nf}\Omega' w'-\sigma B_o^2 u'+\left(\rho\beta\right)_{nf} g\left(T'-T'_d\right) \tag{1}$$

$$\rho_{nf}\left(\frac{\partial w'}{\partial t'}\right)=\mu_{nf}\left(\frac{\partial^2 w'}{\partial z'^2}\right)-2\mu_{nf}\Omega' u'-\sigma B_o^2 w' \tag{2}$$

$$\frac{\partial T'}{\partial t'}=\alpha_{nf}\left(\frac{\partial^2 T'}{\partial z'^2}\right) \tag{3}$$

Where ρ_{nf} is viscosity , α_{nf} is thermal diffusivity and $\left(\rho C_p\right)_{nf}$ is heat capacitance of the nanofluid, which are defined as $\rho_{nf}=\left(1-\phi\right)\rho_f+\phi\rho_s$, $\alpha_{nf}=\dfrac{K_{nf}}{\left(\rho C_p\right)_{nf}}$,

$\left(\rho C_p\right)_{nf}=\left(1-\phi\right)\left(\rho C_p\right)_f+\phi\left(\rho C_p\right)_s$, $\left(\rho\beta\right)_{nf}=\left(1-\phi\right)\left(\rho\beta\right)_f+\phi\left(\rho\beta\right)_s$, $\mu_{nf}=\dfrac{\mu_f}{\left(\rho C_p\right)_{nf}}$ and

$$\kappa_{nf}=\kappa_f\left(\frac{\kappa_s+2\kappa_f-2\phi\left(\kappa_f-\kappa_s\right)}{\kappa_s+2\kappa_f+2\phi\left(\kappa_f-\kappa_s\right)}\right)$$

The boundary conditions for the primary and secondary velocity and temperature are

$\forall t'\le 0: u'=w'=0, T'=T'_d$ for $z'\ge 0$ (4)

$\forall t'>0:\ u'=w'=0, T'=T'_w$ at $z'=0$ (5)

$\forall t'>0: u'=U, w'=0,\ T'\to T'_d$ at $z'=d$ (6)

The modelling equations with boundary conditions (1)-(6) ware solved by FEM after converting in to nondimensional equations by substituting nondimensional parameters such as Primary velocity(u), Secondary velocity (w), time (t), fluid displacement axis (z) Grashof number for heat transfer (Gr), Magnetic(M), rotation parameter(Ω) and Prandtl number(Pr) etc.

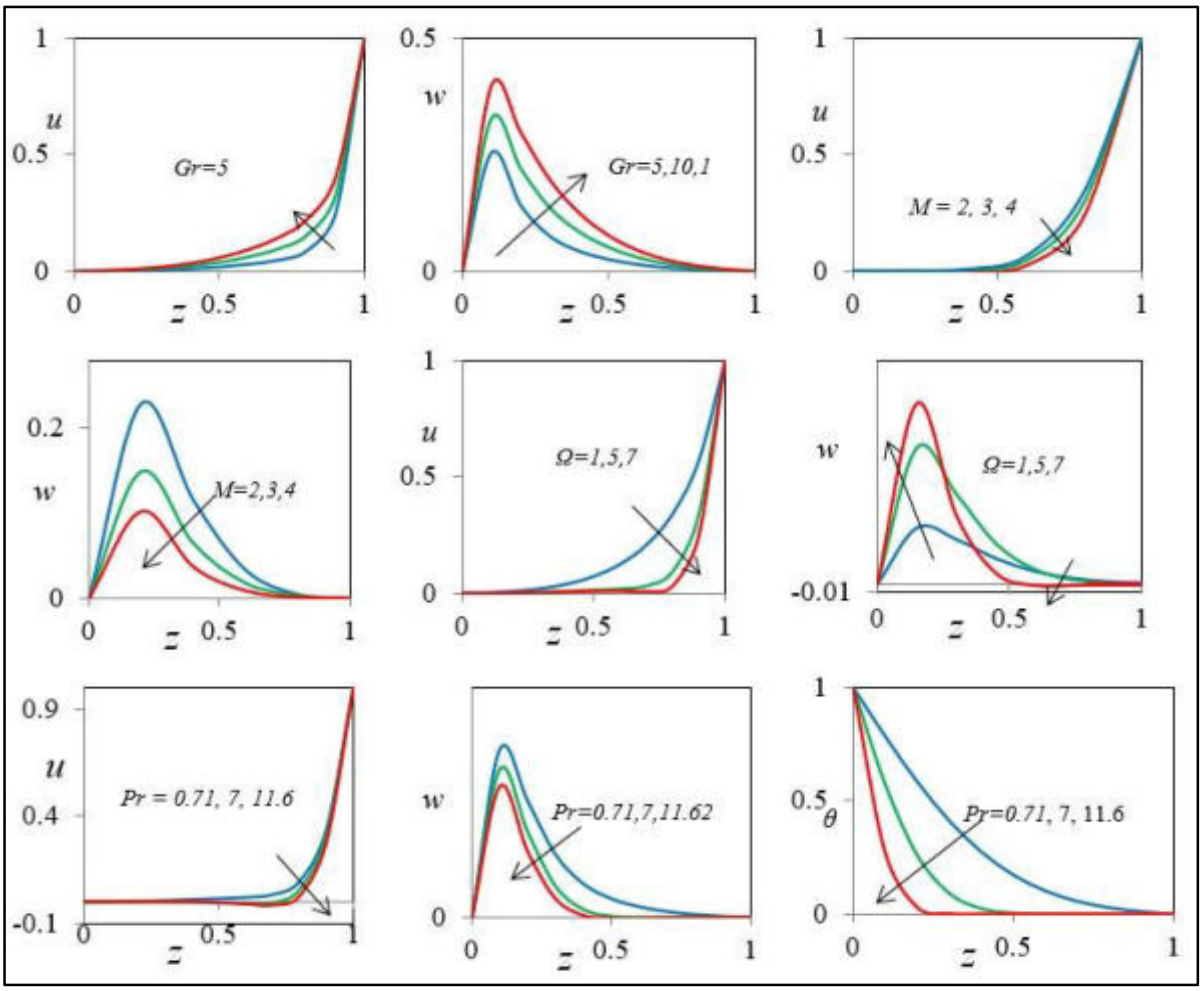

Fig. 2. Primary, secondary velocity and temperature profiles of Cu-water nanofluid.

3. Results and Discussion

The finite element method (FEM) is an efficient numerical and computational method to solving a variety of engineering and real-world problems. The algorithm of the finite element analysis explored by JN Reddy [4] as Discretization of the Domain, Generation of the Element Equations, Assembly of the Element Equations, Imposition of the Boundary Conditions, Solution of Assembled Equations. The nondimensional partial differential equations are solved through these steps by maintaining an accuracy 10^{-6} after imposing the physical properties of the nanofluid (**Table 1.**). The above profiles (**Fig 2.**) are done from the solutions of nondimensional equations with the various values of Grashof number, Magnetic parameter, rotation parameter and Prandtl number.

Table 1: Thermo-physical properties (see [5])

Physical Properties	**Water (H_2O) (Pure fluid)**	**Copper (Cu)**
C_p	4179	385
ρ	997.1	8933
K	0.613	400
$\beta \times 10^{-5}$	21	1.67

4. Conclusions

The following conclusions are dawn from the above study

- The primary and secondary velocity profiles are enhanced as an increase of Grashof number while fall down as an increase of magnetic parameter, Prandtl number and volume of Cu particle.
- Both the primary and secondary velocity of Cu-water nanofluid oscillating as the effect of fluid rotation along with plates.
- The Cu-water nanofluid temperature is low at high Prandtl number.
- The present results are in excellent agreement to the existed literature
- The model is useful for validation of lab experimental results.

5. References

1. S. Das *et al.*, Mathematical and Computer Modelling, 2009, **50**, 1211-1217.
2. M. Sheikholeslami *et al.*, Journal of Applied Mathematics, 2012, Article ID 421320.
3. Kalidad Das *et al.*, Propulsion and Power Research, 2017, **6**(3), 206–213.
4. J. N. Reddy, Introduction to Finite Element Method, McGraw-Hill, New York, 1985. ISBN: 9780072466850.
5. K. Das, Alexandria Engineering Journal, 2014, **53**(3), 757-766.

Fabrication and Comparison between Bio- Bricks to Normal Bricks

E Sadanandam[1], N V Srinivasulu[2], A Krishnaiah[3]
[1]Asistant professor, Department of Mechanical Engineering, Anurag Engineering college, kodad, Telangana & Research scholar at OU.
[2]Professor, Department of Mechanical Engineering, CBIT HYDERABAD, Telangana.
[3]Professor, Department of Mechanical Engineering, OUCOE HYDERABAD, Telangana
Email: sadanandam93@gmail.com

Abstract: In this paper mainly discussed about focuses on the Bio-brick is one such material that has the potential to be a sustainable and cost-effective solution. It acts as good heat & sound insulator and at the same time has an overall negative carbon fact print. From the above project, we have to determine the mechanical properties, and the same properties compare with the normal brick. With further results, it may come under the Ansys analysis. The major concern of the project is to be the development and characterization of Agri waste-based brick and normal brick and also investigate the mechanical, thermal and water absorption properties of bio brick and normal brick.

Keywords: Bio brick, Agri Waste, Epoxy Resin.

I. INTRODUCTION

The main aim of the research is to find a constructive method to turn solid, agricultural wastes into viable building materials, thereby addressing both pressing issues at the same time. This research explores the potential application of 'agro-waste', like sugar cane, sweet corn as the ingredient for alternative sustainable construction materials in the form of bricks. Based on the availability of agro-waste materials, these bio-bricks can be modified to suit the local market and building construction styles. The application of agro-waste as a construction material can result in the reduction of the usage of natural resources as well as of energy consumption. At the same time, it can add to the farmer's income, who can sell the leftover stubbles instead of burning them, thereby reducing air pollution. To achieve this goal, the process of up-cycling (the process of converting waste materials into new products of better environmental value than in their previous use) can be used to convert the agro-waste into usable bricks by combining it with lime binder, lime stone stone dust and water [1-4].

After China, India is the second largest producer of agricultural waste. It produces more than 130 million-tons of Paddy straw out of which only half is used as fodder and the other half goes to waste, either in landfills or is simply dumped somewhere. It also produces more than 50 million-tons of cane bagasse. Table 1 indicates the state wise generation of agricultural waste across India. As can be seen, India has diverse agricultural practices, which produces more than 500 million-tons of agricultural waste every year. The surplus waste (84 - 141 million-tons) is usually burnt by the farmers which results in massive air pollution causing major health hazards. A study based on Punjab alone showed that stubble produced per acre of paddy and wheat is around 23 and 19 quintals respectively. Around 85% of the paddy stubble is burnt in the open fields. In the case of wheat stubble around 11% was burnt. Considering the amount of stubble being produced, even burning a smaller percentage of it can cause considerable damage to the environment around it.

There are several sustainable alternatives that are being currently used in construction industries [5,6]. Some of the most prevalent ones are fly ash, recycled concrete, foam concrete, agro-based panel boards, recycled materials boards, silica fumes, recycled tires, et cetera. A precursory study clearly suggested that the manufacturing technology of so-called 'hempcrete' can be modified best to suit the agro-waste generated in India. Hempcrete which is manufactured primarily from the residue of Hemp plant. Hempcrete is one of the most explored Bio-Crete which is a composed by mixing lime binder, water and

the non-fibrous part of hemp, called ‘shiv’. With passage of time the composition hardens and can be used as bricks. Figure 2 shows the constituent materials of hempcrete and Figure 3 highlights the advantages of hempcrete as a building material.

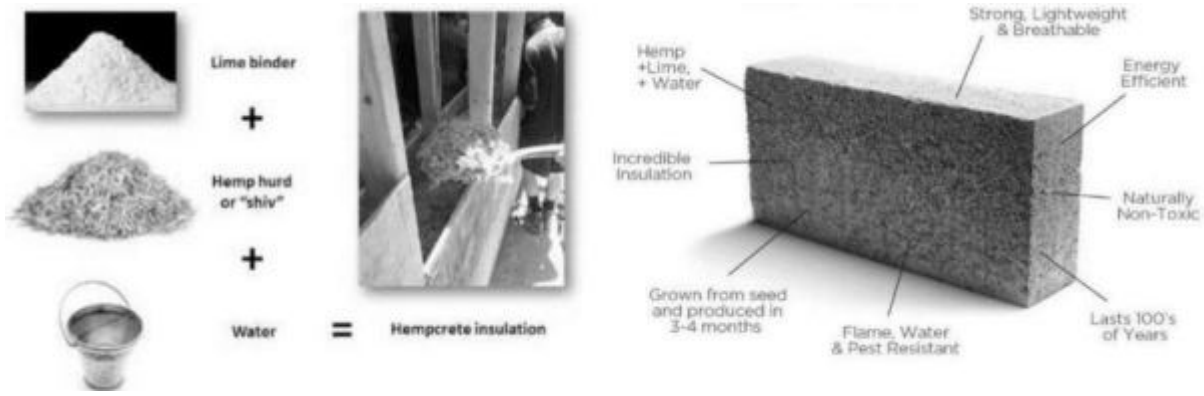

2. MATERIALS AND METHODS :(BIO BRICKS)

The process of making bio-brick starts with careful selection of the dry agro-waste, which is then chopped to the desired size. A lime based slurry is prepared by adding slake lime, binder, stone dust and water. The chopped agro-waste is added to the slurry and mixed thoroughly by hand or mechanical mixer, to create a homogenous mixture. This mixture is poured into moulds and rammed with wooden block to make a compact brick by removing extra water or voids [7,8]. These moulds are left to dry for a day or two, after which the sides of the moulds are removed and the brick is allowed to dry for fifteen to twenty days. It takes approximately a month’s time for these bio-bricks to attain its working strength by air drying.

In this process no controlled or machine drying is used to make the whole process sustainable and reduce the carbon footprint. The time taken to manufacture bio-bricks is comparable to air dried (naturally dried) fired clay bricks. After a month of drying, bio-bricks are covered by a rigid skin, mostly made up of carbonate lime (calcination) thereby increasing its overall strength. Even though these bio-bricks have less compressive strength as compared to fired clay bricks or concrete blocks, they are quite light in weight (1.43 kg per block) i.e. almost 1/8 of fired clay bricks and 1/10 of concrete blocks of similar volume. Hence, they can be effectively used in framed structure as non-load bearing walls with excellent heat and sound insulation with minimal dead load on the structure.

Figure 1.1: Dry sugarcane bagasse was chopped into fine Pie ces

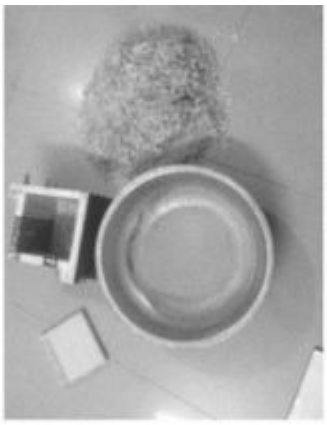

Figure 1.2:. Basic tools used along with lime, stone dust and water

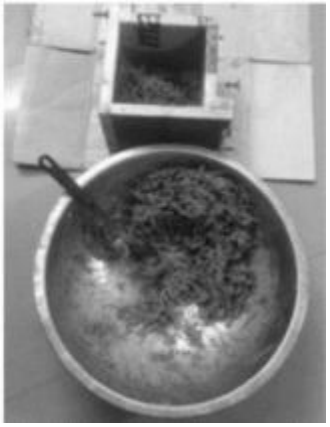

Figure 1.3:. Chopped bagasse, lime, water and stone dust were mixed properly

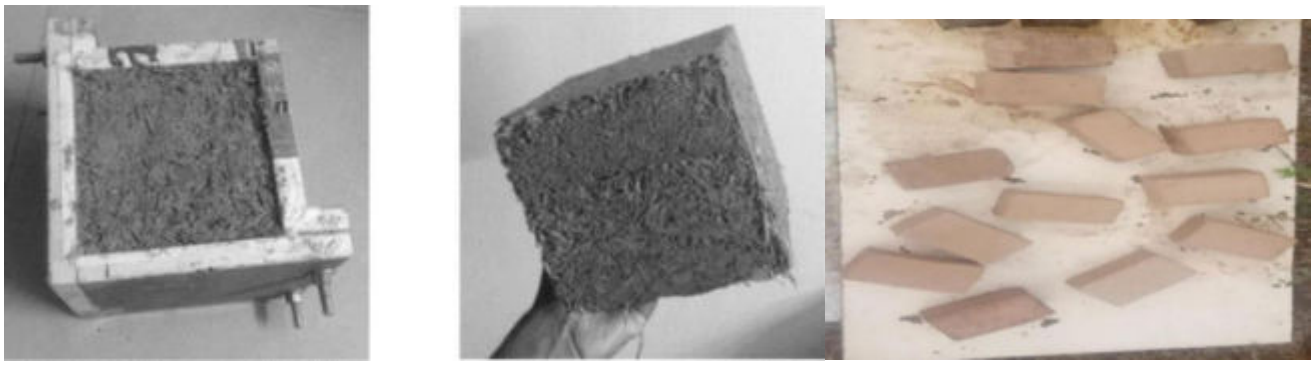

Fig. Raw materials and manufacturing procedure of Specimens.

3. Applications of Bio Bricks:

1. With low thermal conductivity (approx. 0.27 W/mK) these bio-bricks can be effectively used in walls as they provide good insulation to heat and sound. Due its porosity and low density these bio-bricks helps in maintaining humidity of the buildings, making these houses suitable for hot-humid climate like India.

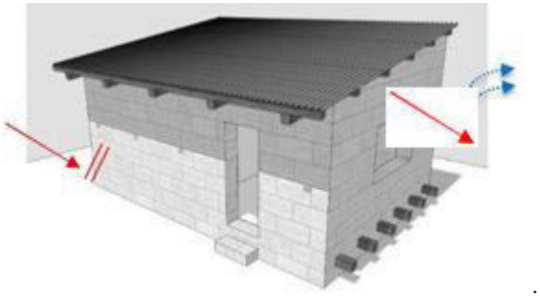

2. Bio-brick with low average density of 423.7 kg/m3 (as calculated from prototypes) is a suitable replacement of burnt clay brick and concrete block for partition walls in column beam structures. This is extremely beneficial for high rise structures as the overall load on the frame structure will be much lower compared to traditional walls as illustrated in Figure 12. Thus, this can result in designing lighter frame structure, thereby reducing the use of concrete, steel and lowering the construction cost.

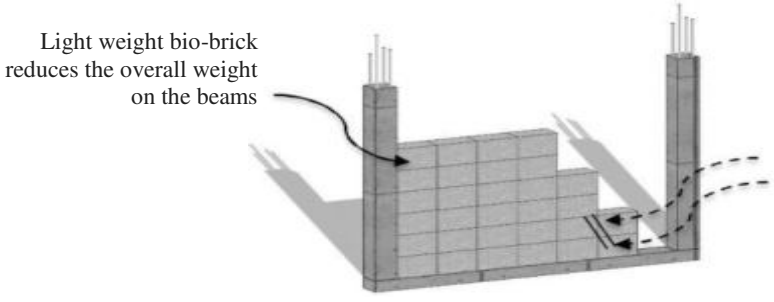

The bio-brick acts as a
sound insulator

4. MATERIALS AND METHODS(NATURAL BRICKS):

Preparation of clay for bricks manufacturing is done in six steps: Un soiling of clay we need pure clay for the preparation of bricks [8-10]. The top layer of soil may contain impurities, so the clay in top layer of soil about 200mm depth is thrown away. This is called un soiling. Digging After the removal of top layer, the clay is dug out from the ground and spread on the plain ground. Cleaning in this stage, the clay is cleaned of stones; vegetable matter etc. if large quantity of particulate matter is present, and then the clay is washed and screened. The lumps of clay are converted into powder with earth crushing rollers. Weathering the cleaned clay is exposed to atmosphere for softening. The period of weathering may be 3 to 4 weeks or a full rainy season. Generally, the clay is dug out just before the rainy season for larger projects. Blending if we want to add any ingredient to the clay, it is to be added in this stage by making the clay loose and spread the ingredient over it. Then take small portion of clay into the hands and tuning it up and down in vertical direction. This process is called blending of clay.

5. EXPERIMENTAL CALICULATION:

1. Hardness Test:

TYPE OF BRICK	LOAD	ROCKWELL HARDESS NUMBER
Normal brick	150 kg	69
	150 kg	65

Bio-brick	150 kg	40
	150 kg	35

2. BRINELL HARDNESS TEST:

BHN = $2P/\pi D\ (D - \sqrt{(D^2 - d^2)})$.

Where,

Load P in kgf,

steel ball diameter D in mm

changed diameter d in mm are the key terms of this calculation.

BHN for normal brick

BHN = $[(2*150)] / [\ 3.14(10)\ ((10-(10^2-0.8^2)^{0.5}]$

= 298.08

BHN for Bio-brick

BHN = $[(2*150)] / [\ 3.14(10)\ ((10-(10^2-0.9^2)^{0.5}]$

= 235.42

Compression strength calculation for normal brick:

Area = 90*50 = 4500 mm^2 Breaking

load=40KN

Breaking stress = Breaking load/Area

= 4000/4500

= 0.88 N/mm^2

Compression strength calculations for Bio-brick:

Area = 90*50 = 4500 mm^2 Breaking

load =35KN

Breaking stress = Breaking load/Area

= 3500/4500
= 0.77 N/mm^2

6. CONCLUSION:

The bio-bricks we generated from common agro-waste, have a tremendously better net carbon footprint than standard building materials and, at the same time, are very cheap and simple in production. Though they may not be suitable for larger loads, they have huge application potential in less-load bearing wall construction, sound reduction and insulation, particularly in the low-cost sector, which, after all, is a substantial market in India. Thus, converting agro-waste into bio-bricks could help to mitigate the pertinent issues of raw material required by the construction industry and the agro-waste created in the agricultural sector.

Further research and development is required to develop bio-bricks for Pan-India application where local agricultural waste can be used as a building material. We will also need to explore options for how the load-bearing capacity of the bricks can be improved as well as how to optimize the manufacturing processes for the bio-bricks to allow for industrial-scale production at a low cost.

REFERENCES:

1. L. Armstrong *et al.*, (2015), "Building a sustainable future: The hempcrete revolution", available at http://www.cannabusiness.com/news/science-technology/building-a-sustainablefuture-the-hempcrete-revolution/ (accessed 4 August 2018).
2. A. Arrigoni *et al.*, Journal of Cleaner Production, Elsevier Ltd., 2017, **149**, 1051–1061.
3. A. Awasthi *et al.*, Science of the Total Environment, Elsevier B.V., 2020, **408** (20), 4440–4445.
4. S.Banerjee *et al.*, (2015), "Brick kilns contribute about 9 percent of total black carbon emissions in India", available at http://www.cseindia.org/brick-kilnscontribute-about-9-per-cent-of-total-black-carbon-emissions-in-india-5713.
5. G.P. Hammond, *et al.*, Proceedings of the Institution of Civil Engineers – Energy., 2008, **161** (2), 87–98.
6. S. Loganathan *et al.*, Journal of Construction in Developing Countries., 2017, **22**, 121–144.
7. M.Madurwar *et al.*, Construction and Building Materials, Elsevier., 2013, **38**, 872–878.
8. C. Meyer *et al.*, Cement and Concrete Composites, Elsevier Ltd., 2009, **31** (8), 601–605.
9. N.K. Son *et al.*, Procedia Engineering., 2017, **171**, 725–733.
10. Y. Singh *et al.*, Proceedings of the Indian National Science Academy., 2014, **80** (1) 95–114.

Indoor radon concentrations in dwellings of Bhadrachalam town and its surroundings, Telangana State, India

B. Sreenivasa Reddy and B. Linga Reddy*
Department of Physics, Chaitanya Bharathi Institute of Technology (A), Gandipet, Hyderabad-500 075, INDIA

***Corresponding author: bandi.lr@gmail.com**

Abstract:

Radon is a ubiquitous, colourless, odourless, tasteless radioactive noble gas bearing Atomic number 86. Radon is being used to monitor atmospheric mixing, to investigate monsoon circulation patterns, to predict volcanic eruptions & earthquakes, mapping geological faults and in geochemical exploration etc. But radon is also a cause of concern because it is radioactive and emits high energy alpha particles with relatively short half-lives and can induce lung cancer by damaging the tissues along the bronchial tree. Indoor radon concentrations were estimated in 10 dwellings selected in and around Bhadrachalam town for about one year on quarterly basis using LR-115 type-II detectors with twin-chamber cup dosimeters. The radon concentration in these dwellings found to vary between 10 Bq m^{-3} and 101 Bq m^{-3} with an average of 41.5±7.8 Bq m^{-3}. Distinct seasonal variation is observed in the radon concentration with minimum in rainy and maximum in winter seasons.

Keywords: Indoor Radon, SSNTD, LR-115, Bhadrachalam

Introduction

Radon is a ubiquitous, colourless, odourless, tasteless radioactive noble gas bearing Atomic number 86. It was discovered by Fredrich Ernst Dorn of Germany in 1895 from Radium. Radon is continuously replenished from the radioactive decay of long-lived precursors in minerals containing uranium and thorium. More than 25 isotopes of radon have been identified. Two major important isotopes of radon are ^{222}Rn generally called as radon and ^{220}Rn generally called as thoron. ^{222}Rn is produced from the decay chain of uranium and having a half-life of about 3.824 days and ^{220}Rn, with an half-life of about 55.6 seconds, is produced from the decay chain of thorium. Another isotope of radon, ^{219}Rn is short lived (3.96 s) and is virtually always produced in much smaller amount than ^{222}Rn, since the natural ^{235}U/^{238}U ratio of these ultimate progenitors is only 0.00719 [1]. Hence ^{219}Rn is largely ignored. Radon is being used to monitor atmospheric mixing, to investigate monsoon circulation patterns, to predict volcanic eruptions & earthquakes, mapping geological faults and in geochemical exploration etc. [2,3]**.** But radon is also a cause of concern because it is radioactive and emits high energy alpha particles with relatively short half-lives and can induce lung cancer by damaging the tissues along the bronchial tree [4].

The prediction of radon concentrations in a given dwelling is extremely difficult. The main sources of indoor radon concentrations are the soil-gas, building materials, tap

water and natural gas used for cooking. The topography, house construction type, soil characteristics, ventilation rate, wind direction, atmospheric pressure and even the life style of the habitants are also having significant influence on indoor radon concentrations [5-7].

Experimental

The Solid State Nuclear Track Detectors LR-115 Type II strippable (pelliculable) films, of Kodak Pathe make supplied by Dosirad company of France, have been used to estimate the radon concentrations inside the dwellings using a twin-chamber dosimeter cup developed at Bhabha Atomic Research Centre, Mumbai. The SSNTDs consists of thin sheets (12-13μm) of red dyed dielectric material called Cellulose Nitrate ($C_6H_8O_9N_2$) on a 100 μm thick polyester base.

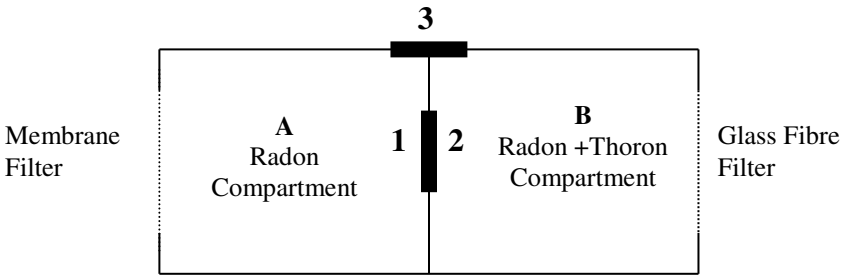

1. Rn Cup mode SSNTD Film
2. Rn+Tn Cup mode SSNTD Film
3. Bare mode SSNTD Film

Fig.1. Twin cup dosimeter

The twin-chamber dosimeter cup is shown in Fig.1. Each chamber has a length of 4.5cm and a radius of 3.1cm. The SSNTD strip of 2.5 cm x 2.5 cm is placed in chamber 1 measures only radon which diffuses into it from the ambient air through a semi-permeable membrane (latex). These membranes have permeability constants for radon gas in the range of 10^{-8} to 10^{-7} cm^2 s^{-1} [8-10] and allow more than 95% of radon gas to diffuse and suppress thoron gas to less than 1% [11-13]. On the other hand, the glass fibre filter paper in chamber-2 allows both radon and thoron gases. The 3rd SSNTD placed on the outer surface of the dosimeter exposed in the bare mode registers alpha particle tracks due to radon/thoron gases and their daughter products. It is mounted on a rectangular card such that it views a hemisphere of air of radius 6.9 cm, the range of alpha particle emitted by ^{218}Po. A detailed methodology for evaluating the gas concentration for the mixed field survey is given by Mayya et al., [14].

The dosimeters were installed in dwellings selected randomly. The dosimeters loaded with a LR-115, Type-II films (2.5 cm x 2.5 cm) were hanged at a height of 2.5 m from the ground and at about 30 cm away from the walls or roof. As the locations were

very far away from the laboratory, dosimeters were prepared on the locations itself by carrying out the required material to the location on the quarterly basis. For every 90 days dosimeters were loaded with a fresh LR-115, Type-II films and at the same time the retrieved exposed films were kept in indexed envelopes and brought back to the laboratory for further processing i.e., etching and subsequent counting. This process was continued for one year on quarterly basis.

The exposed detectors were etched chemically with 2.5N NaOH solution for 90 minutes in a constant temperature bath maintained at 60±0.5°C, without stirring. Etching time was selected through a series of experiments in our laboratory to determine the etching rates under different stirring conditions. The chemically etched films were washed in distilled water and peeled off from their plastic base so as to use for the counting process. Evaluation of etched tracks in solid-state nuclear track detectors by an optical microscope is a difficult and time-consuming task. The attempts to automate track counting have led to the use of image analyser instruments and spark counting systems. The image analyser is rather expensive and can only be adopted by a few laboratories and research centres. The spark counting technique, which is applicable to plastic detectors, provides a convenient, cheap and fast method for track counting. In the present studies a spark counter Supplied by M/s. Polltech Instruments, Mumbai has been employed. The calibration of dosimeters is carried out using the calibration facility at the Environmental Assessment Division (EAD) of Bhabha Atomic Research Centre (BARC), Mumbai.

Results and Discussion

The study was conducted in 10 dwellings in and around Bhadrachalam town of Telangana State, India during September, 1999 to August. 2000 on quarterly basis. The estimated radon concentration in these dwellings in different seasons is presented in the Table 1.

Table 1. The estimated indoor radon concentrations in different seasons

Season	Radon concentration (Bq m^{-3})			
	Minimum	Maximum	Average	Standard Deviation
Autumn	35	67	51	11
Winter	29	101	64.4	31.8
Summer	18	44	32.2	8
Rainy	10	30	18.6	6.3

The radon levels are found to be maximum in the winter season and minimum in the rainy season. The maximum and minimum levels may be due to the ventilation inside the dwellings and meteorological variations. During the winter season, the dwellers normally prefer reduced ventilation to conserve heat. This reduced ventilation may cause

a partial lowering of atmospheric pressure inside a dwelling when compared to outside. This may further cause an increase in the exhalation rate of radon from the floor and walls of the room. The reduced ventilation in winter also leads to a build-up of radon inside the house. On the other hand, during the monsoon season, the rains cause closure of pores on the surface soil, which results in the reduced exhalation of radon gas from the soil. These variations are similar to the variations reported by others [15,16,5].

Conclusions:

Indoor radon concentration levels were measured in 10 selected dwelling places in and around Bhadrachalam town of Telangana State, India using LR-115 type-II detectors with twin-chamber cup dosimeters. The studies were conducted for about one year on quarterly basis. The radon levels were found to vary between 10 Bq m^{-3} and 101 Bq m^{-3} with an average of 41.5±7.8 Bq m^{-3}. It is also observed that the radon levels are significantly affected by the seasonal changes.

REFERENCES

[1]. Ll. Font and C. Baixeras, The Sc. Tot. Environ., 2003, **307**, 55-69.
[2]. H.S. Virk, Himalayan Geol., 1996, **17**, 91-103.
[3]. H.S. Virk et al., Current Science, 1997, **72**, 656-663.
[4] UNSCEAR, 2000: United Nations Scientific Committee on the Effects of Atomic Radiation, Ionizing Radiation: Source and Effects of Ionizing Radiation. United Nations, New York.
[5]. T.V. Ramachandran et al., Current Science, 1990, **59**, 979-982.
[6]. G. Jonsson, Nucl. Tracks Radiat. Meas., 1991, **19**, 335-338.
[7]. U.C. Mishra and T.V. Ramachandran, Proc. 3rd International Conference on Rare Gas Geochemistry, 1995, 310-319.
[8]. F.H. Abdel and G. Somogyi, Nucl. Tracks, 1986, **12**, 697-700.
[9]. R. Ilic and J. Sutej, Radon monitoring devices based on etched track detectors. In: Radon measurements by etched track detectors-Applications in radiation protection, earth sciences and the environment, (Eds. Durrani, S.A., Ilic, R.), World Scientific, Singapore, 1997, 103-128.
[10]. Wafaa Arafa, Radiat. Meas., 2002, **35**, 207-211.
[11]. G. Jha et al., Health Phys., 1982, **42**, 723-725.
[12]. T.V. Ramachandran et al., Nucl. Track. Radiat. Meas., 1987, **13**, 81-84.
[13] P.J. Jojo et al., Radiat. Meas., 1994, **23**, 715-724.
[14]. Y.S. Mayya et al., Radiat. Prot. Dosim., 1998, **77**, 177-184.
[15]. Wilkening Marvin and Wicke Andreas, Health Phys., 1986, **51**, 427-436.
[16]. M.C. Subba Ramu et al., Bull. Radiat. Prot., 1988, **11**, 81-87.

Author Index

CHAITANYA BHARATHI INSTITUTE OF TECHNOLOGY (A)
GANDIPET, HYDERABAD 500 075

COURSES OFFERED

UNDER GRADUATE

1. B.E (IT-Artificial Intelligence and Data Science)
2. B.E (CSE-Artificial Intelligence and Machine Learning)
3. B.E (CSE-Internet of Things Cyber Security with Block Chain)
4. B.Tech (Biotechnology)
5. B.Tech (Chemical Engineering)
6. B.E (Civil Engineering)
7. B.E (Computer Science Engineering)
8. B.E (Electronics and Communication Engineering)
9. B.E (Electrical and Electronics Engineering)
10. B.E (Information Technology)
11. B.E (Mechanical Engineering)

POST GRADUATE

1. M.E Civil (Structural Engineering)
2. M.Tech (Computer Science Engineering)
3. M.E (CAD/CAM)
4. M.E (Thermal Engineering)
5. M.E (ECE – Communication Engineering)
6. M.E (ECE – Embedded System and VLSI Design)
7. M.E (Power Systems & Power Electronics)
8. M.E (Artificial Intelligence and Data Science)
9. MBA
10. MCA

ABOUT CBIT (A)

CBIT is one of the premier Engineering Institute in INDIA, pioneer in Telangana State, which is at idyllic surroundings of Gandipet Lake, Hyderabad. The college offers Nine UG and Eleven PG programs. It has been standing as a temple of knowledge for the past 41 years by producing about 25,000 Eminent and skillful Graduate Engineers, who are successful in their Careers, serving all over the world. The Institute has been accredited by NBA--AICTE and NAAC--UGC. UGC has granted Autonomous Status from the Academic Year 2013-14 onwards. The Grants received from AICTE/UGC are worth about Rs. 2.5 Crores. Brilliant and Meritorious Candidates with good EAMCET Rank are seeking admissions at CBIT. CBIT Students are prepared and perfected to secure Placements in MNCs through College Career Development Center.

INTERNATIONAL E-CONFERENCE ON MATERIALS PROCESSING & CHARACTERIZATION – 2020
(ICMP&C–2020)
18th & 19th September 2020
Organized by Department of Physics
CHAITANYA BHARATHI INSTITUTE OF TECHNOLOGY
(AUTONOMOUS)
GANDIPET, HYDERABAD 500 075, INDIA

Vandana Publications

Branch Office : UG-4, Avadh Tower, Kaysons Lane, Hazratganj, Lucknow-226001, INDIA.
Contact Numbers : 0522-4108552, +91-9839-748474, +9196960-45327
E-mail ID's : info@vandanapublications.com, mail2vandanapublications@gmail.com
Visit us : www.vandanapublications.com

9 788194 647690
Price: ₹600/-